PROCEEDINGS

EIGHTEENTH WORKSHOP
GEOTHERMAL RESERVOIR ENGINEERING

January 26-28, 1993

Henry J. Ramey, Jr., Roland N. Horne,
Paul Kruger, Frank G. Miller,
William E. Brigham, Jean W. Cook
Stanford Geothermal Program
Workshop Report SGP-TR-145

Library of Congress Catalog Card No. 86-643338
ISSN 1058-2525

TABLE OF CONTENTS

MODELING II

PAPERS FOR PROCEEDINGS

PREFACE

The Eighteenth Workshop on Geothermal Reservoir Engineering was held at Stanford University on January 26-28, 1993. There were one hundred and seventeen registered participants which was greater than the attendance last year. Participants were from eight foreign countries: Italy, Japan, United Kingdom, Mexico, New Zealand, the Philippines, Guatemala, and Iceland. Performance of many geothermal fields outside the United States was described in several of the papers.

Dean Gary Ernst opened the meeting and welcomed the visitors to the campus. The key note speaker was J.E. "Ted" Mock who gave a brief overview of the Department of Energy's current plan. The Stanford Geothermal Program Reservoir Engineering Award for Excellence in Development of Geothermal Energy was awarded to Dr. Mock who also spoke at the banquet.

Thirty-nine papers were presented at the Workshop with two papers submitted for publication only. Technical papers were organized in twelve sessions concerning: field operations, The Geysers, geoscience, hot-dry-rock, injection, modeling, slim hole wells, geochemistry, well test and wellbore. Session chairmen were major contributors to the program and we thank: John Counsil, Kathleen Enedy, Harry Olson, Eduardo Iglesias, Marcelo Lippmann, Paul Atkinson, Jim Lovekin, Marshall Reed, Antonio Correa, and David Faulder.

The Workshop was organized by the Stanford Geothermal Program faculty, staff, and graduate students. We wish to thank Pat Ota, Ted Sumida, and Terri A. Ramey who also produces the Proceedings Volumes for publication. We owe a great deal of thanks to our students who operate audiovisual equipment and to John Hornbrook who coordinated the meeting arrangements for the Workshop.

Henry J. Ramey, Jr.
Roland N. Horne
Frank G. Miller
Paul Kruger
William E. Brigham
Jean W. Cook

PRESENTATION OF U.S. DEPARTMENT OF ENERGY CERTIFICATE OF APPRECIATION TO DR. HENRY J. RAMEY, JR.

By

Marshall J. Reed, Program Manager
Geothermal Reservoir Technology Program

The United States Department of Energy wishes to honor Dr. Henry J. Ramey, Jr., for his outstanding achievements in geothermal research and education in support of the Departmental mission in Geothermal Energy. Dr. Ramey's studies for DOE (and predecessor agencies) span nearly twenty years, and, during that time, he has been a world leader in the field of geothermal reservoir engineering.

Dr. Ramey was the first to demonstrate the use of geothermal reservoir engineering, the application of scientific principles to the production and development of geothermal resources. He began applying the methods of petroleum engineering to the characterization of geothermal fields in 1966, and Dr. Ramey presented his first analysis of The Geysers Geothermal Field in 1968. His successful applications of reservoir analysis led him to institute graduate studies in geothermal engineering, and Stanford awarded the first Ph.D. in geothermal research in 1969. Dr. Ramey has had 45 students who received graduate degrees in geothermal reservoir engineering, and he continues to attract top students to the geothermal program at Stanford. He has supplied the geothermal industry and universities with highly qualified engineers who have greatly advanced the development of geothermal energy, and many of his students are now in critical positions in the geothermal development companies.

In 1972, Dr. Ramey and his colleagues established the Stanford Geothermal Program to incorporate the education and research applied to geothermal engineering, and the Stanford Program has remained the premier geothermal engineering research curriculum in the world. Dr. Ramey and others at Stanford began a series of Workshops on Geothermal Reservoir Engineering in 1975 to better disseminate the growing body of knowledge. For eighteen years, these workshops have been the most valuable and effective means of technology transfer from DOE-funded geothermal research to commercial developments. The very important comparison of reservoir simulation codes was initiated and reported at the Stanford Geothermal Reservoir Engineering Workshops, and the major discussions of injection water breakthrough were held during the workshops. The Stanford workshops were instrumental in developing the greater insight into the functioning of The Geysers reservoir that is now used by the developers. More recently, Dr. Ramey used these workshops to introduce the geothermal industry to the concept of large geothermal steam reserves existing as adsorbed water on fracture surfaces.

The outstanding individual achievements and the dedication of Dr. Henry J. Ramey, Jr., in serving the needs of the United States through his educational activities and his studies for the Department of Energy, merit this certificate of appreciation.

STANFORD UNIVERSITY, STANFORD, CALIFORNIA 94305

HENRY J. RAMEY, JR.
KELEEN AND CARLTON BEAL PROFESSOR
OF PETROLEUM ENGINEERING

Wednesday, January 27, 1993
Stanford University Hospital

Marshall Reed read the Award Citation to me and my wife Alyce today. I was completely surprised and she was in tears. It doesn't seem fair to receive awards for doing what you enjoy with people you like and admire. The Stanford program owes the Department of Energy more that we can ever repay. Nevertheless, I accept this award with deep pleasure and humility in behalf of the Stanford Geothermal Program Staff and Alumni. It is my fondest wish that I will spend the next workshop Banquet with you.

Thank you,

Henry

PROCEEDINGS, Eighteenth Workshop on Geothermal Reservoir Engineering
Stanford University, Stanford, California, January 26-28, 1993
SGP-TR-145

NATURAL RESOURCE ECONOMIC IMPLICATIONS OF GEOTHERMAL AREA USE

d'E Charles Darby

Conservation Development Services
New Zealand

ABSTRACT

Large-scale use of geothermal energy is likely to result in depletion of natural resources that support both biodiversity and other human uses. Most of the problems could be averted with competent planning and adherence to agreed conditions, but they commonly develop because they are not perceived to be directly geothermal in origin and hence are not taken into account adequately. Some of the implications of such issues are discussed below, with particular reference to countries where all or most resources are held under traditional principals of custom ownership.

INTRODUCTION

Geothermal areas often play far reaching economic roles for local people, hence large-scale exploitation of such areas may have equally far-reaching consequences. This is particularly so where local people operate in a subsistence economy and have little access to the cash necessary either to benefit from rural electrification or to compensate for resources depleted as a result of new project developments.

The objective here is to outline some of the implications of proposals to use geothermal features for electric energy or process heat. The viewpoints taken are those of local people and of national government agencies that are required to promote responsible rural development.

It is also intended to promote recognition of some of the realities of working within tribal (custom) land and resource ownership systems, and the efficiency with which such systems are normally capable of managing natural resources on the basis of sustainable utilisation.

Despite their effectiveness under normal circumstances, custom resource management systems commonly break down under the pressure of "development". Principal reasons include their inability to take account of the scale, pace and totality of present-day resource exploitation methods; their inability to control exploitation using traditional methods, but supplying new and largely unlimited foreign markets; and the inability of governments and aid agencies alike to integrate northern hemisphere practices of good resource management with equally sound, or better, custom practice.

Subsistence economies vary widely in the quality of life they deliver, from desperate poverty (commonly where the national resource base has been systematically stripped over centuries of non-local domination, with North Africa providing some stark present-day examples), through to a relatively high quality lifestyle in a resource-rich environment. Paradoxically, some of what the conventional classifications would have us believe are among the world's least developed countries are in the latter category, Western Samoa, Vanuatu, Solomon Islands and Papua New Guinea being examples.

IMPLICATIONS OF TRIBAL/ CUSTOMARY RESOURCE OWNERSHIP

The majority of people in Melanesia and much of Polynesia, where the traditional ownership systems of land and maritime resources have not been destroyed by foreign influences, have what most of us in the rest of the world can only dream about. They have the absolute right to build and to occupy a dwelling in their home area free from any charges, and to take from that area materials for building, clothing, food, transport, and other services necessary to support their livelihood. They may have responsibilities towards their community, but no person and no government can charge or tax them for these rights, nor prevent them from being taken up.

For most eastern or western businessmen and "developers" this concept is not easy to comprehend. Even less so is it to understand that the governments of several such countries have no authority over the nation's resources and no rights of access to land except with the permission of the owners. Again, a dream for most of us in the "developed" world.

However, custom land and marine areas are not private property in the northern hemisphere sense, since the custom owners are not free to sell them even though they may sell the resources on or under them. Rather, the land is held permanently in trust, and its living and non-living resources are used as the present generation of human custom owners sees fit. In other words, a type of stewardship.

In this situation it may be helpful to regard the custom ownership clan as similar to a corporation. Members of the corporate body have inherited or

been elected to varying positions of influence, authority and rights to take goods or to be rewarded from corporate resources. These positions may change, but no one can be displaced from the corporate clan. However, neither individually nor collectively can members dispose of the corporate core, the lands and/or sea areas they control. In providing a true homeland, this core is the guarantee of corporate survival.

Whether understandable or not, the reality in such places that all resources have custom owners must be recognised equitably. Custom owners are powerful partners in the development process, and they are the ultimate authority. A well-known example with geothermal connotations is the Bougainville epithermal gold-copper mine. Consistent gross failure to pay equitable attention to custom rights, later coupled with attempts to control custom property by armed force, escalated into a civil war that has cost the national government and the mine owners several hundred million dollars, and that has yet to be resolved.

Defining custom ownership boundaries is often very complex, with boundary markers commonly being kept secret and even regarded as sacred sites. This can be highly frustrating, and may lead outsiders to the cynical conclusion that sacred sites can only be located by resistivity surveys or other prospecting equipment! In the context of corporate property with significant economic value, however, such secrecy is no different from that practiced by most corporate bodies.

Custom ownership also needs to be seen in the perspective of its promotion of sustainability in resource use, which is now recognised as being essential to continuing human socio-economic development. It is worth reflecting on how many of the world's remaining primary resources are located in those parts of South America, the South-West Pacific and South-East Asia where custom ownership is in force, or was until recently, and comparing them with the natural resources of Europe, North Africa and northern Asia that have been molested by humans for centuries.

DEPENDENCE ON THE RESOURCES OF GEOTHERMAL AREAS

Existing users that depend upon geothermal resources also have rights, ethically if not always legally. The fact that outsiders may be in a position to override these rights is no excuse to do so. It is now widely recognised that plants and non-human animals, and the ecosystems in which they occur, have rights that are independent of any uses humans may make of them. Indeed, humans are often parallel beneficiaries when such rights are given precedence, for example in preservation of some of the most spectacular geothermal fields where economic uses are required to be non-destructive, as well as the many living species of economic significance that have been discovered in protected areas.

Para-economic dependence may be defined as human dependence upon resources in a manner that does not involve cash, but where alternatives would need cash if the resources were no longer available. The alternatives may be acceptable only if a method of acquiring the necessary cash is not only available but is regarded as equitable by local people.

Para-economic examples of using natural geothermal features occur in both economically developed and "less developed" countries, but the economic implications of losing those uses are very real for the people involved.

District heating is a common use, but may have adverse consequences which may or may not be reversible. (Recent restrictions on wasteful use of the Rotorua geothermal field have had the desired effect of reversing degradation in the Whakarewarewa geothermal area, thus enhancing one of New Zealand's foremost tourism assets).

Cooking in hot spring water or steam from fumaroles is also common. The alternative cooking heat source is usually fuelwood, but in areas of human habitation good quality fuelwood is usually in short supply. It is also usually the responsibility of women to collect it, which itself has development implications.

Food for humans is an important product of geothermal systems in parts of the Pacific, notably Papua New Guinea and the Solomons. Large birds called megapodes use geothermally heated forest soil to incubate their eggs. Adult birds do not tend either eggs or chicks. Apart from being a "free" food source, the megapodes support an inter-island egg trade that is part of the cash economy to the tune of tens of thousands of dollars per year for the custom owners involved.

Tradition is an important part of the social fabric of human communities everywhere, and is particularly well preserved in the S.W. Pacific where incursion of the cash economy tends to be a recent phenomenon. It is noticeable that areas with the highest levels of lawlessness and resource destruction are those where the local culture has been broken down by northern hemisphere styles of economic activity, with none of its safeguards being emplaced to support the former cultural controls. Maintenance of cultural integrity while still offering a range of economic development options is thus an important part of project planning.

"Bush medicines" are collected from primary forests by people in non-cash economies. Many of these compounds are highly effective, and are related to similar compounds used in "western" medicine that have been derived from similar sources. When forests are degraded as a result of new projects, the goods and services supplied by this free pharmacy decline along with the forest ecosystem. Imported alternatives to the bush medicines require cash which may not be available when required, so all too often no medicine is used and rural health standards decline.

Economic dependence obviously involves cash. However, even in cases where local people earn cash from using natural geothermal features, it is not always easy to develop alternative sources of income that are equally acceptable from the viewpoint of lifestyle or livelihood.

Tourism is perhaps the most widespread cash use, with examples from almost every country where there is naturally heated water or ground. In cash terms, tourism is also the most profitable single use. Other examples are numerous, and include drying pyrethrum plants for insecticide (Kenya), collecting megapode eggs for export (PNG), condensing steam to water for cattle (Kenya), collecting silica for white cement, drying stockfeed, and timber treatment (NZ).

The dollar numbers involved may be substantial. A recent study in a remote part of Solomon Islands assessed the annual value of harvested forest products to be $10,512 per household, and the net loss suffered as a result of forest destruction by logging to be $7545 per household, (Cassells, 1992). A study in the Philippines demonstrated that roading and logging destroyed tourism and fishing industries that were capable of grossing sustainable revenues $4M per year greater than those resulting from once-only logging, (Hodgson & Dixon, 1985). A dive tourism enterprise near the Pokili geothermal area generates some $700,000 per year for the Papua New Guinea economy, (Benjamin, pers. comm.)

So what has wise use of forest resources to do with a geothermal project? In a word, roads. If a forest is made accessible by road, whatever the reason, that forest will usually be logged unless an an effective forest management scheme is in place before roading commences.

FURTHER ECONOMIC IMPLICATIONS OF RURAL RESOURCE DEPLETION

From the macroeconomic viewpoint, the potential negative implications of rural economic development projects need to be addressed seriously before approval to proceed is given.

Degradation of natural resources that are used by people outside the cash economy is counterproductive to the rural socio-economic development objectives that are claimed to be at the core of so many government programmes. Unfortunately for such programmes, collateral damage to natural resources usually results in urban drift, which in turn puts pressure on such facilities and services as energy, health, education, housing, roading, employment and sewerage, all of which have self-evident macroeconomic implications.

Rural electrification is often given as the primary reason for geothermal energy exploitation, but rarely is effective attention given to how scattered rural dwellings are to be supplied with electricity, or how their occupants are to pay either for it or for the appliances to use it. Without such planning, power supply benefits only the towns or base-load industries, while the subsistence resources that supported rural people are all too often destroyed.

RESOURCE LOSS IMPACTS UPON WOMEN

In subsistence economies as in economically developed countries, women usually prepare the family food and act as the principal health practitioners and nutritionists. Women are also usually responsible for obtaining water, and are often also the main horticulturists.

Again, so what for geothermal? And again, careful planning is needed if project development is not to degrade women's lifestyle and prevent their socio-economic advancement by loading more work onto them. Such problems commonly result from depleting local resources of clean fresh water, fuelwood, geothermal cooking sites, garden soils that are not subject to accelerated erosion or droughts or flooding, medicines, and the housing and clothing fibres, fabrics and timbers that are normally obtained from a forest.

MANAGEMENT APPROACHES TO SUSTAINABLE RESOURCE USE

The most cost-effective management approaches are the well- known ones of using a comprehensive Socio-Ecological Evaluation system, (EIA or EIS system), coupled with an effective monitoring and compliance system, and an incentive-disincentive system that is designed to achieve results without need to resort to legal enforcement. All need to be in place before major financial commitments to project development are made.

Further, realistic accounting practices need to be used in assessing natural resource values. Natural resource accounting is an important tool in planning sustainable development, because it helps to assign defensible values to the primary natural resources that represent most of the wealth of economically developing countries. Conventional accounting methods are of limited use since they regard natural resources as having no value unless they are actually harvested or consumed in the year in question.

There is a need to assess the values of resource wealth that is still "in the bank" as represented by the environment; to value resources that are not destroyed when they are used to generate income or support human life, (e.g. geothermal areas used for tourism); and to value the non-replaceability and rarity of surface geothermal features.

Failure to undertake this type of assessment leaves decision-makers with information that is biassed to the disadvantage of the resource-rich but economically underdeveloped landowners and their "developing" nations, and biassed in favour of their resource-depleted but economically developed partners in the development process. The more cynical among us might perceive linkages between the overt reluctance to

introduce natural resource accounting practices and those whose economic interests are served by such bias.

Most of the problems outlined here are not strictly geothermal in their nature, hence it may be tempting to regard them as someone else's business. Professionally, however, it is not pleasant to return in later years to a technically excellent project, and see it presiding over an environmental wasteland populated by the impoverished remnants of human communities that once led a secure if basic lifestyle on lands rich in natural resources whose uses they controlled.

The lesson is to evaluate project proposals on comprehensive criteria of equity and sustainability, and to ensure that conservation principles are implemented effectively throughout all phases of a project. Even those of us whose primary interests lie elsewhere can help, by requiring assurance that such matters have indeed been addressed effectively by others.

REFERENCES

Benjamin, M. 1992. Records of Walindi Plantation, New Britain, Papua New Guinea. (Pers. comm.)

Cassells, R. M., (1992). "Tropical rainforest: subsistence values compared with logging royalties". Conference Proceedings: Development that Works, Massey University, New Zealand.

Hodgson, G. & J. A Dixon, 1988. Logging versus fisheries and tourism in Palawan. Occasional Paper #7, East West Center, Hawaii.

DEFINITIONS

The following meanings are ascribed in this paper to some words which are commonly misunderstood.

Development means changing lifestyle and livelihood, or making something that did not exist before, or supplying new services. Development is not synonymous with exploitation of existing resources.

Sustainable Development means improving the quality of human life while living within the carrying capacity of the natural resources used to support that improvement, i.e. without using up all of the resources or the environment in which they exist.

Exploitation means using a resource in an unsustainable manner so that the resource stock continually declines until there is no longer enough left to use.

Preservation means protecting some living or non-living resource so it is not damaged in any way whatsoever, even by sustainable harvesting. However, that does not preclude making money from it.

Conservation means using natural resources so that people gain the greatest sustainable benefit, while at the same time maintaining biodiversity and retaining all of the ability of the resource to meet the needs of future generations. Conservation does not mean "setting aside" or "locking away" resources and never using them to earn a livelihood or to make money.

PROCEEDINGS, Eighteenth Workshop on Geothermal Reservoir Engineering
Stanford University, Stanford, California, January 26-28, 1993
SGP-TR-145

BULALO FIELD, PHILIPPINES: RESERVOIR MODELING FOR PREDICTION OF LIMITS TO SUSTAINABLE GENERATION

Calvin J. Strobel

Unocal Geothermal Division,
3576 Unocal Place, Santa Rosa, California, 95403-1774

ABSTRACT

The Bulalo geothermal field, located in Laguna province, Philippines, supplies 12% of the electricity on the island of Luzon. The first 110 MWe power plant was on line May 1979; current 330 MWe (gross) installed capacity was reached in 1984. Since then, the field has operated at an average plant factor of 76%. The National Power Corporation plans to add 40 MWe base load and 40 MWe standby in 1995.

A numerical simulation model for the Bulalo field has been created that matches historic pressure changes, enthalpy and steam flash trends and cumulative steam production. Gravity modeling provided independent verification of mass balances and time rate of change of liquid desaturation in the rock matrix. Gravity modeling, in conjunction with reservoir simulation provides a means of predicting matrix dry out and the time to limiting conditions for sustainable levelized steam deliverability and power generation.

INTRODUCTION

Bulalo field development, operations history, geology and geochemistry has been documented by Benavidez, et. al. (1988). Steam deliverability decline in individual wells has been moderate, 3-1/2% per year on average. Beginning in 1989 production makeup wells were needed to offset declines in steam deliverability to maintain peak power generation capacity. All produced brine has been injected since the beginning of production operations.

Conceptual modeling of the Bulalo field was initiated by the author in 1981. During the period 1981 to early 1983, injection flowmeter profiles were run in twenty four wells. A well by well analysis of temperature and pressure gradient profiles, geological data and enthalpy test data was accomplished using methods developed in New Zealand (Grant, Donaldson and Bixley, 1982).

By early 1983 conceptual modeling had led to a general description of the resource: 1) thermodynamic state is distributed vapor to a depth of 5000 ft (1.5 km) bsl, with rising production enthalpy due to increasing vapor saturation, 2) the interconnected network of naturally enhanced permeability increased in area and volume with depth, 3) closed acting boundaries, depletion being from matrix desaturation and recirculation of injectate, and 4) mass in place within the network sufficient to sustain 330 MWe for 30 years at then prevailing evaporation rates.

The conceptual understanding as of 1983 has required little revision after 10 years of additional history and two reservoir simulation studies, except to change from notions of a closed system to one with significant influx. Simulation studies based upon field history through 1986, Atkinson and Pedersen (1988), had modeled the reservoir as a predominantly closed system with pressure support from brine injection. Enthalpy and pressure trends observed since 1986 can not be replicated with a closed system model. The current simulation effort described in this paper demonstrates that influx from above the reservoir, and from the northwest outside of the productive limits of the field is needed to match observed enthalpy and pressure trends and to provide the kind of mass balances necessary to match gravity changes.

THE SIMULATION MODEL

Model configuration and parameter assignments were the combined result of three interdependent processes: 1) conceptual modeling, 2) initial state simulation to reproduce known thermodynamic conditions and the dynamic pressure gradient in the reservoir and to match the initial enthalpy test values of production wells, and 3) history matching simulations to reproduce the trends of various dependent variables measured in the field to include

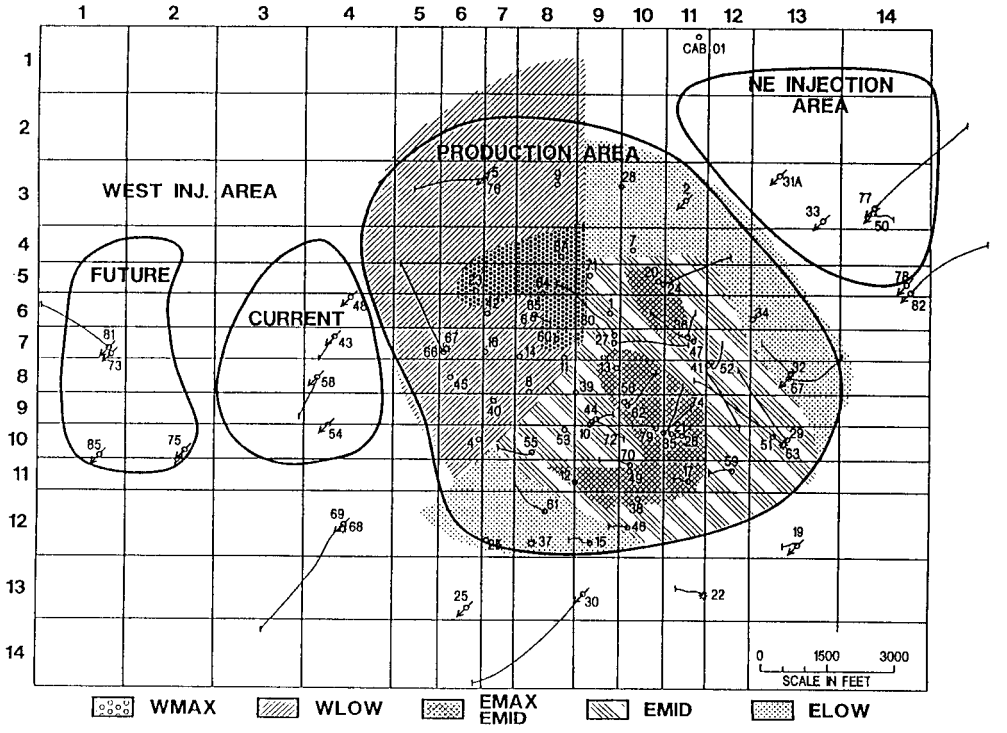

Fig. 1. Geographic distribution of the five enthalpy groups, and the injection strategy as of 1989.

enthalpy trends, pressure trends, cumulative steam production and steam flash (fraction of total mass that is vapor).

To perform the history matching simulations, the actual total mass production and injection histories of each well were imposed on the model. Independent variables discussed in the following sections of this paper were adjusted until the simulation model reproduced known trends and absolute values of the dependent variables.

Gridding and Well Completions

The numerical model has three layers of 196 rectangular blocks each arranged in 14 rows north-south and 14 columns east-west, as shown in Fig. 1. Each physical block is represented mathematically in the numerical model by a fracture block and a matrix block, the whole fracture matrix model being 1760 mathematical blocks.

Fig. 1 shows geographic dimensions of the grid relative to will locations. Total area of the grid is 20,000 feet (6098 m) east-west and 15,000 feet (4573 m) north-south, an area 6887 acres (2787 ha). Grid block size varies from 12 acres (4.86 ha) in the center, to 72 acres (29.1 ha) on the southeast and northwest.

Physically, the top layer represents depth from mean sea level to 1950 feet (595 m) bsl, the middle layer 1950 feet to 4650 feet (595 m to 1418 m) bsl, and the deepest layer 4650 to 7700 feet (1418 m to 2348 m) bsl. These depth intervals are shown in relation to well completion depths along a southwest to northeast cross section, Fig. 2. Injection wells are completed only in layers 2 and/or 3, compare depth intervals (Fig. 2) with injection areas (Fig. 1). Each production well is given layer assignments consistent with known well completion depth and enthalpy history matching results.

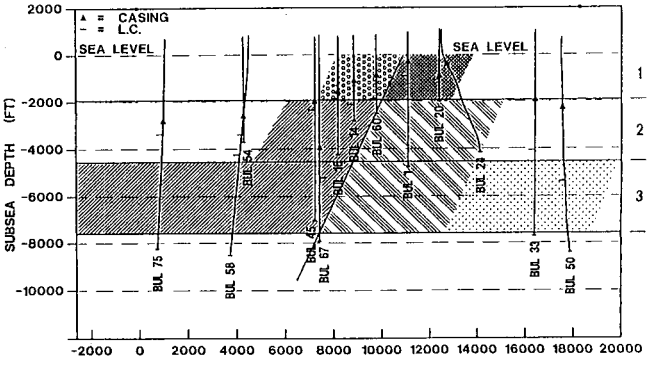

Fig. 2. Southwest - northeast cross section showing relation to the enthalpy groups.

Permeability and Porosity

Fracture and matrix permeability and porosity in the simulation model are summarized on Table 1. Matrix properties were assigned to the model beginning with average properties from core analysis and changing these properties in the model as necessary during the history matching process.

Some of the disparity between model properties and core data exists because cores are taken from specific points, whereas the simulation model requires an average value for the entire geographic area of each grid block. Also removal of the core from the natural hydrothermal environment to laboratory conditions may alter the original pore geometry and transmissibility.

Table 1. Porosity and Permeability

Layer	Model properties kxy,md.	Model properties o,%	Core analysis averages number	Core analysis averages k,md.	Core analysis averages o,%
1 fractures	100	.1	-	-	-
2 fractures	7.5-50	.1	-	-	-
3 fractures	7.5-25	.1	-	-	-
1 matrix	.03	12.5	4	.04	7.1
2 matrix	.03	7.5-9.0	18	.27	14.9
3 matrix	.03-.0045	5.5	18	.37	8.3

Reservoir Thermodynamics

At initial conditions vertical pressure gradient in the reservoir, interpreted from entry point conditions in the wells, exceeded hydrostatic by 10%. The excess gradient is a function of dynamic upward convection within the system, Grant, et. al. (1982 pp 162-165). To reproduce this pressure gradient in the simulation model, vertical permeability and aquifer influence were adjusted until the pressure gradient in the simulation model was the same as observed in the field data; this required low vertical permeability (.5 to 15 md.).

Rock temperatures in the model were set to maintain consistency with known entry point temperatures of the individual wells. At initial reservoir conditions many of the entry point temperatures and pressures were on the vapor pressure curve to a depth of 4650 feet (1418 m) bsl. A finite vapor saturation at initial conditions was necessary to match the beginning enthalpy behaviors of wells in the WMAX, EMAX and EMID enthalpy groups, Figs. 3 and 4. Initial vapor saturations, and therefore initial enthalpy test values, were very sensitive to rock temperature in the well completion blocks. Slight adjustments in grid block average temperatures were necessary to fine tune these initial state vapor saturation conditions.

In the interval from sea level to 1950 feet (595 m) bsl, average initial vapor saturations after initialization simulations were 30% for fracture blocks, and slightly less than 20% for the matrix blocks. Below 1950 feet (595 m) bsl there was no free vapor on the west side of the central barrier. East of the barrier in the interval from 1950 to 4650 feet (595 m to 1418 m) bsl, average initial vapor saturation in fractures was 20% and 7% in the rock matrix. No vapor phase existed below 4650 feet (1418 m) bsl.

Enthalpy and Pressure Trends

Five distinct production enthalpy patterns have been identified in the field, Figs. 3 and 4. Areal relationship of wells exhibiting a particular pattern is shown on Fig. 1 and vertical relationships are shown on Fig. 2.

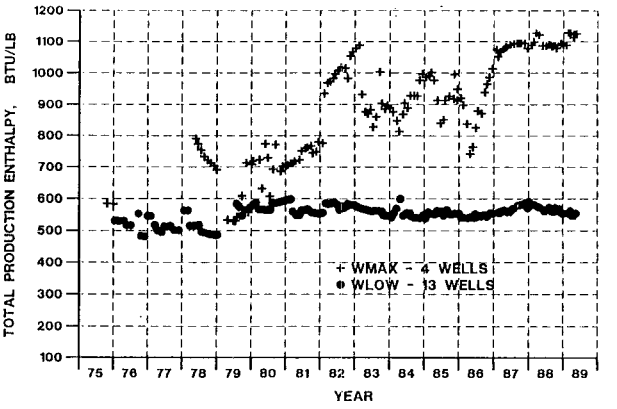

Fig. 3. West Bulalo enthalpy.

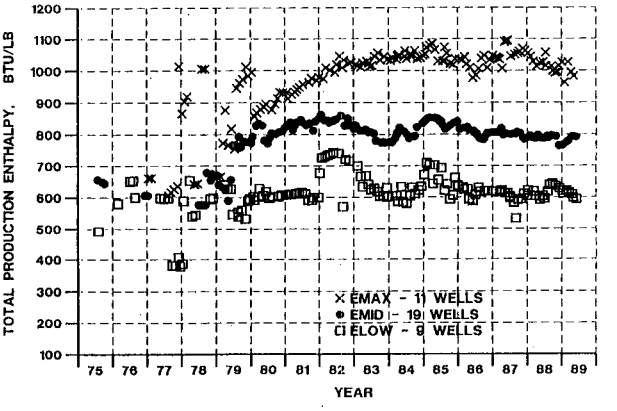

Fig. 4. East Bulalo enthalpy.

Table 2 shows the number of wells included in each group and approximate split of steam deliverability by group and by layer of the model. Although each well is represented individually in the simulation model, wells with similar enthalpy patterns appear to be influenced in unison by gross reservoir structural characteristics that the wells share in common.

Table 2. Percent of Total Steam Deliverability by Group and by Layer.

Group - Wells	Lyr-1	Lyr-2	Lyr-3	Total
WMAX -- 4	10	0	0	10
WLOW -- 16	2	10	3	15
EMAX -- 11	23	0	0	23
EMID -- 23	5	30	10	45
ELOW -- 11	1	3	3	7
TOTAL %	41	43	16	100

Comparison of group allocation percentages on Table 2 with the group enthalpy trends on Figs. 3 and 4 shows a relationship between observed enthalpy changes and well completion depth. On the west side of the reservoir the WMAX group, with all of its steam from layer 1, has rapidly rising enthalpy to 1000 Btu/lb (2326 KJ/kg) whereas the deeper WLOW group, with most of its steam from layer 2, has a very flat trend cycling between 550 and 600 btu/lb (1279 and 1395 KJ/kg). On the east side of the reservoir the EMAX group, with all of its steam from layer 1, has rapidly rising enthalpy to 1150 Btu/lb (2674 KJ/kg), compared to EMID group enthalpy which rises to 850 btu/lb (1977 KJ/kg) then begins gradual decline, and ELOW group enthalpy which has remained flat at 600 Btu/lb (1395 KJ/kg).

Layer 2 of the model, Fig. 2, is the primary production source, Table 2, for wells in the WLOW and EMID groups. Wells in these two groups are at equivalent completion depths, however there is a dramatic enthalpy discontinuity, compare Figs. 3 and 4, caused by the central barrier seen in Fig. 2. Influx from the northwest is held up by the barrier, isolating the east side. The result is higher enthalpy and greater pressure drawdown (Fig. 5) on the east.

History matching to enthalpy, Figs. 3 and 4, and the 500 psi (3.45 MPa) pressure sink on the southeast side of the field, Fig. 5, required a sensitive combination of influences, to include vertical transmissibility barriers, rate of downflux, mass flux across the central barrier, matrix permeability and relative permeability to steam and water in the matrix. The general shape and magnitude of enthalpy trends of the five groups shown on Figs. 3 and 4 were matched successfully, leading to the excellent matches to fieldwide flash trend, Fig. 6, and fieldwide cumulative steam produced, Fig. 7.

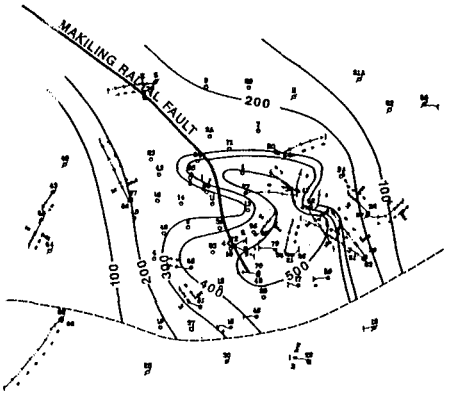

Fig. 5. Pressure drawdown, psi, from field data as of 1/1988.

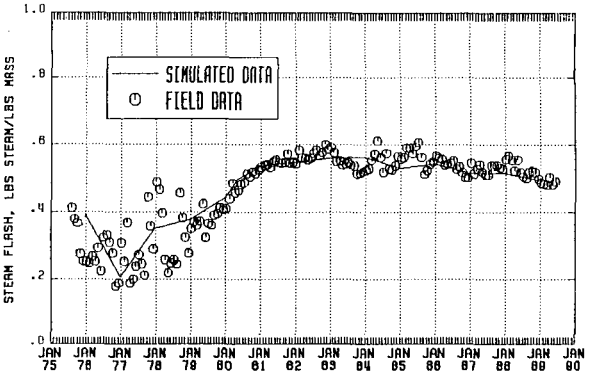

Fig. 6. Bulalo field total steam flash history match.

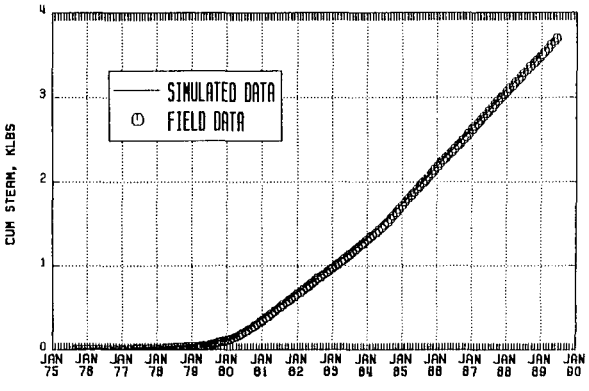

Fig. 7. Bulalo field cumulative steam history match.

At 80% vapor saturation in the fractures, relative permeability to vapor reaches 100%; liquid becomes immobile at 70% vapor saturation. At 80% vapor saturation in the matrix, water in the matrix becomes immobile and relative permeability to vapor reaches 100%. In Fig. 6, the maxima in 1983, and subsequent long term decline in fieldwide flash is due to downflux from above and within the reservoir. In 1983, pressure at the base of the caprock dropped below aquifer pressure reversing the convection path from outflow to inflow.

General shape and magnitude of the pressure sink shown on Fig. 5 was matched. Symmetric arrangement of pressure contours along the northwest trending Makiling Radial Fault indicates extension of high permeability reservoir to the northwest. Influx from the northwest provides pressure support west of the central barrier shown on Fig 2. A 500 psi (3.45 MPa) pressure sink exists east of the barrier. Matching this sink required another permeability barrier to the north between the eastern production area and the northeast injection area, Fig. 1, effectively isolating the eastern side of the field from active pressure support.

PREDICTIVE MODELING

Depletion Mechanisms

Reservoir simulation shows that pro-produced fluid mass originates from three sources currently acting in roughly equal proportions: (1) recovery of injected brine, (2) vaporization of liquid in matrix , and (3) influx from outside the boundaries of the model. Percentage of total mass production rate from each of these sources is shown on Table 3.

Table 3. Depletion Source, Percent of Total Mass Production Rate vs. Time.

Depletion source	1991	2011	2050
Matrix desaturation	33	14	3
Injected brine	37	30	36
Natural influx	30	56	61
Total mass rate	100	100	100

Vaporization of liquid in the rock matrix will become less important with time, influx will become more important and recovery of injected brine will remain fairly constant at approximately 1/3 of the total mass produced. The importance of injectate recirculation is confirmed by tracer testing, Villadolid (1991), which demonstrated widespread and rapid migration of injectate in the reservoir; in the simulation model, fracture/matrix geometry and heat transfer properties qualitatively reproduce the migration phenomena observed by Villadolid. Natural mass influx rate and cumulative were quantified by history matching to observed pressure and enthalpy changes. These influx numbers agreed quantitatively with those determined independently by modeling gravity changes, San Andres and Pedersen (1992).

Sustainable Limits

Predictive simulation incorporated addition of one 55 MWe unit to be operated at 76 % plant factor. This is equivalent to the expected average steam demand of the proposed plan to add 40 MWe base and 40 MWe standby.

Predictive modeling results, Fig. 8, show that by drilling infield production make up wells, existing generation levels (status quo) can be sustained until the year 2011, followed by declining generation. The proposed additions in 1995 (40 MWe base and 40MWe standby) are sustainable to the year 2005; this short term increase being offset by a corresponding long term decrease in power generation. Each of the two cases on Fig. 8 assumes the same limiting number of make up well locations.

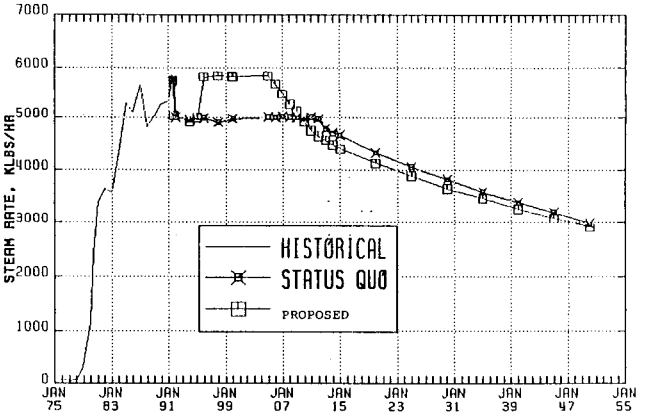

Fig. 8. Bulalo field total steam rate prediction showing the affect of proposed additions to capacity.

Gravity Modeling For Prediction of Matrix Dryout and Limits to Sustainable Deliverability

Observed gravity, San Andres and Pedersen (1992), verified the mass balances of the current reservoir simulation model, Fig. 9. The "1990" trend matches the OBSERVED GRAVITY very well. Difference between the PROD-INJ trend and the "1990" trend is due to influx of liquid. The OBSERVED GRAVITY trend is primarily due to saturation changes as vapor replaces liquid.

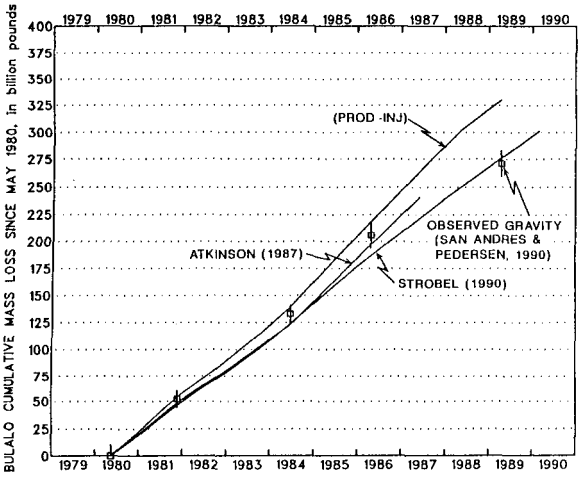

Fig. 9. Cumulative mass loss from observed gravity compared to actual voidage (PROD-INJ) and the simulations in 1987 (closed model) and 1990 (model with influx)

Reservoir simulation in conjunction with gravity modeling demonstrated a relationship between relative permeability in the rock matrix, the influence of relative permeability on rate of change of vapor phase saturation in the matrix, and the influence of vapor phase saturation changes on observed gravity changes. Gravity therefore provided independent validation of the time rate of change in matrix saturations computed in reservoir simulation.

Prediction of matrix dryout using gravity modeling to validate time rate of change in vapor saturations, determined by reservoir simulation, can be an important predictive tool in assessing the limits to sustainable levelized deliverability. As parts of the reservoir reach irreducible liquid saturation the production wells in that area become deprived of a local source of mass transport. Local deprivation precipitates a change in the depletion process of the system as the wells try to make up the local deficit by drainage for more distant sources; if constant mass withdrawal is imposed on that area by make up well drilling, then Darcy's law dictates greater decline in reservoir pressure throughout the area, which in turn translates into accelerated decline in deliverability of all wells in the area. Thereafter the incremental contributions of new make up wells in the affected area will not keep up with the accelerated decline in total area deliverability; a limiting condition for sustainable deliverability from that area has then been reached. This study indicates that such a condition will be reached in the EMID enthalpy group, the major steam supply source (Table. 2), by the year 2000.

Acknowledgements. The simulation technology used in this work is marketed under the brand name TETRAD/ASTRO. Special recognition is due Mr. Larry Murray, Geothermal Division, Unocal Corporation for his patient instruction on the use of ASTRO technology. Thanks to Unocal Corporation management for permission to publish. Most credit goes to the engineers and geoscientists at PGI, Manila, for their professional accountability.

REFERENCES

Atkinson, P.G. and Pedersen, J.R.,(1988), Using precision gravity data in geothermal reservoir engineering modeling studies. Proceedings of the 13th Workshop on Geothermal Reservoir Engineering: Stanford University, Stanford, California, U.S.A.

Benavidez, P. J., Mosby, M. D., Leong, J. K., and Navarro, V. C. (1988) Development and Performance of the Bulalo Geothermal Field. *Proceedings of the* 10th New Zealand Geothermal Workshop, Aukland, New Zealand.

Grant, M. A., Donaldson, I. G, and Bixley, P. F. (1982) *Geothermal Reservoir Engineering*. Academic Press, Inc., New York, N.Y.

San Andres, R. B. and Pedersen, J. R. (1992), Monitoring the Bulalo Geothermal Reservoir Using Precision Gravity Data. Manuscript submitted for publication in *Geothermics Special Issue: Geothermal Systems of the Philippines*.

Villadolid, F. L. (1991) The Application of Natural Tracers in Geothermal Development: The Bulalo, Philippines Experience. *Proceedings of the* 13th New Zealand Geothermal Workshop, Auckland, New Zealand, pp. 69-74.

PROCEEDINGS, Eighteenth Workshop on Geothermal Reservoir Engineering
Stanford University, Stanford, California, January 26-28, 1993
SGP-TR-145

A SURVEY OF POTENTIAL GEOPRESSURED RESOURCE AREAS IN CALIFORNIA

S.K. Sanyal and A. Robertson-Tait
GeothermEx, Inc.
Richmond, California

M. Kraemer and N. Buening
California Energy Commission
Sacramento, California

ABSTRACT

This paper presents the initial results of a survey of the occurrence and characteristics of geopressured fluid resources in California using the publicly-available database involving more than 150,000 oil and gas wells drilled in the State. Of the 975 documented on-shore oil and gas pools studied, about 42% were identified as potentially geopressured. Geothermal gradients in California oil and gas fields lie within the normal range of 1°F to 2°F per 100 feet. Except for the Los Angeles Basin, there was no evidence of higher temperatures or temperature gradients in geopressured pools. The porosity of geopressured pools shows the same normal distribution as for normal pressured pools, with a mode in the range of 20 to 25%. The salinity distribution of both the geopressured and normal pressured pools appear to be bimodal, each with two peak ranges of 0 to 10,000 and 25,000 to 30,000 ppm. Compared to the U.S. Gulf Coast region, geopressured pools in California display much lower water salinities, and therefore, should have a higher solubility for methane. Geopressured pools in California occur in the depth range of less than 1,000 feet to more than 18,000 feet. The modal depth of geopressured pools in California is 2,000 to 4,000 feet, much shallower than that encountered in the Gulf Coast region. The distribution of thickness of geopressured pools is similar to that of normal pressured pools, the majority being less than 250 feet thick. The distributions of the volume of geopressured and normal pressured pools are similar, the modal value being in the range of 1 to 10 billion cubic feet.

INTRODUCTION

Many authors have reported in depth on the potential for commercial recovery of the kinetic energy, thermal energy and dissolved methane from geopressured geothermal reservoirs identified in the U.S. Gulf Coast region. However, the occurrence of geopressured fluids in California has been reported by only a few authors, such as Berry (1973); Berry and Kharaka (1981); Kharaka *et al.* (1981); Lico and Kharaka (1983); Levine and Yerkes (1985); and Price (1988). These studies describe the geologic and tectonic settings of known geopressured zones, and in some cases present data from selected oil and gas wells to characterize the geopressured fluid. The U.S. Department of Energy has recently studied the feasibility of using geopressured fluids for enhanced thermal oil recovery (Negus-De Wys *et al.*, 1991). The present work is part of a systematic survey of the occurrence and characteristics of geopressured fluid resources within on-shore sedimentary basins in the State of California.

THE DATABASE

After reviewing the available literature and consulting with various public agencies and private companies, the primary database chosen for this study was the drilling, well logging and well test data available from oil and gas fields in California. Some of these data are published in California Division of Oil and Gas (1982, 1985 and 1991) but the majority are archived on microfilm at the headquarters of the California Division of Oil and Gas. This database was chosen for several reasons:

- Over 150,000 oil and gas wells have been drilled in California compared to only a few thousand deep geothermal and water wells;
- more extensive logging and testing are conducted in oil and gas wells compared to other types of wells;
- oil and gas well data are more readily retrievable from governmental and private archives;
- the geographical distribution of oil and gas wells is more extensive compared to other types of wells; and
- while numerous oil and gas wells in California have exhibited geopressure, very few occurrences of geopressure from geothermal or water wells have been reported.

For initial screening of data, information on oil or gas pools, rather than on individual wells, were analyzed; an oil or gas field may contain one or more pools. The average initial static pressure, temperature, porosity, salinity, depth, thickness and acreage data available from 975 individual oil and gas pools were gathered from nine different on-shore basins or geographical regions in California (table 1).

Figure 1 is a map of California showing the major regions considered; the subdivisions of the Sacramento Valley and San Joaquin Valley shown in table 1 are not shown in this figure. The only other potentially geopressured areas onshore in California are the Eel River Basin and the Coast Ranges; unfortunately, the publicly available database from these areas proved to be too meager to be useful for this study.

IDENTIFYING GEOPRESSURED POOLS

As the first step in screening the assembled database, plots of the initial static pressure versus datum depth of all pools within a region were prepared. Figure 2 shows a typical plot, representing the oil and gas pools in the Southern

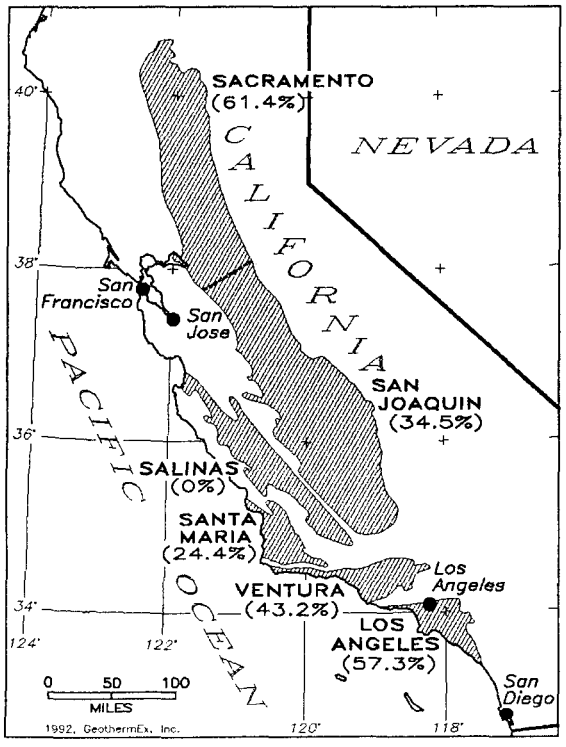

Figure 1. Locations of on-shore oil and gas producing basins, showing the percentage of pools in each basin that are geopressured

Sacramento Valley. On the plot for each region, a visual best fit line was defined; the slope of this line represents the hydrostatic gradient for the region. The estimated hydrostatic gradients fall between 0.40 and 0.45 psi/ft, with the low value being representative of the Salinas Valley, and the highest value being obtained from both the northern Sacramento Valley and the southeast San Joaquin Valley (see table 1).

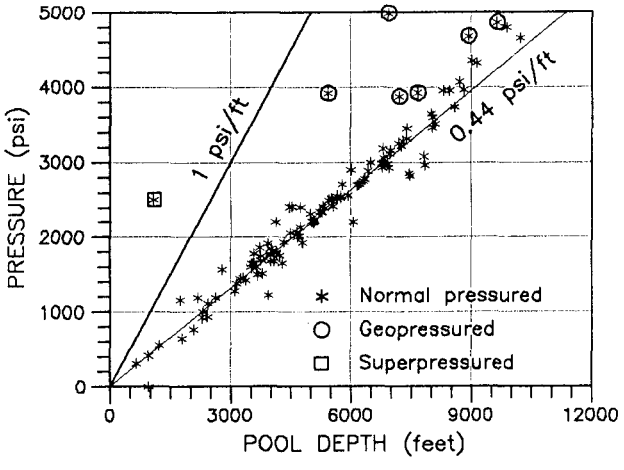

Figure 2. Depth vs. initial pressure for oil and gas pools in the southern Sacramento Valley

On such a plot, any point lying above the hydrostatic line represents an "overpressured" pool. The points lying between the hydrostatic line and the line representing the lithostatic gradient (about 1.0 psi/ft) on each plot represent the "geopressured" pools in the region. Considering the data scatter and the need to prepare a conservative inventory of geopressured pools, only those points falling clearly above the cluster of points along the hydrostatic gradient line were considered to represent distinctly geopressured pools.

These plots display data scatter because of several factors:

- The geothermal gradient and/or water salinity in the various parts of a region can vary significantly, causing variations in the local hydrostatic gradient.
- Unlike the geopressured areas in the well-studied Gulf Coast region, tectonic stresses contribute to the occurrence of geopressure in California; tectonic stresses vary widely even within a given region.
- Static reservoir pressures reported to the State agencies are often imprecise, as these are based on correcting measured pressures from various wells to a common datum, and then volumetrically averaging the datum pressures. Each step in this process is subject to error.
- The assumption of zero pressure at zero depth (used in force-fitting the data) is only an approximation. Some pools may have an artesian condition due to an elevated recharge source or a depressed potential because of depletion due to production.
- Pressures measured in gas pools (and to a lesser extent in oil pools) with high structural relief will be higher than the hydrostatic pressure outside the reservoir; this is clearly not a geopressure phenomenon.

The point falling above the lithostatic line on figure 2 represents a "superpressured" pool. The occurrence of geopressured pools is commonly ascribed to a rapid compaction of shales and consequent entrapment and thermal expansion of excess water in lenticular bodies of sediments enclosed within the shales, with or without any aid from tectonic stresses. The occurrence of superpressured systems, however, requires the presence of a major tectonic stress.

At least 70 distinctly geopressured pools and eight superpressured pools have been identified from such plots. Only the Salinas Valley did not exhibit the occurrence of any overpressured pool. The Ventura Basin had the largest number of distinctly overpressured pools (15 geopressured and two superpressured).

While the above approach identifies distinctly geopressured pools, a more liberal approach can be used to identify potentially geopressured zones by defining a geopressured pool as one with a pressure gradient higher than 0.45 psi/ft, the maximum estimated hydrostatic gradient (based on plots like figure 2) amongst all nine regions. Table 1 shows the number of potentially geopressured pools thus estimated for each region. Table 1 shows that 410 pools, that is, 42% of the on-shore pools in California are potentially geopressured. In terms of the total number of geopressured pools, the San

Joaquin Valley (all three subdivisions combined) has the most (163), nearly 40% of the 410 potentially geopressured pools. In terms of the fraction of pools in a region that are potentially geopressured, the Sacramento Basin (both subdivisions combined) tops the list with 135 geopressured pools out of 220 pools (61.4%); these percentages are also shown on figure 1.

CORRELATION BETWEEN GEOPRESSURE AND TEMPERATURE GRADIENT

Attempts were made to verify the hypothesis that geopressured pools in California display a positive correlation between pressure and temperature gradients. This hypothesis is based on the assumption that the geopressured lenses contain excess water and are, therefore, poorer heat conductors than the surrounding medium, which in turn causes the occurrence of steeper temperature gradients through such lenses. As a first step, a plot of the average reservoir temperature versus datum depth of pools was prepared for each region. Figure 3 is an example of such a plot; it shows the data from the Los Angeles basin.

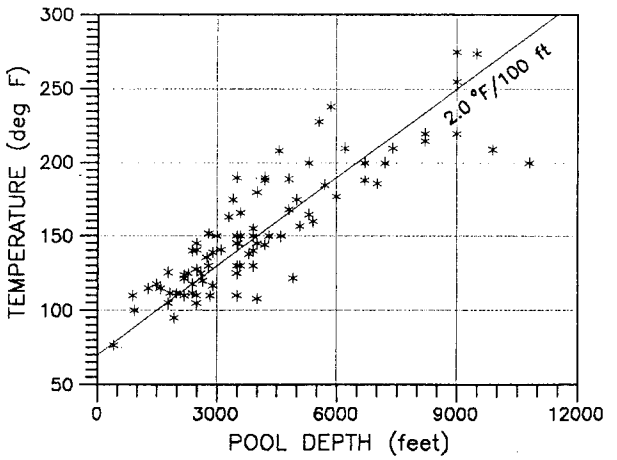

Figure 3. Depth vs. temperature for on-shore oil and gas pools in the Los Angeles Basin

The data scatter on the plots like figure 3 is caused by the inherently inaccurate nature of this database. There are at least two reasons for this inaccuracy:

- The estimates of the average pool temperature is usually based on the maximum temperature recorded in wells during logging runs. A well may not have recovered from the cooling effect of mud circulation by the time a log is run; therefore, the temperature is often underestimated.

- The maximum recorded temperature is usually associated with the total depth of the well during the logging run, which is not necessarily appropriate; the maximum temperature may have been recorded at a shallower depth than at the well bottom.

A visual best fit line through the data points in each plot was defined subject to the constraint that the average ambient surface temperature in central and southern California could not lie outside the range of 60° to 75°F. The geothermal gradients estimated from these plots varied from 1°F/100 ft for the northern Sacramento Valley to 2°F/100 ft for the Los Angeles Basin (see table 1), a perfectly normal range, even though many geopressured reservoirs are known to exist in these regions.

A plot was prepared of the pressure gradient versus temperature gradient for all pools in each region. Figure 4 is an example of a plot of pressure gradient versus temperature gradient representing the Los Angeles basin, and this was the only such plot that indicated a positive correlation between pressure gradient and temperature gradient. A majority of the potentially geopressured pools on this plot indicate an abnormally high temperature gradient (over 2°F/100 ft). In other regions, the above analysis has so far failed to confirm the hypothesis that geopressured pools have a positive correlation between pressure and temperature gradients.

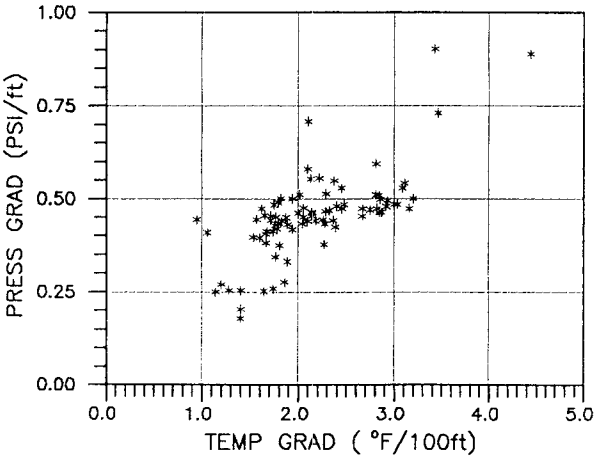

Figure 4. Pressure gradient vs. temperature gradient for on-shore oil and gas pools in the Los Angeles Basin

The most reliable means of verifying this hypothesis is to review equilibrium temperature profiles in known geopressured wells and to verify if a higher temperature gradient exists through the geopressured sections of the wells. Unfortunately, such profiles were available for very few wells. Therefore, attempts were made to develop temperature profiles of wells from the maximum temperatures recorded during the various logging runs in the same well assuming that the maximum recorded temperature during a run was the equilibrium temperature at the total depth of the well during the run.

Figure 5 shows an example of a maximum recorded temperature profile from a well known to have encountered geopressured pools (from mud records, pressure data and well logs). For the well considered in figure 5 (Well 423, Kettleman North Dome field, central San Joaquin Valley), the geopressured zone occurs from about 11,400 feet to total

depth, as indicated by the plot of the mud weight used during drilling as a function of depth (figure 6). Figure 5 does not indicate any obvious steepening of the temperature gradient in the geopressured depth interval.

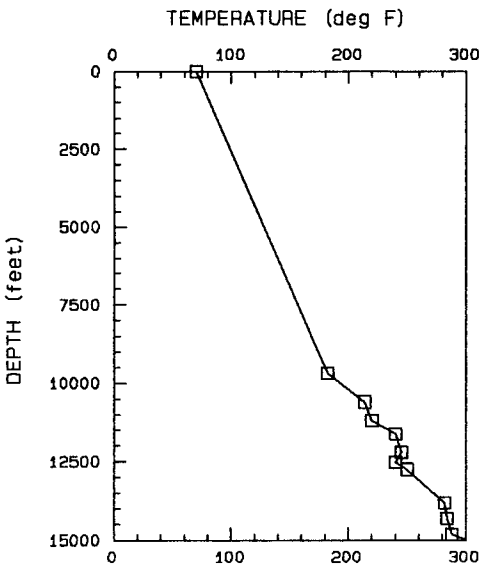

Figure 5. Maximum recorded temperature vs. depth, Kettleman North Dome Field, Well 423

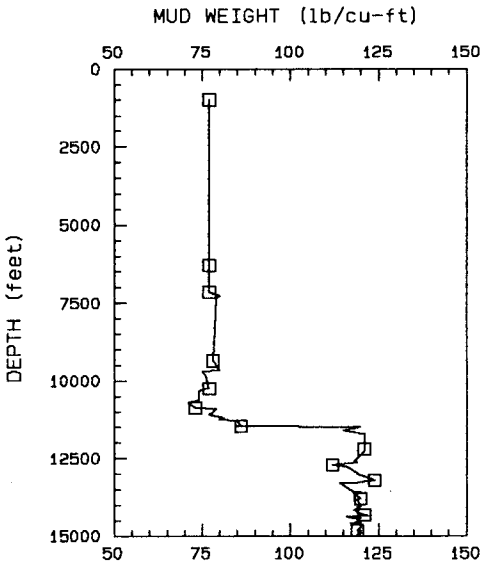

Figure 6. Drilling mud weight vs. depth Kettleman North Dome Field, Well 423

So far we have not been able to confirm the hypothesis that a positive correlation exists between pressure and temperature gradients for geopressured pools in California. If geopressure is caused by tectonic stresses alone, the mechanism postulated above would not be present and, therefore, geopressure need not be associated with a steepening of the temperature gradient.

OTHER CHARACTERISTICS OF GEOPRESSURED POOLS IN CALIFORNIA

Based on the available data on the oil and gas pools, statistical distributions of several characteristics of both geopressured and normal pressured pools were defined and compared. Figure 7 shows a histogram of the porosity values for 878 of 975 pools for which porosity data were available, compared with the porosity histogram for 380 potentially geopressured pools for which porosity data were available. Figure 7 shows that geopressured pools have essentially the same statistical distribution as do all pools, with modal porosity in the range of 20 to 25%.

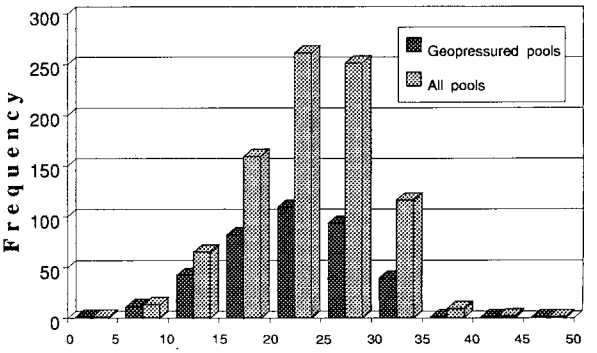

Figure 7. Histogram of porosity (%)

Figure 8 compares the histograms of water salinity based on data from all pools (424 data points) and data from potentially geopressured pools (172 data points). The two histograms are similar, indicating that the water salinity in geopressured pools is statistically the same as in normal pressured pools. The distribution of water salinity appears to be bimodal, the modes being 0 to 10,000 parts per million (ppm) and 25,000 to 30,000 ppm. These ranges of water salinity are much lower than encountered in the geopressured reservoirs of the U.S. Gulf Coast, where it is typically higher than 100,000 ppm. The practical implication of this fact, as pointed out by Kharaka *et al.* (1981), is that higher solubilities for methane can be expected in the geopressured reservoirs in California.

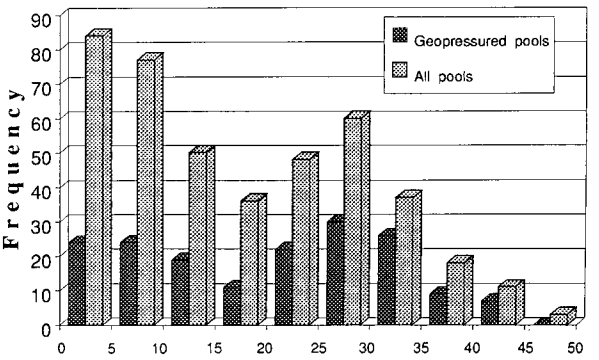

Figure 8. Histogram of salinity (thousands of ppm)

Geopressured pools in California occur in the depth range of 1,000 feet to over 18,000 feet. Figure 9 compares the histograms of the depths of all pools (975 data points) and the depths of the potentially geopressured pools (410 data points). The two histograms are similar, with a mode in the range of 2,000 to 4,000 feet. This depth range is much shallower than that of the geopressured reservoirs in the U.S. Gulf Coast, where geopressure is encountered only below 12,000 feet. Therefore, the drilling cost for any geopressured development should be lower in California than in the Gulf Coast area.

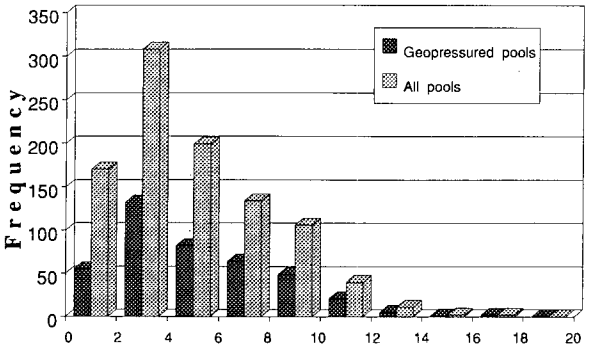

Figure 9. Histogram of pool depth (thousands of feet)

The geopressured pools identified in this study are thin, mostly less than 250 feet in thickness. Figure 10 compares the histograms of all pools (950 data points) and the potentially geopressured pools (400 data points). The highly skewed distributions for both sets of data are similar, with a mode of 0 to 250 feet. It should be noted, however, that the thickness values of oil or gas pools have been used in constructing these histograms; the water aquifer underlying the oil-water or gas-water contact may be much thicker. A statistically significant database on the thicknesses of geopressured aquifers has not yet been developed for California.

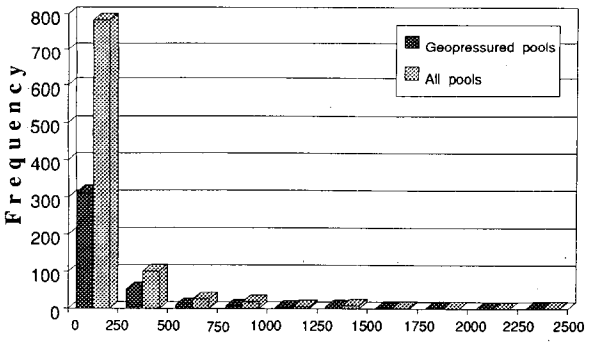

Figure 10. Histogram of thickness (feet)

An attempt was made to define the distribution of the volume of geopressured pools in California. However the effort has not yet been successful because of the scarcity of published data on the areal extent of the pools. Only 264 of the 975 pools provided enough data for estimating the volume; of these 98 were potentially geopressured. Figure 11 shows the two histograms constructed from these data.

Again, the two histograms are similar, with a mode in the 0.1 to 1 billion cubic feet (2,300 to 23,000 acre-feet) range. As mentioned in connection with the thickness data, the volumes of geopressured aquifers must be higher than indicated by the data from the oil and gas pools. Perhaps the volumes of geopressured aquifers would be one or two orders of magnitude higher than they appear from figure 11.

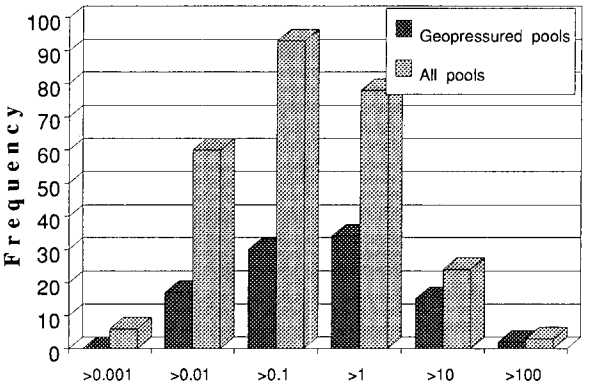

Figure 11. Histogram of volume (billions of cubic feet)

CONCLUSIONS

We have arrived at the following conclusions based on our study to date:

- Of the 975 on-shore oil and gas pools in California, 410 are potentially geopressured with at least 70 distinctly geopressured and eight superpressured. The Sacramento Valley displays the largest relative occurrence of geopressure (61.4%) while the San Joaquin Valley has the largest number of geopressured pools in the State (163). No geopressured pools could be identified in the Salinas Valley.

- Geothermal gradients in the geopressured pools lie within the normal range of 1°F to 2°F per 100 ft, with the pools in the Los Angeles Basin showing the highest gradient. Except for the Los Angeles Basin, the hypothesis of a positive correlation between pressure and temperature gradients could not be validated.

- Both normal pressured and geopressured pools in California show the same distribution of porosity with a mode of 20% to 25%.

- Both geopressured and normal pressured pools in California display a bimodal distribution of water salinity with peaks at 0 to 10,000 and 25,000 to 30,000 ppm; these salinities are much lower than encountered in the U.S. Gulf Coast, and hence, geopressured pools in California should have higher solubilities for methane.

- Both geopressured and normal pressured pools in California occur in the depth range of less than 1,000 feet to over 18,000 feet, the median depth (2,000 to 4,000 feet) for both being much shallower than the depths encountered in the Gulf Coast region; therefore, the drilling cost for any geopressured development would be lower in California.

- The distributions of the thicknesses of the normal-pressure and geopressured pools are the same, with the majority being less than 250 feet thick.

- The distributions of the volume of the normal-pressured and geopressured pools are the same, with the majority being in the range of 1 to 10 billion cubic feet.

ACKNOWLEDGEMENTS

The authors wish to thank the California Energy Commission and the U.S. Department of Energy for financial support for this study.

REFERENCES

Berry, F. A. F., 1973. High Fluid Potentials in California Coast Ranges and Their Tectonic Significance. AAPG Bulletin, Vol. 57, pp. 1219-1249.

Berry, F. A. F. and Y. K. Kharaka, 1981. Origins of abnormally-high fluid-pressure systems in California. Abstracts with Programs - Geological Society of America, Vol. 13, p. 409.

California Division of Oil and Gas, 1985. California Oil and Gas Fields, Volume 1: Central California. California Division of Oil and Gas Report TR11, 3rd Edition.

California Division of Oil and Gas, 1991. California Oil and Gas Fields, Volume 2: Southern, Central Coastal and Offshore California. California Division of Oil and Gas Report TR12, 3rd Edition.

California Division of Oil and Gas, 1982. California Oil and Gas Fields, Volume 3: Northern California. California Division of Oil and Gas Report TR10, 4th Edition.

Kharaka, Y. K., M. S. Lico, L. M. Law and W. N. Carothers, 1981. Geopressured-geothermal resources in California. GRC Transactions, Vol. 5, pp. 721-724.

Levine, P. and R. F. Yerkes, 1985. Distribution of abnormally high pore pressures in the western Transverse Ranges, California. U.S. Geological Survey Open-File Report 85-0522, 19 pp.

Lico, M. S. and Y. K. Kharaka, 1983. Subsurface pressure and temperature distributions in Sacramento Basin, California. Selected Papers of the Pacific Section AAPG 1983 annual meeting; Vol. 1, No. 1, pp. 57-75.

Negus de-Wys, J., O. E. Kimmell, G. F. Hart and M. M. Plum, 1991. The feasibility of recovering medium to heavy oil using geopressured geothermal fluids. Idaho National Engineering Laboratory Report EGG-EP-9840, 107 pp.

Price, C. A., 1988. Fluid Pressures in Overpressured Forbes Formation, Sacramento Valley, California. AAPG Bulletin, Vol. 72, pp. 391-392.

Table 1. Hydrostatic and Temperature Gradients and the Occurrence of Overpressured Pools

Region	Hydrostatic Gradient (psi/ft)	Temperature Gradient (°F/100 ft)	Number of Oil and Gas Pools	Number of Distinctly Overpressured Pools*	Number of Potentially Overpressured Pools**	Percentage of Pools Overpressured
Northern Sacramento Valley	0.45	1.0	98	13	66	67.3%
Southern Sacramento Valley	0.44	1.3	122	6	69	56.6%
Central San Joaquin Valley	0.44	1.6	37	4	20	54.1%
Southwestern San Joaquin Valley	0.43	1.6	212	7	88	41.5%
Southeastern San Joaquin Valley	0.43	1.3	224	10	55	24.6%
Salinas Valley	0.40	1.6	20	0	0	0%
Santa Maria Basin	0.42	1.6	78	9	19	24.4%
Ventura Basin	0.44	1.6	88	15	38	43.2%
Los Angeles Basin	0.44	2.0	96	5	55	57.3%

*Based on plots like figure 2.
**Pressure gradient >0.45 psi/ft.

PROCEEDINGS, Eighteenth Workshop on Geothermal Reservoir Engineering
Stanford University, Stanford, California, January 26-28, 1993
SGP-TR-145

Enthalpy and Mass Flowrate Measurements for Two-Phase Geothermal Production by Tracer Dilution Techniques

Paul Hirtz, Thermochem, Inc.
Jim Lovekin, California Energy Company, Inc.
John Copp, California Energy Company, Inc.
Cliff Buck, Thermochem, Inc.
Mike Adams, University of Utah Research Institute

Abstract

A new technique has been developed for the measurement of steam mass flowrate, water mass flowrate and total enthalpy of two-phase fluids produced from geothermal wells. The method involves precisely metered injection of liquid and vapor phase tracers into the two-phase production pipeline and concurrent sampling of each phase downstream of the injection point. Subsequent chemical analysis of the steam and water samples for tracer content enables the calculation of mass flowrate for each phase given the known mass injection rates of tracer. This technique has now been used extensively at the Coso geothermal project, owned and operated by California Energy Company. Initial validation of the method was performed at the Roosevelt Hot Springs geothermal project on wells producing to individual production separators equipped with orifice-plate flowmeters for each phase.

Introduction

In geothermal fields that produce two-phase fluids, monitoring trends in the enthalpy (heat content) of produced fluids is important for understanding the reservoir's performance. Decreasing enthalpies can indicate breakthrough of injection water or invasion of cooler groundwater. Increasing enthalpies can indicate reservoir boiling and the formation of a steam cap. Enthalpy is essential for the interpretation of geochemical data because it determines the steam fraction at sampling conditions and allows the correction of chemical concentrations back to reservoir conditions. From an operational point of view, the enthalpy and the mass flowrate govern the amount of steam available and ultimately the power output of the plant.

Measuring the total enthalpy of two-phase flow is not a simple process. Defining the pressure and the temperature of the fluids is not sufficient; for a given pressure and temperature, the enthalpy can vary from that of saturated steam to that of saturated liquid, depending on the steam fraction of the mixture. Determining the fraction of vapor ("void fraction") in two-phase flow is a common engineering problem in power generation, oil production and chemical process industries. In a geothermal field, full-flow production separators can be added to the fluid gathering system to allow measurement of steam and liquid flow independently, but this entails the substantial cost of additional piping and pressure vessels. Chemical methods are available to calculate enthalpy over a broad range of values, but require a significant pressure drop in the two-phase flow line to allow comparison of chemical concentrations at different steam fractions. Geochemically derived reservoir temperatures can be used to estimate total enthalpy, provided the well produces from a single-phase liquid resource.

This paper presents a brief overview of available methods for measuring enthalpy and discusses some of the limitations of each. The paper then describes a new chemical method of enthalpy determination based on the use of tracers in the steam and liquid-phases. The tracer dilution technique was developed specifically for the Coso geothermal field, but is applicable to all two-phase geothermal production. This method does not rely on a pressure drop, but simply on the mixing of tracers in the pipeline between the point of injection and the point of sampling. This technique has been verified by testing in geothermal fields at Coso and at Roosevelt Hot Springs.

Methods of Enthalpy Determination

Conceptually, the most straightforward way to measure the enthalpy of a two-phase flow stream is to separate the phases and to measure their individual mass flowrates by well-established single-phase measurement techniques, such as orifice plates, Venturi tubes or annubars. Given the mass flowrates of steam (Q_V) and liquid (Q_L) and the known enthalpies of steam (H_V) and liquid (H_L) derived from steam tables at the separator pressure, the total enthalpy of the mixture (H_T) can be calculated by a simple heat and mass balance equation:

Equation 1.

$$H_T = \left(\frac{(Q_V \times H_V) + (Q_L \times H_L)}{(Q_V + Q_L)} \right)$$

Several authors have described the design of separators that can handle the large flowrates typical of geothermal wells. Lazalde-Crabtree (1984) presents a good overview of this subject. For typical geothermal plants requiring

single-phase steam, separators are an integral part of the gathering system. In some geothermal fields, each production well has a dedicated separator. In many cases, however, separators are shared between several wells to minimize capital costs. This results in a loss of the ability to monitor enthalpy trends continuously for individual wells.

Test separators may be installed for groups of wells, so that the flow from individual wells may be diverted and metered separately during test intervals. Alternatively, the flow lines of individual wells may be designed to allow portable test separators to be connected for periodic testing. Steam venting and production loss can be avoided by piping the separated fluids back to the main production line.

Although shared test separators may be less expensive than dedicated separators, they are still costly. In addition to the separator vessels, the capability of flow diversion to a test separator requires extra production piping and valves. Also, diverting the well flow may change the flowing wellhead pressure, which could cause the enthalpy of the fluids produced on tests to differ from the enthalpy under normal operating conditions.

For wells with relatively low flowrates (less than about 15 kg/s), enthalpy can be measured by a total-flow calorimeter. Grant et al., (1982) provide a summary of this technique. James tube testing with a silencer and a weir box can provide reasonably accurate enthalpy values over a wide range of flowrates (James, 1970). Both these methods require diversion of flow from production, with attendant losses of revenue and fluid disposal costs. The atmospheric venting of steam may also require hydrogen sulfide abatement to comply with environmental regulations.

Ultrasonic and neutron-based meters have been developed to determine the mass ratios of steam and liquid in two-phase flow (Shen, 1992; Woiceshyn et al., 1986). However, such devices typically have limitations on the range of steam fractions and pipe diameters with which they can operate. These devices can also lose accuracy due to deposition of scale at the sensor locations.

Flowing pressure and temperature surveys within production wells can be interpreted to estimate enthalpy (Kaspereit, 1990). This technique is useful when fluid enters the wellbore as a single-phase liquid, but it is less reliable when there are fluid entries above the flash point. In addition, access to wells for repeated surveys may be limited by mechanical constraints, such as the presence of tubing for downhole injection of scale inhibitor.

Geothermometry can be used to estimate the enthalpy of produced fluids (Fournier and Potter, 1982). This technique estimates the enthalpy for saturated liquid based on the corresponding geothermometer reservoir temperature. If some of the fluid enters the wellbore as steam due to boiling within the reservoir, geothermometry will underestimate the enthalpy of fluids produced at the surface.

Other chemical methods to calculate enthalpy involve a comparison of samples collected at two points on the two-phase flow line that differ substantially in pressure. These methods include the gas ratio method (Mahon, 1966) and the chloride method (Marini and Cioni, 1985). Such methods depend on changes in concentration of naturally occurring constituents in the steam or liquid-phases due to flashing between the two sample points. There must be a sufficient pressure drop caused by a flow control valve or other restriction between the sample points to provide a measurable concentration change. If the normal flowing wellhead pressure is close to the gathering system pressure, this technique is not viable. Sufficient pressure drop may be induced by throttling the well, but the total discharge enthalpy may vary with wellhead pressure.

The injection of chemical tracers into two-phase flow allows the determination of individual mass flowrates directly from tracer concentrations and the known injection rates without the requirement of a pressure drop in the flow line. Liquid-phase tracers have been used extensively in surface and groundwater hydrology to estimate the flowrates of water, and to a limited extent in geothermal fields to determine mass flowrates of produced and injected liquid (Ferrer, 1992). The mass flowrates of liquid streams, liquid fractions and steam quality involved in geothermal fluid treatment processes such as H_2S abatement and HCl corrosion mitigation have been routinely determined using sodium ion as the tracer (Hirtz and MacPhee, 1989; Hirtz et al., 1991). Steam flowrates venting from geothermal drilling mufflers at The Geysers are routinely estimated from air to steam ratio measurements of samples collected during air-drilling operations. The current work applies similar principles to determine steam and liquid-phase flowrates simultaneously in a two-phase flow stream and uses the ratio of steam and liquid mass rates to determine the total fluid enthalpy.

Tracer Dilution Testing Technique

Theory of Method

The tracer dilution enthalpy measurement technique requires precisely measured rates of vapor and liquid-phase tracers injected into the two-phase flow stream. Samples of each phase are collected from sampling separators downstream of the injection point, before injection for background analysis, and concurrent with tracer injection. Chemical analysis of the vapor and liquid-phase samples for tracer content is performed, and the mass flowrate of each phase is calculated based on

these measured concentrations and the injection rate of each tracer.

The liquid-phase mass rate is given by:

Equation 2.
$$Q_L = \frac{Q_T}{(C_{TL} - C_{BL})}$$

Q_L = Liquid-phase Mass Rate
Q_T = Tracer Injection Mass Rate
C_{TL} = Liquid-phase Tracer Concentration by Weight
C_{BL} = Liquid-phase Background Concentration by Weight

The vapor-phase mass rate is given by:

Equation 3.
$$Q_V = \frac{Q_T}{(C_{TV} - C_{BV})}$$

Q_V = Vapor-phase Mass Rate
Q_T = Tracer Injection Mass Rate
C_{TV} = Vapor-phase Tracer Concentration by Weight
C_{BV} = Vapor-phase Background Concentration by Weight

The mass rates calculated are valid for the temperature and pressure at the sample collection point. The total fluid enthalpy can then be calculated using the same heat and mass balance equation as shown above for the total fluid enthalpy calculation of separated steam and water (Equation 1).

Tracer Selection Criteria

The selection of liquid and vapor-phase tracers for the tracer dilution technique was based on an evaluation that included the following considerations:

- Each tracer must partition completely into their respective vapor or liquid-phase.
- The tracers must be thermally and chemically stable under the conditions of two-phase geothermal production.
- The liquid-tracer must be highly soluble in water and the gas-tracer must have a high vapor pressure to facilitate injection and metering.
- Quantitative, highly precise analytical methods with wide linear ranges must be available to measure the tracers in a geothermal fluid matrix.
- The natural background levels of the tracers must be fairly low and constant.
- The cost of the tracers must be reasonable for the quantities to be injected given the background levels.

Several inorganic ions were considered for use in the Coso geothermal field as the liquid-phase tracer. These included fluoride (as KF), bromide (as NaBr), lithium (as LiCl), cesium (as Cs_2SO_4), and magnesium (as $MgCl_2$). Organic tracers such as fluorescein dye, rhodamine WT dye, benzoic acid and benzene sulfonates were not considered for this application since these compounds are used in reservoir injection tracer studies and routine use for enthalpy testing would contaminate the reservoir and preclude their primary use (Adams et al., 1992). There is also less certainty that the organic tracers could be used in applications requiring highly quantitative recoveries and analytical detection.

All of the inorganic tracers listed above will partition completely into the liquid-phase at normal two-phase geothermal production temperatures. The inorganic tracers are also thermally stable, but fluoride and magnesium may precipitate under certain conditions. Fluoride can precipitate as fluorite (CaF_2) at reservoir temperatures if sufficient concentrations of calcium and fluoride ions are present. Fluorite is usually undersaturated by one order of magnitude in Coso reservoir fluids. Magnesium can precipitate as magnesite ($MgCO_3$) if sufficient concentrations of magnesium and carbonate ions are present, or co-precipitate in calcite ($(Ca,Mg)CO_3$). Since calcite deposition is a problem for many wells at Coso, a magnesium tracer does not seem to be a prudent choice for flashed liquid already supersaturated in calcium carbonate.

The inorganic tracers considered for use are highly soluble, except for lithium. Due to the low molecular weight of lithium, a maximum solution concentration of only 5 weight % lithium ion can be made from the lithium chloride salt. The highest tracer concentrations can be achieved for bromide and cesium, both at 30 weight % for the respective anion and cation. Low tracer solubility will cause logistical problems during enthalpy tracer testing in the areas of chemical mixing, storage, transport and injection, especially if the background levels of the tracer are high, requiring greater quantities of tracer for injection.

The inorganic tracers listed above are readily detected with modern analytical instrumentation. The anions, fluoride and bromide, can be analyzed precisely by ion-chromatography (IC). The geothermal brine matrix required the development of specific IC methods by Thermochem laboratories for accurate detection of fluoride and bromide in the presence of high chloride concentrations. The cations, lithium, cesium and magnesium can be analyzed precisely by atomic absorption spectrophotometry (AAS) or inductively-coupled plasma emission spectroscopy (ICP). However, the IC methods for the anion tracers are more precise and have a greater linear range than the AAS or ICP methods for the cations.

The background levels of the inorganic tracers range from less than 0.02 ppm_w for magnesium to about 15 ppm_w for lithium in the geothermal liquid produced at Coso. In order to maintain a high degree of accuracy and minimize the effects of background concentrations on the tracer dilution technique, a tracer concentration of at least 10 times the background level is desired during the test. The background levels for all the potential inorganic tracers at Coso are not a problem, with the exception of lithium which has the highest background and lowest solubility, requiring unreasonably high tracer solution injection rates.

The chemical cost per hour of injection, which is the typical duration of an enthalpy tracer test, ranges from $33.00 for magnesium (at 100 times the detection limit) to $1,420.00 for lithium (at 10 times background), given a 50 kg/s liquid flowrate with the average background levels found at Coso.

Based on the criteria outlined above, fluoride was chosen as the initial liquid-phase tracer to be tested at Coso and Roosevelt Hot Springs. Bromide was not tested initially due to analytical problems in the IC procedure caused by the high chloride content of the samples. The analytical procedure was later developed for high-precision bromide analysis by IC, with comparable accuracy and precision to the fluoride procedure.

The gases considered for use in Coso as vapor-phase tracers were ethane, propane, butane and helium. Unsaturated hydrocarbons such as ethene and propene were not considered due to potential chemical and thermal instability. These compounds are also easily hydrolyzed by caustic which is commonly used in geothermal gas collection bottles to absorb CO_2. Sulfur hexafluoride and the halocarbons were not considered for routine use because they are used in reservoir injection tracer studies and this application would contaminate the reservoir (Adams et al., 1991).

Each of these potential vapor-tracers will partition completely into the steam phase with minimal solubility in the liquid at production temperatures. There are also no known chemical or thermal instability problems associated with their use under surface production conditions.

The vapor pressure of the gas tracers is an important parameter in tracer selection. The injection of gas tracers is easiest if the tracer can be maintained as a gas during metering and injection. Since the hydrocarbons considered have relatively low vapor pressures, they must be obtained as gas mixtures, diluted with nitrogen or helium in high-pressure cylinders (140 bar). The vapor pressure limits the maximum tracer concentration possible in these cylinders: ethane mixtures can be as high as 17% by volume and propane up to 2.9%, but butane mixtures are limited to only 0.68% by volume. Pure gases could also be injected from liquefied gas cylinders, but the cylinders would have to be heated to maintain sufficient pressure during injection.

The hydrocarbon gas tracers can be analyzed by gas chromatography with flame ionization detection (GC/FID). This method is highly precise and has a linear range of several orders of magnitude. Trace background levels of hydrocarbons can be easily detected in geothermal steam at low part-per-billion concentrations. Helium can be analyzed by gas chromatography with thermal conductivity detection (GC/TCD). Background levels of helium in the part-per-billion by weight range can also be detected with the proper instrumentation, although the linear range is not as broad.

The background levels of vapor-phase tracers are significantly more variable than the liquid-phase tracer concentrations and make it necessary to inject the gas tracers at about 100 times the average background value. Given this requirement and the maximum volume % of tracer possible in high-pressure cylinders, ethane and butane must be injected at rates that are impractical for routine application at Coso. Due to the low molecular weight of helium, the pure gas injection rate from a high-pressure cylinder is also too high for routine use. Propane mixtures can be injected at rates of 1/4 to 1/10 that of the other gas tracers, given the average background propane level at Coso, about 0.010 ppm_w. Due to the logistical simplifications in handling the smaller quantities of propane required for injection, propane was chosen as the vapor-phase tracer for enthalpy tracer testing at Coso.

The costs of the vapor-phase tracers are relatively low, ranging from $24.00 to $107.00 per hour to measure a 12.5 kg/s steam flowrate at Coso, given average background levels.

Tracer Metering Techniques

The tracer dilution enthalpy technique relies upon accurate and precise metering of the liquid and vapor-phase tracers injected into the two-phase flow stream. Mass flowrate measurement devices were initially chosen as the best means to meter the tracers without errors related to gas and liquid density and viscosity corrections over the wide range of operating temperatures required. Constant injection rates are also necessary to minimize errors and data reduction complications associated with the time delay between injection of tracer and subsequent recovery by sampling downstream.

The liquid-tracer delivery methods evaluated were pressurized reservoir systems, rotary gear pumps and positive displacement metering pumps. Pressurized reservoirs could be designed to deliver tracer at any pressure required, but it is difficult to reproducibly control the injection rate which depends upon the pressure drop across a small orifice, capillary tube or

metering valve. Pressure surges in the two-phase flow line, which are common in geothermal production, will also affect the output rate of these systems. Another consideration is that the system would have to be shut down to replenish the reservoir. Unfortunately, variable-speed rotary gear pumps, which do not suffer from these problems, could not be obtained for the flowrate and discharge pressures required. This left positive displacement metering pumps which typically do not deliver a continuous flow stream, but pulsations that could result in periodic concentration spikes of tracer in the liquid-phase. The liquid delivery system finally selected for testing of the enthalpy tracer method was a positive displacement metering pump, relatively insensitive to discharge pressure fluctuations, operating at a high stroke frequency in conjunction with a pulsation damper to effectively produce a continuous flow stream.

The true mass injection rate of the liquid-tracer is monitored by an electronic balance (50 g resolution, 150 kg capacity) interfaced to a portable computer. The metering pump draws from a 60 liter reservoir placed on the balance, which measures the weight loss continuously during injection. The computer records the weight loss data versus time and calculates the mass injection rate over selected intervals, in addition to running averages and cumulative totals. Although the stroke setting of the metering pump provides reproducible injection rates, monitoring true mass delivery results in the highest possible accuracy.

A mass flow-based system was also selected for gas tracer delivery. The gas tracer is metered directly from a gas pressure regulator manifold connected to the high pressure gas mixture cylinders. An electronic mass flow controller regulates the gas flowrate with high precision by sensing the cooling of an integral heated coil exposed to the flowing gas. This cooling effect is proportional to the mass flowrate of the gas. A solenoid metering valve is continuously adjusted by the control unit to maintain the gas flow at the desired set-point. This is a standard laboratory and industrial device for high-accuracy gas metering, with certain modifications to accommodate the relatively high delivery pressure requirements. A back-pressure regulator was also added to the system to eliminate rapid cycling of the controller caused by pressure surges in the two-phase line.

The liquid and gas tracers are co-injected through a stainless-steel probe inserted into the two-phase flow line near the wellhead. A probe is used to eliminate any possible leakage of tracer from the sample port valve packing or related connections, and to deliver the tracers directly into the flow stream. The tracer injection hoses and probe connections are easily leak-checked during testing. A tracer leak would obviously induce an error in the actual amount of tracer injected into the flow stream, resulting in erroneous flowrate and enthalpy measurements.

Tracer Sample Collection Techniques

Samples of the steam and liquid-phases are collected downstream of the tracer injection point, which is near the wellhead, according to standard two-phase geothermal fluid sampling methods (ASTM E-44). In order to obtain representative samples of each phase, the sampling separator used to collect steam samples is attached to the top of the horizontal two-phase flow line and the liquid separator is attached to the bottom of the line. Since the fluid in most two-phase geothermal production lines is nearly stratified, this configuration usually insures that sufficient quantities of each phase are available to the separators, where a final high-quality separation is achieved.

The sample points at Coso are normally located downstream of the flow control valve(s) for the well tested, and as far downstream of the injection point as possible. The flow control valve provides agitation in a similar manner to a Venturi mixer, effectively distributing the tracers within each phase. The shortest lengths between injection and sampling points at Coso are restricted to 18 meters by the existing gathering system configuration.

The liquid samples are cooled through a sample condenser and collected over a time interval of at least 2 minutes to integrate any short-term fluctuations in tracer concentrations. The samples are stored in plastic bottles without further treatment before analysis. The steam samples are passed through a condenser and the condensate plus noncondensible gases are collected in evacuated glass bottles containing sodium hydroxide. The caustic solution absorbs CO_2, the predominant noncondensible gas, and enables a sufficient quantity of condensate to be collected in the bottle with the gases, resulting in a representative sample of condensed steam and tracer gas. These bottles are filled over a 3 to 5 minute interval, which also helps integrate any short-term tracer fluctuations due to flow surging of the wells. Several liquid and steam samples are collected during the length of the test.

Field Testing

Comparative field tests of the tracer dilution technique to other enthalpy measurement methods were initially conducted at the Coso geothermal field in California and at the Roosevelt Hot Springs geothermal field in Utah. At Coso, separators in the gathering system are typically shared by several production wells, and the tracer dilution tests on individual wells were compared to James tube tests. At Roosevelt, dedicated production separators allowed verification of tracer dilution tests with reference to orifice meter measurements of separated steam and liquid.

Coso

The Coso Geothermal Field produces two-phase fluids from fractured, crystalline rock at depths ranging from approximately 400 to 3,200 meters. Reservoir temperatures range from approximately 200 to 345°C. Commercial production began in July 1987 with a 30 MW, dual-flash power plant. By the end of 1989, plant capacity had expanded to a total of 240 MW from nine turbines at four plant sites. As of December 1, 1992, 68 production wells were in active use. The reservoir was initially liquid-dominated, with a pre-existing steam cap that has expanded with exploitation. The total mass flowrates of individual wells range up to about 125 kg/s and are generally in the range of 10 to 100 kg/s. The enthalpies of produced fluids at the wellhead range from 840 to 2,800 kJ/kg.

Initial tests on Coso wells in the early 1980's used test separators to establish flowrates and enthalpy values. The testing procedure was later simplified so that most of the initial tests at Coso were performed using just James tubes, silencers, and weir boxes. When gathering systems were designed for the first few plants, it was intended to use the gas ratio method to monitor enthalpy trends for wells in production. This technique was successful when the wells first went on line, because wellhead pressures were high enough to allow substantial pressure drops in the flow lines between sampling points.

Within a year of start-up, however, declines in wellhead pressure (often aggravated by wellbore scaling) caused a loss of resolution in the gas ratio measurements, and the enthalpy values from these measurements became unreliable. James tubes and weir boxes were added as permanent components of the gathering system, and a program of quarterly testing of all production wells was implemented in the summer of 1991. This improved the quality of enthalpy determinations, but taking wells off-line for James tube testing decreased the power output of the plants and upset the balance of the other wells in the gathering system. Also, some wells could not be vented to atmosphere at full flowrates without exceeding environmental limits on H_2S emissions. Tracer dilution testing was undertaken in the winter of 1991-92 to establish a reliable means of determining enthalpies without taking wells off-line.

Comparative Test Results for Coso

Propane and potassium fluoride tracers were injected into the two-phase flow lines of three wells at Coso according to the procedures described above. One well produced fairly low enthalpy fluids (900-950 kJ/kg) and the other two produced higher enthalpy fluids in the 1400 to 1900 kJ/kg range. The tests were conducted over intervals of 2 to 3 hours to document the ability of each method to track short term trends in flowrate and enthalpy. The wells were diverted from plant production to the James tube and silencer/weir box facility located on each wellpad and allowed to stabilize before starting the comparative tests. In at least one case the wellhead pressure varied sufficiently after flow diversion to cause a substantial change in the normal discharge characteristics of the well. The wellhead pressure, James tube lip pressure and weir box liquid level were recorded every 10 to 15 minutes during the tests. The distributed computer control system (DCS) for the well field also recorded the upstream orifice pressure, temperature and the differential orifice pressure from the two-phase flow line continuously.

Table 1.0 summarizes the results of these initial tests at Coso. The total flowrate and enthalpy measurements for the lower enthalpy well agreed within 1.4% and 3.7%, respectively. This well produced a fairly high liquid rate of 34 kg/s with minimal flow surging during the test. The differences in total flowrate for the higher enthalpy wells were 5.5% to 25% and the enthalpy differences were 12% to 14%. These wells produced low liquid rates, 8.5 to 15 kg/s, and the discharge from well C-3 surged at regular intervals during the test, with liquid rate variations of ±50%.

The flowrate, enthalpy and differential pressure trends obtained from the C-3 well test are plotted in Diagram 1.0. As shown, variations in total flowrate correlate between the tracer and James tube techniques, and rate peaks correspond to orifice plate differential pressure spikes. A slight delay in the maximums is indicated for the James tube rates relative to the tracer rates. The James tube and weir box are at the very end of the two-phase flow line, while the tracer measurements represent flow conditions within approximately the mid-section of the line. The James tube results do not exhibit the same

Table 1.0 COSO TRACER DILUTION TEST SUMMARY

Comparison of Tracer Results to James Tube Measurements

Well Name	TOTAL FLOWRATE, kg/s			TOTAL ENTHALPY, kJ/kg			COMMENTS
	James Tube	Tracer Test	Δ %	James Tube	Tracer Test	Δ %	
C-1	36.9	37.4	1.4	949	914	-3.7	High Liquid Rate, Stable Flowrates
C-2	20.9	26.8	25	1870	1630	-14	Low Liquid Rate, Variable Lip Pressure
C-3	14.1	13.4	-5.5	1588	1402	-12	Low Liquid Rate, Low Lip Pressure, Flow Surging

Diagram 1

Well C-3
Enthalpy and Flowrate Trends

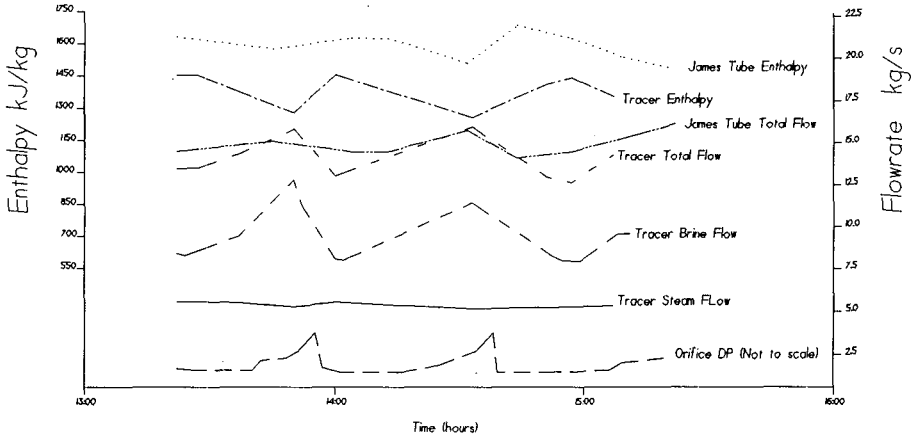

amplitude of variation as the tracer results, which is most likely due to the buffering effect of the large cyclone silencer that drains to the weir box.

The differences between the two methods observed for the low liquid rate wells do not appear to be the result of any systematic error in the tracer technique. Tracer injection rates were varied by up to 100% during these tests, producing consistent flowrate and enthalpy values in the final calculations, which demonstrates a lack of dependence on tracer to liquid or steam ratios. Sampling bias due to low liquid rates was also eliminated as a possible cause; well C-3 liquid was collected from a sampling separator, but the other high enthalpy well (C-2) was sampled directly from the weir box due to a lack of sample ports. Adequate mixing of tracers in the two-phase flow stream was insured by the exceptionally long mixing runs between tracer injection and sample collection points for the low liquid rate wells tested (84 to 90 meters).

However, the James tube results rely on weir box liquid levels for the liquid flowrate measurement, which can easily be in error by up to ± 20 % due to flow surges, scale reading error, and errors in the zero value for the level. These errors are accentuated by low liquid flowrates. Other problems noted for the low liquid rate wells were variable lip pressures for C-2 and low lip pressure readings for C-3.

The results of the initial enthalpy tracer tests were encouraging enough to warrant additional testing against an enthalpy and flowrate standard more reliable than the James tube method, such as the individual production separators and orifice meters in use at the Roosevelt Hot Springs geothermal field. This comparison is described in the following section.

Roosevelt Hot Springs

The geothermal field at Roosevelt Hot Springs is similar to Coso in that it produces two-phase fluids from fractured, crystalline rock. Productive depths range from about 500 to 1,650 meters, and reservoir temperatures are in the range of 230 to 260°C. Commercial production began in 1984. Currently, four production wells supply steam to a single-flash 25 MW power plant. Flowrates per well are in the range of 75 to 125 kg/s, with enthalpies of approximately 1,070 kJ/kg. The production wells were drilled with a spacing of roughly 400 meters. Because of the distance between the wells, the gathering system was constructed with dedicated separators for each well. This afforded an opportunity to test the tracer dilution technique on individual wells with reference to single-phase measurements downstream of the separators.

Comparative Test Results for Roosevelt

Tracer enthalpy testing was conducted at the Roosevelt geothermal field in April 1992, during normal production of the three wells in service. Propane and potassium fluoride tracers were also used for these tests, but a higher capacity metering pump and gas mass flow controller were required to inject sufficient tracer into the generally larger production wells at Roosevelt. The tracers were injected over 2 to 4 hour periods while samples were collected from sampling separators upstream of the production separators, and downstream of the separators from the single phase liquid and steam lines. Production separator pressures, liquid levels and orifice plate differential pressures for steam and liquid were recorded both manually at 20 minute intervals and continuously by the DCS. Minimal flow surging was experienced during these tests.

Table 2.0 ROOSEVELT TRACER DILUTION TEST SUMMARY

PRODUCTION SEPARATOR TRACER RESULTS VERSUS ORIFICE MEASUREMENTS

Well Name	STEAM FLOWRATE, kg/s			LIQUID FLOWRATE, kg/s			TOTAL ENTHALPY, kJ/kg		
	Orifice	Tracer	Δ%	Orifice	Tracer	Δ%	Orifice	Tracer	Δ %
R-1	20.2	20.8	3.08	103	103	0.12	1072	1079	0.65
R-2	18.1	17.8	-2.11	94.3	98.0	3.80	1065	1049	-1.54
R-3	11.8	11.6	-1.93	61.5	60.8	-1.03	1065	1063	-0.22

SAMPLING SEPARATOR TRACER RESULTS VERSUS ORIFICE MEASUREMENTS

Well Name	STEAM FLOWRATE, kg/s			LIQUID FLOWRATE, kg/s		
	Orifice	Tracer	Δ%	Orifice	Tracer	Δ%
R-1	20.2	(1)	–	103	105	2.17%
R-2	18.1	(1)	–	94.3	97.6	3.41%
R-3	11.8	13.2[2]	11%	61.5	149[2]	83%

(1) Adequate steam samples could not be obtained due to improper sample port orientation.

(2) Incomplete mixing of tracer due to short section of pipe between injection and sampling point: 7 meters

Table 2.0 summarizes the Roosevelt comparative test results for steam flowrate, liquid flowrate and total enthalpy. As shown in the comparison of tracer results for samples collected downstream of the production separator, the greatest deviation for any of these parameters was a 3.8% difference in liquid flowrate for well R-2. Sampling upstream of the production separator from the two-phase line was limited by the availability of sample ports in the proper locations and orientations. Adequate steam samples could not be obtained from the two-phase lines of wells R-1 and R-2, which lacked top sample ports for the steam separator. The liquid samples collected from the two-phase lines of these wells generated liquid rate results within 3.4% of the orifice meter values.

The two-phase line for well R-3 was only 7 meters long between the tracer injection point and two-phase sample point, while the mixing runs for wells R-1 and R-2 were 140 to 150 meters long. For this reason, the liquid-phase tracer obviously had not mixed sufficiently, producing an 83% deviation in the sampling separator results for the liquid flowrate of well R-3. However, the steam rate was only in error by 11% given the same mixing run length. The steam phase is fully developed turbulent flow, dispersing the vapor-phase tracer much faster than the liquid-phase tracer which is constrained by the slug flow regime that exists in the two-phase lines of these wells.

Based on the excellent agreement generally observed between the tracer dilution and orifice meter flowrate and enthalpy determinations, tracer dilution was considered a valid measurement technique to be applied routinely at the Coso geothermal field, as well as other geothermal fields where needed.

Fieldwide Enthalpy Testing at Coso

In order to implement the tracer dilution technique on a fieldwide basis at Coso, approximately 120 sample and tracer injection ports had to be installed on two-phase lines throughout the well field. It was determined that port and valve installation by the hot-tap process was less expensive and more expedient than taking wells off-line and isolating the flow lines for the installation procedure. A tracer injection trailer unit outfitted with metering pumps, electronic balance, computer, gas mass-flow controller, generator, gas cylinder racks, and a 750 liter storage tank was fabricated by Thermochem for this application. Tracer storage facilities and chemical mixing equipment to prepare the liquid-phase tracer are also maintained on-site at Coso.

A total of 75 enthalpy tracer tests have been performed to date in Coso on wells ranging in enthalpy from 840 to 2760 kJ/kg. The first fieldwide test was performed with potassium fluoride as the liquid-tracer. Sodium bromide was later substituted for potassium fluoride after fluorite precipitation was observed during tracer tests conducted in wellbores at reservoir temperatures. During these tests, tracer was injected through the downhole scale inhibitor tubing of some wells at Coso to test for inhibitor recovery back up the wellbore, in an effort to optimize the tube setting depth (Lovekin, 1990). The fluoride loss was detected by comparing the recovery of fluoride ion to potassium ion during the down-hole tests where potassium fluoride tracer was injected. Similar comparisons performed for surface enthalpy tests did not indicate any significant loss of fluoride. In order to eliminate any potential for precipitation during downhole recovery or surface enthalpy tests, sodium bromide is now used as the routine liquid-phase tracer at Coso.

The results of the fieldwide enthalpy tests are generally consistent with the historical James tube results for the wells at Coso. However, many wells had not been tested by the James tube method for six months or more, making it difficult to compare results directly in a field where enthalpies can change over short time spans due to processes such as reservoir boiling, wellbore scaling and injection breakthrough. The enthalpy tracer results have

Table 3.0 REPEATABILITY OF TRACER DILUTION ENTHALPY MEASUREMENTS

Well Name	Test Date	Liquid Phase Tracer	Total Enthalpy, kJ/kg	% RSD
C-5	10/20/92	Fluoride	1267	
	11/08/92	Fluoride	1256	0.6
C-9	10/23/92	Fluoride	2349	
	12/18/92	Bromide	2404	1.6
C-10	10/06/92	Fluoride	988	
	10/06/92	Potassium	1011	
	11/07/92	Bromide	1017	1.5

been internally consistent and repeatable. This is demonstrated by the results summarized in Table 3.0 for all repeat tests performed on wells not known to be subject to any of the processes described above that would change the enthalpy between tests. These repeatability results are also based on various liquid-phase tracers: fluoride, bromide and potassium.

Tracer mixing efficiency studies have also been performed during enthalpy testing at Coso. The degree of uniform tracer dispersion within the liquid-phase can be evaluated by collecting liquid samples from sampling separators attached to both the bottom and top ports of the two-phase flow line. Since the bulk of the liquid-phase flows along the bottom of the pipeline, uniform dispersion can be assumed if equivalent tracer concentrations are obtained from the top of the pipeline where liquid is present as the upper crests of wave and slug flow or as annular films. Table 4.0 lists the results of these tests by comparing the liquid-tracer concentrations and derived liquid flowrates for liquid samples collected simultaneously from the bottom and top ports.

In the first case shown in Table 4.0 for well C-4, two sets of bottom and top samples were collected from different points along the pipeline. Upstream of the control valve, after a 38 meter mixing run, the first set shows the greatest difference, 9.4% between flowrates calculated from bottom and top samples. Downstream of the control valve, 58 meters downstream of injection, the bottom versus top derived flowrates differ by only 3.3%. All other tests were conducted on wells with very short mixing runs, 18 to 22 meters long, where the sample ports are downstream of the flow control valve. The greatest deviations are for wells producing high liquid rates (>35 kg/s), with a maximum difference between top and bottom ports of 5.4% for well C-6. This well produces fluid at significantly higher velocities and under a more turbulent two-phase flow regime than well C-5. However, C-5 exhibits essentially perfect mixing, and only produces about 1/5 the liquid of C-6 under a nearly stratified two-phase flow regime. The degree of tracer dispersion within the liquid-phase appears to be more dependent on the total liquid mass than the velocity and the two-phase flow regime under the conditions encountered. Still, sampling downstream of the flow control valve, as is routinely done, seems to provide adequate mixing of the liquid-phase tracer.

Additional mixing data for well C-5 is given in Table 5.0 as a function of mixing run length. The liquid rate derived from samples collected upstream of the flow control valve and only 12 meters downstream of injection is within 1.8% of the rate calculated for the normal downstream sample port. The furthest upstream port, only 3 meters after injection, produced a liquid rate value

Table 4.0 LIQUID PHASE TRACER MIXING EVALUATION

Bottom versus Top Sample Ports

Well Name	*BOTTOM PORT* Liquid, kg/s	*TOP PORT* Liquid, kg/s	Δ %	Mixing Run, m	Two-Phase Flow Regime
C-4	58.6	64.4	9.43	38	Slug Flow
C-4	60.5	62.5	3.28	58(1)	Slug Flow
C-5	11.3	11.4	0.89	18(1)	Wave to Slug Flow
C-6	52.8	50.0	-5.39	18(1)	Slug to Annular Flow
C-7	7.85	7.71	-1.78	18(1)	Annular to Annular Mist Flow
C-8	35.9	37.7	4.79	22(1)	Slug Flow

(1) Flow control valve upstream of sample point

Table 5.0 **TRACER MIXING EVALUATION**

WELL C-5

Sample Port Location	Mixing Run, m	*LIQUID PHASE* Tracer ppm_w	Flow, kg/s	Δ%[1]	*STEAM PHASE* Tracer ppm_w	Flow, kg/s	Δ%[1]
Downstream	18[2]	129	11.3	0	1.20	3.89	0
Midstream	12	131	11.1	-1.8	(3)	(3)	-
Upstream	3	228	6.29	-44	1.37	3.40	-13

(1) **Percent difference relative to downstream port**

(2) **Flow control valve upstream of sample point**

(3) ***No midstream port available for steam samples***

differing by 44% from the downstream rate. Steam samples also collected 3 meters after injection were in error by only 13%, demonstrating the rapid dispersion of gas-tracer in the vapor-phase.

A statistical error analysis for the tracer dilution technique was performed based on the known limits of error for the tracer injection rate, the analytical error which incorporates any error associated with the tracer concentration, and estimated errors attributed to tracer mixing and sample collection. The tracer injection rates are determined by instruments that are regularly calibrated against primary standards traceable to the National Bureau of Standards (NBS). The sampling and mixing errors are estimated from the mixing analyses discussed above and comparisons of samples collected from sampling separators versus full production separators during chemical testing performed by Thermochem in several geothermal fields. The sampling and mixing errors probably represent worst case values, since the mixing analyses include sampling error associated with liquid sample collection from the top pipeline ports, where representative liquid samples can be difficult to collect. The analytical error includes any uncertainty in tracer concentrations: the gas-tracer is actually used as the analytical standard for gas samples, and the liquid-tracer concentration is determined relative to the same standards and procedures as liquid samples. This analysis yields a cumulative error limit of 4.3% for steam flowrate, 6.5% for liquid flowrate, and 3.4% for total enthalpy, as summarized in Table 6.0.

Further Work

Additional work will be performed in determining the minimum pipeline configuration requirements for tracer dispersion under various flow conditions. Correlation of tracer-based flowrate measurements to differential pressure data from orifice meters in two-phase service can now be performed extensively at Coso to improve the accuracy of two-phase orifice meters in measuring total flowrates of known enthalpy. Development of real-time tracer measurement systems would also be useful in applications requiring continuous enthalpy and flowrate determinations.

Conclusions

Based on the comparative enthalpy testing in Roosevelt and the fieldwide testing performed in Coso, the tracer dilution technique is considered an accurate and cost effective well testing procedure for both the discharge rate of steam and liquid and the total enthalpy of two-phase flow. This technique eliminates the need for dedicated production separators for each well in new geothermal fluid gathering systems and the installation of test separators to existing systems. The tracer dilution

Table 6.0 **TRACER DILUTION TECHNIQUE ERROR ANALYSIS**

STEAM PHASE						
Gas Tracer Concentration	Calibration	Gas Tracer Injection Rate	Calibration	Sampling and Mixing Error	Analytical Error	Cumulative Error Steam Flowrate
±2.0%	NBS Traceable Gravimetric	±1.5%	NBS Traceable Liquid Film Flowmeter	±2.0%	±2.0%	±4.3%

LIQUID PHASE						
Liquid Tracer Concentration	Calibration	Liquid Tracer Injection Rate	Calibration	Sampling and Mixing Error	Analytical Error	Cumulative Error Liquid Flowrate
±1.0%	NBS Traceable Gravimetric	±0.5%	NBS Traceable Weight Standards	±5.0%	±1.0%	±6.7%

Cumulative Error Total Enthalpy	±3.4%

method is also applicable to short term well tests in new geothermal fields, precluding the need for fabrication of large test mufflers for liquid separation and measurement. This method may be employed to calibrate existing and/or experimental single and dual-phase flow measurement devices.

Acknowledgments

The authors wish to express their appreciation to California Energy Company and to the Geothermal Program Office of the China Lake Naval Air Weapons Station for permission to publish this paper. We also wish to thank Russell Kunzman, Paul Speilman and Elliott Bell for their assistance with the field testing and data reduction, and Shirlee Johnson and Sophia White for their part in analyzing hundreds of tracer samples.

References

Adams, M. C., Moore, J. N., Fabry, L. G., and Ahn, J. (1992); "Thermal Stabilities of Aromatic Acids as Geothermal Tracers", Geothermics, Vol. 21, No. 3, pp. 323-339, 1992.

Adams, M. C., Moore, J. N., and Hirtz, P. N. (1991); "Preliminary Assessment of Halogenated Alkanes as Vapor-Phase Tracers", Proceedings, Sixteenth Workshop on Geothermal Reservoir Engineering, Stanford Geothermal Program, Stanford, CA, Workshop Report No. SEP-TR-134, pp. 57-62.

ASTM Sub-Committee E-44, "Standard Practice for Sampling Two-Phase Geothermal Fluid for Purposes of Chemical Analysis", in committee review.

Ferrer, H. P. (1992); Personal communication, PNOC-Energy Development Corp., Geothermal Division, Metro Manila, Philippines.

Fournier, R. O., and Potter II, R. W. (1982); "A Revised and Expanded Silica (Quartz) Geothermometer", Geothermal Resources Council Bulletin, Vol. 11, No. 10, pp. 3-12.

Grant, M.A., Donaldson, I.G., and Bixley, P.F. (1982); Geothermal Reservoir Engineering, Academic Press, San Francisco, pp. 118-119.

Hirtz, P. N., Buck, C. L., and Kunzman, R. J. (1991); "Current Techniques in Acid-Chloride Corrosion Control and Monitoring at The Geysers", Proceedings, Sixteenth Workshop on Geothermal Reservoir Engineering., Stanford Geothermal Program, Stanford, CA, Workshop Report SGP-TR-134, pp. 83-95.

Hirtz, P. N., Mac Phee, T. D. (1989); "Development of a Safer and More Efficient Method for Abatement of H_2S during Geothermal Well Drilling", Geothermal Resources Council, Transactions, Vol. 13, pp. 403-407.

James, R. (1970); "Factors Controlling Borehole Performance", U.N. Symposium on the Development and Use of Geothermal Resources, Geothermics, Vol. 2, pp. 1502-1515.

Kaspereit, D.H. (1990); "Enthalpy Determination Using Flowing Pressure-Temperature Surveys in Two-Phase Wellbores in the Coso Geothermal Field", Geothermal Resources Council Transactions, Vol. 14, Part II, pp. 1211-1218.

Lazalde-Crabtree, H. (1984); "Design for Approach of Steam-Water Separators and Steam Dryers for Geothermal Applications", Geothermal Resources Council Bulletin, Vol. 13, No. 8, pp. 11-20.

Lovekin, J., (1990); "Control of Calcium Carbonate Scale Using Concentric Tubing", Geothermal Resources Council, Transactions, Vol. 14, Part II, Aug. 1990.

Mahon, W.A.J. (1966); "A Method for Determining the Enthalpy of a Steam/Water Mixture Discharged from a Geothermal Drillhole", New Zealand Journal of Science, Vol. 9, pp. 791-800.

Marini, L., and Cioni, R. (1985). "A Chloride Method for the Determination of the Enthalpy of Steam/Water Mixtures Discharged from Geothermal Wells", Geothermics, Vol. 14, No. 1, pp. 29-34.

Shen, J. (1992); "Measurement of Fluid Properties of Two-phase Fluids Using an Ultrasonic Meter", United States Patent No. 5,115,670.

Woiceshyn, G.E., Yuen, P.S., John, H. and Manzano-Ruis, J.J. (1986). "Measurement of Steam Quality, Mass Flowrate, and Enthalpy Delivery Rate Using Combined Neutron Densitometer and Nozzle", SPE/DOE Paper 14907, Fifth Symposium on Enhanced Oil Recovery.

PROCEEDINGS, Eighteenth Workshop on Geothermal Reservoir Engineering
Stanford University, Stanford, California, January 26-28, 1993
SGP-TR-145

REVIEW OF RECENT DEVELOPMENT OF THE KAKKONDA DEEP RESERVOIR, JAPAN

Mineyuki Hanano and Morihiko Takanohashi

JMC Geothermal Research and Development Co., Ltd.
72-2 Sasamori, Ukai, Takizawa-mura, Iwate 020-01, Japan

Abstract

There are two reservoirs with different temperature and permeability in the Kakkonda hydrothermal system. The shallow reservoir is permeable and 230 to 260°C, while the deep reservoir is less permeable and 350 to 360°C. However, they are hydraulically connected each other. Recent drilling of deep wells revealed existence of Pre-Tertiary formation below Tertiary formations and neo-granitic pluton younger than 5Ma. This pluton is a heat source of metamorphism found in Pre-Tertiary and Tertiary formations. There is a permeable horizon at the top of the pluton, and is very productive. To date, 4 production wells have been completed in this deep reservoir.

INTRODUCTION

The Kakkonda (Takinoue) geothermal field is located about 600km northeast of Tokyo (Fig.1) and is one of the most active liquid-dominated geothermal fields in Japan. The first power plant, Kakkonda Unit1, 50MWe, has been in operation since 1978 by Tohoku Electric Power Inc. (TEP), where Japan Metals and Chemicals Co., Ltd. (JMC) is a steam supplier. Currently, development for the Kakkonda Unit2, 30MWe, is being continued by Tohoku Geothermal Energy Co., Ltd. (TGE), a joint venture led by JMC. Its power generation is expected to start in 1996 by TEP. In the course of this development, JMC Geothermal Research and Development Co., Ltd. (JMCD), a geothermal development operator fully owned by JMC, has been in charge of exploration, drilling, reservoir engineering studies and fundamental studies.

Before the start of the development for the Kakkonda Unit2, the reservoir shallower than 1,500m has been developed. However, due to the limited horizontal extent of the reservoir, it has become necessary to develop a deeper reservoir than 1,500m for both Unit1 and Unit2. Thus, a deep exploration well KT-208 (T.D. 2,126m) was drilled in 1985 and revealed geological and thermal characteristics of the deep reservoir. Then, the production well K6-2 (T.D. 2,818m) was drilled in 1989 and confirmed that the Kakkonda deep reservoir was very productive. Geological information from these deep wells revealed existence of Pre-Tertiary formation below Tertiary formations, neo-granitic pluton, and thermal metamorphic rocks created by the neo-granitic pluton.

These results encouraged the development of the Kakkonda deep reservoir. To date, 4 deep production wells (1 for Unit1 and 3 for Unit2) were completed without any trouble. In this report, we summarize outline of the development, hydrothermal characteristics and conceptual model of the Kakkonda deep reservoir.

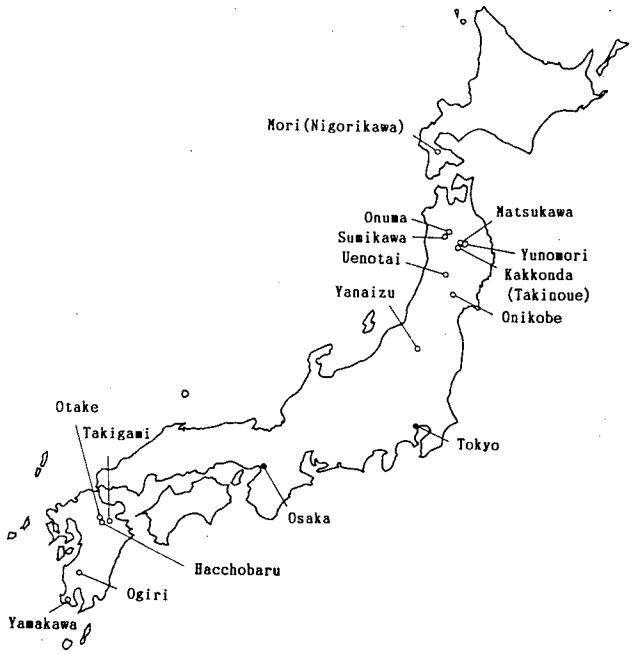

Fig.1 Location of the Kakkonda geothermal field

OUTLINE OF THE DEVELOPMENT

Geothermal exploration in the Kakkonda area was started in 1958 by JMC in cooperation with Geological Survey of Japan. Exploration and development for the Kakkonda Unit1 was described by Nakamura and Sumi (1981) and Sato (1982). Its power generation was started in 1978 at the output of 50MWe, but it gradually decreased due to unexpectedly fast return of reinjected fluid (Nakamura, 1981; Horne, 1982). However, it was not necessarily avoidable, because of the lack of understanding of detailed three-dimensional permeability distribution and the lack of sufficient drilling pads especially for reinjection. Since Kakkonda is at the bottom of a steep valley and included in a national park, the geothermal development was restricted by the difficulty of finding flat land for drilling pads and getting permission for its use. Subsequently, the output was recovered to 45MWe in average, by offsetting reinjection wells to southeast and production wells to northwest. To relocate these wells, we employed a number of tracer tests and a three-dimensional history matching study with a double-porosity reservoir model (Nakamura, 1986).

Depth of production wells for the Kakkonda Unit1 ranged from 1,000m to 1,500m before the start of the development for the Kakkonda Unit2. However, we had been looking for possibilities of development of a reservoir of different depth. Thus, based on the following facts confirmed by existing wells, we thought development of the deep hot reservoir was feasible;

1) In-flow of very hot fluid of more than 300°C at the

bottom of some wells of 1,500m depth, was confirmed though its rate was very small.
2) Some wells showed abrupt increase in bore hole temperature at around the bottom (Fig.2). This suggested that there was a very slow hydrothermal convection in great depth though its permeability was very low.
3) Micro-earthquakes existed below -2km sea level suggesting existence of fractures at such depth.
4) Distribution of the thermal metamorphic minerals suggested that its heat source such as neo-granitic pluton was not very far from the developed zone.
5) Results of interpretation of chemical data and the three dimensional history matching study suggested that there should have been small amount of in-flow of hot fluid into the shallow reservoir from the deep reservoir.

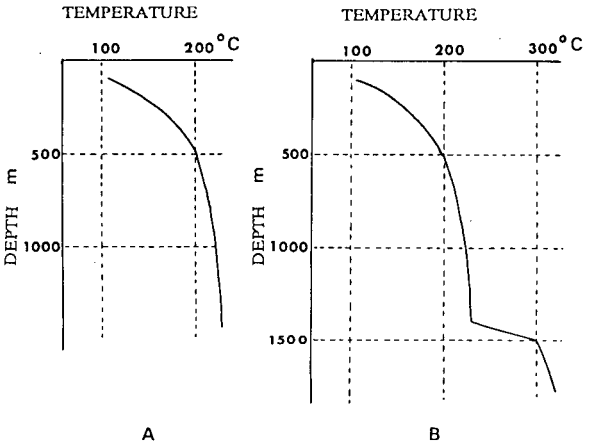

Fig.2 Schematic temperature profiles of the shallow wells (after Kasai et al., 1990). A: Ordinary shallow reservoir wells. B: Wells touched top of the deep reservoir.

The exploration well KT-208 was drilled during 1985 and 1986. From the results of this well (Fig.3), the deep reservoir of totally different hydrothermal characteristics, i.e. temperature and permeability, was confirmed to exist below approximately 1,500m (e.g. Doi et al., 1988). Production test of this KT-208 was tried in 1989. It was successful and confirmed that the deep reservoir was productive enough for commercial geothermal development, because of high pressure and high enthalpy, though its permeability was very low.

To develop this deep reservoir for the Kakkonda Unit2, the first deep production well K6-2, which targeted this deep reservoir, was drilled in 1989. Drilling of this K6-2 was described by Saito (1991; 1992). K6-2 first targeted 3,000m depth, but it encountered fractured zone at around 2,800m. It produces 63t/h of steam and 57t/h of hot water. This drilling revealed existence of Pre-Tertiary formation from 2,167m depth, neo-granitic pluton form 2,778m depth, and productive fractures of more than 300°C in the Pre-Tertiary formation and upper boundary of the neo-granitic pluton (Fig.4).

In 1990, K1-3 (T.D. 2,465m), the second deep production well for the Unit2, was successfully drilled. It encountered neo-granitic pluton exactly at the expected depth (2,344.5 to 2,463.4m) and confirmed horizontal extent of the deep reservoir. K1-3 produces 92t/h of steam and very small amount of hot water.

In 1992, K6-3 (T.D. 3,000m), the third deep production well for the Unit2, was also successfully drilled. It encountered neo-granitic pluton at 2,832m exactly as expected. We tentatively confirmed by early production test, that K6-3 produced more than 100t/h of steam and almost the same amount of hot water.

GEOLOGICAL OUTLINE OF THE KAKKONDA DEEP RESERVOIR

Geology of the Kakkonda shallow reservoir has been described by Sato (1982) and Doi et al. (1988). Based on Doi et al. (1991) and Kato et al. (1993), we summarize geological characteristics of the Kakkonda deep reservoir. Schematic geologic sequence at the Kakkonda geothermal field is shown in Fig.5.

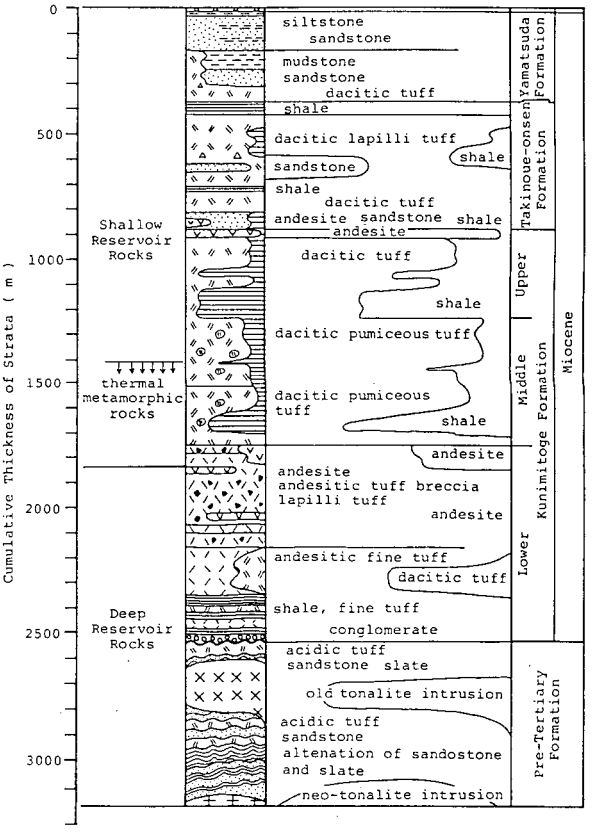

Fig.5 Schematic geologic sequence at the Kakkonda (after Kato et al., 1993).

Based on core samples taken at K6-2, the neo-granitic pluton is not metamorphosed and its alteration is very weak. It has texture of the shallow intrusion and consists of quartz, plagioclase, potassium feldspar, biotite, hornblende, cummingtonite, clinopyroxene and orthopyroxene.

Metamorphic minerals were found in depths deeper than 1,006m. They are in Pre-Tertiary formation, Tertiary formation (Kunimitoge-formation) and intrusive rocks. They consists of green and brown biotite, muscovite, cordierite, anthophyllite, andalusite, hastingsite, cummingtonite, tremolite, pyrrhotite and magnetite. This metamorphism is more notable at depth, and texture of its original rock is sometimes lost at depths deeper than 2,500m. The horizontal area of this metamorphism ranges 2.0 x 2.5km. Accounting for the extent of this metamorphism and the neo-granitic pluton,

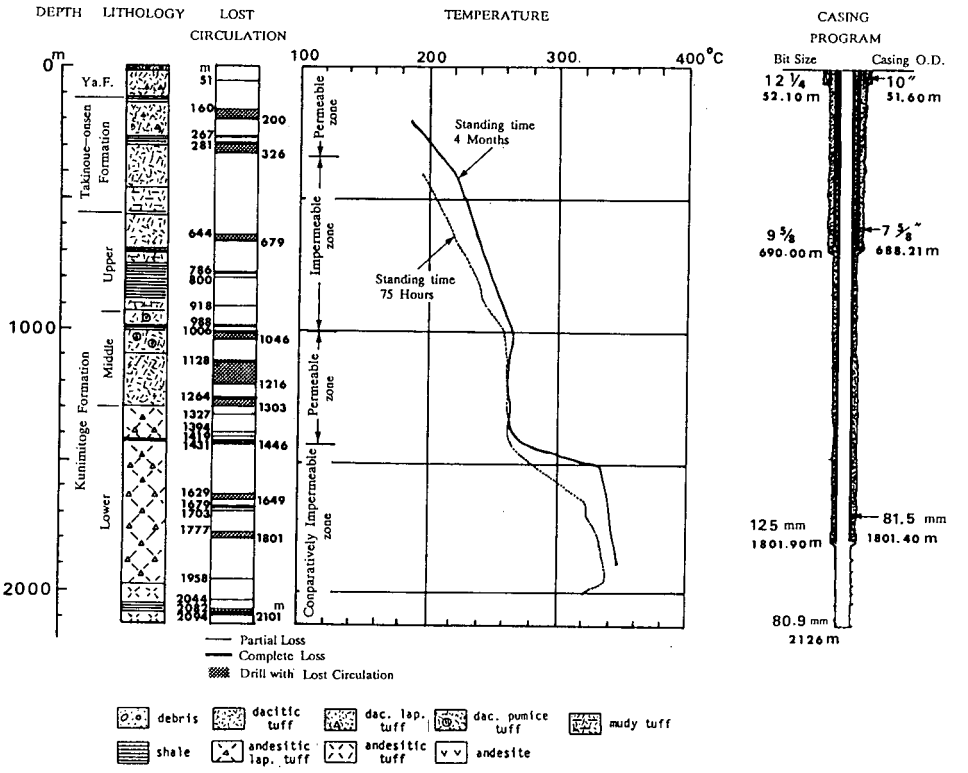

Fig.3 Geologic column and logging data of KT-208 (modified from Doi et al., 1988).

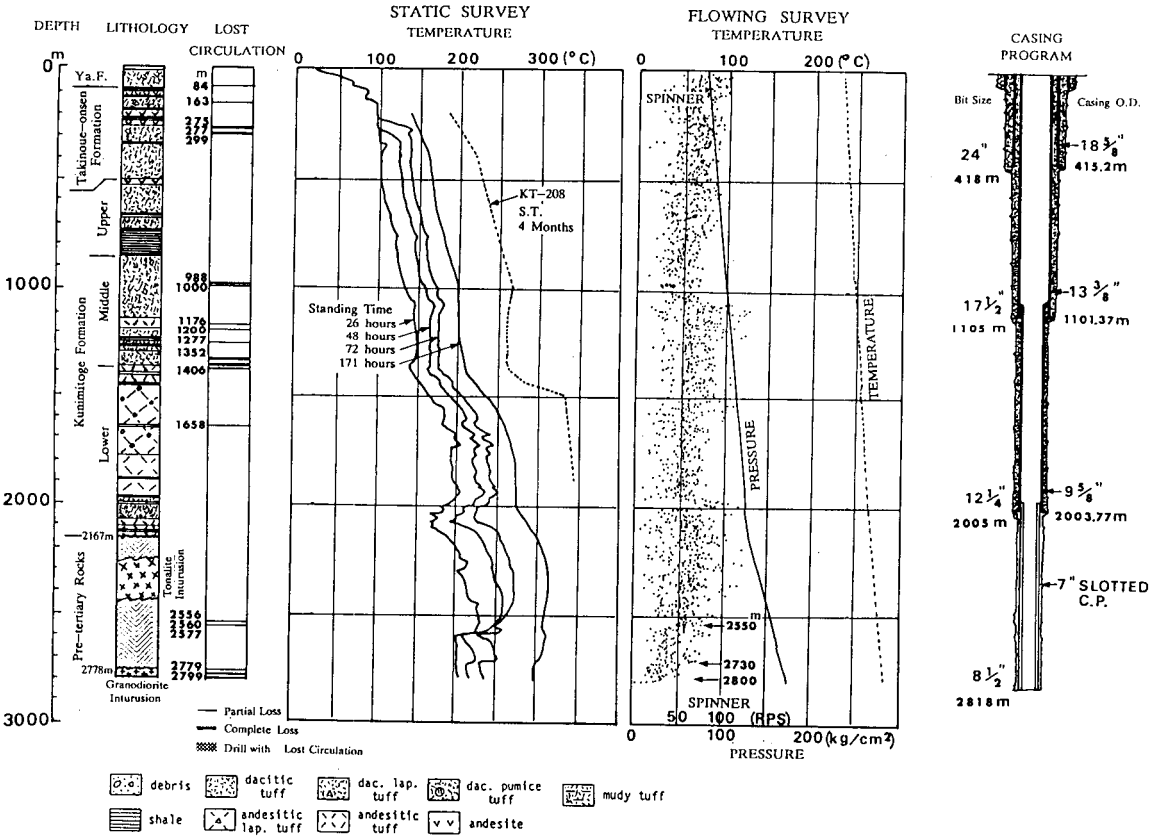

Fig.4 Geologic column and logging data of K6-2

and characteristics of the neo-granitic pluton as described above, it is clear that heat source of this metamorphism is the neo-granitic pluton. On the other hand, the latest rock which was metamorphosed is a dacite dike of 5Ma (Tamanyu, 1980). Thus, the neo-granitic pluton is younger than 5Ma.

The biotite was found at 19 wells and the cordierite was found at 10 wells. Vertical distance between the biotite and the neo-granitic pluton is approximately 1,000m and that between the cordierite and the pluton is approximately 700m (Fig.6). The depths of their appearance are shallower in northeast and slightly deeper in southwest. Thus, isograds of the biotite and the cordierite are good indicators of top of the neo-granitic pluton. Targets of K1-3 and K6-3 were decided based on these isograds.

The top of the neo-granitic pluton is also estimated from micro-earthquake data. The bottom of micro-earthquake distribution in Kakkonda was found to be very close to the confirmed top of the pluton (Fig.7). That is, micro-earthquakes occur in permeable zone of Tertiary and Pre-Tertiary formations but they do not occur within the neo-granitic pluton. Based on trend of the biotite and cordierite isograds, distribution pattern of deep micro-earthquakes in northwest and southeast (Fig.7) probably indicate shape of outline of the neo-granitic pluton.

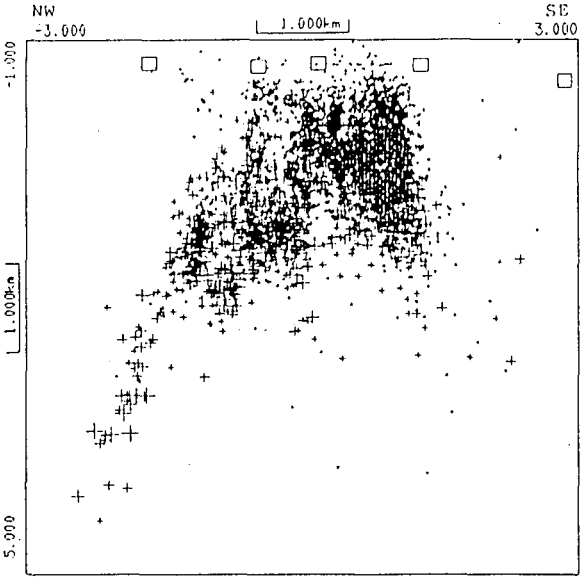

Fig.7 Northwest-southeast cross section of the micro-earthquake hypocenter distribution at Kakkonda (after Sugihara, 1991). Open squares are some of the micro-earthquake observatories.

THE KAKKONDA HYDROTHERMAL SYSTEM

Before the start of the development of the deep reservoir, the model of the Kakkonda hydrothermal system used be as follows (e.g. Sato, 1982). That is, the Kakkonda geothermal reservoir is a combination of horizontal fractures which develop at the bottom of a syncline, and vertical fractures such as faults and shear zones. Temperature profiles of wells in syncline zones are convective, while some of the southeastern wells in lower reach of the Kakkonda river show conductive profiles. Thus, there is a permeable zone with lots of fractures and hydrothermal convection in it, while there is a less permeable zone which dominates in heat conduction surrounding the permeable zone. In this permeable convection zone, high enthalpy fluid which entered from the deep zone heats meteoric-origin fluid and forms the Kakkonda shallow geothermal reservoir.

Later, static temperature of the deep wells, such as KT-208 and K6-2, were found to show abrupt increase at around 1,500m depth (Figs 3 and 4). This indicated existence of two different convection cells, thus the Kakkonda hydrothermal system was found to consist of two reservoirs with different characteristics; the shallow reservoir (shallower than approximately 1,500m) and the deep reservoir. The shallow reservoir is very permeable and 230 to 260°C, while the deep reservoir is less permeable and 350 to 360°C. Fluid flashes in the wellbore at almost all the shallow wells, but because of high enthalpy it flashes in the reservoir at the deep wells.

Reservoir pressures of these deep wells are on a line of current reservoir pressures of the shallow reservoir (Fig.8). Thus, this deep reservoir is hydraulically connected to the shallow reservoir, and responding to the exploitation of the Unit1.

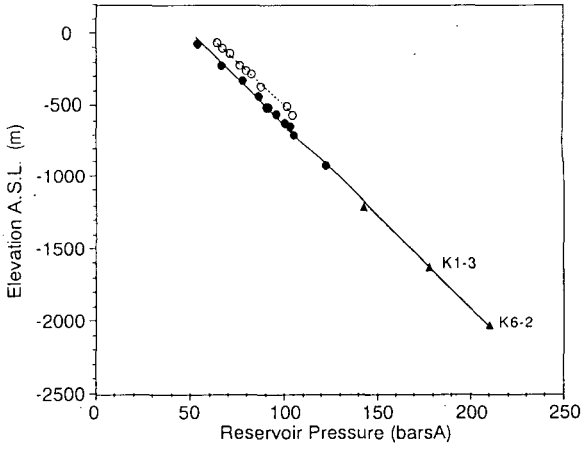

Fig.8 Reservoir pressure profile at Kakkonda. Solid circles: current data of the shallow reservoir. Solid triangles: current data of the deep reservoir. Open circles: initial data of the shallow reservoir.

Applying one-dimensional vertical advection model described by Turcotte and Schubert (1982, p.399), we analyzed temperature profiles of both shallow wells and deep wells. This result suggests that the average vertical permeability is around $10^{-14}m^2$ in the shallow reservoir but it is much lower in the deep reservoir, it is possibly around $10^{-16}m^2$. Based on the linear stability analysis (e.g. Turcotte and Schubert, 1982, p.404), this value ($10^{-16}m^2$) is very close to the minimum critical value for the onset of hydrothermal convection in the deep reservoir. Thus, the hydrothermal convection in the deep reservoir evolved upon very critical hydrothermal conditions.

However, as seen in Figs 3, 4 and 6, complete lost circulation always occurred when the wells encountered the permeable horizon in the deep reservoir, i.e. the top of the neo-granitic pluton. Thus, the permeable horizon in the deep reservoir is very permeable and its kh (permeability thickness product) was found to be order of $10^{-12}m^3$ by both single well tests and a pressure interference test. This relatively high permeability, high pressure and high enthalpy result in high productivity of

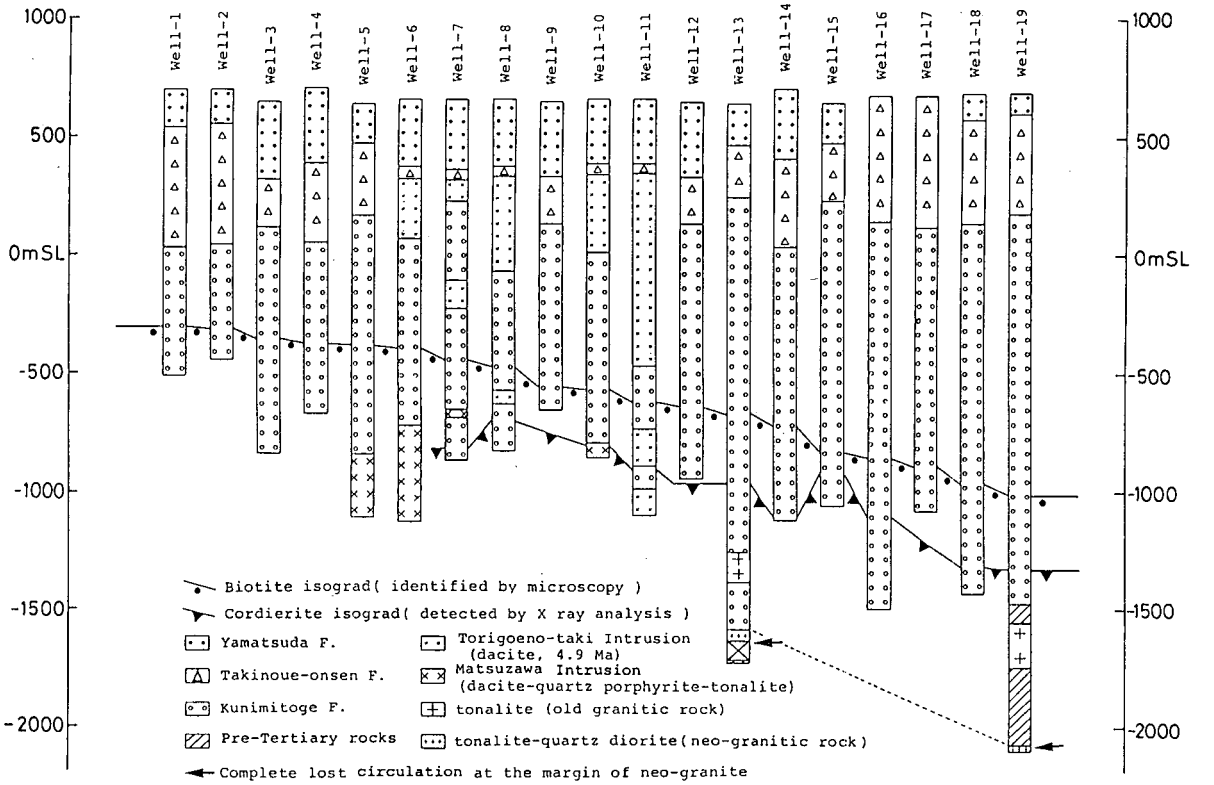

Fig.6 Distribution of metamorphic minerals in wells at Kakkonda (after Kato et al., 1993). Well-13 is K1-3, and Well-19 is K6-2.

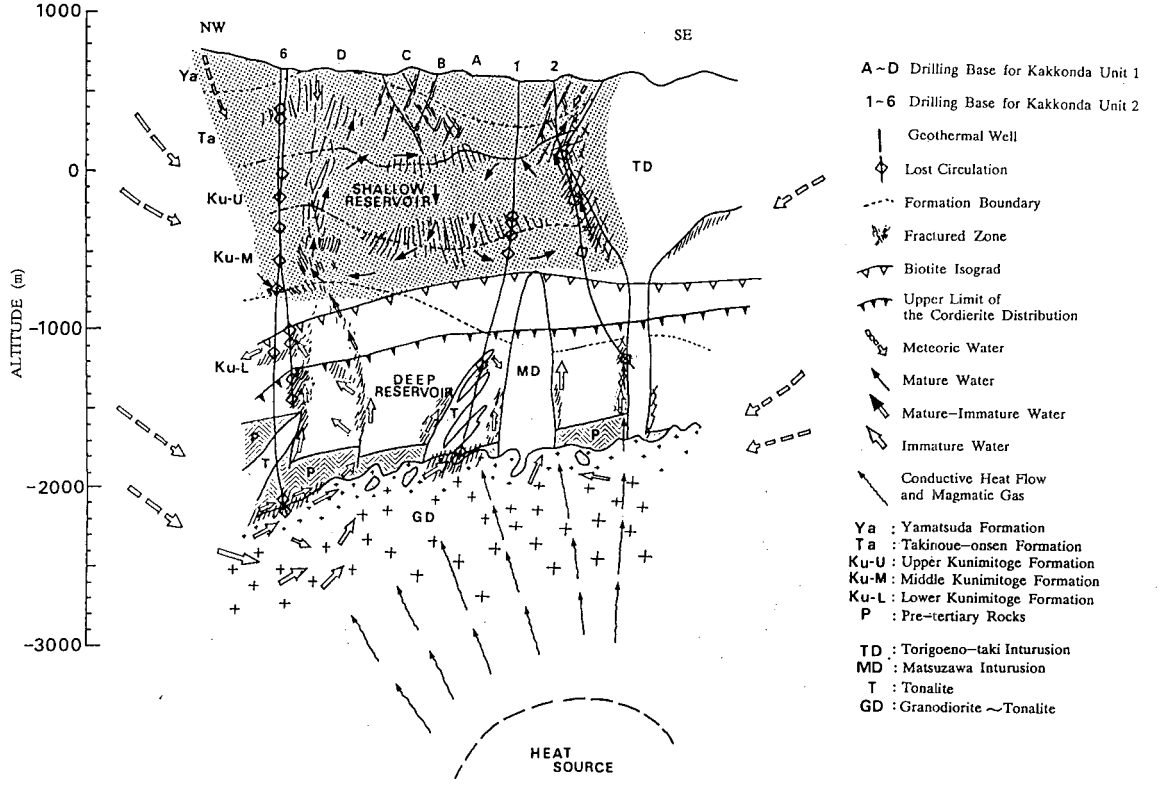

Fig.9 Conceptual model of the Kakkonda hydrothermal system.

the deep wells. The most important fractures for production in the deep reservoir are marginal ones at the top of the neo-granitic pluton and those associated with intrusion of the pluton in the Pre-Tertiary formation, but some minor fractures do exist in the Tertiary formations in the deep reservoir.

Fluid in the shallow reservoir, sampled by a Kuster tool in wells at depths deeper than flashing points, is slightly alkaline and pH is around 8 (e.g. Kasai et al., 1990). However, fluid from deep wells sampled at the well heads is rich in Cl and acid, with pH being 3.3 to 4.5. (Yanagiya, 1990). From an isotope study, this acid fluid was found to be a so-called "immature water", i.e. a mixture of meteoric water and, HCl and SO_2 contained in volcanic gas.

A conceptual model of the Kakkonda hydrothermal system based on above discussions is shown in Fig.9.

CONCLUDING REMARKS

The development of the Kakkonda deep reservoir has become promising by the success of the recent deep wells. The Kakkonda shallow reservoir has been characterized by production of large amount of hot water with steam. This raised a problem of large amount of reinjection and return of reinjected fluid into production wells. However, using deep wells which produce much less hot water than the shallow wells, we will be able to reduce amount of reinjection. This is favorable for our development. With less reinjection, we will be able to reduce rate of the temperature decrease in the shallow reservoir due to return of reinjected fluid, and will be able to continue constant power production not only at the Unit2 but also at the Unit1. Based on the distribution of the metamorphic minerals and micro-earthquakes, the neo-granitic pluton is large enough. Thus, we are planning to confirm its distribution and extent by further deep drilling.

Acknowledgments

Success of the development of the Kakkonda area is a result of efforts by a number of colleagues in Japan Metals and Chemicals Co., Ltd. (JMC), Tohoku Geothermal Energy Co., Ltd. (TGE) and its group. We would like to pay our respects to their continuing efforts. We are grateful to JMC and TGE for their permission to publish this paper. We also would like to thank Ko Sato of JMC for his review of this manuscript, and our colleagues in JMC Geothermal Research and Development Co., Ltd., especially Nobuo Doi and Yutaka Yoshida, for their discussions and suggestions.

REFERENCES

Doi, N., Kato, O. and Muramatsu, Y. (1991) On the Neo-Granitic Pluton and the Deep Geothermal Reservoir at the Kakkonda Geothermal Field, Iwate Prefecture, Japan. Paper presented at the *Geothermal Symposium on Deep Geothermal Systems with Special Reference to Neo Felsic Intrusive Bodies -Examples of the Sengan, Geysers, Tongonan and Larderello-, Nov. 1991, Geol. Surv. Jap.*, pp.9.

Doi, N., Muramatsu, Y., Chiba, Y. and Tateno, M. (1988) Geological Analysis of the Kakkonda Geothermal Reservoir. *Proc. Int. Symp. Geotherm. Energy, 1988, Kumamoto and Beppu, Japan*, pp.522-525.

Horne, R.N. (1982) Geothermal Reinjection Experience in Japan. *J. Pet. Tech.*, Vol.34, pp.495-503.

Kasai, K., Kotanaka, K. and Chiba, F. (1990) Operation and Reservoir Management of the Kakkonda Geothermal Power Station. *Chinetsu (J. Jap. Geotherm. Energy Assoc.)*, Vol.27, pp.1-22. (In Japanese with English abstract)

Kato, O., Doi, N. and Muramatsu, Y. (1993) Neo-Granitic Pluton and Geothermal Reservoir at the Kakkonda Geothermal Field, Iwate Prefecture, Japan. *J. Geotherm. Res. Soc. Jap.*, Vol.15, No.1, in press. (In Japanese with English abstract)

Nakamura, H. (1981) Development and Utilization of Geothermal Energy in Japan. *Trans. Geotherm. Resour. Counc.*, Vol.5, pp.33-35.

Nakamura, H. (1986) Flow of Hot Water in Geothermal Reservoir, Kakkonda, North-east Japan. *Proc. Int. Symp. "Geothermal Energy Development and Advanced Technology", Nov., 1986, Sendai, Japan*, pp.209-215.

Nakamura, H. and Sumi, K. (1981) Exploration and Development at Takinoue , Japan. In *Geothermal Systems* (Edited by Rybach, L. and Muffler, L.J.P.), pp.247-272. Wiley.

Saito, S. (1991) Recent Geothermal Well Drilling Technologies in Kakkonda and Matsukawa, Japan. *Geotherm. Resour. Counc. Bull.*, Vol.20, pp.166-175.

Saito, S. (1992) The Drilling Experience of K6-2, the High-Temperature and Crooked Geothermal Well in Kakkonda, Japan. In *Drilling Technology, PD-Vol.40* (Edited by Vikram Rao, M. and Rowley, J.C.), pp.151-158. Am. Soc. Mech. Eng.

Sato, K. (1982) Analysis of Geological Structure in the Takinoue Geothermal Area. *J. Geotherm. Res. Soc. Jap.*, Vol.3, pp.135-148.

Sugihara, M. (1991) Geophysical Model of the Sengan -Microearthquake Study of the Kakkonda Geothermal Area-. Paper presented at the *Geothermal Symposium on Deep Geothermal Systems with Special Reference to Neo Felsic Intrusive Bodies -Examples of the Sengan, Geysers, Tongonan and Larderello-, Nov. 1991, Geol. Surv. Jap.*, pp.5.

Tamanyu, S. (1980) Radiometric Dating of Igneous Rocks in the Sengan Area. In *Research on Hydrothermal System, Interim Rpt. Japan's Sun-Shine Project, FY1978-1979, Geol. Surv. Jap.*, pp.15-23. (In Japanese)

Turcotte, D.L. and Schubert, G. (1982) *Geodynamics*, Wiley.

Yanagiya, S. (1990) Chemistry of Deep Geothermal Fluid at Kakkonda. *Abstract, 43rd Annual Meeting of the Balneological Society of Jap.*, pp.20. (In Japanese)

PROCEEDINGS, Eighteenth Workshop on Geothermal Reservoir Engineering
Stanford University, Stanford, California, January 26-28, 1993
SGP-TR-145

GEOCHEMICAL STUDIES OF RESERVOIR PROCESSES IN THE NCPA FIELD OF THE GEYSERS A PRELIMINARY REPORT

Alfred Truesdell*, Steve Enedy**, and Bill Smith**

*Consultant, Menlo Park, California
**No. California Power Agency, Middletown, California

INTRODUCTION

A nearly-fieldwide accelerated decline in pressure and steam production occurred at The Geysers in the late 1980s. As a result of this crisis, the U. S. Dept. of Energy has begun a program to examine the reservoir processes at The Geysers in greater detail, with particular attention to understanding the sources of steam and gas and predicting changes in pressure, steam flow and gas content. As part of that program the Lawrence Berkeley Laboratory is supporting the study of the chemical composition of steam, and is modelling processes that affect the composition as well as the temperature, pressure and flow.

The chemistry of steam has been used to indicate the distribution of liquid and gases in the reservoir, and the sources of produced steam.[5,7,17] These studies involve calculation of temperature and fraction of steam in the feed to wells, and tracing compositions of steam originating from partial condensation of steam, evaporation of liquid, and mixing of steam sources. Steam sources now exploited include steam from the open fractures of the system, vaporized liquid from small fractures and the rock matrix, and fluids entering the reservoir from outside, including injected condensate and fluids from undrilled areas. In the next sections methods of tracing reservoir processes will be discussed and applied to the NCPA Geysers steam field.

The Northern California Power Agency (NCPA) field is located in the southeastern part of The Geysers (Figure 1). The field is bounded to the north by Unocal and Calpine leases, to the southwest by the Big Sulfur Creek fault zone, in which low permeability limits steam production, and partially to the south and east by liquid-saturated boundaries. The engineering of the field and power plants and changes in pressure and gas contents of steam up to mid 1989 have been described by Enedy et al.[9] From 1985, extensive collection and analyses of steam were made for gases and isotopes. The sampling and analysis program and composition changes to early 1987 were described by Klein and Enedy.[15]

TRACING USING GAS EQUILIBRIA

At equilibrium, concentrations of gases in reservoir steam and liquid are different because gases partition strongly into the steam. If reservoir liquid vaporizes during production and this steam mixes with original reservoir steam, gas concentrations in the mixture will not correspond to equilibrium in either liquid or steam. By combining gas solubilities and equilibria for two reactions, both reservoir temperature and steam fraction, "y" equal to the fraction of original reservoir steam in the produced mixture (also called effective reservoir steam saturation), can be calculated. Methods for this calculation were described by Giggenbach[12] and D'Amore et al.[7]

The calculations used in this paper were described in detail in D'Amore and Truesdell.[6] The methane breakdown and pyrite-H2S reactions were chosen for the calculation. These reactions are

$$CH_4 + 2\,H_2O = CO_2 + 4\,H_2 \text{ , and}$$

$$3\,FeS_2 + 4\,H_2O + 2\,H_2 = Fe_3O_4 + 6\,H_2S \text{ ,}$$

and the corresponding equilibrium expressions are

$$KC = P_{H_2}{}^4\, P_{CO_2} / P_{CH_4}\, P_{H_2O}{}^2 \text{ , and}$$

$$KS = P_{H_2S}{}^6 / P_{H_2}{}^2\, P_{H_2O}{}^4,$$

where KC and KS are equilibrium constants and P indicates gas partial pressures. At equilibrium the wellhead steam composition is a function of the reservoir temperature and the fraction, y, of the original steam. These functions for the two reactions can be written as,

$$4 \log (H_2/H_2O)WH + \log (CO_2/CH_4)WH$$
$$= \log KC - 2 \log P_{H_2O}$$
$$+ 4 \log A_{H_2} + \log (A_{CO_2}/A_{CH_4}) \text{ , and}$$

$$3 \log (H_2S/H_2O)WH - \log (H_2/H_2O)WH$$
$$= \log KS + 3 \log A_{H_2S} - 2 \log A_{H_2} \text{ ,}$$

where WH refers to wellhead analyses, $A_i = y + (1\text{-}y)/B_i$ and B_i is the gas distribution constant, C_{vapor}/C_{liquid}.

The equilibrium constants KC and KS and the pressure of saturated steam (P_{H_2O}) are functions of temperature so the left-hand sides of the equations are written,

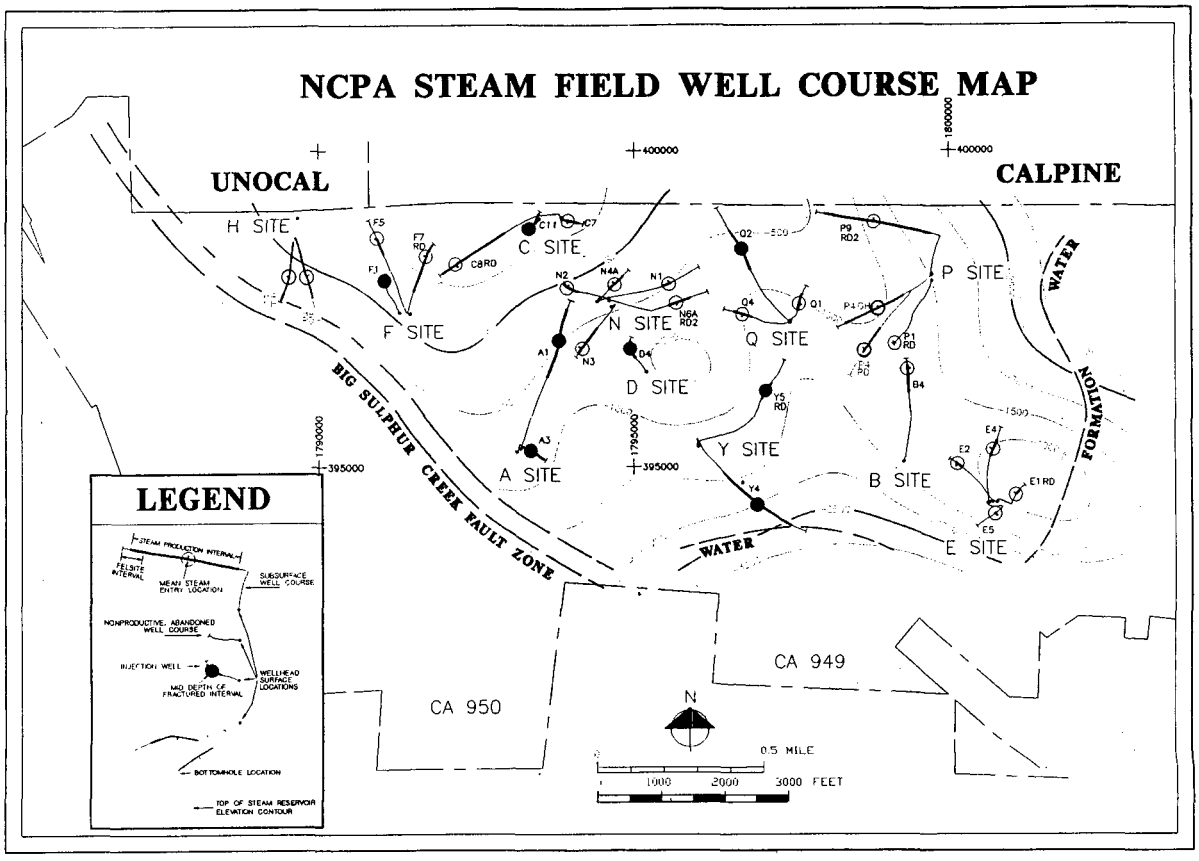

Figure 1. Map of the NCPA field showing locations of field boundaries, and selected well sites, well courses, mean steam entries and mean injection points (solid circles).

$$-15.35 - 3952/T + 4.635 \log T + 4 \log A_{H_2} + \log (A_{CO_2}/A_{CH_4})$$

$$6.23 - 6222/T - 0.412 \log T + 3 \log A_{H_2S} - \log A_{H_2},$$

with T in °K and $A_i = y + (1-y)/B_i$ as before. Values of B_i are calculated from the data in Table 1.

Table 1. Equations for the distribution constant B_i (from[12])

$$B_i = C_i + D_i\, t \text{ (t in °C)}$$

Gas	C_i	D_i
CO_2	4.7695	-0.01096
H_2S	4.0442	-0.00980
H_2	5.9681	-0.01330
CH_4	6.0810	-0.01388

On a grid drawn using these equations (Figure 2) the NCPA steam analyses indicate temperatures from about 210° to 265°C and steam fractions ("y" values) from about 0.005 to 0.25. Most steam analyses are between 225°C and 250°C, and 0.05 and 0.2 y. The indicated temperatures are reasonable. The original temperate at 2000 m depth was probably near 245°C[16,19] with somewhat lower temperatures expected as a result of exploitation. The calculated steam fraction values (5 to 20 weight % steam) indicate substantial liquid reserves.

Figure 3 shows the changes in calculated temperature for each year from 1985 to 1990 along a W-E cross-section of the field with well locations projected on a W-E line. The general locations of groups of wells are shown at the top (compare with Figure 1). Where there were several analyses for a year, the results of the calculations were averaged. The calculations show a range of temperatures for each group of wells of from 20 to 40 (or more) °C. The order to see yearly changes and variations along the section, a power series fit of temperatures for each year was calcu-

lated. Except for 1985, the results show that there is a general tendency for mean calculated temperatures in the center of the field (F to Q wells) to be near 235°C, with higher temperatures for P and E wells and lower temperatures for H wells. The high temperatures indicated in 1985 may be an artifact.

Fitted "y" values vary more widely (Figure 4). The 1985 y values are low across the middle of the field and very low at the western edge. Y values at both east and west edges of the field were low initially, but increased with time more rapidly than in the center. Y values were nearly constant in 1985-86, but increased in 1987-88. The high y values and increase in y at the margins of the field reflect high and increasing gas concentrations.

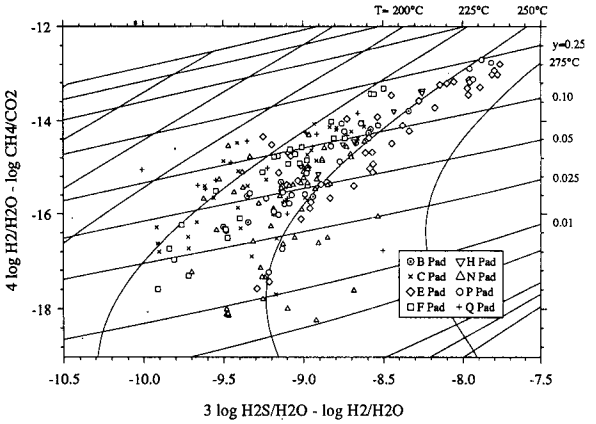

Figure 2. Part of the y-t "grid" diagram for CH_4-CO_2-H_2 and pyrite-magnetite-H_2S reactions showing effective vapor saturation, y, and temperature for selected NCPA steam samples collected from 1985 to 1990.

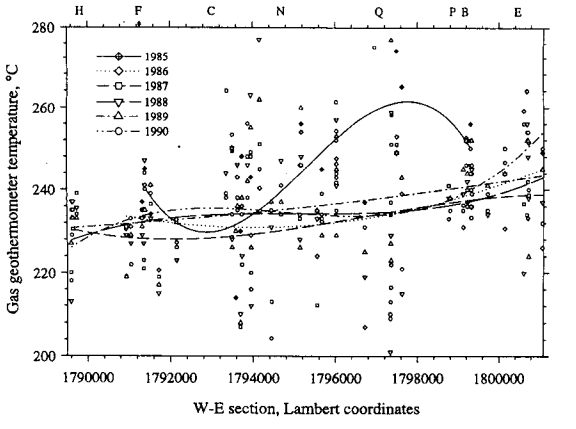

Figure 3. W-E cross-section of the NCPA field showing calculated gas geothermometer temperatures for yearly steam samples and curves fitted to each year's data.

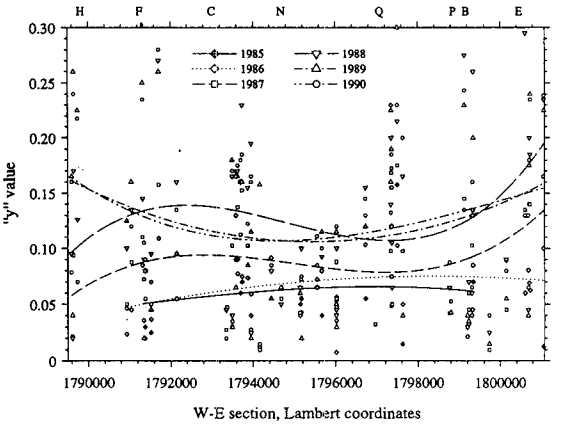

Figure 4. Calculated y values for yearly steam samples presented as in Figure 3.

TRACING USING GAS CONCENTRATIONS

Calculated y values are closely related to total gas concentrations because the balance of original steam (gas rich) to vaporized liquid (gas poor), as measured by y, determines in most cases the concentration of total gas in the mixture. However if the high-gas steam originates separately from the low-gas steam then the changes in the gas concentrations may give a clearer picture of reservoir processes.

Total gas concentrations (as mole fractions) are shown for the section in Figure 5. These values show less scatter than temperatures and y values and vary distinctly with time and position in the field. Large increases occurred at the field margins after 1985, with smaller increases in the center of the field after 1987. These changes can be better seen in Figures 6 and 7 which show changes with time of the gas concentration of wells at the margins (H, P, B and E wells) and center (all others except N wells) of the field. Gas concentrations in steam from N wells is lower and more variable as a result of intense nearby injection (Figure 8). (Injection well locations are shown as filled circles on Figure 1.) These figures show that gas concentrations in almost all steam analyses decreased or were constant until mid-1987 and increased markedly from 1987 to late 1989 or 1990.

Steam may exist in areas beyond the margins of the drilled field. These areas, initially rejected because of high gas or low productivity, eventually contribute to the total steam produced in neighboring wells. Steam at the reservoir margins is distinct chemically from steam in the center. In the SE Geysers and in several areas of Larderello there is a characteristic pattern of steam composition in which water soluble salts (e.g. B) are more concentrated in steam from the center of the field and water insoluble gases (e.g. CO_2) are more concentrated at the margins.[5,21] Oxygen-18 is more soluble in water than oxygen-16 and is depleted in marginal steam. These patterns are produced by natural state (pre exploitation) lateral steam flow with partial con-

densation as heat is lost by conduction to the surface. This can be described chemically as a Rayleigh or open system process which the concentration of a component is a function of the amount of steam condensed and the relative solubility of the component in steam and water. The equation for this process is[5]

$$C/Co = (m/mo)^{(1/K - 1)},$$

where at any point C/Co is the ratio of a component concentration to its original concentration, m/mo is the fraction of steam condensed and K is the distribution coefficient of the component between steam and water (Cs/Cw). The same equation for isotope notation is[5]

$$\delta - \delta o = 1000\,[\,(m/mo)^{(\alpha - 1)} - 1\,],$$

with δ and δo the present and original isotopic compositions (in permil) and α, the fractionation factor between water and steam.

The most easily demonstrated effects of this condensation process in the NCPA field are enrichment of marginal steam in gas (CO_2) and depletion in oxygen-18. Later discussion of isotopic compositions describes the lower ^{18}O composition of steam from H and E wells on the field margins.

High gas at the E, S and W margins of the field is shown in Enedy et al.[8] The increase of gas generally and for wells near reservoir margins can be seen in Figures 5-8 in which the total gas is shown for the period from 1985 to 1991. These figures show gas contents for wells that may show influence of migration of marginal steam (B, E, H and P wells) or vaporization of injectate (N wells), or possibly influences from both process (C, F, and Q wells).

Steam from E and P wells clearly shows the effect of mixture with marginal steam (Figure 6). These wells (except E-1) produce the highest initial (1986) gas contents and (except E-2) have increased in gas with time generally

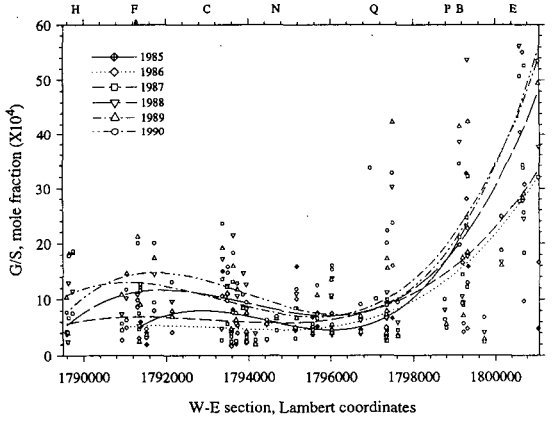

Figure 5. Gas to steam mole fractions presented as in Figure 3.

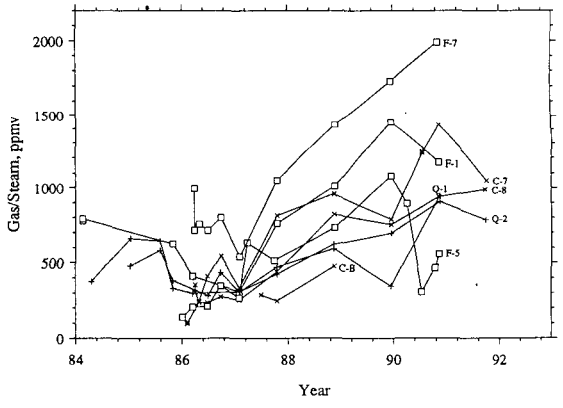

Figure 7. Changes in gas concentrations for steam from wells in the central NCPA field (except N wells).

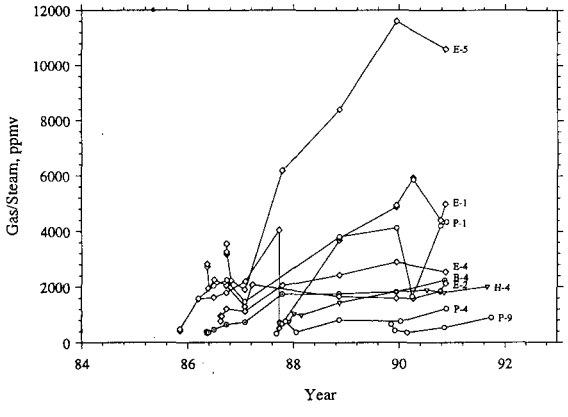

Figure 6. Changes with time of gas concentrations (in ppm by volume) for steam at the margins of the NCPA field (H, P, B and E wells).

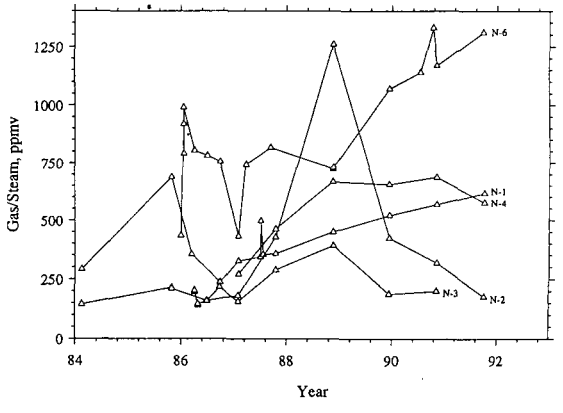

Figure 8. Changes in gas concentrations for steam from N wells.

starting in 1987. Wells E-5, E-1 and P-1 produce the highest gas of the field (to 12000 ppmv) and are nearest to the field margin. Steam from well H-4 on the western margin, which (along with E well steam) was originally low in $\delta^{18}O$, has moderately high gas relative to most wells but much lower than for E wells.

Steam from C, F, and Q wells has somewhat higher gas contents than that from N wells and much lower gas than steam from field margins (Figure 7). Most steam in this group shows large increase in gas after early 1987, similar to that for marginal steam. Some steam from C and F wells increased greatly in δD during the 1989-90 injection experiment in the low pressure area in which most condensate was injected into well C-11. This experiment probably produced the drop in gas (along with increases in δD) observed in F-1 and F-5 steam after 1989 and later in C-7. The decrease in gas content of most steam before 1987 is probably due to dilution of reservoir steam by the continued vaporisation of reservoir liquid. In 1987 this process stopped or slowed markedly and gas content of steam increased.

Steam from N wells has the lowest gas of the NCPA field (Figure 8). This is probably due both to the position of N wells at the center of the field and to gas dilution from vaporization of injectate. Well N-6 steam has shown a rapid increase in gas (but only to 1260 ppmv) and may receive less injection steam. Steam from wells N-1 through N-4 generally has gas contents below 750 ppmv, and has not shown rapid increase in gas. These wells are evidently receiving enough injectate to stabilise gas contents of the produced steam.

TRACING USING ISOTOPES

Isotopes have been frequently used in tracing injection return in steam fields. Studies of injection in a low pressure area of the SE Geysers shared by NCPA, Calpine and Unocal have demonstrated substantial increases in steam flow and reservoir pressure.[10] Isotopic data were used as tracers in this and other studies to estimate the quantity of steam generated from evaporation of injected condensate.[17,1,2,4,11]

Steam condensate from cooling towers is enriched in oxygen-18 and deuterium because these isotopes fractionate strongly into liquid at lower temperatures. This fractionation is an open system or Rayleigh process and follows the equation

$$\delta = \delta o + 1000\ ((m/mo)^{(1/\alpha-1)} - 1),$$

in which δo and δ are the initial and final isotope compositions, m/mo is the fraction of condensate remaining after evaporation and α is the fractionation factor. The derivation of this equation follows that given for steam condensation in D'Amore and Truesdell.[5] At NCPA cooling towers there is about 30% liquid remaining after evaporation at an average temperature of 70°C, and the expected δD change of the condensate is +50 permil, close to the observed difference between produced steam and injectate. Isotope changes for other temperature and residual liquid fractions are given in Table 2.

Table 2. Change in δD for open-system, isothermal evaporation at temperatures from 40 to 100°C and fractions of residual liquid from 0.5 to 0.2.

Liquid	Temperature °C			
Fraction	40	60	80	100
0.5	42	32	25	19
0.4	56	42	33	25
0.3	74	56	44	34
0.2	100	76	59	45

The effects of evaporation on the injected condensate and the results of mixing steam from vaporized condensate with reservoir steam are shown in Figures 9 and 10 in which steam isotope compositions for 1985-86 are compared with those for 1990. In 1985-86 some N and A wells were affected by condensate injection, while in 1990 this effect was felt strongly by F, C and N wells with a small effect for most other wells. F and C wells were intensively sampled during the injection experiment in the low pressure area (LPA)[10] and the results are prominent in the 1990 data (Figure 10). In 1990 only wells far from injection wells (some E and H wells) retained their original isotope compositions. A small number of 1990 steam samples from several areas show δD compositions lower than any in 1985-86. This could only be explained by entry of shallow, low-temperature (<220°C) steam or (less likely) deep, high-temperature liquid.

In Figures 11 and 12 changes in isotopic compositions (omitting the data for F and C wells from the LPA injection experiment) are shown on the cross-section used earlier. The fitted lines show the same increase in heavy isotopes in the east-central field after the 1989 start of the LPA injection experiment as in Figure 10. Except for this change (and an initial high δD analysis at the east margin) δD values are very similar across the field. this is not true of $\delta^{18}O$ values which show (save one number) lighter oxygen at the field margins before the LPA experiment with an increase in $\delta^{18}O$ in the west-central field for 1989 and 1990, similar to that observed for δD.

DISCUSSION

As we have seen the gas and isotope chemistry of produced steam is far from uniform even in a restricted volume of the reservoir. The composition is affected by many factors. Differences in permeability, local existence of gas pockets or perched liquid and the pattern of fracture connection can cause neighboring wells to produce steam of different compositions. This study attempts to separate local effects from general influences by viewing the data across the field and over a period of time. The fits of the trend lines to the data are far from perfect but present a reasonably consistent picture.

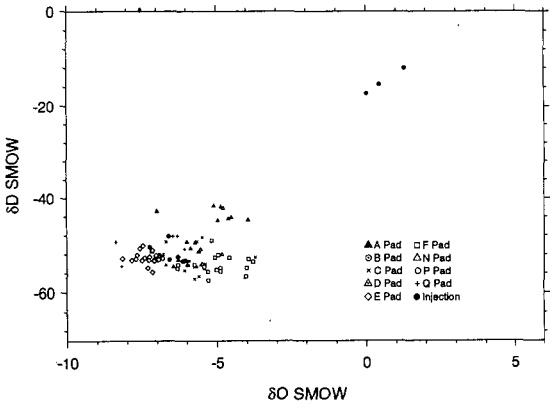

Figure 9. Isotope diagram showing values of $\delta^{18}O$ and δD (in permil SMOW) for 1985-86 NCPA steam samples.

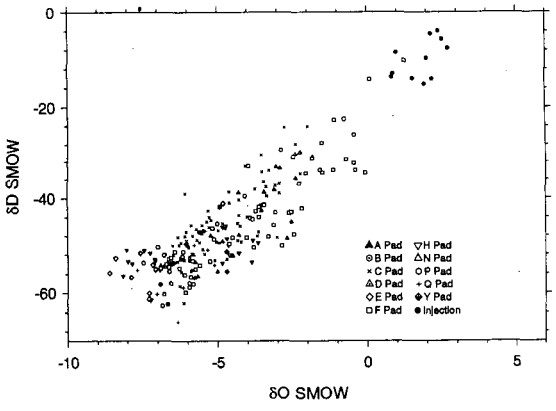

Figure 10. Isotope diagram (as Fig. 9) for 1990 NCPA steam samples.

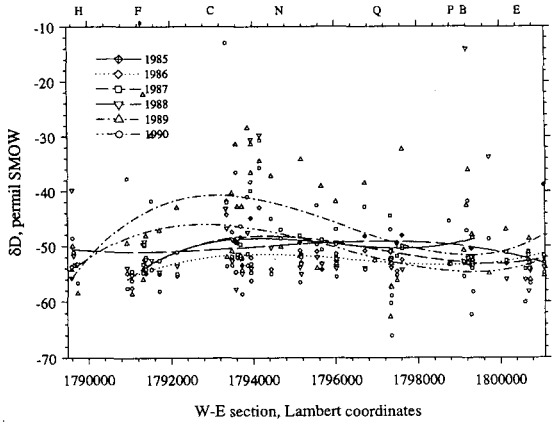

Figure 11. W-E cross-section of the NCPA field showing δD compositions of yearly steam samples and curves fitted to each years points.

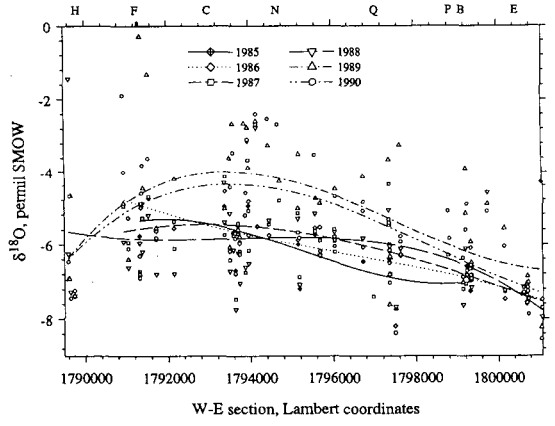

Figure 12. Yearly $\delta^{18}O$ steam compositions presented as in Figure 11.

The main influences on the gas and isotope compositions of steam from the NCPA field include: 1) original (pre-exploitation) gradients produced by the lateral movement of steam, resulting in the presence of high-gas steam at field margins; 2) injection of steam condensate which vaporizes and mixes with reservoir steam to dilute gases; and 3) a decrease in the availability of liquid in the reservoir which has decreased pressures and flows and increased gas.

Natural state gradients in gas and isotope chemistry result from lateral movement of steam from an upflow zone in the west-central part toward zones of condensation mainly to the south and east, with a smaller flow to the west. This movement was accompanied by partial condensation of steam along the flow path causing the residual steam to be enriched in gas and depleted in oxygen-18. This process was described for Larderello by D'Amore and Truesdell.[5] The resulting zones of condensation at the field margins contain sub-commercial quantities of high-gas steam. As pressures decrease during production, the marginal steam is drawn into producting zones causing an increase in gas concentrations. This effect may produce similar results to the general decrease of steam from vaporized liquid.

The second main influence on steam compositions is the injection of condensate in the center of the field. Injection greatly increases heavy isotope (D and ^{18}O) contents of steam fed in part from vaporization of the injectate. Injection has also lowered the content of gas in the center of the field, but this effect has been overshadowed by the general change in steam origins discussed next.

The third and most important influence on steam compositions is the sudden decrease in 1987 of the amount of steam formed by vaporization of liquid water in the reservoir. This is most clearly seen in the change in the gas concentration of steam from individual wells (Figures 6 and 7). Before 1987 steam from most central wells contained less than 1000 ppmv, and wells at the eastern margin contained less than 3000 ppmv. In early 1987, gas contents increased rapidly from minimum values to

maxima in 1990 (2 to 6 times greater). This change is also apparent in the increase of y values after 1987 (Figure 4). The decrease in vaporization of easily available liquid in the reservoir has caused rapid decreases in pressure and steam flow throughout most of The Geysers field. This has important consequences for the continued productivity of the entire field and deserves further discussion.

From simple volumetric calculations it can be shown that the main source of steam from vapor-dominated reservoirs is the vaporization of liquid.[14] But although its presence is certain, the location and mobility of reservoir liquid is still a matter of debate. Static bottom-hole pressure and temperature conditions at The Geysers were initially close to saturation values based on data for pure steam and water.[22,19] This indicates that initial reservoir liquid in equilibrium with steam was thermodynamically equivalent to pure bulk liquid, neither highly saline nor bound to rock surfaces. Downhole static pressure measurements showed low "vaporstatic" gradients and surface heat flow was high even in the near absence of surface discharge.

These observations indicate that the reservoir contains steam and water, with steam flowing upwards in response to a pressure gradient caused by boiling at the bottom and condensation at the top, and liquid condensate flowing downwards by gravity. Thus the counterflow of steam and water acts as a "heat pipe".[22] The upward flow of steam must occur in large fractures but the location of liquid downflow is less certain. Liquid descent could occur in saturated matrix blocks, as liquid sheets on the surfaces of fractures or as a combination in which matrix flow is interrupted by fractures where sheet flow occurs. It is unlikely that downward flow of liquid is limited to matrix block porosity. Observed perched water and liquid in dead-end drill holes show that steam and bulk water coexist.[20]

Numerous modelling studies of mass and heat transfer in vapor-dominated reservoirs have demonstrated steam-water counterflow, but only Pruess and Narasimhan[18] indicate the location of liquid in the reservoir. These authors state that liquid is confined to matrix blocks because it will vaporize if it enters vertical fractures and cannot exist on fracture surfaces. This argument appears limited to very low-permeability rocks in which conductive heat flow is as rapid as fluid flow. For a natural system at equilibrium, thermodynamic arguments indicate that water in rock pores, water on fracture surfaces, and steam can coexist.

It seems likely that the 1987 increase in gas and decline in pressure and flow was due to a decrease in the availability of liquid water in the reservoir. Relating the production history of The Geysers to assumed distributions of reservoir steam and liquid is however difficult. Pressure could be maintaned by producing steam from a large volume of interconnected fractures with minimal vaporization of liquid in each unit volume, or from a smaller production volume with extensive vaporization. Similarly, declining pressure could result from an increasing distance to the source of steam or from decreasing availability of nearby liquid.

The existence of well-defined chemical patterns inherited from the natural state in the long-exploited Larderello field,[5] and in the geochemical results presented here suggest a local source of steam. In this view, rather than the exhaustion of a distant homogeneous source, the recent accelerated decline in pressure and flow at The Geysers resulted from the local disappearance of liquid held in easily accessible sites—liquid on surfaces of major fractures, in minor fractures opening upwards and perched liquid in structural traps. Continued production is from existing steam and vaporization of less-accessible reservoir liquid as well as from injected water, and possibly from underexploited areas at the reservoir margins.

EXISTING STEAM AND LESS-ACCESSIBLE RESERVOIR LIQUID

Before 1987 much of the steam produced from The Geysers probably originated from vaporization of easily-accessible liquid. The fieldwide pressure decline after 1987 indicated that the amount of easily-accessible liquid had declined rapidly throughout the interconnected reservoir. Continued production is largely from existing steam and less-accessible liquid. This liquid is probably contained in limited matrix porosity (< 2% in Geysers graywacke; G.S. Bodvarsson, pers. com., 1992) and in small fractures of matrix blocks. The amount that this "matrix" liquid contributes to steam flow is indicated at least semi-quantitatively by the gas equilibria calculations (Figures 2-4). At the NCPA field vaporization of matrix liquid may still provide more than 75 or 80% of production from most wells. The rate at which the steam produced by vaporization of liquid within the matrix blocks can move to large fractures connecting to wells is limited by permeability. The Geysers cannot boil dry immediately (unlike a teakettle), but the rate of boiling may be limited. If the indication from gas geothermometry that most of present steam is from matrix blocks, then the amount of liquid water in the reservoir may be large but the production rate limited. This suggests that The Geysers will continue to be productive for a long time, but at a lower rate.

OTHER SOURCES OF STEAM

Pressure and flow declines at The Geysers are recognized as due to decrease in reservoir fluid rather than decrease in reservoir temperature or heat content.[8,10] In principle, near-original pressures and flows could be maintained if a quantity of liquid equal to the steam extracted could be recharged into the reservoir to preserve original liquid contents and distribution. However, water available for injection (at present essentialy limited to surplus condensate from cooling towers) is inadequate to maintain reservoir liquid mass. Even if the quantity were sufficient, ideal redistribution of liquid in the reservoir is probably not possible until field pressures decline greatly. Injection of liquid into a reservoir produces local cooling. The now wet, but cooled, volume receiving the liquid can produce steam to the reservoir only if its steam pressure is higher than the reservoir pressure. If the local steam pressure is lower, then higher-pressure steam from the reservoir will condense in the cooled zones and, although a long term increase of reserve fluid occurs, the immediate effect will be a decrease in reservoir pressure and steam production.

However, if the reservoir has dried out and lost pressure, the effect of injection can be immediately beneficial. Although pressures have dropped substantially, rock temperatures are close to original values.[8] Liquid injected into the hot, under-pressured reservoir boils vigorously and an immediate increase in pressure and steam flow results. Injection of water into the low pressure area of the SE Geysers and the Valle Secolo area of central Larderello has demonstrated this effect.[1,2,10] Steam flow to wells increased greatly and it was shown from isotopic and gas compositions that nearly all water injected was produced as steam. Other factors that influence the expected benefits of injection have been discussed by Cappetti et al.[3] Injection of increased amounts of liquid piped from outside the field to augment condensate injection increases the necessity of understanding injection mechanisms.

Recovery of steam from outside the drilled field may not be a major source of steam but the high gas content of this steam may require changes in plant design and field managment. Gas contents increase toward the margins of the field over most of the center and south Geysers.[13,21] In the development of The Geysers it was assumed that the margin of the field was indicated by the limit of productive wells and that steam was locally derived and would have more or less constant gas contents. As a result the gas handling abilities of power plants designed for conditions at the start of production may not be adequate for higher gas steam from field margins and that resulting from reservoir liquid decline. Now, when production from the central field has decreased, entry of marginal steam may be useful although changes in power plants will be necessary. In any case there is little choice. The rapid increases in gas in steam from wells near the field margins show that steam from the undrilled areas is being captured.

Finally it appears from the geochemical study that there will be continued long term production of steam from the NCPA field at a stable rate lower than the maximum observed in the 1980s. The field will also benefit immediately from injection in the lower-pressure, hot area in the west central part of the field. Contributions from marginal steam may require plant modification but will increase total steam production.

ACKNOWLEDGMENTS

The authors wish to thank the Northern California Power Agency for contributing extensive data for this paper. They also wish to thank Marcelo Lippmann and Karsten Pruess of the Lawrence Berkeley Laboratory for helpful reviews and continuing stimulating discussions. This work was supported in part by the Assistant Secretary for Conservation and Renewable Resources, Geothermal Division of the U.S. Department of Energy, through the Lawrence Berkeley Laboratory.

REFERENCES

1 Beall, J.J. and W.T. Box, Jr., 1992, "Recovery of injected condensate as steam in the south Geysers field," Geothermal Resource Council Special Rept. No. 17, p. 151-157.

2 Bertrami, R., C. Calore, G. Capetti, R. Celati, and F. D'Amore, 1985, "A three year recharge test by reinjection in the central area of the Larderello field: Analysis of production data," Geothermal Resource Council Trans., v. 9, p. 293-298.

3 Cappetti, G., A. Giovannoni, C. Ruffilli, C. Calori, and R. Celati, 1982, "Reinjection in the Larderello geothermal field," Proceedings, Int. Conf. on Geothermal Energy, Florence, Italy, v. 1, p. 395-407.

4 D'Amore, F., 1991, "Gas geochemistry as a link between geothermal exploration and exploitation," Application of Geochemistry in Geothermal Reservoir Development, F. D'Amore, ed. UNITAR/UNDP, Rome, Italy, p. 93-117.

5 D'Amore, F. and A.H. Truesdell, 1979, "Models for steam chemistry at Larderello and The Geysers," Proceedings, 5th Workshop on Geothermal Reservoir Engineering, Stanford, CA, p. 283-297.

6 D'Amore F. and A.H. Truesdell, 1988, "A review of solubilities and equilibrium constants for gaseous species of geothermal interest," *Sci. Geol., Bull., 41*(3-4), 309-332.

7 D'Amore, F., R. Celati, and C. Calore, 1982, "Fluid geochemistry applications in reservoir engineering (vapor-dominated systems)," Proceedings, 8th Workshop on Geothermal Reservoir Engineering, Stanford, CA, p. 295-308.

8 Enedy, K.L., 1992, "Downhole enthalpy and superheat evolution of Geysers steam wells," Geothermal Resources Council Special Report No. 17, p. 205-209.

9 Enedy, S., M. Grande and W. Smith, 1990, "A case history of steamfield development, reservoir evaluation, and power generation in the southwest Geysers," Bull. Geothermal Resources Council, v. 19, p. 232-248.

10 Enedy, S.L., K.L. Enedy and J. Maney, 1992, "Reservoir response to injection in the southeast Geysers," Geothermal Resources Council Special Report No. 17, p. 211-219.

11 Gambill, D.T., 1992, "The recovery of injected water at The Geysers," Geothermal Resources Council Special Report No. 17, p. 159-163

12 Giggenbach, W.F., 1980, "Geothermal gas equilibria," Geochim. Cosmochim. Acta, v. 44, p. 393-410.

13 Gunderson, R.P., 1992, "Distribution of oxygen isotopes and noncondensable gas in steam at The Geysers," Geothermal Resources Council Special Report No. 17, p. 133-138.

14 James, R., 1968, "Wairakei and Larderello: power systems compared," *N.Z. Jour. Sci., 11*, 706-719.

15 Klein, C. and S. Enedy, 1989, "Effect of condensate on steam chemistry at The Geysers field," Trans. Geothermal Resources Council, v. 13, 409-413.

16 Lipman, S.C., C.J. Strobel and M.S. Gulati, 1977, "Reservoir performance of The Geysers field," *Geothermics, 7*, 209-219.

17 Nuti, S., C. Calore and P. Noto, 1981, "Use of environmental isotopes as natural tracers in a reinjection experiment at Larderello," Proc. 7th Workshop on Geothermal Reservoir Engineering, Stanford, CA, p. 85-89.

18 Pruess, K. and T.N. Narasimhan, 1982, "On fluid reserves and the production of superheated steam from fractured, vapor-dominated geothermal reservoirs," *Jour. Geoph. Res., 87*, 9329-9339.

19 Truesdell, A.H. and D.E. White, 1973, "Production of superheated steam from vapor-dominated geothermal reservoirs," *Geothermics, 2*(3-4), 154-173.

20 Truesdell, A.H., M. Nathenson and G.A. Frye, 1981, "Downhole measurements and fluid chemistry of a Castle Rock steam well, The Geysers, Lake County, California," *Geothermics, 10*(2), 103-114.

21 Truesdell, A.H., J.R. Haizlip, W.T. Box and F. D'Amore, 1987, "Fieldwide chemical and isotopic gradients in steam from The Geysers," Proceedings, 12th Workshop on Geothermal Reservoir Engineering, Stanford, CA, p. 241-246.

22 White, D.E., L.J.P. Muffler and A.H. Truesdell, 1971, "Vapor-dominated hydrothermal systems compared with hot-water systems," *Economic Geology, 66*(1), 75-97.

PROCEEDINGS, Eighteenth Workshop on Geothermal Reservoir Engineering
Stanford University, Stanford, California, January 26-28, 1993
SGP-TR-145

CORE IMAGE ANALYSIS OF MATRIX POROSITY IN THE GEYSERS RESERVOIR

Dennis L. Nielson, Greg Nash, Jeffrey B. Hulen and Alan C. Tripp

University of Utah Research Institute
391-C Chipeta Way
Salt Lake City, Utah 84108

ABSTRACT

Adsorption is potentially an important consideration when calculating reserves at The Geysers. Our investigations of the mineralogical relationships in core samples have shown matrix pore spaces to be largely associated with fractures. Dissolution of calcite from hydrothermal veins increases porosity in the graywacke reservoir. The high relative surface area of secondary alteration phases could promote adsorption. In order to quantify porosity distribution and surface area, Scanning Electron Microscope (SEM) images were analyzed using software developed for the interpretation of satellite imagery. This software classifies the images as either crystal or pore and then accumulates data on pore size, total porosity and surface area of the mineral-pore interface. Review of literature shows that data on thickness of adsorbed water layer does not exist for many of the mineral phases of interest in The Geysers. We have assumed thicknesses of 10, 100, and 5300 Angstroms for the adsorbed layer and calculated the relative proportions of adsorbed water. These calculations show 0.005%, 0.05%, and 2.5% of total water would be adsorbed using the above thicknesses.

INTRODUCTION

The Geysers vapor-dominated geothermal system is conceptualized in terms of a dual-porosity model where steam is present in major through-going fractures, is highly mobile under production conditions and is the pressure-controlling phase. Liquid water, by contrast, occupies pores in the matrix between these fractures and is largely an immobile phase (Truesdell and White, 1973; Pruess and Narasimhan, 1982). Buffering of the steam at saturated pressure and temperature conditions prior to exploitation demonstrated that the steam is flashing from a liquid reservoir in response to production. The majority of the heat reserves in the reservoir are in the rock and transfer to the steam through the process of flashing. Total reservoir production therefore will be determined by the water content of the reservoir, which is a function of matrix porosity. Although fractures are responsible for extremely rapid and widespread communication within the reservoir, they have not effectively breached either the cap or lateral permeability seals, and the reservoir is generally acknowledged to have little natural recharge (Williamson, 1990).

Recent pressure declines at The Geysers have raised the question of the longevity of the steam field and the most effective means of injection into the resource to prolong its economic life. The potential importance of liquid-water adsorption in reservoir storage has been discussed by a number of researchers (Economides and Miller, 1985; Ramey, 1990) who argue that failure to consider adsorption will lead to underestimation of reserves. Pruess and O'Sullivan (1992) have surveyed the literature on capillarity and adsorption on rock surfaces and point out that there is a large variation in the degree of adsorption in rocks that they attribute to different pore size distribution and variations in composition and activity of mineral surfaces. They also feel that vapor pressure lowering will only become a significant process at liquid saturations of 20% or less and is thus only important during the final stages of reservoir production.

The porosity of reservoir rocks at The Geysers has been determined by standard core analyses (Gunderson, 1990). Gunderson reports an average porosity of 2.3% (range of 0.6% to 5.8%) in the graywacke reservoir. The felsite reservoir has an average porosity of 2% (range of 1.7% to 4.2%). Porosity in the graywacke was found to decrease with increasing depth and with proximity to the felsite. Gunderson also presented a schematic representation of four types of matrix porosity from The Geysers core. A revision of this diagram based on the results of Hulen et al. (1991,1992) and this study is shown in Figure 1. Matrix porosity in the reservoir is largely a function of three different processes. Creation of new void space through rock brecciation (tectonic or hydrothermal) as well as dissolution of calcite, enhances porosity. Precipitation of silicate phases within the pores decreases porosity, but may enhance adsorption.

Core samples from the reservoir show that matrix porosity is heterogeneous. Dissolution of Franciscan calcite produces pores that are more or less randomly distributed through the graywacke. Calcite dissolution from veins forms the largest pores within the vein, but also forms pores marginal to the veins. Unmineralized fractures are porous within and along the fracture. Closely spaced fractures, in addition, are often separated by areas of high matrix porosity. We do not have access to core that samples a steam entry within the normal graywacke reservoir. Since the highest matrix porosity is associated with fracturing, the results of our work probably underestimate total porosity.

Our observations of The Geysers cores also suggest that there is a stratigraphic distribution for matrix porosity. Figure 2 is a schematic diagram showing our concept of porosity within the reservoir. As illustrated in Figure 1, porosity in the graywacke reservoir results from the dissolution of previously existing calcite as well as tectonic and hydrothermal fracturing. An important

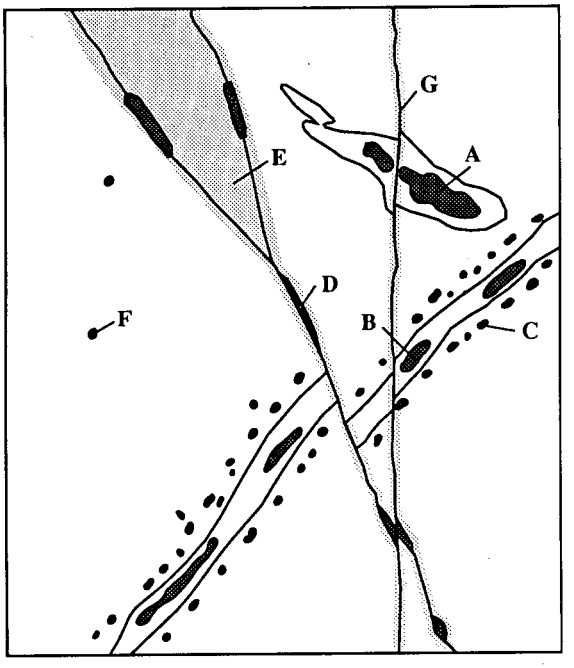

Figure 1 - Schematic diagram of "matrix" porosity in The Geysers normal graywacke reservoir. **A** is pore space created by dissolution of Franciscan calcite in discontinuous pods. **B** is pore space formed form dissolution of calcite in quartz + calcite veins. **C** are pores marginal to the quartz + calcite veins. **D** is porosity in small, partially sealed fractures, and **E** represents the porosity between and adjacent to these young fractures. **F** represents isolated pores. **G** are unmineralized fractures that are the youngest in the field. Modified from Gunderson (1990).

aspect of this portion of the reservoir is the development of low-angle fractures discussed by a number of authors (see Nielson and Brown, 1990 for a summary). Alternatively, we suggest that flat fractures may be developed by strike-slip faulting and generation of associated "flower" structures (Willis and Tosdal, 1992). In the hornfels zone, prograde reactions resulted in conversion of calcite to calc-silicate minerals during contact metamorphism and metasomatism associated with emplacement of the felsite. Matrix porosity here, then, is largely confined to brecciated areas associated with faulting that followed the emplacement of the felsite. Matrix porosity in the felsite, reported by Gunderson (1990), is probably associated with faults and joints or miarolitic cavities. Thus, matrix porosity and associated liquid reserves, are probably highest in the graywacke.

Hulen et al. (1991,1992) have described very intricate and delicate mineral textures within vugs that constitute the matrix porosity of the reservoir rocks. Since adsorption is a function of surface-energy relationships among solid, liquid and vapor phases, it seems likely that mineral species and textures will influence the storage capacity of the reservoir.

OBSERVATIONS

The textural relationships for several mineral phases are shown in Scanning Electron Microscope (SEM) images

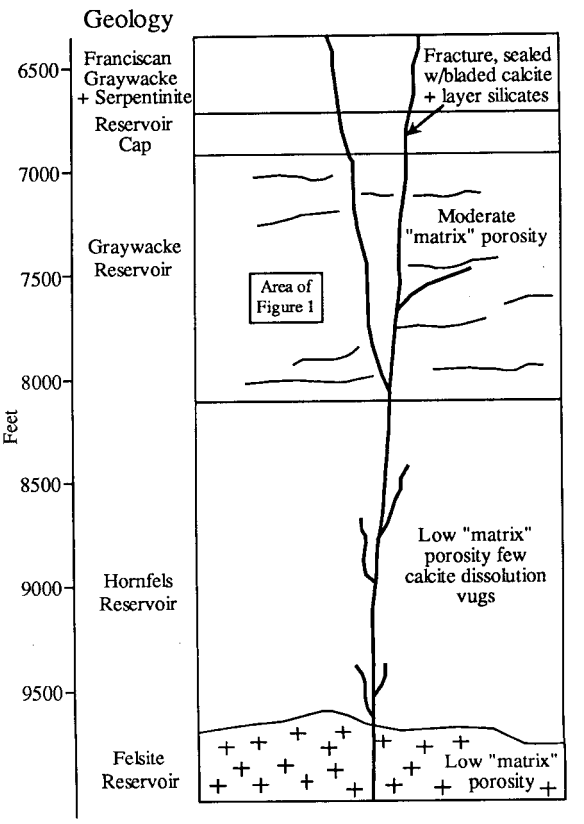

Figure 2 - Reservoir model of The Geysers

in Figure 3. The most common hydrothermal phases in the reservoir are actinolite, epidote, and quartz. Bladed calcite, wairakite and layer silicates are more common in the cap at the top of the reservoir (Hulen et al., 1991). Figure 3a shows the texture formed by actinolite growing within a solution vug while Figure 3b shows the texture formed by epidote in a similar setting. Figures 3c and d show two magnifications of pore space in a sample where the surface has been polished to emphasize the location and geometry of the overall porosity. The pore space is confined to a hydrothermal vein. SEM and thin-section examination of the rock matrix shows that porosity is generally not present along the margins of the original sedimentary grains. This is an important distinction between The Geysers reservoir and conventional siliciclastic hydrocarbon reservoirs.

The observation of these textures suggests that porosity measurements on core only partially describe the relationships necessary to understand reservoir storage. The pore size, size distribution and surface areas of minerals should influence adsorption and capillarity. We have based our measurements of pore characteristics on the interpretation methods described in Krohn and Thompson (1986), Krohn (1988) and Thompson (1991). These works demonstrated a fractal distribution for porosity in a suite of sandstones. However, we have improved upon their image analysis techniques to enable calculations of surface area as well as pore volume.

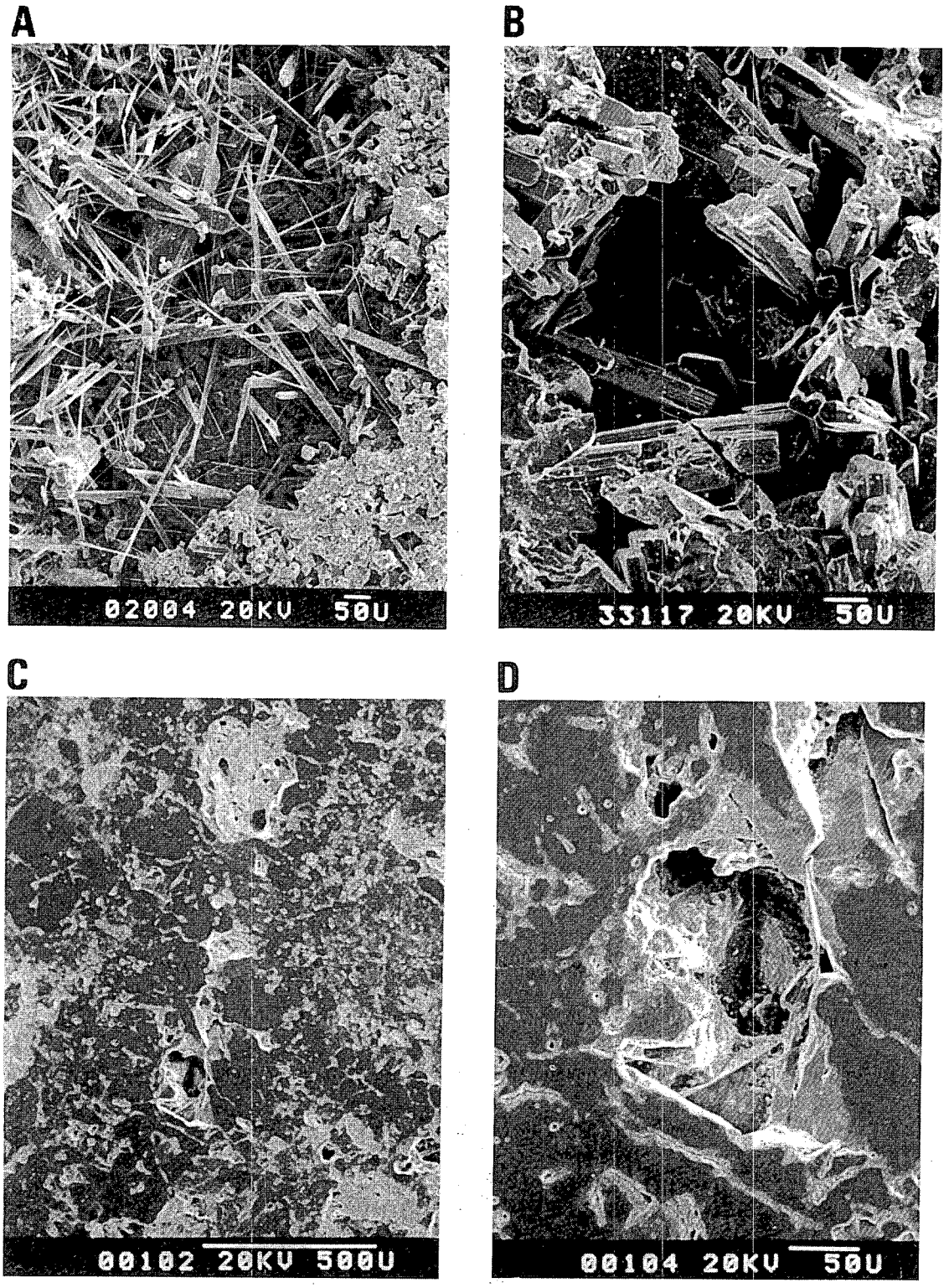

Figure 3. SEM images of core from The Geysers reservoir
A. Actinolite in dissolution pore from well Prati-State 12
B. Epidote in dissolution pore from well NEGU-17
C. Polished sample of vein with dissoution pores from well NEGU-17
D. Same sample as C, higher magnification

ADSORPTION

Adsorption on surfaces can be considered to result from the physical attraction between a liquid or a gas and the solid substrate. The process results in three thermodynamically distinct phases: the solid, adsorbed liquid (or gas) and liquid (or gas) (Jaroniec and Madey, 1988). The theoretical details of the adsorption process can get very complex for The Geysers system, and a comprehensive discussion is beyond the scope of this paper. Different crystallographic orientations of the same mineral will have different adsorption capacities, as will different mineral phases. The adsorbed fluid in The Geysers reservoir is also likely to be chemically variable as evidenced by the chemical differences of fluids trapped within fluid inclusions (Moore, 1992). Thus, complex relationships of electrolyte adsorption would have to be considered in a comprehensive treatment of the reservoir.

The thickness of the adsorbed layer is of considerable interest in determining the potential adsorbed fluid reserves. There are few data that are of use in determining this for the minerals and fluid compositions present in The Geysers field. A conservative approach is to consider adsorption of one molecular layer. He et al. (1987) concluded from a study of tuff that beyond 7 to 8 Angstroms from the mineral surface, the properties of the adsorbed phase were similar to bulk water. Mulla (1986) reviewed different simulation techniques and suggested that attractive forces become negligible at 10 to 15 Angstroms from the mineral surface. Giese and Costanzo (1986) reviewed the literature on adsorption of water by clay and found a potential range of adsorbed thicknesses between 10 and 100 Angstroms. Henneker (1949, as cited in Economides and Miller, 1985) reports water on glass oriented up to a thickness of 5300 Angstroms. It must also be kept in mind that the electrostatic forces that result in adsorption decrease away from the mineral substrate. Therefore, there is a gradational transition between the adsorbed phase and the bulk fluid rather than an abrupt transition as will be implied in our treatment.

MEASUREMENTS

Because pore space within core from The Geysers is heterogeneous, two different techniques have been identified for its characterization. The first is Scanning Electron Microscopy (SEM). This method has been used to image the mineral-void relationships inside pores. It has the advantage of not disturbing the fine textural features while being capable of high magnification. Measurement of the distribution of pores within a sample has utilized a technique known as Laser Scanning Confocal Microscopy (LSCM). The application of this technique requires that the sample be injected with an epoxy doped with a fluorescent dye. LSCM utilizes a laser to focus at different layers of the sample, allowing three-dimensional imaging of the pores. A convenient aspect of LSCM is that the data are recorded digitally. The remainder of this paper will discuss only the analysis of SEM images of pore interiors, the features we consider most important in determining the volume of water that could be adsorbed.

IMAGE ANALYSIS

Studies that have used SEM imagery in the characterization of rock pore space (Krohn, 1988; Krohn and Thompson, 1986), have relied on brightness maxima, often located at the pore edge, to determine feature boundaries (Fig. 3c and d). Although brightness maxima are often present in SEM images, there are circumstances that sometimes prevent their manifestation. Therefore, this study involved development of other methods to handle SEM data.

Digital image processing of SEM data was approached as a micro-scale remote sensing and geographic information system (GIS) problem. This consisted of the use of digital SEM images, at an 8-bit quantization level, to incorporate 256 gray-scale levels to be used in the classification of pore space by albedo. Classifications were made by digitally overlaying GIS files, consisting of maps of the gray-scale images quantified by albedo, onto the original gray-scale images. The ability to digitally overlay mapped data correlation is the heart of GIS. Two methodologies were utilized in this regard (Fig. 4).

Before the geometry of the pore space could be determined, several preprocessing steps were necessary. Initially, SEM images were scanned into a raster format at a resolution of 300 pixels per inch. The resultant raster gray-scale images were then digitally trimmed to remove the remnants of white photographic paper boundaries and mixed pixels along the edge of the image. The trimmed SEM images were then converted into the tag image file format (TIFF), and imported into ERDAS digital image processing software, where they were converted to an ERDAS gray-scale image file format for further processing and classification.

The first classification method involved the reduction of brightness-value data volume. The original gray-scale images consisted of 8-bit data with an albedo (brightness-value) range from 0 to 255. It was believed that the reduction of this range could simplify the classification process and possibly aid in the development of an automated classification procedure.

To accomplish the data reduction, a single SEM digital image was subjected to an iterative self-organizing data analysis technique (ISODATA), a semi-supervised statistical training algorithm. The ISODATA algorithm is similar to a nearest-neighbor classifier, but generally considered to be superior (Campbell, 1987). This technique generates pixel cluster means according to the following criteria: (1) the maximum number of clusters to be considered, (2) the convergence threshold, (3) the maximum number of iterations to be performed, and (4) the minimum number of pixels allowed in a cluster (ERDAS, Inc., 1991). The cluster means are derived from brightness values, with the cluster generation being a function of pixel homogeneity. This process generated the statistics used on subsequent SEM images.

The cluster means generated in training were then utilized in a final classification scheme. This classification strategy consisted of a parallelepiped (Jensen, 1986; Campbell, 1987) preclassification set to a threshold of ± two standard deviations. Cluster means that were found outside of the ± two standard deviation threshold were assigned to an unclassified category. As the outlier data were less homogeneous than the data classified within the parameters set in the parallelepiped method, and due to the fact that some data may fit into overlapping parallelepiped boundaries, a more robust statistical

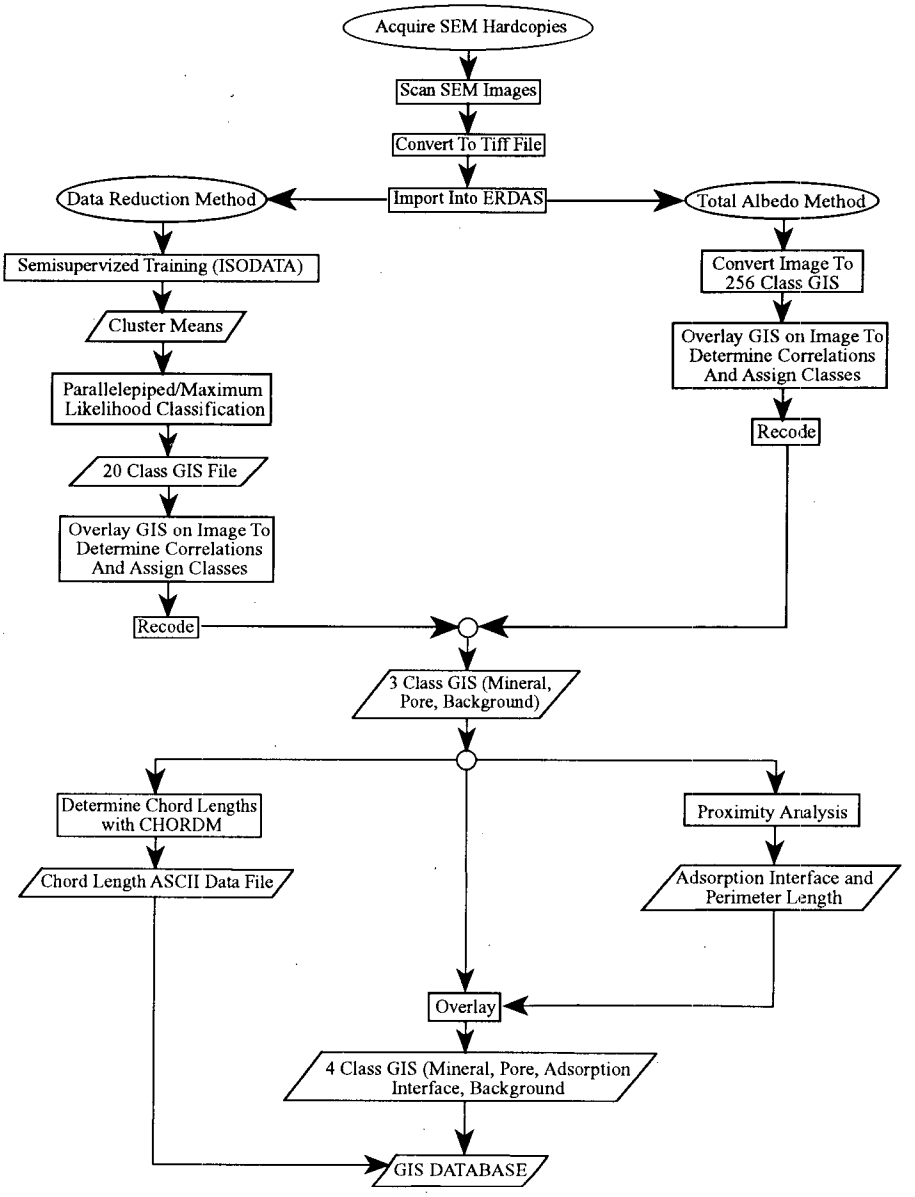

Figure 4. Flow chart for computer assisted porosity determination.

method was utilized to classify the remaining values. The maximum likelihood method was used in this respect (Jensen, 1986; Campbell, 1987). The final output, a twenty class GIS file, consisted of data that had been compressed from 265 to 20 gray-scale levels. Therefore, the albedo data volume was reduced by a factor of 12.19. The twenty-class output GIS file was then utilized to determine which of the new albedo classes best represented solid mineral, pore space, and the interface between the two. The interface is the surface area available for fluid or vapor adsorption. The ISODATA algorithm allows efficient classification as it generates sequential cluster means by albedo level, resulting in gray-scale classes ordered according to brightness values, with class 1 being the closest to black, and class 20 being the closest to white. This 20 gray-scale class GIS file was digitally overlain on the original SEM gray-scale image to determine which classes corresponded with which features. A histogram equalization of the gray-scale image aided in this procedure. Classes 1 - 6 (cluster means of 5.95 - 22.39) were determined to represent pore space best, and classes 7 - 20 (cluster means of 33.44 - 127.67) to represent solid mineral best. The data were then recoded to the two classes indicated above.

This method allows the total automation of all of the above processes. A problem arises in the fact that not all SEM data are consistent. This can be due to scale changes and heterogeneous mineralogy resulting in contrast inconsistencies on the SEM images. Therefore, while data reduction worked very well on a limited number of SEM images, the results were inconsistent on others.

In an attempt to eliminate the problems encountered in the data reduction method, a second, total albedo, approach

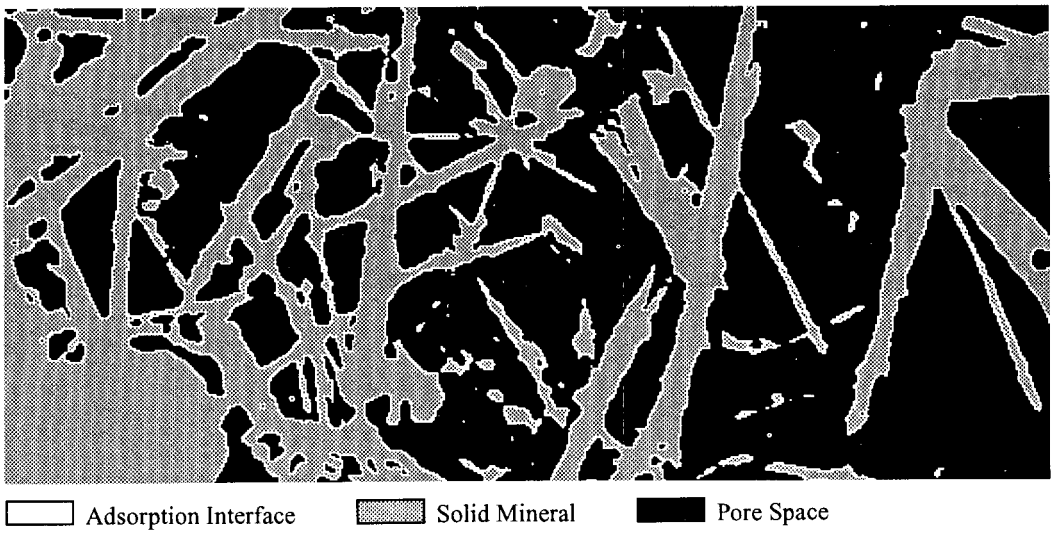

Figure 5. Processed image 02004 (Fig. 3A) with adsorption thickness of 7575 Angstroms

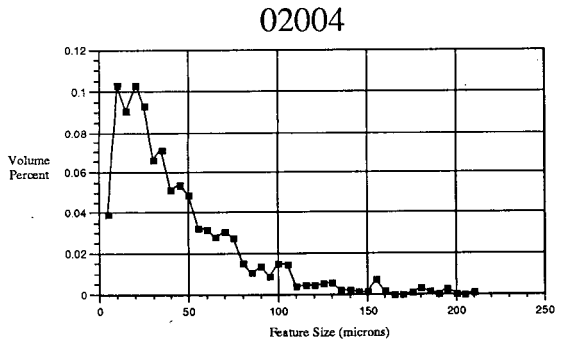

Figure 6. Pore volume relationships from sample 02004 (Fig. 3A)

was developed. In this method, no data reduction was attempted. Therefore, more changes in albedo could be detected. The first step in this method is, again, to transfer scanned SEM images into the ERDAS system.

The gray-scale image is then converted to a GIS file and assigned 256 classes, with class 0 being black, and class 255 being white. The GIS file can then be digitally overlain on the SEM gray-scale image with no further processing. Each of the 256 classes, except zero, are then checked to determine which feature they correspond to. Although there are many more classes to categorize using this method, it was found that it was much more efficient than the data reduction method, as no clustering statistics had to be generated. It was also determined that for the images that did not work well with the data reduction method, each had to be classified as a separate unit. This factor eliminates the possibility of total automation with this method.

The 256-class GIS was then recoded to two classes consisting of solid mineral and pore space. The total albedo method then proceeds in the same manner as the data reduction method. The following methods were applied to both.

The two-class recoded GIS files were used as input to the CHORDM program written by UURI computer specialist Brad Beck. This program measured pore chord lengths which were scaled to microns, and output in ASCII format. The chord lengths were used to determine the statistical distribution of pore dimensions.

The pore space/solid mineral GIS file was then utilized to determine total area of pore space, to determine pore perimeters, and to determine the total length, in microns, scanned by the CHORDM program. Before the statistics of these properties could be compiled, a new class, consisting of adsorption surfaces, had to be generated. It was determined that adsorption surfaces could be estimated by counting the solid mineral pixels at the pore-mineral interface.

To accomplish this task, proximity analysis was utilized. In this process, the area at one pixel depth, immediately adjoining the pore spaces, was determined and reclassified as adsorption interface. Proximity analysis was also utilized to determine the total perimeter of the pore spaces. The ERDAS BSTATS program was then utilized to generate the statistics, which consisted of pore-space area, pore-space perimeter, solid-mineral area, the total adsorption area of the interface between the pore spaces and solid mineral, and the total length of the pixels in the image. Figure 5 is a processed image of sample 02004 (Fig. 3a). The processed image shows solid mineral as stippled, pore space as black, and an adsorbed water layer as white. At this scale, the adsorbed phase is one pixel thick which is equivalent to 7575 Angstroms.

POROSITY DISTRIBUTION

Void space within calcite-dissolution vugs is logarithmically distributed with the greatest volume represented by the lower chord lengths. Figure 6 shows the volume percent as a function of chord length for sample 02004 (Fig. 3A).

Initial observations suggested that the void space in the vugs could be represented by a fractal distribution. The

lengths of chords transecting pore spaces were analyzed using the approach of Krohn (1988). A histogram of chord lengths was constructed using bin sizes appropriate to the scale of the image. These chord lengths were normalized by dividing by the porosity scan length of each individual image. Log-log plots of pore lengths as a function of bin size were prepared. This analysis showed that, for features above 1 micron in size, the distribution of pore volume is not fractal. Sufficient data to analyze feature sizes smaller than this have not been collected at this time.

The objective of this exercise is to estimate the potential liquid reserves due to adsorption. Image analysis provides a measurement of the lengths of chords that traverse pore space and the length of the boundary between the solid and pore. Relative volume calculations of the percent adsorbed fluid assume that the images represented slices of rock that are the thickness of the adsorbed layer. It is also assumed that the total pore space is filled with water resulting in a simple two phase water-adsorbed water relationship. The calculated relative volume of adsorbed water is a function of the magnification of the image. The calculated volume percents were plotted against magnification and then extrapolated to 0. It was found that the actinolite-filled pores had a slightly higher adsorption capacity than epidote-filled pores. The actinolite assemblages supported a 0.005% volume adsorption at an assumed adsorption thickness of 10 Angstroms, 0.05% at 100 Angstroms, and 2.5% at 5300 Angstroms.

CONCLUSIONS

This paper is designed to demonstrate a methodology for using image analysis to determine the proportion of reserves that can be attributed to adsorption in The Geysers reservoir. It should be stressed that this paper is not a comprehensive treatment of matrix porosity since only a few samples have been analyzed in detail. The conclusions from the present work are as follows.

1. Image analysis provides a means for independently measuring porosity distribution and the surface area available for fluid adsorption.

2. Estimates of reserves, using the approach presented here, are highly dependent on the assumed thickness of the adsorbed layer. These data have apparently not been collected for the mineral phases of importance in The Geysers reservoir.

3. The proportion of total water adsorbed to mineral surfaces is small and would not seem to be important in the calculation of total reserves unless extraordinary adsorption thicknesses are present.

ACKNOWLEDGEMENTS

This work was sponsored by the U. S. Department of Energy under contract No. DE/AC07/90ID12929. This support does not constitute a DOE endorsement of the views expressed in this paper. The authors express their appreciation to Wes Martin of Terra Tek for his expert assistance on the Scanning Electron Microscope. We appreciate the technical reviews by P. M. Wright and J. N. Moore of UURI.

REFERENCES

Campbell, J. B., 1987. Image Classification, Introduction to Remote Sensing, Guilford Press: New York, pp. 294-333.

Economides, M. J. and Miller, F. G., 1985, The effects of adsorption phenomena in the evaluation of vapor-dominated geothermal reservoirs: Geothermics, v. 14, p. 3-27.

ERDAS, inc., 1991, Classification, ERDAS Field Guide, pp 105-142.

Giese, R. F. and Costanzo, P. M., 1986, Behavior of water on the surface of kaolin minerals, in Davis, J. A. and Hayes, K. F. (eds.), Geochemical processes at mineral surfaces: American Chemical Society Symposium Series 323, Washington, D.C., p. 37-53.

Gunderson, R. P., 1990, Reservoir matrix porosity at The Geysers from core measurements: Geothermal Resources Council Transactions, v. 14, p. 1661-1665.

He, H. X., Cushman, J. H. and Diestler, D. J., 1987, Molecular dynamics of water near an uncharged silicate surface, in Evans, D. D. and Nicholson, T. J. (eds.), Flow and transport through unsaturated fractured rock: American Geophysical Union Monograph 42, Washington.

Henneker, J. C., 1949, The depth of the surface zone of a liquid: Review Modern Physics, v. 21, p. 322-341.

Hulen, J. B., Nielson, D. L. and Martin, W., 1992, Early calcite dissolution as a major control on porosity development in The Geysers steam field, California--additional evidence in core from Unocal well NEGU-17: Geothermal Resources Council Transactions, v. 16, p. 167-174.

Hulen, J. B., Walters, M. A., and Nielson, D. L., 1991, Comparison of reservoir and caprock core from the northwest Geysers steam field--implications for development of reservoir porosity: Geothermal Resources Council Transactions, v. 15, p.11-18.

Jaroniec, M. and Madey, R., 1988, Physical adsorption on heterogenous solids: New York, Elsevier, 351 p.

Jensen, J. R., 1986. Thematic Information Extraction, *Introductory Digital Image Processing*, Prentice Hall: Englewood Cliffs, pp. 177-233.

Krohn, C. E., 1988, Sandstone fractal and euclidean pore volume distributions: Journal of Geophysical Research, v. 93, p.3286-3296.

Krohn, C. E. and Thompson, A. H., 1986, Fractal sandstone pores: automated measurements using scanning-electron-microscope images: Physical Review B, v. 33, p.6366-6374.

Mulla, D. J., 1986, Simulating liquid water near mineral surfaces: current methods and limitations, in Davis, J. A. and Hayes, K. F. (eds.) Geochemical processes at mineral surfaces: American Chemical Society Symposium Series 323, Washington, D.C., p. 20-36.

Moore, J. N., 1992, Thermal and chemical evolution of the Geysers geothermal system, California: Reprints, Seventeenth Workshop Geothermal Reservoir Engineering, Stanford University.

Nielson, D. L. and Brown, D., 1990, Thoughts on stress around The Geysers geothermal field: Geothermal Resources Council Transactions, v. 14, p. 1685-1690.

Pruess, K. and Narasimhan, T. N., 1982, On fluid reserves and the production of superheated steam from fractures, vapor-dominated geothermal reservoirs: Journal of Geophysical Research, v. 87, p. 9329-9339.

Pruess, K. and O'Sullivan, M., 1992, Effects of capillarity and vapor adsorption in the depletion of vapor-dominated geothermal reservoirs: Reprints, Seventeenth Workshop Geothermal Reservoir Engineering, Stanford University.

Ramey, H. J., 1990, Adsorption in vapor-dominated systems: U. S. Department of Energy Geothermal Program Review VIII, CONF-9004131, p. 63-67.

Thompson, A H., 1991, Fractals in rock physics, in Wetherill, G. W., Albee, A. L. and Burke, K. C., (eds.), Annual Review of Earth and Planetary Sciences, v. 19, p. 237-262.

Truesdell, A. H. and White, D. E., 1973, Production of superheated steam from vapor-dominated geothermal reservoirs: Geothermics, v. 2, p. 154-173.

Williamson, K. H., 1990 Reservoir simulation of The Geysers geothermal field: Proceedings, Fifteenth Workshop on Geothermal Reservoir Engineering, Stanford University, SGP-TR-130, p. 113-123.

Willis, G. F. and Tosdal, 1992, Formation of gold veins and breccias during dextral strike-slip faulting in the Mesquite Mining district, southeastern California: Economic Geology, v. 87, p.2002-2022.

PROCEEDINGS, Eighteenth Workshop on Geothermal Reservoir Engineering
Stanford University, Stanford, California, January 26-28, 1993
SGP-TR-145

PARAMETRIC ANALYSIS OF FACTORS AFFECTING INJECTION AND PRODUCTION IN GEOTHERMAL RESERVOIRS

John W. Hornbrook
Stanford University

D.D. Faulder
Idaho National Engineering Laboratory

ABSTRACT

A program was designed to allow the study of the effects of several parameters on the injection of water into and production of fluid from a fractured low porosity geothermal reservoir with properties similar to those at The Geysers. Fractures were modeled explicitly with low porosity, high permeability blocks rather than with a dual-porosity formulation to gain insight into the effects of single fractures.

A portion of a geothermal reservoir with physical characteristics similar to those at the Geysers geothermal field was constructed by simulating a single fracture bounded by porous matrix. A series of simulation runs were made using this system as a basis. Reservoir superheat prior to injection, injection temperature, angle of fracture inclination, fracture/matrix permeability contrast, fracture and matrix relative permeability, and the capillary pressure curves in both fracture and matrix were varied and the effects on production were compared. Analysis of the effects of these parameter variations led to qualitative conclusions about injection and production characteristics at the Geysers.

The degree of superheat prior to water injection was found to significantly affect the production from geothermal reservoirs. A high degree of superheat prior to injection increases the enthalpy of the produced fluid and causes the cumulative produced energy to nearly equal that from a reservoir which began injection much earlier. Injection temperature was found to have very little effect on production characteristics. Angle of fracture inclination affects the enthalpy of the produced fluid. Fractures dipping toward the production well allow greater flow of water toward the producer resulting in lower enthalpies of produced fluid. The fracture/matrix permeability contrast was shown to influence the production in an expected way: The lower the contrast, the lower the production rate, and the lower the enthalpy of the produced fluid at a given time. Results obtained by varying relative permeability show that the relative permeability curves used have little effect on the production from the reservoir. This indicates that the transfer between the matrix and the fracture is dominated by capillary forces, thus reducing the importance of the shape of the relative permeability curve. Capillary pressure curves were shown to have a strong effect on production characteristics, further emphasizing the importance of capillary forces in Geysers-type geothermal reservoirs.

INTRODUCTION

Due to recent pressure decline in The Geysers geothermal reservoir, much effort has been focused on understanding not only the physics of production from the reservoir, but also the mechanism for possible recharge of the reservoir by injection of fresh water or produced condensate. Over the past several years, numerous field studies and simulations have attempted to answer the unknowns in reservoir depletion and possible recharge. For example, it has been shown that high local levels of superheat may evolve at The Geysers and it has been assumed that these areas provide excellent sites for recharge of the reservoir (Enedy, 1992) and (Enedy, et. al., 1992). Further, simulation studies have been used in an attempt to optimize the rates of injection and production to maximize the producing life of The Geysers (Shook & Faulder, 1991). While field studies indicate that recharge is a viable option for extending the life of a geothermal reservoir and field-scale simulations provide insight into optimization of recharge schemes, much research is still needed to understand the individual effects of the many parameters affecting flow in geothermal reservoirs. This study is directed at understanding the influences of various parameters (superheat prior to injection, injectate temperature, fracture angle, fracture/matrix permeability contrast, relative permeability, and capillary pressure) on the recharge and production in a Geysers-like geothermal reservoir.

SIMULATION PROCEDURE

A slice of a geothermal reservoir with characteristics similar to those at The Geysers was constructed. Injection of water into and the subsequent production of vapor from this system were analyzed under a variety of conditions. A summary of the model follows:

Gridding:

Block Size:	10m x 1m x 10m.
Dimensions:	400m x 1m x 50m.
Fracture:	Single fracture in center of system (Figure 1).
Boundaries:	All boundaries are no-flow.

Matrix Properties:

Porosity:	0.04.
Permeability:	0.10 md.

Rel. Perm:	Various relative permeability curves were tested (S_{wr} = 0.3, S_{vr} = 0.05). See "Relative Permeability".
Cap. Pressure:	Several capillary pressure curves were tested. See "Capillary Pressure".
Initial Pressure:	4000.0 kPa.
Initial Temp.:	240 C.
PVT Data:	Entered via standard steam tables.
Initial S_W:	0.7.

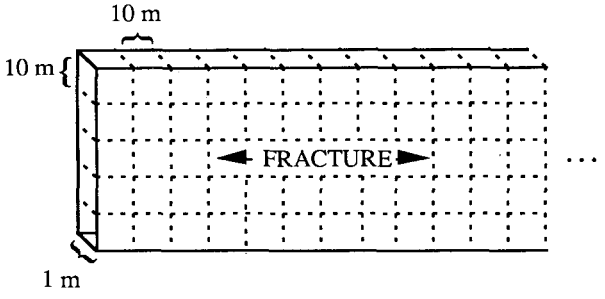

Fig. 1: Simulated reservoir slice

Fracture Properties:

Porosity:	0.0001 (Simulates a 1 mm fracture).
Permeability:	Various fracture permeabilites were tested. See "Permeability".
Rel. Perm:	Various relative permeability curves were tested (S_{wr} = 0.1, S_{vr} = 0.01). See "Relative Permeability".
Cap. Pressure:	Several capillary pressure curves were tested. See "Capillary Pressure".
Initial Pressure:	4000.0 kPa.
Initial Temp.:	240 C.
PVT Data:	Entered via standard steam tables.
Initial S_W:	0.3.

Investigation Procedure:

A systematic procedure for analyzing the effects of various parameters on the injection and production characteristics in a low porosity, fractured reservoir was developed. Since the fracture was to be modeled explicitly, it was first necessary to determine the best way in which to model the fracture. Either a five-point differencing scheme with a small matrix block representing the fracture or a nine-point differencing scheme with a large, low-porosity block representing the fracture may be used to explicitly model a fracture. It was necessary to determine which differencing scheme was more suited to the problems described in this paper. Pruess (1991) indicated that, under certain conditions, nine-point differencing may be superior to a five-point differencing scheme. Although, there are cases in which a five-point differencing scheme may be preferable, cases in which horizontal and vertical forces are on the same order are usually best modeled with a nine-point scheme. For the problems described in this paper, viscous forces (horizontal) dominate as the fracture flow mechanism while capillary forces (vertical) dominate as the matrix/fracture transfer mechanism. Therefore, it was expected that nine-point differencing would be preferable. A series of simulations not included in this paper confirmed that a nine-point differencing scheme should be used for subsequent simulations.

Once the differencing scheme was determined, a base case simulation was carried out which would serve as a comparison basis for all other simulations. Base case properties are as follows:

Base Case Properties:

Rel. Perm.:	Corey curves with n = 1.5.
Cap. Pressure:	Power law : $P_{cmax}*(S_W)^j$ (jmatrix = 8, jfrac = 2) P_{cmax} (matrix = 1075.30, fracture = 38.57).
Prod. Rate:	12.0 kg/hr.
Inj. Rate:	4.0 kg/hr.
Inj. Enthalpy:	126 kJ/kg.
Inclination:	0.0 degrees.

The parameters used in the base case simulation were then varied as described in the following sections and their effects on production rate, enthalpy of produced fluid, and total produced energy were compared.

EFFECTS OF DEGREE OF SUPERHEAT PRIOR TO INJECTION

The effects of reservoir superheat prior to injection were studied by comparing three simulation cases (Figs. 2a - 2d). In the first case, base case properties were used without injection. In the second case, base case properties were used with injection starting at t = 0. In the third case, base case properties were used with injection starting at t = 10,000 days. The first case illustrates the production history of a Geysers-type geothermal reservoir without any injection. It shows the drawdown and eventual depletion of the reservoir. Superheat develops in the reservoir at about 10,000 days and the reservoir becomes completely depleted at about 12,500 days.

The second case shows the effects of injecting water at 33% of the producing rate beginning at t = 0 days. In this case, depletion effects are not seen until about 19,000 days and significantly more energy is produced than in the case without injection.

The third case shows the effects of injecting water at 33% of the producing rate beginning at t = 10,000 days. In this case, depletion effects are first seen at about 13,500 days and the cumulative mass produced falls exactly between that in cases one and two, as it should (Fig. 2b). However, the enthalpy of the produced fluid is significantly higher than that in either of the first two cases. As a consequence of the higher produced enthalpy, the cumulative energy produced in the third case is nearly as high as in the second despite the fact that much less mass is produced.

The above described series of simulations indicates that high reservoir superheat leads to a more efficient conversion of injectate to produced energy. It also implies that geothermal reservoirs should be slightly depleted before an injection program is initiated.

It is noted that while shortcomings in the simulator used resulted in reported enthalpies which are unreasonably high, the trends are qualitatively correct.

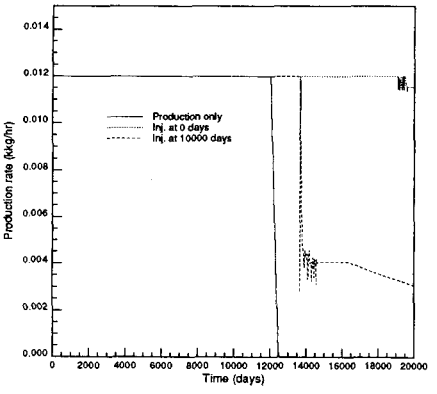

Fig. 2a: Mass production rate

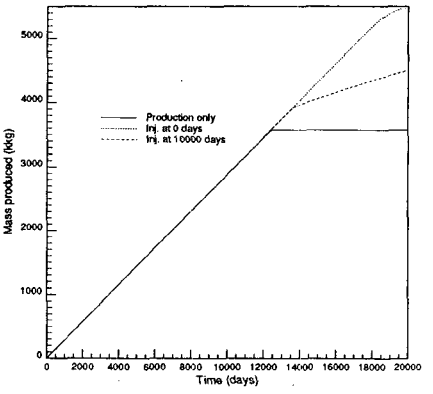

Fig. 2b: Cumulative mass produced

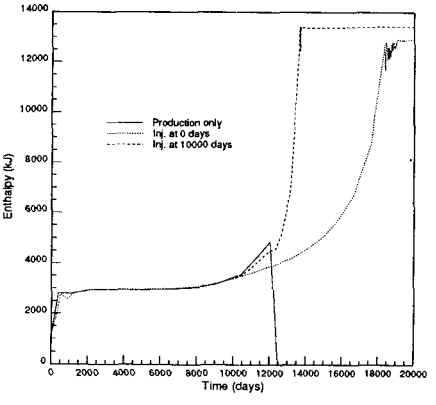

Fig. 2c: Enthalpy of produced fluid

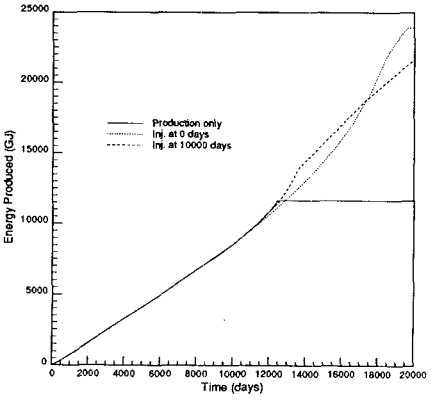

Fig. 2d: Cumulative energy produced

EFFECTS OF INJECTATE TEMPERATURE

The effects of injectate temperature on fluid production were studied by comparing simulation results from three different cases (Figs. 3a - 3d). In case one, injectate enthalpy is 126 kJ/kg (T = 30 C); in case two, injectate enthalpy is 337 kJ/kg (T = 80 C); and in case three, injectate enthalpy is 677 kJ/kg (T = 160 C). Woods and Fitzgerald (1992) and others have indicated that injection fluid temperature equilibrates quickly with reservoir temperature, so injection temperature should not strongly influence the behavior of an injection/production pair in a geothermal reservoir.

Simulation results support earlier research and indicate that the temperature of the injectate has little or no effect on the production history of an injection/production pair in a geothermal reservoir. Figures 3a - 3d show that temperature has no effect on production rate or energy produced and, therefore, should not be considered in designing injection programs in geothermal reservoirs.

EFFECTS OF FRACTURE ANGLE

The effects of fracture inclination were studied by comparing three simulations with varied fracture inclination. In case one, a horizontal fracture was simulated. In case two, the fracture was inclined at 15 degrees to the horizontal from the injector to the producer. In other words, injection fluid would be forced to travel slightly uphill to reach the producer. In case three, the angle of inclination was -15 degrees to the horizontal. Results of the simulations (Figs. 4a - 4d) indicate that while fracture inclination has little or no effect on mass production (Figs. 4a, 4b), it strongly affects energy production (Figs. 4c, 4d).

An fracture inclined upwards toward the producer tends to increase energy production since liquid water flow is retarded while a fracture inclined toward the injector has the inverse effect.

The influence of fracture inclination indicates that this is a very important parameter in the modeling of flow in geothermal reservoirs.

EFFECTS OF FRACTURE/MATRIX CONTRAST IN PERMEABILITY

The effects of the fracture/matrix permeability contrast were studied by comparing two simulations with widely different permeability contrasts (Figs. 5a - 5d). In the first case (base case - fracture permeability = 100 md), the permeability contrast between fracture and matrix was 1000. In the second, the contrast was reduced to 10

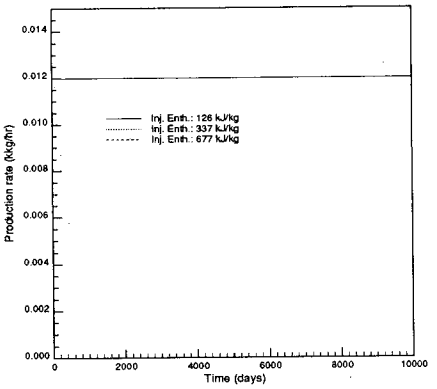

Fig. 3a: Mass production rate

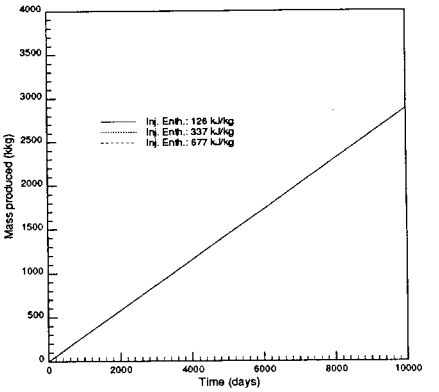

Fig. 3b: Cumulative mass produced

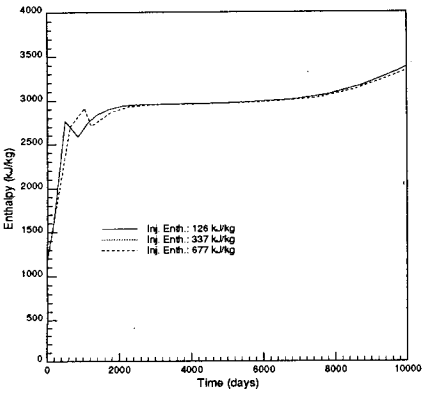

Fig. 3c: Enthalpy of produced fluid

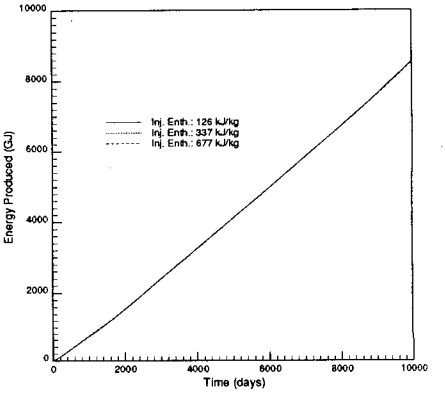

Fig. 3d: Cumulative energy produced

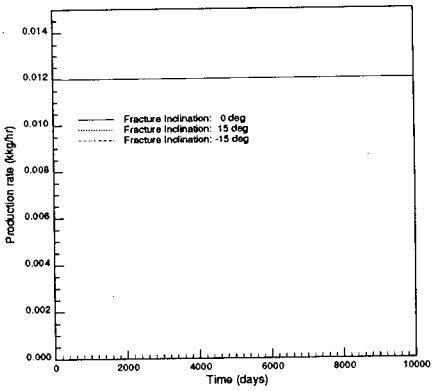

Fig. 4a: Mass production rate

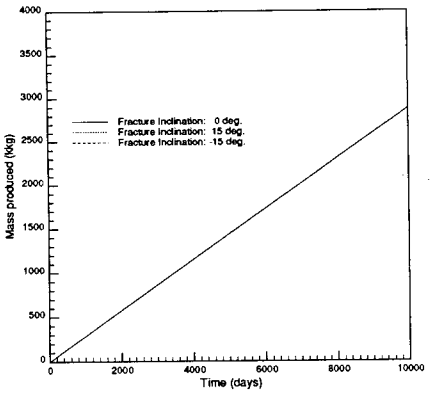

Fig. 4b: Cumulative mass produced

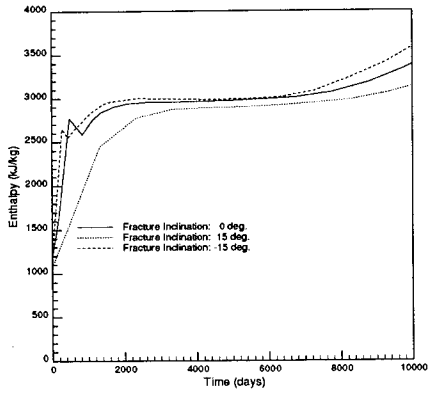

Fig. 4c: Enthalpy of produced fluid

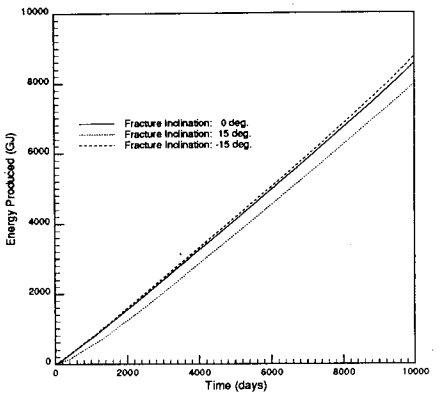

Fig. 4d: Cumulative energy produced

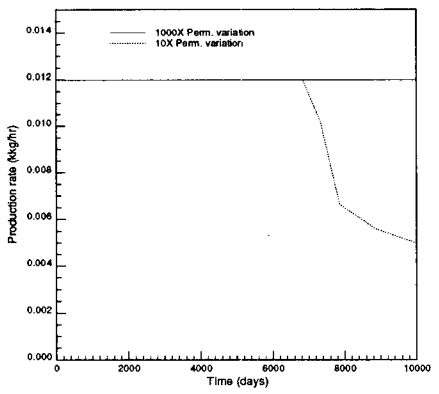

Fig. 5a: Mass production rate

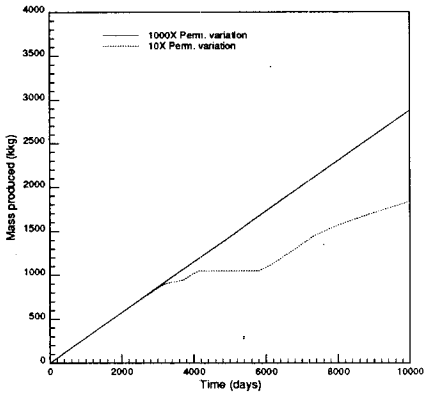

Fig. 5b: Cumulative mass produced

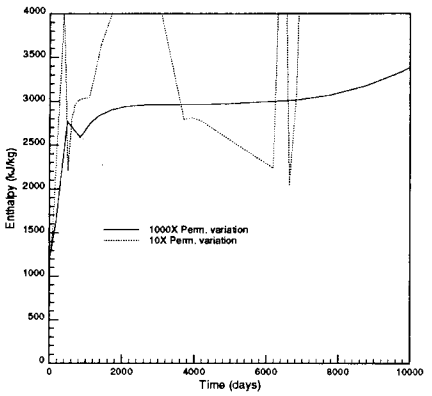

Fig. 5c: Enthalpy of produced fluid

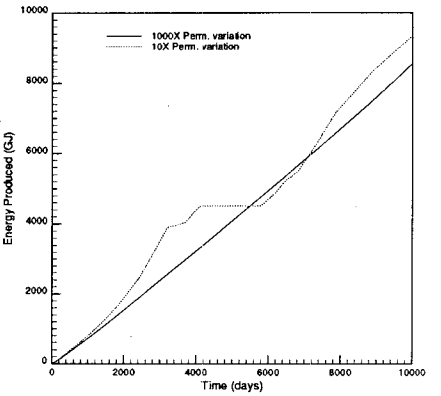

Fig. 5d: Cumulative energy produced

(fracture permeability was reduced from 100 md to 1.0 md). Comparison of the two cases indicates, as expected, that the fracture/matrix permeability contrast strongly effects the production history in geothermal reservoirs. Fig. 5a indicates that production rate, which is controlled by fracture flow, is limited with lower permeability in the fracture. The effect on enthalpy of produced fluid is as significant but is not as obvious. Fig. 5c shows that for the low contrast case, the enthalpy of produced fluid is reduced. This is due to a reduction in pressure drawdown in the fracture and a subsequent reduction in fracture fluid enthalpy. Cumulative mass and energy produced (Figs. 5b and 5d, respectively) are also reduced for the reasons described above.

Therefore, fracture/matrix permeability contrast is significant not only as a rate controlling mechanism, but also as an energy production mechanism.

EFFECTS OF RELATIVE PERMEABILITY

Corey relative permeability curves for both the matrix and the fracture were varied to study the effects of relative permeability variation on the fluid flow in geothermal reservoirs. The exponent in the Corey relationship was varied from 1.0 to 2.0 (Figs. 6a and 6b) and the effects of these changes on the mass and energy production were documented. It was observed that altering the relative permeability curves produced only minor changes in the mass and energy production histories with injection at 33% of the production rate (Figs. 8a - 8d).

Guzman and Aziz (1992) showed that relative permeabilities are important only if capillary forces are small. When capillary forces are dominant, relative permeabilities are of limited importance. It is apparent from simulation results that in Geysers type reservoirs, capillary forces are sufficiently large to make relative permeabilities unimportant.

Therefore, in low permeability, fractured geothermal reservoirs, it is likely that capillary forces dominate as the matrix/fracture transfer mechanism. In these cases, relative permeabilities are of little importance as a mechanism influencing flow.

EFFECTS OF CAPILLARY PRESSURE

Results from the previous section ("Effects of relative permeability") indicate that capillary forces are much more important as a flow controlling mechanism than relative permeability. Three cases with different matrix and capillary pressure curves were studied to determine the effects of capillary pressure. Case one (base case) made use of a power-law relationship (see "Base Case Properties") (Fig. 8a). Maximum capillary pressures for matrix and fracture were chosen to be 1075.30 kPa and 38.57 kPa, respectively. Case two used the same

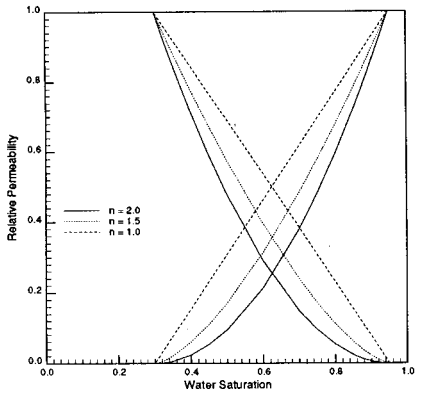

Fig. 6a: Matrix relative permeability curves

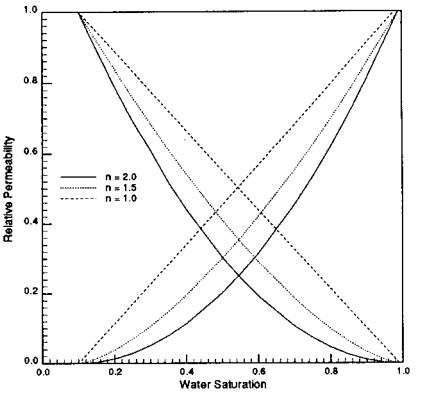

Fig. 6b: Fracture relative permeability curves

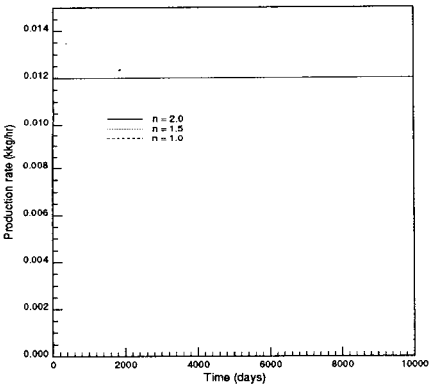

Fig. 7a: Mass production rate

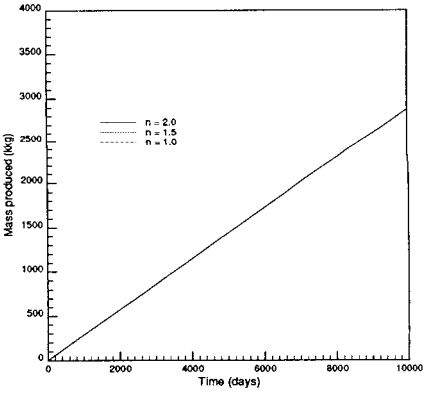

Fig. 7b: Cumulative mass produced

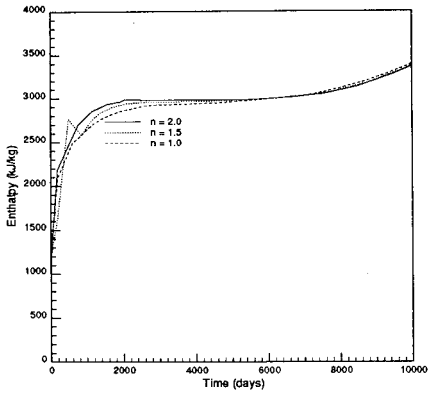

Fig. 7c: Enthalpy of produced fluid

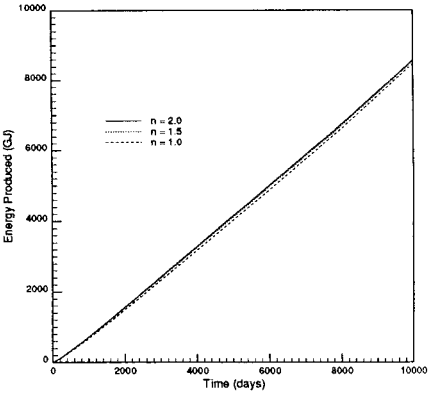

Fig. 7d: Cumulative energy produced

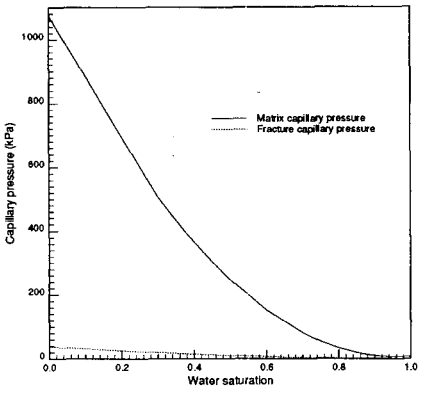

Fig. 8a: Base case capillary pressure curves

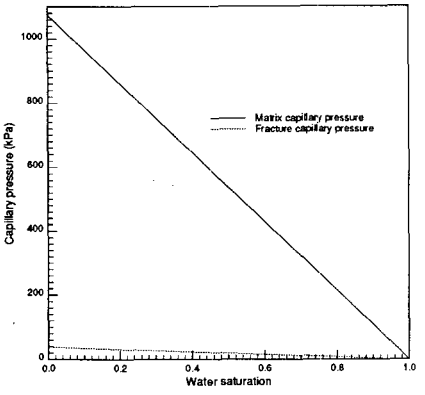

Fig. 8b: Linear capillary pressure curves

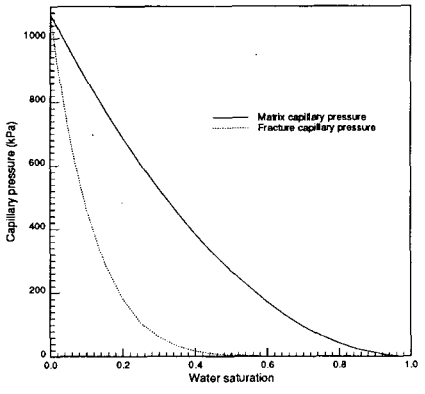

Fig. 8c: Equilibrium capillary pressure curves

enpoint capillary values but varied P_C linearly (Fig. 8b). Case three allowed for endpoint capillary pressure equilibrium at 1075.30 kPa and varied P_C by a power law relationship with n = 2 for the matrix and n = 8 for the fracture (Fig. 8c).

Simulation results indicate that the variations in capillary pressure described above strongly affect the production response in geothermal reservoirs (Figs. 9a - 9d). While mass production is not strongly influenced (Figs. 9a and 9b), the energy production history is (Figs. 9c and 9d). Of the three cases modeled, case two (linear P_C) exhibits the highest capillary pressure over the entire range of water saturation. As a result, vapor is more mobile than water and the result is higher production enthalpy and cumulative produced energy.

Case two exhibits the smallest difference between the fracture and matrix capillary pressures. As a result, water becomes more mobile and lower enthalpy fluid may be produced, especially at low water saturations when matrix and fracture relative permeabilities are almost identical.

Capillary pressure is extremely important in modeling flow in low permeability, fractured geothermal reservoirs. Not only is the shape of the P_C curve important, but also the endpoint characteristics of the matrix and fracture capillary pressure curves. More research is necessary in this area to better understand the role of capillary pressure in fluid flow through geothermal reservoirs.

CONCLUSIONS

1. The degree of superheat prior to injection has a significant impact on production from geothermal reservoirs. High initial superheat translates into higher production enthalpies. High production enthalpies may make up for the reduction in mass produced when injection initiation is delayed until superheat develops.

2. Injection fluid temperature has little effect on the production of fluids from geothermal reservoirs. Neither mass produced nor energy produced are affected to any appreciable degree by the temperature of the injectate.

3. The fracture angle strongly affects the production response in geothermal reservoirs. Fracture inclination between injector/producer pairs reduces water flow and increases the enthalpy of the produced fluid. Fracture declination, conversely, increases water flow in the fracture and decreases the enthalpy of the produced fluid.

4. The fracture/matrix permeability contrast can effect the production of fluids from geothermal reservoirs. The lower the contrast, the lower is the mass production

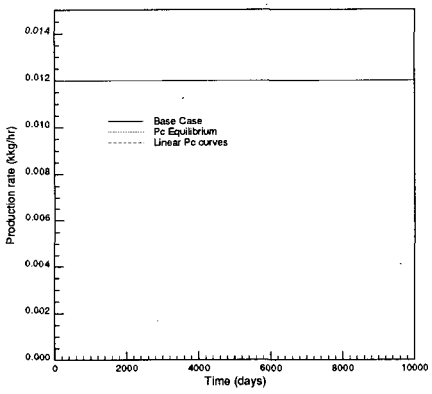

Fig. 9a: Mass production rate

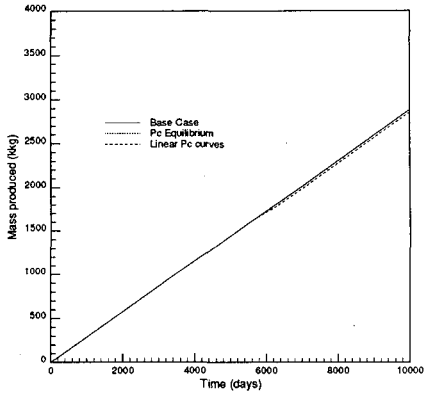

Fig. 9b: Cumulative mass produced

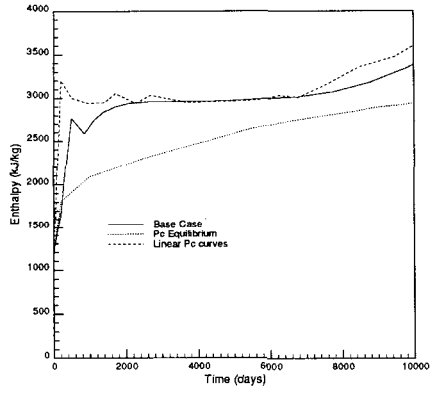

Fig. 9c: Enthalpy of produced fluid

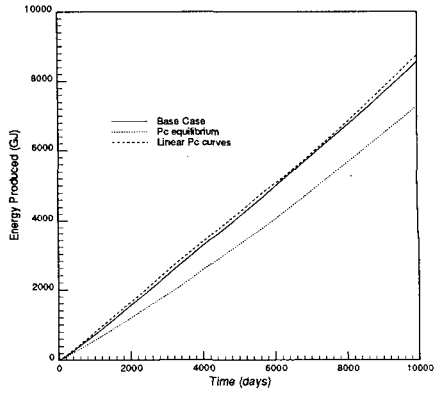

Fig. 9d: Cumulative energy produced

rate and the lower is the pressure drawdown in the fracture. As the pressure drawdown in the fracture decreases, the enthalpy of the vapor in the fracture is also reduced thus resulting in a reduction in produced fluid enthalpy and cumulative energy production.

5. Fracture relative permeabilities have little effect on the production from low permeability, fractured geothermal reservoirs. In these type of reservoirs, the capillary pressure forces dominate and relative permeabilities do not have a significant effect.

6. Capillary forces are extremely important in determining the injection and production characteristics in low permeability, fractured geothermal reservoirs. Due to the dominance of capillary forces in these type reservoirs, the shape and end-point characteristics of capillary pressure curves are both extremely important. More research on capillary forces in geothermal reservoirs is needed, especially at low water saturation, to better understand and model fluid flow in these reservoirs.

ACKNOWLEDGEMENTS

The authors wish to thank Mike Shook of INEL and Marc Hornbrook of BP, Alaska for their help and support and Rafael Guzman of Stanford University for his useful comments.

NOMENCLATURE

Variable Names:

j	Exponent in capillary pressure expression.
K	Permeability [md].
n	Exponent in rel. permeability expression.
P	Pressure [kPa].
S	Saturation [%].
T	Temperature[C].

Subscripts:

c	capillary.
frac	fracture values
matrix	matrix values
max	maximum
r	residual.
v	vapor.
w	water.

REFERENCES

Enedy, K.L. (1992) Downhole Enthalpy and Superheat Evolution in Geysers Steam Wells, *Monograph on The Geysers Geothermal Field,* GRC, pp. 205 - 209, 1992.

Enedy, S.L., Enedy, K.L., and Maney, J. (1992) Reservoir Response to Injection in the Southeast Geysers, *Monograph on The Geysers Geothermal Filed,* GRC, pp. 211 - 219, 1992.

Guzman, R.E. and Aziz, K., Fine Grid Simulation of Two-Phase Flow in Fractured Porous Media, Presented at the 67th Annual Technical Conference and Exhibition of the Society of Petroleum Engineers, Washington, D.C., Oct. 4-7, 1992, SPE 24916.

Pruess, K. (1991) Grid Orientation and Capillary Pressure Effects in the Simulation of Water injection into Depleted Vapor Zones, *Geothermics*, Vol. 20, No. 5/6, pp. 257-277, 1991.

Shook, G.M. and Faulder, D.D. (1991) Analysis of Reinjection Strategies for the Geysers.

Woods, A.W. and Fitzgerald, S.D., The generation of vapour in a hot rock through injection of cold water, Cambridge University, England, Unpublished report, April, 1992.

PROCEEDINGS, Eighteenth Workshop on Geothermal Reservoir Engineering
Stanford University, Stanford, California, January 26-28, 1993
SGP-TR-145

NUMERICAL MODELING OF INJECTION EXPERIMENTS AT THE GEYSERS

Karsten Pruess‡ and Steve Enedy†

‡Earth Sciences Division, Lawrence Berkeley Laboratory
University of California, Berkeley, CA 94720

†Northern California Power Agency, P.O. Box 663,
Middletown, CA 95461

ABSTRACT

Data from injection experiments in the southeast Geysers are presented that show strong interference (both negative and positive) with a neighboring production well. Conceptual and numerical models are developed that explain the negative interference (decline of production rate) in terms of heat transfer limitations and water-vapor relative permeability effects. Recovery and over-recovery following injection shut-in are attributed to boiling of injected fluid, with heat of vaporization provided by the reservoir rocks.

INTRODUCTION

Since the mid-eighties, reservoir pressures and well production rates at The Geysers have entered a period of accelerated decline (Goyal and Box, 1990; Enedy, 1992). Steam shortfalls have curtailed power generation, and have emphasized the need to view injection not just as a means for condensate disposal, but as a reservoir management tool for replenishing dwindling fluid reserves and enhancing energy recovery.

Injection design and interpretation of monitoring data require an understanding of the important reservoir processes. Using detailed data from a series of injection experiments in the southeast Geysers, we attempt to identify fluid and heat flow processes and geometric controls that determine reservoir response to injection.

INJECTION EXPERIMENTS

Recent injection experiments performed by NCPA in the Southeast Geysers have shown dramatic patterns of interference with production. During 1990 water was injected into well Q-2 for periods of from one day to several weeks at rates of 200-600 gpm (approximately 12-36 kg/s). Nearby production well Q-6 responded to injection with rapid strong rate declines. When injection was stopped production not only recovered but over-recovered. As shown in Figure 1, the interference pattern could be repeated over many injection cycles, and (over-) recovery of production was stronger for longer periods of injection shut-in.

Wells Q-2 and Q-6 are located in the north-central portion of the NCPA steam field near the lease line with Calpine's Unit 16 steam field. The wells are completed within the Franciscan graywacke, a metamorphosed sandstone. Greenstone segments within the graywacke serve as a secondary host rock. The main reservoir is overlain by a heterogeneous mixture of rock types which is set behind casing. The entire study area is underlain by a silicic intrusive known as the felsite; although neither Q-2 or Q-6 are drilled deep enough to reach the felsite. The wells are surrounded on all sides by steam production wells which are in hydraulic communication with both wells based on deuterium distribution (Beall et al., 1989) and static pressure analysis.

Prior to 1987, Q-2 was the primary injector for NCPA's Plant #2 with injection rates ranging from 800 to 2,000 gpm. Following the drilling and subsequent completion of several steam wells including Q-6 in 1987, the amount of injection into Q-2 was considerably reduced due to communication with offset steam wells. During 1990, Q-2 served as one of five injection wells utilized to inject condensate in the NCPA steam field and one of 34 injection wells used at The Geysers. Injection rates were normally limited to 200 to 600 gpm in order to minimize the amount of communication with the offset wells. The location of the wells within the field along with the relative volume of water injected into each Geyser injection well is shown in Figure 2.

Wells Q-2 and Q-6 are both directionally drilled. Q-6 is a type of non-conventional well completion known as a "forked hole" which is a well with two legs open to steam production. Both wells have multiple steam entries at depths between 1,300-2,000 m (4,265-6,562 ft) with typical spacing between steam entries of 100 m (328 ft). The distance between steam feeds in Q-2 and those in either leg of Q-6 range from 200-800 m (656-2,625 ft). A plan view and cross-section is shown in Figure 3.

Injection into Q-2 also caused interference with Calpine well 9589, which is located approximately 300 m (984 ft) due north of Q-2 (Tom Box, private communication). Initial effects were beneficial, increasing production rates, but later water breakthrough was observed.

The striking patterns of injection interference between wells Q-2 and Q-6 call for an explanation. In an attempt to identify reservoir conditions and processes that could cause such behavior, we first develop hypothetical models that may be capable of explaining the observations. Subsequently the viability of proposed models is evaluated by means of numerical simulation, and conclusions are drawn for design and monitoring of injection systems.

CONCEPTUAL MODEL

The strength and rapidity of interference between Q-2 and Q-6 suggests that both wells intersect some of the same fractures or fracture zones. These fractures would accept much of the fluid injected into Q-2, and provide important paths for flow of reservoir vapor to well Q-6 steam entries. During injection a plume of heating and partially boiling liquid will spread around the injection well. Depending on rates of fluid injection, and heat transfer from the reservoir rocks to the injection plume, two-phase zones with declining temperatures may develop. Because of the one-to-one correspondence between temperatures and pressures in two-phase conditions, fluid pressures in parts of the injection plume and the surrounding reservoir may decline, causing flow rate declines in neighboring wells. In addition, injected liquid in the fractures may partially block the vapor flow paths from the reservoir "at large" to well Q-6 feeds. This interference of injection-derived liquid with vapor flow can be thought of as a relative permeability effect.

After injection is stopped the injected liquid will, in part, boil away, migrate to greater depth, or be sucked by capillary force away from the fractures into the low-permeability rock matrix. Removal of the liquid will clear the fracture flow paths for vapor, causing production to recover. The observed over-recovery indicates that the injected liquid becomes available as a significant additional source of steam, boiling close to Q-6 ("close" in the sense of good hydraulic communication), with excellent access to reservoir heat. Heat transfer to the fluid could occur either by conduction to the fractures, with fluid boiling in the fractures, or injected liquid could be imbibed into the rock matrix, boiling there from local heat exchange.

Based on the foregoing discussion, the most important component in the model will be the fracture(s) by which Q-2 and Q-6 are connected. The fractures will take a portion of the fluid injected into Q-2, and will supply part of the production to Q-6. They will be coupled to matrix rock of small but finite permeability, that will transfer heat to the fluids in the fractures by conduction, while absorbing liquid from the fractures by capillary force. In addition to the specific fractures that connect Q-2 and Q-6, there is a general "background" reservoir that supplies long-term production to the local fracture system, and may also absorb some of the injected fluid.

The nature of the fracture system at The Geysers has been discussed in recent papers by Beall and Box (1989) and Thompson and Gunderson (1992). Both sub-horizontal and sub-vertical fractures are present. In the southeast Geysers high-angle (nearly vertical) fractures are thought to dominate. Monitoring of natural tracers (deuterium) in the southeast Geysers showed that injected fluids migrate primarily in north-south direction (Beall et al., 1989). The available information from the field does not provide the detailed geometry of the local fracture system on the scale of the distance between Q-2 and Q-6 feeds, of order 300m (984 ft). Our approach is to start with the simplest assumptions and flow geometries that would seem capable of explaining the strong and rapid negative production interference during injection, and the (over-)recovery following injection shut-in. Our modeling assumptions will then be revised and refined as needed to reduce discrepancies between predicted and observed behavior. The most "stripped down" model would seem to need two essential ingredients: (i) a single fracture intersecting both Q-2 and Q-6, and (ii) a large "background reservoir" connected to this fracture. Even in this most simplified model the flow geometry would be three-dimensional, and fluid and heat flows would need to be considered over a very large range of thermo-hydrologic parameters and spatial scales. Indeed, permeabilities range from microdarcies in the rock matrix to perhaps tens or hundreds of darcies in the fractures. Relevant spatial scales for the important flow processes are of the order of centimeters for flow in the fractures and imbibition into the rock matrix, several decimeters for penetration of heat conduction into wall rock over several days, and hundreds of meters for reservoir perturbation from long-term production. When coupled with the extremely non-linear process complexities of two-phase vaporizing flows, this leads to impractical computational demands, and further simplifications must be made.

Flow geometry can be simplified by modeling the fracture and the background reservoir as two separate two-dimensional systems with appropriate coupling, although in reality the local fractures are of course embedded in the reservoir. The background reservoir is modeled as a large radially-symmetric layered (R-Z) system. The fracture is modeled as a rectangular vertical (X-Z) section. Although the fracture itself requires only 2-D gridding, consideration of fluid and heat flow between the fracture and the surrounding reservoir rock will still make the system three-dimensional.

NUMERICAL SIMULATION APPROACH

A schematic of our fracture-reservoir flow model is shown in Fig. 4; the model parameters are summarized in Table 1. These parameters were not specifically selected for the local conditions in the study area; rather, they are intended to be generically applicable to The Geysers reservoir. Generally speaking, hydrologic parameters needed for two-phase flow modeling are not well known for Geysers rocks. As in previous studies of vapor-dominated reservoirs (Pruess and O'Sullivan, 1992), we have borrowed data for welded tuffs from nuclear-waste related studies (Peters et al., 1984). Welded tuffs have permeabilities in the microdarcy or fraction-of-a -microdarcy range, and are believed to have similar capillary and relative permeability behavior as unfractured graywacke or felsite from The Geysers.

We have modeled vertical fractures of different total area, from 300 x 300 to 600 x 600 m^2 (984 x 984 to 1969 x 1969 sq. ft). The fracture is modeled as a high-permeability porous medium with a small effective void space thickness of 1 cm (.39 in.), and a permeability-thickness product of 40 dm (131,200 millidarcy-ft). Relative permeability and capillary pressure behavior of fractures is not well known. Recent theoretical and experimental studies by Pruess and Tsang (1990) and Persoff et al. (1991) have suggested that two-phase flow behavior of fractures may be similar to that of three-dimensional porous media of high permeability. We have assumed that fracture capillary pressures are negligibly small, and that relative permeabilities may be represented by standard Corey-curves.

The distance between injection and production well is 240 m (787 ft). The background reservoir is modeled as a layered porous cylinder of 500 m (1640 ft) height and 1,000 m (3281 ft) radius. It is conceptualized as a dual-permeability fractured porous medium with average porosity of 4% and a total permeability-thickness product of 21.6 dm (70,866 millidarcy ft). Dual permeability behavior is modeled with an "effective porous medium" description. Chiefly, this consists of an effective relative permeability with a very high (80%) irreducible liquid saturation (Pruess and Narasimhan, 1982; Pruess, 1983a). The "background reservoir" serves as a means to provide stabilized long-term flow to the local fractures; simulated injection interference is not sensitive to detailed specifications of the background reservoir.

As a starting point for simulating "natural" pre-exploitation conditions, the entire flow system is initialized with a temperature of 240°C (464 F) and a corresponding saturated vapor pressure of 33.44 bars (485 psi). Initial water saturation is 80% in the background reservoir and 0% in the fracture. Boundary conditions in the background reservoir are held constant to initial conditions at the cylinder mantle (R = 1000 m = 3281 ft). Top and bottom boundaries are modeled as semi-infinite (thermally) conductive half-spaces. Lateral boundaries in the fracture are "no flow"; perpendicular to the fracture plane different boundary conditions were explored, including semi-infinite conductive half-spaces, and permeable matrix rock. The latter requires a fully three-dimensional fracture-matrix grid, while conductive boundary conditions can be efficiently modeled with a semi-analytical technique (Vinsome and Westerveld, 1980; Pruess and Bodvarsson, 1984; Pruess, 1991b).

The production well representing Q-6 is placed on deliverability, with mass flow rate given by

$$q = \sum_{\beta=liq.,\ gas} \frac{k_{r\beta}}{\mu_\beta} \rho_\beta \, PI(P_\beta - P_{wb}) \qquad (1).$$

Here k_r, μ, ρ are, respectively, relative permeability, viscosity, and density of fluid phases in the (fracture) production grid block. PI is the productivity index, a characteristic feature of the well reflecting permeability-thickness and skin (Coats, 1977), and P_{wb} is the flowing wellbore pressure. These parameters are here taken to be PI = 10^{-11} m^3 (35.3×10^{-11} cuft), and P_{wb} = 10 bars (145 psi). Prior to startup of injection we model an extended production period of 5 years, to simulate appropriate reservoir depletion in the area of the NCPA injection experiments. Subsequently water injection is started into the fracture at a distance of 240 m (787 ft) from the production well, and at the same elevation. Water at a temperature of 20°C (68 F) is injected at rates from 12-25 kg/s (191-397 gpm) for periods of from 1 to 3 days. During injection the production well continues to operate at the same deliverability conditions as before, with interference effects manifest in changing flow rates and enthalpies. The simulation is continued past the termination of injection to investigate recovery behavior. So far all of our simulations have only been performed for one single injection cycle; interference effects and constraints from repetition of many cycles have not yet been explored.

All calculations reported in this paper were done on an IBM RS/6000 workstation with LBL's general-purpose reservoir simulator TOUGH2 (Pruess, 1991b). This code incorporates the general "MULKOM" architecture for multiphase fluid and heat flow (Pruess, 1983b), and includes special provisions for modeling geothermal flows in fractured-porous media.

RESULTS AND DISCUSSION

Simulation results for an injection rate of 25 kg/s (397 gpm) and a 600 x 600 m^2 (3.88×10^6 sq. ft) fracture size are given in Figs. 5 through 12. Fig. 5 shows production rate vs. time for the periods before, during, and after injection. Fig. 6 shows the pressure distribution in the fracture at the end of a 5 year production period, prior to start of injection, for a case where the fracture has permeable wall rock. The fracture connection to the background reservoir in the bottom right corner is evident from the shape of the isobars. At the end of the 5 year production period, temperatures in the fracture are 240°C (464 F) throughout. In the background reservoir temperatures have declined somewhat from boiling, with lowest temperatures being approximately 234°C (453 F). Figs. 7-12 give contour maps of water saturations, temperatures, and pressures in the fracture. Results for different cases are summarized in Table 2. Simulated behavior can be briefly described as follows.

After production is first started at a time of -5 years, flow rate initially declines rapidly, and later stabilizes at rates of typically 9.5 kg/s (75,397 lbs/hr). Startup of injection causes rapid interference with production, due to a complex interplay between two-phase flow and heat transfer effects around the injection point (Calore et al., 1986; Pruess, 1991a). Heat exchange between the injection plume and the surrounding reservoir occurs partially through conduction, and partially through transport of sensible and latent heat and associated phase change processes. A boiling injection plume is a very efficient heat transfer system akin to a "heat pipe" (Calore et al., 1986). Reservoir vapor flows towards cooler, lower-pressure regions of the plume where it condenses, depositing large amounts of latent heat. In hotter regions of the plume the saturated vapor pressure exceeds ambient reservoir pressures, causing vapor to flow away from the plume, and inducing boiling. The concurrent condensation and boiling processes tend to diminish temperature variations throughout the injection plume.

Injected water migrates primarily downward and, near the bottom of the fracture, also laterally. Advancement of lower temperatures and pressures from the injection point is much delayed relative to water migration, due to the various heat transfer processes. In a recent study (Pruess, 1991a) it was shown that the simulated movement of injection plumes can be strongly affected by the orientation of the numerical grid, due to the gravitational instability of dense injection water over less dense steam. Test calculations showed that for the flow system modeled here grid orientation effects are insignificant. The reason for this favorable situation is the presence of a strong transversal dispersion in the descending plume, caused by conductive heat transfer from the fracture walls. Due to this heat transfer, the interior region of the plume beneath the injection point tends to have somewhat larger temperatures and pressures. This gives rise to a horizontal (outward) component of liquid (and vapor) flow, and a broadening of the injection plume.

Following start-up of injection the simulations show a brief initial period of increasing production rate. This occurs because initially the injected water is boiling at temperatures high enough so that the saturated vapor pressures exceed vapor pressures in the fracture prior to injection. Production rates then decline as large portions of the injection plume cool to temperatures with saturated vapor pressures lower than initial vapor pressures, inducing condensation of reservoir vapor.

For the simulations shown in Figs. 5-12, the vapor inflow from the background reservoir extends over a length of 120 m (394 ft) at the right lower boundary of the fracture. This path is just beginning to get blocked by injection water after 1.2 days (Fig. 7). At this time production rate has dropped to approximately 60% of the stabilized pre-injection value. The decline is caused by the partial blockage of vapor upflow, and by declining pressures from the cooling effects of injection. At 1.2 days, most of the outer envelope of the injection plume is at pressures of 22 bars (319 psi) or larger, corresponding to temperatures of > 217°C (423 F). After 3 days of injection, a plume of significant water saturations with $S_w > 0.5$ extends all the way across the lower third of the fracture, where it impedes vapor upflow. Pressures of the injection plume surface facing the production well region have declined to values of 16-20 bars (232-290 psi), with saturation temperatures of 201-212°C (394-414 F). Together these effects reduce production rate to less than 30% of the pre-injection value.

As is clear from the water saturation distributions (Figs. 7 and 10), no water breakthrough to the production well was observed in our simulations. However, water breakthrough would have occurred if the production well had been placed at lower elevation, or if injection had been continued for longer time periods.

Shutting-in of the injection well has an immediate impact on production, causing recovery and then over-recovery by about 10% over the stabilized pre-injection rate. It is seen that the permeability of the fracture wall rock, even when it is as low as 2 microdarcies, has a very significant effect. Impermeable wall rock can boil water only by heat conduction to the fracture. When wall rock is permeable it will imbibe injection water by capillary force. Boiling will then proceed at temperatures close to original reservoir temperature, and production rates exceeding stabilized pre-injection values are maintained for much longer periods of time. As long as injection continues the vapor generated in the reservoir rock adjacent to the fracture condenses in the cooler portions of the injection plume, slowing the temperature and pressure

decline there. When injection and further cooling stops, this vapor no longer condenses and becomes available for production.

The extent of flow rate decline during the 3-day injection period is excessive in comparison with the field observations. This may be attributed to a combination of several factors. The "real" fractures may be more extensive than the fracture in our model. In the field experiment, the injected water probably exited well Q-2 through several different fractures, whose combined heat transfer area is likely to be significantly larger than the surface area of the fracture in our model. Furthermore, not all of the fractures accepting injection water will also intersect Q-6, and not all of the fractures feeding Q-6 will intersect Q-2. Therefore, a reduction in production rate from one of the feeds of Q-6 will have a lesser relative impact on production than predicted from our single-fracture model.

Even in the case with dramatic production decline after 3 days of continuous injection, good recovery and over-recovery is observed when injection is stopped. This result is encouraging, indicating that even in cases with very strong negative injection interference production can be recovered by shutting-in the offending injector.

A limited number of variations in problem parameters and flow geometry have been explored. Table 2 summarizes simulated production interference and recovery for different fracture sizes. Injection rates and times, and permeability of the fracture walls, were also varied. In all cases stabilized production rate before start of injection was near 9.5 kg/s (75,400 lbs/hr). Production and injection were always made at the same elevation. As expected, smaller fractures produce more rapid and stronger negative interference with production, and less over-recovery. The permeability of the rocks forming the fracture walls is an important parameter. For impermeable wall rock the over-recovery following injection shut-in is very short-lived.

Different couplings between the fracture and the background reservoir were tried. Placing the coupling either beneath the injector or beneath the producer had very little impact on predicted production rates, although it did have some effects on the shape of the injection plumes. Similarly, introduction of non-zero capillary pressure in the fracture had negligible impact on production rates. There is considerable uncertainty about fracture relative permeabilities, and future studies should explore their sensitivity to production rates. Vapor pressure lowering effects have been neglected so far; as capillary effects are believed to be weak in fractures, vapor pressure lowering is also not expected to be significant.

CONCLUSIONS

(1) Our numerical simulation studies have predicted strong interference between injection into and production from the same fracture. During injection production rates mostly decline, with over-recovery observed after injection is stopped. The simulated behavior is similar to field observations in the Q-2/Q-6 experiments, lending credence to the underlying conceptual and numerical model.

(2) The most significant reservoir processes during injection include gravity-driven downward migration of injected water, local heat exchange with reservoir rock swept by the injection plume, conductive heat transfer from rocks of very low permeability to the injection plume, capillary-driven imbibition of injected liquid into the matrix rock, away from the fractures, vapor condensation in the cooler portions of the plume, and boiling in the hotter portions.

(3) The simulated production declines are stronger than seen in the field. This can be explained by noting that in our model all injected water enters one single fracture, and all production comes from that same fracture, whereas in the field several fractures will participate in taking up injectate, and delivering fluid and heat to the production well.

(4) The simulations clearly demonstrate that injection is subject to heat transfer limitations. Production rate decline from injection is caused primarily by temperature decline in the injection plume and associated drop in vapor pressure. Cool portions of injection plumes act as low-pressure sinks that can consume large amounts of vapor by condensation. Temperature decline depends on injection rate and on the heat transfer capacity of the reservoir, which is a function of available heat exchange volume, heat transfer area, and permeability for vapor flow.

(5) Based on the foregoing, it is to be expected that each injection well has a limitation on the rate at which water can be injected without causing significant reservoir pressure decline, and consequently negative interference with neighboring producers. Acceptable limits for injection rates may be difficult to predict, as they depend on geometric properties of the local fracture system that usually are poorly known. However, in practice such limitations can be established empirically by monitoring neighboring production wells.

(6) Injection should not be concentrated into a few wells that would take up large rates. Because of heat transfer limitations, injection wells should generally be operated at moderate rates well below their capacity for accepting fluids (Enedy et al., 1991).

ACKNOWLEDGMENT

The work presented in this paper was undertaken on the suggestion and with encouragement from Marshall Reed of the Geothermal Division, U.S. Department of Energy. The authors appreciate helpful discussions with Tom Box of Calpine Corporation. Peter Fuller and Curt Oldenburg of LBL provided a data interface for plotting simulation results. For a review of the manuscript, and the suggestion of improvements, the authors are indebted to Marcelo Lippmann. This work was supported by the Assistant Secretary for Conservation and Renewable Energy, Geothermal Division, of the U.S. Department of Energy under Contract No. DE-AC03-76SF00098.

REFERENCES

Beall, J.J. and Box, W.T. (1989), "The Nature of Steam Bearing Fractures in the South Geysers Reservoir," Geothermal Resources Council, Transactions, Vol. 13, 1989, pp. 441-448.

Beall, J.J., Enedy, S. and Box, W.T., Jr. (1989), "Recovery of Injected Condensate as Steam in the South Geysers Field," Geothermal Resources Council, Transactions, Vol. 13, 1989, pp. 351-358.

Calore, C., Pruess, K. and Celati, R. (1986), "Modeling Studies of Cold Water Injection into Fluid-depleted, Vapor-dominated Geothermal Reservoirs," paper presented at 11th Workshop on Geothermal Reservoir Engineering, Stanford University, Stanford, CA, January 1986.

Coats, K.H. (1977), "Geothermal Reservoir Modelling," paper SPE-6892, presented at the 52nd Annual Fall Technical Conference and Exhibition of the SPE, Denver, CO, October 1977.

Enedy, K.L. (1992), "The Role of Decline Curve Analysis at The Geysers," in: C. Stone (ed.), Monograph on The Geysers Geothermal Field, Special Report No. 17, Geothermal Resources Council, Davis, CA, 1992.

Enedy, S., Enedy, K. and Maney, J. (1991), "Reservoir Response to Injection in the Southeast Geysers," Proceedings, Sixteenth Workshop on Geothermal Reservoir Engineering, Stanford University, Stanford, CA, January 1991.

Goyal, K.P. and Box, W.T. (1990), "Reservoir Response to Production: Castle Rock Springs Area, East Geysers, California, U.S.A.," Proceedings, Fifthteenth Workshop on Geothermal Reservoir Engineering, Stanford University, Stanford, CA, January 1990.

Persoff, P., Pruess, K. and Myer, L. (1991), "Two-phase Flow Visualization and Relative Permeability Measurement in Transparent Replicas of Rough-walled Rock Fractures," LBL-30161, presented at Sixteenth Workshop on Geothermal Reservoir Engineering, Stanford University, Stanford, CA, January 1991.

Peters, R.R., Klavetter, E.A., Hall, I.J., Blair, S.C., Heller, P.R. and Gee, G.W. (1984), "Fracture and Matrix Hydrologic Characteristics of Tuffaceous Materials from Yucca Mountain, Nye County, Nevada," Sandia National Laboratory, Report SAND84-1471, Albuquerque, NM, December 1984.

Pruess, K. (1983a), "Heat Transfer in Fractured Geothermal Reservoirs with Boiling," Water Resources Research, Vol. 19, No. 1, February 1983, pp. 201-208.

Pruess, K. (1983b), "Development of the General Purpose Simulator MULKOM," Annual Report 1982, Earth Sciences Division, Lawrence Berkeley Laboratory LBL-15500, 1983.

Pruess, K. (1991a), "Grid Orientation and Capillary Pressure Effects in the Simulation of Water Injection into Depleted Vapor Zones," Geothermics, Vol. 20, No. 5/6, 1991, pp. 257-277.

Pruess, K. (1991b), "TOUGH2—A General-purpose Numerical Simulator for Multiphase Fluid and Heat Flow," Lawrence Berkeley Laboratory Report LBL-29400, May 1991.

Pruess, K. and Bodvarsson, G.S. (1984), "Thermal Effects of Reinjection in Geothermal Reservoirs with Major Vertical Fractures," Journal of Petroleum Technology, Vol. 36, No. 10, September 1984, pp. 1567-1578.

Pruess, K. and Narasimhan, T.N. (1982), "On Fluid Reserves and the Production of Superheated Steam from Fractured, Vapor-dominated Geothermal Reservoirs," J. Geophys. Res., Vol. 87, No. B11, 1982, pp. 9329-9339.

Pruess, K. and O'Sullivan, M. (1992), "Effects of Capillarity and Vapor Adsorption in the Depletion of Vapor-dominated Geothermal Reservoirs," Lawrence Berkeley Laboratory Report LBL-31692, presented at Seventeenth Workshop on Geothermal Reservoir Engineering, Stanford University, Stanford, CA, January 1992.

Pruess, K. and Tsang, Y.W. (1990), "On Two-phase Relative Permeability and Capillary Pressure of Rough-walled Rock Fractures," Water Resources Research, Vol. 26, No. 9, September 1990, pp. 1915-1926.

Thompson, R.C. and Gunderson, R.P. (1992), "The Orientation of Steam-bearing Fractures at The Geysers Geothermal Field," in: C. Stone (ed.), Monograph on The Geysers Geothermal Field, Special Report No. 17, Geothermal Resources Council, Davis, CA, 1992.

van Genuchten, M.Th. (1980), "A Closed-form Equation for Predicting the Hydraulic Conductivity of Unsaturated Soils," Soil Science Society Journal, Vol. 44, 1980, pp. 892-898.

Vinsome, P.K.W. and Westerveld, J. (1980), "A Simple Method for Predicting Cap and Base Rock Heat Losses in Thermal Reservoir Simulators," J. Canadian Petroleum Technology, July-September 1980, pp. 87-90.

Table 1: Specifications of numerical model (#)

FRACTURE ZONE

Vertical X-Z section, 0.1 m thick, 10 % porosity
Areal extent: variable, from 300 x 300 m^2 to 600 x 600 m^2
(984 x 984 to 1969 x 1969 sq. ft)
Permeability-thickness product in fracture plane: 40 darcy-meters
(131,200 md-ft)

Relative permeability: Corey-curves with $S_{lr} = 0.3$, $S_{gr} = 0.05$
Capillary pressure: 0

Wall rock: impermeable, or permeability = 2 microdarcy
relative permeability and capillary pressure: function of van Genuchten (1980), with parameters as measured for welded tuff sample G4-6 by Peters et al. (1984);
parameters: $\lambda = 0.4438$ $S_{lr} = .08$
$P_0 = 17.27$ bar (250 psi)
gas phase relative permeability: $k_{rg} = 1 - k_{rl}$

Discretization: 15x15x1 square blocks (for impermeable wall rock) 15x15x6 blocks (for permeable wall rock; increments perpendicular to fracture: .01 m, .19 m, .8 m, 4 m, 15m, for total wall rock thickness of 20 m)

BACKGROUND RESERVOIR

Radially symmetric layered system (2-D, R-Z), discretized into 5 layers and 16 radial blocks per layer.

Radius: 1000 m (3281 ft)

Layers (from top down)	Thickness		Permeability-Thickness	
1	20 m	(66 ft)	10 dm	(32,808 md-ft)
2	40 m	(131 ft)	4 dm	(13,123 md-ft)
3	80 m	(262 ft)	4 dm	(13,123 md-ft)
4	160 m	(525 ft)	1.6 dm	(5,249 md-ft)
5	200 m	(656 ft)	2 dm	(6,562 md-ft)
total	500 m	(1640 ft)	21.6 dm	(70,866 md-ft)

Porosity: 4 %

Relative permeability: function of van Genuchten (1980) for liquid;
parameters: $\lambda = .4438$
$S_{lr} = .80$ (*)
gas phase relative permeability: $k_{rg} = 1 - k_{rl}$

Capillary pressure: function of van Genuchten (1980);
parameters: $\lambda = .4438$ $S_{lr} = .08$
$P_0 = 1.727$ bar (25.0 psi)

Rock grain properties

density: 2600 kg/m^3 (162.3 lbs/cu-ft)
specific heat: 1000 J/kg°C (.239 Btu/lb x deg-F)
conductivity: 2.51 W/m°C (34.8 Btu/day x ft x deg-F)

(#) Initial and boundary conditions, and well parameters, are given in the text.

(*) Large irreducible water saturation, to approximate effective behavior of a dual-permeability medium (Pruess, 1983a).

Table 2. Injection-production interference. Simulated results for different fracture sizes, and injection rates and times.(*)

Fracture Size	Wall Rock (a)	Injection Rate	Production Interference (b)	Production Recovery (c)
300 m x 300 m	I	12 kg/s	64% at 0.5 days	99% at 1.7 days
450 m x 450 m	I	12 kg/s	80% at 1.2 days 42% at 10 days	110% at 2.0 days 105% at 15.9 days
600 m x 600 m	I	12 kg/s	91% at 1.2 days	113% at 2.0 days
	I	25 kg/s	66% at 1.2 days	113% at 2.0 days 102% at 3.5 days
	P	25 kg/s	60% at 1.2 days	111% at 2.0 days 109% at 3.5 days 103% at 10 days
			28% at 3.0 days	109% at 5.7 days 107% at 10 days

(*) All times relative to start of injection.
(a) I = impermeable wall rock, P = permeable wall rock with $k_m = 2$ μd.
(b) Interference is expressed as a percentage of pre-injection production rate.
(c) Recovery is expressed as a percentage of pre-injection production rate.

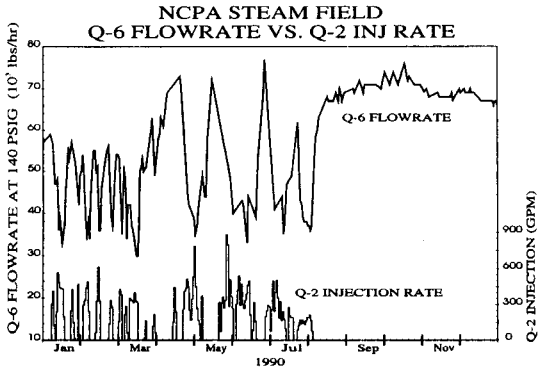

Figure 1. Injection rates into Q-2 and observed production from Q-6.

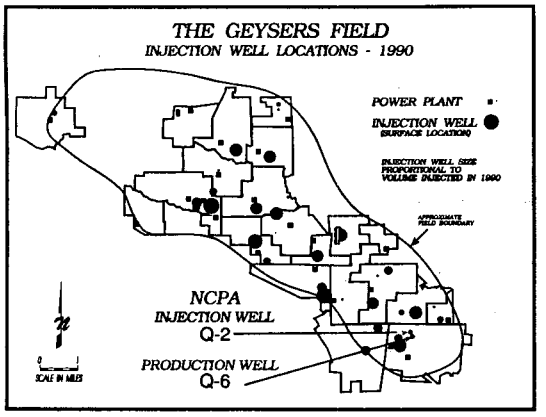

Figure 2. Injection well locations at The Geysers.

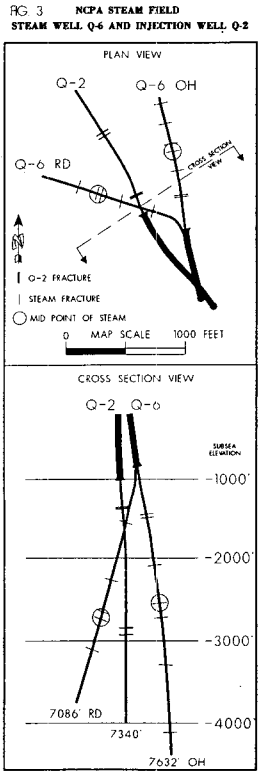

Figure 3. Plan and cross-sectional view of Q-2 and Q-6 well courses.

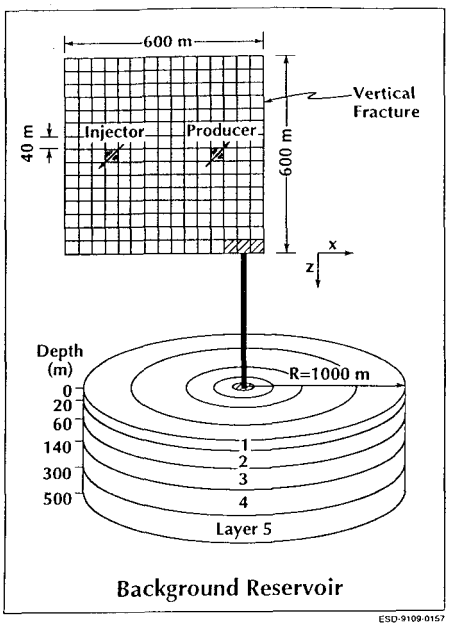

Figure 4. Schematic diagram of fractured reservoir model used in numerical simulations. Injection and production wells are intersected by the same vertical fracture, which is connected to a large background reservoir. Fluid and heat flow perpendicular to the fracture plane is also taken into account.

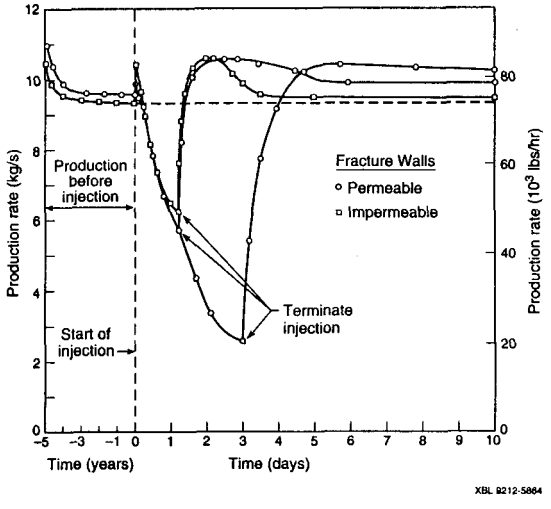

Figure 5. Production rate before, during, and after injection. Note the change of time scale at time = 0.

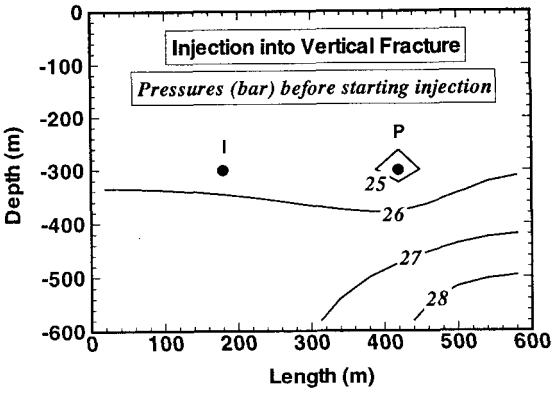

Figure 6. Vapor pressures in the fracture before start of injection, for a case with permeable fracture wall. I and P indicate the points where injector and producer penetrate the fracture.

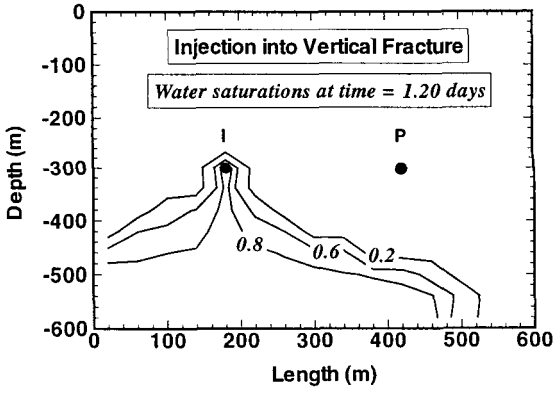

Figure 7. Water saturations in the fracture after 1.2 days of injection (impermeable fracture wall; I-injector, P-producer).

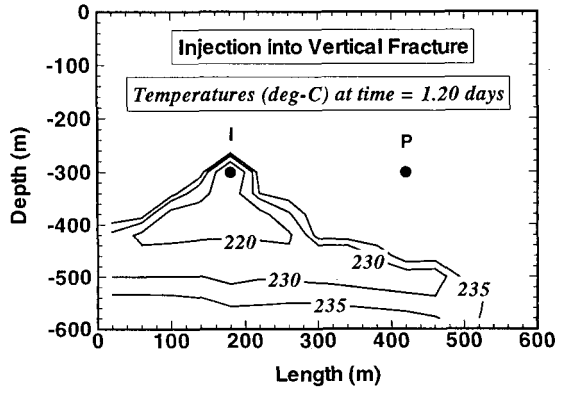

Figure 8. Temperatures in the fracture after 1.2 days of injection (impermeable fracture wall; I-injector, P-producer).

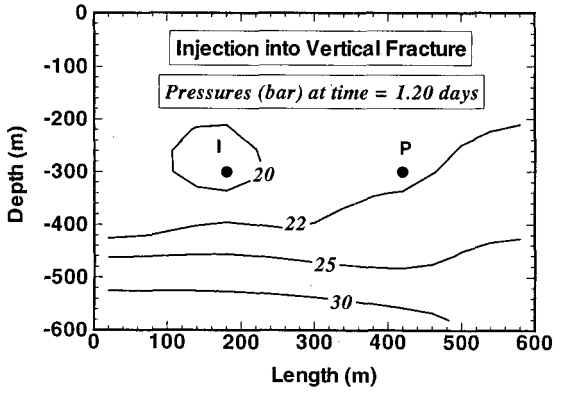

Figure 9. Fluid pressures in the fracture after 1.2 days of injection (impermeable fracture wall; I-injector, P-producer).

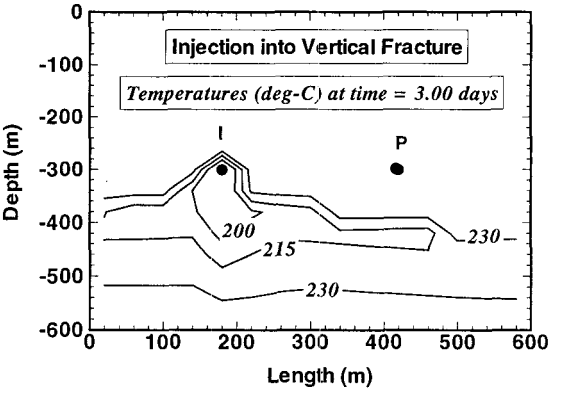

Figure 11. Temperatures in the fracture after 3.0 days of injection (permeable fracture wall; I-injector, P-producer).

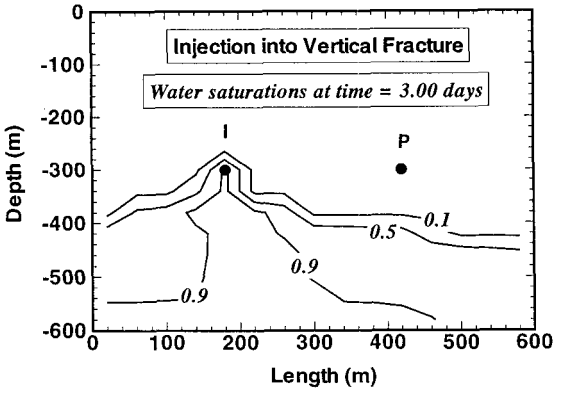

Figure 10. Water saturations in the fracture after 3.0 days of injection, case with permeable fracture wall; I-injector, P-producer.

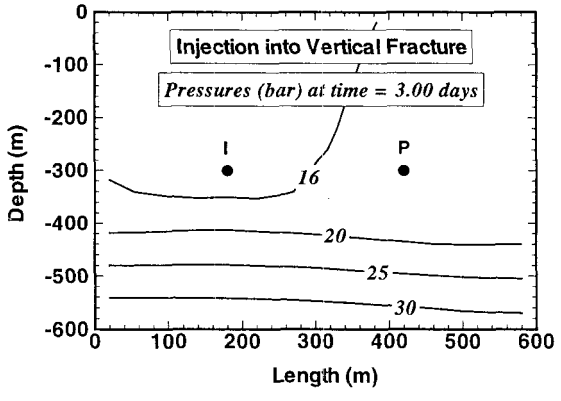

Figure 12. Fluid pressures in the fracture after 3.0 days of injection (permeable fracture wall; I-injector, P-producer).

PROCEEDINGS, Eighteenth Workshop on Geothermal Reservoir Engineering
Stanford University, Stanford, California, January 26-28, 1993
SGP-TR-145

APPLICATION OF MINERALOGICAL METHODS TO ASSESS THE THERMAL STABILITIES OF GEOTHERMAL RESERVOIRS

Patrick R.L. Browne

Geothermal Institute and Geology Department
University of Auckland, Private Bag 92019
Auckland, New Zealand

ABSTRACT

Estimates of temperatures, past and present, in geothermal reservoirs can be made by using now standard mineralogical techniques, including fluid inclusion geothermometry, vitrinite reflectance, calc-silicate and clay occurrence, the extent of clay interlayering, and measuring clay crystallinity. Recent studies of clays in 60 drillcores from 6 wells at Wairakei, for example, show an inverse relationship between reservoir temperatures and crystallinities from 90° to 225°C (195 to 435°F) (Kübler Indices: 1.40 to 0.44 $\Delta°2\theta$). Fluid inclusion geothermometry results require careful interpretation but the method need not be calibrated with respect to the reservoir, as do other geothermometric methods.

INTRODUCTION

Measuring temperatures directly in geothermal wells is obviously an essential part of reservoir assessment. However, in several situations, downwell temperatures are not necessarily the same as those that prevailed immediately prior to drilling as this disturbs the thermal regime and often promotes changes in the patterns of fluid flow. Many wells never reach thermal equilibrium with their reservoir even months after being drilled. Discharge of a well also irrevocably changes temperatures at depths shallower than its feed zones.

For these reasons, indirect estimates of subsurface temperatures made independently can be very useful. In addition, by comparing geothermometric results obtained by using different methods with one another, and with temperatures measured directly, we can assess the thermal stability of a geothermal reservoir, or at least some sections of it.

This paper reviews some of the mineralogical methods available for assessing reservoir temperatures but excludes both fluid and isotope geothermometers.

METHODS

Several methods proposed for estimating temperature have been applied or tested in natural geothermal systems. Some have proved unsuccessful, e.g. Al in hydrothermal quartz (Scotford, 1975; Browne and Wodzicki, 1977), or apply only under very restricted circumstances, e.g. sphalerite and pyrrhotite geothermometers (Kissin and Scott, 1982; Scott and Barnes, 1971).

More useful are mineral geothermometers and methods that are of wider application, and some of these are summarized in this paper. For convenience, the thermal signatures of a geothermal reservoir may be considered, in mineralogical terms, as belonging to one of three categories:

(1) minerals whose presence in a reservoir has a thermal significance;
(2) minerals whose compositions or structures vary with temperature;
(3) determinative methods that depend upon some property of a mineral or material present within the reservoir rocks.

TEMPERATURE SENSITIVE MINERALS

Geothermal experience has extended the results of experiments, thermodynamic calculations and metamorphic studies to determine the thermal stabilities of hydrothermal minerals to temperatures well below 350°C.

Where the altering fluid is of near-neutral pH and of alkali chloride type, the thermally sensitive hydrothermal minerals commonly formed include clays, calc-silicates and zeolites. Not surprisingly, most of these minerals contain essential $(OH)_n$ or nH_2O. Several schemes relating calc-silicate mineral occurrence to temperatures above about 150°C have been suggested in recent years (e.g. Bird et al., 1984; Reyes, 1990) and are not reproduced here. The sensitivities of zeolites at temperatures below 110°C have been very effectively described from drillholes in the low enthalpy reservoirs of Iceland (Kristmannsdóttir and Tómasson, 1978). For example, chabazite and levyne occur below 70°, mesolite from 70 to 90°, and stilbite from 90 to 110°. In many geothermal reservoirs, laumontite is stable to about 210° and wairakite above about 220° persisting to well above 300°C (Browne, 1979; Elders et al., 1981).

Among calc-silicates that are not zeolites, the presence of epidote has long been used to indicate temperatures in excess of 240°, and in some reservoirs its crystal size and abundance increases with increasing temperature (Elders et al., 1981; Browne and Gardner, 1982). Prehnite is usually stable above 220°, hydrothermal amphibole above 290°, and calcium garnet above about 320°.

A few non calc-silicates show a thermal sensitivity that may also be useful in interpreting reservoir temperatures: hydrothermal biotite usually occurs above about 320°, for example, and cristobalite below 150°.

A different assemblage of hydrothermal minerals forms in the presence of acidic fluids; at 250°C, these typically produce pyrophyllite, diaspore and alunite (Reyes, 1990). It is important to realise that the identities of the hydrothermal minerals which form are largely independent of rock type, and that reservoir temperatures can only be interpreted from the presence of a mineral in a core or cutting. The converse, i.e. the absence of a hydrothermal mineral, cannot be cited as evidence that a specific temperature was not reached. This is because the stability of many hydrothermal minerals depends not only upon temperature but also on other factors. For example, the formation of many calc-silicates is prohibited where the altering fluids contain high concentrations of dissolved carbon dioxide.

The other group of minerals whose presence has often been used to interpret temperatures is the clays, all phyllosilicates, with essential $(OH)_n$.

Near neutral pH alkali chloride waters react with the host rocks, or deposit directly from solution, to form a thermally progressive sequence of minerals. Typically, montmorillonite occurs to about 140°, mixed layer clays from 140 to about 210°, with illite or sericite stable at higher temperatures (Browne, 1979). This sequence differs slightly from place to place; for example, montmorillonite prevails to 230° in Icelandic (Kristmannsdóttir, 1975) and to 180° in Philippine geothermal systems (Reyes, 1990).

Where the altering fluids are acidic the usual sequence, with respect to temperature, is: kaolinite occurs to 120°C, dickite ± kaolinite from 120 to 200°C, dickite and pyrophyllite from 200 to 250°C, and pyrophyllite ± illite from 250 to 320°C (Reyes, 1990).

In many geothermal reservoirs, chlorite occurs over a wide range of temperatures and its presence generally offers no useful geothermometer, but in the basaltic rocks of Iceland it occurs only above 230° (Kristmannsdóttir and Tómasson, 1976).

MINERALS WHO COMPOSITIONS OR STRUCTURE VARY WITH TEMPERATURE

Interlayered clays

Alteration zones characterized by mixed layer clays occur in many geothermal systems and the extent of interlayering can usually be related to reservoir temperature. Mixed layer clays are present in several Iceland geothermal fields, for example, where the measured temperatures are between 200 and 230°C (Kristmannsdóttir, 1975). In New Zealand geothermal fields the proportion of illite interlayered with montmorillonite usually increases with temperature above about 100°C until only illite is present above about 200°C.

Recent work (Harvey and Browne, 1991) shows that there are slight but measurable differences in the extent of interlayering within samples from the same depth. These differences can be related to clay size in that fractions less than 0.2μm may contain a higher proportion of the smectite interlayer component than co-existing clays larger than 0.2 μm in diameter (Figure 1).

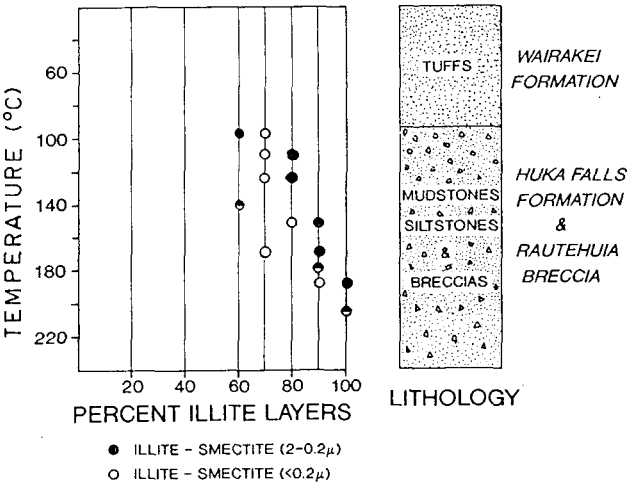

Figure 1: Sequence of mixed-layer clays present in cores from drillhole WK207 compared with the measured downwell temperatures that most closely match the estimated predrilling temperatures (from Harvey and Browne, 1991).

Measuring the extent of interlayering and, indeed, identifying the clay minerals present requires use of an X-ray Diffractometer. Other instruments useful in characterizing clay minerals include Differential Thermal Analysis (DTA), Thermogravimetric Analysis (TGA), and Infrared Spectroscopy. For example, DTA patterns of samples recovered from drillholes at the Ngawha geothermal field, New Zealand, show progressive changes with increasing temperature (Browne and Gardner, 1982; 1985). The reactions the endothermic peaks in these patterns represent can be clearly attributed to the hydration states of the clay minerals they contain. Samples from depths where the measured temperatures are less than 120° to 180°C have a larger endothermic peak at about 150°C and a smaller one at about 550°C. Samples from hotter locations give DTA patterns with progressively smaller low temperature peaks but proportionally larger ones at 580° (Fig. 2). Samples from depths where the reservoir temperatures are above 180°C, however, are almost thermally inert even though some contain appreciable amounts of illite and chlorite. By contrast, chlorite from Icelandic geothermal systems commonly give DTA patterns with large endothermic peaks at 620°C (Kristmannsdóttir, 1975).

Solid solution series

The extent of solid solution among non-stoichiometric hydrothermal minerals has long been recognized as being controlled, at least partly, by temperature. At temperatures prevailing in geothermal reservoirs, for example, the orthoclase content of coexisting albite and adularia provides a usable geothermometer above about 250° (McDowell and McCurry, 1978; Hedenquist and Browne, 1989) but one which has not yet been fully tested.

Potentially more useful, because chlorite is much more widespread than coexisting feldspars, is the chlorite geothermometer (Cathelineau and Nieva, 1985; Cathelineau, 1988) which relies on the temperature dependence of the amount of tetrahedral aluminium incorporated within chlorite. This geothermometer was applied successfully at the Los Azufres and Salton Sea

Table 1: Summary features of mineralogical geothermometers commonly applied to geothermal reservoirs

Minerals or Technique	*Method*	*Effective Temperature Range (°C)*	*Provisos*	*Records*
Occurrence of calc-silicates	Thin section examination	best 200 to 320	Inappropriate where altering fluids have high concentrations of dissolved CO_2	Usually peak temperatures; textural relations show thermal changes
Occurrence of clay minerals	XRD DTA IRS	~100 to 220	Different clay types depending on fluid pH	Usually peak temperatures attained for considerable period
Extent of clay interlayering	XRD	~140 to 220	Slight differences depending on clay size. Not applicable to acid alteration	Usually peak temperatures attained for considerable period
Crystallinity of montmorillonite, illite and their interlayers	XRD	130 to 230	Not applicable to chlorite or kaolins	Peak temperature attained for considerable period
Composition of chlorite	electron microprobe	? >200	Promising method not yet fully established	Temperature at the site of analysis
Feldspar compositions	electron microprobe	>250	Co-existing feldspars needed	Temperature at the site of analysis
Fluid inclusion geothermometry	heating stage, microscope	>100	Powerful method but needs careful interpretation of data	Temperatures at site of inclusions. With sufficient data, changes in the thermal regime can be recognised
Vitrinite reflectivity	reflected light microscope	>100	Requires rocks containing carbonaceous material. Field specific	Peak temperature attained for minimum period of 10-100 years

XRD = X-ray Diffraction
DTA = Differential Thermal Analysis
IRS = Infrared Spectroscopy

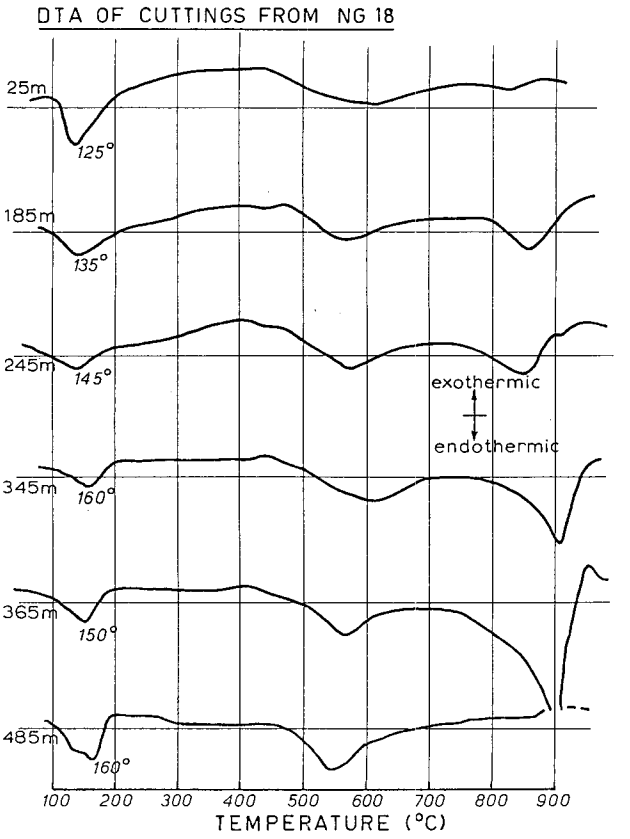

Figure 2: Differential Thermal Analysis charts of selected core and cutting samples from Ngawha drillhole Ng 18, showing typical variations in thermal reactions of samples from depths where measured temperatures differ (from Browne and Gardner, 1985).

geothermal systems (Cathelineau et al., 1985; 1987; Cathelineau, 1988) but it has not worked particularly well elsewhere, such as at Tongonan (Scott, 1988) nor Ohaaki-Broadlands (Lonker et al., 1990). Although there appear to be systematic changes in chlorite compositions with temperature, compositions vary from crystal to crystal in the same sample, and even individual chlorite crystals are commonly inhomogeneous. Cathelineau (1988) describes some of the limitations and values of the method.

Clay crystallinity

A technique commonly used by petrologists working on low grade metamorphic rocks is to measure the crystallinity of any clay minerals present. This is a straightforward method but has seldom been applied to geothermal materials, except in a qualitative way. The crystallinity measurements are made by determining the width, at half peak height, of the (001) reflections of illite and illite/smectite and the (002) reflection of chlorite. Units used are degrees 2θ and the crystallinity is commonly termed the Kübler Index.

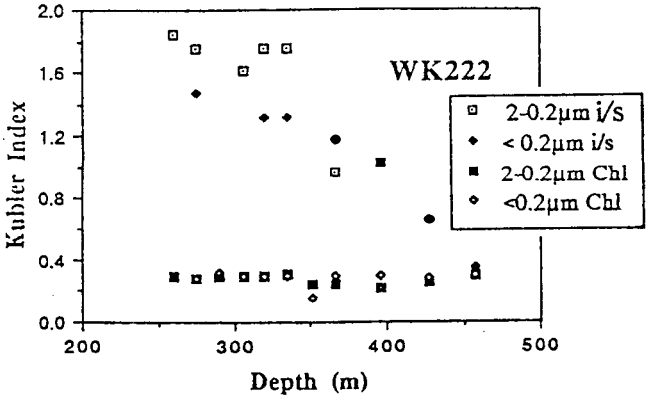

Figure 3: Crystallinity (Kübler Index: Δ° 2θ) of illite/smectite (c/s) and chlorite (Chl) versus measured drillhole temperature in drillhole WK222, Wairakei (from Chi Ma et al., 1992).

Recently, Chi Ma et al. (1992) reported the Kübler Indices for clay minerals present in 60 cores of lacustrine sediments from 6 drillholes in the Te Mihi sector of the Wairakei Geothermal Field. The crystallinity of the illite/smectite mixed layer clays increases with increasing temperature and depth (Fig. 3). Most Kübler Indices range from 1.40 to 0.44 Δ°2θ, where measured reservoir temperatures are between 90° and 225°C (irrespective of host rock), giving the relationship

$$T(°C) = 249 - 89.3 \times K.I.$$

where K.I. is the Kübler Index (Fig. 4).

By contrast, the crystallinity of chlorites present in the same samples do not vary with reservoir temperature (Fig. 4).

Chi Ma et al. (1992) found no measurable difference between the crystallinities of the larger (0.2 to 2.0 μm) and smaller (<0.2 μm) size clay fractions.

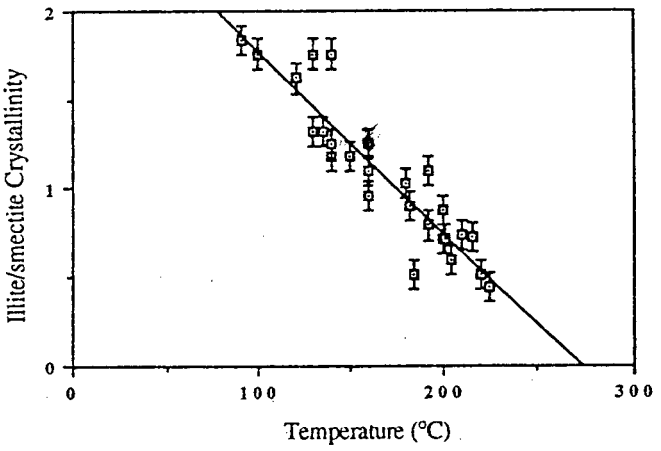

Figure 4: Relationship between temperature and illite/smectite crystallinity in cores from drillholes WK201, 202, 206, 219 and 222, Wairakei (from Chi Ma et al., 1992).

GEOTHERMOMETRIC TECHNIQUES

Fluid inclusion geothermometry

Fluid inclusion homogenisation temperatures have been measured on hydrothermal minerals from geothermal reservoirs for many years (e.g. Browne et al., 1976; Hedenquist et al., 1992).

Comparison of temperatures measured in drillholes and from fluid inclusions allows even slight changes in reservoir temperatures to be recognized. For example, the northern sector of Waiotapu and the eastern sector of Broadlands-Ohaaki have cooled by 20°C or more since quartz crystals there grew (Hedenquist and Browne, 1989; Hedenquist, 1990). The Ngawha geothermal reservoir shows evidence, from fluid inclusion studies, for cooling of its southern margin but heating by 20°C or so of its northern margin since the time the inclusions formed (Browne and Gardner, 1982).

Fluid inclusion geothermometry can thus reveal the direction of thermal evolution of a geothermal reservoir. However, because the ages of the inclusions are rarely known, the rate at which temperature changes occur can not be determined.

Usually, liquid only is trapped in inclusions, and the homogenisation temperatures measured on inclusions that trap two phases are much higher than the actual trapping temperatures and thus erroneous. Another problem is caused by "necking of inclusions" after they form, whereby an inclusion separates into two or more inclusions, usually with different proportions of vapor and liquid that then give spurious homogenisation temperatures. Straightforward statistical analysis of data will lead to incorrect conclusions. Hence, an operator needs to show sound judgement in interpreting fluid inclusion data.

However, fluid inclusion geothermometry is easier to apply to geothermal systems than to other geological environments. Pressure corrections are seldom needed, for example, or can be determined directly from drillhole measurements. The distinctions between primary, secondary and pseudosecondary inclusions are of lesser consequences than elsewhere. Indeed, Youngman (1985) has shown that usable secondary (i.e. geothermal) inclusions occur in primary minerals in the Wairakei system.

The homogenisation temperatures of vapor-rich inclusions are seldom able to be measured because of the difficulty of seeing when homogenisation occurs. However, the mere presence of vapor-rich inclusions demonstrates that the crystals grew under vapor phase conditions, and this information is often important in assessing reservoir temperatures and pressures. It also demonstrates that boiling occurred during their formation.

Vitrinite Reflectivity

This is a powerful method for estimating temperatures in geothermal reservoirs that contain sediments or tuffaceous sediments with carbonaceous material. Although vitrinite reflectivity is a standard technique used for many years by sedimentologists, especially those working on oil reservoirs or coal deposits, the method has only recently been applied to geothermal reservoirs. Barker and Elders (1981) pioneered the application of this method by studying fluviatile sediments comprising the Cerro Prieto reservoir. They showed that vitrinite reflectivity of samples from several wells increases regularly with depth and temperature. Once a relationship between reflectivity and temperature was established, i.e. a vitrinite geothermometer calibrated, this knowledge was then applied to estimating reservoir temperatures using samples as they were recovered from later drillholes. The vitrinite reflectivity method has also been applied successfully to lacustrine sediments at the Wairakei and Ngatmariki geothermal systems (Struckmeyer and Browne, 1988; Gonzales, 1985) in New Zealand and Palinpinon in the Philippines (Hermoso, 1991).

Note that a reflectivity versus temperature calibration curve is system-specific and these curves are not transferable from field to field since reflectivity values depend also on the duration of heating (but see Barker, 1991).

COMPARISON OF MINERALOGICAL THERMOMETERS AND TECHNIQUES

Table 1 summarises some of the salient features of the mineralogical geothermometers and techniques commonly used to evaluate geothermal reservoirs. All methods offer opportunities that are independent of one another, and all have limitations. Obviously, the most important of the latter is first having suitable material. Some methods, such as those relying on chlorite and feldspar compositions, show much promise but are not yet fully established. Both require analyses to be made on an expensive electron microprobe.

All the methods described here, except measuring the homogenisation temperatures of fluid inclusions, essentially rely on calibrations made, either in natural systems or in a laboratory. Uncertainties in the natural systems often arise in deciding how close the measured drillhole temperatures are to the predrilling or true reservoir temperatures. This results from the nature of drilling itself, which introduces cool drilling fluids into a hotter reservoir and disturbs irrevocably its fluid flow patterns. Many geologists do not always carefully evaluate the quality of downhole measurements nor the circumstances under which the data were obtained. This means that some of the temperature stability ranges assigned to thermally sensitive minerals are likely to be in error. Errors are likely to be greatest at shallowest depths where reservoir temperatures are usually coolest and temperature gradients steepest. In fact, any temperatures measured at shallow depths in wells that have discharged should not be used to calibrate mineral geothermometers. Even temperature calibrations based on experiments should be used with caution as equilibrium is achieved only very slowly at low temperatures.

Calc-silicates are usually detected easily by petrographic microscope, and their distribution should be recorded as part of any routine assessment of a reservoir. Some minerals, e.g. epidote, are reliable temperature indicators, irrespective of rock type or field, but others, such as prehnite, have lower temperature stabilities that vary from field to field but remain uniform within each field. The petrographic microscope is also the most important instrument to recognise thermal changes that have occurred within a reservoir. This is done by observing alteration overprints or the sequences of hydrothermal minerals that occur in veins or vugs, and interpreting them with respect to the temperatures they indicate.

Fluid inclusion geothermometry does not rely on field calibration, and also offers a fairly precise tool for determining changes in temperature within a reservoir. This can be done by careful observations of the growth directions within individual hydrothermal crystals in relation to the occurrence of primary inclusions. Theoretically, the chlorite and feldspar geothermometers should also be able to record changes in reservoir temperatures, but this has not been demonstrated to date, so far as I know. In any case, these methods record only the trends of thermal change and not the rates at which changes occur, since the ages of different crystals, let alone different sections within a single crystal, are unknown.

In reality, a single homogenisation temperature tells us only the temperature (albeit precisely) within an area the size of the individual inclusion (~10 μm) at an unknown time. By contrast, the vitrinite geothermometer commonly records (much less precisely) the peak temperatures that a sizable section of a reservoir has attained for periods as brief as 10 to 100 years (Barker, 1991). This is because cooling has no effect on vitrinite reflectivity.

Clay minerals also seldom record retrograde thermal effects except where they overprint hydrothermal feldspars, and these may be due to either cooling, a lowering of fluid pH, or both. Clay crystallinity, the proportions of montmorillonite and illite interlayered together in a single phase and the occurrence of the clays probably also reflect the maximum temperatures attained but, again, for an unknown but "considerable" period. This is because of the slow thermal response of reservoir rocks, since catalysing or reacting fluids do not usually move freely in rocks containing abundant clays.

Chlorite crystallinity has no thermal significance at Wairakei, in contrast to the crystallinity of co-existing interlayered illite/montmorillonite, but whether or not this conclusion applies elsewhere is not known.

In summary, however, the combination of mineralogical techniques and present knowledge of mineral occurrences offers important ways for determining the thermal stability of a geothermal reservoir.

ACKNOWLEDGEMENT

I thank Stuart Simmons and Mary Weston for their help in preparing this paper.

REFERENCES

Barker, C.E. (1991). "Implications for organic maturation studies of evidence for a geologically rapid increase and stabilisation of vitrinite reflectance at peak temperature: Cerro Prieto geothermal system, Mexico." American Association of Petroleum Geologists Bulletin, 75, 1852-1863.

Barker, C.E. and W.A. Elders (1981). "Vitrinite reflectance geothermometry and apparent heating duration in the Cerro Prieto geothermal field." Geothermics, 10, 207-223.

Bird, D.K., Shiffmann, P., Elders, W.A. and A.E. Williams (1984). "Calc-silicate mineralisation in active geothermal systems." Economic Geology, 79, 671-695.

Browne, P.R.L. (1979). "Hydrothermal alteration in active geothermal systems." Annual Reviews Earth and Planetary Science, 6, 229-250.

Browne, P.R.L. and A. Wodzicki (1977). "The aluminium-in-quartz geothermometer: a field test." Geochemistry 1977. DSIR Bulletin 218, 35-36.

Browne, P.R.L. and A.J. Ellis (1970). "The Ohaaki-Broadlands hydrothermal area, New Zealand: mineralogy and related geochemistry." American Journal of Science, 269, 97-131.

Browne, P.R.L. and M.W. Gardner (1982). "Subsurface alteration at the Ngawha geothermal field: a progress report." Proceedings 4th NZ Geothermal Workshop, 49-54.

Browne, P.R.L. and M.W. Gardner (1985). "Hydrothermal alteration of samples from recent wells at Ngawha." In: The Ngawha Geothermal Field, DSIR Geothermal Report 8, ed. M.A. Mongillo.

Browne, P.R.L., Roedder, E. and A. Wodzicki (1976). "Comparison of past and present geothermal waters from a study of fluid inclusions, Broadlands Field, New Zealand." In J. Cadet, J. Paces, eds., Proceedings International Symposium on Water-Rock Interaction, Czechoslovakia, 1974, Prague, 140-147.

Cathelineau, M. (1988). "Cation site occupancy in chlorites and illites as a function of temperature." Clay Minerals, 23, 471-485.

Cathalineau, M., Oliver, R., Garfias, A. and D. Nieva, (1985). "Mineralogy and distribution of hydrothermal mineral zones in Los Azufres (Mexico) geothermal field." Geothermics, 14, 49-57.

Cathelineau, M., Izquierdo, G. and D. Nieva (1989). "Thermobarometry of hydrothermal alteration in the Los Azufres geothermal system (Michoacan, Mexico): significance of fluid inclusion data." Chemical Geology, 76, 229-238.

Chi Ma, P.R.L. Browne and C.C. Harvey (1992). "Crystallinity of subsurface clay minerals in the Te Mihi sector of the Wairakei geothermal system, New Zealand." Proceedings 14th NZ Geothermal Workshop, 267-272.

Elders, W.A., Hoagland, J.R. and A.E. Williams (1981). "Distribution of hydrothermal mineral zones in the Cerro Prieto geothermal field of Baja California, Mexico." Geothermics, 10, 245-253.

Gonzales, R.C. (1985). "Vitrinite reflectance of cores and cuttings from Ngatamariki well NM-2, New Zealand." Geothermal Institute Report 85.10, 60 p.

Harvey, C.C. and P.R.L. Browne (1991). "Mixed layer clay geothermometry in the Wairakei geothermal field, New Zealand." Clays and Clay Minerals, 39, 614-621.

Hedenquist, J.W. (1990). "The thermal and geochemical structure of the Broadlands-Ohaaki geothermal system, New Zealand." Geothermics, 19, 151-185.

Hedenquist, J.W. and P.R.L. Browne (1989). "The evolution of the Waiotapu geothermal system, New Zealand, based on the chemical and isotopic composition of its fluids, minerals and rocks." Geochimica Cosmochimica Acta, 53, 2235-2257.

Hedenquist, J.W., Reyes, A.G., Simmons, S.F. and S. Taguchi (1992). "The thermal and geochemical structure of geothermal and epithermal systems: a framework for interpreting fluid inclusion data." European Journal of Mineralogy, 4, 989-1015.

Hermoso, D.Z. (1991). "Application of vitrinite reflectance geothermometry in wells OR-9D and ML-1RD, Palinpinon Geothermal Field, Southern Negros, Philippines." Geothermal Institute Report, 91.07, 49 p.

Kissin, S.A. and S.D. Scott (1982). "Phase relations involving pyrrhotite below 350°C." Economic Geology, 77, 1739-1754.

Kristmannsdóttir, H. (1975). "Clay minerals formed by hydrothermal alteration of basaltic rocks in Icelandic geothermal fields." Geologiska Föreningens i Stockholm Förhandlingar, 97, 289-292.

Kristmannsdóttir, H. and J. Tómasson (1976). "Hydrothermal alteration in Icelandic geothermal fields (1976)", Soc. Sci. Island, 5, 167-176.

Kristmannsdóttir, H. and J. Tómasson (1978), "Zeolite zones in geothermal areas in Iceland," in 'Natural Zeolites: Occurrence, Properties, Use', ed. by L.B. Sand and F. Mumpton, 277-284.

Lonker, S.W., Fitzgerald, J.D., Hedenquist, J.W. and J.L. Walshe (1990). "Mineral-fluid interactions in the Broadlands-Ohaaki geothermal system, New Zealand." American Journal of Science, 290, 995-1068.

McDowell, S.D. and M. McCurry (1978). "Mineralogical variations in borehole #1, Salton Sea geothermal area: Preliminary Report." Univ. California, Riverside, Report UCR DL 118/24.

Reyes, A.G. (1990). Petrology of Philippine geothermal systems and the application of alteration mineralogy to their assessment." Journal of Volcanology and Geothermal Research, 43, 279-309.

Scotford, D.M. (1975), "A test of aluminum in quartz as a geothermometer." American Mineralogist 60, 139-142.

Scott, G.L. (1988). "The fluid-rock interaction history of the Tongonan Geothermal Field, Leyte, Philippines." Unpublished PhD thesis, University of Auckland, 370 p.

Scott, S.D. and H.L. Barnes (1971). "Sphalerite geothermometry and geobarometry." Economic Geology, 66, 653-669.

Struckmeyer, H. and P.R.L. Browne (1988). "Application of the vitrinite reflectivity method to samples from the Wairakei-Tauhara and Ohaaki geothermal fields." Proceedings 10th NZ Geothermal Workshop, 251-255.

Youngman, K.J. (1985). "The application of fluid inclusion geothermometry based on secondary inclusions in primary igneous quartz crystals." Proceedings 7th NZ Geothermal Workshop, 189-191.

PROCEEDINGS, Eighteenth Workshop on Geothermal Reservoir Engineering
Stanford University, Stanford, California, January 26-28, 1993
SGP-TR-145

SIGNIFICANCE OF CRACK OPENING MONITORING FOR DETERMINING THE GROWTH BEHAVIOR OF HYDROFRACTURES

Toshiyuki Hashida, Kazushi Sato and Hideaki Takahashi

Research Institute for Fracture Technology
Tohoku University
Sendai/980, Japan

ABSTRACT

A method for determining the size of a crack induced by hydraulic fracturing is presented. The procedure is based on the measurement of the crack opening displacement and the fracture mechanics approach. The proposed method has been tested by conducting laboratory small-scale hydraulic fracturing tests on a granite. It is shown from the preliminary tests that the method provides a reasonable prediction of experimentally observed crack sizes.

INTRODUCTION

Massive hydraulic fracturing is one of the most promising means for enhanced recovery of geothermal energy from a deep rock mass. In this application of hydraulic fracturing, it is useful to develop a methodology for the design and control of an artificial crack to be used as heat exchanging surfaces. The evaluation of the size of the crack should be based on the fracture mechanics (Abe, H. et al, 1976, Simonson, E.R., 1976, Takahashi, H. and Abe, H., 1987). Conventionally, the size of the crack by means of hydraulic fracturing has been predicted using the fracture toughness and the volume of the fluid injected, assuming that an estimate of the volume of the induced crack is provided from the fluid volume injected. However, no established method for determining the in-situ fluid loss during hydraulic fracturing exists. It is known that the fluid permeation into a surrounding rock mass strongly depends on pre-existing fractures in actual geothermal reservoirs.

In this paper, we propose a method, which is based on the monitoring of the crack opening displacement and the fracture mechanics approach, to evaluate the size of hydrofractures. Firstly, laboratory small-scale hydraulic fracturing tests were conducted on various sized specimens of a granite, and the results were analyzed in terms of the crack propagation resistance in order to determine a suitable fracture toughness. Secondly, a specially designed deformation gage was applied to preliminary hydraulic fracturing tests to monitor the crack opening behavior. Based on the measured crack opening displacement and fracture toughness, the size of the crack was predicted and compared with experimental observations. It is suggested form the preliminary result that the proposed method provides a potential means for analyzing the crack growth behavior in hydraulic fracturing.

EXPERIMENTAL PROCEDURE

(1) Laboratory small-scale hydraulic fracturing tests

The rock tested in this study was a granite from a quarry in Iidate, Fukushima prefecture, Japan. Iidate granite is a light gray biotite granite. The rock has a rift plane typical of granites. As described below, all the hydrofractures propagated along the rift plane.

A series of hydraulic fracturing tests were conducted on rectangular specimens of various sizes. The geometry and dimensions of the specimens are shown in Fig. 1 and Table1, respectively. Hereafter, the size of the specimens are nominally designated by 15 cm, 20 cm, 30 cm, 50 cm, and 1 m. Simulated vertical boreholes were drilled in the center of all specimens, and bilobed pre-notch was introduced on the borehole to facilitate the analysis of crack propagation resistance. The depth of the pre-notches a_j/λ was approximately 0.5. In most tests the diameter of the holes was 15 mm, but diameter of 29 mm was used for crack opening monitoring experiments. Hydraulic fracturing was achieved by pressurizing the borehole using rubber packers. The pressurization was provided by a plunger pump at a flow rate of approximately 0.2 ml/sec. The rubber packers were made of hard rubber belt-shaped O-rings mounted on a steel shaft through which injection fluid was pumped into the open hole. Dyed hydraulic oil was used as the injection fluid to delineate the shape of the hydraulically induced crack. The viscosity of the injection fluid was 14 cSt. In order to analyze the crack growth behavior rubber packers with different pressurization intervals were utilized to extend the crack step by step in such a way that the subsequent injection interval enclosed the crack created at the preceding stage. During fracturing tests, the borehole pressure vs time was recorded in an X-Y plotter. After the tests, the specimen was broken open along the dyed crack plane, and the fracture surfaces were examined in detail. To determine the fracture toughness of the granite, J-based fracture tests were conducted on 3 inch compact tension specimens. For the experimental procedure of the J-based method, see the literature (Li, V.C. et al, 1987)

(2) Method for monitoring the crack opening displacement

In order to measure the crack opening displacement of hydrofractures, a special displacement gage was made in this study. A schematic of the displacement gage installed between the two rubber packers is given in Fig. 2. The displacement gage consists of three pairs of double cantilever beams. Strain gages are cemented to the both surfaces of each beam and connected as a Wheatsone bridge. The displacement gage monitors the displacement of the borehole wall in three orientations through a sensing steel rod. As indicated in Fig. 3, the instrumented packer with the displacement gage was set in the borehole such that the borehole deformation perpendicular to the rift plane can be monitored during hydraulic fracturing tests. Two specimens of 50 cm size were used for this series of tests. The pressurization interval was 15 cm.

STRESS INTENSITY FACTORS FOR THE FRACTURE MECHANICS ANALYSIS

As shown below, the shape of the hydraulically induced fracture can be approximated by an elliptical crack. In this section, the stress intensity factor of semi-elliptical surface cracks on a borehole is presented.

For semi-elliptical surface cracks on a cylindrical cavity in an infinite elastic body subjected to a constant pressure P acting on the crack surfaces and on the surface of the cavity (see Fig. 4), the stress intensity factor at the deepest point of the crack is written as follows

$$K = M_o P(\pi a)^{1/2}/E(k), \quad k=[1-(a/c)^2]^{1/2} \qquad (1)$$

where M_o is a correction factor, and E(k) is the complete elliptical integral of second kind. Abē et al have found that an approximate estimate of the stress intensity factor at the deepest point can be obtained from a solution for a two dimensional crack irrespective of different aspect ratios (Abē, H., et al, 1985). The relation is given by

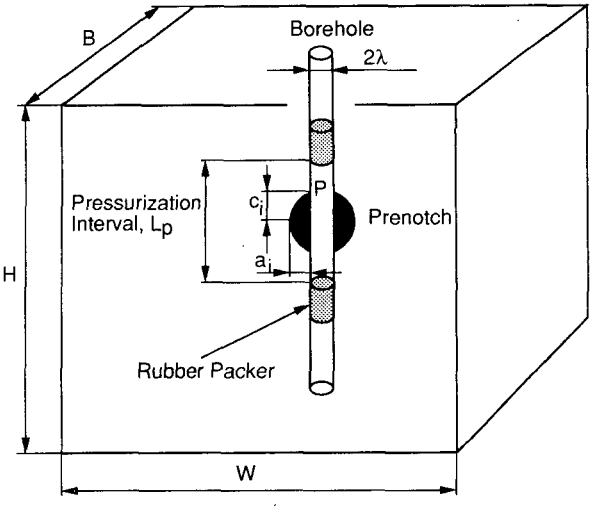

Fig. 1. Specimen used for hydraulic fracturing tests.

Table 1. Dimensions of specimens used.

Nominal Specimen Size	W (cm)	B (cm)	H (cm)	Borehole Diameter 2λ (mm)
15 cm	15	15	15	15
20 cm	20	20	20	15
30 cm	30	30	30	15
50 cm	50	50	50	15
50 cm *	70	50	50	29
1 m	100	100	100	15

* Borehole deformation was measured during the hydraulic fracturing tests

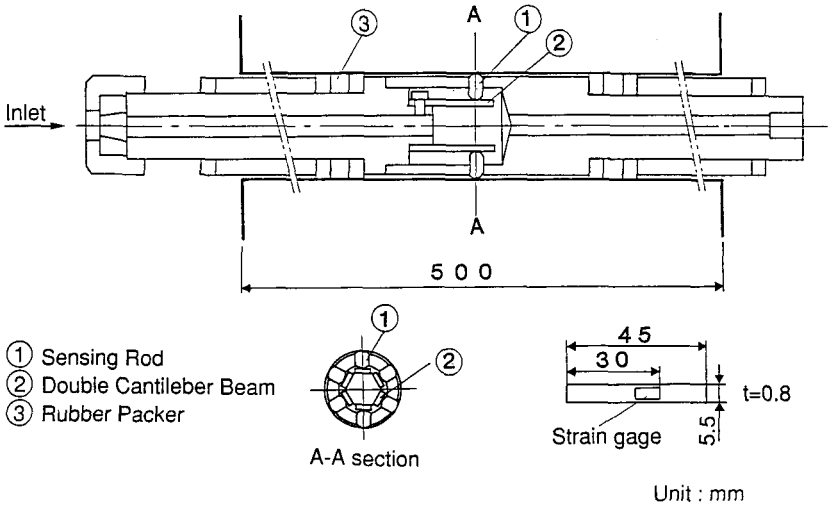

Fig. 2. Displacement gage for monitoring borehole deformation.

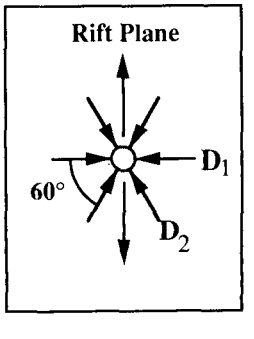

Fig. 3. Orientations for crack opening displacement measurements

$$K \simeq K_2 / E(k) \qquad (2)$$

where K_2 is the stress intensity factor of the two dimensional crack which can be found in the literature (Paris, P.C. and Shih, G.C., 1965). The correction factor calculated using Eqs. (1) and (2) is shown in Fig. 5. In order to correct Eq. (1) for the finite size of the rectangular specimens tested, a method proposed by Nishimura et al is used (Nishimura, A. et al, 1977). Approximating the specimen geometry by a thick-walled cylinder yields the following expression

$$K=[W^2/(W^2-1)]\, M_B\, M_o P(\pi a)^{1/2}/E(k) \qquad (3)$$

where $W= \lambda_o / \lambda$, and λ, λ_o are the radius of the borehole, and the outer radius of the approximated thick-walled cylinder. Data for M_B can be found in the literature (Shah, R.C. and Kobayashi, A.S., 1972).

CRACK PROPAGATION RESISTANCE BEHAVIOR IN HYDROFRACTURE GROWTH

The small-scale hydraulic fracturing tests showed that the crack extended both the sides of the pre-notches within the amount of the crack growth observed in this study ($\Delta a <$ 25 cm). Thus, the induced crack was bilobed, and its shape was nearly circular.

In the following, we describe an evaluation method to determine the crack propagation resistance based on results of the hydraulic fracturing tests. Schematics of crack propagation process and corresponding borehole pressure vs crack length (P- Δa) are shown in Fig. 6. We consider the pressure variation with the crack growth during the stepwise pressurization. The locations, A and B represents the positions of the rubber packer. The pressurization interval for the first cycle is A-A, and B-B for the subsequent cycle, respectively. The point 1 on the P- Δ a curve denotes the crack initiation at the notch tip. When the crack tip along the borehole reaches the location A, the pressure decreases due to the leakage of the injection fluid without significant crack growth. At the subsequent cycle, where the borehole interval B-B is subjected to fluid injection, the crack starts to propagate after the pressure corresponding to the point 2 is reached. When the fluid

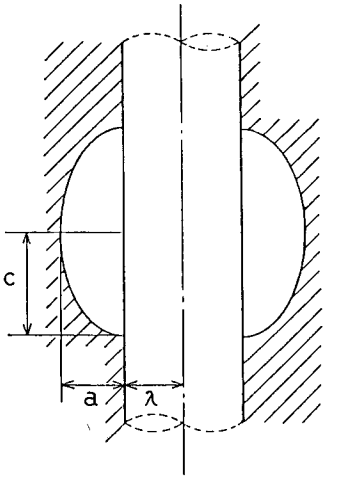

Fig. 4. Two semi-elliptical cracks on a borehole.

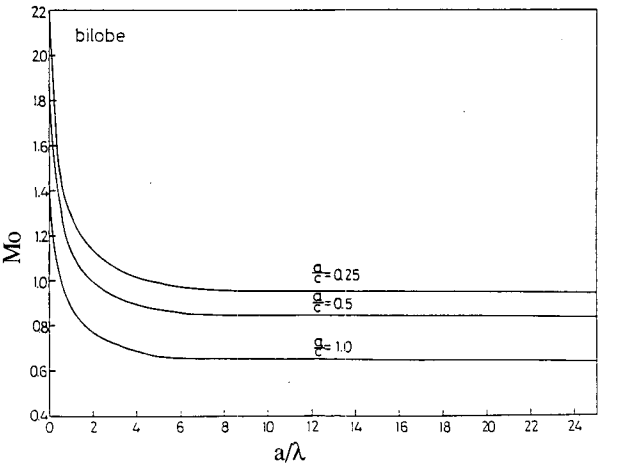

Fig. 5. Correction factor of the stress intensity factor.

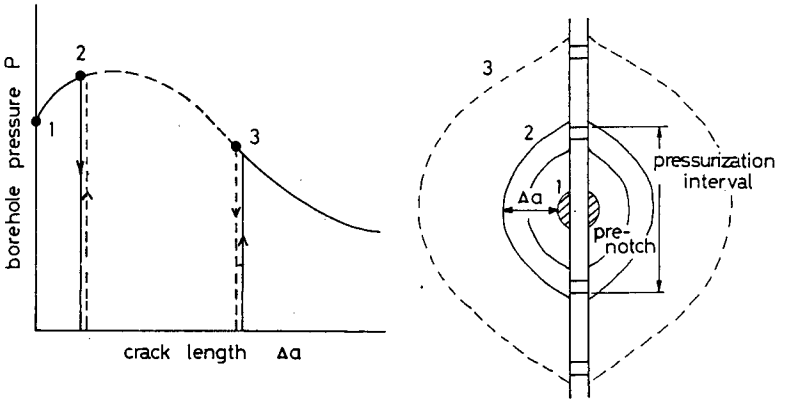

Fig. 6. Procedure for the analysis of crack propagation resistance.

gets over the straddle packer at the location B, the pressure decreases again as mentioned for the first cycle. Thus, the borehole pressure corresponding to the crack length induced at a pressure cycle $P(\Delta a)$ can be found by comparing the magnitude of the maximum pressure achieved at the the cycle P_{pre} and that at the subsequent cycle P_{sub}. Namely, $P(\Delta a) = P_{pre}$, if $P_{pre} \leq P_{sub}$, and $P(\Delta a) = P_{sub}$, if $P_{pre} > P_{sub}$. This discussion enables us to determine the borehole pressure and the corresponding crack size which are needed to construct crack propagation resistance curves.

Fig. 7 shows an example of the borehole pressure vs time curve recorded for the cyclic hydraulic fracturing tests of the 1 m sized specimens. Based on the method illustrated in Fig. 6, the evaluation point to be used for the crack propagation analysis is indicated on the pressure vs time curve by a solid circle. The pressurization was discontinued and unloaded at the end of the tests. Post-test examination showed that the crack propagation at the final pressure cycle was within the pressurization interval. The

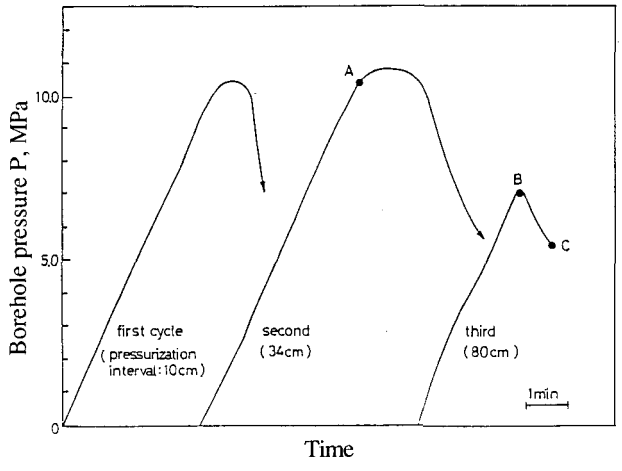

Fig. 7. Pressure vs time record.

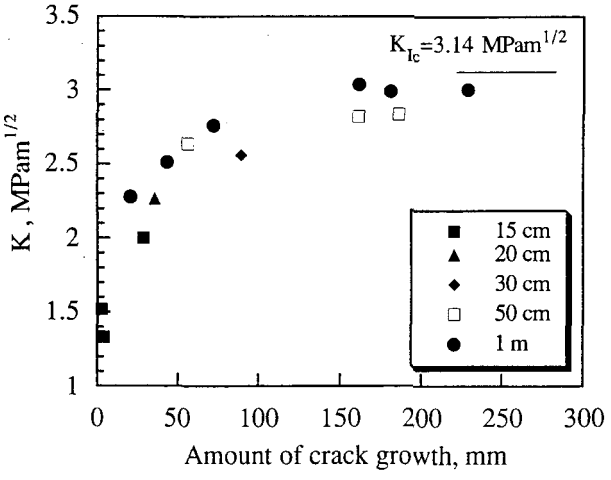

Fig. 8. Crack propagation resistance curve.

stress intensity factor along the periphery of the growing crack may be essentially constant. Abē et al carried out boundary element analyses for a pair of semi-elliptical cracks around a borehole and found the crack shape giving almost constant stress intensity factor along the crack periphery (Abē, H. et al, 1988). It has been shown that the aspect ratio of the crack is close to 1.0. This theoretical prediction agrees with the experimental observation mentioned above. Therefore, the amount of the crack growth at each pressure cycle is estimated from the aspect ratio a/c (=1.0) and the pressurization interval Lp using the following equation

$$a/c = 2(a_i + \Delta a)/Lp = 1.0 \quad (4)$$

The crack propagation resistance curves obtained from the hydraulic fracturing tests are summarized in Fig. 8. It is shown that the crack propagation resistance initially increases and levels off at the crack length of approximately 15 cm. It is particularly noted that the curve gives a nearly constant crack propagation resistance at the larger crack growth stage and steady-state crack growth condition is achieved. The fracture toughness value determined by the J-based testing method K_{Ic} is also indicated in Fig. 8. Note that the constant crack propagation resistance is close to the K_{Ic}. In order to assess the crack growth process in large-scale rock masses, it is required to evaluate an upper limit of fracture toughness values. The result of Fig. 8 suggests that the J-based method can be used to predict the constant value of the crack propagation resistance. Furthermore, it has been demonstrated previously that the J-based method can determine a fracture toughness which is independent of specimen size and confining pressure (Hashida, T., 1990, Hashida, T. et al, 1993). These results show that the K_{Ic} is judged to be an appropriate fracture toughness value which can be applied to the analysis of crack growth behavior during hydraulic fracturing.

CRACK OPENING DISPLACEMENT AND PREDICTION OF HYDROFRACTURE GROWTH BEHAVIOR

Pressure vs borehole deformation curves obtained from a hydraulic fracturing test are shown in Fig. 9. The curve labelled D_1 shows the deformation recorded for the orientation perpendicular to the rift plane, and the data obtained in the direction inclined at 30° to the rift plane is labelled D_2 (see Fig. 3). Note that the D_1-curve gives a larger displacement compared to the D_2-curve. This is because the crack propagation has occurred along the rift plane, as mentioned previously. The relation exhibits significant nonlinear deformation behavior below the breakdown pressure. It has been shown that the development of localized fracture process zone precedes the macroscopic crack propagation in fracture tests of the granite (Hashida, T., 1990, Hashida, T. et al, 1993). The nonlinear displacement prior to the breakdown process can be taken as reflecting the planar fracture process zone along

the rift plane. Thus, the pressure vs borehole deformation curve of Fig. 9 allows the crack opening displacement to be evaluated. From Fig. 9, the measured borehole deformation is 58 μm at the last stage of the crack propagation, and the corresponding linear elastic borehole deformation at this stage is 8 μm. Therefore, by substracting the elastic deformation from the total borehole deformation, the crack opening displacement is obtained to be 50 μm for this hydraulic fracturing experiment. The crack opening displacement data as obtained above are used in the following analysis.

Based on the measurements of the crack opening displacement and the fracture mechanics approach, we predict the length of the crack induced by the hydraulic fracturing tests. The opening displacement of a penny shaped crack at the center, w is written as follows

$$w=8(P-S)a/\pi E' \quad (5)$$

where S is the tectonic stress perpendicular to the crack plane, and $E'(=E/(1-\nu^2))$ is the effective Young's modulus. The stress intensity factor for the penny shaped crack is given by

$$K=(2/\pi)(P-S)(\pi a)^{1/2} \quad (6)$$

The combination of the above two equations provides the following relation

$$a=(E'w\pi^{1/2}/4K) \quad (7)$$

As described in the preceding session, the observation on the shape of the hydrofractures supports the approximation of the penny shaped crack and then the use of Eq. (7) in the prediction of the crack length. The E' of the granite used for the tests is 60 GPa and the fracture toughness K_{Ic} determined by the J-based method is 3.14 MPa·m$^{1/2}$. The crack lengths predicted by Eq. (7) with the measured crack opening displacement value are shown in Table 2, together with the experimental results obtained from post-test observations. The predicted crack length compares well with the experimental results. Though this comparison should be taken as preliminary and further tests are needed, the result demonstrates the feasibility of the present technique to analyze the crack growth behavior in hydraulic fracturing treatments. The method proposed in this study is summarized in Fig. 10. The technique is being currently applied to field hydraulic fracturing experiment.

CONCLUDING REMARKS

A method for determining the size of hydrofractures was proposed, which is based on the measurement of the crack opening displacement and the fracture mechanics approach. The method was applied to laboratory small-scale hydraulic fracturing tests. The results in this paper can be summarized as follows:

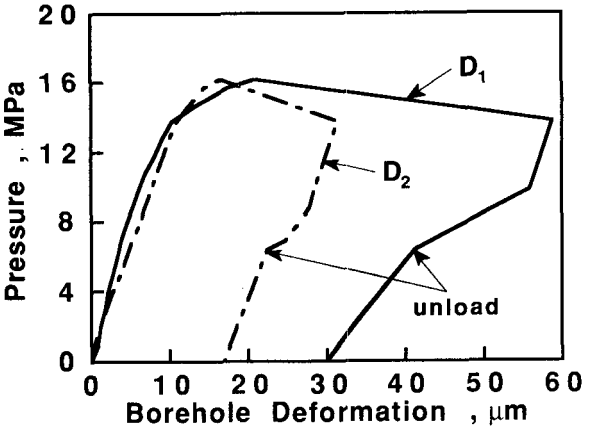

Fig. 9. Pressure vs borehole deformation.

Table 2. Comparison of predicted and experimental results

Specimen No.	Experimental Results a (cm)	c (cm)	w (μm)	Predicted Results a (cm)
H1	13.0	12.0	50	18
H2	12.5	12.0	51	18

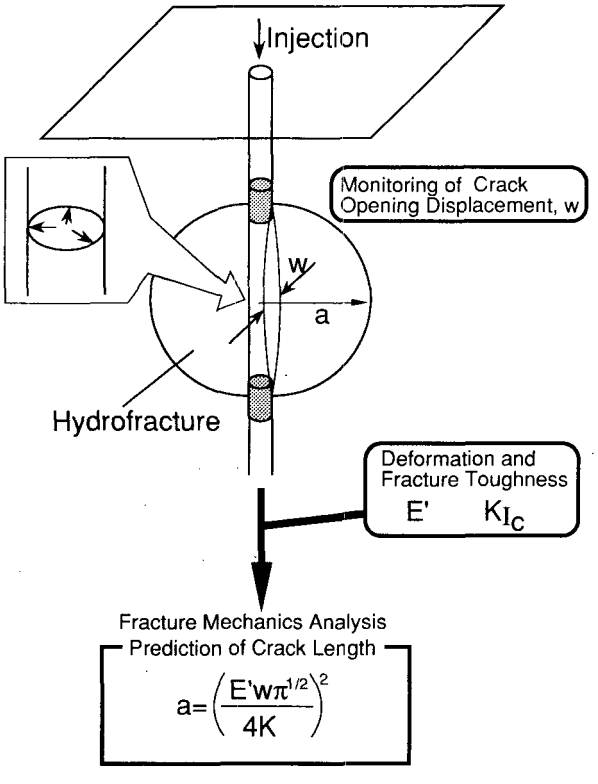

Fig. 10. Method proposed for the analysis of hydraulic fracturing.

(1) Cyclic hydraulic fracturing tests were conducted to determine the crack propagation resistance of a granite. The fracture mechanics analysis of the hydraulic fracturing tests revealed that the crack propagation resistance initially increased with the crack extension and then showed a constant value after the crack extension of 15 cm.
(2) The constant crack propagation resistance in the hydrofracture growth can be predicted by the J-based fracture testing method.
(3) The size of the hyrofractures predicted by the proposed method compares well with the experimental results.

REFERENCES

Abē, H., Mura, T. and Keer, L.M. (1976), "Growth Rate of a Penny-Shaped Crack in Hydraulic Fracturing of Rocks," Journal of Geophysical Research, 81-29, pp. 5335-5340.

Abē, H., Hayashi, K. and Takahashi, S. (1985), "Stress Intensity Factor of Elliptical Cracks Around a Cylindrical Cavity," Transactions of the Japan Society of Mechanical Engineers (A), 51-465, pp. 1350-1358 (in Japanese).

Abē, H. Hayashi, K. and Hashida, T. (1988), "Studies on Crack Propagation Resistance of Rocks Based on Hyrofrac Data of Large Specimens, Fracture of Concrete and Rock (Edited by S.P. Shah and S.E. Swartz), SEM-RILEM Int. Conf., Houston, pp. 354-361.

Hashida, T. (1990), "Evaluation of Fracture Processes in Granite Based on the Tension-Softening Model," Micromechanics of Failure of Quasi-Brittle Materials (Edited by S.P Shah, S.E. Swartz, and M.L. Wang), Elsevier Applied Science, London, pp. 233-243.

Hashida, T., Oghikubo, H., Takahashi, H. and Shoji, T. (1993), "Numerical Simulation with Experimental Verification of the Fracture Behavior in Granite under Confining Pressures Based on-Tension-Softening Model, Int. J. Fracture, in press.

Li, V.C., Chan, C.M. and Leung, C. (1987), "Experimental Determination of the Tension-Softening Curve in Cementitous Composites," Cement and Concrete Research, 17, pp. 441-452.

Nishimura, A., Aoki, a. and Sakata, M. (1977), "Stress Intensity Factor of a Semi-Elliptical Crack on Pressurized Cylindrical Cavity," Transactions of the Japan Society of Mechanical Engineers (1), 43-373, pp. 3192-3199 (in Japanese).

Paris, P.C. and Shih, G.C (1965), "Stress Analysis of Cracks," ASTM STP 381, pp. 30-83.

Shah, R.C. and Kobayashi, A.S. (1972), "Stress Intensity Factor for an Elliptical Crack Approaching the Surface of a Plate in Bending," ASTM STP 513, pp. 3-21.

Simonson, E.R., Abou-Sayed, A.S. and Clifton, R.J. (1976), "Constrainment of Massive Hydraulic Fracture," SPE Paper No. 6089, 51st Annual Fall Meeting of SPE of AIME.

Takahashi, H. and Abē, H. (1987), "Fracture Mechanics Applied to Hot, Dry Rock Geothermal Energy," Fracture Mechanics of Rock (Edited by B.K. Atkinson), Academic Press, pp. 241-276.

PROCEEDINGS, Eighteenth Workshop on Geothermal Reservoir Engineering
Stanford University, Stanford, California, January 26-28, 1993
SGP-TR-145

EXPERIMENTAL STUDY OF WATER ADSORPTION ON GEYSERS RESERVOIR ROCKS

Shubo Shang, Roland N. Horne and Henry J. Ramey, Jr.

Department of Petroleum Engineering
Stanford CA 94305-2220

ABSTRACT

Experimental isotherms of water vapor adsorption/desorption on three geothermal reservoir rock samples have been measured at temperatures of 80, 100, 120 and 140°C. Initial surface status of the sample was found to influence the amount of water adsorbed. At low relative pressures, adsorption is the dominant process of water retention onto the rock samples. Adsorption/desorption hysteresis was observed to exist over the whole pressure range at all temperatures. Similar observations were made for all three samples. The results of this study suggest that adsorption is important in storing water in geothermal reservoir rocks not only in itself, but also in inducing capillary condensation.

INTRODUCTION

In vapor dominated geothermal systems, it has been proposed that liquid might exist as adsorbed liquid in micropores (White, 1973). Evidence from both laboratory studies (Hsieh, 1980, Herkelrath et al., 1983) and field data indicates that storage of liquid as micropore fluid is reasonable. As pointed out by Ramey (1990) that if the only mechanism for liquid storage is adsorbed water, then the desorption curve provides important information for performance matching and production forecasting. It is therefore obvious that measurement of adsorption/desorption of water vapor on reservoir rocks is a crucial step in determining whether adsorption is the storage mechanism for these systems, and if so, what would be the appropriate procedure for performance prediction of vapor dominated geothermal systems.

Water vapor desorption was regarded as a simple and reliable technique in core analysis by Melrose (1988). In a comprehensive study to determine capillary pressure in the low-saturation region, Melrose (1991) compared results obtained using different techniques, and concluded that water vapor desorption method gave capillary pressure in good agreement with those obtained using the centrifuge and the porous plate methods. However, it should be pointed out that water vapor desorption in this case referred to the part of the desorption curve at relative pressures greater than 0.9, and the corresponding saturations are higher than 3.3% for the berea sandstones studied by Melrose (1988). At high relative pressures, adsorption is accompanied and complicated by capillary condensation, and it is likely that water held by capillary force constitutes a large part of the desorbed water.

Literature on water adsorption has been largely concerned with pure adsorbents, with carbon and silica being the most popular (Dubinin, 1980, Stoeckli, et al., 1983). The majority of the water adsorption studies are associated with the characterization of porous material. Willems et al. (1988) reported studies of water adsorption on hardened cement pastes and observed large adsorption/desorption hysteresis at 25°C. Carrott et al. (1991) studied water adsorption on synthetic zeolites in order to elucidate the relative influence of surface chemistry, pore size and pore shape upon the form of the water adsorption isotherm. A common feature of these studies is that the adsorption tests were all made at low temperature (between 0 to 25°C) and some special behaviors of water (Gregg and Sing, 1982) were observed.

Reservoir related water adsorption investigation is limited, particularly at high temperatures. Hsieh (1981) constructed a BET type of apparatus for high temperature water adsorption measurements. He conducted a number of adsorption measurements on berea sandstone and unconsolidated silica sand. Conclusions reached in his study were that adsorbed water is an important source of steam in vapor dominated geothermal systems and that water vapor pressure lowering in a rock is dominated by micropore adsorption (Hsieh and Ramey, 1983). Luetkehans (1988) continued Hsieh's research by improving the apparatus. Measurements of N_2 adsorption were made for berea sandstone, cores from the Geysers, California, and Larderello, Italy. Water adsorption/desorption tests were also conducted. However, the true magnitude of the amount adsorbed was suggested to be in question due to difficulties in establishing equilibrium. In addition, the long equilibrium time required made the leakage of high temperature valves a significant factor in causing the experimental error. Laboratory studies of water adsorption on porous media were also conducted by Herkelrath *et al.* in association with their work on steam

flow in porous media (Herkelrath et al., 1983) and the disposal of nuclear waste (Herkelrath and O'Neal II, 1985) They reported similar findings to those by Hsieh and Ramey (1983). Linear adsorption isotherms were claimed to fit data on Topopah Spring welded tuff up to a relative vapor pressure of 0.9. The problem of leakage in long equilibrium time was also identified in their work.

Clearly, there was a need to improve the apparatus in order to obtain reliable data of water adsorption at high temperatures. Harr (1991) performed preliminary investigation on the use of an automated sorptometer from Porous Material Inc. (PMI) for high temperature water adsorption measurements. To our knowledge, this is the first commercial sorptometer built for high temperature adsorption tests. Considerable time was spent to investigate various problems associated with the sorptometer both by Harr and in the present study.

APPARATUS AND PROCEDURES

The sorptometer consists of basically three parts. (1) a set of valves and pressure transducers kept in a high temperature chamber, (2) a sample chamber for loading and unloading samples, and (3) the electronic part for automatic control. During normal operation, the operator only needs to load the sample and the rest of the procedures are accomplished via a computer keyboard.

The principle of the adsorption/desorption measurement is the same as a BET type of experiment. The quantity one measures is the pressure of water vapor in the system before and after adsorption/desorption. System volumes are predetermined by expanding N_2 and measuring the corresponding pressures. The amount adsorbed/desorbed can then be calculated from mass balance. Knowing the weight of the rock sample, we can obtain the amount of water adsorbed per unit weight at a given pressure.

Due to the limitation of the size of the sample holder, rock samples had to be broken into granulars with equivalent diameters of approximately 8mm. New samples were all heated at 180°C under vacuum overnight to get rid of any surface residuals before running the adsorption test. Upon adsorption, water vapor is added incrementally to the system from a steam reservoir, which is kept at a temperature higher than the test temperature, and time was allowed for the system to reach equilibrium. Desorption commences at the end of adsorption test. In this case, water vapor is gradually pumped away until the adsorbed water is completely desorbed. The sample is reweighed at the end of the tests.

RESULTS AND DISCUSSION

The experimental studies reported here are the results of water adsorption/desorption tests performed on Geysers shallow reservoir core, Monteverdi well #2 rock and berea sandstone using the PMI sorptometer. As mentioned previously, the size of the rock samples used for an adsorption test is limited by the geometry of the sample holder. This should not impose any problem since the only change caused by breaking the core is surface area and the change is likely to be small. It was found to have negligible effect on the amount of water adsorbed (Harr, 1991). On the other hand, using small size samples reduces diffusional time and the time required for adsorption/desorption equilibrium. Knowing the complexity of the adsorption process, it is important to ensure that the rock surface has the same condition prior to each adsorption/desorption isotherm test. This was achieved by heating the sample at 180°C under vacuum for 3 to 4 hours. Reproducible isotherms were obtained after this pretreatment.

Figures 1 to 3 show the adsorption/desorption isotherms obtained at 120°C for Geysers shallow reservoir core, berea sandstone and Monteverdi #2 sample, respectively. As shown in the figures, the amount of water adsorbed at a relative pressure of 0.7 is 1.3mg/g for Geysers shallow reservoir core, 1.0mg/g for berea sandstone and 0.5mg/g for Monteverdi #2 samples. These quantities agree reasonably well with data

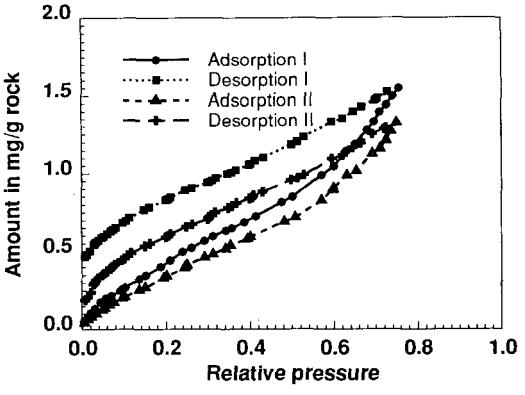

Figure 1 Isotherms on Geysers Shallow Reservoir Core

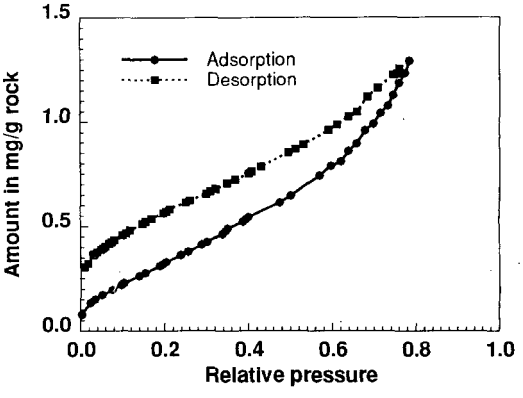

Figure 2 Isotherms on Berea Sandstone

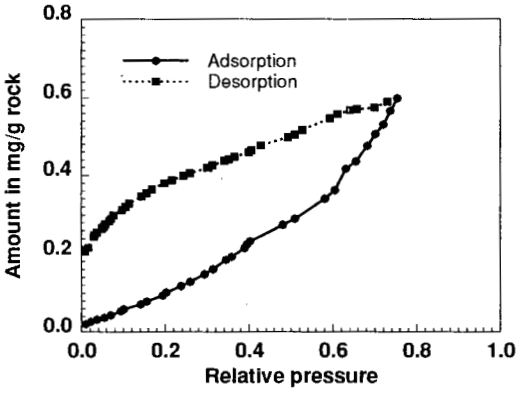

Figure 3 Isotherms on Monteverdi #2 Core

obtained by Hsieh (1980) and Luetkehans (1988). There is an obvious adsorption/desorption hystersis in each case, and it exists at near zero pressure. In Figure 1 are two sets of adsorption/desorption isotherms from two tests. The difference between these tests are that test II was performed without pretreating the sample, i.e. starting the second adsorption test at the end of the first desorption cycle. Comparison of the two sets of isotherms indicates the presence of irreversible adsorption.

Adsorption/desorption hysteresis

It is clear that significant hysteresis exists for steam adsorption/desorption on all samples tested. As shown by scanning electron micrographs (SEM), all the rock samples have complicated physical structures. This physical heterogeneity of the rock must be responsible for the presence of the adsorption/desorption hysteresis. Capillary condensation provides a basic explanation of the phenomena at high relative pressures (Adamson, 1990), and it can be quantitatively described using network models while applying the Kelvin equation to both adsorption and desorption isotherms (Mason, 1982, 1988)

However, hysteresis exists at very low relative pressures in the samples tested in this work. A plausible explanation for this behavior is that irreversible changes may occur in the pore structure on adsorption so that the desorption situation is different from the adsorption one (Bailey et al., 1971). For the adsorption of water at high temperatures, it is likely that the interaction of polar water molecules with rock surface causes irreversible adsorption at low relative pressures, *i.e*, there is some weak chemisorption for the first monolayer. Weak chemisorption of water onto cement pastes was reported by Willems *et al.* (1988) at room temperature. The observed low pressure hysteresis in this work is at least partly caused by weak chemisorption. The repeated tests without pretreatment in between provide some support for this assumption. Evacuation at test temperature mainly removes physically adsorbed water. So for the subsequent test, the surface of the sample was partly, if not completely, covered by chemisorbed water molecules. Thus, the amount of water adsorbed in the subsequent tests is smaller than that for the first one, and the amount of water retained at the end of desorption isotherms was also reduced.

Due to the presence of adsorption/desorption hysteresis, the measured desorption isotherms can be very different from the adsorption one. Understanding of the hysteresis phenomena bears significance to the reinjection process since the desorption isotherm is directly related to steam production in geothermal reservoirs.

Adsorption and capillary condensation

Adsorption is a surface phenomena and is affected not only by the surface area of the material but also by its chemical composition. Capillary condensation is related to the geometry of the porous media and for a given adsorbate it only depends on the geometric structure of the porous material. These processes are similar in nature, *i.e* they both cause vapor to condense onto the solid. They are related in such a way that adsorption provides a precursor for capillary condensation. One can divide the physical processes of adsorption in porous materials into three steps: (1) submonolayer adsorption, (2) multilayer adsorption with transition to (3) capillary condensation. The pressure range at which the transition from multilayer adsorption to capillary condensation occurs depends on the structure of the material. If the material is microporous (pore diameters not exceeding 20 Å), the pore space will be filled up (commonly termed as volume filling) before multilayer adsorption is developed. What happens physically is that as multilayer adsorption develops, the micropores become filled by a meeting of the adsorbed molecules from opposing walls. In large pores, multilayers of adsorbed water form as pressure increases. In reservoir rocks, there exist pores of different shapes and sizes. Due to the variation in pore size, capillary condensation occurs at different relative pressures. Since it is difficult to obtain the actual pore size distribution, it is hard to tell at what pressure capillary condensation will take place. Volume filling exists to a small extent in the rock samples studied in this work, and this suggests the presence of micropores in the rocks. However, the percentage of the micropores must be small judging from the shape of the adsorption isotherms. Thus, volume filling is not considered in the present discussion.

Figure 4 shows adsorption isotherms on the three rock samples obtained at 80°C. At relative pressure below 0.6, the amount of water adsorbed can be approximated by a linear function of relative pressure in all three cases. However, the linear relationship breaks down as pressure increases and the amount of water adsorbed increases rapidly with pressure. This change in the shape of adsorption

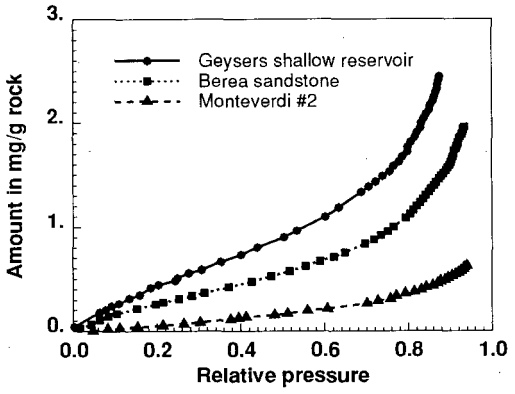

Figure 4 Comparison of Adsorption Isotherms at 80°C

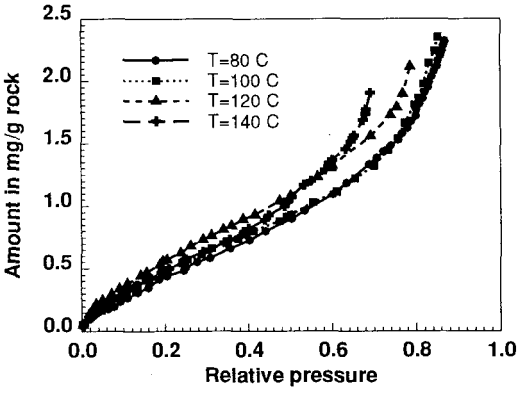

Figure 5 Comparison of Isotherms on Geysers Shallow Reservoir Core

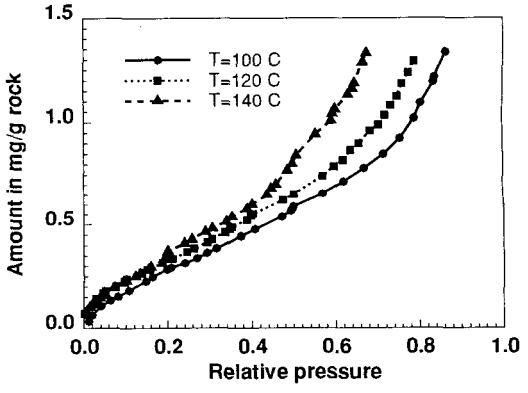

Figure 6 Comparison of Isotherms on Berea Sandstone

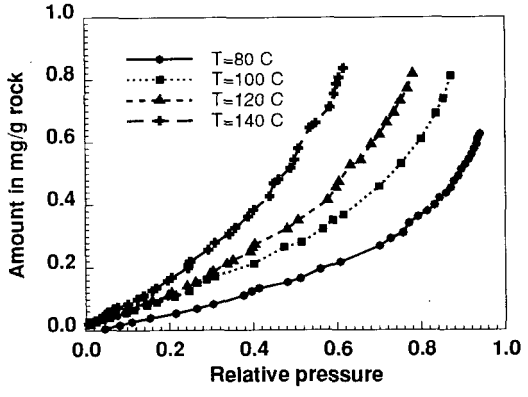

Figure 7 Comparison of Isotherms on Monteverdi #2 Core

isotherm is an indication that capillary condensation takes place and its contribution to total water retention onto the reservoir rock becomes more significant as pressure is further increased.

Due to equipment problems, we have not yet been able to obtain reliable data at relative pressures greater than 0.9 for higher temperatures. Based on the above discussion and the experimental data at 80°C, we expect similar adsorption/condensation phenomena for higher temperatures. The magnitude of water retention is yet to be measured.

Effect of temperature on water adsorption

Figures 5 to 7 show comparison of adsorption isotherms at different temperatures obtained on Geysers shallow reservoir core, berea sandstone and Monteverdi #2, respectively. The effect of temperature on the amount of water adsorbed varies from sample to sample. For Geysers shallow reservoir core and berea sandstone, as shown in Figures 5 and 6, appreciable changes in the amount of water adsorption did not occur until the relative pressure reached 0.65. However, for the Monteverdi #2 sample, considerable difference in the amount of adsorption at different temperatures appears at very low relative pressures, and this difference increases as the relative pressure increases, as shown in Figure 7. The reason for the different temperature dependence is not clear.

Salt in solution has long been considered to cause the low vapor pressure of water in vapor dominated geothermal systems (Ramey, 1990). So far in our discussion, we have ignored the possible effect of salt on water retention and vapor pressure lowering. We believe that if there are minerals present in the rock sample, they will dissolve in the adsorbed water film and influence the adsorption/condensation process.

CONCLUSIONS

Adsorption is important in geothermal reservoirs, not only in itself but also in inducing condensation to take place easier than in the absence of adsorption. It is logical to suggest that the system is adsorption dominated at lower relative pressures, and changes to capillary condensation dominates as pressure increases. Both adsorption and capillarity cause vapor pressure lowering.

However, it is hard to determine the cause of this vapor pressure lowering since the status of the rock surface is largely unknown.

Significant hysteresis exists for water adsorption/desorption on the rocks tested and it is shown to be caused, at least partly, by weak chemical interaction. The amount of water adsorption is affected by temperature and its effect is found to be sample dependent.

Much work needs to be done to measure the amount of water adsorbed/condensed at higher relative pressure. Additional work will be undertaken to investigate the possibility of running adsorption test at temperatures higher than 140°C so that we can simulate geothermal field conditions as closely as possible.

There is an obvious need to develop a model to describe the adsorption--capillary condensation process. The combination of Frenkel--Halsey--Hill (Halsey, 1952, Adamson, 1990), used for adsorption, and the Kelvin equation, used for capillary condensation, provides a good basis for such a model. Current work on this subject is in progress.

ACKNOWLEDGMENTS

The authors acknowledge the financial support from DOE, geothermal division. We thank Mr. Paul Pettit for help in the face of hardware problems.

REFERENCES

Adamson, A.W., Physical Chemistry of Surfaces, Wiley, 1990.

Baily, A., Cadenhead, D.A., Davis, D.H., Everett, D.H., and Miles, A.J., Trans. Faraday Soc., **67**, 231 (1971).

Carrott, P.J.M., Kenny, M.B., Roberts, R.A., Sing, K.S.W. and Theocharis, C.R., 'The Adsorption of Water Vapor by Microporous Solids', in Characterisation of Porous Solids II F., Rodriguez-Reinoso et al. (Editors), Elsevier Science Publishers, 1991.

Dubinin, M.M., 'Water Vapor Adsorption and the Microporous Structures of Carbonaceous Adsorbents', Carbon, **18**, 355 (1980).

Gregg, S.J., and Sing, K.S.W., Adsorption, Surface Area and Porosity, Academic Press, 1982.

Halsey, G.D., Jr., 'On Multilayer Adsorption', J. Am. Chem. Soc., **74**, 1082 (1952).

Herkelrath, W.N., Moench, A.F. and O'Neal II, C.F., 'Laboratory Investigation of Steam Flow in a Porous Medium', Water Resources Research, **19(4)**, 931--937 (1983).

Hsieh, Chih--Hang, 'Vapor Pressure Lowering in Porous Media', PhD Thesis, Stanford University, 1980.

Hsieh, Chih--Hang and Ramey, H.J., Jr., 'Vapor-Pressure Lowering in Geothermal Systems', SPEJ, 23(1), 157--167 (1983).

Harr, M.S., 'Laboratory Measurement of Sorption in Porous Media', MS Dissertation, Stanford University, 1991.

Leutkehans, J., 'A Laboratory Investigation of Steam Adsorption in Geothermal Reservoir Rocks', MS Dissertation, Stanford University, 1988.

Mason, G., 'The Effect of Pore Space Connectivity on the Hysteresis of Capillary Condensation/Desorption Isotherms', J. Colloid Interface Sci., **88**, 36--46 (1982).

Mason, G., 'Porous Materials and Percolation Theory' in Characterisation of Porous Solids, K.U. Unger et al. (Editors), Elsevier Science Publishers, 1988.

Melrose, J.C., 'Use of Water-Vapor Desorption data in the Determination of Capillary Pressures at Low Water saturations', SPE Reservoir Engineering, 913--18, (Aug. 1988).

Melrose, J.C., Dixon, J.R. and Mallinson, J.E., 'Comparison of Different Techniques for Obtaining Capillary Pressure data in the Low--Saturation Region', paper SPE 22690, presented at the 66th SPE Annual Technical Conference and Exhibition, Dallas, TX, Oct. 6--9 1991.

Ramey, H.J., Jr., 'Adsorption in Vapor--Dominated Systems', Geothermal Program Review VIII, April 18--20, 1990, San Francisco, CA.

Stoeckli, H.F., Kraehenbuehl, F., and Morel, D., 'The Adsorption of Water by Active Carbons, in Relation to the Enthalpy of Immersion', Carbon, **21(6)**, 589 (1983).

Willems, H.H., Massen, C.H., Hardon, J.J., Poulis, J.A. and Robens, E. 'Investigation of the Microstructure of Hardened Cement Pastes', in Characterisation of Porous Solids, K.K. Unger et at. (Editors), Elsevier Science Publishers, 1988.

White, D.E., 'Characteristics of Geothermal Resources', in Geothermal Energy, Kruger and Otte (Editors) Ch.4, P69 Stanford Press, 1973.

PROCEEDINGS, Eighteenth Workshop on Geothermal Reservoir Engineering
Stanford University, Stanford, California, January 26-28, 1993
SGP-TR-145

Numerical Investigations into the Formation of a 'High Temperature Reservoir'

Mike Shook

Idaho National Engineering Laboratory
P.O. Box 1625 MS 2107
Idaho Falls, ID 83415

Introduction

This paper summarizes an ongoing numerical modeling effort aimed at describing some of the thermodynamic conditions observed in vapor-dominated reservoirs, including the formation of a high temperature reservoir (HTR) beneath the "typical" reservoir. The modeled system begins as a hot water geothermal reservoir, and evolves through time into a vapor-dominated reservoir with a HTR at depth. This approach taken here to develop a vapor-dominated system is similar to that of Pruess (1985), and involves induced boiling through venting. The reservoir description is intentionally generic, but serves to describe a means of evolution of conditions observed (in particular) at The Geysers.

The formation of vapor-dominated geothermal reservoirs, such as The Geysers in northern California, Larderello in Tuscany, Italy, and Kamojang, Indonesia, has been subjected to intense scrutiny over the last several decades. These reservoirs are characterized in their native state by vapor-static pressure gradients and near-isothermal temperatures that extend vertically for up to thousands of meters. These conditions were explained conceptually by White et al. (1971) and Truesdell and White (1973) as manifestations of countercurrent flow of vapor (upward) and liquid (downward) in a "heat pipe" (Eastman, 1968). Steady state heat pipes result in large vertical heat flows with vanishingly small net mass flux.

It has been recognized since the early 1980's that, beneath portions of the "typical" vapor-dominated reservoir at The Geysers, there exists areas of high temperature; the temperature gradient in these zones approaches a conductive gradient The transition between what has come to be known as the "typical" reservoir and the "high temperature reservoir" (HTR) occurs over a very small distance— on the order of hundreds of meters, and is not accompanied by any observed permeability barrier or other massive change in rock properties (eg, thermal conductivity) (Walters, et al., 1988). Evidence for the presence of a HTR at Larderello is less complete, and while most of the high temperature data can be explained by the presence of a liquid-dominated heat pipe at depth (Pruess et al., 1987), at least some of the temperature data is inconsistent with this model (Truesdell, 1991).

Several theories have been advanced concerning the formation of the HTR. Truesdell (1991) recently summarized three models for HTR formation, originally proposed by Drenick (1986). These three models can be summarized as: 1) an active liquid system, separated from the "typical" system by permeability barriers; 2) local heating from an intrusive, resulting in dry conditions and essentially conductive temperature gradients; and 3) a "fossil liquid system", which has recently (geologically speaking) boiled dry. Model 1 is discarded because such a permeability barrier has not been observed, and because of the observed pressure continuity between reservoirs. Truesdell discards model 3 from energy balance considerations and discrepancies in possible temperature gradients in the HTR, and ultimately offers a modification of Drenick's model 2, and suggests that the high temperature reservoir is due to recent downward extensions of an existing vapor-dominated reservoir into dry rock.

This study addresses the question of HTR formation numerically. The reservoir model and approach used is similar to that of Pruess (1985); however, vapor pressure lowering effects were included for the rock matrix. Results of this study indicate that a high temperature reservoir may occur as a steady state component of a "typical" vapor-dominated reservoir. Fractures within the HTR are dry; however, saturated conditions exists in the rock matrix. Pressures at depth follow a vapor pressure with depth relationship. Temperatures at depth are large (relative to saturated conditions) because of superheat in the fractures and vapor pressure lowering in the matrix. Drying out the fracture network at depth appears to be what drives the system to form a high temperature reservoir; however, adsorption in the rock matrix allows for saturated conditions to prevail.

Numerical Model

The model used in this study is a one-dimensional, fractured, vertical reservoir. The Warren and Root (1963) dual porosity model is used, with matrix-matrix interactions allowed in the vertical direction. The dimensions of the reservoir are 100 m by 100 m areally, and 1200 m vertically. Fracture spacing is also 100 m. The permeability field used was 10^{-14} m^2 (10 md) for the fracture network, and 10^{-17} m^2 (10 md) for the rock matrix. Thermal properties of the rock were taken from the geothermal literature, and are summarized in Table 1. These properties were selected to be representative of Geysers rock properties.

Additional properties required in the simulation study include relative permeability and capillary pressures for the fractures and rock matrix. There are no published laboratory data for Geysers rock, and therefore these properties were selected somewhat arbitrarily. For relative permeabilities, the following functional form is used:

$$k_{rl} = k^{o}_{rl} (S)^{e_l} , \qquad k_{rv} = k^{o}_{rv} (1 - S)^{e_v}$$

$$S = \frac{S_l - S_{lr}}{1 - S_{lr} - S_{vr}}$$

Parameters used for relative permeability are given in Table 1, and the relative permeability curves are shown in Figures 1 and 2. In the lower quarter of the reservoir, "matrix" relative permeabilities were used in the fractures and matrix alike. Rocks in the HTR are more thermally altered, and it was thought that changes in wettability (and therefore in relative permeability and capillary pressure) could be partially responsible for formation of the HTR.

Capillary pressures are of the form:

$$P_c = P_{c\text{-}max} (1\text{-}S_l)^n$$

A maximum capillary pressure was arbitrarily selected as 1380 kPa (13.8 bars). We further assume that the full range of capillary pressure is also encountered in the fractures, albeit over a much smaller range of saturation values. This is done by assigning substantially more curvature to the capillary pressure curve in the fractures than in the matrix, and allows for capillary equilibrium between the two domains (Pruess et al., 1985). Capillary pressure curves are given in Figure 3.

The simulation model used in this study was TETRAD (Vinsome, 1991; Vinsome and Shook, 1993). A numerical grid of 24 vertical elements was selected, with vertical grid dimensions of 50 m. The fluid was assumed to be pure water in this preliminary study. Further studies are planned to include the effects of brine and noncondensible gases.

A final important feature of the reservoir model involves vapor pressure lowering (VPL). VPL effects were incorporated in the rock matrix by including adsorption, and was implemented in TETRAD in a manner described by Holt and Pingle (1992). Langmuir parameters A and B were as reported by Nghiem and Ramey (1991). The resulting vapor pressure ratio β vs. saturation is given in Figure 4.

Model Implementation

Initial conditions for the base case simulation were hydrostatic equilibrium, and a constant (240°C) temperature. Pressure at the top of the reservoir was set at 3580 kPa, slightly above saturation pressure. A heat flux of 0.5 W/m^2 was proscribed at the base of the reservoir, and the top surface was held at constant temperature and pressure. All other boundaries were considered no-flow. In response to the heat flux at the bottom, the reservoir undergoes transient behavior, in which some mass is expelled (due to thermal expansion) into the caprock. After 2000 years, the system is perturbed by withdrawal of mass, simulating natural venting. The pressure boundary at the top of the reservoir is replaced with a no (mass) flow boundary, however, energy is lost to the caprock via conduction. A well is completed in the top grid block of the fracture network, and mass is withdrawn at a rate of 0.4 kg/s, corresponding to a discharge rate of 40 kg/s/km^2. This discharge rate is similar to estimated natural discharge of many geothermal fields (Pruess, 1985). Fluid is discharged for a period of 20 years, at which time approximately 5% of the initial mass in place has been removed.

The imposed discharge gives rise to rapid boiling in the fractures, which causes cooling at the top of the reservoir. This cooling is partially mitigated by large vertical upflow of vapor, which condenses at the top of the reservoir and releases latent heat. Boiling also occurs in the matrix, though to a lesser extent. At early times large differences in temperatures and pressures exist between fracture and matrix at any given elevation, similar to that noted by Pruess (1985). However, as boiling is induced in the matrix elements, vapor pressure lowering effects cause a reduction in vapor pressure within the matrix, and steam enters the matrix. This influx of steam largely offsets cooling effects of boiling. When discharge is terminated after 20 years, fracture temperature has fallen by an average of 18°C, and matrix temperature by 5°C. Two phase conditions exist in throughout the fracture system, and in the top 40% of the matrix blocks. The top portion of the fracture network contains a small mobile liquid saturation, characteristic of a vapor-dominated heat pipe. Appreciable liquid ($S_l > 0.8$) exists at depth in the fractures.

After terminating discharge, the reservoir is again isolated and allowed to attain steady state. Heat flux at the base of the reservoir is maintained at 0.5 W/m^2, and heat loss is allowed through the caprock via conduction. Heat loss does not balance influx for nearly 20,000 years; however, at 10,000 years heat loss to the caprock is 95% of heat influx at the bottom. In attaining steady state, all elements undergo monotonic changes in thermodynamic conditions. Figures 5 - 7 show temperature, pressure, and saturation profiles, respectively, at 10,000 and 30,000 years. These figures clearly show that steady state conditions nearly apply at 10,000 years. Heat loss to the caprock finally balances heat flux applied to the bottom at approximately 20,000 years, and all elements exhibit steady state behavior from that point. Simulations have been run through 100,000 years with virtually no change in the thermodynamic properties in any grid.

Steady state conditions of the reservoir are very interesting. Figures 5 and 6 very clearly show vapor-dominated conditions in the upper 70% of the reservoir, overlying a high temperature reservoir. The pressure gradient in the fractures is slightly in excess of vapor-static, which is sufficient to allow for the downward movement of the small mobile liquid phase. The temperature gradient in Figure 6 also shows the near-isothermal conditions typically found in a vapor-dominated reservoir. Although not shown on these figures, the vapor dominated reservoir came to near steady state about 4,000 years after discharge was terminated. Thermodynamic conditions in the associated matrix blocks are slightly different than adjacent fractures, with temperatures larger by about 4.5° C and pressures less by 700 kPa. The pressure difference causes secondary convection cells to form, with steam moving from fractures to matrix, condensing, and heating the rock.

Below the vapor-dominated reservoir is a transition zone, characterized by relatively large (45%) liquid saturations in the fractures, with a high temperature reservoir below. The transition begins just above the "modified relative permeability zone" in the fractures, and extends

downward 200 meters. Mobile liquid in this zone is approximately 5%. This water trickles downward into the high temperature zone, where it is immediately vaporized. No mobile water exists in the HTR in the fracture network, though average liquid saturation in the matrix is about 75%. This lack of liquid in the fractures appears to be directly responsible for the occurrence of high temperatures, as insufficient mass is available for efficient heat pipe behavior. Liquid recharge into this portion of the reservoir is largely due to gravity drainage in the matrix blocks.

While this numerical model is extremely simple relative to real geothermal systems, it shows the possible genesis of a vapor dominated reservoir from a liquid dominated system. One aspect of this vapor-dominated reservoir is the formation of a steady state, high temperature reservoir below the "typical" reservoir. Use of a zone of reduced mobility in the lower portion of the fractures makes this model similar in some regards to the "permeability barrier model of Drenick (1986). Further studies are planned to examine what effect other causes of reduced mobility at depth have on HTR formation; for example, a decrease in absolute permeability (rather than relative permeabilty) with depth.

Summary and Conclusions

A numerical study has shown that a high-temperature reservoir can develop as a steady state component of a vapor-dominated reservoir. The reservoir model used here began as a hot water geothermal system. Through simulated natural venting, a perturbation was introduced, during which the reservoir underwent long (> 20,000 years) transient behavior. At termination of the venting, the reservoir moved monotonically toward steady state. Steady state conditions nearly applied at 10,000 years, with heat loss approximately 95% of the heat influx. Steady state prevailed at approximately 20,000 years, and conditions remained constant through a simulated time of 100,000 years. The steady state conditions included a vapor-dominated reservoir overlaying a high temperature reservoir at depth. Matrix liquid saturations are 100% in the "typical" reservoir, and average approximately 75% in the HTR. Saturations in top of the fractures are as typically observed in a vapor-dominated reservoir, with small mobile liquid saturations. No liquid exists in the HTR fractures.

It should be emphasized that several ad hoc assumptions were implemented in this study. In particular, a zone of reduced mobility in the fracture system was used. Insufficient measurements have been made to evaluate the validity of this assumption. Future studies are planned to investigate these and other aspects of this model.

Acknowledgements

I gratefully thank Mark Walters of RREC and Greg Anderson of UNOCAL for many useful conversations on this topic, and Jackie Brower of EG&G for help with manuscript layout. Funding for this work was provided by the U.S. DOE, Assistant Secretary for Conservation & Renewable Energy, Office of Utility Technologies, under DOE Contract No. DE-AC07-76ID01570. Mention of specific products and/or manufacturers in this document implies neither endorsement of preference nor disapproval by the U.S. Government, any of its agencies, of EG&G Idaho, Inc of the use of a specific product for any purpose.

References

Drenick, Andy, "Pressure-Temperature-Spinner Survey in a Well at The Geysers," *Proceedings*, 11th Workshop on Geothermal Reservoir Engineering, Stanford University, Stanford, CA., January 21-23, 1986.

Eastman, G. Y., "The Heat Pipe," Scientific American, Vol. 218, 1968, pp 38-46.

Holt, R., and A. Pingol, "Adding Adsorption to a Geothermal Simulator," *Proceedings*, 17th Workshop on Geothermal Reservoir Engineering, Stanford University, Stanford, CA., January 29-31, 1992.

Nghiem, C.P., and H.J. Ramey, "One-Dimensional Steam Flow Under Desorption," *Proceedings*, 16th Workshop on Geothermal Reservoir Engineering, Stanford University, Stanford, CA., January 23-25, 1991.

Pruess, K., Y.W. Tsang, and J.S.Y. Wang, "Modeling of Strongly Heat Driven Flow in Partially Saturated Fractured Porous Media," presented at the IAH 17th International Congress on the Hydrogeology of Rocks of Low Permneability, University of Arizona, 1985.

Pruess, Karsten, "A Quantitative Model of Vapor Dominated Geothermal Reservoirs as Heat Pipes in Fractured Porous Rock," *Transactions*, Geothermal Resource Councel, Vol. 9, II, August, 1985.

Pruess, K., R. Celati, C. Calore, and G. Cappetti, "On Fluid and Heat Transfer in Deep Zones of Vapor-Dominated Geothermal Reservoirs," *Proceedings*, 12th Workshop on Geothermal Reservoir Engineering, Stanford University, Stanford, CA., January 20-22, 1987.

Truesdell, A.H., and D.E. White, "Production of Superheated Steam from Vapor-Dominated Geothermal Reservoirs," *Geothermics*, Vol. 2, Nos. 3-4, 1973, pp 154-173,

Truesdell, Alfred H., "The Origin of High-Temperature Zones in Vapor-Dominated Geothermal Systems," *Proceedings*, 16th Workshop on Geothermal Reservoir Engineering, Stanford University, Stanford, CA., January 23-25, 1991.

Vinsome, P.K.W., "TETRAD Users Manual," Dyad Engineering, Calgary, Alberta, Canada, 1991.

Vinsome, P.K.W., and G.M. Shook, "Multi-Purpose Simulation," *J. Petroleum Science and Engineering*, to appear, 1993.

Walters, M.A., J.N. Sternfeld, J.R. Haizlip, A.F. Drenick, and Jim Combs, "A Vapor-Dominated Reservoir Exceeding 600° F at The Geysers Sonoma County, California," *Proceedings*, 13th Workshop on Geothermal Reservoir Engineering, Stanford University, Stanford, CA., January 19-23, 1988.

Warren, J.E., and P.J. Root, "The Behavior of Naturally Fractured Reservoirs", *Society of Petroleum Engin. J.*, Sept. 1963.

White, D.E., L.J.P. Muffler, and A.H. Truesdell, "Vapor-Dominated Hydrothermal Systems Compared with Hot-Water Systems," *Economic Geology*, Vol. 66, 1971, pp 75-97

Table 1: Petrophysical Properties and Initial Conditions

Petrophysical Properties	Matrix	Fractures
Porosity	0.04	0.01
Permeability (md)	0.01	10.
Relative Permeabilities		
$k_{rl} = k^o_{rl} (S)^{e_l}$	$k^o_{rl} = k^o_{rv} = 1$	$k^o_{rl} = k^o_{rv} = 1$
$k_{rv} = k^o_{rv} (1 - S)^{e_v}$	$e_l = 4.;\ e_v = 2.5$	$e_l = 2.;\ e_v = 1.5$
$S = \frac{S_l - S_{lr}}{1 - S_{lr} - S_{vr}}$	$S_{lr} = 0.4;\ S_{vr} = 0.05$	$S_{lr} = 0.05;\ S_{vr} = 0$

Rock Heat Capacity = 1. kJ/kg

Rock Density = 2650 kg/m^3

Rock Thermal Conductivity = 2.1 W/m°C

Matrix Block Size = 100. m

Heat Flux = 0.5 W/m^2

Initial Conditions

Pressure = Hydrostatic Gradient, P_{avg} = 8260 kPa

Temperature = 240° C

Grid Data

Nx = 1	Ny = 1	Nz = 24
Δx = 100 m	Δy = 100 m	Δz = 50 m

Figure 1. Matrix Relative Permeability vs. Liquid Saturation.

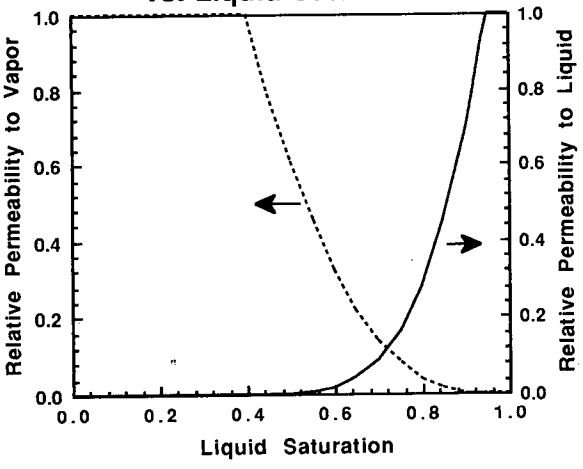

Figure 2. Fracture Relative Permeability vs. Liquid Saturation.

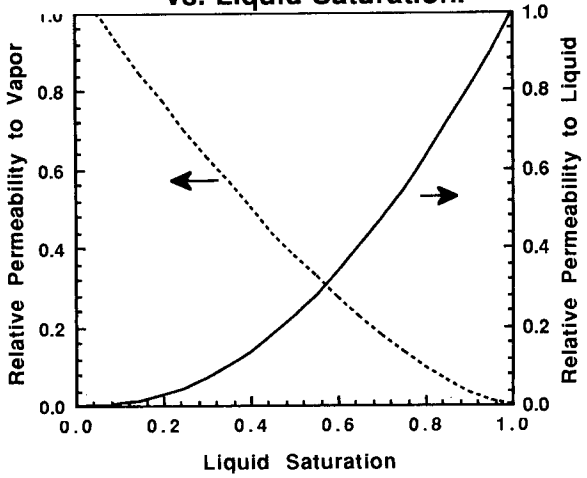

Figure 3. Capillary Pressure Curves for Matrix and Fracture Grid Blocks.

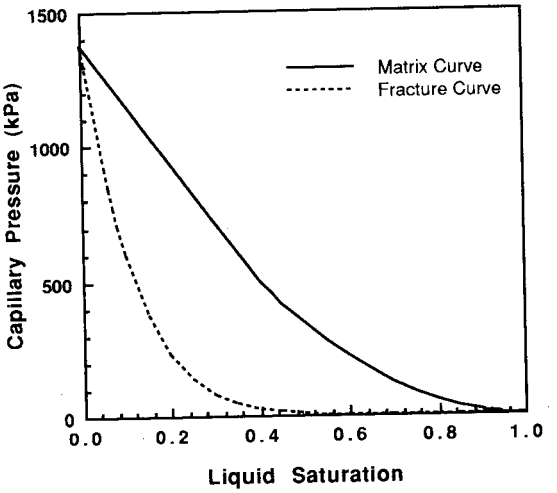

Figure 4. VPL Effects Used in Model.

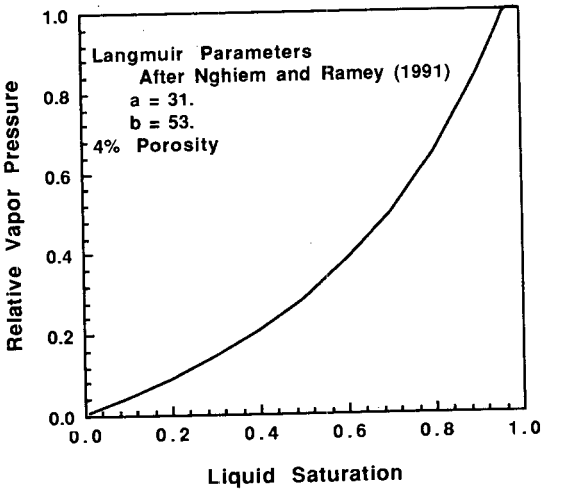

Figure 5. Pressure Profiles for 10,000 and 20,000 Years.

Figure 7. Saturation Profiles at 10,000 and 20,000 Years.

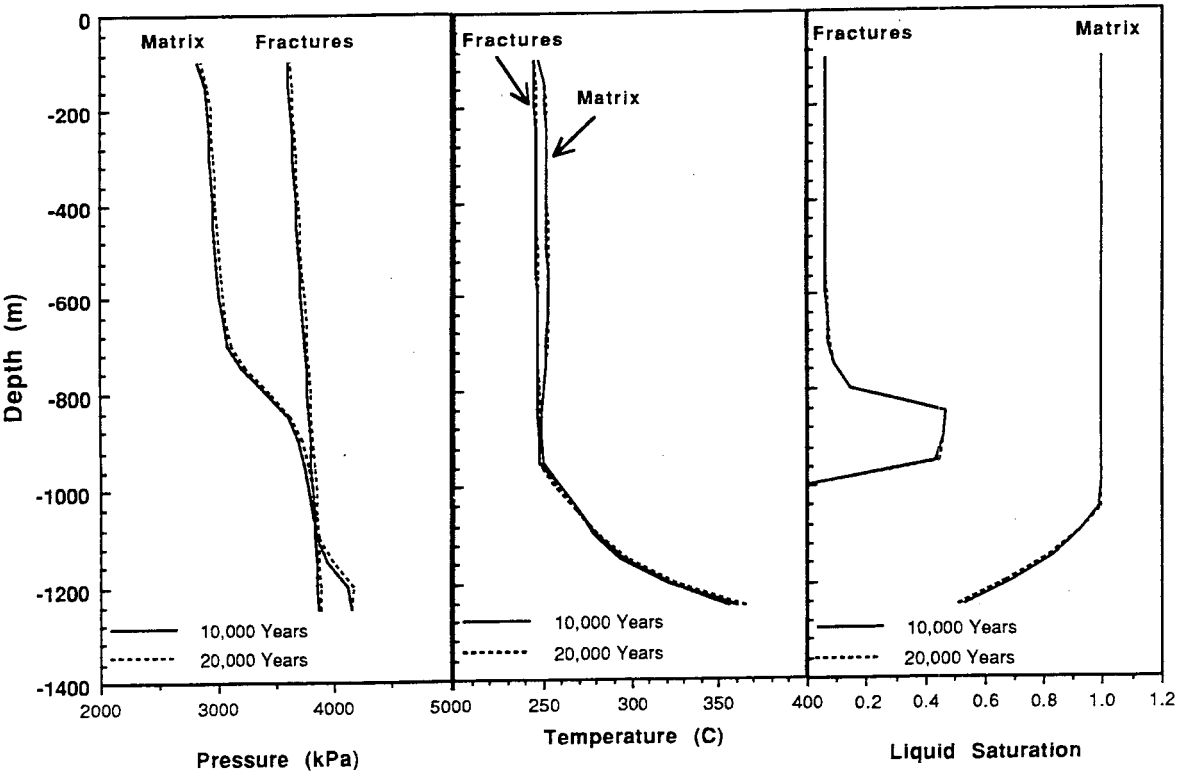

Figure 6. Temperature Profiles at 10,000 and 20,000 Years.

GEOSYS: AN X/MOTIF-BASED SYSTEM FOR ANALYSIS AND MANAGEMENT OF GEOTHERMAL DATA

J. L. Stevens, S. K. Garg, L. Luu, T. G. Barker, J. W. Pritchett and A. H. Truesdell
S-Cubed, P.O. Box 1620, La Jolla, CA 92038

Luis Quijano
Comision Federal de Electricidad, Morelia, Mich., Mexico

ABSTRACT

The Geothermal Data Management System (GEOSYS) has been developed to allow storage, retrieval, and analysis of the large volume of data associated with a geothermal reservoir, including well drilling data, well log data, production (chemical and flow) data, and geographical data. The system allows the user to display overlays of well locations, faults, and surface features on maps or topographic images. Subsurface cross-sections can be displayed by selecting any two points on the map. Cross sections show subsurface topography together with the projections of wells along the cross section. The structure of each individual well can also be displayed in detail. Downhole well logs can be selected, displayed, and expanded to arbitrary scale. Time histories of production data can be displayed for the field and for each well. Data from the Cerro Prieto geothermal field has been used for development and testing of the system.

This type of system has been made possible by recent advances in hardware and software technology, and the dramatic reduction in cost of high speed workstations and disk storage. GEOSYS was developed using the X Window System and the OSF/Motif widget set. The X Window System was designed specifically to provide hardware independence for interactive systems based on bit-mapped graphics with a Graphical User Interface (GUI). Systems developed using X run on most modern workstations, and can run across a network with the application being resident on only one computer, but accessible to all others.

INTRODUCTION

The exploration, testing, development, and operation of geothermal reservoirs generates a great quantity and variety of data. Geothermal reservoir analysis and assessment require access to these data in ways that are often difficult to predict. The purpose of the Geothermal Data Management System described in this paper is to provide access to all of the data that are collected related to a particular geothermal reservoir, and to allow interactive extraction and display of these data in a wide variety of formats. The development of modern high speed workstations, and advances in both hardware and software design have made it possible to develop a system with much more extensive capabilities than have been feasible in the past.

GEOTHERMAL DATA MANAGEMENT SYSTEM–CONCEPTUAL DESIGN

The Geothermal Data Management System is an example of a general class of system built on four basic elements: data, analysis tools, a relational database, and a graphical user interface. In this case the data include well log data (e.g., pressure, temperature, and spinner); related well data such as well locations, deviation logs, and drilling logs; historical data such as production and well test histories, and physical data such as topography and fault locations. The analysis tools operate on this data and extract and/or display information. Examples of analysis tools are programs to display well logs and time histories, and to overlay event and geographic information on maps and images. The data are maintained within a relational database system. The database structure is designed to allow virtually any type of data to be stored and accessed within the system. The relational database performs the function of keeping track of raw data and related information, and keeps track of any changes to the database. The graphical user interface (GUI) allows the user to interact with the data, database, and analysis tools. All user interaction takes place through the graphical user interface. The GUI is designed to minimize the amount of keyboard entry and to allow most selections to occur though mouse driven menus and displays.

GEOSYS consists of a hierarchy of programs: a master program and a set of analysis modules which may in turn start additional modules. At the top level is the master program whose primary function is to start the other analysis programs. This top level program allows the user to obtain a summary of available data, to select the geothermal field to be processed in analysis modules, and to select analysis tools to apply to the data. By design, the master program is both small and simple. Because of this, it is easy to expand the program to add additional analysis modules as required.

SYSTEM REQUIREMENTS

The graphical user interface is based on the X Window System (X11, currently in revision 5, refs: Scheifler and Gettys, 1990; O'Reilly, 1988). X is a client/server windowing system that was designed specifically to allow hardware independence and transportability of applications across different hardware platforms. GEOSYS is being designed and implemented on a Sun workstation, however because the interface is based on X, transfer to any other system that supports X and Unix could easily be accomplished. Also, because X is a client/server system, GEOSYS can run on one computer (the client) while the display and all interaction with GEOSYS occurs on a different computer (the server).

GEOSYS has been written in the C and FORTRAN programming languages. C is required because calls to Xlib (the X Window System interface) are in C, and because C is better suited to the design of complex systems with a variety of data structures than FORTRAN. FORTRAN is being used because it is better suited to certain types of computational analysis than C. As a result, the top level programs, interactive modules, database interface, and graphics routines are written in C, and when necessary these routines call FORTRAN subroutines and start executable FORTRAN programs.

The X interface is being written using the X toolkit (Asente and Swick, 1990; Young, 1990). The X toolkit enforces an object-oriented approach to programming by combining the windows and the operations on the windows into "widgets". GEOSYS uses the Motif widget set developed by the Open Software Foundation (OSF, 1990) and some additional special purpose widgets.

The relational database tables used in GEOSYS are independent of the particular relational database management system used for accessing the tables. Currently, GEOSYS is being developed using an internal database manager that accesses the tables as required by the system. All database tables are documented in a standard format before being created or used within the system. All files required for defining the database structure in SQL, as well as internal data structures used within the GEOSYS system are generated directly from this documentation. This way typographic errors are avoided and any changes in the database structure can be made throughout the system by changing only the documentation and regenerating dependent files.

SYSTEM COMPONENTS

The Geothermal Data Management system currently consists of 7 modules:

GEOSYS

This is the master program to select data and execute other modules. This and all of the other modules contain on-line help to aid the user in understanding the options available for each module.

MAP

The Map module allows display of a background image which may be an aerial or satellite photograph, a color or grayscale representation of topography, an image displaying a subsurface parameter (e.g. temperature at a given depth), or any other geographic image. Other information may be overlaid on top of this image. Some types of overlays include well locations, hot spring locations, faults, topographic contours, roads, towns, and other surface or subsurface features. Wells can be selected by pointing at any well on the Map. Any of the other GEOSYS modules can then be started using the selected well. The Cross Section module can be started by selecting any two points with the mouse.

CROSS SECTION

The Cross Section module displays the topography, subsurface geology, and the projection of each well along the selected cross section. This module is normally started from the Map module, although it can be started directly from GEOSYS to display a cross section through a selected well.

WELL

The Well module shows the structure of each well in detail, including well deviations along North-South, East-West, and vertical projections, hole/casing structure, cemented and slotted regions, circulation loss points, surface elevation, and stratigraphic layers along the well. Additional information about the well can be displayed in tabular form.

WELL LOG

The Well Log module is used to display subsurface profiles of temperature, pressure, spinner, and other downhole measurements. The displays can be expanded to show fine details of the profiles by simply drawing a rectangle with the mouse around the region to be expanded. Well logs can be displayed as a function of measured depth, true depth, or elevation. The well structure, hole/casing size and locations of circulation loss points can be displayed together with the profiles, and automatically rescale when a region is expanded.

PRODUCTION

The Production module allows production data taken over the history of the field and individually for each well to be accessed, displayed, and correlated. Any type of production data including mass flow rate, enthalpy, temperature, and chemical measurements can be stored and accessed by this module. The Cerro Prieto production database used to test the system contains over 120,000 measurements taken from 200 wells over a period of 25 years.

DATABASE

The Database module is the link to the relational database that allows data to be entered, changed, and removed from GEOSYS. Forms are provided for data entry and review for each of the 24 database tables, however data may also be added by reading from a file in a format that mimics interactive entry. This can be a very significant convenience when a large amount of data is to be added to the system. Data added by file can then be reviewed, edited, and corrected interactively.

CONCLUSIONS

The development of systems such as GEOSYS has been made both necessary and feasible for three reasons:

1. The volume of data associated with a geothermal field and used in reservoir assessment has been rapidly increasing. This volume of data has great benefits in the ability to analyze a field, but is difficult to analyze by traditional means.

2. Over the last few years, the cost of high speed workstations and disk storage has decreased dramatically, while the computational speed and storage capacity have simultaneously increased dramatically. The capabilities of these systems make it possible to develop interactive systems that access and analyze large volumes of data.

3. The development of the X Window system has made it possible to develop sophisticated systems with a transportable Graphical User Interface capable of operating on machines from a wide variety of vendors and on different types of machines across a network. Because of this, the software no longer is restricted to a particular brand of hardware, and can be easily transported to different machines as hardware technology improves.

As a result, it is now possible to maintain nearly all of the data associated with a geothermal field on a workstation, and to provide the capability to access and analyze this data. GEOSYS has been developed for this purpose.

REFERENCES

Asente, Paul J. and Ralph R. Swick (1990), "X Window System Toolkit", DEC Press, ISBN 1-55558-051-3.

O'Reilly (1988), "The X Window System Series" (8 volumes), O'Reilly and Associates, 1988, 1989, 1990.

ISBN 0-937175-50-1, 0-937175-26-9, 0-937175-27-7, 0-93715-14-5, 0-937175-38-2, 0-937175-33-1, 0-937175-56-0, 0-937175-57-9.

OSF (1990), Open Software Foundation, OSF/Motif Series (5 volumes), Prentice Hall. ISBN 0-13-640491-X, 0-13-640525-8, 0-13-640517-7, 0-13-640509-6, 0-13-640483-9.

Scheifler, Robert and James Gettys (1990), "X Window System", Second Edition, DEC Press. ISBN 1-55558-050-5.

Young, Douglas A. (1990), "X Window System: Programming and Applications With Xt", OSF/Motif Edition, Prentice-Hall. ISBN 0-13-497074-8.

PROCEEDINGS, Eighteenth Workshop on Geothermal Reservoir Engineering
Stanford University, Stanford, California, January 26-28, 1993
SGP-TR-145

RESULTS FROM A DISCRETE FRACTURE NETWORK MODEL OF A HOT DRY ROCK SYSTEM

G W Lanyon, A S Batchelor, and P Ledingham

GeoScience Ltd., UK

INTRODUCTION

The dream of clean, economic power derived from the huge volumes of naturally hot rock that lie beneath us (Parsons, 1904) is as yet unfulfilled. The technical difficulties in engineering heat-exchangers of sufficient area and volume at depth have not yet been solved (Garnish et al, 1992).

In the mid 1970s and early 1980s models of HDR systems assumed "penny-shaped" hydraulic fractures (for example MAGES 1979), which were assumed to have been created by hydraulic fracturing of a homogeneous, isotropic, impermeable, elastic crystalline host-rock. Even at this time some authors were drawing attention to the importance of natural fracture systems (Batchelor, 1976, 1977). Subsequent experience during all large scale field tests has shown that the interaction between the in-situ stress field and the natural fracture system is of supreme importance and new models such as FRIP (Pine and Cundall, 1985) were developed. These models were vital for the understanding of field experiments such as those performed at Rosemanowes (Parker, 1989). However, these models only considered a gross idealisation of the natural fracture system. The work described in the Summary of the Work section represents a move towards better representations of the natural fracture system.

The discrete fracture network model used during the study was the NAPSAC code (Grindrod et al, 1992). NAPSAC has been developed as part of the OECD/NEA Stripa Project.

OBJECTIVES

The goals of the work were to investigate the application of discrete fracture network models to Hot Dry Rock systems, increase the understanding of the basic thermal extraction process and more specifically the understanding of the Rosemanowes Phase 2B system. The aims of the work were:

a estimation of the area, extent and aperture of the hydraulically important natural fractures using pre-stimulation permeability measurements;

b estimation of the effective properties of porous media equivalents of the natural fracture system including directional permeabilities;

c examination of a model of reservoir creation due to aperture enhancement of natural fractures;

d application of the tools developed to the fracture system at Rosemanowes and comparison with field data from that site.

The aim in applying the work to the Rosemanowes site was to use the discrete fracture network approach to integrate a diverse set of field measurements into as simple a model as possible.

CONCEPTUAL MODELS

The limited nature of measurements of natural fracture system properties at depth forces the use of many simplifying assumptions. These assumptions were chosen to simplify the model while still being compatible with experimental observation.

Natural fracture system

The natural fracture system was idealised as a stochastic process with fracture properties such as orientation, size and hydraulic aperture described by probability distributions. Realisations are instances of the stochastic process. In NAPSAC the probability distributions are approximated by "random number" generators and a realisation is specified by the random number seed used to initialise the generator.

The models that have been used in the study assume that the basic fracture properties are independent of each other. Correlations may exist in nature, for example between fracture length and transmissivity, but they have not been included in the models because of the difficulty in deriving estimates of the strengths of such correlations. The probability distributions used to specify fracture orientation, transmissivity and size have been chosen to fit the limited observations available. This means that the models are compatible with observation but are not uniquely so.

It has also been necessary to limit the fractures that are included within the models. Discontinuities within the granite exist on many scales from micro-cracks to major faults extending tens of kilometres. The models have assumed that features not visible by borehole televiewer (BHTV) are hydraulically unimportant. Measurements

from core or Formation MicroScanner (FMS) show many more features than the BHTV but experimental evidence suggests that these features are hydraulically unimportant. In fact only a small percentage of those features identified by the BHTV show any appreciable flow (see Summary of the Work section).

Flow within fractures and boreholes

It has been assumed throughout the study that flow in fractures can be approximated as laminar flow within a parallel plate. It has been suggested that flow is in fact "channelled". If this is the case at the pore pressures and stresses of interest, the thermal performance of the underground heat-exchanger may be markedly worse than that predicted here. In this way the models described here are optimistic. Similarly the assumption of laminar flow within the fracture system may underestimate the resistance to flow at the inflows and outflows to boreholes.

It has been assumed that flow through sufficiently large volumes of the fracture network can be treated as flow through an equivalent porous medium. In such a medium the mass flowrate $\underline{q}$ through an area A is related to the non-hydrostatic pressure P by Darcy's Law:

$$\underline{q} = -\frac{\mathbf{K}A}{\mu}\nabla P \qquad \text{Eq 1}$$

where μ is the fluid viscosity and **K** is the effective permeability tensor of the equivalent porous medium. For a given network **K** is estimated by calculating the flow through several realisations of volumes of the network under unit pressure gradients. The network volumes used should be sufficiently large that **K** is independent of realisation. Values of **K** derived in this way can be used in porous medium models of fluid-flow to describe the large-scale behaviour of flow within the fracture network.

Fracture system stimulation

The use of homogeneous, isotropic, elastic models of the rock mass to describe the effects of Massive Hydraulic Fracturing (MHF) is well established in the oil industry. However, it is believed that they are of only limited utility in modelling the stimulations necessary to create a HDR reservoir in low-permeability pervasively fractured granite. Field observations suggest that flow is controlled by the natural fracture system even after stimulation. It is believed that although axial fractures may be created close to the borehole, fracturing fluid will be quickly diverted into the most transmissive and compliant natural fractures rather than creating new fractures. In this way the major effect of MHF programmes away from the vicinity of the borehole is in the dilation of existing natural fractures.

Fully coupled three-dimensional models of the mechanical interaction between the fluid, the fracture system and the rock mass are only now becoming available and demand substantial computing resources to model even small numbers of random fractures. The scale of the Rosemanowes system made such an approach impractical. Even if sufficient computing resources had been available it is not clear that there is sufficient knowledge of the dynamic properties of fractures and their load-paths to make such an approach viable. Instead it was assumed that all fractures within the stimulated volume had been exposed to similar pressure disturbance and that each fracture could be treated independently. This approach was taken using a range of fracture deformation parameters to calculate effective properties of stimulated networks. Having done this the observed hydraulic performance of the stimulated rock mass was used to identify a range of deformation parameters that were compatible with observation.

Tracer transport in the fracture system

Tracer transport has been modelled as the advective transport of non-reactive particles within the flow-field. It has been assumed that the porosity of a fracture is larger than the fracture volume calculated from fracture area and hydraulic aperture. In reality fracture surfaces are rough and resistance to flow is controlled by bottle-necks within the fracture, resulting in hydraulic apertures considerably smaller than the mechanical aperture of the fracture. Travel times in fractures have therefore been calculated using a delay factor based on a transport aperture to hydraulic aperture ratio.

SUMMARY OF THE WORK

The undisturbed fracture system

The Carnmenellis granite is one surface expression of the Cornubian batholith underlying the the South Western peninsula of England (Whittle and McCartney in Parker, 1989). It is relatively homogeneous in composition and character, with pervasive orthogonal jointing. At the Rosemanowes site three deep boreholes were drilled between 1980 and 1983 at depths between 2000 m and 2600 m. The wireline logging data available from Rosemanowes provided information on the orientation, spacing and percentage of hydraulically active fractures at depth.

The fracture orientations derived from borehole televiewer (BHTV) images from RH12 and RH15 showed two clear fracture sets. Set 1 comprises sub-vertical fractures dipping between 80° and 90° and striking approximately NW-SE. Set 2 fractures are again sub-vertical dipping between 70° and 90° but nominally strike NE-SW. Set 1 fractures are more numerous in all the deep boreholes.

An important parameter that cannot be measured from boreholes is fracture length. Early FRIP models assumed infinite, equally-spaced fractures although subsequent work has used discontinuous fractures. NAPSAC,

however, needs estimates of the fracture length distribution. Microseismic source diameters derived from analysis of events generated during hydraulic tests at the Rosemanowes site were therefore used as a basis for fracture length studies. These estimates will be shown to correspond to fracture system geometries that are compatible with the results of hydraulic and tracer data from the site. An alternative would have been to look for suitable out-crop data (Gale et al, 1991).

Although it would have been possible to measure individual fracture transmissivities in the deep boreholes at Rosemanowes, it would have been impractical to perform complete surveys of each borehole. Such surveys were performed at the Carwynnen test site to depths of 700 m using lightweight equipment (Hodgkinson, 1984). This latter data was used as an initial estimate of the fracture transmissivity distribution at Rosemanowes despite the discrepancy in depth and hence normal stress. These fracture transmissivities were used to calculate equivalent hydraulic apertures using the 'cubic law'. At a later point the data was used only as a measure of the variation in hydraulic aperture, the mean aperture being adjusted so that network permeability matched the observed in situ permeability.

In view of the inevitable incompleteness of the data available to characterise the natural fracture system, a parametric approach was taken. The parameter used in the study was fracture length. Experimental uncertainties, together with observations from local mines suggested that the microseismic source diameters might be an over-estimate of fracture length. Several different distributions of fracture length were studied; these included distributions estimated from trace-mapping in local mines and scaled versions of the microseismic source diameters. For each distribution the percolation frequency was calculated. This is the frequency at which the fracture network becomes connected over large distances. Below this frequency the network is made up of discrete unconnected clusters of fractures. There is no evidence for such a disconnected fracture system at Rosemanowes and it was assumed that the fracture system was above the threshold, thus limiting the range of fracture lengths that were considered.

Three distributions were used throughout the rest of the study. These were scaled versions of the log-normal fits to the microseismic source diameters. The three distributions had mean fracture lengths of 24 m, 16 m and 11 m respectively. The distribution with a mean length of 24 m was that derived directly from the microseismic data with no scaling reduction.

Equivalent permeability tensors were calculated for networks with the three different fracture length distributions by performing flow simulations on 200 m side cubes of fractured rock. Figure 1 shows a sample 200 m cube for each of the three length distributions.

The permeability was found to increase with fracture-length. All the permeability tensors were anisotropic with the greatest permeability in the vertical and NW-SE directions. Typically permeability in the NE-SW direction corresponding to the set 2 strike direction was a factor of four to seven times lower than the vertical permeability. The permeability tensors were more anisotropic for the smallest fracture length distribution.

Constant-head well tests were also simulated for models including a 200 m length of pressurised borehole for each of the length distributions. Only the 11 m fracture length distribution network had permeabilities close to those measured. However, since there were no measurements of hydraulic aperture at Rosemanowes and the data from Carwynnen had been used as an estimate of the hydraulic aperture distribution, it was not possible to exclude the higher fracture length models. Instead the aperture distribution was scaled by a factor chosen for each length distribution to match the field permeability of 5×10^{-17} m^2 (50 μDarcy). In this way a range of fracture aperture and length distributions was identified that were consistent with the well-test observations. The estimated mean hydraulic aperture and anisotropy (given as the ratio of maximum to minimum principal permeability) are given in Table 1.

Geological constraints on the fracture system

In order to assess whether the models of the fracture system were realistic it was essential to consider the geological context of the modern fracture system, and to assess what 'soft' geological information might contribute to the modelling effort.

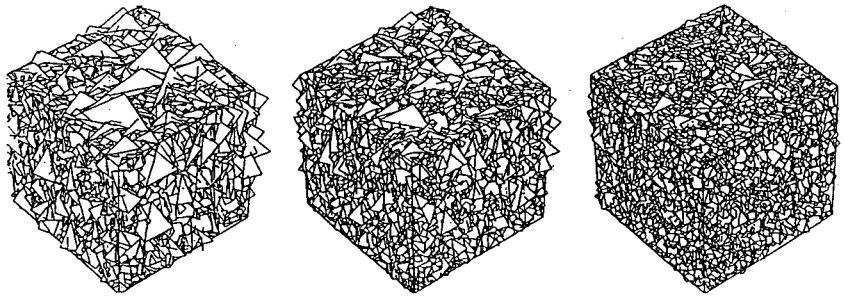

Figure 1 Realisations of 200m cubes of fracture system, for three distributions of fracture length with means of 24, 16 and 11m.

TABLE 1 CALCULATED AND EXPERIMENTAL PERMEABILITIES FOR UNDISTURBED FRACTURE SYSTEM AT ROSEMANOWES

Mean Fracture Length (m)	Mean Fracture Aperture (μm)	Mean principal permeability values (m^2)			Ratio of max/min	Simulated well-test permeability (m^2)
		Set 2	Set 1	Vertical		
24.4	22	$1.3\ 10^{-17}$	$2.8\ 10^{-17}$	$5.0\ 10^{-17}$	4	$1.1 - 6.6\ 10^{-17}$
16.4	27	$1.2\ 10^{-17}$	$2.6\ 10^{-17}$	$5.0\ 10^{-17}$	4	$0.7 - 4.6\ 10^{-17}$
11.0	59	$0.7\ 10^{-17}$	$1.7\ 10^{-17}$	$5.0\ 10^{-17}$	7	$0.9 - 7.0\ 10^{-17}$
Experiment		Falling head tests led to estimates of permeability in the range 1 to $5\ 10^{-17}$				

The scope of this geological study was limited to a review of existing literature. The review indicated that the models described in the previous section were consistent with the overall pattern of fracturing in the Carnmenellis. The major sets identified in BHTV mapping related to "master joint" sets identified by Ghosh (1934). The relationship between fractures and larger scale flow-structures (eg the cross-courses) was also considered.

Data from the south west England Seismic Experiment (SWESE, Brooks et al, 1984) suggested that the fracture patterns observed at Rosemanowes and elsewhere in the Carnmenellis might extend to a depth of 6 km or more. The shallowest of the four major reflectors in the granite being estimated to be at approximately 8 km depth. It was also suggested that there might be some medium-scale (200-500 m) block structure within the granite. It was thought that this block structure might be related to the zones of relatively highly fractured rock found in the deep boreholes.

In general the study concluded that most of the assumptions made in the fracture network modelling were reasonable, but that larger scale structures (dykes etc) might be important factors at reservoir scales. This conclusion may prove to be of great significance in the exploitation of the HDR resource.

The stimulated fracture system

A massive stimulation programme was undertaken at Rosemanowes between 1982 and 1985, using a variety of fluids from water to highly viscous gels. The programme could be broadly divided into Phase 2A (attempting to link RH11 and RH12) and Phase 2B (linking RH12 and RH15). In almost all experiments, RH12 was used as the injection well.

It was assumed that away from the immediate vicinity of the wellbore, all permeability enhancement occurred by changes in the hydraulic aperture of existing fractures. Practically all inflows and outflows have been correlated with natural fractures visible on the BHTV (Pearson R A in Parker, 1989).

Axial fracturing resulting from the stimulations did not appear to effect flowing locations. No BHTV logs are available for RH11 and RH12 prior to stimulation, so it is not possible to state definitively that only natural fractures flow in this case. However, this hypothesis has been confirmed for RH15.

The stimulation model used represents an upper bound on the performance of the stimulation rather than a prediction of the effects of the various massive hydraulic fracturing tests. The model considered two modes of aperture enhancement:Shear induced dilation and normal dilation. Shear induced dilation was assumed to be a permanent deformation resulting from failure of the fracture, while normal dilation was assumed to be a reversible elastic response to the pore pressure within the fracture. For each of the two modes, permeability tensors were calculated for a range of parameters using 200 m cubes of the largest (mean 24 m) and smallest (mean 11 m) fracture length distributions.

The model used for the in-situ stresses is that given by Pine and Kwakwa (1988) which had been derived from data including a suite of hydro-fracture stress measurements at depth in RH12 and RH15. At reservoir depths the maximum principal stress was horizontal and oriented at approximately 310° N. The intermediate stress was vertical. There was considerable anisotropy in the stress field, with total stresses at 2000 m vertical depth being estimated to be σ_{Hmax} = 71, σ_V = 52 and σ_{Hmin} = 30 MPa. The estimated stresses were used with a simple Mohr-Coulomb failure law for estimating shear failure and a bilinear compliance law for normal dilation.

Figures 2 and 3 show the variation in network permeability with shear induced dilation and fracture normal compliance for the 11 and 24m cases. For the range of values considered, shear induced dilation is the dominant mechanism. It is evident that the smaller fracture length case needs far greater dilations to achieve the same permeability. The very large dilations needed to attain permeabilities of order 10^{-15} m^2 imply that it would be impossible to create viable HDR systems in such networks and that the study of the Rosemanowes system

can be limited to cases with either a larger fracture length or a major singular feature that carries the majority of the flow. It is impossible to discriminate between the different length distribution networks until the stimulation properties are considered, suggesting that borehole observations alone will not be able to assess the suitability of the natural fracture system for HDR development.

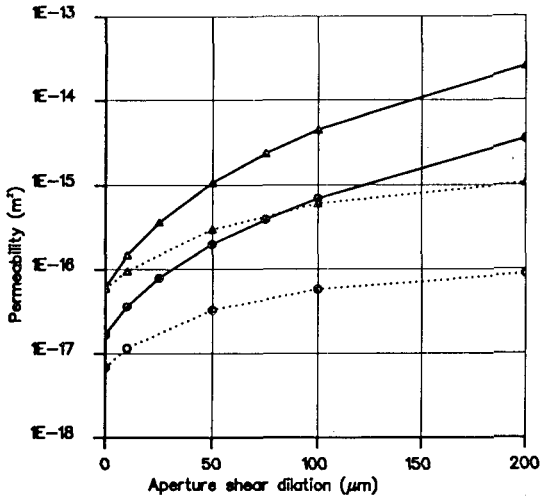

Figure 2 Change in maximum and minimum prinicipal permeability with shear induced dilation. Solid line shows 24m network, dotted line shows 11m network.

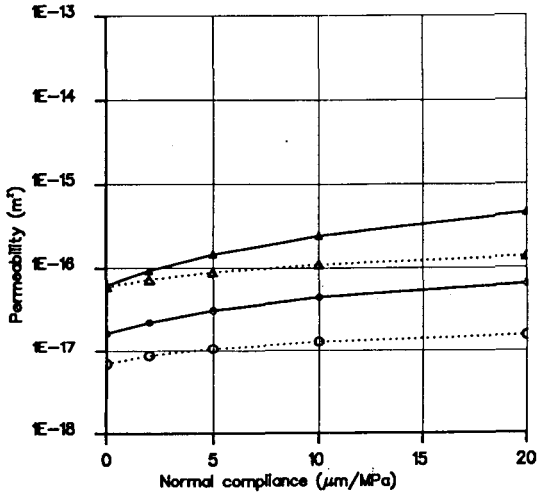

Figure 3 Change in maximum and minimum prinicipal permeability with normal compliance.

In the shearing mode only the set 1 fractures dilate. Similarly, in the normal mode the set 1 fractures are under lower normal stress and hence dilate more. The permeability tensors are therefore more anisotropic in the stimulated system than in the undisturbed fracture system. Typically, the NE-SW enhanced permeability is an order of magnitude lower than that in the vertical direction. The anisotropy in the enhanced permeability is in agreement with the overall shape of the microseismic cloud generated during stimulations. These events are believed to correspond to shear failures on the set 1 fractures.

Circulation performance

The permeability tensors calculated by NAPSAC for the largest fracture length network were used in porous medium models of the entire reservoir using the NAMMU computer code (Rae et al, 1982). Two models were developed: the first assumed a totally homogeneous reservoir bounded by undisturbed rock; the second included a high permeability vertical zone extending between the two wells. This vertical zone was located at the point where the RH12 and RH15 trajectories intersect in the plan view.

The effective permeabilities for the reservoir zones used in the NAMMU models were interpolated from the NAPSAC results and adjusted until the impedance and water loss matched that observed at Rosemanowes during the early low-flow (2-7 l/s) circulation. Table 2 shows the final values of the permeabilities for the two models. The reservoir permeabilities used within the models are between 100 and 1,000 times that of the undisturbed fracture system. Synthetic flow logs were calculated from the models. In both models flow occurs at too shallow a depth compared to the data from Rosemanowes. The logs for the high permeability zone model are ,however, a better match to the observed flow distribution.

The permeabilities derived from the porous medium models were then used to estimate the fracture dilations within the reservoir and to provide boundary conditions to a large NAPSAC model of the reservoir. Two NAPSAC simulations were performed for both the homogeneous and high permeability zone reservoir models. The NAPSAC results were in good agreement with the porous medium models. Preliminary estimates of tracer travel times and effective surface areas derived from the NAPSAC models matched experimental data.

Tracer and heat transport within the reservoir

An important advantage of models like NAPSAC is their direct representation of the fracture system geometry. This means that it is possible to make direct comparisons of predictions of tracer and heat transfer from NAPSAC with experimental data.

Tracer transport within NAPSAC is simulated by tracking large swarms of particles through the calculated flow field. In order to calculate travel times for such particles it is necessary to estimate the flowing porosity of the fractures. In natural fractures cored at approximately 350 m depth in the Stripa mine in Sweden, it was found that the tracer aperture was between two and seven times greater than the hydraulic aperture (Herbert and Lanyon, 1992). It is expected that this factor will be small for large open fractures and higher for more closed fractures. However, this factor is not known for Rosemanowes and was adjusted to get the best possible match to the observed tracer breakthrough.

TABLE 2 PERMEABILITIES AND FLOWS FROM POROUS MEDIA RESERVOIR MODELS

	Far-field (m^2)	Reservoir (m^2)	Inner zone (m^2)	RH12 flow (l/s)	RH15 flow (l/s)	Recovery
Observed				7.0	5.0	70%
Model 1	$5.0\ 10^{-17}$	$6.0\ 10^{-15}$	$6.0\ 10^{-15}$	7.1	5.0	72%
Model 2	$5.0\ 10^{-17}$	$2.4\ 10^{-15}$	$3.4\ 10^{-14}$	7.0	5.1	73%

It was necessary to implement a heat-transfer solution method within NAPSAC. It would be computationally intensive to solve the heat flow in the rock by discretisation of the blocks between the fractures. Instead, an approximate solution has been implemented based on that used by Cacas (Cacas and Bruel, 1990). Heat transfer is modelled using a one-dimensional finite difference scheme in a block of rock associated with each fracture. This scheme will work well where cooling is dominated by fluid flow in the fracture system rather than conduction within the rock. This method has been verified against analytical solutions for very simple geometries. Heat transport was not coupled to fluid or rock mass properties such as viscosity or thermal expansion/contraction.

As part of the testing of the tracer and heat transport facilities a parameter study was conducted to consider the performance of a single heat-exchanger module 150 x 150 m in plan and 250 m high. To simplify the calculations no wells were included and no account was made for the geothermal gradient. The rock within the model was assumed to be at a constant 80°C and fluid was injected at 20°C at the top surface with an overpressure of 5 MPa. It was also assumed that hydraulic aperture and tracer aperture were equal.

Six different configurations were considered for the fracture system within the block (see Table 3) and heat and tracer transport was modelled for each. The heat transport calculations were for a six-year circulation. The tracer simulations assumed a 1.4kg pulse injection of conservative tracer. A wide variety of thermal and tracer responses were predicted by the models. Only three realisations of each of the six configurations were analysed and so only a very approximate estimate of the variability within each configuration can be made. In all configurations the long-term thermal behaviour was dominated by variations in the mass flowrate.

The results from the study indicate that a well connected evenly stimulated volume is needed for good thermal performance. Part sealing of throughgoing high permeability features (zones or discrete features) provided some delay in thermal breakthrough but long-term performance was still compromised by the concentration of flow within the unsealed portion of the feature.

The thermal responses of the homogeneous heat-exchangers (models 1 and 2) were analysed in terms of the analytical model commonly used to estimate system lifetime (Armstead and Tester 1987). In all cases the effective heat-transfer area estimates represented only about 20% of the total area of hydraulically active fractures in the models. Since it has been estimated that only 10-15% of observed fractures will be hydraulically active, this suggests that only 2-3% of the observed fracture surface area can be used in analytic models of reservoir thermal performance.

In order to investigate the links between tracer and heat transport responses of a reservoir, cross-plots of thermal and tracer breakthrough volumes were produced. Figure 4 shows a plot of the produced volume at the time when production temperature drops by 1°C (T_1) against the volume produced when 5% of the tracer mass has been recovered (C_5) for all the models used in the study. There is a simple linear relationship between the breaktrhough volumes. The relationship would be complicated by the presence of a geothermal gradient. However, these results suggest that if fracture transport properties are known, the early time tracer response can be used to estimate system longevity.

The results of this study, combined with the results of the earlier NAPSAC models of the Phase 2B system, suggested that the Rosemanowes thermal and tracer responses could be modelled by considering only a very small volume of rock, little larger than those used in the study. The tracer and thermal curves for models 3 and 5 were similar in form to those from the Rosemanowes site.

TABLE 3 HEAT EXCHANGER STUDY CONFIGURATIONS

Model	Mean Fracture Length	Shear Induced Dilation	High permeability feature	Flowrate l/s
1	24m	100 μm	Absent	7.1 - 7.6
2	16m	110 μm	Absent	6.0 - 10.0
3	24m	80 μm	Vertical zone	7.0 - 7.6
4	24m	80 μm	Discrete vertical feature	4.9 - 8.7
5	Model 3 with zone extending to 50 m of base			6.0 - 7.1
6	Model 4 with feature extending to 50 m of base			5.9 - 6.0

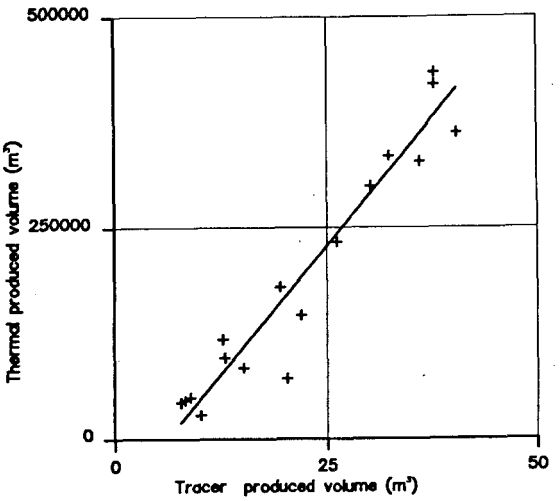

Figure 4 Thermal breakthrough volume versus tracer breakthrough volume.

The tracer responses were faster than those observed but this could be due to the discrepancy between tracer and hydraulic apertures and to increased dispersion due to the geometry ofthe injection and production wells.

Review of other data and models of the Phase 2B system suggested that the zone of high permeability extending from the bottom of RH12 does not link directly to RH15. This is similar to case 5 of the heat-exchanger study. Using the locations of microseismic data from the viscous stimulation of RH15 (test RT2B022) to delimit the zone, a NAPSAC model was created to test this hypothesis. Five realisations of approximately 7 l/s steady state flows were calculated. For all except one realisation a good match to the observed tracer was obtained by assuming a ratio of 1.5 between tracer and hydraulic apertures. This small value of the ratio is what might be expected for large planar high transmissivity fractures.

In order to compare the models with the experimental thermal drawdown from the Phase 2B system, thermal calculations were performed for one realisation at a mass flowrate equivalent to 14 l/s. The model and experimental tracer recoveries and drawdowns are shown in Figure 5.

Although a similar drawdown rate is observed, the model temperatures are approximately 10°C higher than the experiment. This can be partially explained by the approximations used to model thermal drawdown in the boreholes. This cannot, however, fully explain the discrepancy.Re-examination of temperature logs from the drilling of RH15 and the work-over of RH12 at the beginning of Phase 2B suggests that the zone below RH12 was already thermally depleted prior to the start of circulation. This was almost certainly due to the large volumes of fluid injected during Phase 2A.

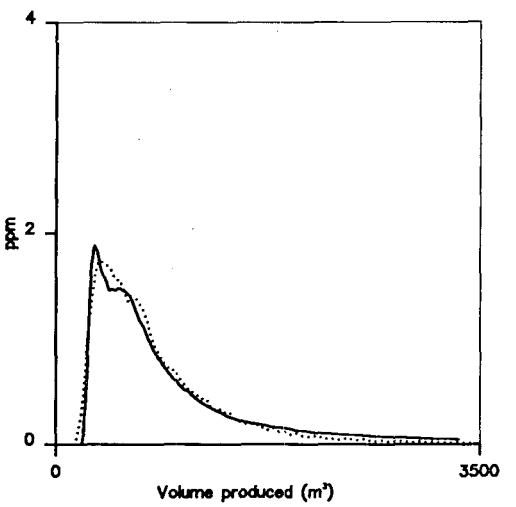

Figure 5a Comparison of experimental (solid line) and calculated tracer response.

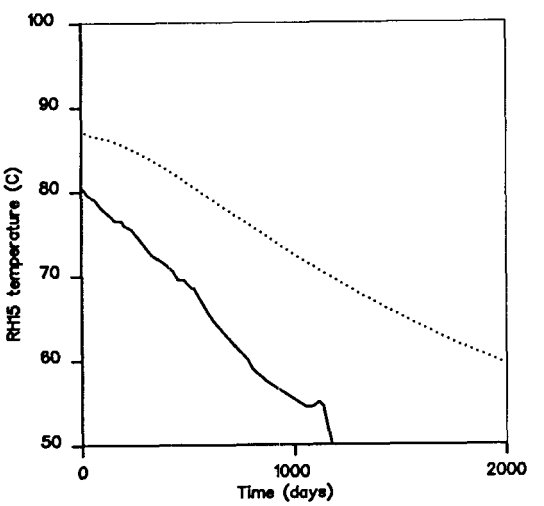

Figure 5b Comparison of experimental (solid line) and calculated thermal response.

Figure 6 shows a sequence of plots illustrating the growth of the thermally depleted zone away from RH12 towards RH15 as calculated by the model. Note that thermal breakthrough to RH15 occurs on a single flow entry, as was observed at Rosemanowes.

DISCUSSION

The work described in this paper represents a geologically realistic approach to the modelling of HDR reservoirs and reflects the progressive movement away from idealised penny-shaped fracture geometries towards systems dominated by natural fractures.

Various results from the model demonstrate possible causes of the difficulties encountered by the large scale field experiments, and are potentially highly significant for the development of HDR technology. These are summarised below.

a The hydraulic performance of the Phase 2B Rosemanowes reservoir was controlled by a very small volume of rock.

b The ability of engineers to create regions of enhanced permeability in a controlled manner away from the wellbores is limited by the geometry of the natural fracture system. In particular the stress regime at Rosemanowes leads to stimulated zones with highly anisotropic permeability.

c Large scale geological features in the undisturbed rock might be important at reservoir scales. The high permeability zone needed to fit tracer and heat-transfer results at Rosemanowes may be related to such a feature.

d Heat extraction calculations suggest that fracture systems similar to Rosemanowes may contain insufficient effective heat transfer area for current commercial designs.

e The models have shown that blocking off short circuits close to the production wells would be of limited benefit. In fact the models described here suggest that the Phase 2B system can be considered as a partially blocked short circuit.

The logical conclusion from these findings is that it is necessary to develop reservoir creation concepts which rely on less radical permeability enhancement. One approach would be to engineer reservoirs consisting of multiple cells, each of a similar size to the Rosemanowes reservoir (Green and Parker 1992). One risk attached to the development of such a large overall system would be that zones of differing levels of fracturing would be encountered, making stimulation difficult to control and potentially leading to a small number of very low impedance connections that might severely degrade overall thermal performance.

An alternative approach has been set out by Garnish et al (1992) and involves the study of naturally more permeable systems which require little or no stimulation, but which are able to support sufficient flow. Many naturally fractured geothermal systems are maintained over their lifetimes by reinjection, yet they exhibit little or no thermal drawdown, demonstrating that the flow is evenly distributed or that the systems are very large. Studies of the nature of these successful fractured reservoirs should be used to influence strategy for the creation of artificial (ie HDR) systems, and geologically realistic modelling has a crucial part to play in our understanding of such systems.

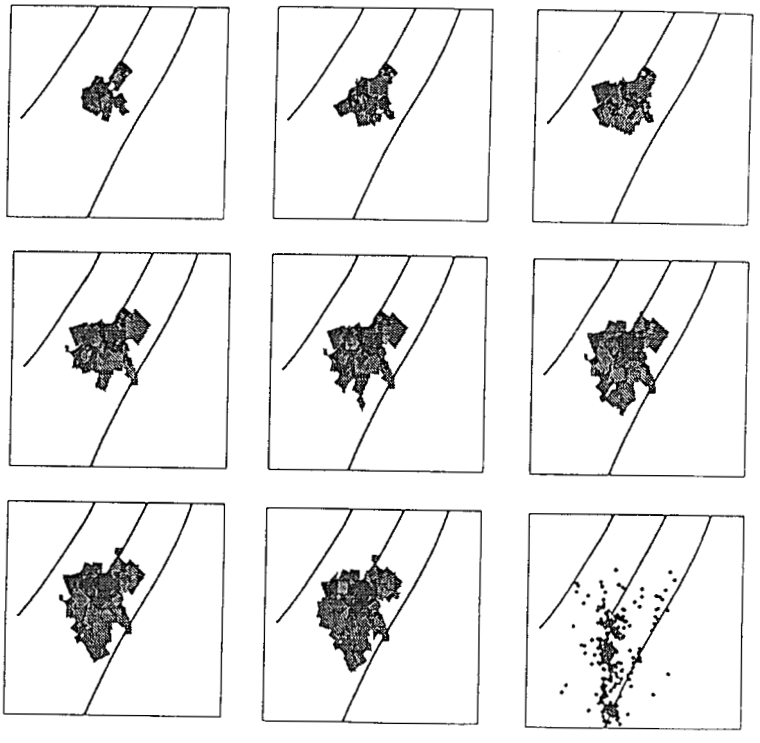

Figure 6 Growth of thermally depleted volume in model of Rosemanowes thermal drawdown. Views at half year intervals, with only fractures with surface drawdowns of 30°C or greater shown. Last view shows microseismic events from stimulation of RH15.

It is the distribution of effective heat-transfer surface area within the reservoir that determines the lifetime of HDR systems and in order to predict the performance of any design it is necessary to have models that adequately represent this. The network models that have been described in this report have resulted in a numerical model of the Rosemanowes system that integrates many of the field observations and has hydraulic, thermal and tracer properties that match the real system. Models of such systems need to be three-dimensional to incorporate the effects of stress and thermal gradients. Such models also need to be based on a geologically realistic fracture system, grid models will be dominated by the orientation of the grid system with regard to the regional stresses and will not be able to account for the large variation in fracture orientation and length found in nature. For these reasons it is important to apply the ideas and tools described in this report to other sites and other HDR concepts.

ACKNOWLEDGEMENTS

The study on which this paper was based was performed with the help of Roger Kingdon and Alan Herbert of AEA Technology and was funded and managed by the UK Department of Energy. The views expressed in this paper are those of the authors and do not necessarily reflect those of the Department of Energy.

REFERENCES

ARMSTEAD H C, TESTER J W (1987). Heat Mining, A new source of energy. E&F Spon Ltd, London and New York. 478 pp.

BATCHELOR A S (1976). The Development of Permeability Control Methods for the Exploitation of Geothermal Energy in South-West England. Proposal to UK DEn from Camborne School of Mines.

BATCHELOR A S (1977). Brief Summary of Some Geothermal Related Studies in the United Kingdom. Contribution to 2nd NATO/CCMS Geothermal Conference Los Alamos, USA 1977.

BROOKS M, DOODY J, AL-RAWI F R J (1984). Major crustal reflectors beneath South-West England. Journal of Geological Society. Vol 141, pp 97-103.

CACAS M C, BRUEL D (1989). 3-Dimensional Stochastic Fracture Network Model. Proceedings of Hot Dry Rock: Camborne School of Mines International Conference 1989.

HERBERT A W, LANYON G W (1992). Modelling tracer transport in fractured rock at Stripa. Stripa Project Technical Report 92-01.

GALE J E, SCHAEFER R A, CARPENTER A B, HERBERT A W (1991). Collection, analysis and integration of discrete fracture data from the Monterey formation for fractured reservoir simulations. Proceedings of the 66th Annual Technical Conference and Exhibition of the SPE.

GARNISH J, BATCHELOR A S, LEDINGHAM P (1992). Hot Dry Rock: Fringe technology or key component? Transactions of the Geothermal Resources Council 1992 Annual Meeting, San Diego, USA.

GHOSH P K (1934). The Carnmenellis granite: its petrology, metamorphism and tectonics. Quarterly Journal of the Geological Society of London. Vol 90 pp 240-276.

GRINDROD P, HERBERT A W, ROBERTS D L, ROBINSON P C (1992). NAPSAC Technical Document. AEA D&R report 0270.

GREEN A and PARKER R J (1992). A multi-cell design of a HDR reservoir. Transactions of the Geothermal Resources Council 1992 Annual Meeting, San Diego, USA.

HODGKINSON D P (1984). Analysis of steady state hydraulic tests in fractured rock. AERE report AERE-R-11287.

MAGES (1979). Man-made geothermal energy systems. InterMAGES 1979. Man-made geothermal energy systems. International Energy Agency. OECD Paris, (two volumes) unpublished.

PARSONS C A (1904). President's address to the engineering section. British Association for the Advancement of Science. Transactions of section G, BAAS report for 1904, pp 667-676.

PARKER R H (editor) (1989). Hot dry rock geothermal energy. Phase 2B final report of the Camborne School of Mines Project. Pergamon Press.

PINE R J, CUNDALL P A (1985). Applications of the fluid rock interaction program (FRIP) to the modelling of hot dry rock geothermal energy systems. Proceedings of the International Symposium on Fundamentals of Rock Joints. Bjorkliden, Sweden, pp 293-302.

PINE R J, KWAKWA K A (1988). Experience with hydrofracture stress measurement to depths of 2.6 km and implications for measurements to 6 km in the Carnmenellis granite. Presented at 2nd International Workshop on Hydraulic Fracturing Measurements, Minneapolis USE, June 16-18 1988.

RAE J, ROBINSON P C, WICKENS L M (1982). Coupled heat and groundwater flow in porous rock. Harwell Theoretical Physics Division Report TP-944.

PROCEEDINGS, Eighteenth Workshop on Geothermal Reservoir Engineering
Stanford University, Stanford, California, January 26-28, 1993
SGP-TR-145

THERMAL DRAWDOWN ANALYSIS OF THE HIJIORI HDR 90-DAY CIRCULATION TEST

Paul Kruger
Stanford Geothermal Program
Stanford University
Stanford CA USA

Tsutomu Yamaguchi
Geothermal Energy Technology Department
NEDO
Tokyo, Japan

ABSTRACT

The Hijiori 90-day circulation test is unique in the development of HDR technology in that it was the first (and thus far the only) multi-production well test run for a sufficient production period to obtain observed cooldown curves at multiple production horizons in the stimulated reservoir volume. The experimental data have been analyzed by the SGP 1-D linear heat sweep model to examine the extent of thermal cooldown in this relatively small, multi-well, multi-zone reservoir. Although changes in production flow were carried out in specific wells at specific times during the 90 days of circulation, matching of the observed cooldown curves in conjunction with the structural and temperature logging data allows estimation of the reservoir volume and the mean fracture spacing between rock blocks for heat extraction during the 90-day test.

INTRODUCTION

In 1991, a 90-day circulation test was conducted at the Hijiori geothermal site in Japan (Yamaguchi, 1992) as part of the New Energy and Industrial Technology Development Organization (NEDO) program for the development of HDR technology. It was the first multi-well, multi-production zone circulation test in a HDR reservoir during which extensive diagnostic data were accumulated. In addition, from frequent downhole logging, production fluid temperature histories were measured at the respective feed zones of each production well. These data provide a unique opportunity to examine thermal drawdown in a fractured HDR reservoir under sustained production. They also allow study of two major problems existing in assessing economic feasibility of long-term thermal energy extraction from deposits of high-temperature rock formations, namely: (1) the size of the reservoir available for heat transfer (the total extractable heat content), and (2) the mean size of the rock blocks in the formation which are in contact with circulating fluid (the heat transfer capacity for a given production flowrate).

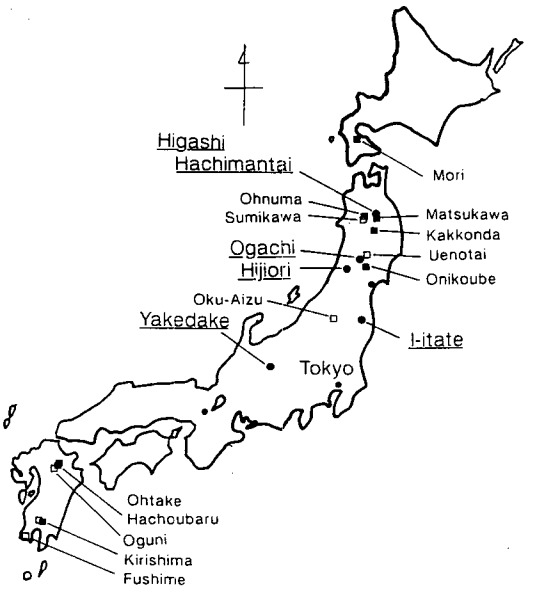

Fig. 1. Location of the Hijiori HDR test site in northern Honshu.

The Hijiori test is the second of two existing HDR circulation tests which provide data for matching an observed cooldown history with simulated cooldown based on models of reservoir geometry and production flow. The first example of thermal drawdown matching in a sustained HDR circulation test was reported by Kruger (1990) for the shallow (2-km) Rosemanowes experimental HDR reservoir in Cornwall, England. The 3-year continuous production history and observed fluid temperature cooldown were provided by Nicol (1989). An estimate of the reservoir volume, made from tracer tests (Nicol and Robinson, 1990) and an ellipsoid envelope around the swarm of microseismic locations observed during the hydraulic stimulation of the reservoir (Parker, 1989) indicated a reservoir volume of about 5×10^6 m^3. The observed cooldown could not be matched for that volume for any value of rock block mean fracture spacing. A match was obtained for the set of reservoir volume of 3.25×10^6 m^3 and a mean fracture spacing of 50 m. The model was extended to a proposed deeper (6-km) reservoir in the same formation (Kruger, Hicks, and Willis-Richards, 1992) to evaluate the energy extraction capability for a commercial-size system.

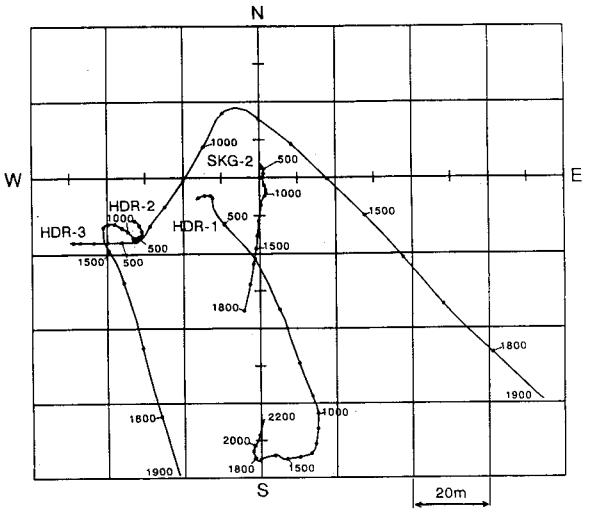

Fig. 2. Plan view of the 4-well system at the Hijiori HDR test site.

Analysis of the observed thermal drawdown for the shallow Rosemanowes reservoir was much simpler than for the Hijiori reservoir in that the experiment was run at constant production rate as a two-well doublet system (one injection well - one production well) over a long period of time (3 years). In contrast, the Hijiori experiment was run as a four-well system (one injection well - three production wells) at constant injection rate over a short period of time (90 days), but with an early brief excursion in flowrate to test enhanced stimulation and occasional shutin of two of the wells to test the third well. However, with the detailed data acquired by the Hijiori staff over the lifetime of the system, analysis of the observed cooldowns at the main feed zones in the three production wells reveals much insight on the volume and mean fracture spacing distributions in the reservoir.

THE HIJIORI 90-DAY CIRCULATION TEST

The Hijiori geothermal site is located in northern Honshu as noted in Figure 1. It has been a site for development of HDR technology since 1985 (Yamaguchi, 1992). In 1986, hydraulic fracturing studies were initiated in well SKG-2. Two wells, HDR-1 and HDR-2 were subsequently drilled, each with short (2 weeks to 1 month) circulation tests to characterize the results of the stimulation. In 1991, following creation of well HDR-3, a 3-month circulation test was carried out to test the reservoir.

A plan view of the Hijiori HDR test site is shown in Figure 2. The horizontal distances from the bottom hole of injection well SKG-2 to the main production zones of the three wells were 41 m for HDR-1, 38 m for HDR-2, and 80 m for HDR-3. A general synopsis of the 90-day test is given in Table 1. The test was run from August 6 through November 3. The injection flowrate was kept

Table 1
Parameters of the Hijiori 90-Day Test*

Parameter	Value
Production Wells	HDR-1,2,3
Injection Well	SKG-2
Injection Flowrate	16.7 kg/s
Injection Pressure	3 MPa
Injection Temperature	55 °C
Production Temperature	160-190 °C
Pumping Duration	90 days
Fluid Recovery	77 %
Thermal Output	8 MW

*from Yamaguchi (1992).

essentially constant at 1 ton/min (16.7 kg/s) except for two early excursions for enhanced stimulation. Following the first 23 days of circulation, single well production tests were conducted for about 5 days each, in order. The result of the two 5-day shutins of each well was a perturbation in the constant-flowrate cooldown curves for the production wells. During the test, frequent (weekly) logs were run downhole to measure pressure, temperature, and flowrate (PTS) in each production well (Miyairi, et al, 1992).

A schematic view of the wellbore geometry at depths 1500-1900 m is shown in Figure 3. It was noted (NEDO, 1992) that each of the three production wells had multiple feed zones. From the frequent PTS downhole surveys, the depth and interval of each feed zone was estimated for each production well. Figure 4 shows the multiple feed zones inferred from the data and confirmed after the test with a borehole televiewer. For each well a feed fraction was defined as the ratio of production flowrate to the total flowrate for that well. A summary of the production flow distribution is given in Table 2.

The results of the 90-day test were reported by Yamaguchi (1992) and Yamaguchi, et al, (1992). The history of injected fluid recovery showed the effects of the two stimulation efforts at the early part of the 90-day test. Initial recoveries were less than 60 % and following the two stimulations, water recovery increased to nearly 80 %. The mean value of water loss over the test period was 23.1 %. Figure 5 shows the observed fluid temperature history at the main production interval at depths about 1750-1780 m. The fluid temperature of well HDR-1, with the smallest flowrate, reached a surface temperature of 190 °C and was still increasing at the end of the test. In contrast, wells HDR-2 and HDR-3, with larger fractional flowrates, exhibited measurable cooldown with decline to temperatures of 145 °C and 165 °C, respectively, at the end of the test.

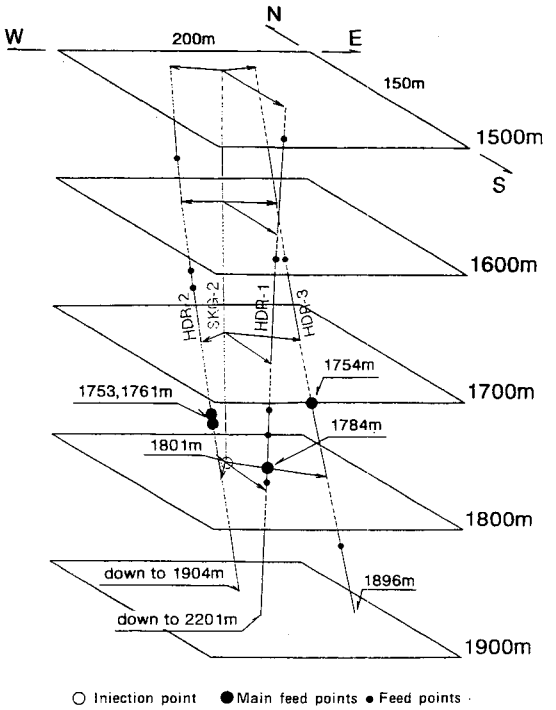

Fig. 3. Schematic view of injection well SKG-2 and production wells HDR-1, 2, and 3 for the 90-day circulation test.

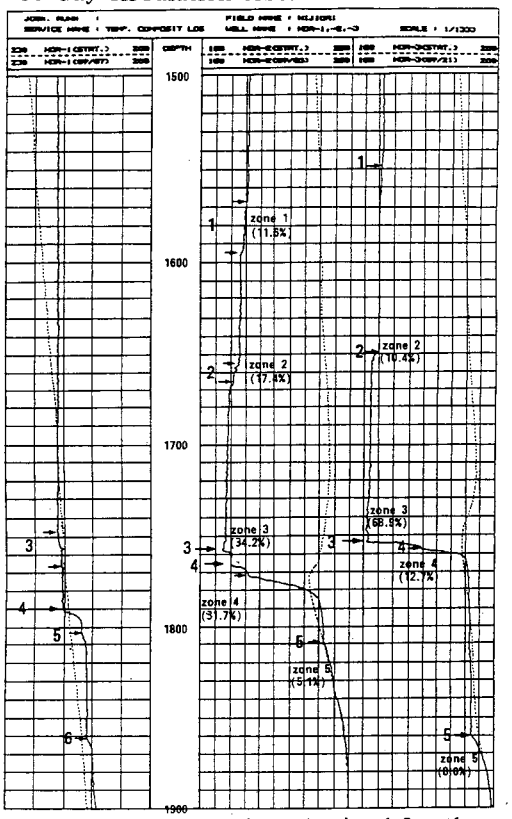

Fig. 4. Temperature profiles obtained for the three production wells showing the indicated zonal thicknesses for the feed zones relative to the injection depth at 1801 m (from Miyairi, et al, 1992).

Table 2
Production Flow Distribution*

Well	Designated Main Feed Zone (m)	Production Interval (m)	Feed Fraction (%)
HDR-1	1790	1530	15
		1628-1767	30
		1790-1803	55
		1860	
HDR-2	1753-1775	1564-1594	11.6
		1654-1668	17.4
		1753-1759	34.2
		1766-1775	31.7
		1810	5.1
HDR-3	1754	1550	0.0
		1649	10.4
		1754	68.9
		1759	12.7
		1861	8.0

*from Yamaguchi, et al (1992).

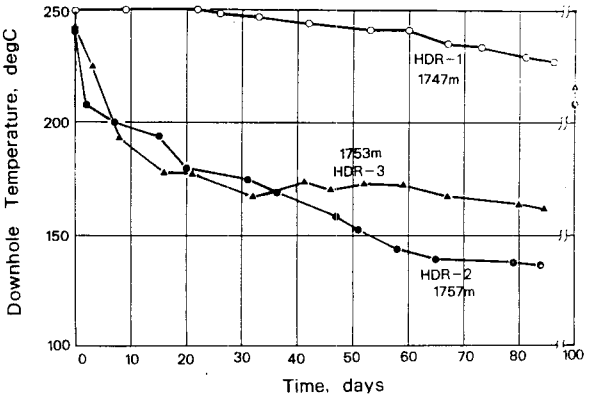

Fig. 5. Fluid temperature histories for the main production zone at depths about 1750-1780 m calculated from downhole logs.

THE SGP 1-D HEAT-SWEEP MODEL

The SGP 1-D Heat Sweep Model was developed experimentally by Hunsbedt, et al (1978) to simulate heat extraction in fractured reservoirs with fluid reinjection or circulation. The model is based on heat transfer properties of regular-shaped rock blocks surrounded by circulating heat-carrier fluid. Kuo, et al (1977) showed from experimental measurements that heat transfer properties of irregular-shaped rock blocks can be successfully approximated as spherical-shaped rocks of equivalent radius for which the heat transfer equations can be solved analytically (Carslaw and Jaeger, 1973). Iregui (in Hunsbedt, et al, 1979) showed that a distribution of varying size and shape rock blocks could be effectively modeled for heat transfer by a single mean size spherical rock with mean equivalent radius.

The governing equations describing heat transfer from the equivalent spherical rock blocks to the circulating fluid under linear heat sweep are given in Hunsbedt, et al (1983). The solution for prescribed linear sweep boundaries and initial conditions is obtained by conversion to Laplace transform equations with numerical inversion by the Stehfest (1970) algorithm. Two major model parameters are the effective reservoir volume and the mean fracture spacing.

For the Hijiori flow regime, with injected fluid partitioned between water loss, three production wells, and multiple feed zones in each well, one-dimensional heat sweep was difficult to define. In prior applications of the model to two-well systems, 1-D linear flow geometry was developed for rectangular, radial, and doublet flows.

To model the heat sweep in the Hijiori experiment from one injection well to three production wells with multiple feed zones and significant water loss, a conceptual model was adopted in which the injection flow was divided into a set of independent flows for each production well and each feed zone. Figure 6a shows the model of the Hijiori zonal flow distribution including water loss and radial flow to the production wells proportional to the flow recovery measured for each zonal thickness. Figure 6b shows the simplified zonal sector flow geometry for the 1-D radial flow heat sweep model.

Table 3 lists the resulting calculated zonal sector flowrates, Q(i,j), where i is the production well number and j is the feed zone number, adjusted for constant water loss of 23.1 %. Testing of the conceptual model was made for the observed cooldowns given in Figure 5. The set of input data for these cases is given in Table 4. Constants in the data set for the zonal sector simulations included injection temperature, porosity, well diameter, and thermal properties of the sector rock blocks.

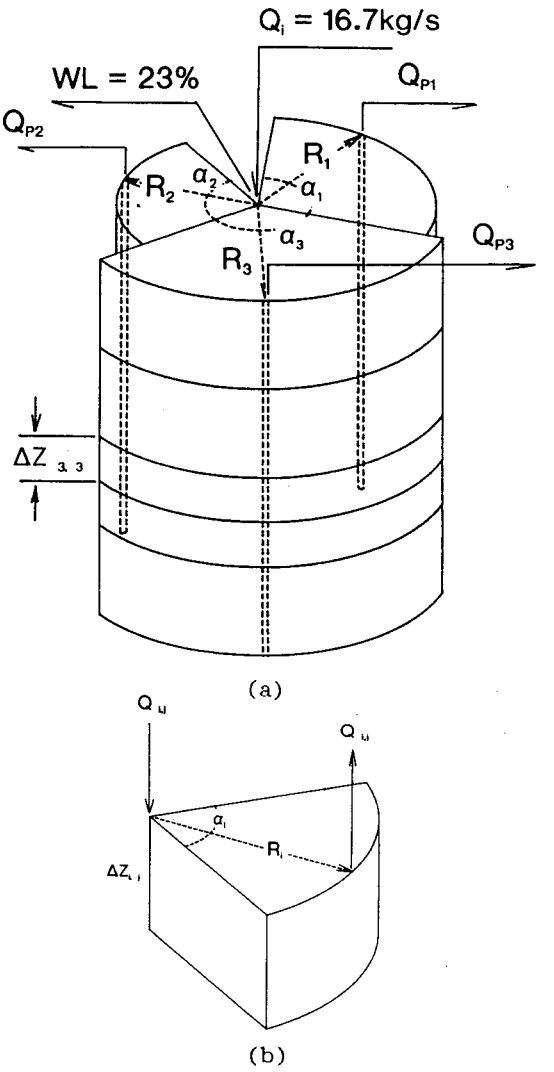

Fig. 6. (a) Conceptual model of the Hijiori zonal flow distribution; (b) radial flow model for each individual zonal sector.

Table 3
Sector Sweep Flowrates
Injection Flowrate = 16.7 kg/s
Production Flowrates

WL = 0.231 Q(i,j) kg/s
j = zonal fraction i = well fraction

zone	for HDR well:			1	2	3
j	1	2	3	0.138	0.299	0.332
1	0.15	0.116	--	0.346	0.578	0
2	w/3	0.174	0.104	--	0.867	0.576
3	0.30	0.342	0.689	0.691	1.71	3.81
4	0.55	0.317	0.127	1.27	1.58	0.703
5	w/4	0.051	0.080	--	0.254	0.443

Table 4
Input Data for the Simulations
Heat Sweep Zonal Data

Constants:
T_r = 55 °C R_i = 0.01 m
porosity = 0.01 Thermal Data

Main Zone Data:

	HDR-2,Z3	HDR-3,Z3	HDR-1,Z4
Temp (init) °C	240.6	240.6	252
Q(i,j) kg/s	1.71	3.81	1.27
Thickness m	5	5	13
Radius m	38	80	41
Flow Angle (°)	140	155	65

Several characteristics of the zonal sectors can be estimated from the data in Table 4: the rock block volume, $V=(\alpha/360)\pi ZR^2$; the maximum MFS as a cubic block with no intrinsic permeability, $MFS=V^{1/3}$; the equivalent radius as a sphere for heat transfer with equal surface to volume ratio, $R_{eq}=(3V/4\pi)^{1/3}$; and the initial heat content above a given abandonment temperature, $HC=\rho VC_v(T_i-T_a)$. Table 5 lists these characteristics for the three test zonal sectors for an abandonment temperature of 150 °C.

Table 5
Calculated Zonal Sector Characteristics

	HDR-2,Z3	HDR-3,Z3	HDR-1,Z4
Volume ($10^3 m^3$)	8.82	43.3	12.4
MFS(cubic) (m)	20.7	35.1	23.1
R_{eq}(sphere)(m)	12.8	21.8	14.4
HC (10^{12} J)	2.16	10.6	3.41

SIMULATIONS

The first case examined was the third zone of well HDR-2, where the accumulated data seemed to offer the most definitive input data for sector flow at the feed level of 1754 m. Figure 7 shows the simulation results for the data given in Table 4. Although the observed cooldown curve shows the excursion in bottom-hole temperature due to the two one-week shutins of the well after day 23, two trends are clear: (1) the initial cooldown proceeds with MFS consistent with the dimensions estimated in Table 5; and (2) all of the family of MFS cooldown curves show an area for heat extraction less than the heat extraction indicated by the observed cooldown curve. For the given thermal properties, it is evident that the estimated volume of zonal sector HDR-2,Z3 is too small. Figures 8a and 8b show the effect of doubling the volume, Z changed to 2Z, and quadrupling the volume, R changed to 2R. In the first case, the initial cooldown follows a MFS of 20 m, but the total heat extracted is still too small; in the second case, the initial cooldown follows a MFS greater than 25 m, but the full curve shows a better fit. The excursion in temperature over the critical early period makes it difficult to distinguish between these two alternate cases. The sector volume probably falls between these two values, with some degree of doublet flow accounting for a greater sector radius that the direct linear distance between the two wells.

Figure 9 shows the results for zonal sector HDR-3,Z3 for the data given in Table 4. Here again the observed cooldown follows an initial cooldown simulated by MFS of about 20 m, but the

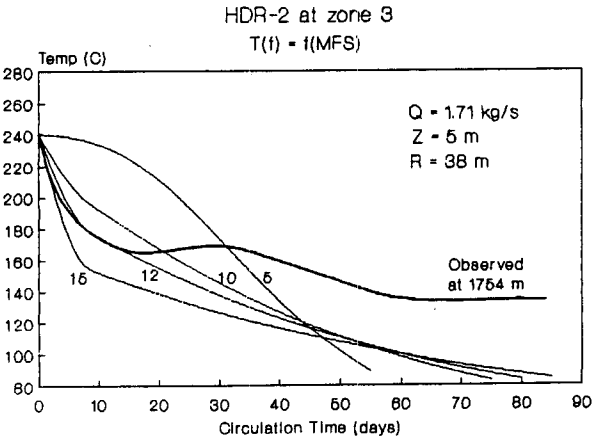

Fig. 7. Simulated cooldown curves of bottom-hole fluid temperature as a function of mean fracture spacing for zonal sector HDR-2,Z3 for the initial estimated dimensions.

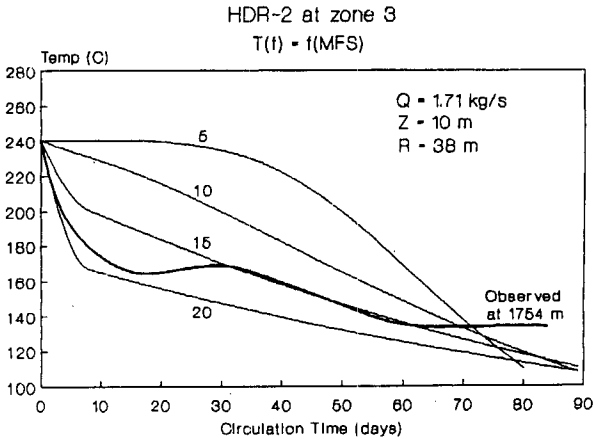

(a)

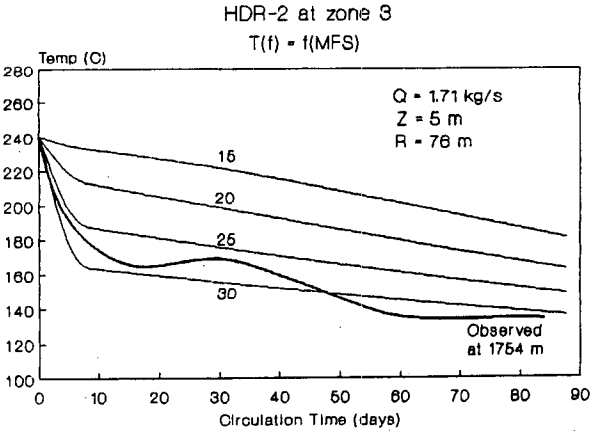

(b)

Fig. 8. Simulated cooldown curves for HDR-2,Z3 with (a) twice the zonal thickness (2Vo) and (b) twice the zonal radius (4Vo).

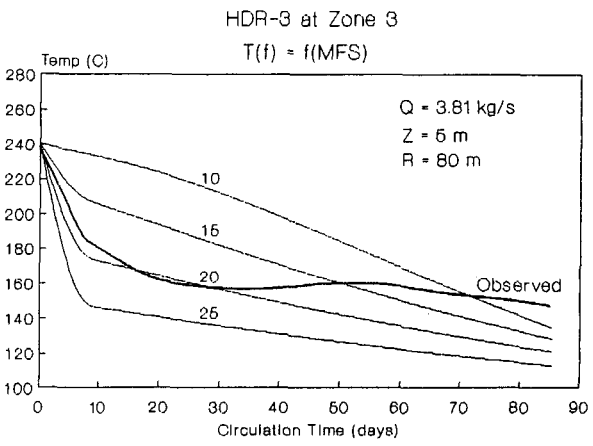

Fig. 9. Simulated cooldown curves of bottom-hole fluid temperature as a function of mean fracture spacing for zonal sector HDR-3,Z3 for the initial estimated dimensions.

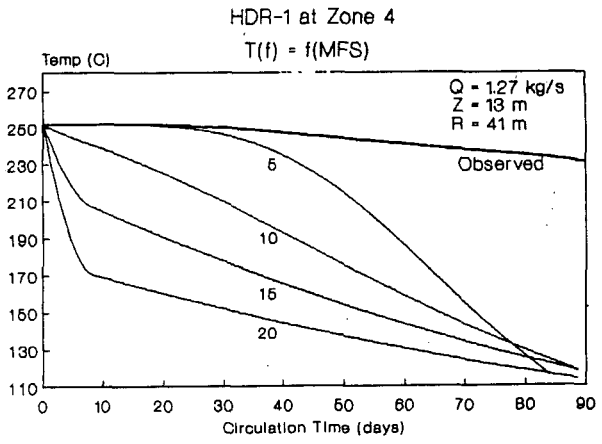

Fig.10. Simulated cooldown curves of bottom-hole fluid temperature as a function of mean fracture spacing for zonal sector HDR-1,Z4 for the initial estimated dimensions.

longer-period temperature excursion on ten days of well shutin prevents greater definition of the unperturbed cooldown. However, here again, the trend does indicates a zonal sector volume greater than that initially estimated.

The observed cooldown for zonal sector HDR-1,Z4 in Figure 5 indicates a more classical S-shaped cooldown curve (or a very long perturbation period on shutin) and greater effort to match it is underway. Figure 10 shows the simulations for the data set in Table 4. The observed cooldown follows a small MFS, but the heat extraction area is much larger than the simulated curves for all MFS. Figure 11 shows the results of the analysis to match both the volume of the zonal sector and its mean fracture spacing with the constraint of maintaining a constant aspect ratio (0.3171) of thickness, Z = 13 m, to radius, R = 41 m. The figure shows the progression of simulated cooldowns for varying MFS with increased volume, from 2Vo to 5Vo, where Vo = 12,400 m^3 (Table 5). It is clear, even for the short 90-day test, that for volume 2Vo, the observed cooldown will have an area greater than the curves for all MFS and that for 5Vo, the observed cooldown will fall below the curves for maximum MFS. Even with the excursion in temperature during the shutin periods, the best fit appears to be for a volume between 3Vo and 4Vo with MFS between 13 and 17 m. The corresponding dimensions of the zonal sector would be a thickness of 19-21 m and a mean flow radius of 59-65 m, The larger flow radius is consistent with the larger radius apparent for zonal sectors HDR-2,Z3 and HDR-3,Z3, where the major part of the injected flow was recovered.

DISCUSSION

The thermal analysis of the 90-day Hijiori test points out several interesting aspects with respect to the extent of heat extraction from the reservoir. First, it is apparent that the test itself can hardly be called a long-term flow test; it is essentially a time-connected string of experiments with several, conflicting objectives: to stimulate fracture growth with flow surges, to evaluate behavior of individual wells on shutin of the other wells, and to test heat extraction from the reservoir. Second, following the early experiments, the test was not run sufficiently long at constant flowrate to overcome the shutin perturbations and establish cooldown trends. In spite of these perturbations, the detailed downhole observations were sufficient to narrow the range of the two key parameters of a HDR reservoir for heat extraction, the volume of rock and MFS accounting for the observed cooldown.

Table 6 shows the extent to which the heat-sweep simulations with the available thermal drawdown data can indicate the range of reservoir heat content and heat extraction parameters. The estimates of reservoir rock block volume and mean fracture spacing were obtained for a constant aspect ratio of zonal sector thickness to radius as estimated from pressure, temperature, spinner logs. Other dimensions for the same volume could have been used. The heat extracted was calculated from

$$HE = \int_{t_o}^{t_a} Q(t)\,\Delta h(T_r - T_i, t)\,dt$$

where $\Delta h(T_r - T_i)$ is the increase in enthalpy of the produced fluid above the enthalpy of the injected

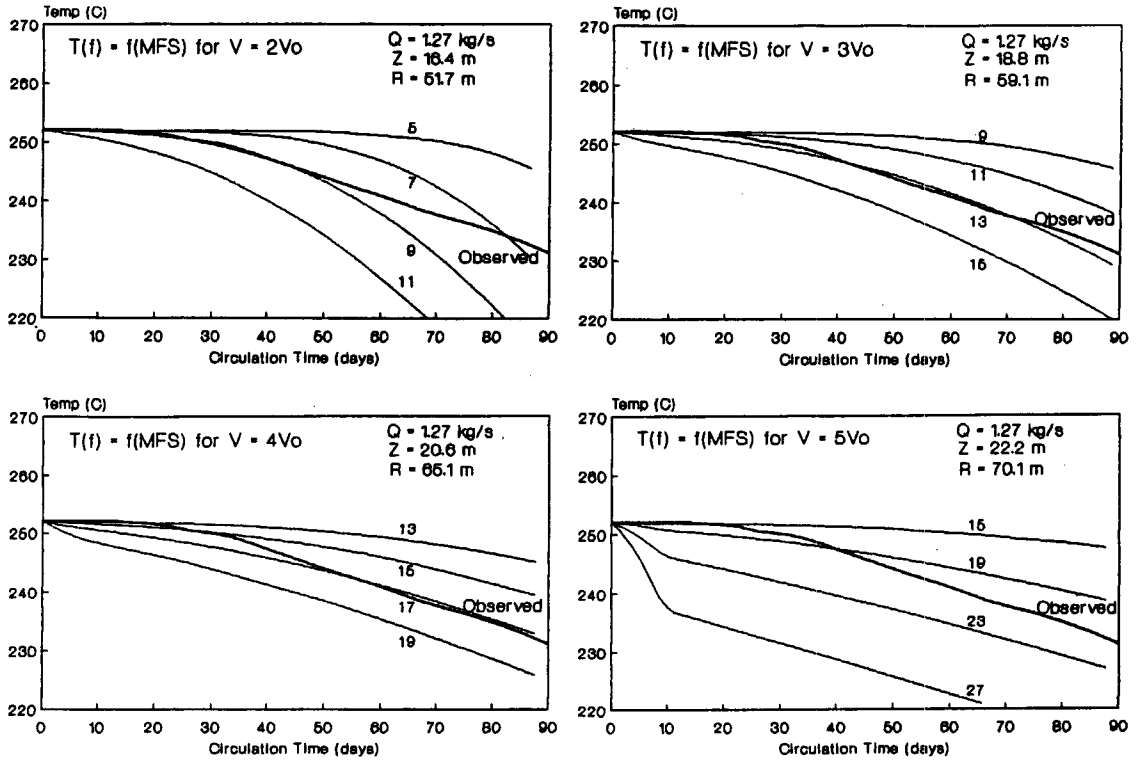

Fig.11. Simulated cooldown curves for HDR-1,Z4 for the progression of zonal sector volume from 2Vo to 5Vo.

Table 6
Simulation Results

Zonal Sector	Sector Dimensions Z (m)	R (m)	V ($10^3 m^3$)	Mean Fr.Sp (m)	Heat Content (10^{12}J)	Heat Extracted (10^{12}J)	Fraction Produced (%)
HDR-2,Z3	5+	38+	>9	15-30	>2.16	5.75	266
HDR-3,Z3	5+	80+	>40	15-20	>10.6	13.7	129
HDR-1,Z4	19-21	59-65	36-50	13-17	>3.41	8.05	236
			for 3.5Vo		11.9		67

fluid. For $T_a >> T_i$, the heat extracted can be approximated from mean parameters as

$$HE = \bar{Q}\,\Delta\bar{h}\,\Delta t$$

The fraction produced is the ratio HE/HC.

The fractions produced for the three well sectors, shown in Table 6, were based on initial estimated dimensions of the sectors. They range from 129 to 266 %, again indicating that the actual sector size (and heat content) is much larger. For example, for sector HDR-1,Z4, with sector dimensions of 20 m thickness and 62 m radius (3.5Vo), the heat content would be 11.9 x 10^{12} J and the fraction produced at T_a = 150 °C would be 67 %. The 1-D heat sweep simulation for these dimensions gives a fraction produced of 77 %. Considering the large uncertainty in the cooldown data, these values are in good agreement. For these dimensions of sector HDR-1,Z4, the simulation estimates a lifetime to the abandonment temperature of 150 °C of 0.67 years.

One further uncertainty is noted which affects the definition of observed cooldowns noted for the zonal flows. The observed temperature of the downhole fluid in HDR-3,Z3, for example, is the temperature of the mixed fluid from zones, 5, 4, and 3 as it passes the PTS log. Thus, the temperature shown for HDR-3,Z3 is actually an estimate calculated from the logging data. This is

also true for HDR-2.Z3. However, for HDR-1, where spinner logging was not possible because of the well casing, the data shown are the actual measured temperature of the produced fluid at zone 4. In view of the compounding problem of the temperature excursions during the shutins, the extent of uncertainty of the observed cooldown curves due to mixed production fluid are difficult to estimate.

CONCLUSIONS

Several conclusions can be inferred from the thermal analysis of the Hijiori 90-day flow test, primary among them is the apparent need to run flow tests for both sufficient time and at constant flowrate to establish a clearly defined cooldown history. The thermal analysis indicates that the feed zones deduced from the PTS logs are representative of the rock-block dimensions for heat extraction and that the observed cooldown curves can be approximately modeled with mean fracture spacing for equivalent cubic or spherical dimensions. Another primary conclusion is the that in spite of the many problems associated with the data as a 'long-term' flow test, it is possible to estimate the approximate size of the Hijiori reservoir as it was constituted during the 90-day test period. If it is assumed that the approximate fraction recovered for sector HDR-1,Z4 is representative of the whole reservoir, then the total heat extracted would be $Q_p/Q_s \times HE_s$, where the total production flowrate, $Q_p = Q_i (1-WL) = 12.8$ kg/s. The total heat extracted would be $(12.8/1.27) \times 11.9\times10^{12}$ J = 1.2×10^{14} J. For a recovery fraction of 0.67 (Table 6), the available heat content of the reservoir above the abandonment temperature of 150 °C would be 1.8×10^{14} J and the volume of the reservoir would be 6.6×10^{5} m^3.

The uncertainty in reservoir size and available heat content caused by the water loss of 23 % remains. If "available", the reservoir volume would be 8.7×10^{5} m^3 and the heat content would be 2.3×10^{14} J. Whether this difference in available heat is actually 'lost' or 'stored' needs to be determined.

For the multi-purpose test at Hijiori, the zonal sector model does permit at least a cursory evaluation of the sector rock-block dimensions, the extractable heat content for a given application abandonment temperature, and an idea of the lifetime expectancy for a given circulation flowrate. These data should be of great value in planning the next (deeper) phase of the Hijiori test facility in the near future.

REFERENCES

Carslaw, H.S. and J.C. Jaeger, "Conduction of Heat in Solids", 2nd Edi., (Oxford University Press, Glasgow, 1973).

Hunsbedt, A., P. Kruger, and A.L. London, "Energy Extraction from a Laboratory Model Fractured Geothermal Reservoir", J.Petr.Tech. 30, 712-718 (1978).

Hunsbedt, A., R. Iregui, P. Kruger, and A.L. London, "Energy Recovery from Fracture-Stimulated Geothermal Reservoirs", Proc. ASME/AIChE Heat Transfer Conference, Paper 79-HT-92, 1979.

Hunsbedt, A., S. Lam, and P. Kruger, "User's Manual for the 1-D Linear Heat Sweep Model", Stanford Geothermal Program Technical Report SGP-TR-75, 1983.

Kruger, P., "Heat Extraction from Microseismic Estimated Geothermal Reservoir Volume", Trans.Geoth.Res.Council 14, 1225-1232 (1990).

Kruger, P., T. Hicks, and J. Willis-Richards, "The Potential for Thermal Energy Extraction from Cornish Granite", Trans.Geoth.Res. Council 16, 465-472 (1992).

Kuo, M.C.T., P. Kruger, and W.E. Brigham, "Shape-Factor Correlations for Transient Heat Conduction from Irregular-Shaped Rock Fragments to Surrounding Fluid", Proc. AIChE-ASME Heat Transfer Conference, Paper 77-HT-54, 1977.

Miyairi, M., M.Sorimachi, and Y.Ohsaki, "Quantitative Analysis of Multi-feed Zones with PTS Combination Log", Proceedings, 1992 Symposium, Geothermal Research Society of Japan, 1992.

NEDO, "FY 1991 Summary of Hot Dry Rock Geothermal Power Project in Japan", 1992 (in preparation).

Nicol, D.A.C., private communication, 1989.

Nicol, D.A.C. and B.A. Robinson, "Modelling the Heat Extraction From the Rosemanowes HDR Resevoir", Geothermics 19, 247-257 (1990).

Parker, P., "Hot Dry Rock Geothermal Energy Research at the Camborne School of Mines", Geoth.Res.Council Bull. 18, 3-7 (1989).

Stehfest, H., "Numerical Inversion of Laplace Transforms", Algorithm No. 368, Comm.ACM 13, No.1, 47-49 (1970).

Yamaguchi, T., "Recent Developments in Japan's HDR Program", Proceedings, 10th DOE Geothermal Review, San Francisco, CA, 24 March 1992.

Yamaguchi, T., N. Hiwaki, A. Tsuyoshi, and Y. Oikawa, "90-Day Circulation Test at Hijiori HDR Test Site", Trans.Geoth.Res. Council 16, 417-422 (1992).

PROCEEDINGS, Eighteenth Workshop on Geothermal Reservoir Engineering
Stanford University, Stanford, California, January 26-28, 1993
SGP-TR-145

FRACTAL CHARACTERIZATION OF SUBSURFACE FRACTURE NETWORK FOR GEOTHERMAL ENERGY EXTRACTION SYSTEM

K. Watanabe and H. Takahashi

Research Institute for Fracture Technology
Faculty of Engineering, Tohoku University, Sendai 980, Japan

ABSTRACT

As a new modeling procedure of geothermal energy extraction systems, the authors present two dimensional and three dimensional modeling techniques of subsurface fracture network, based on fractal geometry. Fluid flow in fractured rock occurs primarily through a connected network of discrete fractures. The fracture network approach, therefore, seeks to model fluid flow and heat transfer through such rocks directly. Recent geophysical investigations have revealed that subsurface fracture networks can be described by "fractal geometry". In this paper, a modeling procedure of subsurface fracture network is proposed based on fractal geometry. Models of fracture networks are generated by distributing fractures randomly, following the fractal relation between fracture length r and the number of fractures N expressed with fractal dimension D as $N = C \cdot r^{-D}$, where C is a constant to signify the fracture density of the rock mass. This procedure makes it possible to characterize geothermal reservoirs by the parameters measured from field data, such as core sampling. In this characterization, the fractal dimension D and the fracture density parameter C of a geothermal reservoir are used as parameters to model the subsurface fracture network. Using this model, the transmissivities between boreholes are also obtained as a function of the fracture density parameter C, and a parameter study of system performances, such as heat extraction, is performed. The results show the dependence of thermal recovery of geothermal reservoir on fracture density parameter C.

INTRODUCTION

Recently, HDR(Hot Dry Rock) and HWR(Hot Wet Rock) have attracted considerable attention as new geothermal energy extraction systems. In order to evaluate the performance of these systems, it is necessary to establish a modeling procedure of fluid flow and heat exchange in fractured rock.

Traditionally, models of ground water flow have used parallel fractures, or a continuum approximation such as a "permeable zone". Such models are often valid when a representative volume of rock can be defined that is much smaller than the region of interest. However, it has been becoming difficult to approximate the behavior of geothermal reservoirs by such models. In fractured rocks, ground water flow and solute transport occur predominantly through the connected network of discrete fractures. For the performance evaluation of such geothermal energy extraction systems, interest has grown in more direct models of water flow and heat exchange in fractured rock.

Recent geophysical investigations have confirmed that a subsurface fracture network can be described by fractal geometry. In the field of seismology several reports are available which have characterized subsurface fractures and fault systems based on fractal geometry. Hirata [1989] has investigated several fault systems in Japan, and characterized them by fractal geometry. In his paper, fractal geometry was considered as a useful tool to characterize the geometry of the fault line. The fractal dimensions of those fault systems were calculated by the so called "box-counting method". Furthermore, Meredith [1990] has noted that subsurface fractures could also be characterized by using a methodology in which the number of fractures was related to the fracture length.

In this paper, two and three dimensional modeling procedures of subsurface fracture network are proposed, based on the relationship between the fracture length and the number of fractures as reported by Meredith. The importance of the parameter is discussed to describe the fracture density of rock mass. This procedure is attractive, since this parameter can be measured from field data such as the core sample, and it is also possible to characterize subsurface fracture network by the same parameter.

For geothermal energy extraction systems, the transmissivity and changes in temperature of geothermal reservoir are important. So, based on this modeling procedure, the transmissivity are discussed in terms of probabilities. Finally, we present one of the results of changes in temperature at reservoir outlet as computed by our model, which suggests the strong dependence of temperature change on fracture density.

FRACTAL DISTRIBUTION OF FRACTURE LENGTH

Fractal geometry is a branch of mathematics that has lingered in the realms of theoretical geometry since the last century. Mandelbrot [1983] realized its great potential for characterizing and simulating the geometry of complex shapes, especially the shapes of nature. The shapes which can be explained by fractal geometry have two important properties. Firstly they have self-similarity. Secondly they are characterized by their fractal dimension.

In nature, there are several irregular shapes which can be explained by fractal geometry. The geometry of subsurface fractures is one of the typical example of such shapes. Hirata [1989] has shown that subsurface fractures such as fault systems can be explained by fractal geometry and he computed the fractal dimensions of several fault systems in Japan. Usually, the fractal dimensions of subsurface fractures or fault systems signify the spatial distribution of fractures. These kinds of fractal dimensions are calculated by the "box-counting method".

Meredith [1990] has reported the investigation of the relationship between the fracture length and the number of fractures. He used the data of several scale fault systems shown in Figure 1.

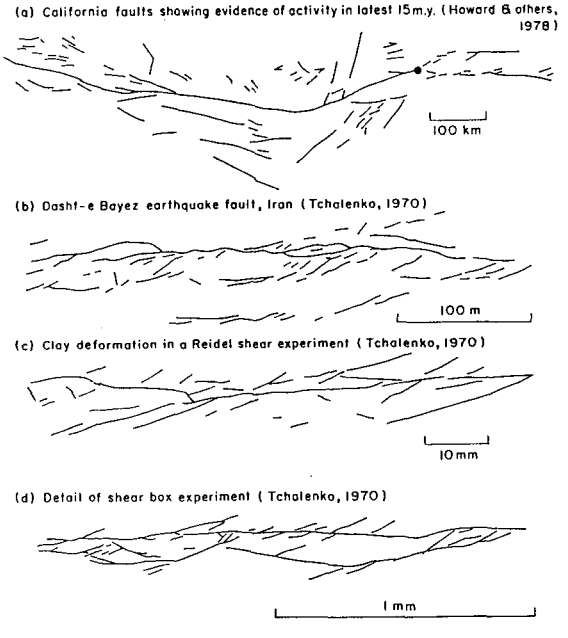

Figure 1 Geometry of fracture system over a range of scales, after Shaw & Gartner [1986].

Figure 2 shows the relationship between the normalized fracture length and the number of fractures. This revealed that the relation between fracture length r (in his paper, fracture length is represented by the symbol L) and the number of fractures N whose lengths are equal to or larger than r can be expressed by the following fractal equation :

$$N = C \cdot r^{-D} \qquad (1)$$

where C is a constant and D is the fractal dimension. The parameter C signifies the fracture density of rock mass. In this paper, C is defined as the fracture density parameter.

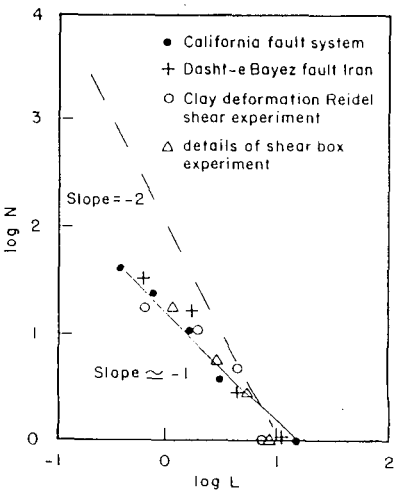

Figure 2 Normalized discrete frequency - length distribution of fracture shown in Figure 1, after Meredith [1990].

Meredith reported that the fractal dimensions were almost equal to 1 for all fault systems he investigated, Figure 1. The meaning of this fractal dimension D is different from that of the fractal dimension calculated by "box-counting method". The former is a measure of the geometry of fractures (branching geometry), while the latter is a measure of the spatial distribution of fractures.

Furthermore, Thomas et al [1989] have investigated the width (opening) distribution of fractures observed on core samples and boreholes. The result showed that the relationship between the fracture width w and the number of fractures whose widths are equal to or larger than w can be also explained by the same formula as Equation (1) and it can be represented by the following equation (although the importance of fracture width distribution is not included here) :

$$N' = C' \cdot w^{-D'} \qquad (2)$$

In the modeling procedure proposed here, the models of fracture network are regarded as being composed of discrete fractures. These fractures are distributed to satisfy Equation (1).

TWO DIMENSIONAL NUMERICAL MODEL

1. Characteristic features of individual fractures

For the two dimensional model of subsurface fracture network, imagine the square area of edge length L between boreholes as shown in Figure 3. Within this area discrete fractures are distributed following the fractal relationship between the length and the number of fractures. In other words, the fracture network model is generated in this area by using fractures that satisfy Equation (1). In order to simplify the discussion, the area and the fractures are normalized by the length L as shown in Figure 3.

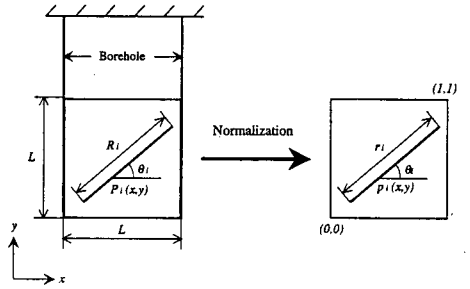

Figure 3 Concept of two dimensional fracture.

In this model, the total number of fractures is expressed by the symbol n, and ith(i=1,2,...,n) fracture is characterized by the following three parameters: (1) Middle point, p_i, (2) Angle from the horizon, θ_i, (3) Length, r_i. In this paper, these parameters are determined as follows.

(1) Middle point of the fracture, p_i

It is assumed that the fractures do not form a cluster around any point. So, x and y co-ordinates of the point p_i are determined by using random numbers lying between 0 to 1.

(2) Angle from the horizon, θ_i

The distribution of θ_i seems to be random, however field data sometimes shows that there exist preferred directions of fracture orientation. So, if it is possible to obtain the preferred direction, θ_i must be determined to have the same tendency as that of the field data. In this paper, two types of angle distribution are used as examples.

(3) Length of the fracture, r_i

Since the lengths of fractures are ruled by fractal geometry, r_i distribution must satisfy Equation (1). In order to satisfy Equation (1), r_i is determined by the following formula :

$$r_i = (C / i)^{1/D} \qquad (3)$$

(4) Total number of fractures, n

Theoretically, if we need to consider very small fractures whose lengths approach 0, n would approach infinity. However, very small fractures can not be observed, and is dependent upon the resolution of measuring instrument. In this paper, r_{min} is defined as the smallest length of fracture which can be observed. According to the data reported by Meredith [1990], r_{min} is between 0.04 and 0.11. So, we let the value of r_{min} as 0.04, and the smallest i which satisfies $r_i > r_{min}$ as the value of n.

2. Fractal Dimension : D

Although some fault systems have been investigated and their fractal dimensions calculated by the "box-counting method", the fractal dimensions required for Equation (1) are not available. The data from Meredith [1990] is the only published information from which we can obtain the fractal dimension D. Meredith [1990] has measured the relationship between the fracture length and the number of fractures at 4 different scale fault systems and shown that the fractal dimensions of all fault systems are almost equal to 1 as shown in Figure 2. In this present work, we adopt the same value of fractal dimension, i. e. D=1.

3. Examples of fracture network model

Figure 4 shows some sample patterns of fracture network model for 3 different values of the fracture density parameter C. Two types of fracture network model are shown. One model has a random distribution of fracture angle (Type 1), the other has two preferred directions (Type 2). Figure 4 illustrates the strong influence of the fracture density parameter C on fracture network patterns.

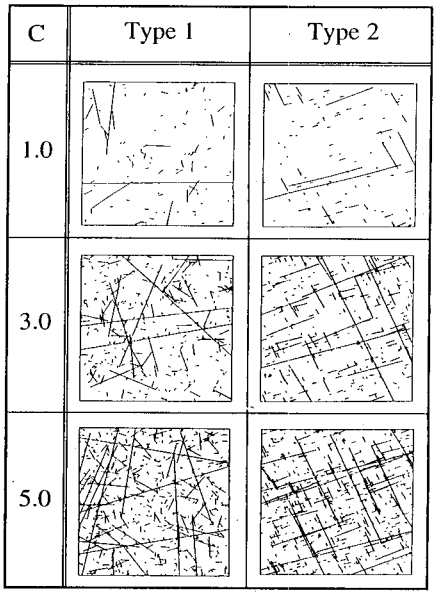

Figure 4 Some of fracture patterns generated numerically based on modeling procedure proposed here.

THREE DIMENSIONAL FRACTURE NETWORK MODEL

For the estimation of practical system performance such as transmissivity and thermal recovery, two dimensional geothermal reservoir model may not be accurate. It is necessary to extend two dimensional modeling procedure into a three dimensional one. However, there is no information about three dimensional shape of subsurface fractures. In this paper, we assume that the subsurface fractures are penny-shaped. Figure 5 shows the concept of three dimensional fracture network model. The network is formed by distributing penny-shaped fractures in the box randomly.

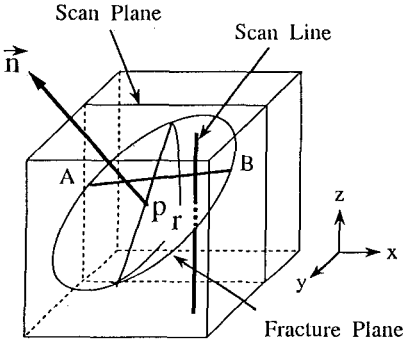

Figure 5 Concept of three dimensional fracture model.

As in the two dimensional modeling procedure, each fracture is characterized by the following parameters :

(1) Central point of the fracture : p

(2) Normal of the fracture plane : $\vec{n}$

(3) Diameter of the fracture : r

In this paper, these parameters are determined by following the same way as the two dimensional modeling procedure. Central point and normal of the fracture are determined by random numbers. Diameter of the fracture is calculated by Equation (3).

Figure 6 is a schematic figure of the three dimensional fracture network model.

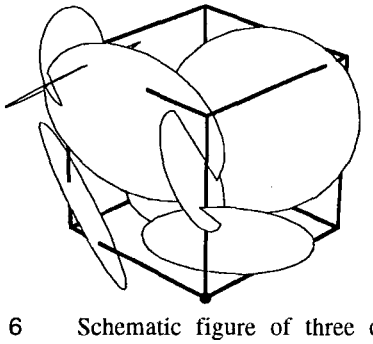

Figure 6 Schematic figure of three dimensional model.

RELATIONSHIP BETWEEN TWO DIMENSIONAL AND THREE DIMENSIONAL MODELS

Length distributions of fractures observed on two dimensional area are fractal. Therefore length distributions of fractures observed on any two dimensional section area of this model must be fractal. Scan planes are introduced to examine fracture pattern and length distribution as shown in Figure 5. Figure 7 shows one of the fracture patterns on a scan plane obtained from three dimensional fracture network model. Figure 8 shows length distributions of fractures on four scan planes randomly chosen from a model (D=1.8, C=5.0). It is possible to say that the three dimensional model which has fractal length distribution of fractures shows fractal characteristics on its two dimensional sectional areas. The relationship between the fractal dimensions of two dimensional fracture network model and that of the three dimensional model is obtained as shown in Figure 9.

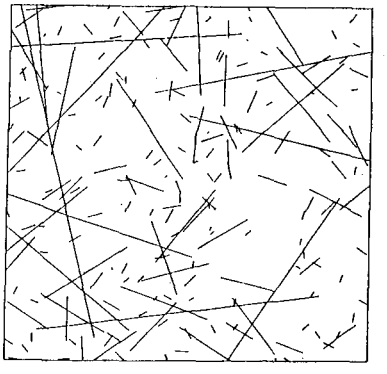

Figure 7 One of the fracture patterns on a scan plane.

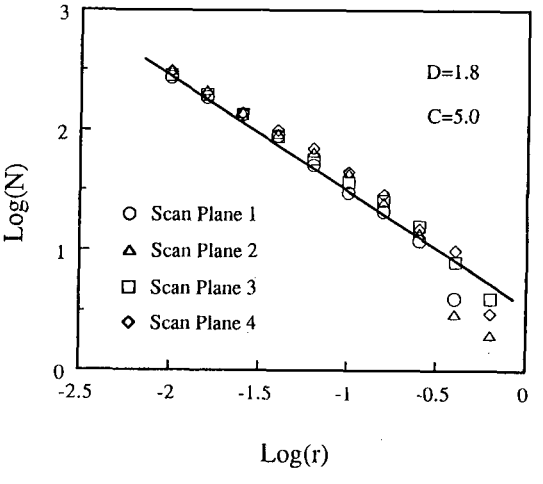

Figure 8 Length distribution of fracture on scan planes.

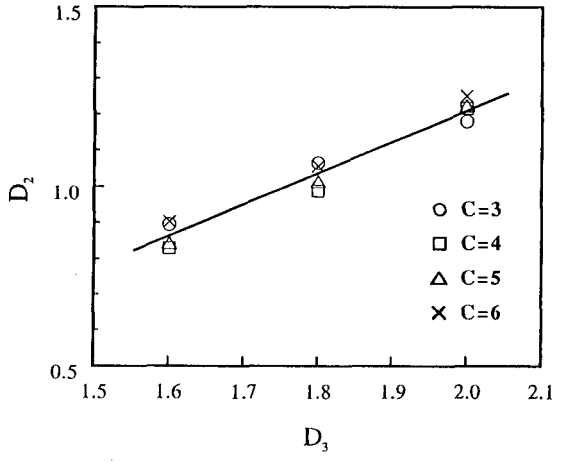

Figure 9 Relationship between fractal dimension of two dimensional model and that of three dimensional model.

ESTIMATION OF THE VALUE OF PARAMETER C

It is possible to measure the number of fractures which are observed on a core sample or borehole per unit length of depth. Considering a borehole as a scan-line of a subsurface fracture network as shown in Figure 5, it is possible to predict the number of fractures observed on core sample per unit length of depth m by the following equation :

$$m = \overline{\sin\theta_i} \cdot \left\{ \int_{r_{min}}^{1} \pi \cdot \left(\frac{r}{2}\right)^2 \cdot \left(-\frac{dN(r)}{dr}\right) \cdot dr + C \right\} \quad (4)$$

where $\overline{\sin\theta_i}$ is the average of θ_i. From Equation (4), the fracture density parameter C can be calculated using the following equation :

$$C = \frac{4m}{\sin\theta_i \cdot \left\{ 9\pi \cdot \left(1 - r_{min}^{0.2}\right) + 1 \right\}} \quad (5)$$

APPLICATIONS

Transmissivity

Transmissivities of fracture network are calculated by using the following equation :

$$k_x \cdot \frac{d^2P}{dx^2} + k_y \cdot \frac{d^2P}{dy^2} + k_z \cdot \frac{d^2P}{dz^2} = 0 \quad (6)$$

where P and Q stand for pressure and quantity of water respectively. k_x, k_y and k_z represent rock mass permeability in each of the x, y, z directions, which are determined by the fractures.

Three types of water flow models used for the calculation are (Figure 10)
(1) Plane - Plane flow
(2) Plane - Borehole flow
(3) Borehole - Borehole flow

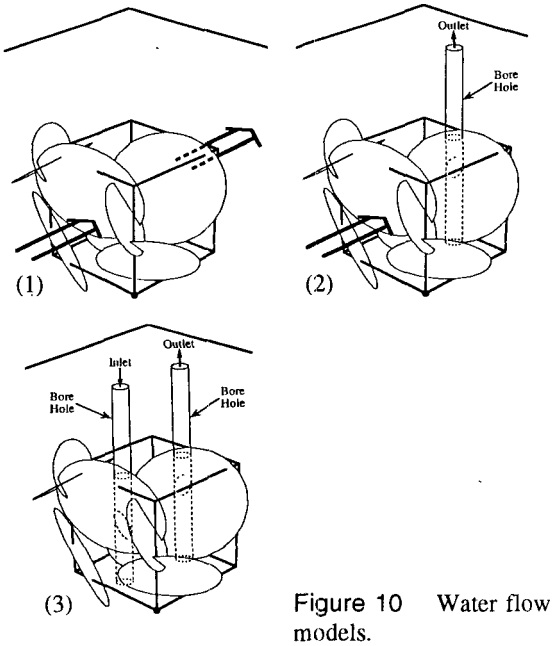

Figure 10 Water flow models.

Figure 11 shows one of the results of the calculation. For this calculation, 100m square reservoir is used and the assumption that the width of the fracture is proportional to its length is adopted.

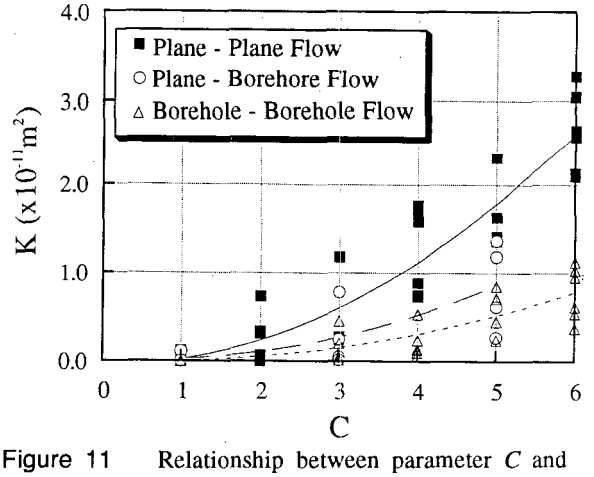

Figure 11 Relationship between parameter C and transmissivity.

Heat Extraction

The change in temperature at the outlet of the reservoir as the time passes is calculated. The model used for thermal calculation is shown in Figure 12.

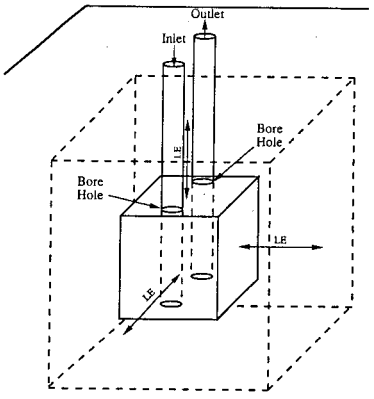

Figure 12 A model used for thermal calculation.

In Figure 12, dashed line expresses adiabatic boundary for thermal calculation and LE represent the distance to the boundary. Equation (7) is adopted for thermal calculation.

$$C_R \cdot \rho_R \cdot \frac{\partial T}{\partial t} + C_W \cdot \rho_R \cdot \left(v_x \cdot \frac{\partial T}{\partial x} + v_y \cdot \frac{\partial T}{\partial y} + v_z \cdot \frac{\partial T}{\partial z} \right)$$

$$= \lambda \cdot \left(\frac{\partial^2 T}{\partial x^2} + \frac{\partial^2 T}{\partial y^2} + \frac{\partial^2 T}{\partial z^2} \right) \qquad (7)$$

where T stands for the temperature of rock (equal to the temperature of water in this paper). λ is thermal diffusivity of rock. C_R and C_W represent specific heats of rock and water, ρ_R and ρ_W represent the densities of rock and water. v_x, v_y and v_z are flow velocities in each of directions.

Figure 13 shows the results of the calculation with following parameters :

Size of reservoir	: 100m cubic
LE	: 100m
Initial temperature of rock mass	: 300 °C
Temperature of water at outlet	: 200 °C

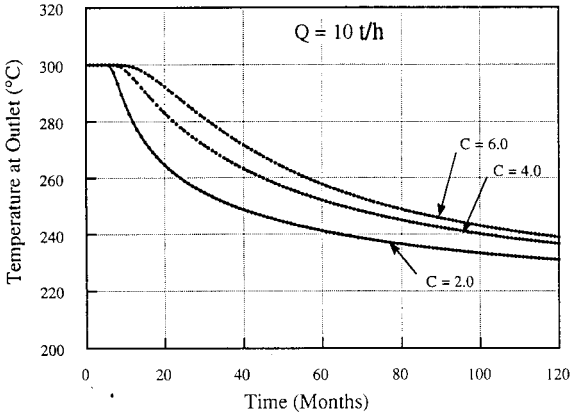

Figure 13 Changes in temperature at reservoir outlet.

In Figure 13 we plot the reservoir outlet temperature versus time by ranging the parameter C which represents the fracture density of rock mass. It can be clearly seen from the graph that there is a strong relationship between the outlet temperature and the fracture density.

CONCLUSION

A modeling procedure based on fractal geometry is quite effective for characterizing subsurface fracture networks. Borehole data have not been used in the past, although it is one of the few datas which contain subsurface information. For this modeling procedure, borehole data gives significant bases for the characterization of geothermal reservoir. Once the model of geothermal reservoir is established, it is possible to predict the transmissivity of fluid path and thermal recovery of geothermal reservoir.

Using the fracture network model proposed here, hydrological and thermal behavior, including long-term performance, of several types of geothermal reservoir can be simulated numerically. This modeling procedure should also make it possible to predict the effectiveness of hydraulically stimulated fractures, since hydraulical stimulation increases the density of fracture in geothermal reservoirs.

REFERENCES

Gringarten, A. C., Witherspoon, P. A. and Ohnishi, Y., "Theory of Heat Extraction From Fractured Hot Dry Rock", Journal of Geophysical Research, Vol. 80, No. 8, 1120-1124, 1975.

Harlow, F. H. and Pracht, W. E., "A Theoretical Study of Geothermal Energy Extraction", Journal of Geophysical Research, Vol. 77, No. 35, 7038-7048, 1972.

Hirata, T., "Fractal dimension of fault system in Japan : Fractal structure in rock fracture geometry at various scales", Pure and Applied Geophysics, Vol. 131, 157-170, 1989.

Mandelbrot, B. B., "The Fractal Geometry of Nature", Freeman, New York, 1983.

Meredith, P. G., "Scattering Attenuation and the Fractal Geometry of Fracture System", Pure and Applied Geophysics, Vol. 133, 283-304, 1990.

Shaw, H. R. and Gartner, A. E., "On the Graphical Interpretation of Palaeoseismic Data", U.S.G.S. Open File Report, 86-394, 1986.

Thomas, A., Blin-Lacroix., "Stochastic modeling of fractured reservoir", Proceeding of International Hot Dry Rock Geothermal Energy Conference, Camborne School of Mines, 1989.

PROCEEDINGS, Eighteenth Workshop on Geothermal Reservoir Engineering
Stanford University, Stanford, California, January 26-28, 1993
SGP-TR-145

IMPACT OF INJECTION ON RESERVOIR PERFORMANCE IN THE NCPA STEAM FIELD AT THE GEYSERS

S. L. Enedy, J. L. Smith, R. E. Yarter, S. M. Jones, P. E. Cavote

Steam Field Operations
Northern California Power Agency
The Geysers, California

ABSTRACT

A managed injection program implemented by the NCPA in The Southeast Geysers reservoir continues to positively impact reservoir performance. Injection effects are determined by the application of geochemical and geophysical techniques to track the movement of injectate. This information, when integrated with reservoir pressure, flowrate, and thermodynamic data, is used to quantify the overall performance and efficiency of the injection program.

Data analysis indicates that injected water is boiling near the injection wells, without deeper migration, and is recovered as superheated steam from nearby production wells. Injection derived steam (IDS) currently accounts for 25 to 35 percent of total production in the NCPA steamfield. Most importantly, 80 to 100% of the injectate is flashing and being recovered as steam. The amount of IDS has increased since 1988 due to both a change in injection strategy and a drying out of the reservoir. However, significant areas of the reservoir still remain relatively unaffected by injection because of the limited amount of injectate presently available.

That the reservoir has been positively impacted in the injection areas is evidenced by a decrease in the rate of pressure decline from 1989 through 1992. Correspondingly, there has been a reduction in the rate of steam flow decline in the areas' production wells. Conversely, little evidence of reservoir cooling or thermal breakthrough is shown even in areas where IDS accounts for 80 percent or more of production. Finally, since injection water is a relatively low-gas source of steam, noncondensible gas concentrations have been reduced in some steam wells located within the injection dominated areas.

BACKGROUND

The Northern California Power Agency (NCPA) owns and operates two geothermal power plants with an installed capacity of 246 and a geothermal steam field in the Southeast Geysers. Plant 1 started operation in 1983 and Plant 2 in 1985. The units were operated in a base loaded manner until 1988 and operated as load following units thereafter with an annual average output of approximately 150 MWG. The steamfield, located on Federal Leases CA 949-950, consists of 69 steam wells and seven injection wells located on 12 sites. The injectate is mainly cooling tower condensate supplemented with some rain water collected in two ponds located near the power plants.

Water injection in the NCPA steamfield began with the start of power plant operations in January 1983. In the ten years following startup, 65 billion pounds of water have been injected into nine injection wells. That cumulative mass injected represents approximately 34 percent of total steam produced. Although the percentage of condensate available from the plants remains relatively constant on an annual basis, the net mass loss of fluid, which through 1992 is 123.5 billion pounds, continues to increase. Because The Geysers is essentially a closed system, the rate of reservoir fluid loss and resultant reservoir pressure decline will continue unchecked, unless injection augmentation programs are activated.

The accelerated decline of reservoir pressure starting in 1986 indicated a need to develop an injection augmentation program (Enedy, Grande, Smith 1990). Toward this goal, the NCPA constructed two containment ponds located near the power plants that increase the amount of injectate between 5 to 10 percent annually, depending on rainfall. Further, the NCPA implemented an overall reservoir management program with the objective of maximizing the value of energy production from the geothermal resource. Efficiency improvements implemented by the NCPA and shown to be cost effective include 1) load following operations, 2) improved distribution of injection for reservoir support, and 3) a well workover and cleanout program using the NCPA's drilling rig on an as-needed basis.

Future enhancements planned by NCPA include installation of a new turbine to better utilize low pressure steam. Additionally, the economic feasibility of several other augmentation projects is being considered with the goal of at least doubling the current annualized rate of injection which is between 1,600 -1,800 gallons per minute (GPM).

EVOLVING INJECTION STRATEGIES

The initial operating philosophy regarding injection was to dispose of condensate in "peripheral" wells to minimize the chance of liquid water breakthrough to steam wells. Little consideration was given to individual well injection rates. The original developer of this leasehold (Shell Oil), constructed injection lines to sites located near the edge of the developed area where no productive steam wells existed. That strategy reflected the prevailing concept at that time that condensate injection was primarily a disposal problem without potential reservoir benefit.

Starting in 1986, high flowrate declines were experienced in the Southeast Geysers This led to studies to determine if revised injection strategies could lead to improved reservoir performance. In order to better understand the effects of "internal" injection (i.e., injection within the NCPA developed area), a joint injection project was begun to quantify the ability of the reservoir to support and benefit from augmented water injection. That study, along with other supporting evidence, showed that a properly planned injection strategy could 1) lead to the extraction of additional heat from the reservoir rock, 2) positively impact both reservoir pressures and flowrates, and 3) minimize thermal breakthrough to offset steam wells. (Enedy, Enedy, Maney 1992).

The reservoir still continues to show the ability to support and benefit from increased injection. For this reason, the operating strategy continues to gradually evolve and improve. Injectate is now distributed throughout the reservoir and injected at rates of 500 - 1,500 GPM per well. This strategy of utilizing additional injection wells at lower rates is shown in Table 1, which lists the wells and masses injected from 1988 through 1992. Only two wells were used in 1988 compared to seven wells in 1992. Injection well locations are shown in Figure 1.

Communication of unflashed effluent to steam production wells has not been a major problem in the NCPA steam field, except on a few occasions when rates

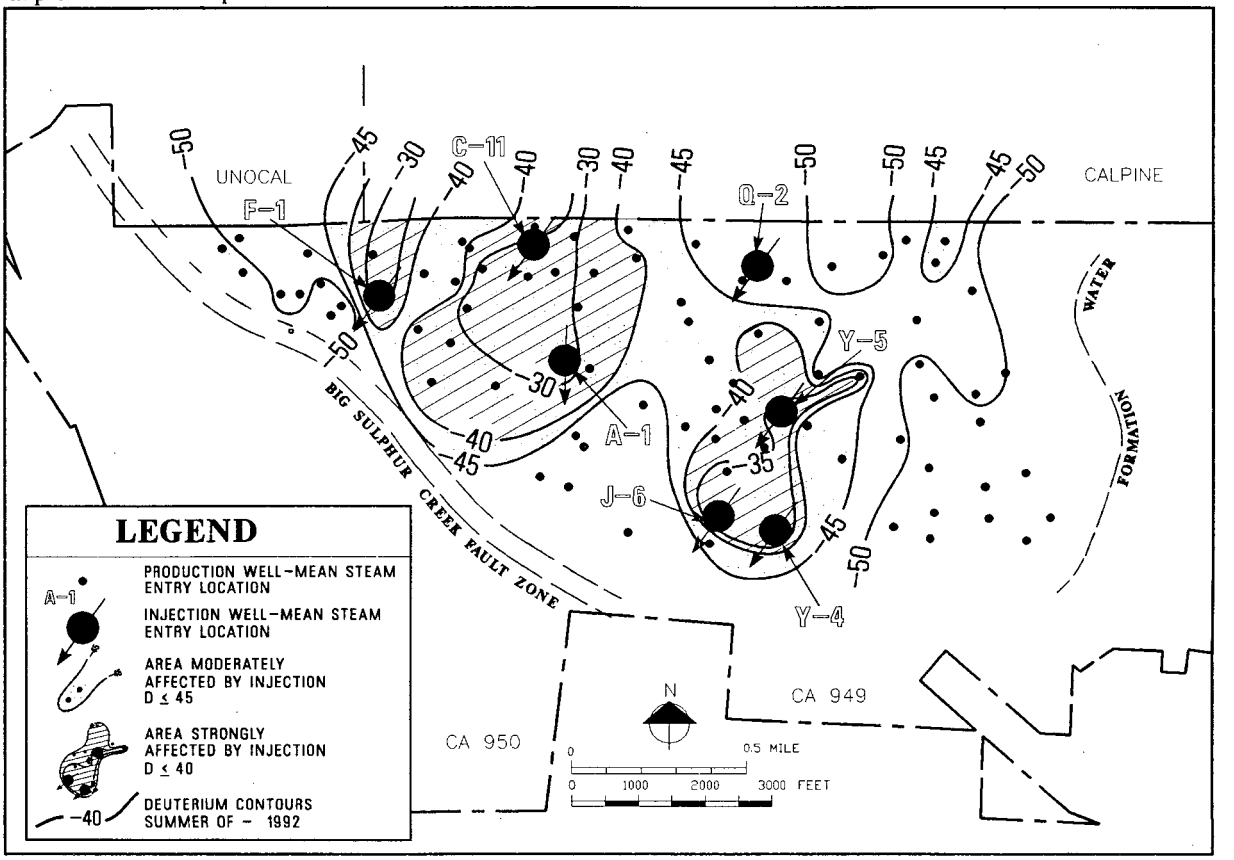

Fig. 1 Fieldwide deuterium distribution from samples taken June through August, 1992

Table 1

Annual Mass Injected And Wells Utilized

	1988		1989		1990		1991		1992	
Well	B-lb	%	B-lb	%	B-lb	%	B-lb	%	B-lb	%
A-1	2.7	34	1.5	20	0.6	8	1.0	15	0.8	9
C-11			0.7	9	1.7	22	2.7	40	2.6	31
F-1							1.0	15	1.0	12
J-6									1.0	12
Q-2					0.5	6			0.3	4
Y-4	5.3	66	2.0	26	3.5	44	1.7	25	1.2	14
Y-5			3.4	45	1.6	20	0.3	5	1.5	18
TOTAL	8.0		7.6		7.9		6.7		8.4	

of injection have been unusually high for a prolonged period of time. At injection rates over 1,000 GPM, injector A-1 communicates with two N-Site steam wells. The only problems experienced below 1,000 GPM occur between injection well Y-5 and steam well D-7, and injection well Q-2 and steam well Q-6.

TRACING INJECTATE MOVEMENT BY DEUTERIUM ANALYSIS

The power plant condensate sent to the injection wells has an elevated deuterium concentration that is a result of the evaporation process in the cooling towers. Consequently, periodic analysis of deuterium in the produced steam provides a means of tracing the movement and quantifying the recovery of injection derived steam (IDS). It is now general practice at The Geysers to use the difference in deuterium concentrations of the original steam and the injected water as a means to trace and quantify the recovery of injected water (Beall, Enedy, Box 1992). Deuterium is useful because it is stable at high temperatures, and undergoes very little fractionation between steam and water phases during the reservoir boiling process. It is also far less susceptible to ion exchange between rock minerals and water molecules than is ^{18}O. However, there are several problems with using deuterium as a tracer including difficulty in determining spatial and temporal patterns since the deuterium is injected continuously in all injection wells. Although, the amount of IDS can be quantified, it is often difficult to determine both the exact sources of the IDS, especially if several injection wells are in close proximity, or the relative contribution of old versus recent injection.

Deuterium concentration is reported as the difference between the isotopic ratios in the sample and a standard. The ratio is of the heavier deuterium to the lighter hydrogen with the small difference in ratios between the sample and the standard reported in per mil (o/oo) relative to V-SMOW (Vienna standard mean ocean water). Additional explanation of the terminology, sampling and testing methods used in isotopic analysis is provided by Reed (1991). For steam without injection, deuterium (D) ranges between -52 to -56 o/oo SMOW. Injectate ranges between -8 and -24 with an average of -16 o/oo SMOW.

Results of a fieldwide deuterium survey taken during the summer of 1992 are shown on Figure 1. The survey indicated that D concentration is increased (i.e., less negative - o/oo values) near active injection wells, with three distinct anomalies centered on the injection areas. These anomalies are somewhat elongated in a north-northeast direction indicating a preferential flow path in this direction. These anomalies are indicated by a cross-hatching on Figure 1, within the -40 per mil contour. The area indicated to be strongly affected by injection represents approximately 30 percent of the reservoir development area, which is very close to the percentage of steam returned as condensate to the reservoir. The most wide-spread deuterium anomaly includes the area of C-11 and A-1. Its large size is probably related to the relatively large amount of injection into C-11 (i.e., 34 percent of all injection in 1992 as shown in Table 1). A small (fourth) deuterium anomaly exists in the northeast portion of the field that is probably related to the operation of an injection well located further north. Injector Q-2 is not associated with an anomaly because it was not an active injector prior to the survey.

TRACING INJECTATE MOVEMENT BY MEQ MONITORING

Microearthquake (MEQ) activity at The Geysers has been studied since 1975, as recently summarized by Stark (1992). In many areas of the steamfield these events are recognized to have a spatial and temporal correlation with injection. This same correlation was recognized during NCPA's first MEQ survey on the leasehold in 1987, and as a consequence, arrangements were made to have a permanent MEQ recording network extended into this area. The expanded network is managed by Unocal and has been continuously operated

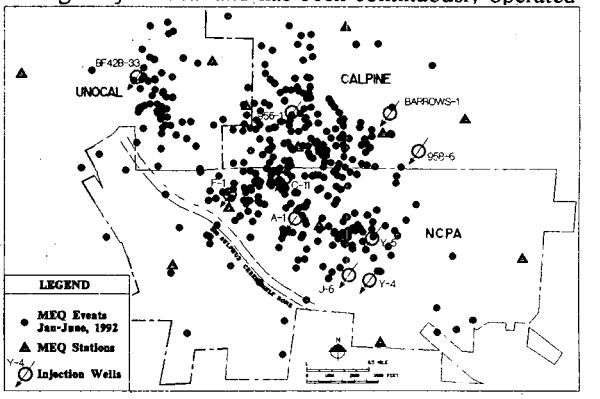

Fig. 2 MEQ epicenters at SE Geysers

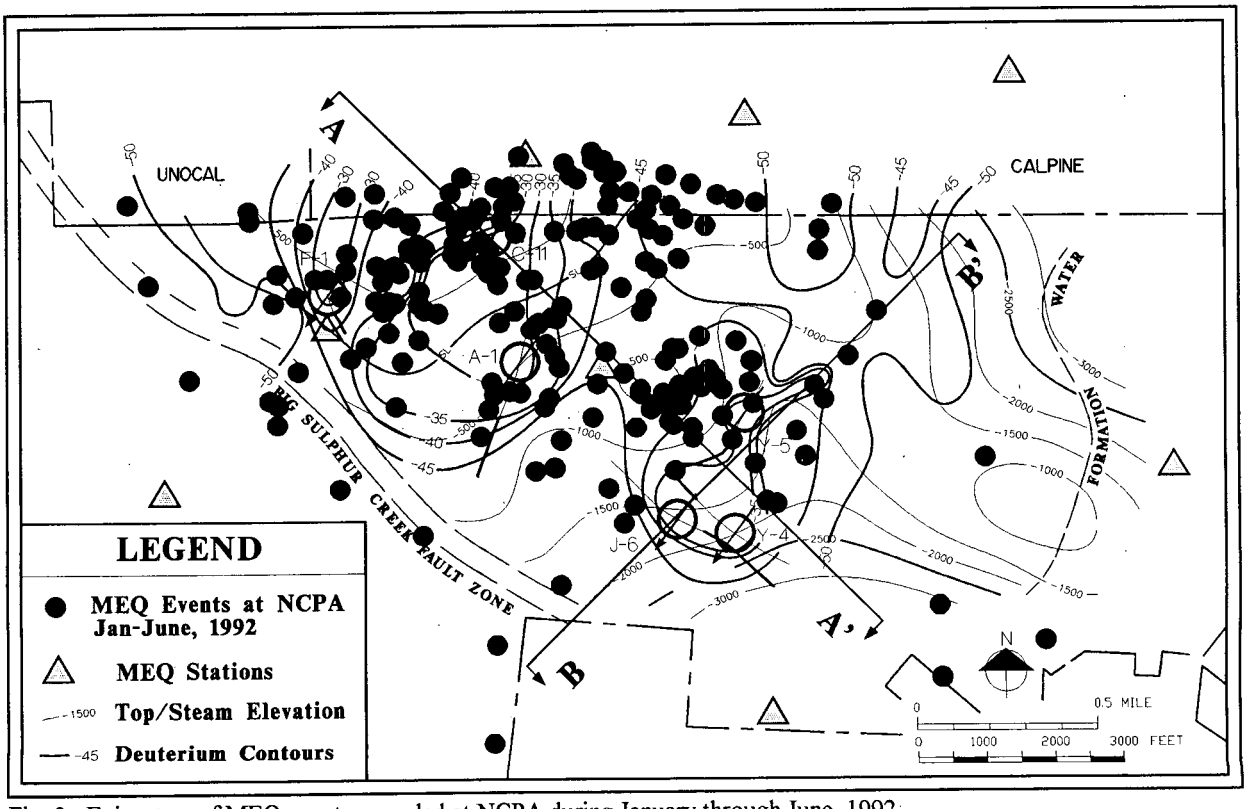

Fig. 3 Epicenters of MEQ events recorded at NCPA during January through June, 1992

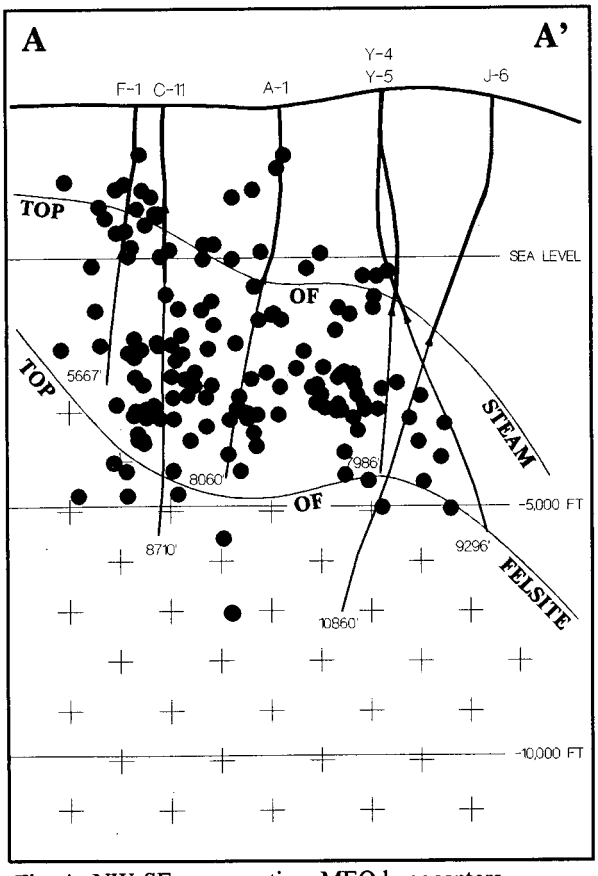

Fig. 4 NW-SE cross section, MEQ hypocenters

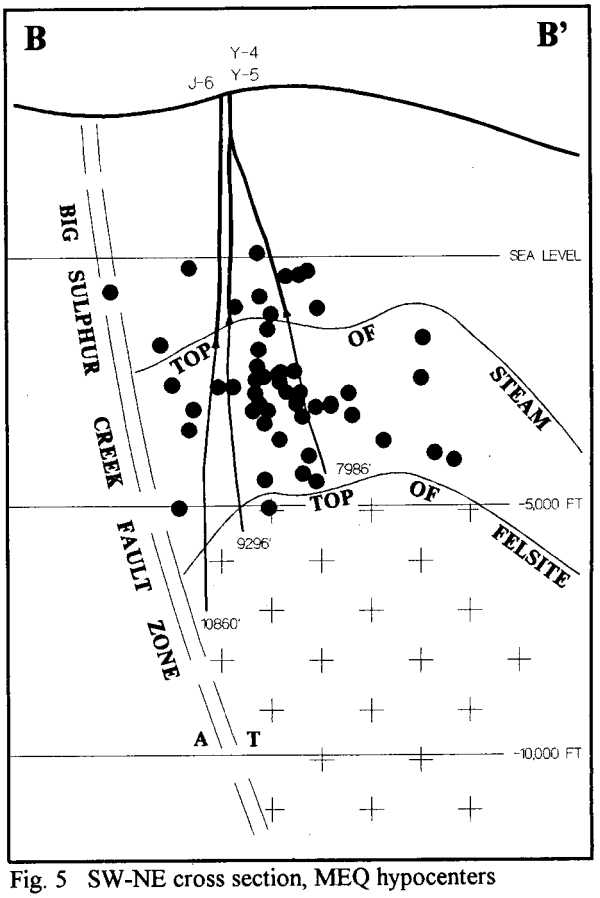

Fig. 5 SW-NE cross section, MEQ hypocenters

since September 1989. Recently, additional recording stations were installed in the Southeast Geysers area by Lawrence Berkeley Laboratory (LBL) and Lawrence Livermore Laboratory. All subsequently recorded events are now being processed in a collective manner.

Figure 2 is a map of Southeast Geysers MEQ events recorded during the first six months of 1992 and processed by LBL. A distinct clustering of events occurs near Unocal's isolated BF42B-33 injection well. Somewhat more widespread clouds of MEQ events occur also near the Calpine 956-1 injector and in the general vicinity of the five NCPA injectors that were active during that same time.

Viewing this data within the NCPA area in more detail, Figure 3 shows those same event locations superimposed on both the Summer 1992 deuterium anomalies presented in Figure 1, and a top of the steam reservoir contour map. The vast majority of MEQ events recorded at NCPA are shown to occur within the deuterium-mapped areas of significant injectate influence. In fact, MEQ events are almost non-existent elsewhere, including throughout the injectate-poor region of the NCPA steam reservoir development area that extends almost a mile east of injection well Y-5.

Figures 4 and 5 are cross sections representing the relationships of the calculated hypocenter depths of these MEQ events to the known injection intervals of the NCPA active injectors, and to the basic geologic/reservoir units present. The MEQ events are shown to take place at depth intervals that rarely exceed the maximum depth of the injection wells in use. The clear indication is that the liquid injectate is boiling near the injectors, without significant migration deeper into the reservoir. The result is that within this NCPA area, under these injection conditions, most of the IDS appears to be immediately available for migration to the surrounding production wells.

QUANTIFYING INJECTATE RECOVERY

It is general practice at The Geysers to use Deuterium in the produced steam to quantify both the amount of injection derived steam (IDS) and the percentage of injectate that is flashing and returning as steam over some reasonable time period. Deuterium surveys of the NCPA wells have been taken once or twice a year since 1985. The contribution of IDS to a well's total flow was calculated assuming each sample is a mixture of a reservoir fluid and condensate and applying a mixing ratio. The well's flowrate potential at 130 psig was then multiplied by the IDS fraction to obtain the IDS flowrate potential at 130 psig. Figure 6 is a plot of both the total IDS flowrate potential and the IDS flowrate potential as a percentage of the total flowrate potential for the NCPA steam field. Figure 7 is a plot of the IDS flowrate potential as a percentage of the average injection rate during the previous six month period. It is a measure of the amount of injectate recovered as steam. The current amount of steam recovered from old versus recent injection has not been quantified on a continuous basis. The injection wells utilized in the three months prior to each survey are annotated on the plots.

As shown on Figure 6, IDS production potential was relatively constant between 1985 - 1988 at 280 to 350 kpph (thousand pounds per hour) at 130 psig. However, starting in 1989, IDS flowrate potential increased to a high of 950 kpph at 130 psig in 1992. This increase in IDS flowrate potential is due to the change in injection strategy that resulted in the use of more injection wells located closer to the producing wells (e.g., C-11, Y-5, F-1) and injection rates averaging 800 GPM per well or less. The IDS flowrate potential in 1992 is 26 percent of total flowrate potential. Actual IDS production varies between 25 and 35 percent of production due to NCPA's load following operation. The deferred production of original steam caused by the increased production of IDS is believed to be small for this case and has not been estimated.

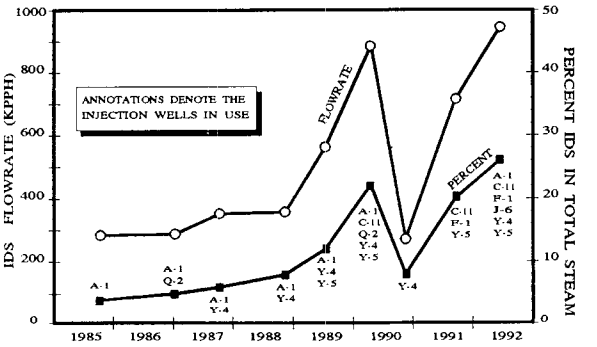

Fig. 6 Injection derived steam flowrate potential and IDS as percent of total flow potential

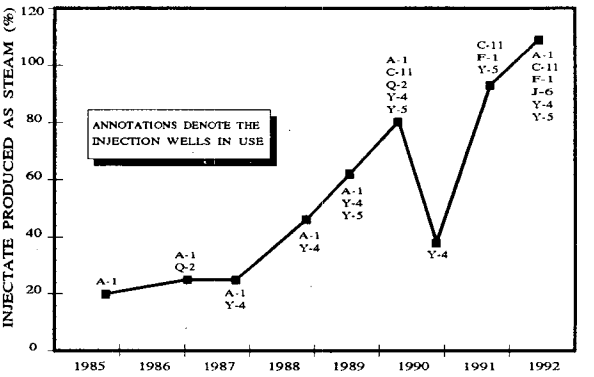

Fig. 7 Percent of condensate recovered as steam, 1985 through 1992

As shown on Figure 7, the percentage of injectate being recovered as steam increased between 1989 and 1992 with values of 93 and 109 percent in 1991 and 1992. The cause of the IDS values exceeding 100 percent of the average injection rate is unclear but could be due to 1) uncertainty in the calculations due to natural fluctuations in the concentration and amounts of deuterium in the injectate, 2) an incorrect assumption regarding the estimate of average injection rate prior to the sampling survey (i.e., a six month average may be high), 3) the wells are actually producing IDS previously injected which would allow for values greater than 100 percent and 4) average well production rates may vary from the flowrate estimated at 130 psig. Due to NCPA's load following operation, actual production of IDS as a percentage of average injection rate varied between 80 and 100 percent in 1992.

IDS production potential decreased in late 1990 because only Y-4 was used during most of the previous summer to dispose of injectate. The other injection wells experienced temporary operating problems at this time. The IDS potential dropped below 300 kpph due to both the low volume of condensate being injected during the previous summer months and the location of Y-4 as a "peripheral" injector.

An example of an individual well's deuterium history is shown on Figure 8 for steam well F-5, which is located near injection well F-1. F-5 has produced IDS since 1989.

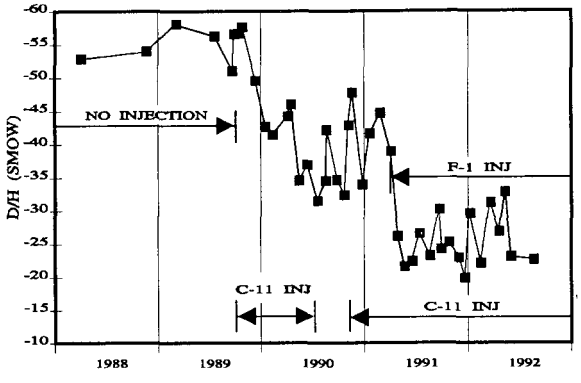

Fig. 8 F-5 deuterium shift, 1988 through 1992

F-5 produced approximately 50 percent IDS starting in 1990 (-35 o/oo). However, with the conversion of F-1, the percentage of IDS increased to over 75 percent (-25 o/oo). Despite the large amount of IDS, and close proximity of this steam well to injectors F-1 C-11, F-5 continues to produce super-heated steam and with no observable decrease in flow temperature. Figure 9 is the plot of two Temperature and Pressure Surveys on F-5. One survey was taken prior to the start of injection in 1989 and the other survey was taken in 1992, following

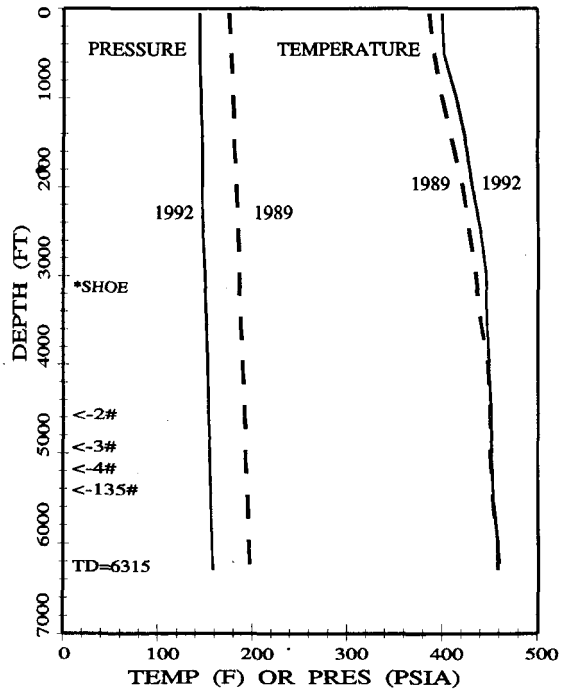

Fig. 9 F-5 T/P/S surveys, Mar., 1989 & Nov., 1992

nearly three years of injection. Continuous injection has not caused any cooling in F-5 as the downhole temperatures are still approximately 460 °F.

RESERVOIR PRESSURE DECLINE

It is general practice at The Geysers to measure reservoir pressure using both pressure buildup tests and the continuous monitoring of observation wells. NCPA routinely conducts static pressure surveys during the spring to develop an isobaric map for the developed area. The rate of decline of static reservoir pressure is a direct measure of the rate of depletion of the reservoir fluid. Also, the decline in reservoir pressure governs the rate of steam flow decline (i.e., the lower the decline in reservoir pressure the lower the decline in steam deliverability).

Figure 10 represents the percentage decline in deliverability caused by pressure decline for the developed NCPA production area between March 1989 and March 1992. It was during this time period that the amount of IDS from wells located near injectors increased. The decline in deliverability pressure for Figure 10 was calculated with Equation 1 and is based on the back-pressure equation. This approach allows for the calculation of a relative rate of deliverability decline caused by pressure decline. Also, a direct correlation can be made between the decline rate in both the low and high pressure areas of the field.

$$\frac{\left(P89^2 - 143^2\right) - \left(P92^2 - 143^2\right) \times 100}{\left(P89^2 - 143^2\right)} \quad (1)$$

Where *P89* represents the individual well static pressure (psia) taken between February and March 1989 and *P92* represents the individual well static pressure taken between February and March 1992. A pressure of 143 psia is the average wellhead pressure of the field.

Figure 10 shows three areas of reduced pressure decline: 1) an anomaly associated with injectors C-11, A-1, and F-1, 2) an anomaly associated with injector Y-5, and 3) the eastern edge of the productive area. Both of the injection supported anomalies are related to areas of significant deuterium shifts and MEQ activities as previously shown in Figures 1 and 3. An area of reduced decline not associated with injection is the eastern edge of the field. This is an area that produces little or no IDS but has been shown to be influenced by the influx of steam from the edge of the field of higher than average noncondensible gas concentration. (Truesdell, Enedy, Smith, 1993)

The highest degree of pressure support is received from injectors C-11 and F-1 which is partially due to the elevated, but not excessive injection rates. These two wells received half of the available injectate during 1991 and 1992 (Table 1). Also, there are certain reservoir characteristics, including lower pressure and decreased fracture spacing, which increases the recovery of injectate.

The pressure support associated with injector Y-5 is smaller than the C-11 anomaly. This is due in part to the reduced injection rate into Y-5 (20 percent of injection in 1991-92). Also, this area is at higher pressure than the C-11 area and has fewer productive wells, especially to the south of Y-5. The relative impact of Y-4 and J-6 to this pressure support anomaly is not clear.

The individual well static pressure histories for two NCPA steam wells (F-4 and B-3) are shown on Figure 11. Also, shown on Figure 11 is the combined injection rate into injectors C-11 and F-1. The location of each well is shown on Figure 10.

Well F-4 is an observation well located 2,400 feet southwest of injector C-11 and 500 feet southeast of injector F-1. F-4 is within the deuterium anomaly associated with F-1 and as such receives an elevated amount of IDS. The pressure history for F-4 is dominated by changes in the injection rates of C-11 and F-1. A 3 psi per year decline for the last three years is estimated from the pressure history. By contrast, steam

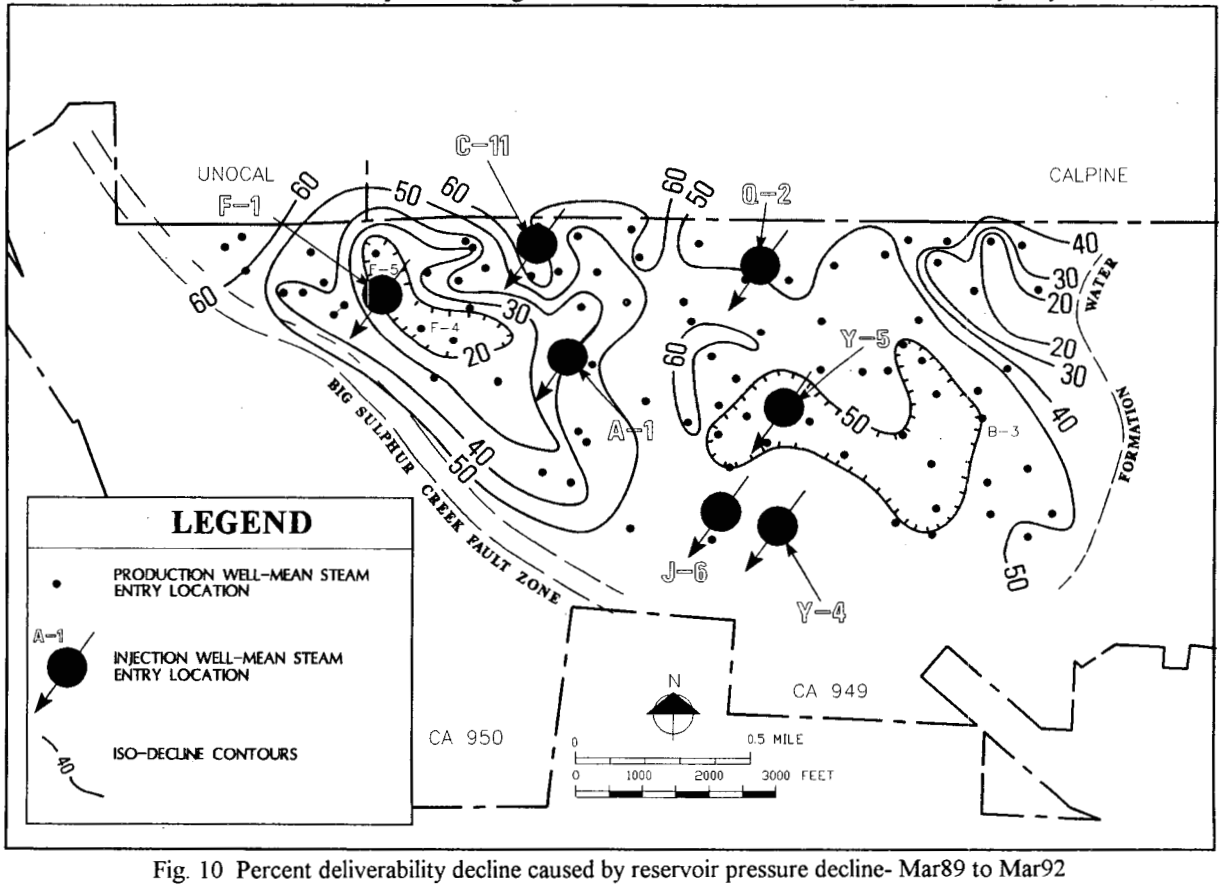

Fig. 10 Percent deliverability decline caused by reservoir pressure decline- Mar89 to Mar92

well B-3 is located near the eastern edge of the field and shows little IDS production. The estimated pressure decline is 18 psi per year.

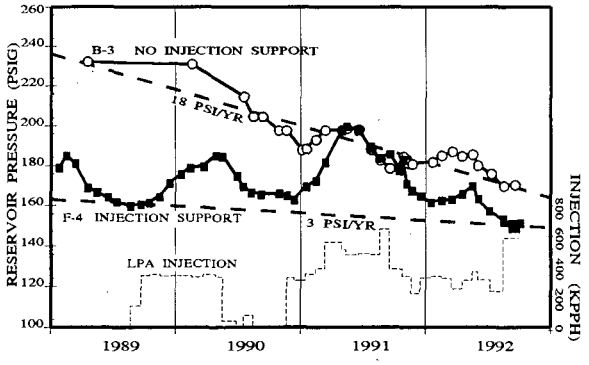

Fig. 11 Reservoir pressure history for steam wells F-4 & B-3, 1989 through 1992

STEAM FLOWRATE DECLINE

Steam flowrate decline is influenced by several factors including reservoir pressure decline, wellhead pressure, interwell interference, and wellbore effects such as bridging in the open-hole, scaling, and condensation. The NCPA routinely calculates the rate of flowrate decline on both an individual well and fieldwide basis. Individual well flowrate declines were calculated for the period August 1991 to July 1992. During this period, the recovery of injectate ranged between 80 - 100 percent and the production of IDS increased to approximately 26 percent of total flowrate potential. The individual well decline rates ranged between 0 and 50 percent with an arithmetic average of approximately 15 percent. The data is plotted and contoured on Figure 12 along with the location of the seven injection wells utilized during this period.

Areas of reduced flowrate decline shown on Figure 12 correlate with areas of injection with the exception of the reduced decline rate near the eastern edge of the field. Reduced decline rate anomalies are centered on injectors A-1 and Y-5. Also, the decline rates of steam wells located near C-11 and F-1 are often lower than the field average or lower than wells located increasing distances from those injectors. Many of the wells showing reduced decline rates are located near areas of increased production of IDS and MEQ activity.

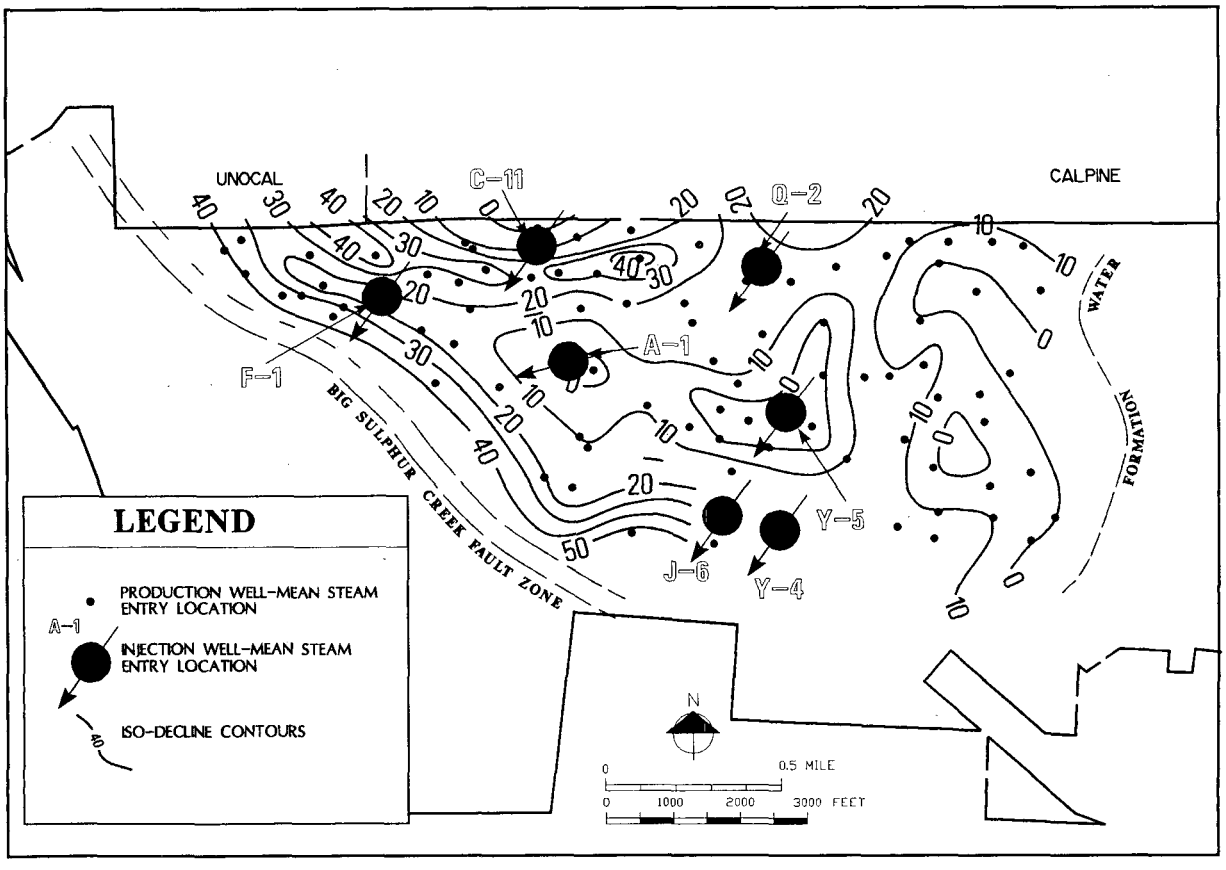

Fig. 12 Annual percentage flowrate decline map, August 1991 to July 1992

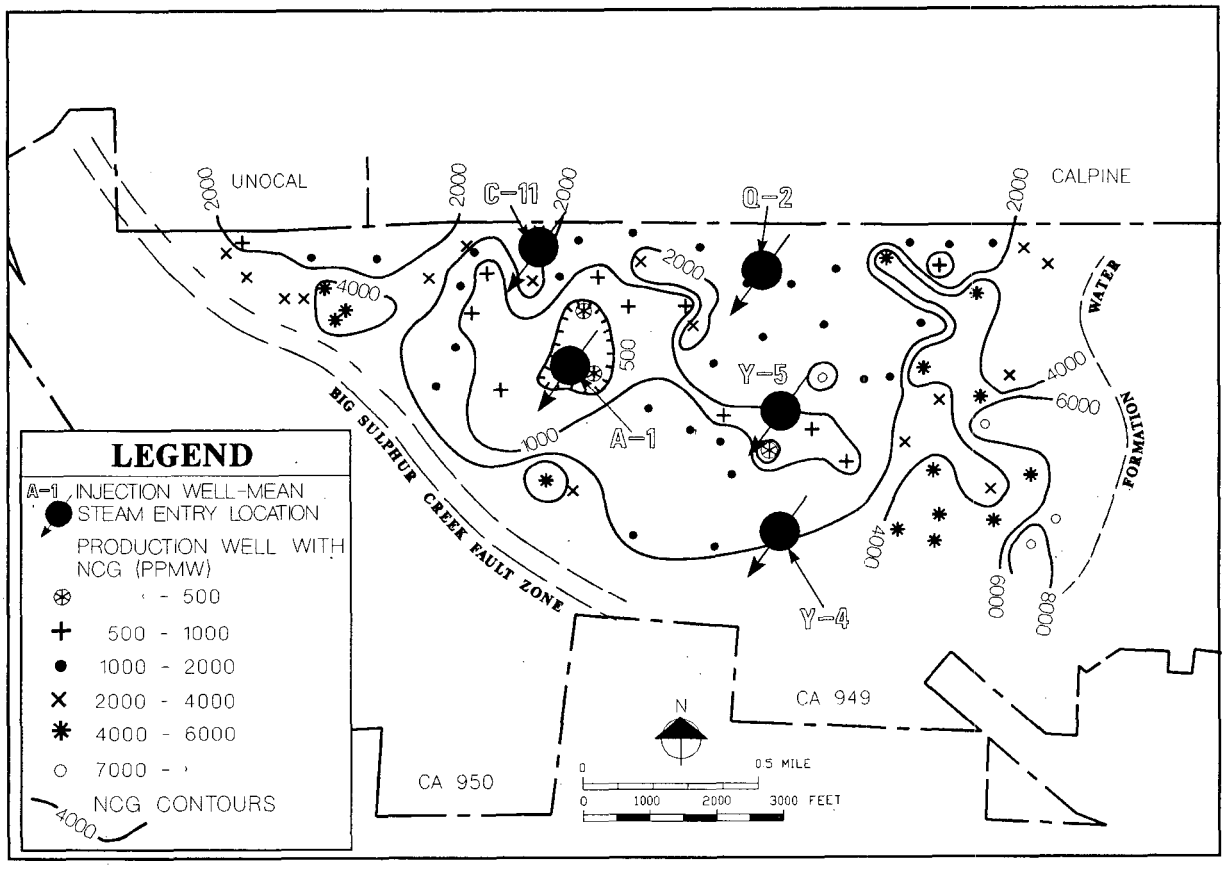

Fig. 13 Fieldwide NCG distribution from samples taken July 1991

NCG DISTRIBUTION

Many of the wells showing injection effects as measured by stable isotope analysis also demonstrates a decrease in noncondensible gas concentrations, including H_2S, and CO_2. Also, these same wells often show evidence of increased NH_3, N_2, and AR (Klein, Enedy 1992).

Figure 13 is the distribution of NCG on the NCPA lease. The gas concentration generally increases from the center of the field toward the reservoir boundaries to the east and west with the highest concentrations being near the eastern boundary. The eastern and western boundaries are affected by an influx of higher gas steam that may be caused by Rayleigh condensation processes (Truesdell, Enedy, Smith, 1993). Steam wells within the 1,000 ppm contour, located near Injection wells A-1, Y-5 and C-11, have reduced gas concentration due to the relatively large component of injection derived steam. IDS is a low-gas source of steam. It is an economic and environmental benefit to produce steam with lower gas concentration as less chemical abatement is required at the power plants. NCPA plans to inject water into wells located near the eastern and western boundaries of the steamfield with the dual purpose of mining the heat of the rock and decreasing the NCG production.

Figure 14 is a plot of NCG versus deuterium concentration. A trend showing lower gas concentration for steam wells with a greater concentration of deuterium (i.e., more IDS) indicates that injection decreases gas concentrations in produced steam.

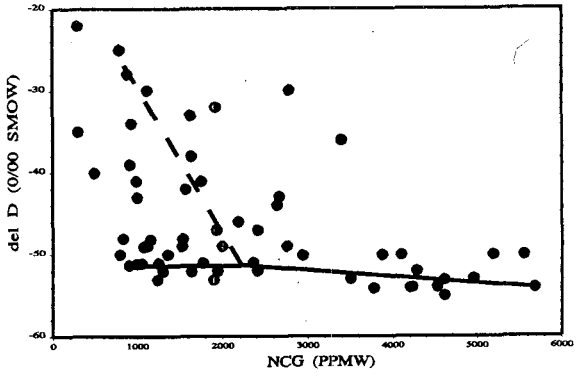

Fig. 14 NCG versus deuterium - July, 1991

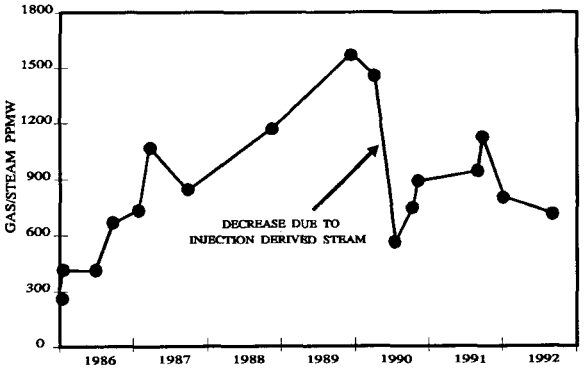

Fig. 15 Gas/Steam history, 1986-92

Steam well F-5 is an example of a well producing reduced concentrations of NCG as a result of increased IDS. The gas history for F-5 is plotted as Figure 15. The well is located within an area that has produced IDS since 1989. Gas concentration for F-5 steadily increased between 1987 - 1989. However, following startup of off-set injector C-11 and later F-1 gas concentration was reduced by approximately 50 percent.

CONCLUSIONS

1. MEQ activity related to injection indicates that liquid injectate is boiling near the injectors without significant migration deeper into the reservoir. The resulting injection derived steam is readily available for lateral migration within the reservoir.

2. Based on deuterium analysis, the flashed injectate is produced by wells located near the injectors. The areas strongly influenced by injection (-40 per mil or less) represent approximately 30 percent of the field, which is very close to the percent of steam returned as condensate. This suggests that the rate of production of IDS is almost equal to the rate of injection. Large areas of the reservoir are not receiving injection support due to the limited amount of available condensate.

3. Deuterium analysis also indicates that the production of injection derived steam increased between 1989 and 1992 to a high in 1992 of 950,000 pounds per hour or 26 percent of total flowrate potential. The amount of injectate being recovered as steam also increased to a high of 80 - 100 percent in 1992. The increase in IDS recovery is believed primarily due to the change in injection strategy. The new strategy results in the use of more injection wells located closer to the producing wells together with lower individual well injection rates.

4. Wells located within the injection areas show significant reductions in the rates of reservoir pressure and flowrate decline. Also, noncondensible gas concentrations have decreased in many steam wells influenced by injection.

5. Based on the above analysis, the overall impact of ten years of injection is clearly favorable. The benefits of augmenting condensate injection are increasing because the need for injection within the "dry" areas of the field continues to grow as the supply of condensate available for injection continues to decrease. NCPA presently views augmented injection as a reservoir management tool that will extend field life and increase electrical production from its geothermal power plants.

REFERENCES

Beall, J.J., S.L. Enedy, W. T. Box, (1992), "Recovery of Injected Condensate as Steam in the Southeast Geysers Field," Monograph on The Geysers Field, Special Report #17, Geothermal Resources Council, Davis, CA. pg. 151-158

Enedy, S. L., K. Enedy, J. Maney, (1992), "Reservoir Response to Injection in the Southeast Geysers," Monograph on The Geysers Field, Special Report #17, GRC, Davis, CA. pg. 211-220

Enedy, S., M. Grande, J. L. Smith, (1990), "A Case History of Steamfield Development, Reservoir Evaluation, and Power Generation in the Southeast Geysers," GRC Bulletin, October, 1990, pg. 223-248

Klein, C., S.L. Enedy, (1992), "Effect of Condensate Injection on Steam Chemistry at The Geysers Field," Monograph on The Geysers Geothermal Field, Special Report #17, GRC, Davis, CA. pg. 145-150

Reed, M. J., R. H. Mariner, "Quality Control Of Chemical And Isotopic Analyses Of Geothermal Water Samples," Proceedings, Sixteenth Workshop on Geothermal Reservoir Engineering, Stanford University, January 23-25, 1991, pg. 9-13

Stark, M.A., (1992), "Microearthquakes - A Tool to Track Injected Water in The Geysers Reservoir," Monograph on The Geysers Field, Special Report #17, GRC, Davis, CA. pg. 111-120

Truesdell, A.H., S.L. Enedy, J.L. Smith, (1993), "Geochemical Studies of Reservoir Processes in the NCPA Field Of The Geysers," Proceedings, Eighteenth Workshop on Geothermal Reservoir Engineering, Stanford University, January 26-28, 1993,

PROCEEDINGS, Eighteenth Workshop on Geothermal Reservoir Engineering
Stanford University, Stanford, California, January 26-28, 1993
SGP-TR-145

RESERVOIR ENVIRONMENT OF THE ONUMA GEOTHERMAL POWER PLANT, NORTHEAST JAPAN, ESTIMATED BY FORWARD ANALYSIS OF LONG-TERM ARTIFICIAL-TRACER CONCENTRATION CHANGE, USING SINGLE-BOX-MODEL SIMULATOR

Shigeno, Hiroshi,*1 Takahashi, Masaaki*2 and Noda, Tetsuro*3

*1 Geological Survey of Japan, Hokkaido Branch, Nishi-2, Kita-8, Kita-ku, Sapporo 060, Japan
*2 Geological Survey of Japan, Geothermal Research Department, Tsukuba 305, Japan
*3 Geological Survey of Japan, Environmental Geology Department, Tsukuba 305, Japan

ABSTRACT

A single-box-model numerical simulator for personal computer analysis was developed in order to estimate macroscopic parameter values for exploited geothermal reservoirs and essential fluids coming from the depth. The simulator was designed to compute history data concerning total production and reinjection fluids at geothermal power plants from the assumed parameter values, based on conservation laws for water mass, heat energy and masses of conservative chemical constituents of geothermal fluids. Using two kinds of forward analysis techniques, i.e. the cast-net and pursuit methods, programs containing the simulator can semiautomatically select the optimum combination of the unknown parameter values by minimizing the differences between the simulated and measured history data for specific enthalpy and chemical compositions of the production fluids.

The forward analysis programs were applied to the history data from the Onuma geothermal power plant (production capacity, 10MWe) where waste hot water reinjection, chemical monitoring and artificial tracer tests have been conducted since 1970, almost the beginning of the geothermal exploitation. Using the history data, enthalpy and iodine concentrations of the total production fluids with the amounts of KI tracer injected as spikes, the macroscopic parameter values for the exploited reservoir and the essential hot water from the depth were uniquely determined as follows: mass of the hot water convecting in the exploited reservoir (M0), 3.23×10^9kg; recycling fraction of the reinjected waste hot water to the reservoir (R), 0.74; specific enthalpy of the essential water from the depth (H1), 385kcal/kg; iodine concentration of the water (I1), 0.086mg/kg with chlorine concentration (C1), 259mg/kg. These results support the conceptual model that the exploited Onuma reservoir mainly in the Tertiary volcanics is supplied with the neutral Na-Cl type hot water of abnormally high B/Cl mole ratio of around 1.0 by a large essential reservoir distributed at depth in the Paleozoic to Mesozoic detrital marine sedimentary rocks.

INTRODUCTION

Producing large amounts of geothermal fluids for power generation causes dynamic changes in reservoir, such as boiling, cold groundwater invasion and essential fluid inflow from the depth. Reinjection of the produced hot waters after steam separation to the reservoir, as at most geothermal power plants in Japan mainly for the purpose of environmental protection, has a large effect on the changes. Therefore, it is very important to optimize allocation of geothermal wells, and their production and reinjection rates, through understanding the nature of these changes and predicting their future, for the purpose of long-term stable operation of geothermal power plants.

In Japan, monitoring concentrations of major chemical constituents in production fluids has been conducted at almost all the geothermal power plants. Also, artificial tracer tests have been tried at many Japanese geothermal power plants. These chemical history data have been analyzed by many kinds of methods for various objectives (e.g. Shigeno, 1992a).

Among these, the studies for the hydrothermal system of the Onuma geothermal power plant by Ito et al. (1978), Matsubaya and Kubota (1987), Kubota and Matsubaya(1987), and Kubota et al. (1989) are very important concerning not only the optimization of geothermal reservoir exploitation but also resource assessments of hydrothermal systems. They tried to estimate macroscopic values for the exploited reservoir, i.e. total amount of the hot waters convecting in the reservoir and recycling fraction of the reinjected waste hot waters to the reservoir, based on a single box model using artificial tracer (iodine ion, I) test data and chemical (especially chlorine ion, Cl) monitoring data. Concerning a well at the Palinpinon geothermal power plant in the Philippines, Malate and O'Sullivan (1991) reported an application of the similar lumped-parameter model to the analysis of the production fluid chemistry changes.

We developed semiautomatic forward analysis programs for personal computers in order to estimate macroscopic values for exploited geothermal reservoirs and essential geothermal fluids from the depth, through repetitions of single-box-model numerical simulations, using chemical monitoring data. These programs were applied to the monitoring data from the Onuma area, and the results were compared with those by the above papers, and with the previously proposed hydrothermal-system models for the Onuma area. In this paper, these methods and results were reported. For more details of this paper, refer to Shigeno et al. (1992b) and Shigeno (1992c).

ANALYTICAL METHOD

Single box model, and difference equations

Fig. 1 shows the very simple single box model of exploited hydrothermal systems used for the numerical simulations in this study. This model is based on Matsubaya and Kubota (1987). An exploited geothermal reservoir is represented by a single homogeneous box, in which only hot water circulates as the fluid phase (shown with suffix 0). Non-steady-state inflow to, and outflow from the reservoir box are as follows: an inflow of an essential hot water from the depth (1); outflows of total hot

water (2), and total steam (3) through all the production wells; and an inflow of the waste production hot water which was reinjected through all the reinjection wells and partly recycled. The total production fluid, the sum of the separated total hot water and steam (1+2), is shown with suffix P. Neither conductive heating by high-temperature sources from the depth nor cold sweep process of the heat stored in rocks by the reinjected waters in and around the reservoir is included in this model.

In this model, the total hot water convecting in the reservoir box, the fluid flow rates, and the recycling fraction of the reinjected total hot water to the reservoir are shown with M0 ($x10^9$kg), F ($x10^9$kg/y), and R, respectively. Time-series data used in the analysis are specific enthalpies (H kcal/kg), Cl concentrations (C mg/kg), and I concentrations (I mg/kg) of the above geothermal fluids. Amounts of KI, which was injected into the reinjection wells as spikes during tracer tests, are also used as time-series data (AI kg).

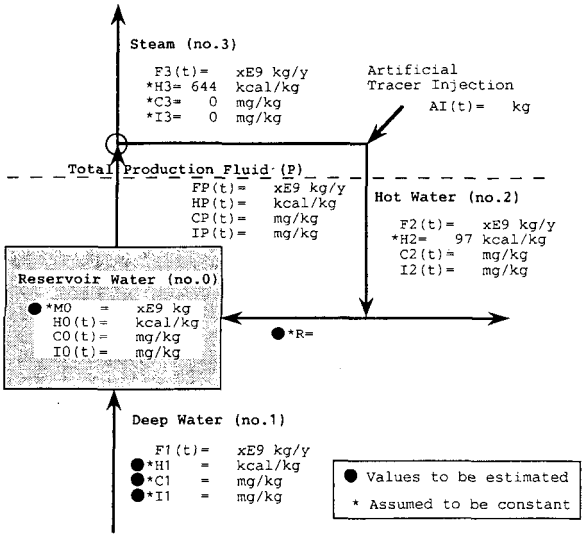

F: Flow rate *M0: Mass of convecting reservoir water
H: Specific enthalpy *R: Recycling fraction of reinjected water
C: Cl concentration *H1: Specific enthalpy of deep water
I: I concentration *C1: Cl concentration of deep water
AI: KI tracer amount *I1: I concentration of deep water

Fig. 1. Single box model of exploited hydrothermal system for numerical simulation forward analysis based on chemical history data.

Concerning the above single box model, the time difference equations {1} to {4} in Fig. 2 are assumed, based on the conservation laws of water mass, heat energy, and masses of Cl and I for the geothermal fluids. In addition to these, the equations {5} to {7}, and {8} to {11} are assumed for the relationships of the total production fluid and the hot water convecting in the reservoir, and for those of the total production fluid, and the hot water and the steam generated from the total fluid, respectively.

Algorithms of analysis, and programs

The objective of the present analytical method is to estimate systematically the unknown macroscopic parameter values for the exploited reservoir and the essential hot water from the depth, M0, R, H1, C1 and I1, when the history data of the production fluids, FP (or F2 and F3), HP (or H2 and H3), CP (or C2), and IP (or I2), as well as the history data of the artificial tracer injection (AI), are available.

The temporal changes of H0(t), C0(t) and I0(t) for the reservoir hot water, and of HP(t), CP(t) and IP(t) for the total production fluid can be simply numerically simulated using the history data of FP(t) and AI(t), based on the equations {1} to {11}, when the above five unknown parameter values are assumed, and the measured values of HP(1), CP(1) and IP(1) are used as the initial values, H0(0), C0(0) and I0(0). This is because the supplemental equations {5} to {11} are available, although the fundamental equations {1} to {4} are seemingly of implicit scheme. By the way, the measured values of HP(t), CP(t) and IP(t) are also available. Therefore, the optimum combination of the above parameter values can be obtained, using forward analysis methods, by minimizing the objective functions, σHP, σCP and σIP, which are defined by the equations {12} to {14} in Fig. 2.

In the present analytical method, the optimum combination of the unknown parameter values is semiautomatically determined by repeating the following two simple techniques, namely cast-net and pursuit methods. (1) Cast-net method (cover-all method): The parameter space, in which the objective functions have low values, is selected by systematic repetitions of the numerical

Fundamental equations:

$$M0 = M0 + F1(t)*\Delta t - (1-R)*F2(t)*\Delta t - F3(t)*\Delta t \quad \{1\}$$

$$H0(t)*M0 = H0(t-1)*M0 + H1*F1(t)*\Delta t - (1-R)*H2(t)*F2(t)*\Delta t - H3(t)*F3(t)*\Delta t \quad \{2\}$$

$$C0(t)*M0 = C0(t-1)*M0 + C1*F1(t)*\Delta t - (1-R)*C2(t)*F2(t)*\Delta t - C3(t)*F3(t)*\Delta t \quad \{3\}$$

$$I0(t)*M0 = I0(t-1)*M0 + I1*F1(t)*\Delta t - (1-R)*I2(t)*F2(t)*\Delta t - I3(t)*F3(t)*\Delta t + R*AI(t)*0.76*E6 \quad \{4\}$$

Supplemental equations:

$$HP(t) = H0(t-1) \quad \text{(Calculated)} \quad \{5\}$$

$$CP(t) = C0(t-1) \quad \text{(Calculated)} \quad \{6\}$$

$$IP(t) = I0(t-1) \quad \text{(Calculated)} \quad \{7\}$$

$$FP(t) = F2(t) + F3(t) \quad \{8\}$$

$$HP(t)*FP(t) = H2(t)*F2(t) + H3(t)*F3(t) \quad \{9\}$$

$$CP(t)*FP(t) = C2(t)*F2(t) + C3(t)*F3(t) \quad \{10\}$$

$$IP(t)*FP(t) = I2(t)*F2(t) + I3(t)*F3(t) \quad \{11\}$$

Parameters to be estimated:

M0 *E9 kg (Mass of convecting reservoir water)
R (Recycling fraction of reinjected water)
H1 kcal/kg (Specific enthalpy of deep water)
C1 mg/kg (Cl concentration of deep water)
I1 mg/kg (I concentration of deep water)

History data:

FP(t)	*E9 kg/y	
HP(t)	kcal/kg	(Measured)
CP(t)	mg/kg	(Measured)
IP(t)	mg/kg	(Measured)
AI(t)	kg	

Objectives: Estimate the M0, R, H1, C1 and I1 values (constants) that minimize σ_{HP}, σ_{CP} and σ_{IP}.

$$\sigma_{HP} = (\Sigma(HP(t)calc - HP(t)meas)^2/N)^{0.5} \quad \{12\}$$

$$\sigma_{CP} = (\Sigma(CP(t)calc - CP(t)meas)^2/N)^{0.5} \quad \{13\}$$

$$\sigma_{IP} = (\Sigma(IP(t)calc - IP(t)meas)^2/N)^{0.5} \quad \{14\}$$

Fig. 2. Equations, parameters to be estimated, history data and objective functions used for single-box-model numerical simulation forward analysis of exploited hydrothermal system.

simulations with the series of assumed parameter values, which are arranged to cover broad ranges with appropriate step sizes. (2) Pursuit method (gradient method): In the parameter space, values of the objective function(s) are calculated for a point of an initial combination of the parameter values, and for the adjacent points, at which one small step value is added to or subtracted from one of the parameter values, by a series of the numerical simulations. By this procedure, the point which has the lowest value(s) for the objective function(s) is selected. The same procedure is repeated around the newly selected point, until the point which has the optimum combination of the parameter values is settled. Two personal computer programs, which contain the single-box-model numerical simulator, were developed for the semiautomatic forward analysis of the chemical history data from exploited geothermal areas, based on the above two algorithms.

OUTLINE OF THE ONUMA AREA

The Onuma area is located in the Sengan regional geothermal field, Northeast Japan. Mitsubishi Metal Co. (presently Mitsubishi Materials Co.) has been conducting geothermal exploration and well drilling in and around this area since 1965, and began the operation of the Onuma geothermal power plant (capacity, 10MWe) in 1973.

The Onuma area is locate in an extension of the Hanawa graben of N-S trend. The Quaternary andesite composite volcanoes, Hachimantai and Akita-Yakeyama, are distributed to the east and west of the Onuma area, respectively. At the Onuma area, a hot-water system of around 215°C is developed at the exploited level, mainly along fractures, in the Neogene formations composed mainly of volcanic and pyroclastic rocks. The hot waters are basically of the neutral Na-Cl type with low Cl concentrations of about 400 mg/kg but abnormally high B/Cl mole ratio of around 1.0.

At the Onuma area, all the produced hot waters have been reinjected underground since the beginning of the geothermal exploitation (see Fig. 3). Ito et al. (1977, 1978) systematically conducted artificial tracer tests during 1975-76, by injecting KI tracer (total amount, 1500kg) into four reinjection wells (depth, 600-1200m), and measuring the changes of I ion concentrations at five production wells (depth, 1400-1800m). The fifth tracer test (KI, 300kg) was tried in 1983, using the temporarily-used reinjection well O-8R, when the production from the well O-10R began (Kubota et al., 1989).

Concentrations of major dissolved components in the hot waters from the production wells have been periodically measured at the Onuma area since the beginning of the geothermal exploitation. Kubota et al. (1989) reported the annual averages of the total production fluids, from 1970 to 1987, for the wellhead pressure, flow rate, specific enthalpy, Cl and I concentrations, Cl/B mole ratios, and the reservoir temperatures estimated by the SiO_2 and Na-K-Ca geothermometers.

The Sumikawa area, which is located about 1.5 km west to the Onuma area, has been under intensive geothermal exploration since 1981. Mitsubishi Materials Co. and Tohoku Electric Power Co., Inc. have been conducting well drilling and production tests with a schedule of opening a geothermal power plant (capacity, 50MWe) in 1995 (Sakai et al., 1986; Ueda et al., 1991).

FORWARD ANALYSIS OF THE ONUMA HISTORY DATA

Data and methods

Concerning this forward simulation analysis of the Onuma hydrothermal system, history data used were basically the annual average values of the total production fluids: flow rate (FP), specific enthalpy (HP) and I concentration (IP) during 1970-1987, and the injected KI tracer amount (AI) (Ito et al., 1978; Kubota et al, 1989). The changes of the allocation and the use of the wells during the period (Kubota et al., 1989), were not regarded in this study. The KI tracer injection into the O-8R well, which was temporarily used as a reinjection well in 1983 (Kubota et al., 1989), was not included in this analysis, because the KI tracer was seemingly not mixed with the hot waters convecting in the exploited reservoir.

The two kinds of the newly developed programs were used for the data analysis. The major unknown parameters determined were M0, R, H1 and I1, and the objective functions were σIP and σHP. The time-step numbers a year used for the numerical simulations were basically 4 times , but 12 times during 1974-1978 when the IP values rapidly changed due to the KI tracer injections. The assumed

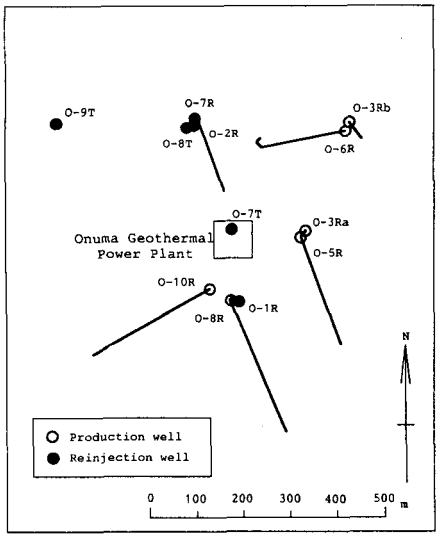

Fig. 3. Distributions of production and reinjection wells at the Onuma geothermal area (modified from Kubota et al. (1989)).

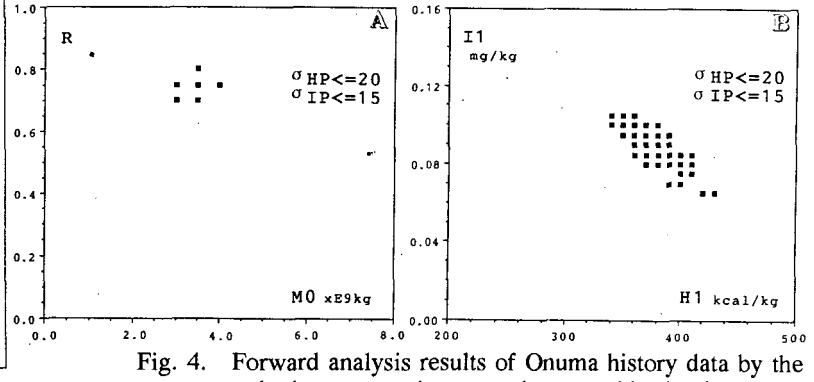

Fig. 4. Forward analysis results of Onuma history data by the cast-net method program using σIP and σHP as objective functions: Cases with suitable combinations of parameter values were projected on M0-R plane (A) and on H1-I1 plane (B).

parameter value, I1, was used as the initial I0 value for each case of the numerical simulations, because the IP values before 1974 were not available (Kubota et al., 1989). The objective function, σIP, was accordingly calculated for 1974-1987.

Results by the cast-net method

Table 1 shows an example of the data analysis by the cast-net method for the Onuma hydrothermal system. Fig. 4 (A) and (B) show the results of this example, plotting the points of suitable parameter-value combinations on M0-R and H1-I1 parameter planes, respectively. Fig. 4 indicates that the points gather in one place in the four-dimensional space, suggesting that the unique solution exists in the limited space. However, the correlations between σIP and σHP indicate that σIP and σHP do not take their minimum values at the same time. Hence, the point, at which the modified optimum condition that the lowest σIP value is obtained with the σHP value close to the minimum value is satisfied, was searched for. Based on these results for the large parameter space, the cast-net method was applied, several times, to the gradually limited space with smaller step sizes of the parameter values. As the result, the optimum combination of the parameter values, M0, R, H1 and I1, obtained were 3.23 x10^9kg, 0.74, 385 kcal/kg and 0.086 mg/kg, respectively.

Results by the pursuit method

Fig. 5 (A) and (B) show analytical results of one case by the pursuit method, in which σIP and σHP were used as the main and associate objective functions, respectively, plotting the pursuit trail on the M0-R and H1-I1 parameter planes. Fig. 6 shows the changes of the σIP and σHP values with increasing pursuit step numbers. The decrease of the σIP value by this pursuit was associated with the increase of the σHP value after passing the minimum point of the σHP value (no. 237). Hence, this point was selected to be appropriate as the solution point. All the parameter values of the above point were consistent with those obtained by the cast-net method. These results were certified by several times of applications of the pursuit method analysis with different initial parameter values.

Summary of the results

Using the optimum-value combination of the parameters, M0, R and H1, the optimum Cl concentration of 259 mg/kg was obtained by the cast-net method with the objective function, σCP. Fig. 7 shows the monthly

Table 1. An example of the cast-net method forward analysis using single-box-model numerical simulator for the history data (IP and HP) from the Onuma geothermal power plant (see Fig. 4).

(1) Run number: N-124

(2) Assumed parameter values:

		Minimum value	Maximum value	Step value	Number of cases
M0	*10^9kg	0.5	7.5	0.5	15
R		0.05	0.95	0.05	19
H1	kcal/kg	250	450	10	21
I1	mg/kg	0.050	0.150	0.005	21

(3) Objective functions: σ_{HP}<=20 and σ_{IP}<=15

(4) Total numbers of simulated cases: 125,685
Suitable cases for the objective functions: 70
Suitable case ratio: 0.000557

changes of HP, CP and IP, which were calculated by the numerical simulation method with the above optimum parameter values and 12 time-steps a year, in comparison with the measured values. The temperature of the essential hot water from the depth was calculated to be 342°C from the above optimum H1 value. Fig. 8 conceptually shows the reserves and the flows of water mass, heat energy and aqueous ions of Cl and I in and around the exploited geothermal reservoir of the Onuma area in 1976.

DISCUSSIONS FOR THE ONUMA HYDROTHERMAL SYSTEM

Comparisons of results obtained with single box models

Table 2 shows the macroscopic parameter values for the exploited reservoir at the Onuma area estimated by the previously reported studies and by this study, based on single box models using the artificial tracer test and chemical monitoring data. Matsubaya and Kubota (1987), Kubota and Matsubaya (1987), and Kubota et al. (1989) used the history data stabilized or changed in one year, assuming that the Cl and I concentrations of the essential hot water from the depth were equal to those of the total production fluids obtained at the initial stage of the geothermal exploitation.

The M0 value, which is about 30% smaller than the present result, by Matsubaya and Kubota (1987) using the changes of the Cl concentrations and the $\delta^{18}O(H_2O)$ values

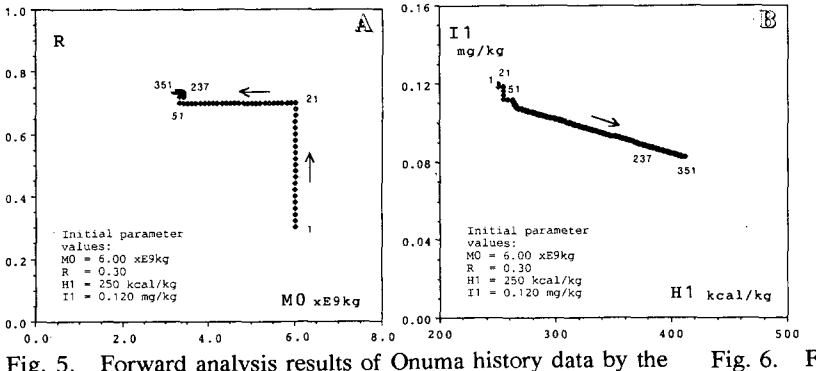

Fig. 5. Forward analysis results of Onuma history data by the pursuit method program using σIP with σHP as objective functions: Pursuit trail for more suitable combinations of parameter values was projected on M0-R plane (A) and on H1-I1 plane (B) (step numbers are shown in the figure; refer to Fig. 6).

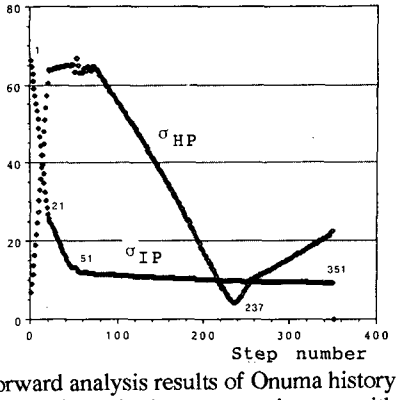

Fig. 6. Forward analysis results of Onuma history data by the pursuit method program using σIP with σHP as objective functions: Changes of σIP and σHP values along the pursuit trail for more suitable combinations of parameter values (refer to Fig. 5).

for the production fluids may indicate that the convection cell size of the exploited reservoir before 1976 was smaller than after 1976 due to the allocation of the wells. However, the smaller M0 value might be obtained by the less reliable calculation: the Cl concentrations and the $\delta^{18}O$ values showing relatively small temporal changes were used, and the Cl concentration and the $\delta^{18}O$ value of the essential hot water from the depth were assumed as mentioned above.

In contrast, the results by Kubota and Matsubaya (1987), and Kubota et al. (1989), using the changes of the I concentrations during 1976-1983, coincide with the present results, within 10% differences except the I1 value, when the assumed cold sweep effect of the reinjected hot water was imposed on the specific enthalpy of the essential hot water from the depth, H1. The high I1 values by Kubota and Matsubaya (1987), and Kubota et al. (1989) were probably caused by the procedure that the I1 value was assumed with the I concentration measured for the total production fluids in 1974, 0.11 mg/kg, which had already been concentrated by the geothermal exploitation. The other macroscopic parameter values estimated by Kubota and Matsubaya (1987), and Kubota et al. (1989) might change, to some extent, if the I1 value estimated by the present study had been used.

Deep hydrothermal environment at the Onuma area

At the Onuma area, the optimum total amount of the hot waters convecting in the exploited reservoir, M0, was estimated to be about 3.2×10^9kg, as shown in Fig. 8. For the Onuma power plant, the total amount of the geothermal fluids produced in a year, about 4.0×10^9kg, is fairly close

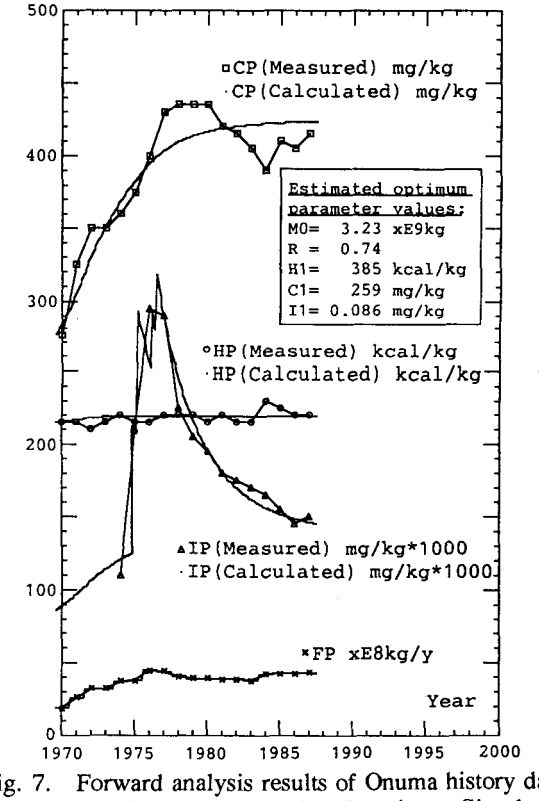

Fig. 7. Forward analysis results of Onuma history data using σIP and σHP as objective functions: Simulated temporal changes of IP, HP and CP with the optimum parameter values (calculated with 12 time steps/year).

Table 2. Comparisons of the macroscopic parameter values estimated by single-box-model calculations using the chemical history data for the Onuma hydrothermal system.

Study report		Ito et al. (1978)	Matsubaya & Kubota (1987)	Kubota & Matsubaya (1987)	Kubota et al. (1989)	Shigeno et al. (1992)
Applied data		IP 1975-1977	CP, HP 1970-1983?	IP, HP 1976-1983	IP, HP 1976-1983	IP, HP 1970-1987
M0	$*10^9$kg	5-8	2.0	3.0	3.1	3.23 *
R		-	0.71 (0.75) *1	0.70	0.70	0.74
H1	kcal/kg	-	-*2	-*2	230 *2 (359) *3	385
C1	mg/kg	-	-*2	-	275 *2	259
I1	mg/kg	-	-	-*2	0.110 *2	0.086

*1 $\delta^{18}O(H_2O)$ values of production fluids were used instead of CP.
*2 Assumed with the data obtained at the reservoir development initial stage.
*3 Corrected value by simply imposing heat energy derived by cold sweep effect estimated for recycling reinjected hot-water on deep essential water inflow.

to the value, and the total amount of the production fluids during 1970-1987, about 6.8×10^{10}kg (refer to Fig. 7), is more than 20 times the value. For this fluid mass outflow, only about 58% of the mass has been recharged by the waste hot-water reinjection, because neither the steam, about 22% of the total production fluids nor about 26% of the reinjected hot waters has returned to the exploited reservoir. Concerning the heat energy outflow associated with the large mass outflow, neither cold sweep process of the reinjected hot waters in and around the reservoir nor thermal conduction from the depth was probably sufficient to keep the enthalpy of the reservoir hot waters very constant through the 18 year operation history (see Fig. 7), especially if cold groundwater invasion to the reservoir occurred. These results indicate that the deep environment of the exploited Onuma reservoir is prosperous enough to supply the reservoir with large amounts of the high-temperature waters that have been able to compensate

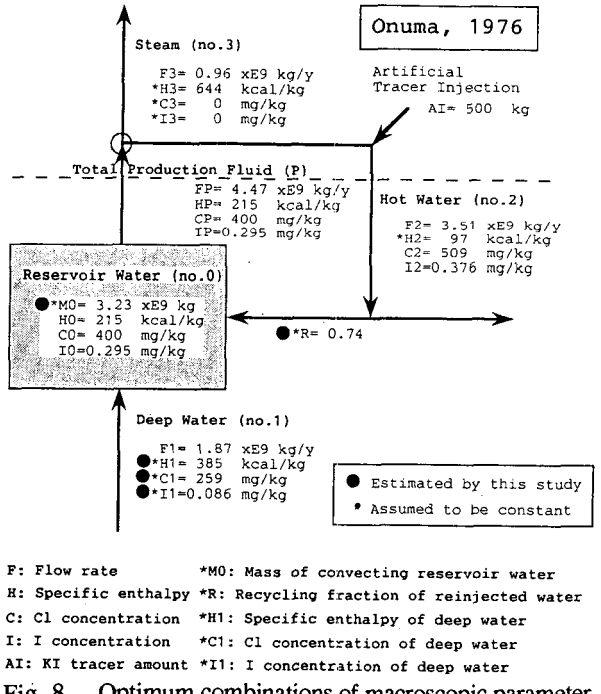

Fig. 8. Optimum combinations of macroscopic parameter values for the Onuma hydrothermal system estimated by single-box-model numerical simulation forward analyses based on chemical history data.

the above large losses of the water mass and the heat energy caused by the geothermal exploitation.

Shigeno and Abe (1983, 1987) suggested that a high-temperature hot-water convection system of meteoric water origin is developed in the basement rocks under the exploited reservoir at the Onuma area, based on the very high B/Cl mole ratios of about 1.0 for the neutral Na-Cl type hot waters of low salinity from hot springs and the geothermal wells, as well as on the geologic structures and the volcano distributions in and around this area. Namely, the essential geothermal reservoir is developed in the Paleozoic to Mesozoic detrital marine sedimentary rocks, which probably have relatively high porosity and permeability with abundant fractures, at the Onuma area, which is located in the extension of the Hanawa graben of N-S trend. And, the deep reservoir is probably heated mainly by the thermal conduction from the magma chambers of the two Quaternary composite volcanoes located to the east and west of the area. The results of the present study: the high recharge ratio of the deep essential fluid flow to the fluid production from the exploited reservoir, 0.42, and the low Cl concentration of the essential fluid, 259mg/kg, clearly support the above conceptual hydrothermal-system model. Also, the stable neutral pH and the slightly increasing high B/Cl ratios of the total production fluids observed by the long-term monitoring (Kubota et al., 1989) support the model.

The Na-Cl type reservoir hot waters from the Sumikawa area, which is also located in the extension of the Hanawa graben, show almost the same abnormally high B/Cl mole ratios of about 1.0 as those from the Onuma area with high temperatures (higher than 300°C at maximum) (Sakai et al., 1986; Ueda et al., 1991). These data suggest that the essential reservoir at the Sumikawa area is also developed at the depth in the Paleozoic to Mesozoic detrital marine sedimentary rocks. At the eastern part of the Sumikawa area, SN-7D well, which was drilled by the New Energy and Industrial Technology Development Organization, reached to the Neogene granitic rocks at about 2500m deep level, and discharged the neutral Na-Cl type hot water with the very high B/Cl mole ratio close to 1.0 (Ueda et al., 1991). By the pressure transient test of this well, the distribution of a large-scale reservoir of more than $3km^3$ was estimated at depth (e.g. Ishido, 1990). These results suggest that the shallow and deep geothermal reservoirs at the Onuma and Sumikawa areas are three-dimensionally connected, and have such a large-scale as of the whole width of the graben structure (Shigeno et al., 1992b; Shigeno, 1992c).

ACKNOWLEDGEMENTS

We are very grateful to Drs. Tsuneo Ishido, Yusaku Yano and Yoshinori Miyazaki, Geological Survey of Japan, for their helpful comments and suggestions.

REFERENCES

Ishido, T. (1990): Geothermal development through reservoir engineering. Jour. Japan Geothermal Energy Assoc., vol. 27, p. 73-92 (in Japanese with English abstr.).

Ito, J., Kubota, Y. and Kurosawa, M. (1977): On the geothermal water flow of the Onuma geothermal reservoir. Jour. Japan Geothermal Energy Assoc., vol. 14, p. 139-151 (in Japanese with English abstr.).

Ito, J., Kubota, Y. and Kurosawa, M. (1978): The tracer-tests applied at the Onuma geothermal power station, and the considerations about the geothermal reservoir and the water-shielding of the wells. Jour. Japan Geothermal Energy Assoc., vol. 15, p. 87-95 (in Japanese with English abstr.).

Kubota, Y. and Matsubaya, O. (1987): A box model of Ohnuma geothermal reservoir based on the changes in chemical and isotopic compositions of geothermal water (2). Abstr. 1987 Annual Meeting Geothermal Res. Soc. Japan, p. 84 (in Japanese).

Kubota, Y., Hatakeyama, K., Bamba, M. and Katoh, H. (1989): Chemical changes of Ohnuma geothermal fluid since operation and related reservoir management. Jour. Japan Geothermal Energy Assoc., vol. 26, p. 1-20 (in Japanese with English abstr.).

Malate, R. C. M. and O'Sullivan, M. J. (1991): Modelling of chemical and thermal changes in well PN-26 Palinpinon geothermal field, Philippines. Geothermics, vol. 20, p. 291-318.

Matsubaya, O. and Kubota, Y. (1987): A box-model of Ohnuma geothermal reservoir based on the changes in chemical and isotopic compositions of geothermal water. Abstr. 1987 Annual Meeting Geothermal Res. Soc. Japan, p. 83 (in Japanese).

Sakai, Y., Kubota, Y. and Hatakeyama, K. (1986): Geothermal exploration at Sumikawa, North Hachimantai, Akita. Jour. Japan Geothermal Energy Assoc., vol. 23, p. 281-302 (in Japanese with English abstr.).

Shigeno, H. and Abe, K. (1983): B-Cl geochemistry applied to geothermal fluids in Japan, especially as an indicator for deep-rooted hydrothermal systems. Extended Abstr. 4th Internat. Symp. on Water-Rock Interaction, Misasa 1983, p. 437-440.

Shigeno, H. and Abe, K. (1987): Conceptual hydrothermal system model for the Sengan area based on geochemistry of hot springs and fumaroles. Rept. Geol. Surv. Japan, no. 266, p. 251-283 (in Japanese with English abstr.).

Shigeno, H. (1992a): Applications of geochemistry in geothermal-field development of Japan. in D'Amore, F. ed., Applications of Geochemistry in Geothermal Reservoir Development, U. N. Institute for Training and Research, New York, p. 365-382.

Shigeno, H., Takahashi, M. and Noda, T. (1992b): Forward analyses of production fluid chemistry changes at the Onuma geothermal power plant, Northeast Japan, using a single-box-model numerical hydrothermal-system simulator. Bull. Geol. Surv. Japan, vol. 43, p. 573-594 (in Japanese with English abstr.).

Shigeno, H. (1992c): Estimating deep environments of hydrothermal systems based on geochemical data from Japanese geothermal power plants. Chishitsu Nyusu (Geology News), no. 457, p. 16-33 (in Japanese).

Ueda, A., Kubota, Y., Katoh, H., Hatakeyama, K. and Matsubaya, O. (1991): Geochemical characteristics of the Sumikawa geothermal system. northeast Japan. Geochem. Jour., vol. 25, p. 223-244.

PROCEEDINGS, Eighteenth Workshop on Geothermal Reservoir Engineering
Stanford University, Stanford, California, January 26-28, 1993
SGP-TR-145

THE INJECTION OF WATER INTO AND EXTRACTION OF VAPOUR FROM BOUNDED GEOTHERMAL RESERVOIRS

Shaun D. Fitzgerald & Andrew W. Woods

Institute of Theoretical Geophysics, Departments of Applied Mathematics
and Theoretical Physics, and Earth Sciences, University of Cambridge, England

ABSTRACT

When liquid is injected into a geothermal reservoir, a fraction of the liquid may vaporise if the reservoir is sufficiently hot. The vapour forms at an approximately planar liquid-vapour interface and diffuses towards the far boundary of the reservoir. If vapour is extracted from the far boundary, then once the new vapour has diffused across the reservoir, the rate of production of vapour at the liquid-vapour interface approximately balances the rate of extraction. We find that if the pressure at the injection pump and extraction well is fixed, then the fraction of the liquid which vaporises and the rate of extraction of vapour from the reservoir increase with time. However, the rate at which liquid is pumped into the reservoir may initially decrease but subsequently increases with time, if a sufficient fraction of the liquid vaporises. If the mass flux of liquid injected into the reservoir is fixed, then again both the fraction of the liquid which vaporises and the mass flux of vapour which may be extracted increase with time. In this case, the pressure at the injection pump may increase but subsequently decreases with time, again if a sufficient fraction of the liquid vaporises.

INTRODUCTION

Fluids extracted from vapour-dominated geothermal reservoirs such as The Geysers, California and Larderello, Italy have for many years been used to generate electricity. The successive developments of these geothermal reservoirs through the installation of new power plants and wells has increased the rate of extraction of the hydrothermal fluids. However, the exploitation of these reservoirs and the subsequent decrease in fluid levels has caused the average vapour pressures to fall. Consequently, the rate of extraction of vapour from the wells to supply power plants has also decreased (Kerr, 1991; Enedy, 1989). The rate of vapour extraction can be enhanced through the injection of water (Schroeder *et al.*, 1982; Bertrami *et al.*, 1985; Pruess *et al.*, 1987). Previous studies have investigated the production of vapour through the injection of water into an unbounded reservoir (Pruess *et al.*, 1987; Woods & Fitzgerald, 1992). It has been shown that as the rate of injection of liquid increases, the fraction of this liquid which can vaporise decreases but the total mass of vapour produced increases.

In this paper, we examine the behaviour of water injected at one boundary of a closed region as vapour is simultaneously extracted from a far boundary. Once the new vapour has diffused across the reservoir, the system typically attains a quasi-steady state if the vapour produced at the moving liquid-vapour front migrates across the reservoir more rapidly than the liquid-vapour front itself. We develop a simple model which may be used to investigate how the mode of injection of water affects the subsequent rate of extraction of vapour. We use this model to examine the long time response of the system if water is injected at a constant rate or with a constant pressure.

THE MODEL

As a highly simplified model, we consider the injection of water from a planar source into a one-dimensional porous rock of length L, porosity ϕ and permeability k. We restrict attention to flows in which the imposed pressure gradients exert much larger forces than the gravitational acceleration, and

we also neglect the effects of surface tension.

Just ahead of the point of injection, there is a liquid region of length $l(t)$ (figure 1) which advances into the reservoir with mass flux Q per unit area according to Darcy's Law

$$\rho_w u_w = Q = \left(\frac{k(P_p - P_I)}{\mu_l l} \right) \tag{1}$$

where P_p is the pressure at the pump, P_I is the pressure at the liquid-vapour interface, μ_l is the liquid viscosity, ρ_w the liquid density and u_w the liquid velocity.

Woods & Fitzgerald (1993) showed that the isotherms within the liquid region lag the advancing liquid-vapour interface so that the fluid is supplied to the liquid-vapour interface with the temperature of the interface. A fraction of this liquid vaporises at the interface and the vapour produced diffuses away from the migrating interface towards the far boundary where vapour is extracted (figure 1). We assume that the liquid and vapour are in thermodynamic equilibrium at the liquid-vapour interface and that the pressure and temperature are coupled by an empirical form of the Clausius Clapeyron relation

$$T_{sat}(P) = 6.7P^{0.23} \tag{2}$$

in the temperature range $150 < T < 240°\mathrm{C}$ (Haywood, 1972). The fraction of injected water which vaporises, F, is given by the Stefan condition across the moving interface

$$F = 1 - \frac{\phi\rho_w (h_{v\infty} - C_{pw}T_i)}{\phi\rho_w (h_{v\infty} - C_{pw}T_i) + (1-\phi)\rho_r C_{pr}(T_\infty - T_i)} \tag{3}$$

where h is taken to represent the specific enthalpy, C_p the specific heat capacity, ρ density, T_i the saturation temperature associated with the pressure at the liquid-vapour interface, subscript r a property of the rock and subscript ∞ to denote a property of the vapour at the far boundary (Woods & Fitzgerald, 1993). Since a fraction F of the liquid vaporises, the liquid interface moves with velocity $dl/dt = (1-F)u_w$. The maximum fraction of liquid which may vaporise occurs when the interfacial temperature attains the minimum value $T_{sat}(P_o)$ where P_o is the pressure at the site of extraction.

Woods and Fitzgerald (1993) have shown that ahead of the interface, the vapour is isothermal and of temperature equal to the far field of the rock. By coupling the Darcy equation with the equation of state for the vapour (Young, 1988), we obtain the nonlinear diffusion equation describing the vapour pressure

$$P_t = \alpha(PP_x)_x \tag{4}$$

where $\alpha = k/\phi\mu$ and μ is the dynamic viscosity of the vapour (Elder, 1981). Fitzgerald and Woods (1993a) have shown that for times longer than the typical diffusion time $\tau_d = \phi\mu L^2/kP_r$, where P_r is a reference pressure, the vapour distribution through the rock becomes quasi-steady, with the rate of production of vapour approximately equal to the rate of extraction. Typically, τ_d is of the order of 1 day - 1 month. In this quasi-steady regime, the mass flux of vapour produced from the vaporising liquid, FQ, is given by the first integral of the right hand side of (4), integrated from the liquid-vapour interface $x = l$ to the far-boundary of the reservoir, $x = L$ (figure 1),

$$FQ = \frac{k\rho_v(P_I^2 - P_o^2)}{(2\mu(L-l)P_o)} \tag{5}$$

Here ρ_v is the density of the vapour at pressure P_o and at the temperature of the rock, T_∞. This quasi-steady model, which we investigate below, is valid for times longer than the diffusion time τ_d. Furthermore, it requires that the rate of migration of the liquid-vapour interface is much slower than the rate of migration of vapour

$$F \gg \frac{1}{1 + \rho_w/\rho_v} \tag{6}$$

In all the calculations we present, condition (6) is satisfied.

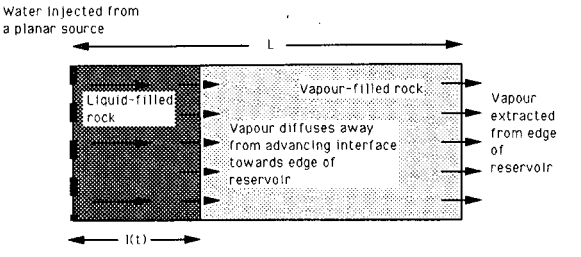

Figure 1. Schematic showing the flow configuration considered.

INJECTION AT A CONSTANT RATE

If water is injected at a constant rate into a bounded domain while vapour is simultaneously extracted from the far boundary at a constant pressure then, as the liquid-vapour interface advances further towards the far boundary, the distance that the liquid has to traverse increases. As a result, the difference in pressure between the liquid-vapour interface and the point of injection increases. In fact, the interfacial pressure decreases, and so the fraction of the injected liquid which vaporises actually increases, thereby producing a greater flux of vapour. This is a consequence of maintaining a fixed pressure at the point of extraction and may be understood in terms of the contradiction which arises if instead the interfacial pressure were to remain constant or increase - in this situation, the mass fraction of the injected liquid which vaporised would remain constant or decrease (equation 3); however, the flux of vapour required to satisfy Darcy's Law would increase, owing to the greater pressure gradient acting over the ever shrinking vapour region.

In figure 2 we show how the fraction of injected water which vaporises varies with time as water is injected at three different rates. After the initial diffusion time τ_d, the quasi-steady model calculations (solid lines) are indistinguishable from those obtained using a full numerical model in which the time-dependent diffusion equation for the vapour has been solved (see Fitzgerald and Woods, 1993b) (dashed lines). At low rates of injection, the pressure required to drive the vapour away from the liquid-vapour interface is relatively small. Consequently, the fraction of water which vaporises is initially larger than for high rates of injection. However, at high flow rates, the interfacial pressure falls more rapidly and so the mass fraction of water which vaporises increases towards the maximum value more rapidly. Eventually, there is a time at which a greater fraction of water vaporises at higher rates of injection.

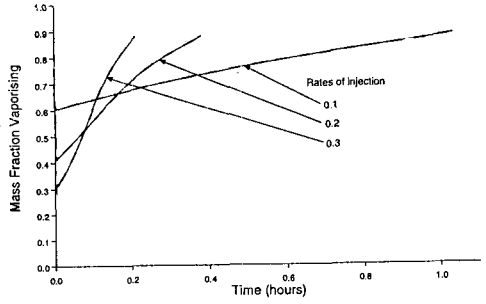

Figure 2. Mass fraction of injected water which vaporises as a function of time (hours). Water is injected from a planar source at a constant rate of 0.1, 0.2 and 0.3 kg/m^{2}s into the liquid region, intially of length 1 m, of a bounded rock of length 10 m while vapour is simultaneously extracted from the far boundary at a pressure of 6 bar. Quasi-steady model (solid) and full numerical model (dashed).

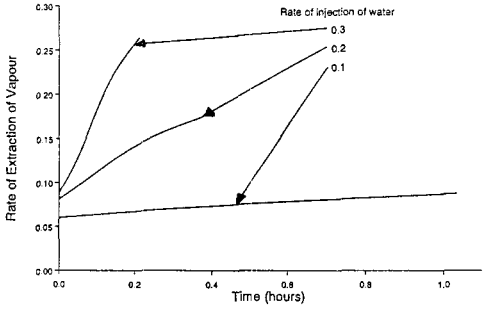

Figure 3. Rate of extraction of vapour (kg/m^{2}s) as a function of time (hours). Water is injected from a planar source at a constant rate of 0.1, 0.2 and 0.3 kg/m^{2}s into the liquid region, intially of length 1 m, of a bounded rock of length 10 m while vapour is simultaneously extracted from the far boundary at a pressure of 6 bar.

In our quasi-steady model, the mass flux of vapour extracted from the reservoir equals the rate of production of vapour at the liquid-vapour interface; this flux depends upon the rate of injection of water and the fraction of the injected water which vaporises. In figure 3 we show how the rate of extrac-

tion of vapour varies with time for the three injection rates used in figure 2. The rate of extraction of vapour increases with time as the mass fraction vaporising increases and is greater at higher flow rates, even though at early times, the mass fraction which vaporises is smaller (figure 2). Although the efficiency of injection may be low during early times, the rate of vapour production at the liquid-vapour interface is dependent primarily upon the rate of injection of water.

The pressure at the point of injection may vary non-monotonically with time as shown in figure 4. During early times, $t \sim \tau_d$, the increase in pressure difference across the liquid region occurs more rapidly than the decrease in interfacial pressure. Consequently, the pressure at the plane of injection rises. However, for times $t \gg \tau_d$, the decrease in interfacial pressure is more rapid than the increase in the pressure difference across the liquid region (as is required to maintain the constant liquid flow rate) and so the injection pressure falls.

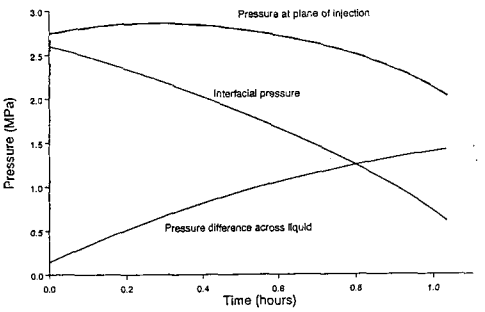

Figure 4. Pressure (MPa) as a function of time (hours). Water is injected from a planar source at a rate of 0.1 kg/m^{2}s into the liquid region, initially of length 1 m, of a bounded rock of length 10 m while vapour is simultaneously extracted from the far boundary at a pressure of 6 bar.

Note that in geothermal reservoirs of length scale 10^3 m and diffusivity 10^{-1}m^2/s, the transient diffusion-controlled period may last for up to several months. In these cases, the evolution towards the quasi-steady state is also of interest and recourse to a full numerical model is necessary (Fitzgerald and Woods, 1993b). During the transient period, the rate of extraction of vapour decreases significantly with time if the pressure at the extraction well is lower than that originally in the reservoir. However, as the new vapour advances into the reservoir and compresses the vapour originally in place, the rate of extraction increases towards those predicted by the quasi-steady model.

INJECTION AT A CONSTANT PRESSURE

The quasi-steady model of the simultaneous injection of water and extraction of vapour may be used to investigate the situation in which water is injected at a constant pressure. We again consider the injection of water from a planar source into a bounded domain. During early times, the pressure difference across the liquid region is relatively small and therefore, the interfacial pressure is approximately equal to the pressure at the point of injection. Consequently, the energy available for vaporisation is relatively small and the mass fraction which vaporises is low (equation 3; figure 5). As in the previous case of injection at a constant rate, the mass fraction which vaporises increases as the size of the liquid region increases and the interfacial pressure decreases. The mass fraction which vaporises during early times is lower when the pressure at the plane of injection is high. However, the rate of addition of water is greater when the injection pressure is high and thus the liquid-vapour interface advances more rapidly. This causes the interfacial pressure to decrease more rapidly with time and the mass fraction which vaporises increases more rapidly at high injection pressures (figure 5).

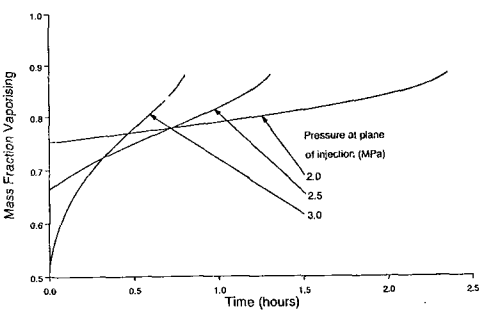

Figure 5. Mass fraction of injected water which vaporises as a function of time (hours). Water is injected from a planar source at a constant pressure of 2, 2.5 and 3 MPa into the liquid region, initially

of length 1 m, of a bounded rock of length 10 m while vapour is simultaneously extracted from the far boundary at a pressure of 6 bar.

For injection at a large constant pressure, the rate of injection of water initially decreases with time as the size of the liquid region, and hence pressure difference across the liquid, increases (figure 6).

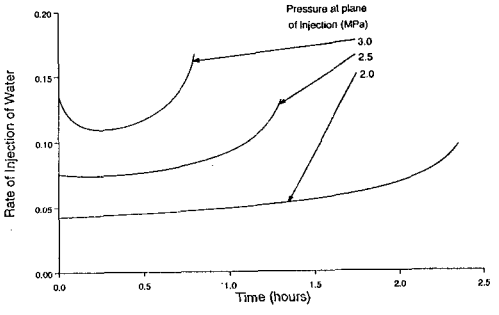

Figure 6. Rate of injection of water (kg/m^{2}s) as a function of time (hours). Water is injected from a planar source at a constant pressure of 2, 2.5 and 3 MPa into the liquid region, initially of length 1 m, of a bounded rock of length 10 m while vapour is simultaneously extracted from the far boundary at a pressure of 6 bar.

However, as the liquid-vapour interface approaches the far boundary, the interfacial pressure decreases rapidly since the mass transfer ceases to be rate limited by the diffusion of vapour. This results in an increase in the flux of water into the system and also the mass fraction which vaporises. At low injection pressures, the flux of water injected into the reservoir increases monotonically with time because the transport of a relatively small flux of vapour across the reservoir does not suppress the vaporisation process as much, and so the interface pressure is smaller *ab initio*.

The rate of extraction of vapour is a function of both the rate of injection of water and the mass fraction which vaporises (figure 7). It increases monotonically with time for all cases considered.

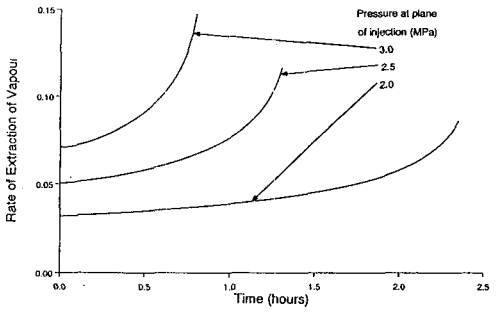

Figure 7. Rate of extraction of vapour (kg/m^{2}s) as a function of time (hours). Water is injected from a planar source at a constant pressure of 2, 2.5 and 3 MPa into the liquid region, initially of length 1 m, of a bounded rock of length 10 m while vapour is simultaneously extracted from the far boundary at a pressure of 6 bar.

Again, these results are valid only for times greater than the timescale of diffusion of vapour across the reservoir. As in the case of injection at a constant rate, during the transient period before the quasi-steady state has been attained, the rate of vapour extraction may decrease significantly with time if the pressure at the extraction well is lower than that originally in the reservoir.

CONCLUSIONS

The rate of extraction of vapour from a geothermal reservoir can be significantly increased through the injection of water. In quasi-steady state, the rate of production of vapour from the liquid is approximately equal to the rate of extraction. If water is injected at one point while vapour is simultaneously extracted from a second point (figure 1), then the rate of production of vapour increases with time, particularly at high pressures or high rates of injection. In contrast, if liquid is injected into a bounded reservoir and vapour is *not* extracted then the production of vapour is suppressed as the interfacial pressure increases.

The mass fraction which vaporises increases with time for both injection at a constant pressure and with a constant liquid flow rate. In both cases, the total flux of vapour extracted from the reservoir increases with time. Initially, most of the pressure drop across the reservoir occurs across the new vapour, since this must migrate across a large fraction of the reservoir; however, with time, the ever increasing efficiency of vaporisation causes a rapid decrease in the interface pressure, changing the dynamic response of the system. For injection at constant pressure, the mass flux of liquid may initially decrease but then increases as the vaporisation efficiency increases. In contrast, for injection with constant liquid flux, the pump pressure may initially increase but then decreases as the vaporisation efficiency increases. Only in the extreme case in which a very small fraction of the liquid vaporises is the process rate-limited by the migration of the liquid (Fitzgerald and Woods, 1993).

REFERENCES

Bertrami, R., Calore, C., Cappetti, G., Celati, R. & D'Amore, F. 1985 A three-year recharge test by reinjection in the central area of Larderello field: analysis of production data. *Geoth. Res. Counc., Trans.* **9**(2), 293–298.

Elder, J. 1981 Geothermal systems, Academic Press.

Enedy, K.L. 1989 The role of decline curve at The Geysers. *Geoth. Res. Counc., Trans.* **13**, 383–391.

Fitzgerald, S.D. & Woods, A.W. 1992 Vapour generation in a hot permeable rock through injection of water. *Proc. Stanford Workshop on Geoth. Res. Eng.* **17**.

Fitzgerald, S.D. & Woods, A.W. 1993a Vapour flow in a hot porous rock. *J. Fluid Mech., subjudice.*

Fitzgerald, S.D. & Woods, A.W. 1993b The injection of water into and extraction of vapour from a geothermal reservoir. *Geothermics, subjudice.*

Haywood, R.W. 1972 Thermodynamic tables in SI (metric) units, Cambridge University Press.

Kerr, R.A. 1991 Geothermal tragedy of the commons. *Science* **253**, 134-135.

Pruess, K., Calore, C., Celati, R. & Wu, Y.S. 1987 An analytical solution for heat transfer at a boiling front moving through a porous medium. *Int. J. Heat Mass Trans.* **30**(12), 2595-2602.

Schroeder, R.C., O'Sullivan, M.J., Pruess, K., Celati, R. & Ruffilli, C. 1982 Reinjection studies of vapour-dominated systems. *Geothermics* **11**(2), 93–119.

Woods, A.W. & Fitzgerald, S.D. 1993 The vaporisation of a liquid front moving through a hot porous rock. *J. Fluid Mech., in press.*

Young, J.B. 1988, An equation of state for steam for turbomachinery and other flow calculations. *J. Eng. Gas Turbines Power* **110**, 1–7.

PROCEEDINGS, Eighteenth Workshop on Geothermal Reservoir Engineering
Stanford University, Stanford, California, January 26-28, 1993
SGP-TR-145

ROCK THERMAL CONDUCTIVITY AT THE CAP ROCK AND INITIAL CONDITIONS IN TWO-PHASE VOLCANIC HYDROTHERMAL SYSTEMS

Mario César Suárez Arriaga

Gerencia de Proyectos Geotermoeléctricos
Comisión Federal de Electricidad. Fax : (45) 144735
A.P. 31-C, 58290 Morelia, Michoacán, México.

ABSTRACT

Numerical experiments are performed to investigate the rock thermal conductivity influence in the formation of the thermodynamic initial conditions of two-phase systems located in volcanic rocks. These systems exhibit pressure and temperature profiles characterized by a sudden change or discontinuity in their vertical gradients. Vapor dominated, two-phase fluids are found at the upper reservoir's levels. Liquid is the dominated phase within the layers below some critical point.

Numerical results presented in this paper, suggest that the vertical location of this point of discontinuity be controlled by the thermal conductivity existing between the limit of the reservoir and the caprock. Too high values could originate liquid dominated reservoirs. Small values would be at the origin of vapor dominated reservoirs. A characteristic middle value could be responsible for the formation of a counter flow mechanism originating the initial conditions observed at some locations of the Los Azufres, Mexico, geothermal field.

INTRODUCTION

In several volcanic geothermal fields, the temperature difference between top and bottom of the reservoir is remarkable. For example, at Tejamaniles, the southern sector of the Los Azufres, Mexico hydrothermal system, the deepest drilled well (Az-47) has a temperature of 358 °C at the bottom (2964 meters depth); while at the surface the average temperature is about 15 °C. In this sector, the measured thermal conductivity has a mean value of 1.86 W/m/°C (Contreras et al, 1988). Thus the average conductive heat flow is about 0.22 W/m^2, corresponding to an average thermal gradient of 0.12 °C/m. A value four times the normal geothermal gradient of the Earth's surface (0.03 °C/m). At Los Humeros, Mexico the temperature difference is about 400 °C between the bottom (2847 m depth) and the surface, which corresponds to an average thermal gradient of 0.14 °C/m; with an average measured thermal conductivity of 2 W/m/°C (Contreras et al, 1990). This originates a conductive heat flow of about 0.28 W/m^2. In this paper, the effect of thermal conductivity on the initial thermodynamic state at the Tejamaniles geothermal subsystem is discussed.

THERMAL CONDUCTIVITY AND INITIAL STATE

The rock thermal conductivity within any geothermal reservoir is a clue parameter to the conductive heat flow, to the distribution of temperatures and to the definition of a barrier to hold the accumulated energy. The thermal conductivity of volcanic rocks depends mainly on the characteristics of its mineral elements, on the conductivity of the fluids filling the pores and on the size and geometry of the pore space (Zimmerman, 1988).

At Los Azufres, the rocks that have been found to form the reservoir's lithology are fractured andesites, rhyolites and some dacites. The andesites forming the reservoir show several degrees of hydrothermal alteration (Viggiano,1987). An impervious cap rock overlying the reservoir, is formed by rhyolites having zero or very low local permeability associated to small fractures and cracks. A cap rock just obstructs the escape of mass and heat through convection. But the heat loss through conduction is only partially prevented by the rhyolites. Two questions emerge: a) What amount of thermal energy outflows from the reservoir to the atmosphere ? b) How this loss influences the natural thermodynamic conditions of the reservoir ?

The natural state observed at Los Azufres, showed that vertical pressure and temperature gradients were small between 1700 - 2250 masl, showing nearly vaporstatic conditions. From 0 to 1700 masl the observed gradients correspond to boiling hydrostatic conditions (Fig.1).

Fig. 1.- TEMPERATURE AND PRESSURE PROFILES AT TEJAMANILES

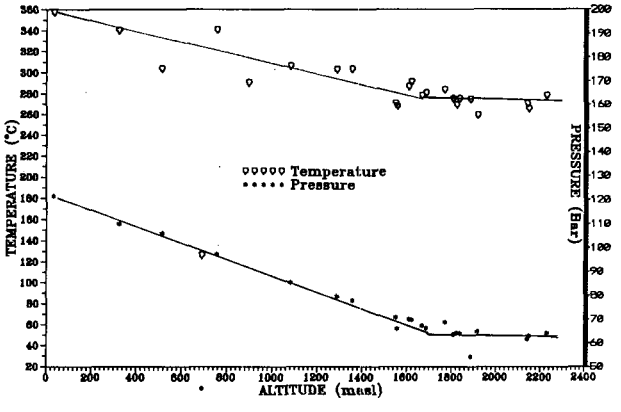

Thereafter the thermodynamic gradients have a discontinuity in the vicinity of 1700 masl. This discontinuity appears also in the vertical distribution of the rock thermal conductivity, having the critical point located around 1800 masl.

Several petrophysical measurements were performed in drilling cores from Los Azufres geothermal field. The reported results involved thermal and mechanical properties belonging to 24 cores of 17 wells (Contreras et al,1988). The measured properties are: density of dry rock, porosity (total and effective), absolute permeability, rock compressibility, Young and Poisson's modulus, specific heat, thermal difussivity and thermal conductivity.

Figure 2 shows the vertical distribution of thermal conductivity of cores from wells in the southern sector. Assuming a linear relation between K_T and the altitude Z, the resulting graph suggests that around 1850 masl, the slope of the straight line changes abruptly.

The functional relation $K_T(Z)$ is approximately represented by the following model (R^2 is the correlation coefficient):

$$K_T(Z) = 1.87 - 1.76\ 10^{-4}\ Z \quad [W/m/°C]$$
$$\text{if } Z \in [-79,1850] \text{ masl; } R^2=0.93$$

$$K_T(z) = 7.65 - 2.66\ 10^{-3}\ Z \quad [W/m/°C]$$
$$\text{if } Z \in [1850,2850] \text{ masl; } R^2=1.0$$

The slope discontinuity is:

$$\{\text{slope}\}_{1850} = 2.66\ 10^{-3}/1.76\ 10^{-4} = 15.11$$

On the other hand, the vertical thermal gradient is heterogeneous at Tejamaniles, as is illustrated in Table 1. From this table it is implied that in the portions of the reservoir with no evidence of cap rock (wells Az-7 and Az-8), the shallow thermal gradient is 7 to 10 times larger than the normal gradient, suggesting the existence of an important heat outflowing the reservoir by conduction. The cap rock reduces considerably the thermal gradient at the same depth (well Az-26). Below the rhyolites the thermal gradient increases rapidly until it reaches a zone where the temperature is almost constant. The thermal gradient at well Az-10, outside the reservoir, corresponds to a normal geothermal gradient. These simple facts originate a plausible hypothesis: The caprock obstructs partially the loss of heat by conduction. Possibly the value of its thermal conductivity could greatly affect the formation of the natural thermodynamic conditions of two-phase reservoirs.

Table 1.- SOME THERMAL GRADIENTS MEASURED AT TEJAMANILES.

WELL	dT/dZ (°C/m)	DEPTH (m)	ROCK TYPE
Az-07	0.21	300	Andesites
Az-07	0.31	500	Andesites
Az-08	0.34	400	Andesites
Az-10	0.07	100	Out of the Reservoir
Az-10	0.03	500	"
Az-26	0.06	100	Rhyolites
Az-26	0.11	400	Rhyolites
Az-26	0.54	600	Andesites
Az-26	0.84	700	Andesites
Az-26	0.01	1200	Andesites

Figure 2.- THERMAL CONDUCTIVITY AT TEJAMANILES

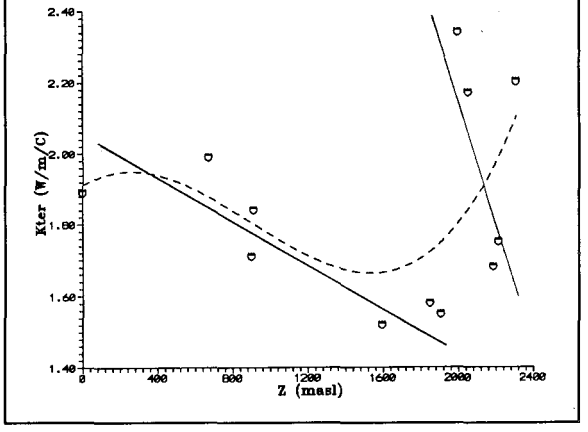

NUMERICAL EXPERIMENTS

To understand the thermal conductivity influence on the behavior of this type of system, a number of steady state simulations were performed. The complex real geology was idealized by a vertical section with 10^4 m^2 cross sectional area and a total depth of 3000 m. The geometric model is divided into 15 single-porosity elements (Fig.3). Thirteen elements (Tej N, N=1,13) represent the permeable reservoir. Element AQUITARD, with fixed boundary conditions (T=350°C; P=171 bar), represents the bottom of the andesitic column in contact with an assumed deeper HORNFELS of 500 m total thickness and acting as a continuous heat source. Element Tej01 is overlaid by a caprock of 600 m total thickness, which is connected at the top to a larger element representing atmospheric boundary conditions (T=15 °C; P = 0.73 bar).

Other parameters (most obtained from actual field data) for the numerical simulations are given in Table 2. The calculations were performed using the LBL code MULKOM, with a water-carbon dioxide equation of state (Pruess, 1988).

DISCUSSION OF RESULTS

A first simulation started from uniform thermodynamic conditions throughout the system. In response to the temperature difference at the bottom, the system goes through a very long transient evolution, reaching a steady

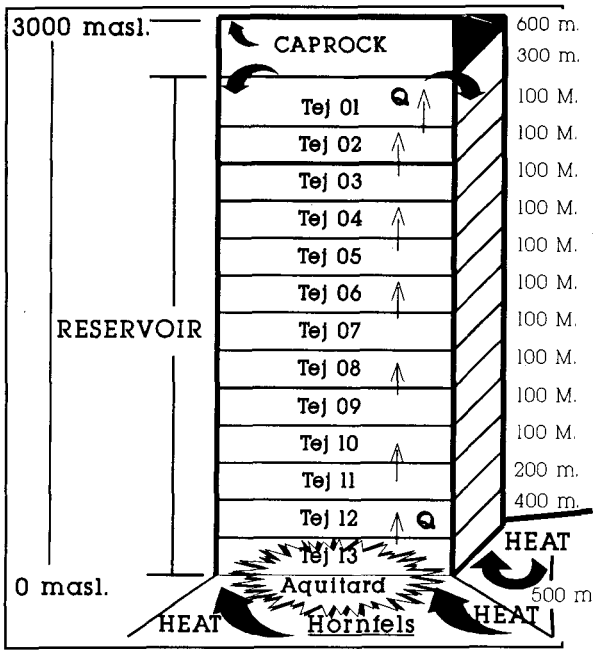

Fig.3- Vertical Geometric Model.

state. The steady state conditions achieved in the first experiment were used as initial conditions for subsequent simulations. Keeping the initial parameters shown in Table 2, several simulations were performed, with different values of K_T at the caprock and with the same boundary conditions. Different steady states were achieved for each value of thermal conductivity at the caprock. Results for ten states are presented in figures 4-7. Figs. 4 and 5 show that a value of $K_T \approx 0.175$ W/m/°C reproduces observed P and T profiles at Tejamaniles. On the other hand, the lowest thermal conductivity value measured in available drill cores is 1.05 W/m/°C. The shorter K_T required, can be interpreted as a simple weighted average of different mineral and fluid components, each having its own thermal conductivity. More complex averages were shown by Zimmerman (1988). Furthermore, results of McKibbin & Pruess (1988), and of Suárez,Pruess & Lippmann (1989), showed that CO_2 tends to accumulate in a condensation zone at the upper limit of the reservoir. A series model can be used to obtain the desired effective average value of K_T:

$$K_T^{-1} = (1-\phi)\, K_{rock}^{-1} + \phi\, K_{fluid}^{-1}$$

Assuming a porosity $\phi = 10$ %, $K_{rock} = 1.65$ W/m/°C and $K_{fluid} = 0.02$ W/m/°C (gas).
The corresponding $K_T = 0.18$ W/m/°C (!)

CONCLUSIONS

The numerical simulations described, proved that natural thermodynamic conditions existing in some regions of two-phase systems such as Los Azufres reservoir, are remarkably influenced by the thermal conductivity of the caprock. The breaks in pressure and temperature profiles, the associated sharp drop in vapor saturation and the vertical position of the discontinuity point, are controlled by the thermal conductivity value at the reservoir/caprock interface. High values could give origin to liquid dominated reservoirs. Small values would originate vapor dominated reservoirs at high temperature. A middle effective value could be the cause of the initial conditions at Los Azufres geothermal field.

REFERENCES

CONTRERAS E.,DOMINGUEZ B.,IGLESIAS E.,GARCIA A.,HUITRON R.,(1988). "Compendio de Resultados de Mediciones Petrofísicas en Núcleos de Perforación del Campo Geotermico de Los Azufres,Mich.", Geotermia-Revista Mexicana de Geoenergia, Vol.4 No.2, pp. 79-105.

CONTRERAS E.,DOMINGUEZ B. AND RIVERA,O., (1990). "Mediciones Petrofísicas en Núcleos de Perforación del Campo Geotérmico Los Humeros", Geotermia - Revista Mexicana de Geoenergia, Vol.6 No.1, pp. 7-42.

IGLESIAS E.,ARELLANO V.,(1988). "El Campo Geotérmico de Los Azufres: Prototipo de los Sistemas Hidrotermales "VAPLIQ". Geotermia-Revista Mexicana de Geoenergia, Vol.4. No.1, (pp. 229-246).

McKIBBIN R., PRUESS K.,(1988). "Some effects of Non-Condensible Gas in Geothermal Reservoirs with Steam-Water Counterflow". (LBL-24973), 13th Workshop on Geothermal Reservoir Engineering, Stanford Ca.

PRUESS K.,(1988). "SHAFT, MULKOM, THOUGH: A Set of Numerical Simulators for Multiphase Fluid and Heat Flow." Geotermia-Revista Mexicana de Geoenergía, Vol.4, No.1, pp. 185-202.

SUÁREZ,C.,PRUESS,K. Y LIPPMANN,M. (1989). "Preliminary Modeling Studies on Los Azufres Geothermal Field: Free Convection in Tejamaniles." Proceedings: Symposium in the Field of Geothermal Energy; Agreement DOE-CFE. San Diego, Ca., April 4-5, 1989, pp.161-184.

VIGGIANO,J. (1987). "Régimen de Flujo en base a Mineralogía Autigénica en el Campo Geotérmico de Los Azufres, Mich." GEOTERMIA-Revista Mexicana de Geoenergia, Vol.3, No.3, pp. 191-213.

ZIMMERMAN,R. (1988). "Thermal Conductivity of Fluid-Saturated Rocks." Preprint LBL-25197. Lawrence Berkeley Laboratory, Earth Sciences Division.

Table 2.- PARAMETERS USED IN THE SIMULATIONS

Thickness (m)	Element	Rock Density (kg/m^3)	Porosity (%)	Vertical Permeability (m^2)	Initial Pressure (bar)	Initial Temp. (°C)	Initial Partial $P(CO_2)$	Thermal Conductivity (W/m/°C)
-	ATMOS	-	-	$1.0\ 10^{-12}$	0.73	15	$3.\ 10^{-4}$	0.025
600	CAP01	2251	1.95	$1.0\ 10^{-20}$	55	265	5	K_T
300	TEJ01	2355	11.95	$1.0\ 10^{-14}$	55	265	5	1.65
100	TEJ02	2434	8.32	$1.0\ 10^{-15}$	55	265	5	2.19
100	TEJ03	2434	8.32	$1.0\ 10^{-15}$	55	265	5	2.45
100	TEJ04	2434	8.32	$1.0\ 10^{-15}$	55	265	5	2.72
100	TEJ05	2434	8.32	$1.0\ 10^{-15}$	55	265	5	1.56
100	TEJ06	2434	8.32	$1.0\ 10^{-15}$	55	265	5	1.58
100	TEJ07	2528	5.50	$1.0\ 10^{-15}$	55	265	5	1.59
100	TEJ08	2528	5.50	$1.0\ 10^{-15}$	55	265	5	1.61
100	TEJ09	2528	5.50	$1.0\ 10^{-15}$	55	265	5	1.63
100	TEJ10	2528	5.50	$1.0\ 10^{-15}$	55	265	5	1.65
100	TEJ11	2677	2.95	$1.0\ 10^{-15}$	55	265	5	1.66
200	TEJ12	2677	2.95	$1.0\ 10^{-15}$	55	265	5	1.69
400	TEJ13	2677	2.95	$1.0\ 10^{-15}$	55	265	5	1.74
500	ACUIT	2834	1.59	$1.0\ 10^{-18}$	171	350	1	1.82

K_T (W/m/°C)	0.100	0.125	0.150	0.175	0.200	0.225	0.300	0.460	0.600	1.000

Complementary Parameters

Rock Specific Heat = 1165 J/kg/°C (homogeneous)
Residual Liquid Saturation = 0.30 Residual Vapor Saturation = 0.05 {Corey's Relations}
Diffusive Vapor Flux Coef. = $1.38\ 10^{-5}$ m^2/seg
Initial Steam Saturation = 0.30
Capillary Pressure --------- neglected

Fig.4 – VERTICAL PRESSURE DISTRIBUTIONS

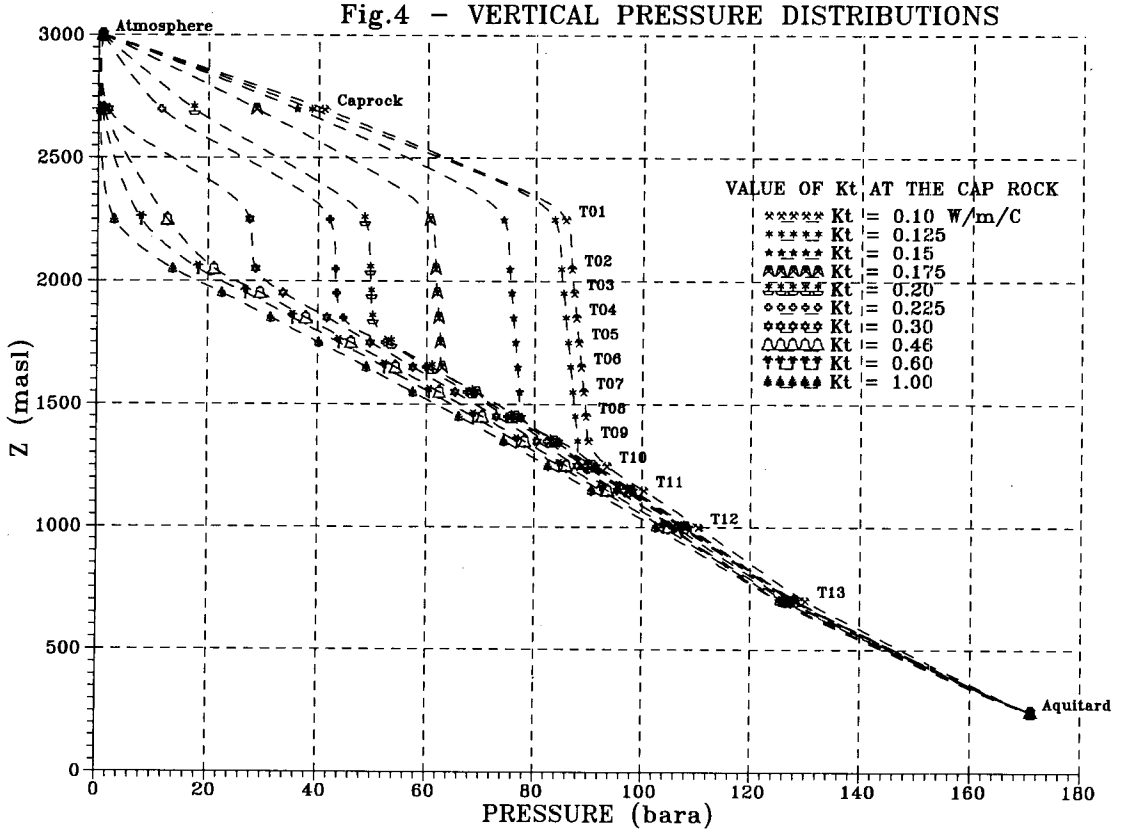

Fig.5 – VERTICAL TEMPERATURE DISTRIBUTIONS

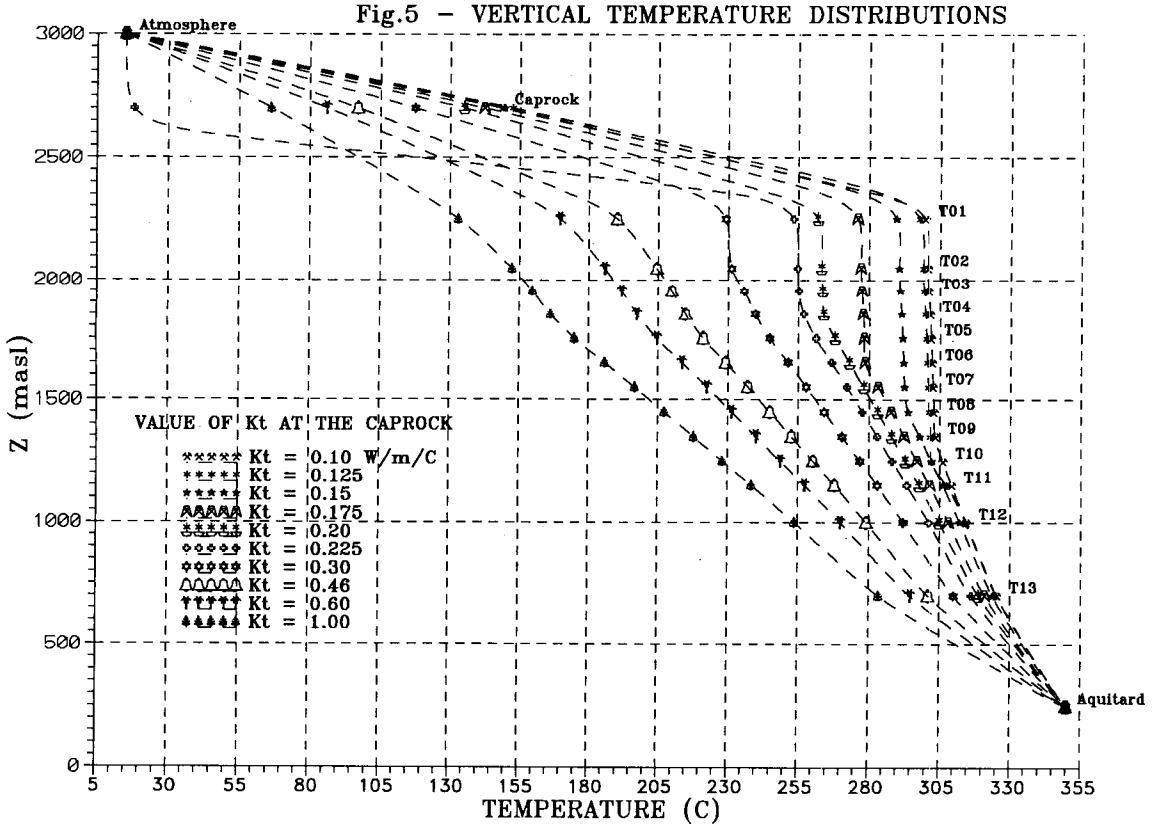

Fig.6 – VAPOR SATURATION AND Kt.

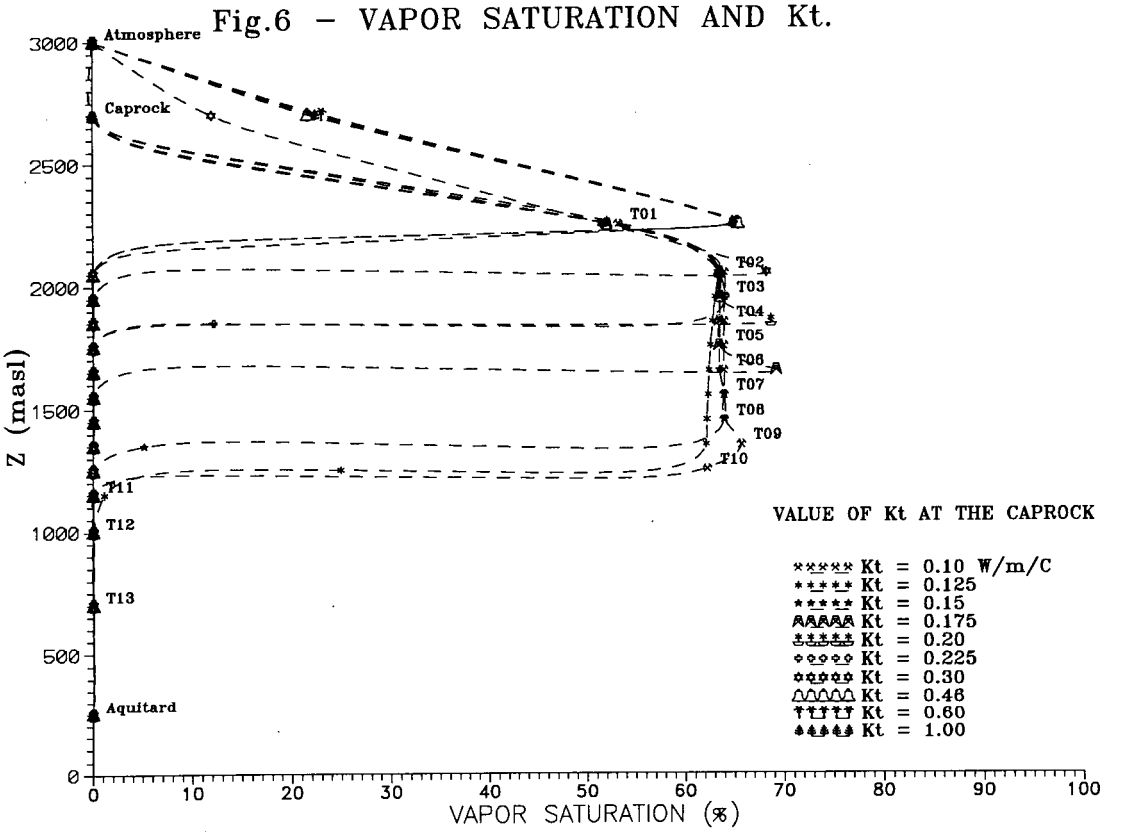

Fig.7 – PARTIAL PRESSURE OF CO2 AND Kt .

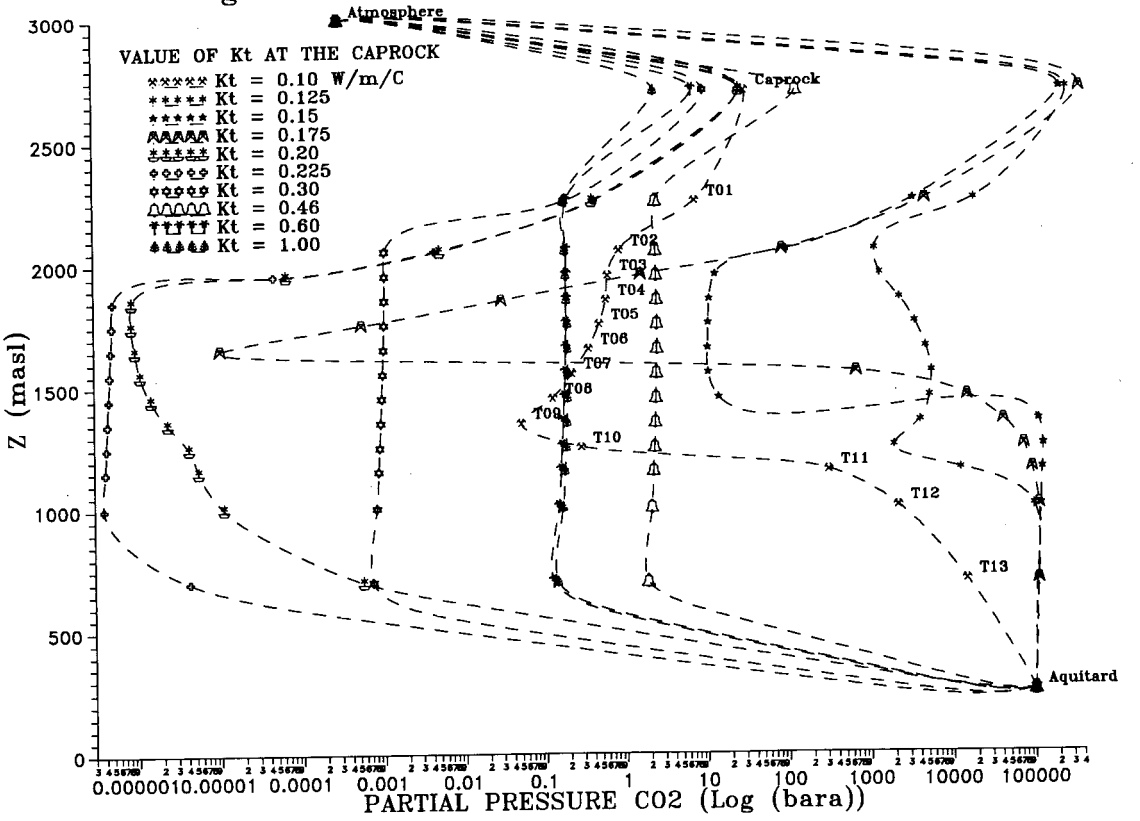

PROCEEDINGS, Eighteenth Workshop on Geothermal Reservoir Engineering
Stanford University, Stanford, California, January 26-28, 1993
SGP-TR-145

NUMERICAL MODELING OF THE EVOLUTION OF TWO-PHASE ZONE UNDER FISSURED CAPROCK

Y. Yano and T. Ishido

Geological Survey of Japan
Higashi 1-1-3
Tsukuba 305, Japan

ABSTRACT

A vapor-dominated two-phase zone would be formed in a geothermal reservoir under fissured caprock, if the permeability of the fissure is much smaller than a critical permeability which is estimated by an energy balance. If the permeability of the fissure is large, then the rule of minimum mass input would be applied.

INTRODUCTION

Yano and Ishido(1989) discussed about the conditions for the development of two-phase zones under fissured caprock. Situations are found in many geothermal reservoirs in Japan where two-phase zones in the natural state and surface manifestations such as fumaroles may be related with permeable flow path through caprocks.

The Ginyu reservoir in the Kirishima geothermal field is characterized by surface manifestations along a fault and vapor-static pressure profile in the upper part of the reservoir under the fault. A simple two-dimensional model was created after the Ginyu reservoir, and it was used for the discussion of the conditions for development of two-phase zones under fissured caprock. Ideas of the model settings in Ingebritsen and Sorey(1988) were taken into consideration.

Simulation results showed several things. (1) A two-phase zone may form so long as sufficient deep fluid mass recharge is present. (2) Or, so long as deep input energy is great enough. (3) The final steady states do not depend on initial conditions. For the simulations above in Yano and Ishido(1989), the permeability of the fissure was the same as that of the reservoir, and was pretty high. Pressure in the two-phase zones formed with large mass input were much greater than vapor-static. In order to create a two-phase zone with small mass input, extreme energy input was required. Both didn't match the actual situation.

After that, we made further elaborations on model parameters such as temperature of the deep input fluid and permeability of the fissure. In this paper, the results of the recent simulations are shown with brief review of the previous work. A part of the previous work was also shown in Yano et al.(1988), and a part of the recent simulations was shown in Yano and Ishido(1990).

THE GINYU RESERVOIR

The Ginyu reservoir is located in the Kirishima geothermal field which is one of the promising fields under exploitation for geothermal power plants in southern Kyushu in Japan(Figure 1). The Kirishima field is situated near the Kirishima volcanos which are located about five kilometers to the northeast. Several faults and lineaments trending ENE-WSW are related to hot springs, fumaroles and alteration zones. The most prominent geothermal anomalies are seen near the Ginyu fault and the Shiramizugoe fault. Geophysical surveys including gravity survey, electrical survey and surface heat flow measurements confirmed the configuration of the major faults and heat anomalies. Many wells were drilled in the Kirishima field, especially near the major faults for over ten years until now. Depth of these wells ranges from several hundred meters to over two thousand meters. Temperature and pressure measurements were performed in these wells.

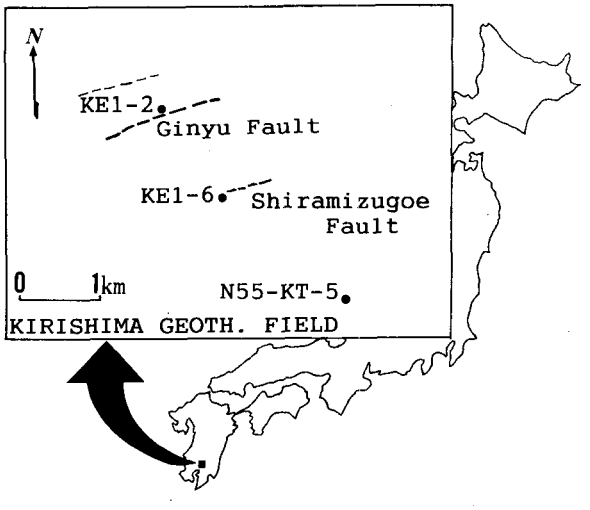

Fig 1. Location of the Ginyu reservoir, modified from Kitamura et al.(1988).

Figure 2 shows the relation between elevation and pressure(Kodama and Nakajima, 1988) in the Kirishima geothermal field. It is shown in this figure that there are two separate hydrostatic pressure-elevation relations. One of these is of the Ginyu reservoir. The slope of the fitted line corresponds to the hydrostatic pressure of hot water at 225 ℃. Measurements in the Ginyu reservoir shows uniform temperature at 232 ℃. The uniformity of temperature in the reservoir implies high permeability within it. In the upper part of the reservoir, pressure-elevation relations are clearly different from hydrostatic. They show vapor-static relations. Two phase zones are assumed by this data. Also, production tests in wells KE1-2 and KE1-6 showed very high steam content in the produced fluid(Kodama and Nakajima, 1988). Thus, a two phase zone with vapor-static pressure is supposed to exist over hydrostatic hot water zones in the Ginyu reservoir.

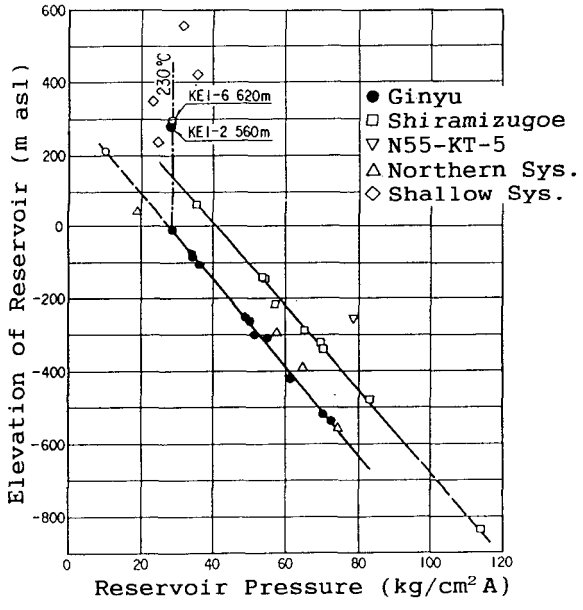

Fig 2. Pressure-elevation relationship in the Ginyu reservoir (Kodama and Nakajima,1988).

The Ginyu fault is featured by a 200m wide subsided zone, active fumaroles, hot springs, an alteration zone, an ENE-WSW lineament, a low resistivity zone, and an anomaly of mercury(ditto). A low permeable layer of 200m to 400m thickness at the depth of several hundred meters is supposed to exist over the geothermal area. The low permeable layer is a lava layer, in which fractures are filled with alteration minerals. Highly permeable reservoirs are developed under the low permeable layer in the Kirishima area.

Figure 3 is a schematic model of the Ginyu reservoir based on above considerations. The deep hot water supply is essentially meteoric water which is heated up by the heat source of the Kirishima volcanos. It is fed into the high permeable Quaternary volcanic layer under the low permeable alteration layer through the deep part of the Ginyu fault. At the top of the hot water reservoir, a two phase zone is formed under the low permeable caprock. Some of the steam is running out of the reservoir through the Ginyu fault to the surface, and forms fumaroles and hot springs.

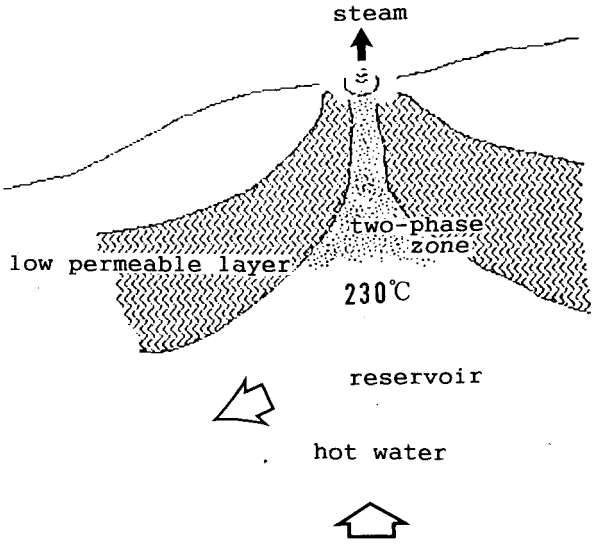

Fig 3. Schematic model of the Ginyu reservoir.

NUMERICAL RESERVOIR MODEL

In order to study the Ginyu type reservoir, we set up a numerical model with geometric components shown in Figure 4. This rather simplified two-dimensional vertical section model incorporates many of the major structural features of the Ginyu reservoir. Quantitative details concerning the representation are summarized in Yano and Ishido(1989).

The size of the highly permeable reservoir, designated as A in Figure 4, is about one square kilometer in vertical section, which is inferred from exploration data. The reservoir is covered by a low permeable altered caprock(D). There is a permeable conduit(F) between the reservoir and the land surface through the caprock. Here we call it a fissure. In the Ginyu area, the fissure corresponds to the Ginyu fault. It is a fractured zone which has some width. Below the reservoir, a permeable conduit(E) also related to the Ginyu fault is supposed to exist for hot water(Mo) to flow into the reservoir. The reservoir is located at a high elevated place related to the volcanic activity. We assume a steady state for the natural state of the system, so the mass inflow rate into the reservoir and the outflow rate must be balanced. A horizontal permeable conduit(B) is assumed for this mass balance. Country rocks(C) around the reservoir have some permeability compared to the caprock, but it is very small, so heat conduction is dominant in them.

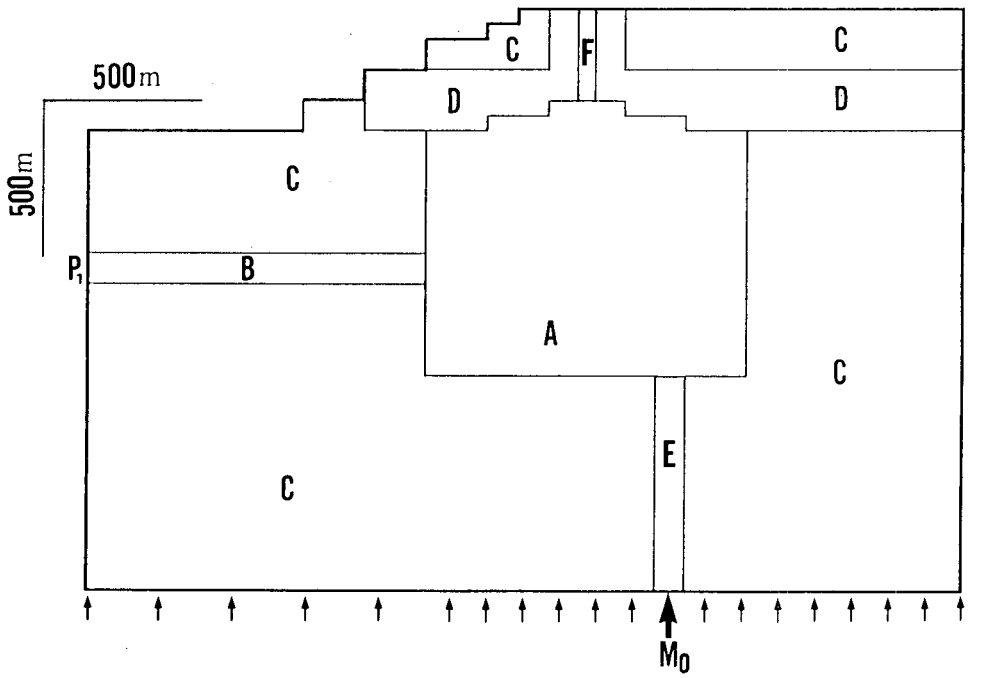

Fig 4. Geometry of the numerical model.

Both side boundaries are insulated except for the outlet of the horizontal conduit. The pressure there(P_1) is hydrostatic pressure which corresponds to initial temperature gradient. The initial pressure of the system is hydrostatic pressure, and the initial temperature gradient is conductive profile according to heat flux from bottom. The heat flux from bottom(intensity designated by arrows) is high on the right part of the system where land surface is elevated. As the heat flow boundary condition of the upper surface of the system, we used "convective-radiative" boundary condition (J.W.Pritchett, personal communication). Details are also shown in Yano and Ishido(1989).

Numerical calculations were all performed using the THOR reservoir simulator (Pritchett,1988), which is designed to solve multidimensional unsteady multi-phase problems in geothermal reservoir flow.

PREVIOUS RESULTS

Using the numerical model in Figure 4, we performed simulations of the evolution of two phase zone in the natural state. We started with conditions that temperature of the deep input fluid is about 260 °C, and the permeability of the fissure is 100 md, which is as same as the permeability of the reservoir. We expected that, if the deep inflow rate exceeds the flow rate through the horizontal conduit, then fluid would flow upwards into the fissure and form a two-phase zone; otherwise, downflow in the fissure would occur.

The amount of mass flowing out of the reservoir through the horizontal conduit(Mesc) can be roughly estimated by the following equation:

$$Mesc = k A (Pa - P_1) / (\nu L) \quad (1)$$

where k, A and L are the permeability, cross-section area and length of the horizontal conduit. The kinematic viscosity of water is represented by ν. P_1 is the boundary pressure applied at the conduit outlet(see Figure 4), and Pa is the initial hydrostatic pressure below the fissure at the elevation of the conduit (8.5 MPa). Assuming appropriate viscosity for the fluid, we calculated the value of Mesc by equation (1) as 47 kg/s.

Actually, simulations showed that a two-phase zone is formed with Mo greater than 47kg/s, and that it is collapsed by the downward flow of cold water with Mo less than 47kg/s.

We tried Mo = 100 kg/s at the beginning and reduced it gradually until it becomes less than the critical rate. For each set of conditions, calculations were continued until nearly steady states were reached. One to five thousands simulated years were needed for these calculations. Figure 5 is a steam saturation distribution for Mo = 60 kg/s. The highly saturated steam is restricted in the uppermost grid block in the fissure. But this two-phase zone is larger than those formed with larger mass input. Temperature in the reservoir becomes nearly uniform at the inflow temperature, though pressure at the fissure is much higher than vapor-static pressure, even higher than the hydrostatic pressure if Mo is as large as 100 kg/s. We cannot expect a vapor-dominated two phase zone in this case of very high fissure permeability. Even a two-phase zone is formed by

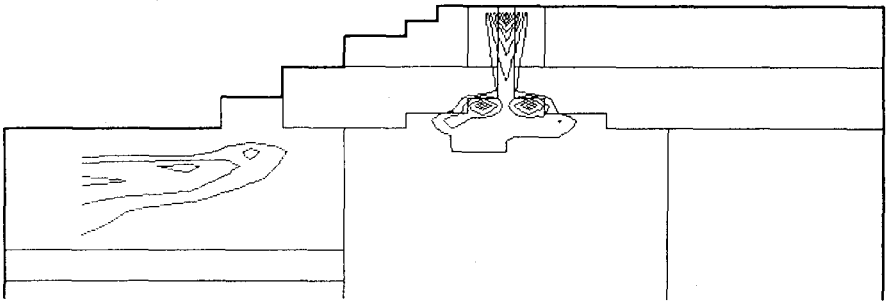

Fig 5. Computed steam saturation with highly permeable fissure, large mass source from below at temperature 260°C(Yano and Ishido,1989). Contour interval is 0.05.

mass input larger than the critical rate, it is collapsed by downflow of cold water when the input mass becomes a bit smaller than the critical. If Mo is less than 47 kg/s, we cannot sustain the two-phase zone unless we assume extremely large energy input accompanying the mass input.

In the whole simulation work for this paper, we tried various conditions and their change at certain time stages. But we couldn't find different final steady states for the same final conditions, even if the histories of them are different.

EFFECT OF TEMPERATURE OF DEEP INFLOW

The internal energy of deep inflowing fluid we used in the above simulation corresponds to hot water at temperature about 260 °C. Because the permeability of the reservoir is pretty high, the hot water spreads within it at a considerable speed. As a result, temperature within the reservoir becomes almost uniform at 260 °C. In the Ginyu reservoir, uniform temperature at 232 °C was observed (Kodama and Nakajima,1988), which indicates high permeability of the reservoir. As long as the permeability through the entire system including the deep conduit, the reservoir and the outlet conduit is so high, the reservoir temperature is controlled by the deep inflowing fluid. If it is the case with the Ginyu reservoir, the deep inflow temperature should be 230-240 °C.

We tried to see how the state would be changed by the change of temperature of deep inflow. We made calculation with Mo = 48 kg/s. As was described above, a significant two-phase zone was formed as long as the temperature of the deep inflow is about 260 °C. Instead, we tried simulation with temperature at about 240°C. As a result, we could not form two-phase zones in the reservoir by this temperature, except for the uppermost grid block in the fissure.

Then we made calculation with temperature at about 280 °C. Figure 6 shows the computed two-phase zone under this condition. Compared to the result with deep input temperature at 260 °C, steam saturation in the two-phase zone becomes higher and the size of the zone also becomes larger. However, steam saturation in the fissure itself is still small, and the pressure gradient is still far larger than a vapor-static pressure. Furthermore, though this is a large and substantial two-phase zone, we found this two-phase zone was also collapsed when we reduced the deep inflow mass rate Mo to 42 kg/s, which is less than the critical rate 47 kg/s.

As we see in the above simulations, the size and saturation of the two-phase zone are sensitive to the temperature of deep inflowing fluid. However, a vapor-static pressure is not attained, and the criteria of minimum mass input is applicable to these high-permeable fissure cases.

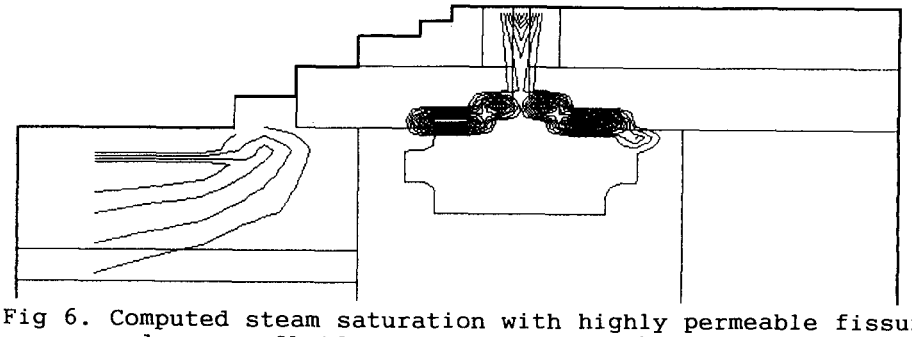

Fig 6. Computed steam saturation with highly permeable fissure and source fluid at temperature 280 °C.

EFFECT OF PERMEABILITY OF FISSURE

In case of the Ginyu, permeability of the reservoir is estimated to be uniformly high, based upon well data. However, permeability of the fissure which connects the reservoir and land surface is unknown. In the simulations above, we have supposed it to be 100 md which is as same as the reservoir. The very high permeability enables a large amount of steam to flow up to the surface forming active fumaroles, when the pressure in the reservoir is maintained by a large deep mass input. But if the deep mass input is small, the high permeability of the fissure allows cold surface water flow down into the reservoir.

For a large vapor dominated two-phase zone to be sustained, high permeability through the caprock is unfavorable. If there is no permeable conduit in the caprock, an extensive vapor dominated two-phase zone would be formed. Actually, we got a highly vapor-saturated, large two-phase zone when we made the net vertical permeability of the fissure to be zero. But if we assume that the reservoir is completely sealed by impermeable caprock, the existence of active fumaroles or other surface manifestations are hard to be explained. The fissure must have permeability to some extent for steam to flow up.

However, if the permeability of the fissure is small, the minimum mass input criterion may become ineffective as we saw in the case of extreme energy input(Yano and Ishido,1989), where small mass recharge from the deep conduit makes a large, vapor dominated two-phase zone. The idea is that, if the cooling rate from above by the downflowing cold water in the fissure at a vapor-static pressure gradient is trivial compared to the cooling power needed for changing the total vapor-phase mass produced per unit time into liquid phase, the two-phase zone would not be collapsed.

The downward convective cooling flux from above for zero vertical pressure gradient is given by $Af \cdot kf \cdot Cvf \cdot \rho \cdot g \cdot \Delta T / \nu$, where Af is cross sectional area of the fissure, kf is the permeability of the fissure, Cvf is fluid heat capacity, ρ is fluid density, g is acceleration due to gravity, ΔT is temperature difference across the fissure zone, and ν is fluid kinematic viscosity. The cooling power needed is given by $Mo \cdot X \cdot Hsw$, where X is the mass fraction of vapor-phase produced from the upward hot water flow, and Hsw is the latent heat at the two-phase zone temperature. X can be calculated by a simple energy conservation equation of the source hot water and fluids in the two-phase zone. If we assume that the downward cooling flux is much smaller than the needed cooling power, then the following inequality is derived.

$$kf << Mo\ X\ Hsw\ \nu\ /\ (Af\ \rho\ g\ Cvf\ \Delta T) \qquad (2)$$

Assuming the two-phase zone temperature to be 230 °C, the source fluid temperature to be 280 °C, and Mo to be 36 kg/s, the right side of the inequality (2) is roughly estimated as 20 md.

Figure 7 is calculated steam saturation of a model in which permeability of the fissure is 5 md. Temperature of the deep inflow is at 280 °C, and mass input rate is 36 kg/s which is less than the critical mass rate. If permeability of the fissure is very high, cold water downflow will occur as we found it previously. But in this case, steam saturations at the top of the reservoir and the fissure are very high, forming a large vapor-dominated two-phase zone. As expected, we could make a substantial two-phase zone with small mass input and small permeability of the fissure. Mass of the rising steam and the liquid water in the uppermost grid block(depth of centroid is 25 m) of the fissure is 2.1 kg/s and 2.0 kg/s respectively. In the grid block whose depth of centroid is 125 m in the fissure, 3.9 kg/s of steam is rising and 0.007 kg/s of liquid water is flowing downward. That is, the fluid rising in the fissure is mostly steam in lower level, but a part of it becomes liquid water as it reaches to the shallow part.

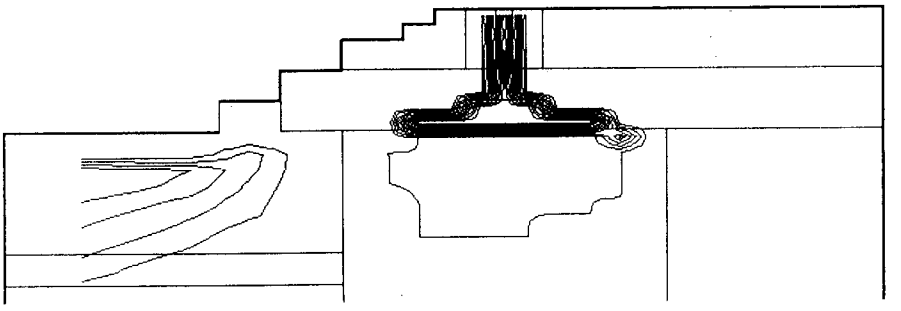

Fig 7. Computed steam saturation with low permeable fissure and small mass source at temperature 280 °C.

SUMMARY

Two-phase conditions in geothermal reservoirs with fissured caprocks in the natural states are greatly influenced by the permeability of the fissure, as we found it in the last calculation.

As far as the permeability of the fissure is very high, the rate of mass input from below determines whether there is a downflow of cold water in the fissure or not. A minimum mass input rate is required to sustain the two-phase zone. This critical mass rate is given by equation (1). Even though the temperature of the deep inflow has influence on size and steam saturation of the two-phase zone, the steam saturation in the fissure is small and the pressure gradient is much higher than the vapor-static profile in the case of this "mass-sustained two-phase zone".

On the other hand, if the permeability of the fissure is so small that the amount of downflowing cold water in the fissure is negligible compared to the produced steam in the two-phase zone, a vapor-dominated two-phase zone can be sustained by a small mass input from below. The permeability of the fissure must be small enough as given by inequality (2) for this "heat-sustained two-phase zone".

REFERENCES

Ingebritsen, S. E. and M. L. Sorey(1988), "Vapor-Dominated Zones within Hydrothermal Systems: Evolution and Natural State," J. Geophys. Res., Vol. 93, pp.13635-13655.

Kitamura, H., T. Ishido, S. Miyazaki, I. Abe, and R. Nobumoto(1988), "NEDO's Project on Geothermal Reservoir Engineering - a Reservoir Engineering Study of the Kirishima Field, Japan," Proc. 13th Workshop on Geothermal Reservoir Engineering, Stanford University, pp.47-51.

Kodama, M. and T. Nakajima(1988), "Exploration and Exploitation of the Kirishima Geothermal Field," Journal of Japan Geothermal Energy Association, Vol. 25, pp.201-230.

Pritchett, J. W.(1988),"THOR User's Manual," SSS-IR-88-9408, S-Cubed, La Jolla, California, 109p.

Yano, Y., K. Yasukawa and T. Ishido(1988), "On the Behavior of Two-Phase Geothermal Reservoirs," Proc. International Symposium on Geothermal Energy 1988, Geothermal Research Society of Japan, pp.220-223.

Yano, Y. and T. Ishido(1989), "Stability of Two Phase Zones below Fissured Caprock," Proc. 14th Workshop on Geothermal Reservoir Engineering, Stanford University, pp.241-246.

Yano, Y. and T. Ishido(1990), "Development of Two-Phase Geothermal Reservoirs," Abst. 1990 Annual Meeting of the Geothermal Research Society of Japan.

PROCEEDINGS, Eighteenth Workshop on Geothermal Reservoir Engineering
Stanford University, Stanford, California, January 26-28, 1993
SGP-TR-145

DETAILED THREE-DIMENSIONAL MODELING OF THE BOTN HYDROTHERMAL SYSTEM IN N-ICELAND

Gudni Axelsson and Grímur Björnsson

National Energy Authority, Grensásvegur 9, 108 Reykjavík, ICELAND

ABSTRACT

A detailed three-dimensional numerical model has been developed for the low-temperature hydrothermal system at Botn in Central North Iceland. It is based on a conceptual reservoir model which has evolved during two decades of geothermal research in the area and on the 10 year production history of the system. The model consists of: (1) A powerful recharge system at depth, (2) a shallow production reservoir and (3) a cold ground-water system at the surface. About 10 million tons of hot water have been extracted from the production reservoir since late 1981. The presence of the powerful recharge system results in a very slow long-term pressure decline. Flow of water in the production reservoir appears to be controlled by a highly permeable, vertical fracture-zone confined by low-permeability rocks. Cold ground-water flows down into the fracture-zone during production causing some cooling of the extracted water.

INTRODUCTION

The low-temperature geothermal field at Botn is one of four geothermal fields utilized for space-heating by the town of Akureyri (pop. 13000) in Central North Iceland (Figure 1). Two production wells, HN-10 and BN-1, have been drilled in the Botn field in addition to four exploration wells (Table 1). Prior to production a 18-22 bar well-head pressure was observed in the production wells.

The total production from the field, from 1981 through 1992, is about 10 million tons. Well HN-10 has produced an average of 25 l/s of 84° C water and well BN-1 5 l/s of 96° C water, during this period. The mass withdrawal has induced a 40 bar draw-down in well HN-10, but it is somewhat less in well BN-1. Most of this drawdown took place in the first months of production. Since then, draw-down in production wells has remained almost stable due to recharge from the overlaying ground-water and from a powerful recharge system of an unknown location. In addition to the pressure draw-down, a 3 - 4 °C temperature decline has occurred in well HN-10 (Flóvenz et al., 1992).

The Botn geothermal system has been studied extensively during the last two decades (Flóvenz et al., 1989 and 1991; Axelsson et al., 1988). Detailed

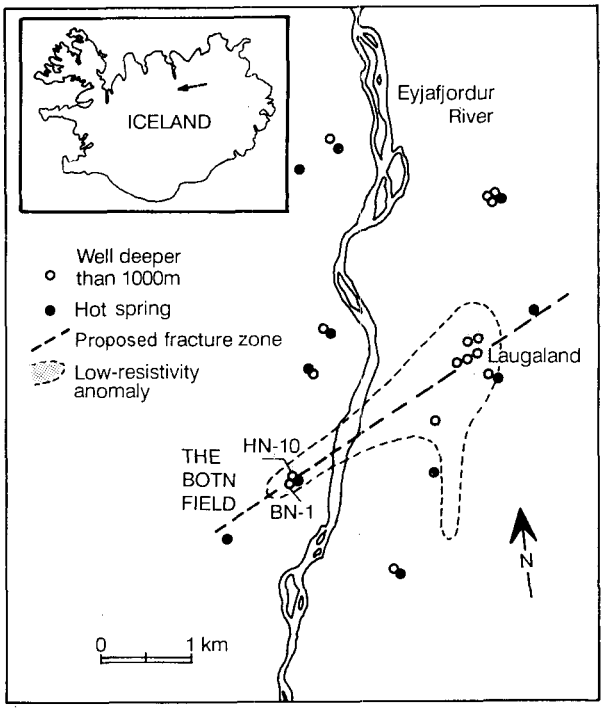

Figure 1. *Location of the Botn geothermal field and the proposed fracture zone.*

Table 1. *Wells in the Botn hydrothermal field.*

Well	Drilled	Depth (m)	Type
BN-1	1981	1830	Prod. well
BY-2	1989	446	Expl. well
BY-3	1989	300	Expl. well
BY-4	1989	403	Expl. well
HN-10	1980	1050	Prod. well
HY-12	1989	318	Expl. well

subsurface resistivity mapping has been carried out, four exploration wells have been drilled, the production response has been monitored carefully and lumped modeling of the Botn system performed. The main objective of this work has been to locate permeable zones in the recharge system mentioned above. However, the results have been too inconclusive for locating sites for new production wells.

As the final stage of geothermal research in the area, a detailed three-dimensional numerical model was developed for the Botn geothermal system (Axelsson and Björnsson, 1992). A brief overview of this modeling study is given here. The numerical model simulates available information on the nature and structure of the system, downhole temperature- and pressure data as well as the production response of the system during the last decade. The computer code PT was utilized for calculations in the modeling study (Bodvarsson, 1982).

Simple modeling, such as lumped modeling, has been used extensively to model pressure responses due to production from low-temperature geothermal systems in Iceland (Axelsson, 1989 and 1991). The numerical model of the Botn system is, however, the first model of it's kind for a low temperature system in Iceland. Previously detailed three-dimensional numerical models have been developed for two high-temperature geothermal systems and much simpler two-dimensional modeling has been performed for a few other geothermal systems in Iceland (e.g. Tulinius and Sigurðsson, 1991; Bodvarsson et al., 1990; Vatnaskil Consulting Engineers, 1989; Tulinius et al. 1987; Bodvarsson et al., 1984).

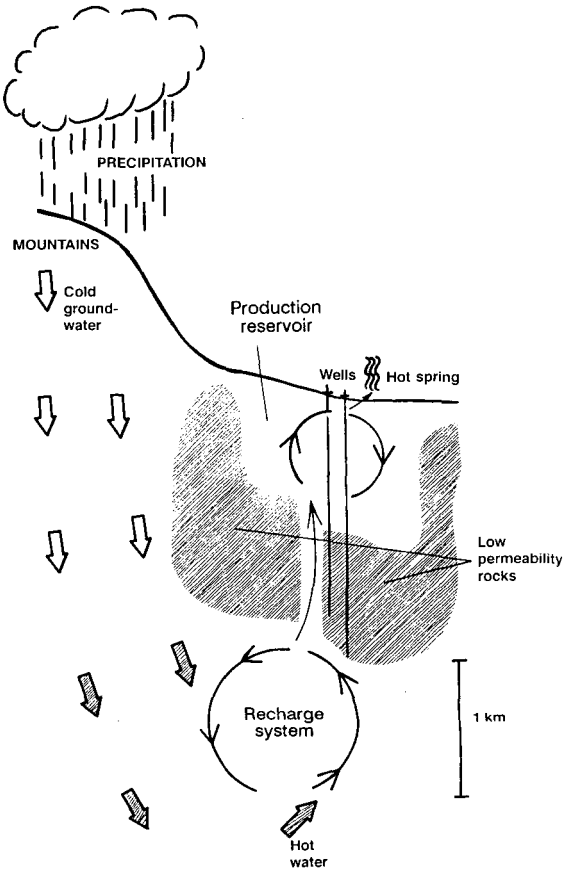

Figure 2. *Simplified sketch of the conceptual model of the Botn geothermal system.*

THE CONCEPTUAL MODEL

The numerical model of the Botn system is based on a conceptual model which has evolved during two decades of geothermal research in the area (Axelsson and Björnsson, 1992). An important element in the conceptual model is a NE-striking feature, probably a fracture-zone, which passes through the Botn area as well as the Laugaland geothermal area NE of Botn (Figure 1). This feature is evident as a common trait in resistivity, subsurface temperature and water-level data. Productive/successful wells in both areas as well as locations of hot springs support the existence of this feature. Well HN-10 is believed to produce from this zone.

A simple sketch of the conceptual model of the Botn geothermal system is presented in Figure 2. The main features of the model are the following:

- Flow of water in the upper part of the geothermal system (above 1000-1500 m depth), or the **production reservoir**, is controlled by a fracture-zone with a northeasterly direction (the NE-striking feature). This fracture-zone intersects older N-S striking structures such as dikes and faults.
- The production reservoir is small in volume and the fracture-zone is confined by low-permeability rocks. In fact the production reservoir appears to be horizontally isolated. Interference from the Botn area is not seen in wells located 1-2 km to the north and east and warm springs to the SW and SE are still unaffected despite the great drawdown at Botn. In addition, a fault to the west of the Botn area probably acts as an impermeable barrier.
- A thin (100 m) caprock confines the Botn system from above. Yet some isolated channels through the caprock link the geothermal system with the ground-water system. Prior to production these channels allowed hot water to escape to the surface and form hot springs.
- At depth, perhaps below 1500 m, a powerful geothermal system, or the **recharge system**, exists. It's exact location is not known. This system has a large reservoir storage coefficient, probably because of it's connection to ground-water systems in the mountains west of the Botn area (Figure 2). Pressure changes are slow in the recharge system due to it's

great storage coefficient. A low-permeability layer, perhaps intersected by one or more fractures, separates the production reservoir from this deeper part.

- The initial pressure and temperature distribution in the Botn system indicates temperatures greater than 100° C in the recharge system whereas temperatures in the production reservoir are quite variable, or between 60 and 90° C (Axelsson and Björnsson, 1992). The entire geothermal system was overpressurized prior to production, probably because of the caprock and the hydrological connection to the mountains in the west. It is estimated that in the natural state pressure at 750 m depth was about 95 bars and greater than 191 bars at 1750 m depth.

THE NUMERICAL MODEL

The structure of the numerical model for Botn is shown in figures 3-5. It is composed of 8 horizontal layers with a total of 429 blocks, that vary in size from 0.00025 to 1 km^3. The blocks are connected by 1361 connections. Figure 3 shows a surface view of the model, which has an area of 5 km^2. The model is closed on all sides to simulate the systems apparent horizontal isolation.

Figure 4 shows a simplified three-dimensional view of the numerical model. It consists of three main units: (1) The recharge system below 1500 m depth, simulated by layers F and G. (2) The production reservoir, between 100 and 1000 m depth, composed of layers B, C and D. (3) The ground-water system above the geothermal system (layer O, not shown in Figure 4). Layer E,

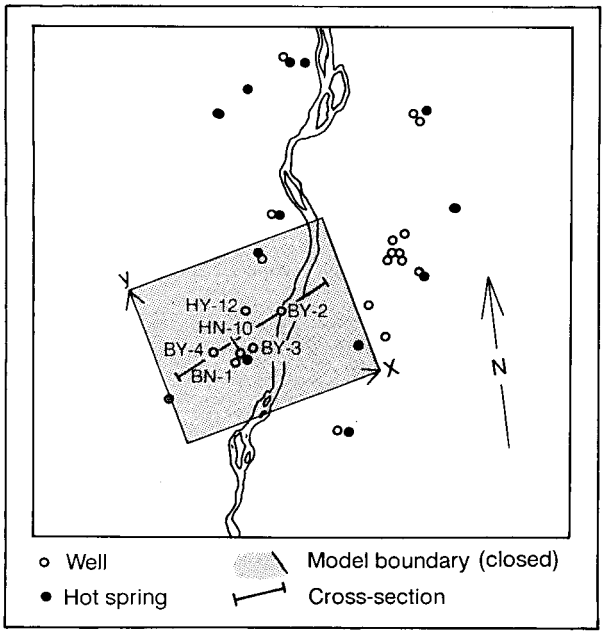

Figure 3. *Surface view of the numerical model.*

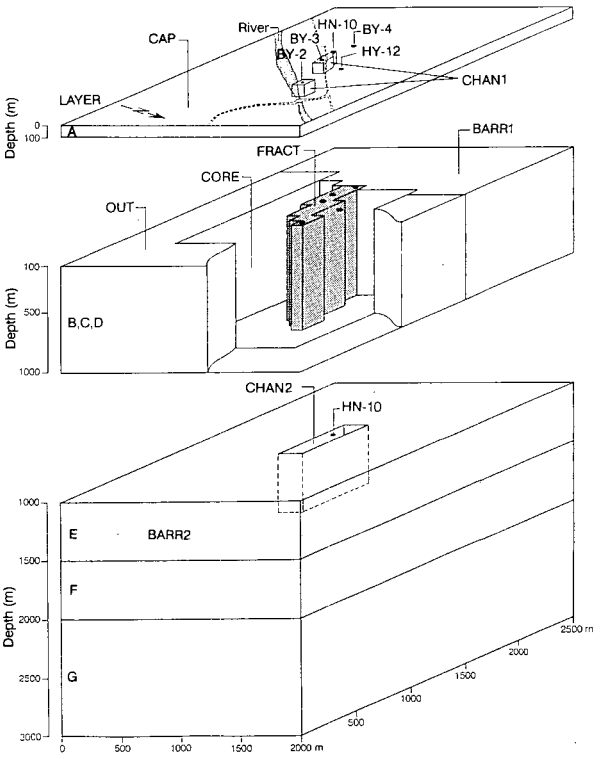

Figure 4. *Simplified three-dimensional view of the numerical model.*

which separates parts 1 and 2 of the model has a very low permeability except for a narrow channel, which connects the recharge system and the production reservoir. Layer A simulates the caprock above the geothermal system (0-100 m depth). Two channels are introduced through the caprock to simulate the connection between the ground-water system and the production reservoir (i.e. hot spring channels).

Figure 5 shows the division of layers B, C and D into blocks and rock types. The grid for these layers is presented as an example, whereas the grids for the additional layers are presented by Axelsson and Björnsson (1992). Note that layers A, B, C and D include 348 of the 429 blocks in the model. This is due to the detailed data available for the uppermost 500 m of the geothermal system. The hydrological and physical properties of the 10 different rock types used in the model are presented in table 2 below.

The numerical model simulates the following: (i) The natural state of the system. (ii) Observed long-term water-level changes and temperature decline of water produced from well HN-10. (iii) Water-level changes observed in exploration wells during a pressure recovery test in the summer of 1990. When a satisfactory natural state simulation had been obtained some changes were made in the model such that it also simulated items (ii) and (iii) above. This in turn required a recalibration of

Table 2. *Properties of different rock types in the model.*

Rock type	Permeability (10^{-15}m^2)	Anisotropy k_y/k_x	Porosity (%)
CAP	0.01	1.0	5
CHAN1	14	1.0	10
BARR1	0.01	1.0	5
FRACT	180	0.0002	10
WELL	800	0.0002	10
CHAN2	40	0.1	1
OUT	0.5	1.0	10
CORE	2	0.2	8
BARR2	0.1	1.0	5
LAYERS F,G	5	1.0	20

Rock matrix heat capacity = 850 J/kg° C
Heat conductivity = 2.1 - 2.5 W/m° C
Rock matrix density = 2900 kg/m^3
Rock matrix compressibility = 2×10^{-11}Pa^{-1}
Compressibility of water = 5×10^{-10}Pa^{-1}

the model for the natural state simulations. Thus several iterative cycles had to be completed until a "best model", which simulated all three items, resulted. The authors believe that this procedure is the most accurate way of reservoir modeling, even though it turned out to be very time consuming.

Natural state simulations

During the natural state simulations a **fixed inflow**, or recharge, into layer G was assumed to have started about 10,000 years ago, or at the end of the last glacial period in Iceland (Bodvarsson, 1982). At this time, a uniform 60° C/km thermal gradient was assumed in the model and the pressure followed a hydrostatic gradient. The simulations then involved adjusting the permeability distribution of the model and the inflow until a satisfactory match between measured and calculated data was obtained. In the "best model" a recharge of 6.5 l/s of 105° C hot water was required. Figure 6 presents a comparison between initial and calculated temperatures

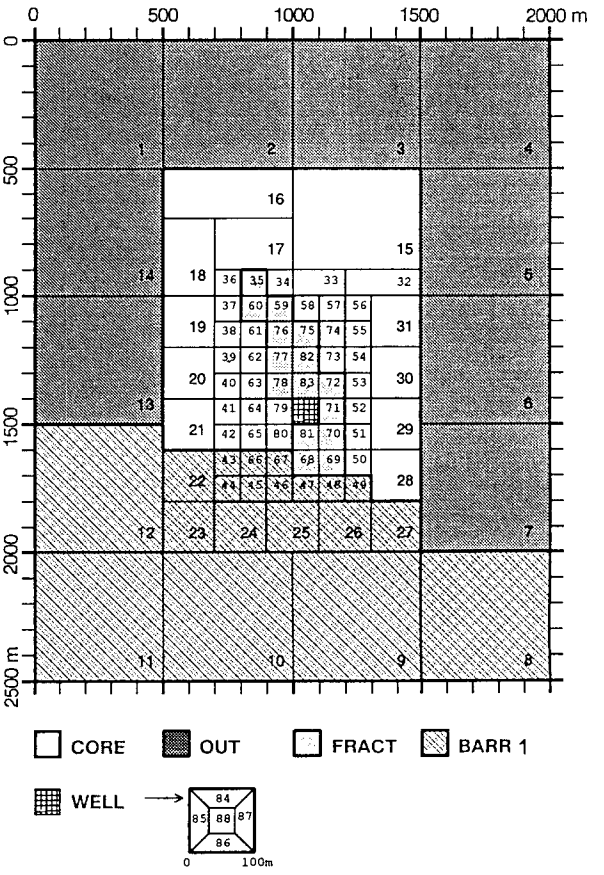

Figure 5. *Division of layers B, C and D of the numerical model into blocks and rock types.*

in wells in the area. It should be mentioned that the numerical model was close to steady state conditions at the end of the natural state simulations.

Figure 7 shows the calculated temperature distribution along a SW-NE cross-section through the center of the numerical model. The temperature distribution reflects clearly that hot water flows from the recharge system below 1500 m up through the fracture-zone and into the ground-water system at the surface.

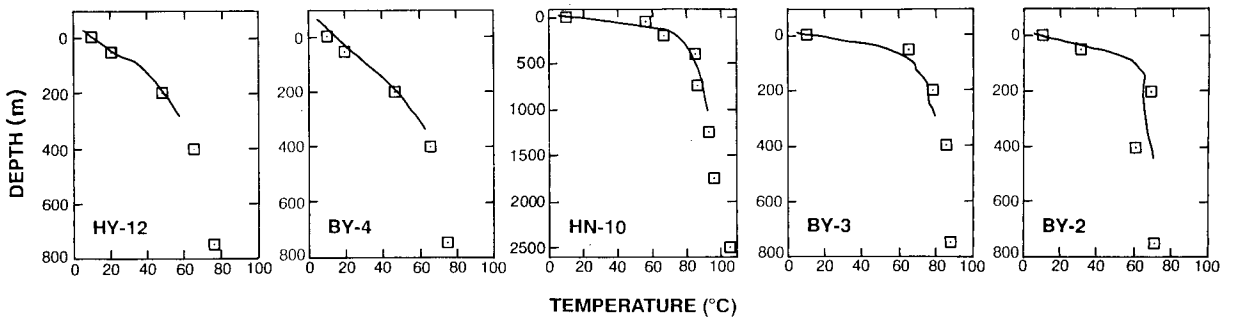

Figure 6. *A comparison between observed temperature profiles (solid lines) and model temperatures (small squares).*

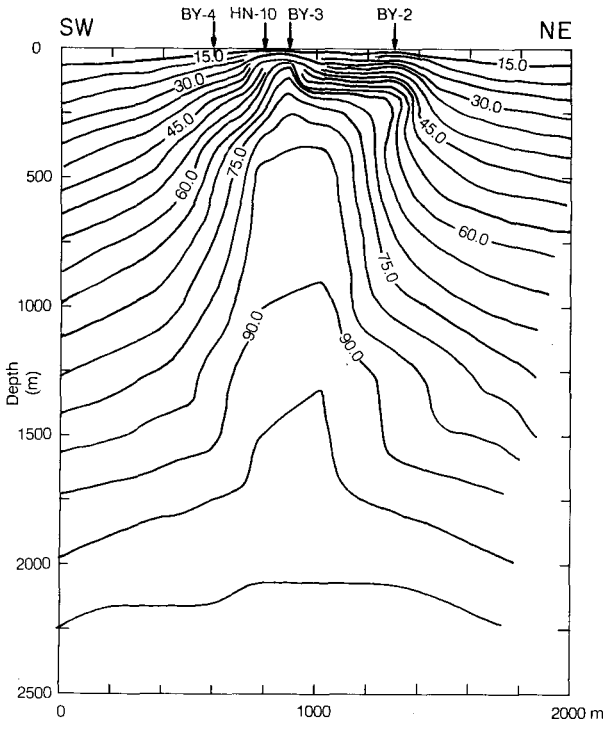

Figure 7. *Calculated temperature distribution along a cross-section shown in Figure 3.*

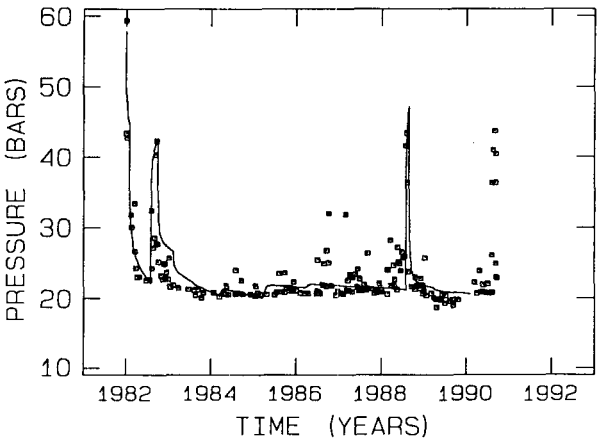

Figure 8. *Comparison between observed (squares) and calculated (solid line) pressure response of production well HN-10.*

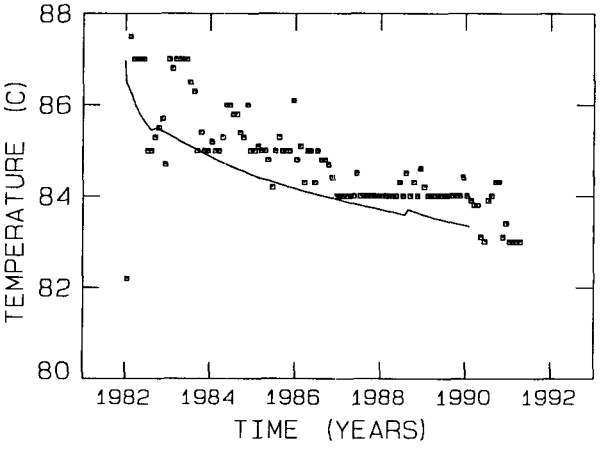

Figure 9. *Comparison between observed (squares) and calculated (solid line) temperatures for production well HN-10.*

Production simulations

The production simulations basically involved adjusting the permeability distribution of the model, the properties of the fracture-zone (FRACT) and the size and porosity of the recharge system (layers F and G). The production simulations were for the most part constrained by a 10 year history of water level measurements in well HN-10 and measurements of the production temperature of the same well. The comparison between the observed data and the response of the "best model" are presented in figures 8 and 9.

As already mentioned flow of water in the production reservoir appears to be controlled by a permeable fracture-zone with a northeasterly direction. In the numerical model this fracture-zone was simulated by a thin volume of blocks, 900 m high and about 900 m long, labeled FRACT (see figures 4 and 5). The decline rate of production temperatures, as well as water-level changes in well HN-10, are very sensitive to the fracture-zone properties, in particular it's thickness. The properties of the fracture-zone were consequently scaled to simulate a variable thickness until a satisfactory match between the observed and calculated response was obtained. As it turned out a thickness of 10 m resulted in the best match.

The simulated long-term pressure decline in well HN-10 is controlled by the storage properties of layers F and G (the recharge system), which in turn is simulated by their volume and porosity. A volume of 300 km^3 and porosity of 20% was used. These are a very great volume and high porosity, which probably indicates storage not only due to rock/water compressibility but also due to lowering of a free liquid surface. This is most likely caused by a hydrological connection with ground-water systems in the mountains west of the Botn area. Therefore, neither the size, porosity nor position of the recharge system in the numerical model should be considered to be real.

Figure 10 shows calculated cooling of the production reservoir in a cross-section along the fracture-zone, after ten years of production. One of the channels linking the production reservoir and the ground-water system is located below a now extinct warm spring, Botnslaug (by well BY-3). A second channel, situated

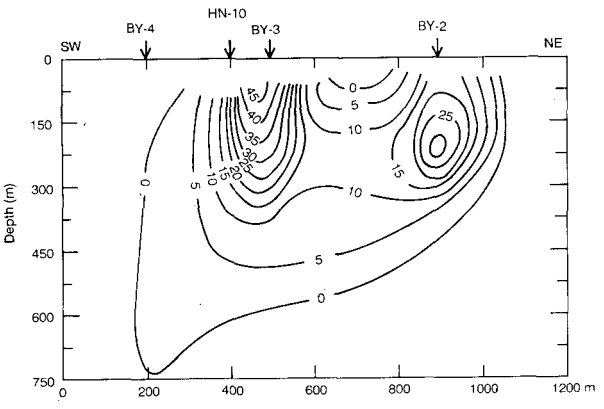

Figure 10. *Calculated cooling of the cross-section shown in Figure 3 after 10 years of production.*

½ km northeast of the production wells (by well BY-2), was required in the numerical model for a satisfactory match. A hot spring is not known there, but since the bedrock in this location is covered by about 100 m of alluvial sediments and a major river flows through the area, a subsurface hot spring is not unlikely. Figure 10 shows that the pressure draw-down allows cold groundwater to flow down through these channels causing a considerable cooling of the uppermost part of the fracture zone. A cooling of water produced from wells HN-10 and BN-1 follows in accordance with the measured data.

According to the numerical model, about 10 % of the water currently produced originates as cold groundwater. Changes in the chemical content of the water produced support this result (Axelsson and Björnsson, 1992). The recharge system provides 85 % of the mass produced and the remaining 5 % are taken from storage above 1500 m depth.

Pressure recovery simulations

In the summer of 1990 production from well HN-10 was discontinued for about a month. During this period water level changes were monitored very carefully in all available wells in the Botn area, and in several wells in surrounding areas. The data from this extensive build-up and interference test were used for a more detailed calibration of the permeability distribution of the numerical model. A comparison between the observed and calculated pressures in wells BY-2, BY-3, BY-4 and HY-12 is presented in Figure 11.

This final stage of the simulations resulted in the following: The fracture-zone (rock-type FRACT) was defined in more detail, in particular extended slightly further to the NE and it's anisotropy increased considerably. The channel, up through the caprock, close to well BY-2 was required. In addition the barrier on the western edge of the Botn system (BARR1 in figures 4 and 5) had to be moved closer to well BY-4.

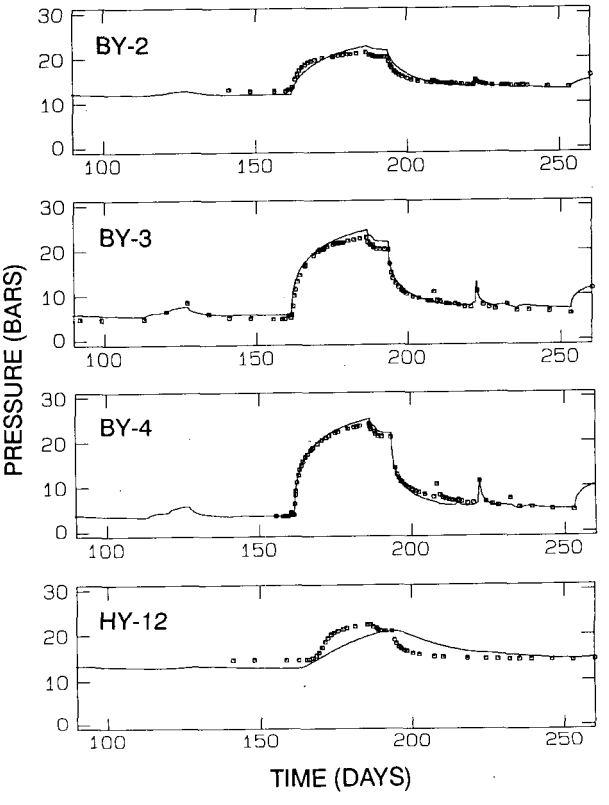

Figure 11. *Comparison between observed (squares) and calculated (solid lines) pressure changes during a recovery test in 1990.*

Predictions

Finally the "best model" was used to predict draw-down and cooling of wells for twelve different future scenarios. Axelsson and Björnsson (1992) present results for several production cases as well as predictions for cases of cold water injection into the exploration wells BY-2 and BY-4, which are about 540 and 220 m from well HN-10, respectively. Figures 12 and 13 provide examples of the predicted water level and production temperatures for the main producer HN-10. Four cases of constant future production from wells HN-10 and BN-1 are considered.

In general the numerical model predicts that decline of production temperatures at Botn will slow down in the future and remain within economical limits for some decades. As an example the production temperature of well HN-10 will most likely stay above 80 °C for the next 20 years. If the average 29,5 l/s production during 1986 - 1992 is maintained, lowering or replacement of the present rotary shaft pumps in the production wells will not become necessary. A 25 % increase in production, on the other hand, requires pumps to be lowered down to 400 m from the present depths of 246 m and 175 m in wells HN-10 and BN-1,

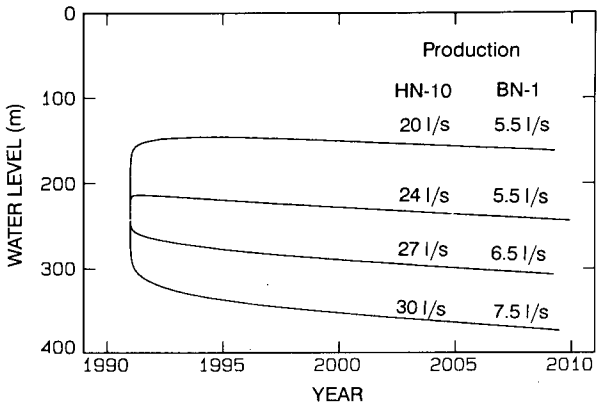

Figure 12. *Predicted water level changes in well HN-10 for different cases of future production.*

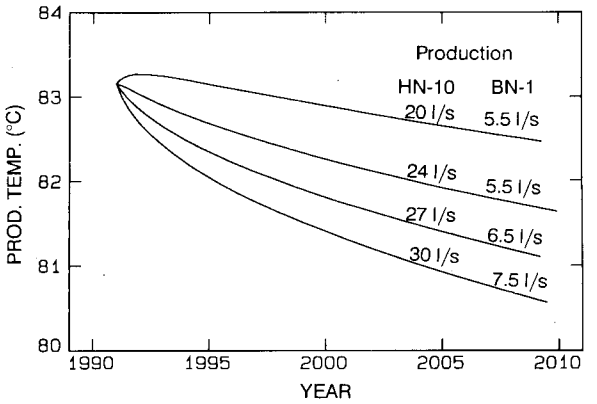

Figure 13. *Predicted changes in production temperature of well HN-10 for different cases of future production.*

respectively. Such an increase in production will only cause an additional 1 °C temperature drop for well HN-10 during the next 20 years..

According to the numerical model injection of cold water into some of the exploration wells reduces the pressure draw-down in the area. However, cold water injection of only 5 l/s into well BY-4 will double the cooling rate of water produced from well HN-10. A moderate injection into two of the exploration wells, 4 l/s into BY-2 and 2 l/s into BY-4, allows a 10 % increase in mass and energy production from well HN-10, without requiring a pump replacement.

CONCLUDING REMARKS

The most important aspects of the detailed three-dimensional modeling of the Botn geothermal system may be summarized as follows:

- The numerical model consists of 429 blocks in 8 horizontal layers. It is one of the most complex models of geothermal systems in Iceland developed to date.
- The numerical model is based on a conceptual model which has evolved during two decades of geothermal research in the Botn area. The model simulates available information on the nature of the system, the natural-state temperature- and pressure distribution, data on the production response during the last decade as well as data from an extensive pressure recovery test.
- The numerical model consists of three main units : (1) A powerful recharge system below 1500 m depth, (2) a production reservoir above 1000 m depth and (3) a ground-water system at the surface. To date production has mostly been from unit 2.
- The recharge system is over-pressurized and has a very large reservoir storage coefficient, probably because of its connection to ground-water systems in the mountains west of the Botn area. It is simulated by 300 km^3 of permeable rocks with 20% porosity.
- The production reservoir is small in volume and appears to be horizontally isolated. Flow of water in this part is controlled by a highly permeable fracture-zone. Decline rates of production temperatures, as well as water-level changes in several wells, are very sensitive to the properties of this zone, in particular it's thickness.
- The Botn system is linked with the ground-water system above through the channels of now extinct warm springs. Cold ground-water flows down through these channels during production causing some cooling of the production wells. According to the numerical model, about 10% of the water currently produced originates as cold ground-water. About 85% originate in the recharge system and the final 5% are taken from storage.
- The numerical model predicts that if the average past production from the Botn field (29.5 l/s) is maintained, replacement of pumps in production wells will not become necessary and temperature of water produced will only drop by an additional 1-2° C during the next 20-30 years. Therefore, this field will continue to provide an important energy base for the district heating system of the town of Akureyri.

ACKNOWLEDGEMENTS

The authors would like to thank the Akureyri District Heating Service for allowing publication of the data from the Botn geothermal field. We also thank our colleagues at the National Energy Authority for their contributions and Drs. Valgarður Stefánsson and Ólafur G. Flóvenz for reviewing the paper.

REFERENCES

Axelsson, G., 1991: Reservoir engineering studies of small low-temperature hydrothermal systems in Iceland. *Sixteenth Workshop on Geothermal Reservoir Engineering, Jan. 1991*, Stanford University, 7 pp.

Axelsson, G., 1989: Simulation of pressure response data from geothermal reservoirs by lumped parameter models. *Fourteenth Workshop on Geothermal Reservoir Engineering, Jan. 1989*, Stanford University, 257-263.

Axelsson, G. and G. Björnsson, 1992: Botn in Eyjafjordur County (in Icelandic). Report OS-92012/JHD-01, National Energy Authority, Reykjavík, 71 pp.

Axelsson, G., H. Tulinius, Ó.G. Flóvenz and Þ. Thorsteinsson, 1988: Geothermal resources of the Akureyri District Heating Service (in Icelandic). Report OS-88052/JHD-10, National Energy Authority, Reykjavík, 35 pp.

Bodvarsson, G., 1982: Glaciation and geothermal processes in Iceland. *Jökull, 32*, 21-28.

Bodvarsson, G.S., 1982: Mathematical modeling of the behavior of geothermal systems under exploitation. Ph.D. Thesis, University of California, Berkeley, 348 pp.

Bodvarsson, G.S., S. Björnsson, Á. Gunnarsson, E. Gunnlaugsson, Ó. Sigurðsson, V. Stefánsson and B. Steingrímsson, 1990: The Nesjavellir geothermal field, Iceland; 1. Field characteristics and development of a three-dimensional numerical model. *J. Geotherm. Sci. and Tech., 2*, 189-228.

Bodvarsson, G.S., K. Pruess, V. Stefánsson and E.T. Elíasson, 1984: The Krafla geothermal field, Iceland; 3. The generating capacity of the field. *Water Resour. Res., 20*, 1545-1559.

Flóvenz, Ó.G., G. Axelsson and G. Sverrisdóttir, 1992: The Akureyri District Heating Service. Geothermal monitoring during 1991 (in Icelandic). Report OS-92020/JHD-07 B, National Energy Authority, Reykjavík, 34 pp.

Flóvenz, Ó.G., G. Axelsson and Á. Guðmundsson, 1991: Geothermal research in the Botn and Hrafnagil areas 1989-1990. Exploration drilling and water-level monitoring (in Icelandic). Report OS-91008/JHD-02, National Energy Authority, Reykjavík, 89 pp.

Flóvenz, Ó.G., Á. Guðmundsson, Þ. Thorsteinsson and G.P. Hersir, 1989: The Botn geothermal area. Results of geothermal research 1981-1989 (in Icelandic). Report OS-89018/JHD-03, National Energy Authority, Reykjavík, 92 pp.

Tulinius, H. and Ó. Sigurðsson, 1991: Krafla. Three-dimensional simulation of the Hvíthólar production area (in Icelandic). Report OS-91046/JHD-07, National Energy Authority, Reykjavík, 37 pp.

Tulinius, H., A.L. Spencer, G.S. Bodvarsson, H. Kristmannsdóttir, Þ. Thorsteinsson and A.E. Sveinbjörnsdóttir, 1987: Reservoir studies of the Seltjarnarnes geothermal field, Iceland. *Twelfth Workshop on Geothermal Reservoir Engineering, Jan. 1991*, Stanford University, 9 pp.

Vatnaskil Consulting Engineers, 1989: Svartsengi. A reservoir simulation (in Icelandic). Report OS-89031/JHD-05, National Energy Authority, Reykjavík, 111 pp.

PROCEEDINGS, Eighteenth Workshop on Geothermal Reservoir Engineering
Stanford University, Stanford, California, January 26-28, 1993
SGP-TR-145

THE PRODUCTIVE PERFORMANCE PREDICTION OF SOME WELLS IN HACHIJOJIMA HYDROTHERMAL FIELD,JAPAN.

Nobuhiro Demboya*, Jun-ichi Ishikawa*,
Nobuyuki Iwai** and Yoneko Tada**

* New Energy and Industrial Technology Development Organization (NEDO)
3-1-1,Higashi-Ikebukuro , Toshima-ku, Tokyo,JAPAN,104
**Kaihatsu Computing Service Center Co., Ltd.(KCC)
2-2-18, Fukagawa, Kohtoh-ku, Tokyo, JAPAN, 135

ABSTRACT

New Energy and Industrial Technology Development Organization (NEDO) did "Geothermal Development Promotion Survey" in the Hachijojima Island which is a volcanic island with 70km^2 located in the Izu-Mariana Island Arc. In that national project, NEDO drilled 8 wells in the field and the maximum temperature of the field was 317°C at 1200m depth of a well. Of these survey NEDO confirmed the existence of geothermal reservoir,and using a well named HJ-5, NEDO did short time discharge test. The authors calculated borehole temperature and pressure under production the of the well in comparison with the measured data. The authors also calculated productive performance of another well named HJ-8.

INTRODUCTION

New Energy and Industrial Technology Development Organization (NEDO) was established as a governmental agency in October 1980 after the Second Oil Crisis. Its purpose is to act as an implementing agency of the Japanese Government in fields related to technological development. One of the most important activities is to develop and promote of new energies, such as geothermal energy.

In fields of geothermal energy, NEDO is working to research and development of technology for example hot dry rock technology (e.g. Hirakawa et al (1989)). Not only such kind of R/D projects, but NEDO is also working to promote geothermal resource development for private corporations, and in order to facilitate such development. It is implementing the "Geothermal Development Promotion Survey" project sponsored by Ministry of International Trade and Industry (MITI). Since 1980, surveys have been conducted in 40 areas across Japan to prospect geothermal resources in this project. Of these, surveys of 32 areas have been completed by the end of 1992. NEDO selects two or three new areas for this project each year, and each area is surveyed for two to four years.

In 1989 NEDO selected Hachijojima area as one of those new areas for this project, and started surveys. The island is one of the volcanic islands in the Izu-Mariana Island Arc. The main surface survey methods are geological surveys, geochemical surveys, geophysical surveys. As drilling survey NEDO drilled 8 slimholes named HJ-1 to HJ-8, and measured borehole temperature, physical properties of their boring core and did injection test. The minimum depth of these wells is 500m and the maximum depth is 1500m. The maximum borehole temperature measured in those wells is 317°C at 1200m depth of well HJ-7.

In 1990 NEDO drilled one of those wells named HJ-5 which was planned with 1000m depth, but NEDO gave up to continue drilling when it arrived 500m depth because of its difficulties to prevent loss circulation and too high formation temperature. Its borehole temperature arrived about 250°C at 200m depth. After completion of this well with 511m depth, in 1991 NEDO tried short time discharge test using this well. During this discharge test NEDO measured borehole temperature and pressure distribution during discharge. Before this discharge test the authors tried to predict the productive performance of this well. But there were much differences between the prediction and measured data. After discharge test the authors kept trying to calculate one to match with measured data. The authors introduce those calculated borehole temperature and pressure distribution during discharge compared with measured data.

NEDO drilled another well named HJ-8 with 1200m depth in 1991 which recorded 305°C at 1200m depth. The authors tried the productive performance of this well. But unfortunately because of casing damage NEDO gave up to do discharge test using this well, so it is impossible to compare the calculated results with measured data.

GEOLOGICAL STUDY

Hachijojima Island is one of the volcanic islands in the Izu-Mariana Island Arc in the northwestern Pacific Ocean and about 300km

south of Tokyo. Fig.1 shows the location of this island. The shape of the island is as like as a cocoon and its area is about 70km^2 with 14km x 7.5km of width. Fig.2 shows the topographic map of this island and location of wells.

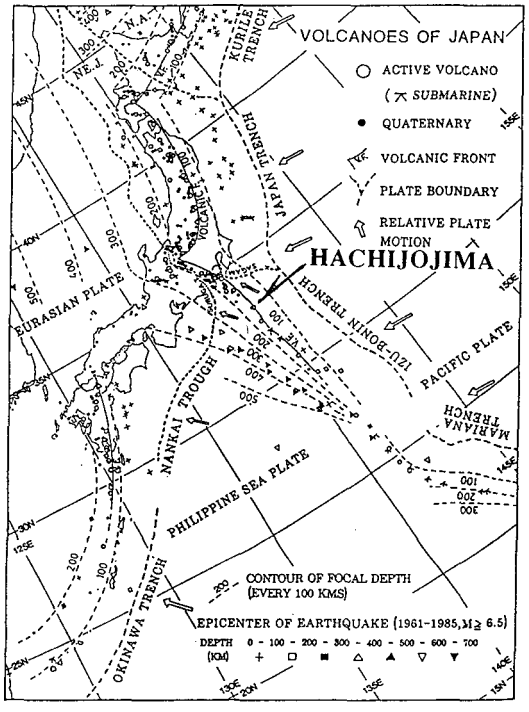

N. A.: North American Plate, NE J.: NE Japan Micro Plate

Fig.1 INDEX MAP OF THE HACHIJOJIMA

There are two Quaternary strato-volcanoes named Nishiyama(mean Western Mountain) and Higashiyama(mean Eastern Mountain) with many parasitic cones (Isshiki (1959)). They have another name "Hachijo-Fuji" and "Miharayama." Volcanic eruption were recorded at Nishiyama Volcano in the 17th century but there are no volcanic eruption record at Higashiyama Volcano.

These Quaternary volcanic rocks lie on the basement of Neogene volcanic rocks and Pleistocene sedimentary and volcanic rocks. Those basement rocks do not crop out in this island but they are identified in boring core.

The volcanic activity at Higashiyama Volcano was prior to Nishiyama Volcano. Its volcanic activity was from about 400,000 years BP to 4,000 years BP. The volcanic activity at the Nishiyama Volcano began after one of the Higashiyama Volcano and its activity continued on into present.

There are several hot springs on the seaside of the Higashiyama Volcano in the southern to eastern part of the island. For example at the southern seaside of the Volcano, there are several hot springs with temperature of 50 to 70^{o}C at the surface. These hot water contains much Na and Cl contents, so it is regarded as heated up sea water. Except these hot springs, there are no hydrothermal manifestations all around the island.

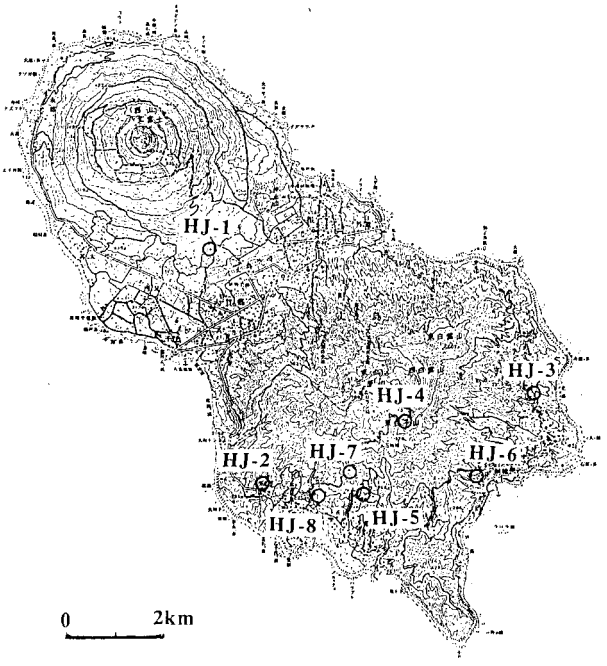

Fig.2 TOPOGARAPHIC MAP OF THE HACHIJOJIMA ISLAND

PROSPECTING METHOD OF THE SURFACE SURVEY

The prospecting method of surface survey which were implemented by NEDO are geological survey, fluid geochemical survey, soil gas geochemical survey, gravity and airborne magnetic survey(analysis only), electromagnetic survey (TDEM method), seismic survey (reflection method using Vibroseis on the land and air gun offshore), and so on.

As results of these surface prospecting, much information and knowledge were got in reference to the geological structure in and around this island especially for basement structure. And they suggest that the southern part of Higashiyama Volcano is the area which has the largest possibility in this island that geothermal reservoir is existence. But they do not suggest no more information about the reservoir, for example its distribution, depth, permeability, temperature, pressure or chemical composition of the geothermal fluid.

UNDERGROUND SURVEY

Specification of drilling and measurement of wells

NEDO drilled 8 wells named HJ-1 to HJ-8 with 500m to 1500m depth in this project. These wells were specified to have their diameters of final drilling step as 98mm or 76mm. These diameters are small in comparison with normal size of geothermal production wells or reinjection wells drilled at geothermal power plant.

Wells named HJ-1 to HJ-3 were drilled in 1989, wells named HJ-4 to HJ-6 were drilled

in 1990 and wells named HJ-7 and HJ-8 were drilled in 1991. Of all these wells, only well HJ-1 were located in Nishiyama Volcano area, other 7 wells were located in Higashiyama Volcano area. Well HJ-4 were located the summit part of the volcano, well HJ-3 and HJ-6 were located in the eastern side of the volcanic body, and well HJ-2, HJ-5, HJ-7 and HJ-8 were located in the southern side of the volcanic body. Fig.2 shows the locations of these wells.

Standard program of measuring data using these wells were well logging (temperature, resistivity and so on) injection test and measuring physical properties using boring cores.

Fig.3 shows the borehole temperature distribution of all wells with elevation in meters ASL VS temperature in degrees in Celsius. These temperature distribution suggested formation temperature near the wells. In the wells HJ-1 to HJ-4, the maximum measured temperature was 182°C at 1500m depth in well HJ-4 and it had not yet confirmed existence of geothermal reservoir.So until this time it had been said that there were no manifestation that suggested geothermal reservoir with high temperature and geothermal fluid.

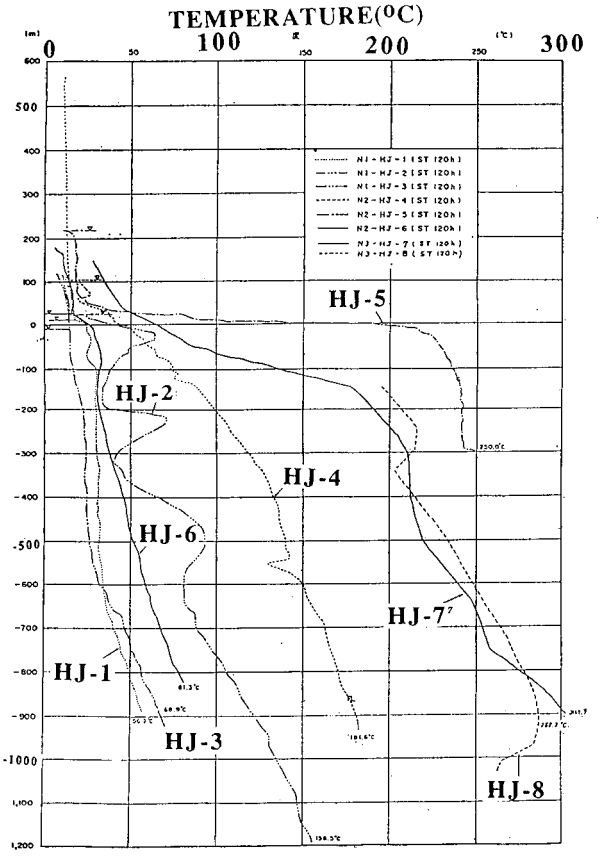

Fig.3 BOREHOLE TEMPERATURE DISTRIBUTION IN THE HACHIJOJIMA AREA

Well HJ-5 were planned with 1000m depth and small diameter. Fig.4 shows the planned cross section of this well. During drilling it was very difficult to continue drilling because of frequently and large lost circulation, over flow and high borehole temperature. At the end NEDO gave up to continue drilling at 511m depth. Fig.4 also shows the completed cross section of this well. From well head to 203m depth casing pipe were set with cement, and from 203m depth to bottom of the well slotted liner were set without cement.

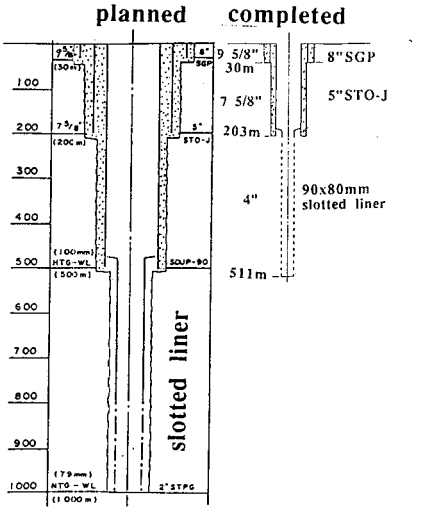

Fig.4 PLANNED AND COMPLETED CROSS SECTION OF WELL HJ-5

Discharge Test of Well HJ-5

After well completion of well HJ-5, NEDO logged borehole temperature and pressure in static condition. Fig.4 shows the borehole temperature and pressure distribution VS depth in m. in static condition. This temperature profile is characterized by a sharp boundary of the formation temperature at 250m depth. The shallower part of this boundary the formation is characterized by very low formation temperature which is lower than 30°C, it results from penetration of meteoric water with low temperature. The deeper part of this boundary is characterized by high formation temperature which is about 250°C cased of existence of up flow of geothermal fluid. At this time they presumed the condition of the reservoir as vapor dominated condition or mixture of vapor and liquid water because of high temperature and relatively lower pressure. During drilling many lost circulation or over flow zone were identified,but it is recognized that important point as feed points are two points with 204m and 346m depth. But it was impossible to identify which is more important for feed point.

From the result of injection test, permeability are presumed as 0.6 to 3.0 darcy-m using type curve matching method or semi-log plot method. But it is supposed that this test were influenced by the skin effect of near the well and blow of gas during drilling, so there were

much inaccuracy of this value of permeability. In 1991 NEDO tried discharge test of this well. Unfortunately lack of reinjection well and of other reason the period of this test was limited very short as 4days. Fig.5 shows the productive performance of well HJ-5 and Fig.6 shows the borehole temperature and pressure distribution in production condition VS depth in meters.

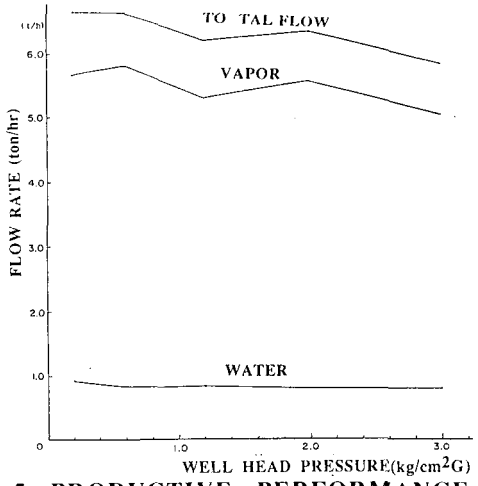

Fig.5 PRODUCTIVE PERFORMANCE OF WELL HJ-5

It is indicated that the phase of fluid in the reservoir is liquid in static condition, and during production the reservoir fluid began flashing in the formation so the borehole temperature and pressure are much lower than those of static condition.
Table1 shows the chemical composition of gas, condensed water and water discharged from well HJ-5. Even though it is feared that there remained influence of injected surface water and mud used during drilling, it is possible to say that the water is not such kind of influenced water nor condensed water of vapor after flashing. The chemical and isotopic composition of those fluid suggest that the origin of fluid water in the reservoir is meteoric water penetrated from the surface of the volcano not ocean water.

BOREHOLE CALCULATION OF WELL HJ-5

The authors had tried to predict the productive performance of HJ-5 prior to the discharge test. But there were much differences between the calculated results and the measured data.
After the discharge test the authors tried to calculate borehole temperature and pressure under production matching with measured data. Fig.6 shows the calculated borehole temperature and pressure distribution VS depth in meters compared with measured data under production. The final term of its calculation is to fix the pressure at the hypothetical production point and well head pressure.There are 4 cases of the calculation. In the case 1 and 2, the vapor/water ratio of the fluid inflow at the production zone are fixed as 0.797. In the case 3 and 4, the temperature at the hypothetical production point as 171.4°C. In the case 1 and 3, we use the heat transfer coefficient as 25 $W/m^2{}^oC$ and in the case 2 and 4, as 0 $W/m^2{}^oC$. Other parameters are shown below.

production zone : 360m depth
formation temperature

20°C	0 to 160 m depth
110°C	160 to 200 m depth
230°C	200 to 360 m depth

Table 1 CHEMICAL AND ISOTOPIC COMPOSITION OF GAS, CONDENSED WATER AND HOT WATER DISCHARGED FROM WELL HJ-5

VAPOR		H_2O	vol.%	97.64
		Gas	vol.%	2.36
		H_2S	vol.%	4.2
		CO_2	vol.%	92.5
		R	vol.%	3.3
		H_2	vol.%	85.1
		N_2	vol.%	12.5
		CH_4	vol.%	2.4
	$\delta^{13}C$ (CO_2)		‰	-1.8
	$\delta^{34}S$ (H_2S)		‰	+6.0
CONDENSED WATER	pH		—	4.3
	Na		mg/ℓ	0.18
	Cℓ		mg/ℓ	0.15
	SO_4		mg/ℓ	2.64
	As		mg/ℓ	0.011
	Hg		ppb	5.5
	δD		‰	-26.6
	$\delta^{18}O$		‰	-1.1
WATER	pH		—	8.5
	SiO_2		mg/ℓ	575
	Cℓ		mg/ℓ	138
	SO_4		mg/ℓ	518
	Na		mg/ℓ	461
	K		mg/ℓ	30.4
	Ca		mg/ℓ	7.15
	Mg		mg/ℓ	0.21
	Fe		mg/ℓ	0.33
	Aℓ		mg/ℓ	1.18
	As		mg/ℓ	0.06
	B		mg/ℓ	114
	Hg		ppb	1.9
	HCO_3		mg/ℓ	319
	CO_3		mg/ℓ	8
	H_2S		mg/ℓ	18.9
	EC		μS/cm	2,190
	δD		‰	+7.8
	$\delta^{18}O$		‰	+4.7
	$\delta^{13}C$ (CO_2)		‰	+1.5
	$\delta^{34}S$ (SO_4)		‰	+10.0
	Tritium		TR	0.31±0.10

PRODUCTIVE PERFORMANCE PREDICTION OF WELL HJ-8

In 1991 NEDO drilled well HJ-8 with 1200m depth which located 1000m west of well HJ-5. After completing the well, temperature logging recorded 305°C at 1200m depth. Injection test showed its permeability is 0.59darcy-m, but as same as well HJ-5 this value has much inaccuracy. Fig.7 shows the cross section of this well.

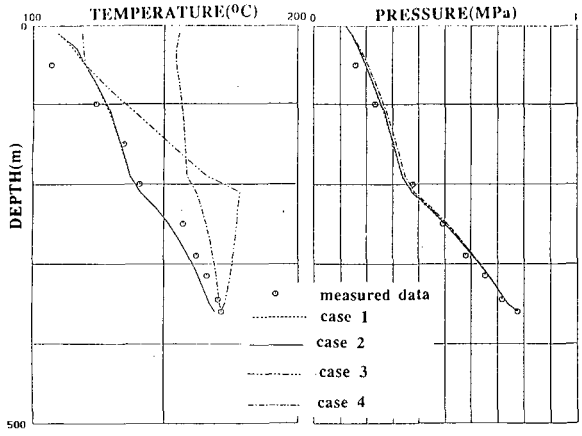

Fig.6 CALCULATED AND MEASURED BOREHOLE TEMPERATURE AND PRESSURE UNDER PRODUCTION OF WELL HJ-5

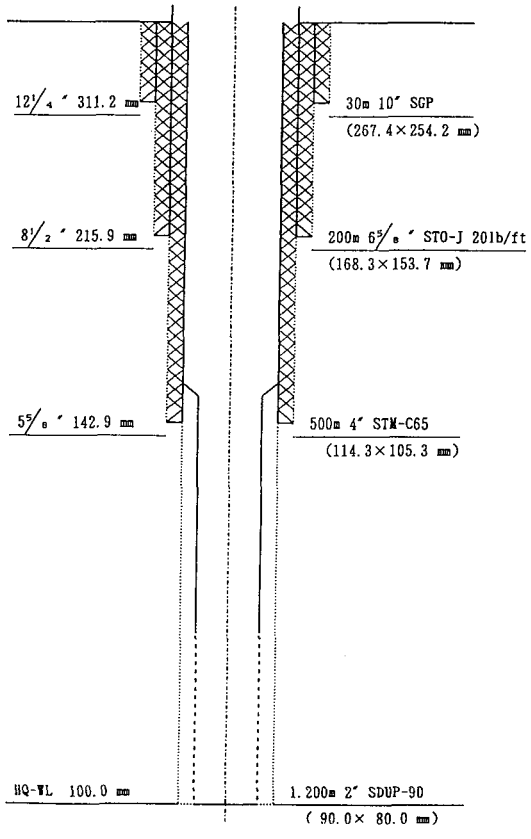

Fig.7 CROSS SECTION OF WELL HJ-8

The authors predicted the productive performance of well HJ-7. Fig.8 shows the calculation result of the relationship of well head pressure and flow rate as productive performance. The parameters of this calculation

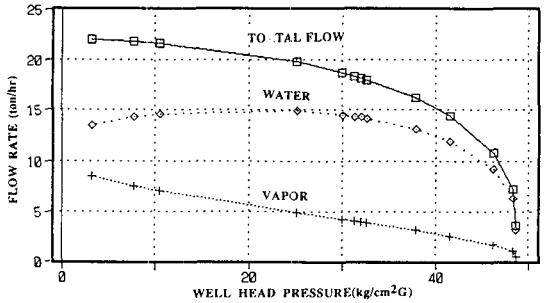

Fig.8 RELATIONSHIP OF WELL HEAD PRESSURE AND FLOW RATE DISCHARGED FROM WELL HJ-8

are shown below.
feed point : 1020m depth
temperature at feed point under static condition : 285°C
pressure at feed point under static condition : 92.96kg/cm^{2}G
In the case 1 and 3, we use the heat transfer coefficient : 0 W/m^2°C
Unfortunately NEDO gave up discharge test of this well because of casing damage and fear of blowing out caused too high formation temperature and pressure to preserve the well for such kind of slimhole. To prevent blowout NEDO completely plugged this well after injection test.
So it is impossible to compare this calculation with measured data

CONCLUSION

Through these survey and analysis of their datum clarified some knowledge about the geothermal reservoir showed below.
1)a geothermal reservoir exists in the southern part of Higashiyama Volcano.
2)the depth of the reservoir are 200 to 1500m in depth, but no information about detail distribution and shape
3)the temperature of the reservoir is 250 to 300°C
4)the phase of geothermal fluid in the reservoir is liquid with formation flashing under production or mixture of liquid and vapor water in reservoir.
5)quality of geothermal resource is enough for geothermal generation but its quantity is unknown.
6)more investigation is needed especially to get more information about distribution of permeability

ACKNOWLEDGMENT

The authors would like to thank Mr. Takahisa Mimura for valuable discussion and Mr. Kazunaga Murakami and other members of KCC for their support and facilities during simulation.

REFERENCES

Hirakawa, S., Miyazaki, Y. and Satoh, Y. (1989) "Reservoir Physics and Hot Dry Rock in Current National R/D Projects", Proceedings

Fourteenth Workshop Geothermal Reservoir Engineering, Stanford University, p.227-232.

Issiki, N. (1959) "Explanatory Text of the Geological Map of Japan, in Scale 1:50,000 HACHIJO-JIMA", Geological Survey of Japan, 58p. (in Japanese with English abstract, 5p.)

PROCEEDINGS, Eighteenth Workshop on Geothermal Reservoir Engineering
Stanford University, Stanford, California, January 26-28, 1993
SGP-TR-145

USE OF SLIM HOLES FOR GEOTHERMAL EXPLORATION AND RESERVOIR ASSESSMENT: A PRELIMINARY REPORT ON JAPANESE EXPERIENCE

S. K. Garg
S-Cubed, P.O. Box 1620
La Jolla, California

J. Combs
Geo Hills Associates
Los Altos Hills, California

ABSTRACT

The publicly available Japanese data on the use of slim holes in geothermal exploration and reservoir assessment are reviewed in this report. Slim holes have been used for (1) obtaining core for geological studies, (2) delineating the stratigraphic structure, (3) characterizing reservoir fluid state (pressure, temperature, *etc.*), and (4) defining the permeability structure for reservoir assessment. Examples of these uses of slim hole data are presented from the Hohi Geothermal Area and the Sumikawa Geothermal Field. Discharge data from slim holes and production wells from the Oguni Geothermal Field indicate that it may be possible to infer the discharge rate of production wells based on slim hole measurements.

1. INTRODUCTION

The principal cost associated with the identification, assessment, and development of geothermal reservoirs for electrical power production is the high cost of drilling the exploration, production, and injection wells. A major impediment to the exploration of new geothermal areas is the high cost of conventional rotary drilling. A conventional 1200 to 1800 m deep rotary-drilled well can cost millions of dollars. Compared to conventional large-diameter wells, the drilling costs for small-diameter (less than 10 cm) slim holes are relatively low. Because of this cost differential, it would be desirable to use slim holes for geothermal exploration and reservoir assessment. At present, there exists little experience in the U. S. geothermal industry in the use of slim holes for exploration and reservoir assessment purposes. Combs and Dunn (1992) have argued the need for a U. S. Department of Energy (DOE)-industry coupled slim hole research and development program.

In contrast to the situation in the United States (*i.e.*, lack of sufficient experience with slim holes in geothermal exploration), the Japanese routinely employ small-diameter core holes in geothermal exploration and reservoir assessment. Besides obtaining core for geological studies, slim holes have been used for characterizing reservoir fluid state and reservoir permeability structure. Most of the Japanese data pertaining to slim holes are proprietary. Sufficient published data are, however, available to produce a preliminary report on Japanese experience, and to provide some tentative conclusions about using slim holes to predict production capability of large-diameter wells.

The publicly-available Japanese data on the use of slim holes in geothermal exploration and reservoir assessment are reviewed in Section 2. It is often difficult to induce deep small-diameter holes (depths >> 300 m) to discharge. A parallel theoretical study discussing the effect of well-diameter on the production behavior of geothermal boreholes is presented elsewhere (Pritchett, 1992); important conclusions of that study are summarized in Section 3. Prediction of the production characteristics of large-diameter wells on the basis of tests performed in small-diameter core holes is also discussed in Section 3.

2. REVIEW OF PUBLISHED JAPANESE SLIM HOLE DATA

The first commerical scale geothermal power station in Japan (Matsukawa Geothermal Power Plant) was commissioned in 1966. As of March 1991, the total installed capacity stood at ~ 270 MW. Additional geothermal power plants are under development at several sites in the Tohoku and Kyushu districts (see Figure 1).

Since the first oil crisis in 1974, the Japanese government (primarily through the Geological Survey of Japan, Agency of Industrial Science and Technology, New Energy and Industrial Technology Development Organization (NEDO)) has actively promoted the exploration and development of geothermal resources (see JGEA, 1992). As discussed by Maki and Kawano (1988), NEDO has been carrying out government subsidized geothermal surveys throughout Japan since 1980. Under its "Geothermal Development Promotion Survey" program, NEDO drilled 189 wells. The report by Maki and Kawano (1988) presents a statistical analysis of penetration rates for 47 HQ (98 to 101 mm) and NQ (76 to 78 mm) core holes drilled during Japanese fiscal years 1984–1986. Most of the boreholes drilled by NEDO have been injection tested; in addition, a small number (5 to 10 percent) of boreholes have been discharged (Kawano, personal communication, 1992).

In addition to core holes drilled by NEDO and other governmental agencies, a large number of core holes have been drilled by private developers. Unfortunately, because

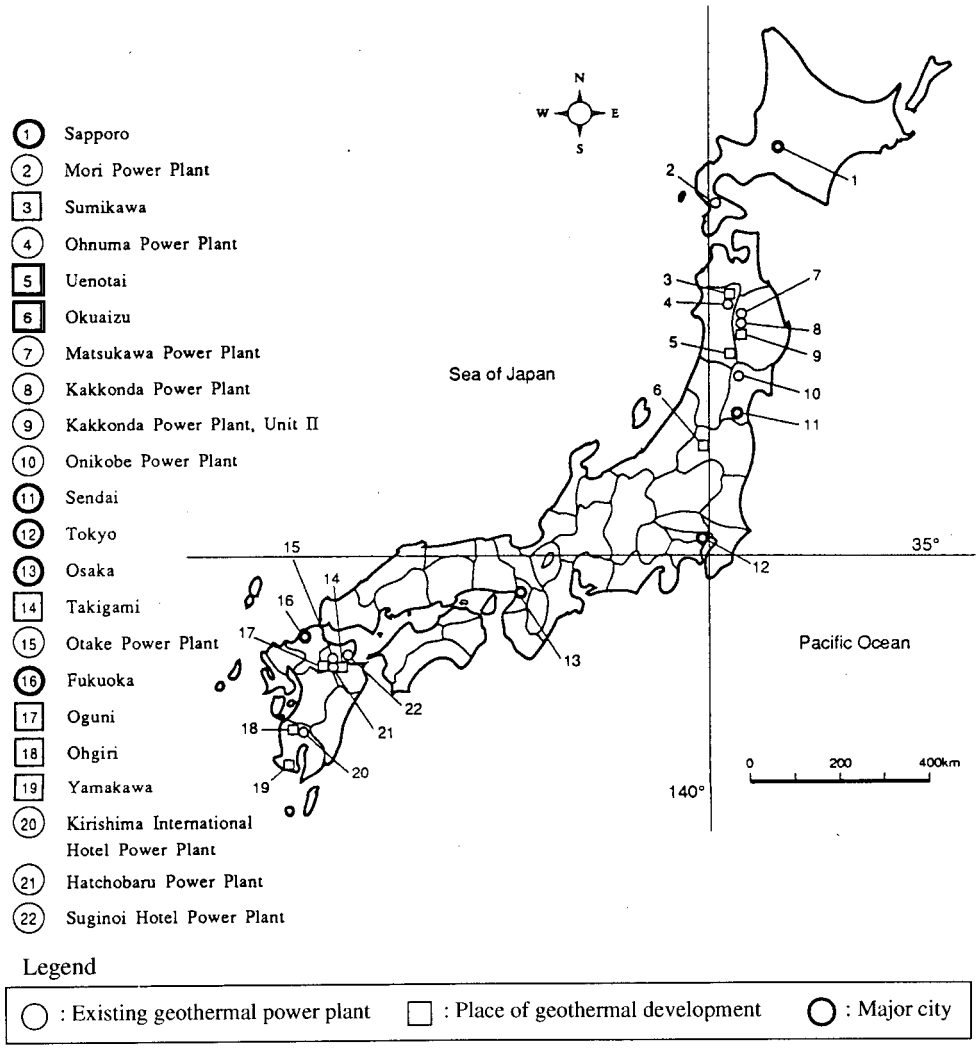

Figure 1. Geothermal power plants and places of geothermal development in Japan (from JGEA, 1992).

of proprietary and other (*e.g.*, language) reasons, most of the data obtained from these core holes are not easily accessible. In the following paragraphs, we briefly describe the publicly available reports on the use of core holes for reservoir assessment purposes.

2.1 HOHI GEOTHERMAL AREA

During the years 1978–1985, the Ministry of International Trade and Industry conducted a regional exploration survey in the Hohi area, Kyushu, Japan (NEDO, 1987). The main area of the survey encompassed 200 km^2 centered on Mt. Waita. As part of this exploration program, both small-diameter core holes ("DB" and "DW" series) and large-diameter production-size wells ("DY" series) were drilled. All of the "DB", "DW", and "DY" series boreholes were injection tested. Since no downhole pressure measurements were made during these injection tests, the injection test data are not useful for inferring formation properties for reservoir assessment purposes. None of the small-diameter "DB" and "DW" series slim holes were discharged; of the "DY" series wells, only two wells (DY-1 and DY-5) could sustain discharge. Murakami, *et al.* (1986) discuss the discharge characteristics of well DY-1. The well was continuously discharged for a six-month period in 1982 at discharge rates between 16 kg/s and 60 kg/s.

Pritchett, *et al.* (1985) present a preliminary reservoir engineering study of the western portion of the Hohi area (see Figure 2). Although the southeastern part of the study area contains the Hatchobaru and Ohtake geothermal fields, no data from these fields were made available for Pritchett, *et al.'s* (1985) study. Available downhole data consisted of (1) drilling data (circulation loss data, well completion information, and geologic data), and (2) repeat temperature and water level surveys. No downhole pressure measurements were taken; feedpoint pressures were estimated from temperature and water level data. Production data (mainly water and steam flow rates, and wellhead pressure) were available from only one well (*i.e.*, DY-1). Core-hole data were invaluable for defining (1) the stratigraphic sequence, and (2) reservoir temperature and pressure

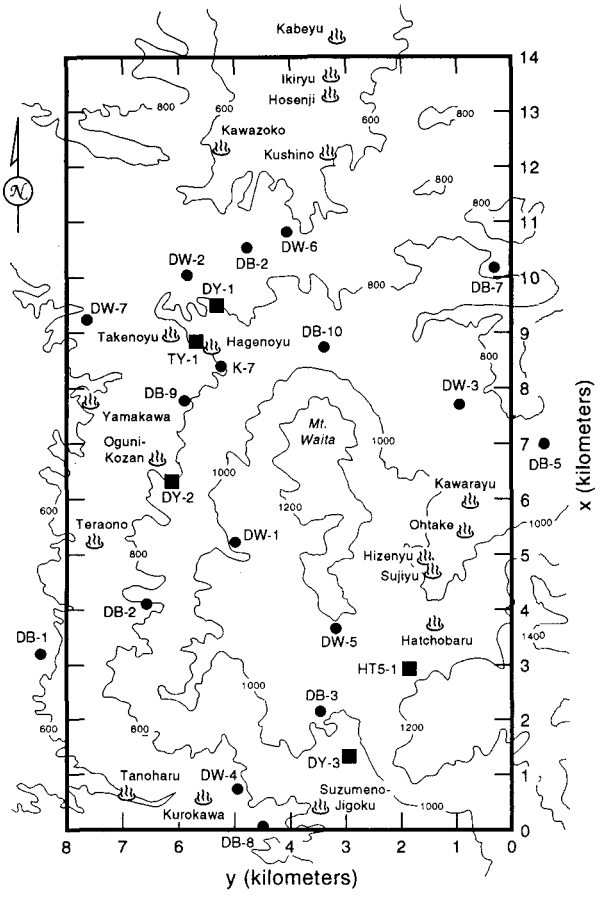

Figure 2. Outline of western Hohi study area showing boreholes, hot springs and surface elevation contours (m ASL) (from Pritchett, *et al.*, 1985). Slim holes are indicated by ● and production wells are represented by ■.

distribution (see Figures 3–5). It can be seen from Figures 3 and 4 that a very large volume of hot reservoir rock is present in the northwestern part of the study area. The feedzone pressures for seven boreholes (five slim holes DB-4, DW-2, K-7, DW-6, and DW-7; and two large-diameter production wells TY-1 and DY-1) in the northwestern area all lie on a straight line (Figure 5); this straight line comprises a lower bound on all the data. Apparently, the northern reservoir forms a separate hydrological entity. The circulation loss data from the northern wells indicated that most of the permeability in the northern reservoir is associated with a horizontal fracture zone in the upper part of pre-Kusu formation near sea-level elevation. Using the reservoir pressure distribution derived essentially from the slim-hole data and the hot spring flow data, Pritchett, *et al.* (1985) estimated a permeability-thickness product of 40 darcy-meters for the northern reservoir.

Since the completion of the above mentioned regional survey of the Hohi area, EPDC and NEDO have carried out additional drilling and well testing programs in the northern Hohi area (Oguni and Sugawara geothermal fields). These new data from production wells have in the main confirmed

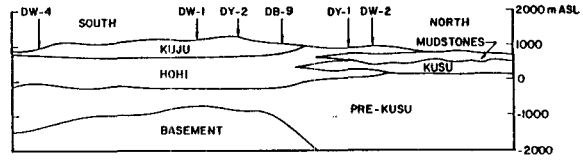

Figure 3. Stratigraphic sequence at Hohi (from Pritchett, *et al.*, 1985).

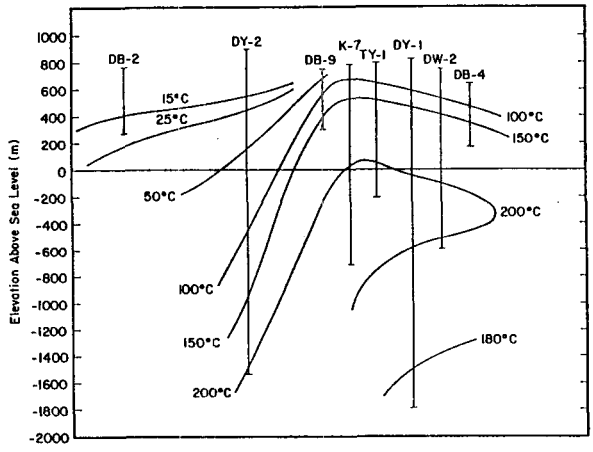

Figure 4. Vertical temperature distribution at Hohi along a line extending from borehole DB-2 to borehole DB-4 (from Pritchett, *et al.*, 1985).

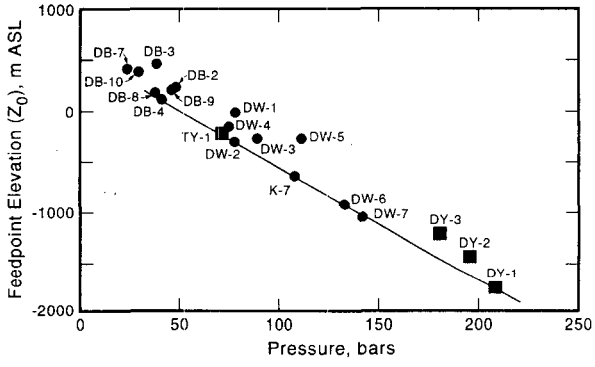

Figure 5. Pressure as a function of elevation for all boreholes in the western Hohi area (from Pritchett, *et al.*, 1985). Slim holes are indicated by ● and production wells are represented by ■.

the conceptual model of Pritchett, *et al.* (1985) for the northwestern Hohi area (surface area ~ 40 km^2; Figure 2) based primarily on the data obtained from slim holes.

It is worthwhile to recall here that Pritchett, *et al.*'s model for the northern Hohi area was based almost entirely on data from (1) seven boreholes (DB-4, TY-1, DW-2, K-7, DW-6, DW-7 and DY-1) of which five were slim holes and (2) surface geological and geophysical surveys (including hot spring discharge rates and temperatures). Of the seven boreholes, five (DB-4, DW-2, DW-6, DW-7 and DY-1) were

drilled under the NEDO program; the remaining two wells (TY-1 and K-7) were drilled by local authorities. As already mentioned, production data were available for only one well (DY-1). The modeling experience for the northern Hohi area indicates that a minimum amount of borehole data (water level and temperature data, stratigraphy and circulation loss data from drilling surveys, discharge data from 1 hole) along with surface surveys (*i.e.*, hot spring data, gravity survey) can be used to derive a preliminary estimate of the power potential of a geothermal area. It should be stressed here that while the amount and type of data required for reservoir assessment will vary from case to case, small-diameter core holes can be used to obtain many of the data (*e.g.*, reservoir pressure and temperature estimates, stratigraphy, *etc.*) needed in reservoir engineering studies.

2.2 SUMIKAWA GEOTHERMAL FIELD

Because of their limited capacity, small-diameter core holes are often unsuitable as production or injection wells in a pressure interference test. The amplitude of the pressure signal generated by production from or injection into a core hole is often too weak to be monitored in neighboring wells. On the other hand, small-diameter core holes can be used as monitoring wells. Garg, *et al.* (1991) present a discussion of the pressure-interference testing of the Sumikawa geothermal wells.

The Sumikawa Geothermal Field is located in the Hachimantai volcanic area in northern Honshu, Japan. The region of particular interest is shown in Figure 6. The Sumikawa Geothermal Field lies in the western part (area around boreholes S-1, S-2, S-3 and S-4) of the region depicted in Figure 6. To the east, the Ohnuma power station has been producing about 10 MW of electrical power for several years. The subsurface stratigraphic structure in the Sumikawa area is shown in Figure 7. This is based almost exclusively on drilling experience. The major formations in order of increasing depth are (1) surficial andesite tuffs, lavas and pyroclastics (ST formation), (2) lake sediments (LS

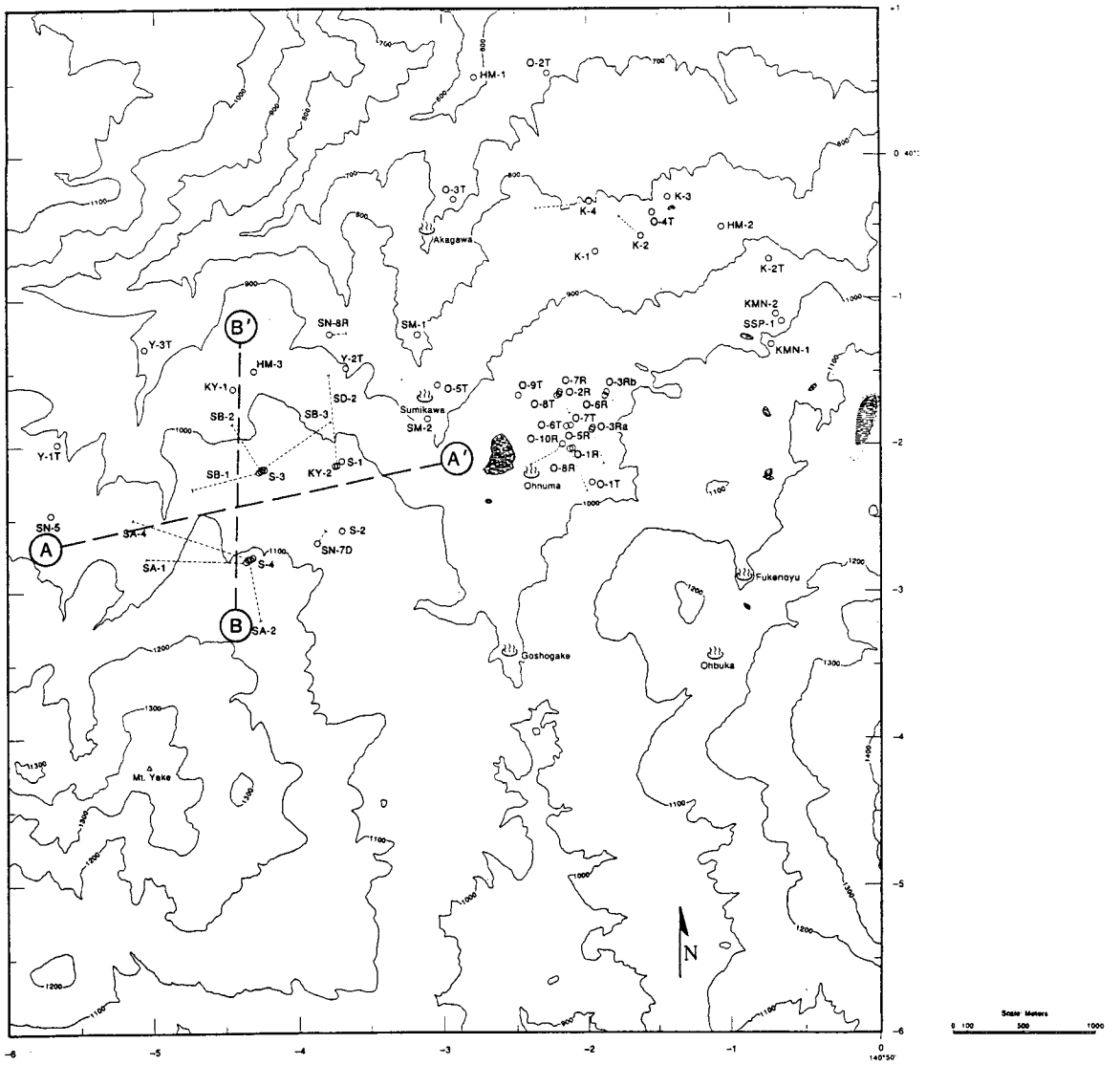

Figure 6. The Sumikawa/Ohnuma area, showing locations of boreholes and cross-sections A–A′ and B–B′ (from Garg, *et al.*, 1991).

formation), (3) Pliocene dacites and tuffs (DA formation), (4) interbedded Miocene dacitic volcanic rocks and black shale (MV or marine/volcanic complex), (5) altered and fractured andesites (AA formation) and (6) crystalline intrusive rocks (GR formation).

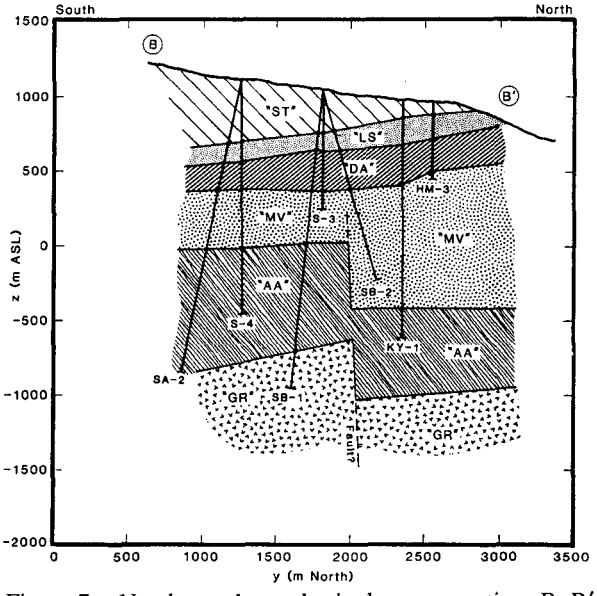

Figure 7. North-south geological cross-section B–B′ through the Sumikawa area (from Garg, *et al.*, 1991).

In April and May 1989, cold water was injected into several wells (SA-1, SA-2, SA-4, S-4, SB-1, SB-2 and SB-3). Slim hole KY-1 responded to injection into wells S-4, SB-1 and SB-2 (see *e.g.*, Figure 8). Apparently, wells S-4 and SB-1 communicate with slim hole KY-1 through the altered andesite layer (AA formation); well SB-2 is connected to slim hole KY-1 through an interbedded dacite layer in the marine/volcanic complex formation.

Pressure response of slim hole KY-1 to production (injection) from well S-4 was interpreted by Garg, *et al.* (1991) to indicate the presence of a very high permeability channel in the altered andesite layer (main production zone at Sumikawa). Pressure interference between slim hole KY-1 and well SB-2 was used to confirm the presence of a moderately high transmissivity layer in the "marine-volcanic complex" formation (main injection zone at Sumikawa). The experience at Sumikawa (as well as several other fields in Japan) has clearly shown that the small diameters of core holes pose no limitations on their use as pressure monitoring wells.

2.3 OGUNI GEOTHERMAL FIELD

In at least some cases, small-diameter core holes have been discharged (1) to collect fluid samples, and (2) to obtain first indications of the productivity of a geothermal formation. Abe, *et al.* (1992) gives tabular values for water and steam flow rates from both the small-diameter core holes and large-diameter production wells in the Oguni Geothermal Field

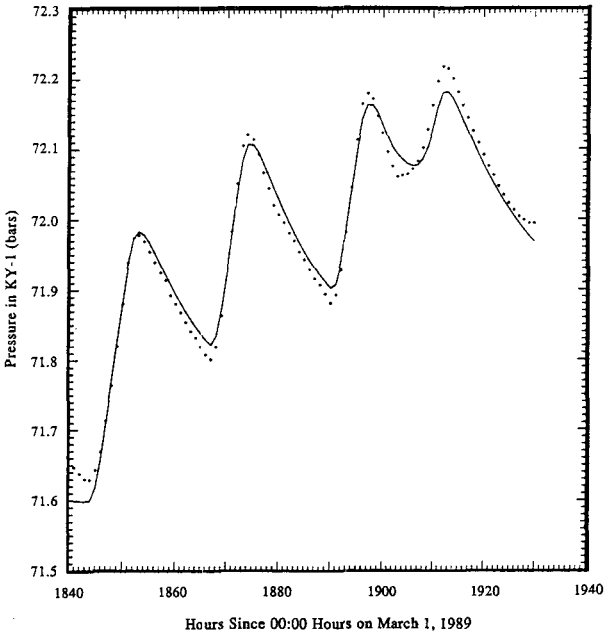

Figure 8. Comparison of computed pressure response of small-diameter core hole KY-1 at Sumikawa with measurements due to cold water injection into well S-4 (—computed, • measurements) (from Garg, *et al.*, 1991).

(the Oguni Geothermal Field forms a part of the northern Hohi area). According to Abe *et al.* (1992), several HQ and NQ size core holes have been successfully discharged (see Table 1). Of course, the production rate of the small-diameter core holes is a small fraction of the large-diameter production-size wells. Ideally, one would like to predict the productivity of large-diameter production wells based on results of injection into or production from small-diameter core holes. The question of the scale-up of production/injection data from core holes to forecast the production behavior of large-diameter wells is considered in Section 3.

3. EFFECT OF BOREHOLE DIAMETER ON PRODUCTION CHARACTERISTICS

Production characteristics of a geothermal borehole are in the main determined by (1) pipe friction and heat losses in the wellbore, and by (2) pressure losses associated with flow in the reservoir rocks. Ignoring pressure transient effects, the flow resistance (or pressure losses) of the reservoir rocks can be represented by the productivity (or injectivity) index. The productivity indices of slim holes and production wells are discussed in Section 3.2.

Pritchett (1992) has carried out a theoretical study of the discharge characteristics of slim holes compared to production wells. To compare the fluid carrying capacity of a borehole as a function of diameter (d), it is convenient to define the "area-scaled well discharge rate" M^* as follows:

$$M^* = M \times \left(\frac{d}{d_o} \right)^2 \qquad (1)$$

Table 1. Diameter, depth, maximum temperature, and production rate for small-diameter core holes and large-diameter production wells in the Oguni area (from Abe, *et al.*, 1992).

Well Name	Final Stage Well Dia. mm	Drilling depth m	Max temp. °C	Steam flow rate t/hr	Hot water flow rate t/hr	Completion year	Note
HH-1	76	700	206	–	–	1984	
HH-2	76	1,000	231	3	2	1984	
HH-3	76	500	210	–	–	1984	
GH-1	76	1,950	175	–	–	1983	
GH-2	76	1,800	155	–	–	1984	
GH-3	76	1,500	223	5	15	1985	
GH-4	76	1,000	239	6	18	1985	
GH-5	76	1,500	235	2	17	1985	directional
GH-6	76	1,000	222	8	28	1985	
GH-7	98	1,544	230	6	20	1985	directional
GH-8	78	1,300	223	7	28	1986	directional
GH-9	81	1,600	243	–	–	1986	directional
GH-10	159	1,063	239	49	119	1986	directional
GH-11	216	1,381	235	45	166	1987	directional
GH-12	216	1,100	230	45	152	1988	directional
GH-13	159	900	181	—	—	1987	directional
GH-14	216	650	225	65	238	1989	directional
GH-15	216	1,190	232	9	28	1990	directional
GH-20	216	1,790	248	82	287	1990	directional

where M is the actual borehole discharge and d_o is the internal borehole diameter (cm). Assuming that (1) the boreholes feed from an all liquid-zone, and (2) the feedzone pressure and temperature are independent of borehole diameter, calculations were carried out for a variety of borehole diameters varying between 5 cm and 35 cm; the results of these calculations are displayed in Figure 9. The wellhead pressure/flowrate relationships for the various borehole diameters do not collapse to a single curve (Figure 9), even when flow rates are adjusted to account for differences in cross-sectional area. Clearly, the area-scaled maximum discharge rate declines with a decrease in borehole diameter. As discussed by Pritchett (1992), both frictional pressure gradient and heat loss effects are more significant for the smaller-diameter slim holes than for the larger-diameter wells. The difference in heat loss effects is probably responsible, at least in some cases, for the difficulty encountered in inducing deep slim holes (depths >> 300 m) to discharge. Theoretical results suggest that to induce deep slim holes to discharge, it may be necessary to employ unusual techniques such as preheating the borehole prior to startup.

For the conditions (feedzone depth = 1500 m, flowing feedzone pressure = 80 bars, feedzone temperature = 250°C, uniform diameter wellbore) considered by Pritchett (1992), the maximum discharge rate (*i.e.*, flow rate at 1 bar wellhead pressure) scales with borehole diameter according to the following relation:

$$M_{\max} = M_o\left(d/d_o\right)^{2.56} \qquad (2)$$

where M_o denotes the maximum discharge rate for a borehole of diameter d_o. Equation (2) implies that the "area scaled" maximum attainable flow rate increases approximately with the square root of borehole diameter.

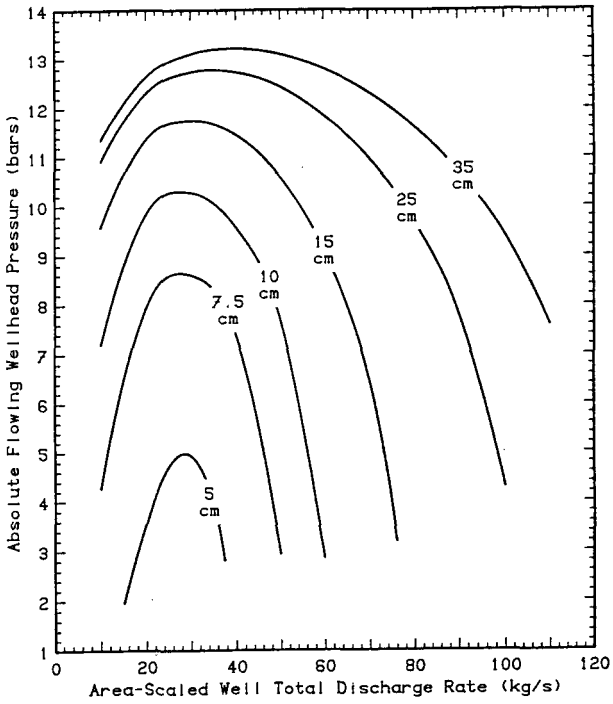

Figure 9. Influence of diameter on borehole performance characteristics (from Pritchett, 1992).

3.1 PREDICTION OF DISCHARGE RATE OF PRODUCTION WELLS FROM SLIM HOLE DATA AT OGUNI GEOTHERMAL FIELD

Abe, *et al.* (1992) do not make it clear if the indicated flow rates for Oguni boreholes in Table 1 are the maximum attainable flow rates for these boreholes. There also exists little reason to expect that the Oguni boreholes conform to the conditions assumed by Pritchett (1992) for his theoretical study. Despite these uncertainties about the Oguni data set, it was decided to investigate the possibility of predicting the discharge rate of the Oguni production wells (GH-11, GH-12, GH-14, GH-15, GH-20) from the slim hole data. Scaled discharge rates for production wells using (1) simple area scaling (Equation 1) and (2) a scaling rule for maximum flow (Equation 2) are given in Table 2. The measured discharges for wells GH-11 (211 t/h), GH-12 (197 t/h), and GH-14 (303 t/h) are bracketed by the average area-scaled discharge rate (176 t/h) and by the average scaled maximum discharge rate (311 t/h) obtained from the measured slim hole discharge data. While the measured discharge rate for well GH-15 (37 t/h) is anomalously low, the measured discharge rate for well GH-20 (369 t/h) is about 20 percent higher than the average scaled maximum discharge rate. The Oguni data are consistent with the premise that it should be possible to infer the discharge rate of large-diameter wells based on production data from small-diameter core holes. It should, however, be stressed that the latter conclusion needs to be tested with data from a statistically significant collection of geothermal fields.

Table 2. Predicted discharge rates for the production-size wells at Oguni (wells GH-11, GH-12, GH-14, GH-15, GH-20) derived from scaling measured discharge rates of slim holes at Oguni Geothermal Field.

Well Name	Final Stage Well Diameter (mm)	Measured Discharge Rate (t/hr)[a]	Area-Scaled Discharge Rate (t/hr)[b]	Scaled Maximum Discharge Rate (t/hr)[c]
HH-2	76	5	40	72
GH-3	76	20	162	290
GH-4	76	24	194	348
GH-5	76	19	153	275
GH-6	76	36	291	522
GH-7	98	26	126	197
GH-8	78	35	268	475
		Average	176	311

(a) Data from Abe, *et al.* (1992)
(b) Equation (1), $d = 216$ mm
(c) Equation (2), $d = 216$ mm

3.2 INJECTIVITY AND PRODUCTIVITY INDICES OF SLIM HOLES AND PRODUCTION WELLS

Theoretical considerations (Pritchett, 1992) imply that apart from any systematic differences resulting from skin effects, the productivity index should exhibit only a weak dependence on borehole diameter. At present, published data comparing the productivity indices (and skin factors) for small-diameter slim holes and production-sized wells are simply unavailable. There is also a need to establish a relationship between injectivity index obtained from cold water injection tests and productivity index obtained from discharge tests. Classical analyses which assume porous-medium flow (see *e.g.*, Garg and Pritchett, 1990) suggest that the injectivity index should be a strong function of the sandface injection temperature. (Note that the dynamic viscosity of water varies greatly with temperature and according to Darcy's law, pressure drop or increase is directly proportional to fluid viscosity.)

Grant, *et al.* (1982) have, however, argued that the conclusions derived on the basis of porous medium flow do not apply to geothermal systems. Most geothermal systems are associated with fractured igneous and metamorphic rocks. The following quotation from Grant, *et al.* (1982) is pertinent:

> "The productivity of a well is found to be less than injectivity. It was argued above (Section 5.6 and A1.4) that transmissivity measured with injection tests is that of the hot reservoir fluid. That is, transmissivity or injectivity measured in injection tests is equal to transmissivity or productivity in discharge. Often this is so. When it is not so, it is usually the case that injectivity is greater than productivity, despite the lower viscosity of hot water."

We do not know what data were used by Grant, *et al.* (1982) in reaching their conclusions. At present, sufficient published data are unavailable which would enable one to state with a high level of confidence that the productivity and injectivity indices are essentially equal for geothermal boreholes.

4. ACKNOWLEDGMENT

This work was supported through Geo Hills Associates under Contract AA-7144 from Sandia National Laboratories. The authors thank James Dunn for his review and comments on this report.

5. REFERENCES

Abe, M., S. Kurishima, and Y. Mezaki (1992) "Drilling of Geothermal Well in the Onikobe Geothermal Field and Developing Oguni Geothermal Field," *Chinetsu, Vol. 29 (1)*, pp. 1–32.

Combs, J. and J. C. Dunn (1992), "Geothermal Exploration and Reservoir Assessment: The Need for a U. S. Department of Energy Slim-Hole Drilling R & D Program in the 1990s", *Geothermal Resources Council Bulletin, Vol. 21., No. 10*, in press.

Garg, S. K. and J. W. Pritchett (1990), "Cold Water Injection Into Single- and Two-Phase Geothermal Reservoirs," *Water Resources Research, Vol. 26*, pp. 331–338.

Garg, S. K., J. W. Pritchett, K. Ariki, and Y. Kawano (1991), "Pressure-Interference Testing of the Sumikawa Geothermal Field," *Proceedings Sixteenth Workshop on Geothermal Reservoir Engineering*, Stanford University, Stanford, California, January 23–25, pp. 221–229.

Grant, M. A., I. G. Donaldson, and P. F. Bixley (1982), *Geothermal Reservoir Engineering*, Academic Press, New York, p. 310.

Japan Geothermal Energy Association (JGEA) (1992), "Annual Report on Geothermal Energy Development in Japan: 1992", Tokyo, Japan, 12 pp.

Maki, H. and Y. Kawano (1988), "Statistical Analysis of Penetration Rate and Lost Circulation in Geothermal Wells," *Proceedings International Symposium on Geothermal Energy: Exploration and Development of Geothermal Resources*, Kumamoto and Beppu, Japan, November 10–14, pp. 388–391.

Murakami, K., T. Ishido, T. Yoshimura, S. Nakanishi, M. Fukushima, J. W. Pritchett, and S. K. Garg (1986), "Discharge Performance Analysis of Well DY-1 in the Hohi Geothermal Area," *Journal of the Geothermal Research Society of Japan, Vol. 8*, pp. 15–36.

New Energy Development Organization (NEDO) (1987), "Survey of Large-Scale Deep Geothermal Development With Regard to Environmental Conservation: Integrated Evaluation (Hohi Area)," report submitted to Ministry of International Trade and Industry (MITI), Tokyo, Japan, March, 116 pp.

Pritchett, J. W. (1992), "Preliminary Study of Discharge Characeristics of Slim Holes Compared to Production Wells in Liquid-Dominated Geothermal Reservoirs," Report No. SSS-TR-92-13133, S-Cubed, La Jolla, California, July, 48 pp.

Pritchett, J. W., S. K. Garg, W. E. Farrell, T. Ishido, T. Yoshimura, K. Murakami and S. Nakanishi (1985), "The Hohi Geothermal Area, Kyushu, Japan," *Proceedings Tenth Workshop on Geothermal Reservoir Engineering*, Stanford University, Stanford, California, January 22–24, pp. 79–87.

PROCEEDINGS, Eighteenth Workshop on Geothermal Reservoir Engineering
Stanford University, Stanford, California, January 26-28, 1993
SGP-TR-145

PRELIMINARY STUDY OF DISCHARGE CHARACTERISTICS OF SLIM HOLES COMPARED TO PRODUCTION WELLS IN LIQUID-DOMINATED GEOTHERMAL RESERVOIRS

J. W. Pritchett
S-Cubed, P.O. Box 1620
La Jolla, California 92038-1620

ABSTRACT

This paper presents a theoretical study of the discharge characteristics of slim holes compared to production wells. Assuming that (1) the boreholes feed from an all-liquid zone, and (2) the feedzone pressure and temperature are independent of borehole diameter, calculations have been carried out for a variety of borehole diameters. The wellhead pressure/flowrate relationships for the various borehole diameters do not collapse to a single curve, even when flow rates are adjusted to account for differences in cross-sectional area. The area-scaled discharge rate declines with a decrease in borehole diameter. Both frictional pressure gradient and heat loss effects are more significant for the smaller-diameter slim holes than for the larger-diameter wells. The difference in heat loss effects is probably responsible, at least in some cases, for the difficulty encountered in inducing deep slim holes (depths >> 300 m) to discharge. Scaling up the discharge capacity of slim holes to those of production wells by the cross-section area ratio provides a conservative estimate of production-size hole discharge.

1. INTRODUCTION

During the exploration of a geothermal prospect, so-called "slim holes" offer an attractive alternative to full-size production well drilling for preliminary characterization of the reservoir, owing both to lower cost and reduced drilling time requirements. The most important problem in reservoir exploration is to establish the underground temperature distribution and the presence of a thermal resource, and large-diameter wells are not required for downhole temperature measurements. Slim holes can also serve to help characterize geological structure, and many geothermal well logging tools can be run in relatively small-diameter holes.

The fluid discharge capacity of a typical slim hole will generally be significantly less than that of a corresponding production-size hole, however. This means, of course, that if a productive region is discovered using slim-hole exploration, it will be necessary to subsequently drill production-size wells to exploit the resource. Also, due to their relatively low fluid discharge capacity, slim holes are not usually useful as signal sources for pressure interference testing (they may, however, be used as shut-in observation wells in interference tests in which the flowing wells are of conventional diameter).

If a slim hole is drilled into a geothermal prospect and can be induced to discharge, the rate of steam production from the slim hole is presumably much less than would have occurred had the well been of conventional diameter. Accordingly, one question of interest is how one might estimate the steam delivery capacity of future production-size wells based upon results from testing slim holes. The discharge characteristics of a geothermal well involve the relationships among stable wellhead flowing pressure, total mass discharge rate, and wellhead fluid enthalpy (i.e., steam/water ratio). If these characteristics are known for one or more slim holes in a prospective geothermal field, is it possible to estimate the corresponding characteristics of future production wells in any meaningful way?

This paper describes a preliminary examination of this question from a purely theoretical point of view. The WELBOR computer program (Pritchett, 1985) was used to perform a series of calculations of the steady flow of fluid up geothermal boreholes of various diameters at various discharge rates. Starting with prescribed bottomhole conditions (pressure, enthalpy), WELBOR integrates the equations expressing conservation of mass, momentum and energy (together with fluid constitutive properties obtained from the steam tables) upwards towards the wellhead using numerical techniques. This results in computed profiles of conditions (pressure, temperature, steam volume fraction, etc.) as functions of depth within the flowing well, and also in a forecast of wellhead conditions (pressure, temperature, enthalpy, etc.). Pipe friction (for both single- and two-phase flow regions) is treated using the formulation of Dukler, Wicks and Cleveland (1964). Liquid holdup (that is, the relative motion between the liquid and vapor phases) is treated using Hughmark's (1962) correlation. Heat transfer through the casing between the fluid within the wellbore and the formation outside is treated using a method derivable from results presented by Minkowycz and Cheng (1976).

For all calculations performed in this preliminary study, it was assumed that:

(1) the reservoir fluid may be treated as pure H_2O (negligible dissolved solids and/or noncondensible gases),

(2) the thermal conductivity of the rock outside the borehole is equal to 4 Watts/meter/degree Celsius,

(3) the borehole is vertical, of uniform interior diameter (D), and its interior surface is hydraulically smooth,

(4) the borehole has a single feedzone, at a depth of 1500 meters,

(5) the undisturbed reservoir pressure at 1500 meters depth is 80 bars absolute, and

(6) the distribution of reservoir temperature with depth may be obtained by linear interpolation among the following values:

zero depth	...10°C
200 m	...100°C
500 m	...180°C
1000 m	...230°C
1500 m	...250°C

The borehole produces fluid from 1500 meters depth in the formation at a temperature of 250°C. Note that the bubble point pressure for water at 250°C is only 39.8 bars (compared to 80 bars reservoir pressure) so the reservoir fluid is all single-phase liquid near the borehole's feedpoint. For most of the calculations reported herein, the borehole's inside diameter D was taken to be either 10 centimeters (typical of a "slim hole") or 25 centimeters (a typical "production well"). Several calculations were also performed for other values of D. Figure 1 illustrates a typical computed downhole profile.

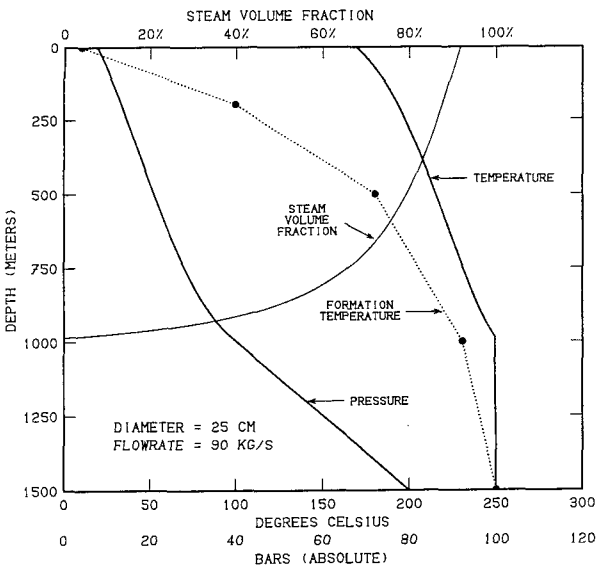

Figure 1. Typical flowing conditions in production well.

2. RESULTS NEGLECTING RESERVOIR FLOW RESISTANCE

It is first instructive to examine the fluid carrying capacity of the well as a function of borehole diameter without consideration of the resistance of the reservoir to fluid discharge. Therefore, for the first series of calculations, it was assumed that the bottomhole flowing pressure is the same as the reservoir pressure (80 bars). In reality, of course, the bottomhole flowing pressure will be somewhat lower than the stable reservoir pressure—the effects of finite reservoir flow resistance are taken up later in this paper.

The simplest approximation for scaling fluid carrying capacity between boreholes of different diameters is to assume that the fluid flow rate (for a given pressure difference between wellhead and bottomhole) will vary in proportion to the cross-section area of the interior of the borehole. Therefore, we define the "area-scaled borehole discharge rate" M^* by:

$$M^* = M \times (25\text{ cm}/D)^2 \qquad (1)$$

where M is the actual borehole discharge rate. Thus, if the borehole diameter D is equal to 25 centimeters (that of our "typical" production well), the "area-scaled" discharge rate will be equal to the actual discharge rate. If $D > 25$ cm, $M^* < M$ and if $D < 25$ cm, $M^* > M$. In particular, if $D = 10$ cm (our "slim hole"), then

$$M^*(D = 10\text{ cm}) = 6.25M \qquad (2)$$

Calculations were carried out for a variety of borehole diameters (D); Figure 2 shows how the stable flowing wellhead pressure varies with area-scaled discharge rate (M^*). In each case, a "minimum" and "maximum" value of the discharge rate is present. For flowrates outside these bounds, the borehole cannot spontaneously discharge (with wellhead pressure above one bar absolute pressure). At some intermediate flowrate, the wellhead flowing pressure takes on a maximum value. The flowrate/wellhead pressure relationships for the various borehole diameters do not collapse to a single curve, even when flow rates are adjusted to account for differences in cross-sectional area. As borehole diameter increases, (1) the maximum area-scaled discharge rate increases, (2) the minimum area-scaled discharge rate decreases, and (3) the maximum attainable flowing wellhead pressure increases, and occurs at a higher area-scaled discharge rate.

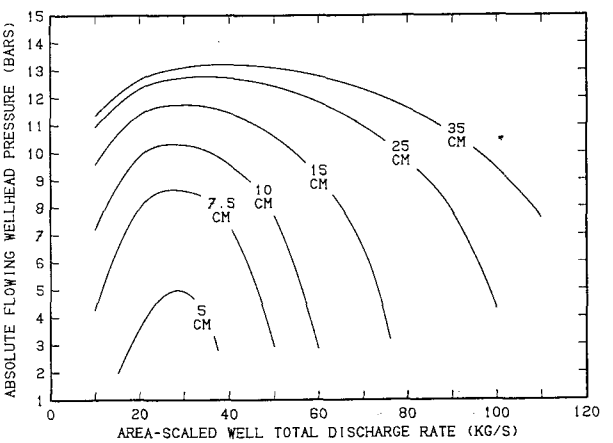

Figure 2. Influence of borehole diameter on borehole performance characteristics (no reservoir flow resistance).

3. THE INFLUENCE OF PIPE FRICTION

One reason why the discharge characteristics (scaled by cross-section area) depend upon borehole diameter is the influence of frictional forces in the pipe. The effects of

friction are most important at high flow rates. The pressure gradient within the borehole consists of three components: (1) the hydrostatic pressure gradient due to gravity, (2) an acceleration term associated with fluid expansion, and (3) pipe friction. In the special case of single-phase flow, the pressure gradient due to pipe friction may be written (in the pertinent high Reynolds number range):

$$\left(\frac{dP}{dz}\right)_{friction} = 2f\left(\frac{M}{A}\right)^2 \Big/ \rho D \qquad (3)$$

where f is a "friction factor" which depends weakly on Reynolds number, A is the cross-section area of the pipe, D is pipe diameter and ρ is fluid density. For two-phase flow, Dukler, *et al.*, (1964) provide modifications to this formula, but the general form is the same. If two wells of different diameters flow at the same "area-scaled" flow rate M^* (so that M/A is the same for both), the frictional pressure gradient will be more important for the smaller-diameter hole. Since the frictional pressure gradient increases with the square of the discharge rate, this effect is most important at high flow rates. Figure 3a shows how the maximum attainable flow rate depends upon borehole diameter. Except for very small diameters, the maximum flow rate (M_{max}) increases with borehole diameter (D) raised to the power ~2.5. Therefore, the "area-scaled" maximum attainable flow rate (M^*_{max}) increases approximately with the square root of borehole diameter.

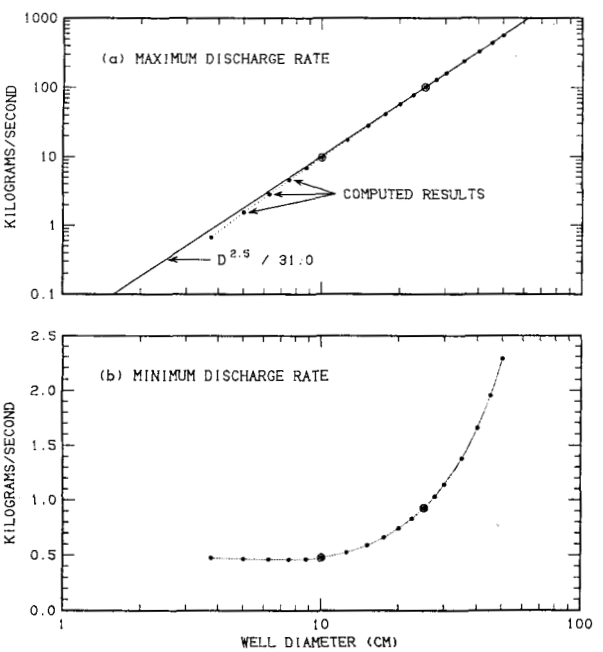

Figure 3. Maximum and minimum fluid discharge rates as functions of borehole diameter in the absence of reservoir flow resistance.

4. THE INFLUENCE OF HEAT LOSSES

At relatively low flow rates, the effect of frictional pressure gradient is less important. We note, however, that the discharge performance curves shown in Figure 2 do not converge at low area-scaled flow rates either. For any value of the borehole diameter D, the discharge rate must lie between a particular maximum value and a particular minimum value for spontaneous flow to be possible. The variation of the minimum permissible flow rate with wellbore diameter is indicated in Figure 3b. For small borehole diameters (less than 10 cm or so) the minimum permissible discharge rate is nearly independent of diameter and equal to about 0.5 kilogram per second. For larger pipe diameters, the minimum flow rate is greater, but the "area-scaled" minimum flow rate decreases monotonically with increasing borehole diameter.

This behavior results from heat losses from the rising fluid within the borehole to the formation outside; Figure 1 shows that the formation temperature is lower than the interior temperature, particularly at shallow depths. For these calculations, the feedpoint flowing enthalpy is 1086 Joules per gram, but the enthalpies at the wellhead are lower. Figure 4 shows the difference between bottomhole and wellhead enthalpies as functions of well diameter and of area-scaled discharge rate M^*.

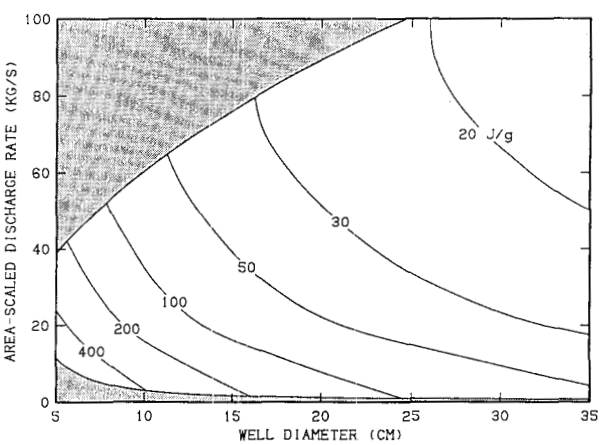

Figure 4. Wellhead fluid enthalpy decrease (relative to bottomhole flowing enthalpy) as a function of borehole diameter (D) and area-scaled discharge rate (M^*) neglecting reservoir flow resistance.

Wellhead fluid enthalpies are lower than bottomhole enthalpies due to three effects: (1) increases in kinetic energy due to fluid expansion, (2) work done against gravity raising the fluid from the feedpoint level (1500 meters deep) to the wellhead, and (3) lateral conductive heat losses to the formation. The work done against gravity is the same in all cases, and is equal to 14.7 Joules per gram. The effects of kinetic energy changes are even smaller. The enthalpy changes illustrated in Figure 4 are, therefore, mainly due to lateral heat loss.

In these calculations, heat losses to the formation are treated by assuming an outward-directed heat flux from each element of the well surface given by:

$$\text{Heat flux} = U\left(T_{fluid} - T_{rock}\right) \qquad (4)$$

where T_{fluid} is the local temperature of the fluid within the well, T_{rock} is the undisturbed rock formation temperature distant from the borehole at the same depth, and U is a heat transfer coefficient (i.e., Watts per square meter per degree Celsius). This heat transfer coefficient, in turn, may be approximated by:

$$U = 0.6K/D \tag{5}$$

(where D is borehole diameter and K is the effective thermal conductivity of the rock formations outside the borehole—taken as 4 W/m/°C for the present calculations) as shown by Pritchett (1981) based upon the work of Minkowycz and Cheng (1976). In effect, heat conduction takes place through a "thermal boundary layer", with temperature equal to the borehole temperature at the inner edge of the boundary layer and equal to the reservoir temperature outside the boundary layer. Beyond the conductive boundary layer, heat transfer is dominated by convection in the porous reservoir rock. Minkowycz and Cheng (1976) showed that the thickness of the boundary layer, at equilibrium, will be proportional to the borehole diameter. Based upon the above expression, it may easily be shown that the total power (i.e., Watts) lost by the fluid within the borehole is given by:

$$\text{Total Power} = 0.6\pi KZ\overline{\Delta T} \tag{6}$$

where Z is the depth of the borehole and $\overline{\Delta T}$ is the vertically-averaged temperature difference between the borehole and the surrounding formation. Dividing the heat loss rate (from Eq. 6) by the rate of fluid production (M) yields the specific fluid enthalpy decrease due to heat losses:

$$\Delta H = 0.6\pi KZ\overline{\Delta T}/M \tag{7}$$

Note that heat losses tend to increase with increasing well depth. For two boreholes of equal depths but of different diameters (D_1, D_2), the ratio of the enthalpy change due to heat losses at the same area-scaled discharge rate (M^*) will be:

$$\frac{\Delta H_1}{\Delta H_2} = \frac{\overline{\Delta T_1}}{\overline{\Delta T_2}}\left(\frac{D_2}{D_1}\right)^2 \tag{8}$$

In other words, heat losses will always be more significant for the slimmer of the two boreholes; the enthalpy loss will vary inversely with "area-scaled" discharge rate and also inversely with the square of the borehole diameter. As shown in Figure 4, the greatest enthalpy declines occur for relatively small-diameter boreholes operating at low discharge rates.

This difference in relative heat loss is responsible for the fact that "area-scaling" fails to produce the same discharge characteristics for production-size wells and for slim holes, even at low flow rates. The computed wellhead pressure is shown in Figure 5 as a function of area-scaled flow rate (M^*) for 10-cm slim holes and for 25-cm production wells both for the calculations described above (solid lines) and for a special series of calculations in which the heat-transfer coefficient was set to zero (dotted lines). The following are noteworthy: (1) for all flow rates, the wellhead pressure is larger if heat losses are neglected, (2) the difference in wellhead pressure between the "no-heat-loss" and "heat-loss" cases (for a fixed borehole diameter) is greatest for the lowest discharge rates, (3) the influence of heat losses upon wellhead pressure is much greater for the 10-cm slim hole than for the 25-cm production well, and (4) in the absence of heat losses (compare the two dotted curves) the wellhead pressure becomes independent of borehole diameter and depends only on area-scaled discharge rate for low flow rates (where the effects of pipe friction are relatively unimportant).

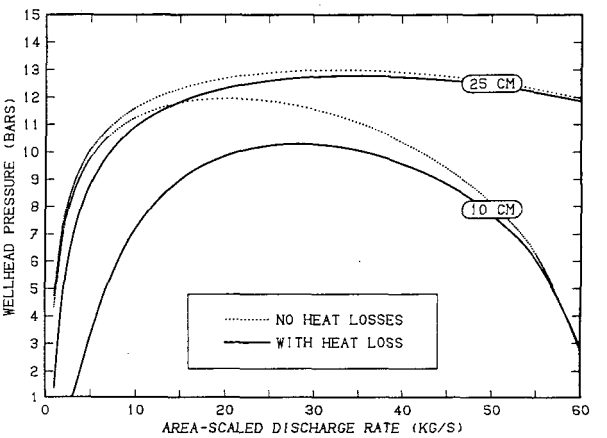

Figure 5. Relative effects of heat losses to the formation on flowing characteristics of production wells (25 cm diameter) and slim holes (10 cm).

The mechanism by which heat loss influences wellhead pressure may be understood by consideration of the flowing pressure distribution indicated in Figure 1. Note that, below the boiling interface, the vertical flowing pressure gradient is approximately hydrostatic (~80 bars per kilometer) but that within the two-phase zone above the boiling level the flowing pressure gradient is significantly lower (~35 bars per kilometer in Figure 1). If heat losses increase, then the liquid temperature below the boiling surface will decline. As a result, the boiling level will occur at a shallower depth within the borehole, at the boiling-point pressure for the lower temperature. Therefore, a greater portion of the borehole will contain the high-pressure-gradient single-phase liquid region and a smaller portion will contain the low-pressure-gradient two-phase region. As a consequence, the average pressure gradient for the borehole as a whole will increase. Since the bottomhole flowing pressure is fixed, this means that the wellhead pressure must decline with increasing heat loss.

5. THE DIFFICULTY OF INITIATING SLIM-HOLE DISCHARGE

Field experience has shown that it is frequently difficult (and sometimes impossible) to induce stable self-sustained discharge from deep slim holes drilled into a field from which spontaneous discharge is readily obtained using wells of conventional diameter. While the greater importance of pipe friction in slim holes may play a limited role in this problem,

the main reason appears to be the relatively larger heat losses to the surrounding formation for boreholes of small diameter.

As noted above, heat losses from the borehole to the formation under stable steady-flow conditions may be adequately represented using a heat transfer coefficient of the form:

$$U = 0.6\,K/D \qquad (9)$$

The problem is that the above formula is only applicable after a stable condition has been reached. The stable heat-transfer model discussed above involves a conductive boundary layer around the borehole of which the thickness is proportional to the borehole diameter. Prior to discharge initiation, however (assuming that the borehole has previously been left in a shut-in condition for a long period of time), the temperature distribution within the borehole will closely resemble that in the formation outside. When discharge begins, temperatures within the borehole change almost discontinuously to higher values. This induces the formation of a thermal boundary layer around the borehole of which the thickness increases with time, eventually reaching the asymptotic value described by Minkowycz and Cheng (1976). At early times, however, the boundary layer will be thinner than at steady-state, so that conductive heat transfer will be augmented. In short, the transient case may be regarded as a succession of states in which the heat transfer coefficient is a decreasing function of time which reaches the above asymptotic value only at infinite time. This situation may be described by defining a "heat loss multiplier" which declines toward unity as time goes on. Computed values for the heat transfer multiplier as a function of time after flow startup for various borehole diameters are illustrated in Figure 6.

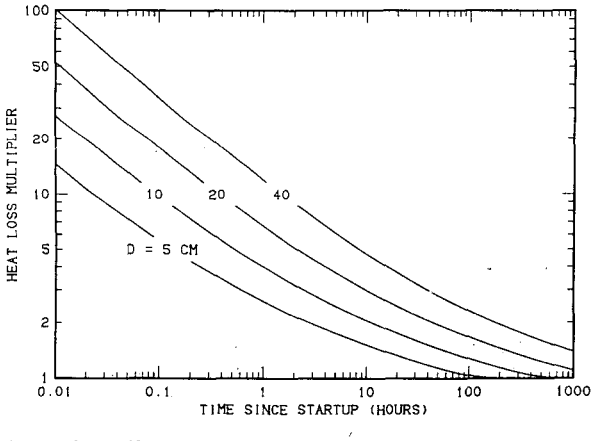

Figure 6. Effective heat transfer coefficient multiplier as a function of time for various borehole diameters.

Therefore, under transient conditions, the results computed above for the discharge capacities of boreholes of various diameters are overly optimistic since these calculations, by assuming steady heat transfer, underestimate the effects of heat losses at early times. To investigate this issue, a series of calculations was performed involving boreholes of both 10 cm and 25 cm diameters, with the "heat transfer coefficient" augmented by various factors relative to the stable steady value. Results are indicated in Figure 7, which shows the ranges of area-scaled discharge rates within which flow may occur as functions of this heat loss multiplier factor. The maximum flow rate is only weakly influenced by increases in heat loss (as expected in light of the above discussion), but the minimum possible discharge rate rises significantly with increases in heat loss. For each borehole diameter, the "critical" heat loss multiplier is reached when the borehole can no longer discharge at any rate. This critical value is much larger (~148) for the 25-cm production well than for the 10-cm slim hole (critical multiplier value ~16.2).

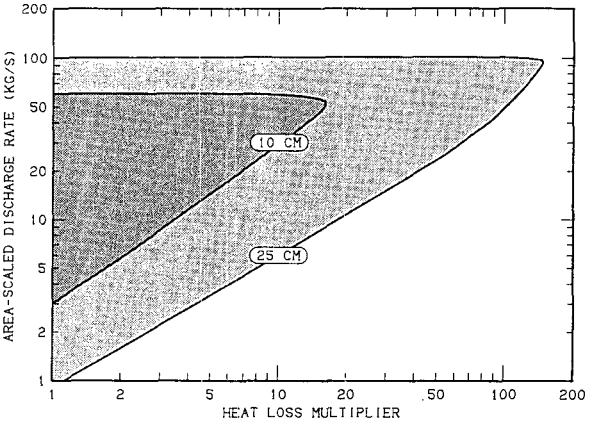

Figure 7. Regions of possible spontaneous discharge for 10-cm slim holes and 25-cm productivity wells as functions of heat loss multipler (no reservoir flow resistance).

This difference in heat loss effects is probably responsible for the difficulty often encountered in inducing deep slim holes (depth >> 300 meters) to discharge (heat losses are relatively unimportant for shallow wells). For example, if we assume that for stable discharge to occur the heat-loss multiplier must drop below one-fourth of the above "critical value", as shown in Figure 8, it should be possible to sustain stable discharge in a 25-cm production well after a transient period of about two minutes. To reach a comparable state for the 10-cm diameter slim hole requires nearly one hour. Since transient processes associated with conventional flow-initiation techniques (swabbing, pressurization, gas injection etc.) usually involve time-scales of only a few minutes, this may explain why deep slim holes often fail to sustain discharge even after several initiation attempts when larger-diameter wells start flowing without difficulty. This implies that to induce deep slim holes to discharge, it may be necessary to employ unusual techniques such as pre-heating the borehole prior to startup.

6. INCORPORATION OF RESERVOIR FLOW RESISTANCE

Up to this point, all calculations presented have assumed that the resistance of the reservoir itself to fluid flow may be neglected compared to the resistance imposed by the borehole; in other words, all calculations have assumed a

bottomhole flowing pressure of 80 bars absolute at the feedpoint (at a depth of 1500 meters in the borehole). For extremely permeable geothermal reservoirs, this may be an appropriate approximation. Under many realistic circumstances, however, the finite permeability of the reservoir causes the bottomhole flowing pressure to be appreciably less than the stable reservoir pressure, and the amount of such pressure decline increases with increasing discharge rate.

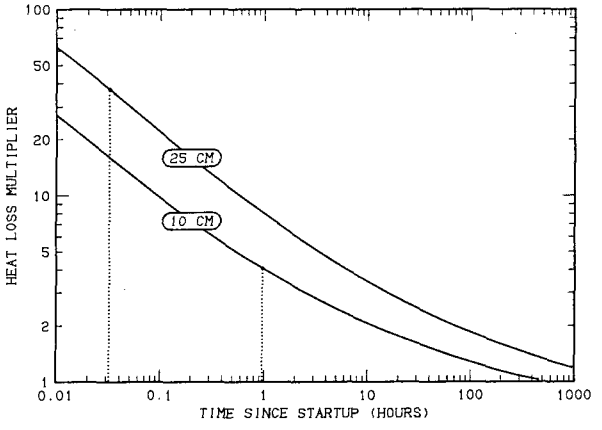

Figure 8. Time required for heat loss multiplier to drop to 1/4 of critical value for 10-cm diameter slim holes and 25-cm diameter production wells.

In light of the purpose of this study, it is appropriate to ignore pressure-transient effects and to assume that the bottomhole flowing pressure may be related to the reservoir pressure and the discharge rate by a "productivity index" (I) so that:

$$P_{bottomhole} = P_{reservoir} - (M/I) \qquad (10)$$

where M is the discharge rate and the productivity index (I) may be regarded as a constant for each borehole. For the remaining calculations, this general form was assumed, and it was further assumed that the fluid flows isenthalpically from "reservoir" conditions (at $P = P_{reservoir} = 80$ bars, $T =$ 250°C) to "bottomhole" conditions (at $P = P_{bottomhole}$), then up the borehole.

The essential difficulty involved in performing calculations with non-zero reservoir flow resistance (that is, values of the productivity index I which are less than infinity) is that of estimating the proper value to use for I for various borehole diameters. It is frequently observed that, if several production wells (of about the same physical characteristics) are drilled into the same reservoir, they are found to be characterized by a wide variety of values of I. This is particularly true in fractured reservoirs, in which the productivity index of a particular well depends mainly on the degree to which it happens to intersect productive fractures. For purposes of this study, the essential question is: if a "slim hole" is drilled into a particular location, what is the relationship likely to be between the productivity index of the slim hole (I_{slim}) and the productivity index that would have been obtained if instead a production-size well had been drilled (I_{prod})? It is useful to adopt the following mathematical form for the productivity index ratio of two boreholes of different diameters (D_{slim}, D_{prod}):

$$\frac{I_{slim}}{I_{prod}} = \left(\frac{D_{slim}}{D_{prod}} \right)^{p} \qquad (11)$$

where the appropriate (presumably non-negative) value for the exponent p remains to be established.

Eventually, it is hoped that the appropriate value for p will be determined empirically by analyses of actual field measurements. One approach would be to examine data sets from geothermal fields in which a sufficient number of both slim holes and production wells have been drilled and tested to provide a statistically significant sample. If sufficient productivity-index determinations are not available, the same p exponent should, in principle, govern the ratio of "injectivity indices", so that injection-test data could be substituted.

For the present, lacking such empirical evidence, we are forced to try to estimate the value of the exponent p. For example, it may be shown that the steady line-source solution results in a value for p which asymptotically approaches zero as the "drainage radius" becomes large. This suggests that the productivity index should be independent of well diameter, all else being equal. In geothermal reservoirs, fluid often enters wells through discrete feedpoints, rather than a long continuous section of hole. In such cases, the point-source (or spherical-source) solution is more appropriate. Evaluation of such solutions suggests that the proper value for p lies somewhere between zero and unity.

Therefore, a final series of calculations was performed involving three well configurations:

(1) a 25-cm diameter production well with productivity index I_{prod},

(2) a 10-cm diameter slim hole using $I_{slim} = I_{prod}$ (that is, $p = 0$ scaling for productivity index), and

(3) a 10-cm diameter slim hole using $I_{slim} = 0.4 \times I_{prod}$ ($p = 1$ productivity index scaling).

Numerous values for I_{prod} were considered, from 1 kg/second/bar upwards. Computed results are indicated in Figure 9, which shows both the maximum attainable wellhead pressure and the maximum area-scaled total mass discharge rate M^* (at one bar wellhead pressure) as functions of the reciprocal of the production-well productivity index ($1/I_{prod}$).

It is noteworthy that changing the reservoir flow resistance has a greater influence upon the discharge characteristics of the production size (25 cm) well than upon those of the slim hole (10 cm). The reason is simply that the total resistance to flow is the sum of the effects of the reservoir and of the

borehole itself. As discussed above (see Figure 3), the capacity of the borehole to deliver fluid to the wellhead varies approximately as $D^{2.5}$, whereas the capacity of the reservoir to deliver fluid to the feedpoint varies as D^p, with $0 < p < 1$. Consequently, the reservoir resistance comprises a greater proportion of the total resistance for larger diameter holes, and therefore large holes are more sensitive to variations in reservoir flow resistance.

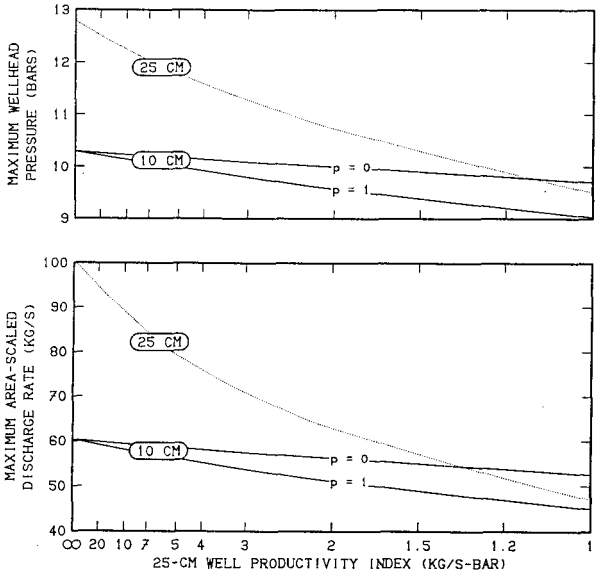

Figure 9. Effects of reservoir flow resistance on performance characteristics of 10-cm diameter slim holes and 25-cm diameter production wells.

It is also noteworthy that, despite the shortcomings of "area-scaling" of discharge rates (arising from the failure of the effects of pipe friction and of heat losses to scale in this manner), scaling-up the discharge characteristics of the 10-cm slim hole using cross-section area provides a conservative estimate of the probable productivity of larger diameter wells so long as the reservoir flow resistance is not too large (productivity index > 1 kg/second/bar or so), at least for conditions similar to those considered in this study.

10. ACKNOWLEDGMENT

This work was supported through Geo Hills Associates under Contract AA-7144 from Sandia National Laboratories. The author thanks James Dunn, Charles Hickok, Roger Eaton, Sabodh Garg, and Jim Combs for their reviews and comments on this paper.

11. REFERENCES

Dukler, A. E., M. Wicks III and R. G. Cleveland (1964), "Frictional Pressure Drop in Two-Phase Flow—B. An Approach Through Similarity Analysis", *A. I. Ch. E. J., v. 10*, p. 44.

Hughmark, G. A. (1962), "Holdup in Gas-Liquid Flow", *Chem. Eng. Progr., v. 53*, p. 62.

Minkowycz, W. J. and P. Cheng (1976), "Free Convection about a Circular Cylinder Embedded in a Porous Medium", *Int. J. Heat and Mass Transfer, v. 19*, p. 805.

Pritchett, J. W. (1981), "The LIGHTS Code", S-Cubed Report Number SSS-R-80-4195-R1.

Pritchett, J. W. (1985), "WELBOR: A Computer Program for Calculating Flow in a Producing Geothermal Well", S-Cubed Report Number SSS-R-85-7283.

PROCEEDINGS, Eighteenth Workshop on Geothermal Reservoir Engineering
Stanford University, Stanford, California, January 26-28, 1993
SGP-TR-145

ENERGY POLICY ACT OF 1992 OPENS DOORS FOR INDEPENDENT GEOTHERMAL POWER PRODUCERS

John E. Mock, Director
Geothermal Division, U.S. Department of Energy

Gene V. Beeland
Meridian Corporation

ABSTRACT

The Energy Policy Act of 1992 embraces and implements many of the actions recommended by the President in the National Energy Strategy. Independent geothermal power producers may be direct beneficiaries of 1) further deregulation of IPPs through their exemption from the provisions of the Public Utility Holding Company Act and 2) potentially freer access to utility-owned transmission facilities. However, these doors will not be fully opened to geothermal energy until this resource can compete with other fuels in cost considerations. While changes in public policy, such as inclusion of externalities in the price of power or financial penalties on carbon dioxide emissions, will level the playing field somewhat, reductions in cost will be the ultimate marketing tool. This is particularly critical in the economics of power derived from "new," as yet undiscovered reservoirs which will reflect the high costs of today's exploration methods. The Department of Energy's geothermal R&D program, in cooperation with industry, is undertaking, as described in this paper, to achieve the technology cost reductions needed to permit this resource to enjoy a status equal to or better than that of competing fuels at the utility least-cost bargaining table.

INTRODUCTION

The Energy Policy Act of 1992 is described by Energy Secretary James D. Watkins as "the most comprehensive and balanced energy legislation ever enacted (which) will bring new jobs, greater energy security, and a cleaner environment." The Act, he continued, will stimulate domestic energy production, promote energy efficiency, increase competition in the electricity sector reducing consumer costs, and develop alternatives to imported oil.

PROVISIONS OF THE ACT FAVORABLE TO GEOTHERMAL POWER PRODUCERS

A number of the Act's provisions are favorable to geothermal development. Some of them that will directly benefit the geothermal industry and open new doors for growth are not directed specifically toward geothermal power per se, but are broad enough to encompass independent geothermal power producers along with other IPPs. These provisions include further deregulation of their structure and operations and a strong mandate for IPP access to transmission facilities. The first of these is accomplished by creating new entities known as "exempt wholesale generators" (EWG's) that may generate and sell power without the restrictions of the Public Utility Holding Company Act. Structuring project ownership to avoid triggering PUHCA regulation has long been considered a major impediment to IPPs, and the freedom granted by the Act is designed to encourage companies that are not electric utilities to get into the power generating business and *compete* to sell electricity to any utility that will buy it. Significantly, EWGs do not lose their status as qualifying facilities under the Public Utility Regulatory Policies Act (PURPA), and its requirement for utilities to purchase the power of such facilities remains intact. However, the geothermal industry should be alert to the fact that at least one influential senator in the energy field has served notice that this issue will surface again in the Congress recently convened due to his belief that PURPA "creates a huge advantage" for QFs over other IPPs.

Perhaps one of the most important provisions of the Act for the geothermal power industry, as it is currently structured, continues another trend established in PURPA -- i.e., affiliation of an EWG with a utility does not preclude the utility from purchasing power from the EWG if cognizant state regulators determine that such transactions meet certain criteria -- e.g., that they will benefit consumers, are in the public interest, and would not provide the utility affiliate unfair competitive advantage. Certainly, given the benign geothermal characteristics compared to those of other available fuel choices for power generation, unregulated utility subsidiaries should have little difficulty substantiating consumer benefit and public interest in its use.

Transmission access for EWPs is provided through authority granted to the Federal Energy Regulatory Commission (FERC) to order utilities, upon application by a qualified EWG, to provide wholesale transmission

services under terms that would 1) permit the utility to recover all of its costs in connection with the transmission services, and 2) would not unreasonably impair the continued reliability of the affected electrical systems. While the legislation as passed omitted earlier language that left FERC no discretion to do otherwise, numerous observers say that regardless of the change in wording, "mandated access will be the order of the day."

According to Electric Power Alert, a leading utility representative described the legislation as "a hell of a bill with a wonderful balance between meaningful access and effective PUHCA reform. The combination is unbeatable. This makes the future a lot less scary for IPPs and utilities alike."

While these portions of the Act will tend to make geothermal development somewhat less onerous and lessen tensions over transmission access in some areas, the geothermal power industry cannot share this unrestrained anticipation of the conventional segments of the industry until it can *compete* with them on cost. Put another way, competitiveness, as we all know, is the key which will open these doors of opportunity.

SECTIONS OF THE ACT WHICH MAY POTENTIALLY IMPACT GEOTHERMAL R&D

While other sections of the Energy Policy Act are specifically designed to support increased competitiveness of geothermal energy and other renewable energy resources, their frame of reference in this particular legislation should alert the geothermal community that they do not yet constitute a mandate for action. That is, those portions that would most directly impact and expand federal/industry research and industry development are only *authorized*, and the extent to which they are ultimately implemented is subject to the availability of *appropriated* funding. This is both a challenge to make the industry's voice heard in the new Congress and an opportunity to acquaint newcomers with the nationwide benefits of geothermal energy. The geothermal community should not stand silently by while their R&D support is committed to more vocal competitors.

The provision of the Act that would most immediately impact the R&D program, if funded for geothermal, is the call for support of "demonstration and commercial application" projects that utilize high- and low-temperature geothermal energy and other renewable energy resources. DOE is required to solicit proposals for projects within nine months of enactment of the Act on the basis of advice provided by an Advisory Committee on Demonstration and Commercial Applications of Renewable Energy and Energy Efficiency Technologies. $50 million total is *authorized* for fiscal 1994.

In addition, subject to the availability of appropriations, DOE is directed to establish a "production incentive program for renewable energy" which would provide payments to "qualified renewable energy facilities" for a 10-year period at a cost of 1.5¢/kWh, adjusted for inflation. Power plants using dry geothermal steam would not qualify.

Fortunately, extension of the 10 percent business energy tax credit for qualified geothermal energy property on a *permanent* basis is a "done deal" and requires no further legislation. As before, qualifying geothermal property includes equipment to produce, distribute, or use geothermal energy, but excludes electrical transmission structures.

Other provisions that may provide longer range benefit for the economics of the geothermal industry are embraced in provisions to promote the export of domestic renewable energy products and services and to investigate the feasibility of reducing greenhouse gases. In addition, there are requirements for utility integrated resource planning that is to include evaluation of renewable energy resources and cost recovery mechanisms for demand-side management strategies that may encourage increased use of geothermal heat pumps and other direct uses of the resource.

Considerations such as these, regulatory reform, and the geothermal-specific support if it is funded, combined with movement at the state level toward public policy changes -- such as inclusion of externalities in the price of power and/or financial penalties on carbon dioxide emissions -- will gradually level the playing field for geothermal competitiveness. Yet, reductions in geothermal costs will be the ultimate marketing tool. This, then, is the goal of the DOE geothermal R&D program -- to achieve, in cooperation with industry, the technology cost reductions that will enable this resource to enjoy a status equal to or better than that of competing fuels at the utility least-cost bargaining table.

ELEMENTS AND OBJECTIVES OF THE DOE GEOTHERMAL R&D PROGRAM

At this point, this presentation will to a large extent repeat the program discussion at the workshop a year ago. However, this repetition may have two benefits. First, at this stage of geothermal development, and at current levels of research funding on the part of both government and industry, our efforts are essentially a process of gradually evolving technology improvements, efforts which can only benefit from repeated examination of their merits or need for change. Second, although it is the strong intent of the R&D program to keep industry continually informed of its activities and direction, it is understood that this

information is not reaching all interested parties. This is a matter of considerable concern to the Geothermal Division, and it is hoped that repetition here will help funnel the information to all who have a need to know.

Exploration and Reservoir Assessment Tools

A particularly critical element in geothermal economics is the high cost of identifying "new" reservoirs and assessing their commercial potential. The deep production-size wells used for these purposes with today's technology cost from $1.5 to $3.5 million each, representing prohibitive costs for many developers or potential developers. Thus, a major objective of the DOE geothermal drilling R&D is to reduce by 50 percent the costs currently required to obtain financing for power plant development. In support of this objective, and at the request of the Hard Rock Penetration Industry Review Panel, DOE has initiated an effort at Sandia National Laboratory to determine whether slimhole drilling can adequately substitute for the costly wells drilled with conventional rotary rigs. This effort will be carried out in a cooperative DOE/industry program that will also support development of geothermal energy in the Pacific Northwest to meet utility needs.

Sandia will first evaluate the slimhole concept through review and documentation of Japanese slimhole data, and then drill and test, in partnership with industry, slimholes at several locations where reservoir parameters are known from large hole flow tests. By comparing these data with those developed from the same formation by large and small wells, it can be determined whether sufficient data can be obtained with the far less costly wells alone.

One cost-shared project has been initiated at Steamboat Hills, Nevada, with Far West Capital using slimhole flow tests and multiwell tracer tests. Other DOE/industry partnerships are under discussion which would involve three geothermal sites in the Cascades.

Further improvements in exploration and reservoir assessment technology are expected to accrue from other R&D program elements which are also directed to other stages of development.

Reservoir Technology

This program element is dedicated to developing better methodology for analyzing the performance of known reservoirs and predicting and managing the effects of fluid injection, in addition to exploration technologies. Currently, the emphasis in reservoir technology is on measures to remedy the decline in production and deterioration of steam quality at The Geysers. These include:

- development of conceptual geological, geochemical, geophysical, and hydrological models of the steam field and immediate environs
- modeling of injection performance, development of means to predict the effects of water injection into the reservoir, and injection strategies.
- development of means to model the reservoir on a fieldwide and subregional scale
- determine methods for improvements in efficiency of power plants, both in the long-term and short-term.

In addition, a cost-shared program with industry is underway to: 1) design, develop, and test the most innovative exploration methods for an integrated exploration technology, and 2) conduct exploratory drilling to identify new resource areas and expand the available geothermal data base. Also in conjunction with industry, the predictions provided by advanced brine chemistry models developed previously are being correlated with actual site data, and model parameters refined where needed. Improvements on submodels are ongoing on such parameters as aluminosilicates, sulfate/bisulfate, and methane.

Drilling Technology

In addition to the slimhole research described above, drilling R&D includes development of technologies for controlling lost circulation, improving the mechanics of rock penetration, and innovative downhole measurement. Activities associated with lost circulation control include, among others:

- field testing the recently-developed rolling float meter under a variety of conditions. This equipment provides early indications of fluid gain or loss which will reduce blow-out and lost circulation problems.
- continued development of the drillable straddle packer, a packer assembly for isolating and directing the flow of cement into a selected loss-zone interval.
- improvement in data analysis techniques and display software of the borehole televiewer for measuring downhole fracture apertures.
- development of several cementitious drilling mud systems for various applications.

Rock penetration mechanics research includes, in addition to slimhole drilling, development of a new concept for measurement while drilling data transmission. This research will be correlated with an

industry-developed system for seismic imaging-while-drilling.

The focus of the downhole instrumentation activity is development of a suite of memory logging tools applicable to geothermal operations. Consultation with operators has resulted in a program to develop three different slim (2 inches in diameter), high-temperature (400°C) tools.

Conversion Technology

The focus of the heat cycle research project is the use of the Rankine binary power cycle with the hydrothermal resource to produce electric power, with emphasis on the utilization of mixed hydrocarbon working fluids. Investigations to define the technology base for allowing binary cycle performance to approach the thermodynamic maximum, and thus reduce costs, are being completed this year. Final tests of the supercritical cycle will provide data for different heat exchanger tube mass and heat flux conditions, allowing a more complete evaluation of the capabilities of the Heat Transfer Research Inc. (HTRI) heat exchange design codes. Field investigations of the condensation behavior of supersaturated turbine expansions are being conducted utilizing a two-dimensional expansion nozzle and laser droplet detection system with the isobutane/hexane working fluid family. These tests are needed to validate the predicted absence of condensate during the supersaturated turbine expansions with hydrocarbon working fluids in order to assure both turbine manufacturers and users that the turbines can be operated in this manner without equipment damage or performance degradation. Operation of the Heat Cycle Research Facility, a small-scale (50kW) binary plant which is the basic tool for conducting these experiments, is being transferred from the Idaho National Engineering Laboratory to the National Renewable Energy Laboratory. It is currently located adjacent to the B. C. McCabe plant in Imperial Valley.

Materials Development

This is a very important research element, the results of which industry is believed to have made considerable use. Its FY 1993 development activities include:

- advanced high-temperature lightweight cements to improve the life expectancy of geothermal well completions
- chemical systems for lost circulation control (in conjunction with drilling research)
- thermally conductive composites for heat exchanger tubing to reduce scaling, corrosion, and other brine handling problems
- corrosion mitigation at The Geysers which involves optimization of previously developed polymer cement formulations and polymer coating systems for use in high acidic environments at high temperatures
- advanced high-temperature coupling systems needed to bond high-temperature elastomers to metal reinforcements.

Biochemical Processes for Geothermal Brines

This activity is a laboratory effort to develop methods for the utilization and/or low-cost environmentally acceptable disposal of toxic geothermal residues. In this work, microorganisms which can interact with toxic metals and convert them into soluble species for subsequent injection or concentration have been identified that are highly efficient at elevated temperatures (>55°C) and acidic pH (1-2). It is anticipated that the new biotechnology will reduce the cost of surface disposal of sludges derived from geothermal brines by 25 percent or more.

SUMMARY

While many of the Stanford geothermal reservoir workshop attendees are participants in certain aspects of DOE's geothermal R&D program, and others are very knowledgeable on all developments affecting the costs and use of this resource, it is hoped that these thumbnail sketches of the broad range of R&D activities will serve to establish their close interrelationships in technology improvements and cost reductions. It is also hoped that those attendees or their colleagues and associates who are not yet conversant with the details of the program will attend the Geothermal Division's annual program review in San Franciso, April 27-28 of this year. Please convey this invitation to whomever you encounter who may have a need or desire to learn more about the federal program.

It is also hoped that the recitation of the favorable or potentially favorable actions impacting geothermal development will encourage those who might tend to listen to the "naysayers" on geothermal's future. And, finally, it is hoped, and expected, that when and where increased power demand exists in "geothermal" areas, geothermal power will be economically prepared to provide a major share of the required capacity.

PROCEEDINGS, Eighteenth Workshop on Geothermal Reservoir Engineering
Stanford University, Stanford, California, January 26-28, 1993
SGP-TR-145

HDR Reservoir Flow Impedance and Potentials for Impedance Reduction

Robert DuTeau and Donald Brown
Los Alamos National Laboratory
Earth and Environmental Sciences Division
Los Alamos, New Mexico 87545

ABSTRACT

The data from flow tests which employed two different production zones in a well at Fenton Hill indicates the flow impedance of a wellbore zone damaged by rapid depressurization was altered, possibly by pressure spallation, which appears to have mechanically propped the joint apertures of outlet flow paths intersecting the altered wellbore. The rapid depressurization and subsequent flow test data derived from the damaged well has led to the hypothesis that pressure spallation and the resultant mechanical propping of outlet flow paths reduced the outlet flow impedance of the damaged wellbore. Furthermore, transient pressure data shows the largest pressure drop between the injection and production wellheads occurs near the production wellbore, so lowering the outlet impedance by increasing the apertures of outlet flow paths will have the greatest effect on reducing the overall reservoir impedance. Fenton Hill data also reveals that increasing the overall reservoir pressure dilates the apertures of flow paths, which likewise serves to reduce the reservoir impedance. Data suggests that either pressure dilating the wellbore connected joints with high production wellhead pressure, or mechanically propping open the outlet flow paths will increase the near-wellbore permeability. Finally, a new method for calculating and comparing near-wellbore outlet impedances has been developed. Further modeling, experimentation, and engineered reservoir modifications, such as pressure dilation and mechanical propping, hold considerable potential for significantly improving the productivity of HDR reservoirs.

INTRODUCTION

The Hot Dry Rock (HDR) geothermal reservoir designed for mining heat at Fenton Hill, New Mexico has shown that thermal energy contained within large bodies of crystalline basement rock can be harvested for use on the earth's surface. The Fenton Hill reservoir demonstrates how a large volume of hot rock at considerable depth can be hydraulically opened with high pressure to circulate water and mine heat with minimal water consumption. Furthermore, many months of reservoir circulation and heat removal have shown no drawdown in the mean temperature of the water produced from the reservoir. Therefore, the major remaining technical challenge is to engineer a reduction in reservoir flow impedance to increase the productivity of an HDR system to a commercial level. The data from Fenton Hill offers valuable information for designing methods for significant reductions in flow impedance.

BACKGROUND

While the creation of an HDR reservoir in deep basement rock is determined by the initial volume of highly pressurized water used to open and extend an originally impermeable joint and fracture system, the working size of a reservoir is determined by the hydraulic pressure maintained on the reservoir. After the initial hydraulic fracturing, the reservoir can be sustained at a stable volume by operating the reservoir below a hydraulic pressure which would induce microseismicity at the reservoir boundaries and cause reservoir growth. Below this seismic threshold, water pressure acts against the in situ stress regime to open joint systems and elastically deform reservoir rock to create flow paths connecting an injection and production wellpair. While the volume of the flow paths within the reservoir is strictly a function of pressure, the rate of fluid flow through a jointed system is both a function of the size of flow path apertures and the driving pressure difference across the system. Two conceptual models used to simulate the fluid flow in the deep Precambrian jointed system at Fenton Hill are the Gangi joint opening law and the cubic law for fluid flow through parallel plates.

The Gangi opening law describes the size of a flow path aperture as a function of pressure and is given by

$$a(P) = a_0[1 - (P/P_0)^m],$$

where P is the fluid pressure at the aperture, P_0 is the closure stress of the flow path joint, a_0 is the initial joint opening at closure stress, and m is a characteristic of the asperity heights in the joint where ($0 < m < 1$).[1] The cubic flow equation relates the rate of flow through a joint to the cube of the joint aperture by

$$q = a^3 / (12\, u\, f) * (dP / dx),$$

where q is the flow rate, a is the joint aperture size, u is the dynamic viscosity of the fluid, f is the friction factor or joint tortuosity, and dP/dx is the pressure gradient across the joint.[2]

Since the flow rate follows a cubic function of flow path aperture, increasing the joint aperture greatly enhances the flow (and reduces the impedance), while the driving

pressure difference across a joint has only a linear influence on flow. These concepts incorporated into an implicitly coupled finite element model have successfully simulated flow test results for experiments conducted at Fenton Hill.

To analyze HDR reservoir impedance, data from the Initial Closed-Loop Flow Test (ICFT), performed in 1986, and data from the Long Term Flow Test (LTFT) and other recent flow tests conducted in 1992 were investigated. A brief history of Fenton Hill follows in order to explain the distinctly different wellbore zones of the ICFT and the LTFT, because the lower portion of the original well used for the ICFT was redrilled and the redrilled wellbore has produced the flows of the LTFT and subsequent flow tests.

The original wellbore, designated EE-2, was used in 1983 to conduct a Massive Hydraulic Fracturing (MHF) reservoir creation test which stimulated intense microseismic activity with the injection of 21000 m^3 of water (5.7 million gallons) at rate of 106 l/s (840 gpm). During this injection, the wellbore was altered and a portion of casing was damaged when a flange at the wellhead failed and a rapid back-flow of water, steam, and about 0.3 m^3 of rock fragments were ejected from the reservoir. In 1986, this damaged EE-2 wellbore served as the production well during the ICFT.

Then in 1987, the original EE-2 wellbore was sidetracked and redrilled through the same fractured reservoir on a trajectory essentially parallel to, but 15 to 30 meters away from the old wellbore. The redrilled well, designated EE-2A, serves as the current production well, and has carried the outlet flow for the LTFT and other recent flow tests. The difference in the flow behavior of the two wellbores suggests that a mechanism, possibly mechanical propping, changed the outlet flow character of the EE-2 well and reduced its outlet impedance.

RAPID DEPRESSURIZATION OF EE-2

During the MHF test when the hydraulic fracturing pressure was accidentally vented, the rapid depressurization of the wellbore flashed water to steam and threw shards of rock from the wellbore. The fragments of rock were apparently broken from the surface of the wellbore by pressure spallation. Pressure spallation is thought to occur when microcracks beneath the surface of a rock fill with water at a pressure higher than the tensile strength of the rock, then when the pressure at the surface is quickly released, the force of the pressure difference between the interior and the surface of a rock causes spallation. Investigation of the outlet impedances of the two wellbores, EE-2 and EE-2A, indicates distinct differences in the outlet flow impedances of the wellbores which may be explained by mechanical propping due to pressure spallation. The pressure spallation seems to have occurred on the surfaces of outlet flow paths as well as on the wellbore surface, which allowed fragments of rock to lodge within and prop open the reservoir connections to the outlet wellbore as flow paths were closing with the release of the pressure. A laboratory experiment designed to verify the principle of pressure spallation has been planned but has not yet been carried out. Therefore, pressure spallation and the resultant mechanical propping of the damaged wellbore zone remains just a hypothesis at this time, however flow test data strongly supports this hypothesis.

The following paragraphs first discuss the overall impedance results from the ICFT, LTFT and more recent flow tests, then go on to analyze the outlet impedances of these flow tests and distinguish the differences in outlet impedances for the two wellbores. The results suggest that two methods of increasing the flow path apertures, pressure propping and mechanical propping, have been demonstrated at Fenton Hill.

ICFT OVERALL IMPEDANCE RESULTS

In May and June of 1986 the ICFT was divided into two 15 day flow segments. Table 1 shows the measured parameters at selected times during each flow segment of the test, along with the calculated impedance. The flow impedances shown in Table 1 were calculated from the pressure drop between the wellheads divided by the produced flow rate.

	ICFT 1st Segment	ICFT 2nd Segment
	6/2/86	6/18/86
Injection Pressure, MPa (psi)	26.8 (3890)	31.5 (4570)
Production Pressure, MPa (psi)	2.4 (351)	3.4 (495)
Production Flow Rate, l/s (gpm)	8.5 (135)	13.5 (214)
Production Temperature, °C (°F)	173 (343)	190 (374)
Impedance, MPa/l/s (psi/gpm)	2.87 (26.2)	2.08 (19.0)

Table 1. ICFT Performance Results

A comparison of overall impedances derived from the first and second segments of the ICFT illustrates the result of impedance reduction by pressure propping. During the second segment of the ICFT, the higher mean reservoir pressure reduced the overall reservoir impedance by pressure dilating the flow paths connecting the injection and production wells. Similar results are also seen in the data of more recent flow tests.

RECENT FLOW TESTS AND OVERALL IMPEDANCE RESULTS

During 1992, the LTFT operated for 16 weeks with a steady injection pressure controlled below a seismic threshold of 27.3 MPa (3960 psi) while the production pressure was held constant at 9.67 MPa (1400 psi). After a pump breakdown which interrupted the test, a series of interim flow tests (IFT's) were conducted to continue gathering data until the pressure and flow conditions of the LTFT could be resumed. Table 2 displays the flow

conditions attained with various injection and production pressures and the resulting overall flow impedances.

	LTFT	IFT	IFT2	IFT3
	7/28/92	9/29/92	12/10/92	12/27/92
Injection Pressure, MPa (psi)	27.29 (3958)	22.36 (3243)	27.32 (3963)	27.32 (3962)
Production Pressure, MPa (psi)	9.66 (1401)	9.65 (1399)	15.18 (2201)	12.40 (1798)
Production Flow Rate, l/s (gpm)	5.66 (89.7)	3.85 (61.1)	5.34 (84.6)	5.71 (90.5)
Production Temperature, °C (°F)	183 (361)	165 (329)	177 (351)	183 (361)
*Impedance, MPa/l/s (psi/gpm)	3.11 (28.5)	3.30 (30.2)	2.27 (20.8)	2.61 (23.9)

Table 2. Recent Flow Tests and Overall Impedance Results

* As the production rates vary with different pressure conditions, production temperatures also vary because more heat loss per unit of fluid is conducted away from the production wellbore at reduced flow rates. Density differences in the produced flow rates have been normalized.

Again, the empirical parameters of the LTFT and IFT3, which show similar flow rates and production temperatures, reveal a reduction in overall impedance due to the pressure dilation of flow paths. Even with a reduction in the pressure difference across the reservoir, the flow rate measured at a backpressure of 1798 psi was not less than the flow rate produced at 1401 psi with nearly the same injection pressure. That is, because the apertures of flow paths were dilated with a higher mean reservoir pressure, the overall flow impedance declined enough to maintain the level of production flow in spite of a smaller driving pressure difference across the reservoir. An even higher backpressure of 2200 psi, shown in column IFT2, further reduced the overall impedance of the system at LTFT conditions by about 27% with only a 5% reduction in flow. These data suggest that within a certain range of wellhead pressures the reservoir productivity is a much stronger function of absolute pressure level than the driving pressure difference between wellheads, and that experimentation, modeling, and system modifications may be employed to optimize the system.

IMPEDANCE ANALYSIS FROM SHUT-IN PRESSURE RESPONSE

When the injection and production wellhead valves are rapidly closed, the pressure response at the wellheads displays valuable information about the magnitude and location of reservoir impedance. Figure 1 shows the time response of pressure at both wellheads when the wellheads were quickly closed during steady state flow conditions on July 31, 1992. The injection pressure showed a step decrease of about 100 psi followed by a slow pressure decline toward the mean reservoir pressure. At the same time the production wellhead pressure rose rapidly almost 1700 psi when the well was shut in and then slowly increased toward the mean reservoir pressure. These responses illustrate how the pressure gradient between the injection and production wells levels out rapidly where the gradient is steep but slowly across the body of the reservoir where the gradient is moderate. The small steep pressure drop at the injection well quantifies the small reservoir inlet impedance due to the pipe friction of the injection wellbore casing, since the reservoir inlet flow paths are dilated by cooling as well as propped open by high injection pressure. The magnitude of the pressure rise at the production well, however, illustrates the location of a steep gradient which defines a large pressure drop over a small distance near the production well. This sizable gradient identifies the largest pressure drop between the wells and therefore the greatest portion of the overall impedance. Finally, the residual pressure difference between the injection and production wells, after the initial rapid changes, represents the moderate pressure drop across the body of the reservoir.

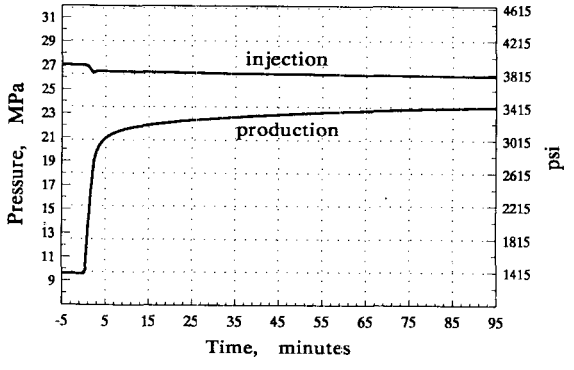

Figure 1. Wellhead Shut-in Pressure Responses

The nature of this pressure response allows the overall reservoir impedance to be divided into three impedances, an inlet impedance, a body impedance, and an outlet impedance. Thus, the pressure measurements in Figure 1 show the LTFT reservoir conditions where a small percentage of the pressure drop between the wellheads occurs on the injection side while the majority of the pressure drop occurs near the production well, leaving a moderate amount of the pressure drop to occur within the body of the reservoir. This asserts that a reduction in the production well impedance will have the greatest impact on reducing the overall reservoir impedance. Therefore, further analysis of the outlet impedance follows.

PRODUCTION WELL SHUT-IN PRESSURE ANALYSIS

In order to more precisely quantify the pressure drop near the production well, the method illustrated in Figure 2 is being developed. Further work in modelling the buoyancy, compressibility, and heat transfer of the water in the wellbore and near wellbore region will be presented in a subsequent paper. Figure 2 plots the pressure rise at the production wellhead when the production valve is quickly closed.

During the initial transient pressure rise, the slope of the curve reflects wellbore and near-wellbore phenomena such as the compressibility of water and heat transfer from the wellbore, but after the short steep rise the pressure at the wellhead shows the gradual relaxation of the pressure gradient across the body of the reservoir. At the same time, flow paths connecting the production wellbore to the body of the reservoir are dilating and storing water due to the increasing pressure. The combination of all these phenomena yields the pressure response measured at the wellhead. Accordingly, the contributions of these influences allow the curve to be divided into two regions, one which follows the steep transient behavior, and a second which follows the gradual long term pressure rise. For the purpose of analysis these two regions of the pressure rise have been modeled with curve fits. The initial slope, which is highly influenced by compressibility and wellbore heat transfer, is nearly linear for a brief few minutes. Therefore, the initial transient is modelled with a linear curve fit whose slope depends upon the initial temperature, pressure, and flow conditions. The subsequent slow pressure rise, which is determined by the relaxation of the pressure gradient across the reservoir and the increasing storage of water in dilating joints near the production wellbore, correlates well with a geometric equation of the form $P = C1\ (t)^{C2}$, where the pressure P is a function of time, C1 is a large constant with the magnitude of the steep transient pressure rise, t is time, and C2 is a very small constant which delineates the long term gradual pressure rise.

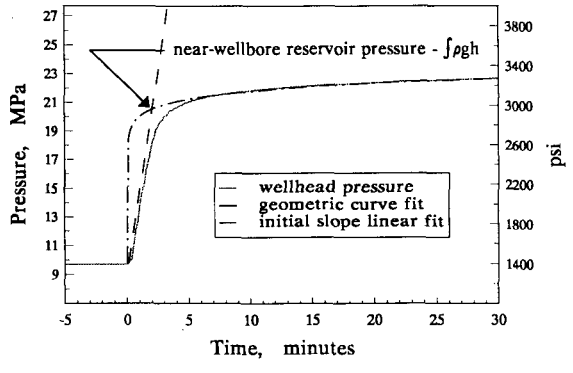

Figure 2. Production Wellhead Shut-in Pressure Analysis

Figure 2 shows the intersection of a linear curve fit following the initial slope of the pressure rise and a geometric curve which models the long term pressure response. The intersection of these curves determines a pressure which represents the reservoir pressure a small distance from the production wellbore. This small distance defines the production zone of steep pressure gradient in a consistent manner for different shut-in curves. Thus, when added to the pressure of the fluid column in the production well, this determined pressure represents the near-wellbore reservoir pressure, which can be used to quantify the pressure drop from the reservoir to the production wellbore in a way that allows comparison of outlet impedances at different production wellhead backpressures.

Figure 3 shows a shut-in pressure rise at the production wellhead from an initial backpressure of 2200 psi, considerably higher than the initial backpressure of 1400 psi shown in figure 2. The effect of the higher backpressure, which dilates the flow paths connecting the production wellbore to the reservoir, is to decrease the near-wellbore outlet pressure gradient. Since the difference between the reservoir body pressure and the wellbore pressure is reduced, the near-wellbore impedance is also reduced. This is evidenced by the smaller pressure rise recorded at the production wellhead when the production well is shut in.

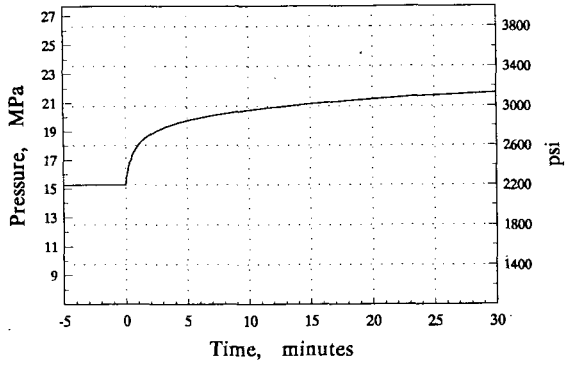

Figure 3. High Backpressure Shut-in Response

Table 3 records the calculated near-wellbore outlet impedances from the earlier ICFT test, with the mechanically propped production outlet, and recent flow tests with the redrilled production well where the outlet impedance is highly dependent upon backpressure. Once again, ongoing work which models compressibility, buoyancy, and heat transfer will refine these numbers, but the qualitative differences in outlet impedances of the two wellbores is evident.

Date	Injection Pressure MPa (psi)	Production Back-pressure MPa (psi)	Near-Wellbore Outlet Pressure Drop MPa (psi)	Production Flow l/s (gpm)	Outlet Impedance MPa/l/s (psi/gpm)
6/2/86	26.82 (3890)	2.42 (351)	6.33 (918)	8.52 (135)	0.743 (6.8)
6/18/86	31.51 (4570)	3.41 (495)	10.13 (1469)	13.63 (216)	0.743 (6.8)
7/31/92	26.96 (3910)	9.64 (1398)	10.73 (1557)	5.85 (92.7)	1.83 (16.8)
12/15/92	27.27 (3955)	15.19 (2203)	4.12 (598)	5.25 (83.2)	0.785 (7.18)

Table 3. Comparison of Near-Wellbore Outlet Impedances

The impedances shown in Table 3 attest to the dependence of outlet impedance upon backpressure for the redrilled wellbore EE-2A, while the ICFT production zone, which connects the reservoir to the EE-2 wellbore, exhibits a considerably reduced and constant outlet impedance. In fact, the constant outlet impedance supports the hypothesis that outlet flow paths of EE-2 were mechanically propped at a fixed aperture when the fluid pressure was below the in situ closure stress of the joints. The composite of all the preceding information allows a number of conclusions to be drawn.

CONCLUSIONS

1. The fluid flow character of the two wellbores, EE-2 and EE-2A, is distinctly different and the reason for the difference is hypothesized to have been caused by pressure spallation and the resultant mechanical propping of EE-2 outlet flow paths by rock fragments.

2. A laboratory experimental verification of pressure spallation should be carried out. (LANL has planned an experiment for summer '93)

3. Two of the potential methods for increasing the size of production flow path apertures are mechanical propping (possibly by pressure spallation) and pressure propping (by holding an elevated backpressure on the production wellhead).

4. Because the largest portion of the pressure drop across the reservoir occurs near the production well, reducing the near-wellbore outlet impedance will have the greatest impact on reducing the overall reservoir impedance.

5. HDR reservoir productivity is a stronger function of the mean reservoir pressure level than the driving pressure difference across the reservoir within a range of the operating pressures employed at Fenton Hill. This is due to the dependence of the flow rate upon the size of the apertures of flow paths, which are a function of pressure.

6. Maintaining a high backpressure reduces both the body impedance and the outlet impedance by pressure dilating flow path apertures throughout the reservoir. In fact, a low backpressure at the production well allows the in situ stresses to pinch off production flow, unless the outlet flow paths are mechanically propped open.

7. The optimization of HDR productivity may be accomplished through modeling, experimentation, and system modifications such as mechanical and pressure propping.

8. Finally, a new method for calculating and comparing near-wellbore outlet impedances at different production wellhead backpressures has been developed.

REFERENCES

1. Brown, D. W., B. A. Robinson. 1990. The Pressure Dilation of a Deep, Jointed Region of the Earth. In *Proceedings of the International Symposium on Rock Joints,*pg. 519-525, June 4-6, 1990. at Loen, Norway.

2. Fox, R. W., and A. T. McDonald. 1985. In *Introduction to Fluid Mechanics*, pg. 336, New York: John Wiley & Sons

3. Dash, Z. V., ed., 1989. ICFT: An Initial Closed-Loop Flow Test of the Fenton Hill Phase II HDR Reservoir, Los Alamos National Laboratory Report, LA-9080-SR.

PROCEEDINGS, Eighteenth Workshop on Geothermal Reservoir Engineering
Stanford University, Stanford, California, January 26-28, 1993
SGP-TR-145

Tracer Experiment Results During the Long-Term Flow Test of the Fenton Hill Reservoir

Nelson E. V. Rodrigues
CSM Associates
Rosemanowes, Penryn, Cornwall
TR10 9DU, U. K.

Bruce A. Robinson, and Dale A. Counce
Los Alamos National Laboratory
Earth and Environmental Sciences Division
Los Alamos, New Mexico, 87545

Abstract

Three chemical tracer experiments and one extended injection of fluid low in concentration of dissolved species have been carried out during the Long Term Flow Test (LTFT) of the Fenton Hill Hot Dry Rock (HDR) reservoir. The tracer tests results illustrate the dynamic nature of the flow system, with more fluid traveling through longer residence time paths as heat is extracted. The total fracture volumes calculated from these tests allow us to determine the fate of unrecovered injection fluid, examine the pressure-dependence of fracture volume, and, through a comparison to the hydraulic performance, postulate a model for the nature of the pressure drops through the system. The Fresh Water Flush (FWF) test showed that while no dissolved specie behavior is truly conservative (no sources or sinks), several breakthrough curves are well explained with a pore fluid displacement model. Other dissolved components are clearly influenced by dissolution or precipitation reactions. Finally, the transient response of the chemistry during the FWF to an increase in production well pressure showed that some fractures connected to the production well preferentially open when pressure is raised.

Introduction

The HDR concept has been under investigation at Los Alamos since the early 1970's at the Fenton Hill site. The site is located on the west flank of the Valles Caldera in the Jemez Mountains of northern New Mexico. On April 10, 1992 a Long Term Flow Test (LTFT) was initiated with the objective of demonstrating that heat can be extracted from the reservoir for a sustained period of time without produced fluid temperature decline. The operational goal was to maintain continuous circulation for a period of one to two years. However, technical problems occurred which necessitated a shut down at the beginning of August to replace the high pressure injection pumps. Injection resumed on August 14, and production resumed on the 19th, though at somewhat lower flow rates than during the period April 10 - July 30.

During this phase of the LTFT, three tracer tests have been performed using p-toluenesulphonic acid (p-TSA) and sodium fluorescein. The fluorescein apparently underwent some thermal degradation in the reservoir. The results discussed here are only for p-TSA tracer tests as these were inert or conservative tracer tests. A summary of test dates and tracer injection masses is provided in Table 1.

TABLE 1. Summary of p-TSA tracer tests.

test	date	mass of tracer injected
first	May 18, 1992	162.1 g
second	July 7, 1992	181.1 g
third	Sept 1, 1992	181.1g

Tracer tests in HDR systems are invariably pulse inputs of a large mass of tracer over a short period of time. However, a step input of a tracer can be simulated in a Fresh Water Flush (FWF) test, in which the following steps are carried out: 1) the system is circulated in closed-loop until quasi-equilibrium is reached with respect to dissolved species in the produced water, 2) circulation is suddenly changed to open-loop with the injection of "fresh water" from a source of fluid low in concentration of dissolved species; and 3) the concentration versus time of dissolved species is measured in the produced fluid. Then, the outlet concentration since the beginning of open-loop circulation can be interpreted as a step tracer test. If a dissolved specie is not produced or consumed by any source or sink mechanism, then its behavior can be predicted from the tracer response curve. Any deviations from this predicted behavior is then evidence of a source or sink within the reservoir.

During the long term circulation test at Fenton Hill one FWF test was conducted essentially simultaneously with the p-TSA tracer test of September 1. The test lasted about 160 hours, during which time fresh water from a domestic water well was injected while the produced fluid was vented temporarily to a storage pond. The present study summarizes the tracer tests and this FWF test, comparing the two to draw inferences about the nature of flow and the source of dissolved species in the circulating fluid.

Analysis of tracer data

The following analyses of the tracer data are presented below:

- calculation of the external and internal residence time distributions ($f(t)$ and $\chi(t)$ respectively, e.g Robinson and Tester, 1986);
- analysis of reservoir conditions during the three tests to infer possible changes in reservoir flow patterns throughout this period;
- comparison of the variation of the integral mean volume with the "water loss"; and

- under the assumption of a simplified geometry, analysis of the variation in volume and area of reservoir with time.

Figure 1 shows the experimentally determined tracer breakthrough curves for the three tracer tests. To interpret these results quantitatively, we define the following functions. First, f(t)dt is the fraction of particles in the exit stream with residence time between t and t+dt, and is given by $f(t) = qC(t)/m_p$, where q is the mass flow rate of fluid and m_p is the mass of tracer injected. Then, $\chi(t)dt$ is the fraction of particles *inside the system* that will eventually have a residence time between t and t+dt, and is equal to $tf(t)/\tau$, where τ is the mean residence time, computed from a first-moment integration of f(t).

When we plot the cumulative distributions of these two functions (F(t) is the cumulative distribution for f(t) and X(t), also known as the internal residence time distribution (RTD), is the cumulative distribution of $\chi(t)$) against one another, we obtain a quantitative picture of the nature of the flow paths within the reservoir. Figure 2 is such a plot for the three tracer tests. Plotting the data in this way shows, for example, that in the first two tracer tests, the 50% of the injected fluid that is traveling fastest sweeps through only 12% of the internal fluid volume of the reservoir (obtained from the point on the curve at 0.5, 0.12). Thus, although there is a tendency for fluid to short circuit directly between the wells, a significant percentage of the fluid sweeps through a very large volume.

Note also that the total fluid volume (computed as the mean residence time times volumetric flow rate) increased during operation at constant flow conditions between the first and second tests (Table 2). There is a shift to longer residence times, with fluid possibly circulating through a greater number of flow paths. The alternative model is that the increased fluid flow volume is simply due to some additional dilation of existing flow paths, without accessing additional rock. It is impossible to distinguish between the models, although we note that curves for the first two tracer tests in Figure 2 are almost identical despite the shift to longer residence times and larger fluid volumes. This might suggest that the existing flow paths are more dilated with no change in the flow distribution through the rock mass.

The third test was conducted at lower flow rates and pressures, and the resulting total fracture volume was considerably lower. Furthermore, Figure 2 indicates that any given fraction of the injected fluid travels through a greater fraction of the total volume in the third test than in the previous two tests. One explanation is that at lower pressures, some joints that previously conducted fluid no longer are open enough to do so. Thus the joints that continue to transmit fluid have smaller volume, and fluid does not percolate as readily through the long-residence-time, tortuous flow paths. Greater rock volumes are almost certainly accessed at the higher pressure conditions.

Another issue that has interested HDR researchers for many years is the fate of the injected fluid that is not recovered at the production well. These tracer results show that during steady flow operation between the first and second tests, the volume of "active flow paths" (those that transmit fluid between the wells) increased by 520 m^3, compared to a total fluid consumption of 3400 m^3 during the same period. Thus, during this test about 16% of the "water loss" actually resulted in increased volume of active flow paths, with the remaining fluid probably diffusing into rock between the fractures or at the boundary of the fractured reservoir.

FIGURE 1. Normalized tracer breakthrough curves for the p-TSA experiments.

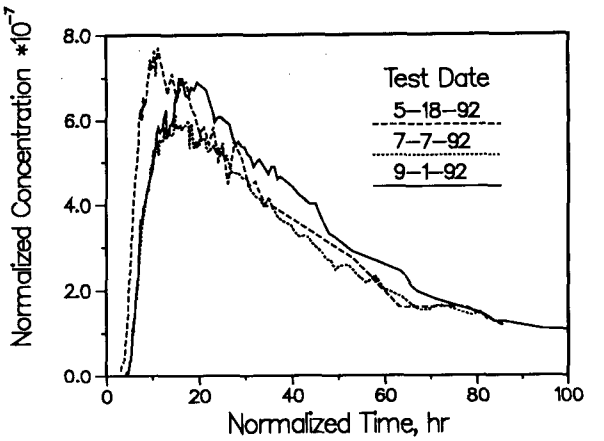

TABLE 2. Integral Mean Volume Variation

Test	Integral Mean Volume	Variation in volume
First	2246 m^3	
Second	2766 m^3	+520 m^3
Third	2044 m^3	-722 m^3

FIGURE 2. Internal volume fraction versus fluid flow fraction for the three tracer tests.

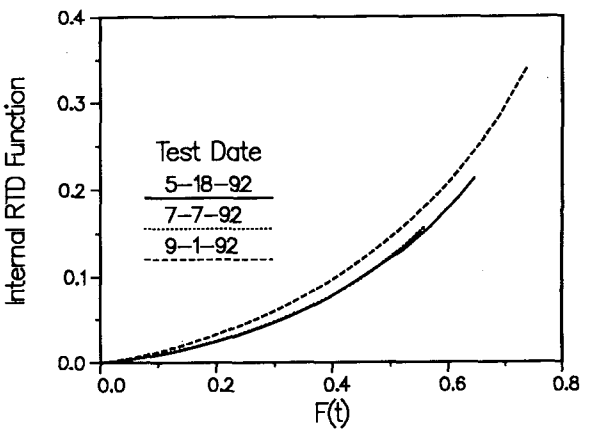

Inferences about the nature of flow and pressure drop through the reservoir can be made by estimating joint apertures, using both pressure drop and tracer information. Information needed for the pressure drop computation and the

corresponding assumptions used for the calculation are: 1) flow velocity based on the known distance between the wells and a measured transit time based on the first arrival of the tracer; 2) mean joint spacing of 20 m based on the heat transfer study of Robinson and Kruger (1992); 3) rock volume dimensions of 150 x 80 x 240 m cut by a three-dimensional array of evenly spaced fractures; and 4) tracer-determined total fracture volume of 2246 m^3 (first tracer test). The resulting apertures obtained are summarized in Table 3 below.

TABLE 3. Estimates of joint apertures.

aperture (m)	reference
$2.1*10^{-4}$	cubic law aperture (Snow, 1969)
$3.0*10^{-5}$	friction law aperture (Abelin et al., 1987)
$2.0*10^{-5}$	radial flow (Witherspoon et al., 1980)
$5.2*10^{-3}$	storage aperture

The first three aperture values are so-called hydraulic apertures, based only on the pressure drop across the reservoir and assumed fracture and flow parameters without consideration of the tracer-determined fracture volume. Contrast these values with the storage aperture, the value obtained using the total fracture volume and the assumed fracture geometry. The actual storage volume in the joints is much larger than would be suggested based on the pressure drop through the reservoir. Even assuming a larger reservoir and closer fracture spacing, the large discrepancy remains. This result is very typical of flow through fracture rock, and is thought to be due to the fact that the hydraulic aperture is dominated by flow constrictions (small apertures) that the fluid is forced to traverse. By contrast, the storage aperture is a straight average of all apertures encountered by flowing fluid. Conceptually, the hydraulic system in the reservoir is one of large pressure drops through some crucial fractures or portions of fractures of small aperture, with fluid experiencing almost no pressure drop through the large aperture fractures that contribute most to the fluid storage volume.

Fresh Water Flush (FWF) Test

Since the concentration of almost all dissolved species is lower in the fresh water than in the circulating fluid during a FWF experiment, the results are analyzed as a *negative step tracer test*, and the washout function, W(t), can be directly calculated from the following expression:

$$W(t) = \frac{C(t) - C_i}{C_o - C_i} \qquad (1)$$

where C(t) is the outlet concentration at time t, C_i is the concentration of the injected fluid, and C_o is initial produced fluid concentration at the beginning of the FWF.

Analysis of a FWF test must account for the following possibilities, each of which could result in a concentration-time response that differs from that of a conservative tracer:

- a constant source of the specie in the form of indigenous pore fluid of high concentration that is swept into the produced fluid as new flow paths are accessed;
- production or consumption of the specie via rock-water interactions in the reservoir. Some possible processes are dissolution of minerals, ion exchange, or interaction with pore fluid. In each case the results can be analyzed assuming a source or sink of the specie;
- reversible adsorption of the specie onto the rock surface. Here the specie is delayed compared to one that does not undergo sorption.

Since it will be shown that many species appear to have a source in the reservoir, we develop a method for interpreting the data in the presence of a source. Assuming a constant source of solute, the dimensionless concentration may be obtained from a revised form of Eqn. (1):

$$\bar{C} = \frac{(C'(t) - C_i)}{(C'_o - C_i)} \qquad (2)$$

where $C'(t) = C(t) + C_s$, $C_o' = C_o + C_s$, and C_s is the source concentration.

Using these equations, the source concentration can be calculated as follows:

$$C_s = \frac{(C'(t) - C_i - W(t) \times (C_o - C_i))}{1 - W(t)} \qquad (3)$$

This value is actually a weighted source concentration, equal to the actual concentration of the added fluid (assumed to be pore fluid in this discussion) times the ratio of the pore fluid flow rate to the total flow rate. If the source of solute is indeed from pore fluid, then a mass balance yields:

$$q \times C'(t) = q_o \times C(t) + q_p \times C_p \qquad (4)$$

$$q \times C_o' = q_o \times C_o + q_p \times C_p \qquad (5)$$

where q_p is the mass flow rate of pore fluid, C_p is the concentration of the pore fluid, and $q = q_O + q_p$. Calculating the value of q_p and using Eqn. (2), the following relation is obtained:

$$q_p = C_s \times \frac{q}{(C_p - C_i)} \qquad (6)$$

During the FWF test, chemical analyses were made of the following dissolved species: Al, As, B, Br, Ca, Cl, F, Fe, HCO_3, Li, Mg, Na, NO_3, PO_4, Si, SO_4, Sr, and Total Dissolved Solids (TDS).

To analyze the test, the washout function W(t) for the p-TSA tracer test was first derived from an integration of the p-TSA tracer response curve. Then, the washout response of each specie was computed using Eqn. (1), with C_i obtained from a chemical analysis of the injected fresh water and C_o determined from an average of all concentrations measured during the 15 hours before breakthrough of the fresh water (values for C_o are listed in Table 4). The comparison of the tracer-determined washout function with the dissolved species B, Br, Cl, K, Li, Na, SO_4, Sr and TDS are presented in Figures 3 to 5 and discussed below.

A truly conservative species would have a concentration-time response coincident with W(t) determined from a tracer experiment. As shown in the figures, none of the species analyzed behaved as a truly conservative tracer. In many cases, the deviation of the dimensionless concentration curves from the tracer-determined W(t) curve can be explained assuming a constant source of the specie. Using the mathematical development outlined above, the source concentration C_s for B, Br, Cl, Li, Na, K, SO_4, Sr have been calculated: the results are given in Table 5.

TABLE 4. Initial Concentrations C_0 at the start of the FWF (ppm)

B	Br	Cl	K	Li	Na
46.7	6.7	1371	106	17.4	1107
SO4	**Sr**	**T.D.S.**			
398	0.91	3947			

FIGURE 3. Dimensionless concentrations of B, Br, and Cl during the FWF

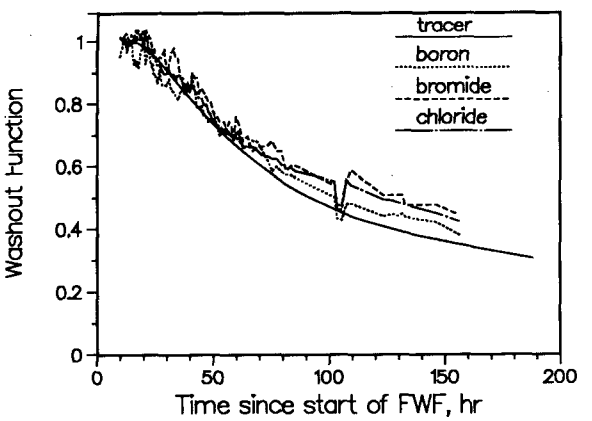

FIGURE 4. Dimensionless concentrations of K, Li, and Na during the FWF

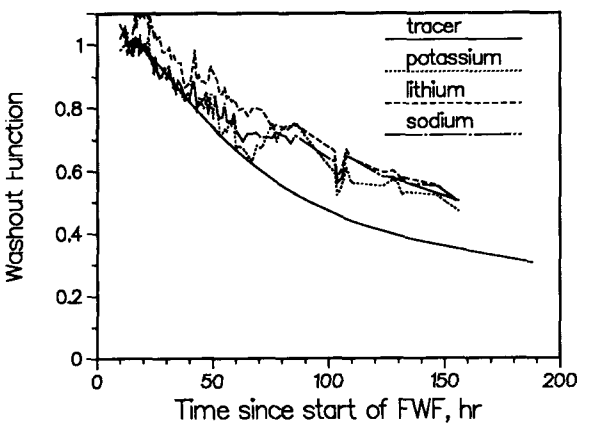

FIGURE 5. Dimensionless concentrations of SO_4, Sr, and TDS during the FWF.

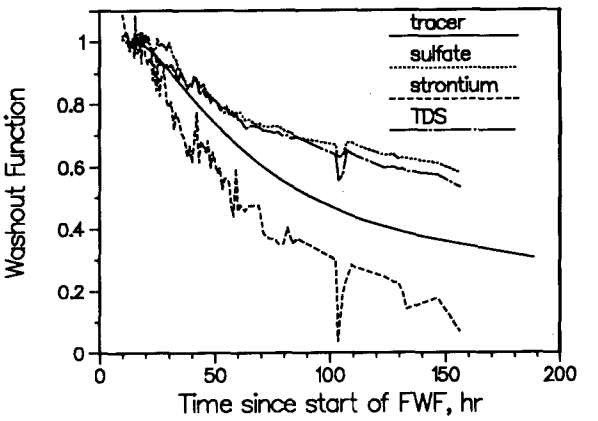

FIGURE 6. Fluoride ion behavior during the FWF.

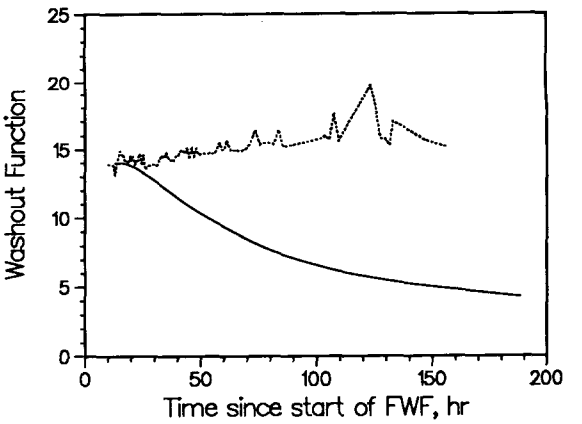

TABLE 5. Calculated average source concentrations (ppm)

B	Br	Cl	Li	Na	K
11.7	1.5	273.7	6.0	423.4	35.6
SO_4	**Sr**	**TDS**			
164.5	-0.18	1310			

Of the species listed in the table, the origin of boron and chlorine is almost certainly pore fluid, because there are no minerals in the host rock that can be a source for these elements (e. g. Laney et al, 1981). Using as the composition of the pore fluid the composition of downhole samples developed during the development of EE-2 (Table 6, from Grigsby et al, 1989), the approximate contribution of pore fluid to the produced flow can be calculated. The results for several of the species, in the form of percent of the outlet flow that was derived from pore fluid, is given in Table 7.

TABLE 6. Approximate Pore Fluid Composition in ppm (Grigsby et al, 1989)

pH	Conductivity(uS)	SiO_2	Na	K	Li	Ca
6.46	18000	435	3310	401	76.1	94.0
Mg	**B**	**SO_4**	**Cl**	**HCO_3**	**F**	**Br**
3.0	178.0	64	5870	692	6.1	42.3

TABLE 7. Percent pore fluid contribution in the produced fluid if pore fluid is the only source of the specie

B	Br	Cl	Li	Na	K	SO4
7	4	5	8	13	9	n.a.

n.a. = not applicable.

From the results of B, Br, and Cl, we conclude that the pore fluid flow rate is approximately 4-7%. The remaining cationic species in the table probably are influenced by rock-water interactions in addition to pore fluid addition. For example, Na could be added to the produced fluid by dissolution of feldspars, and Li may undergo an ion exchange reaction in which it is liberated from the rock in exchange for Ca.

Several other dissolved species, such as Si, F, Mg, and Ca, exhibited behavior that can not be explained using a pore fluid model or a slight deviation from such a model. The easiest of these to interpret is dissolved Si, which declined in concentration only very slightly during the FWF (down to a dimensionless concentration of only about 0.95). The quartz geothermometer during steady state operation agrees with the known rock temperature in the reservoir. The nearly constant concentration during the FWF suggests that in this system the fluid has sufficient time to come to equilibrium with respect to quartz in one pass through the reservoir. This is in contrast to the Fenton Hill Phase I reservoir, showed very little active dissolution of quartz during a FWF (Grigsby and Tester, 1989). The difference in temperature (240°C versus 200°C) in the two reservoirs is apparently sufficient to cause this difference in geochemical behavior.

The behavior of fluorine was unique in that it *increased* in concentration during the test, from about 13 ppm to 15 ppm (Figure 6). The concentration of fluorine in the pore fluid was 6.1 ppm (Table 6). Assuming that this was the concentration of fluorine in the pore fluid, then this indicates the existence of another source of fluorine in addition to pore fluid. The excess of fluorine may be due to dissolution of some mineral present in the host rock (for instance mica, fluorite, or fluorapatite).

Finally, Ca and Mg exhibited a decrease in concentration despite the fact that the concentration in the injected water was *greater* than the initial concentration of these species in the production fluid. The most probable explanation for these results is the precipitation of most of the injected calcium and magnesium immediately upon entering the reservoir. Considering Ca, fluid high in concentration but low in dissolved CO_2 concentration, is being injected. When this fluid reaches the reservoir, it mixes with fluid of considerable dissolved CO_2 concentration, thereby creating a large driving force for deposition of Ca in the reservoir. Figure 7 shows the results of calculations for calcium assuming low "apparent" injection concentrations (0, 2.5 and 5 ppm, compared to the actual injection concentration of 92 ppm) for an initial output concentration of 19 ppm. Note the similarity of these curves to those of other dissolved species. This analysis suggests that the effective injection concentration of Ca after the initial deposition takes place is low, and that Ca behaves like other dissolved species thereafter.

FWF Results During Production Well Pressure Increase

Roughly 92 hours after the start of the FWF, the fluid injection pump failed temporarily, leading to a sequence of events that affected the subsequent geochemical behavior. When the injection shutdown occurred, the control system automatically increased the production well pressure to cut back on the production flow rate.

The traditional method for examining the effect of pressure and flow rate changes on hydraulic performance is to compute the impedance, defined as the pressure drop divided by production flow rate. Defined in this way, the impedance is inversely proportional to the hydraulic conductivity of the reservoir. Figure 8 shows the calculated impedance along with the production pressure during the FWF. The decrease in impedance accompanying the increase in production pressure is thought to be a result of fractures near the production well becoming more dilated at the higher pressure.

FIGURE 7. Dimensionless concentration for calcium during the FWF for different "apparent" injection concentrations

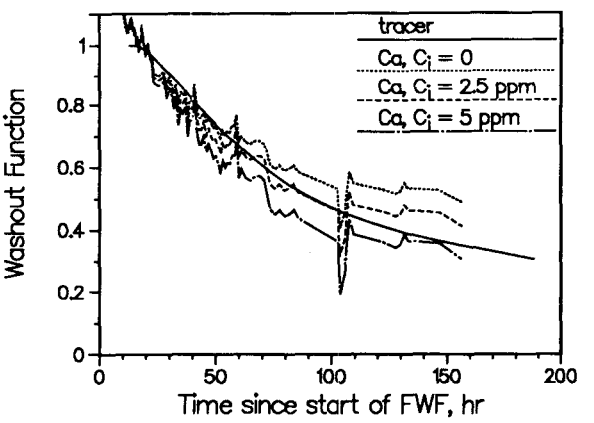

FIGURE 8. Calculated impedance and production well pressure during the FWF.

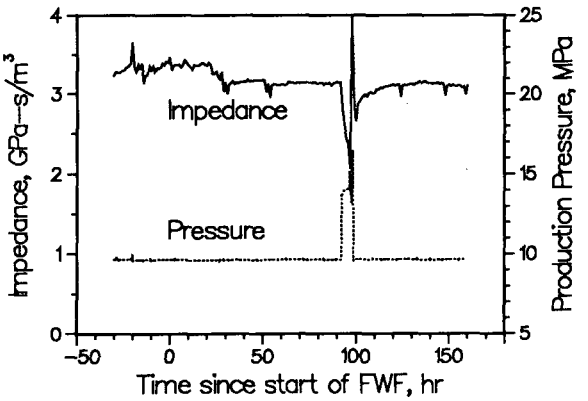

The pressure change also resulted in a short-term transient change in the chemistry of the produced fluid, as shown in Figure 9, which compares the production pressure to the fluid conductivity measurements at the surface. Increases in the pressure result in decreases in the conductivity, while subsequent decreases in pressure result in an increase to the previous conductivity level. This behavior suggests that during the FWF, the pressure rise and accompanying joint opening causes relatively fresh water to surge into the production well.

The delay time between the pressure change and subsequent conductivity change represents the transit time for a parcel of fluid to travel up the wellbore. This information allows us to pinpoint which fractures connected to the production well are opening during this pressure transient. Table 8 lists the specific pressure and conductivity changes numbered on the figure. Using a temperature log measured in the well during production, the variation of the density of the fluid with depth was calculated as a function of temperature and pressure. Then, the average travel time for a parcel of fluid from a given depth to the surface was computed. The transit time from a given depth is itself time dependent, since the flow rate was changing during the time of this analysis. Figure 10 represents the transit time for parcels of fluid entering the well at different depths. Depths chosen for the curves represent the depths of specific fluid entry positions identified from the temperature logs. The points are the transit times for the six transients identified in the fluid conductivity data.

Clearly, the uppermost fractures along the wellbore (10770 and 11050 ft) are preferentially opening, and furthermore, breakthrough of fresh water has occurred before 90 hr in these joints. However, it cannot be concluded that joints lower in the reservoir are not also undergoing this behavior, since this method can only be used to pinpoint the uppermost joints that are opening. Nonetheless, two important conclusions can be gained from this analysis. First, these uppermost joints experience breakthrough of fluid within 90 hr. There was some thought that the deepest joints, being physically closest to the fluid exit points in the injection well, might be short-circuiting flow paths that are responsible for the early residence times of the tracer breakthrough curve. Although this may still be the case, breakthrough also occurs fairly early in these upper joints. This implies that fluid sweep through the reservoir is fairly uniform. Second, increasing the production well pressure preferentially opens the upper joints, rather than simply dilating joints lower in the well, which are of most concern from the standpoint of thermal cooldown. Thus, high production well pressure does not appear to result in increased flow short-circuiting and concomitant rapid thermal decline.

FIGURE 9. Pressure and fluid conductivity during the episode of increasing production well pressure. The numbers correspond to the transients identified in Table 8.

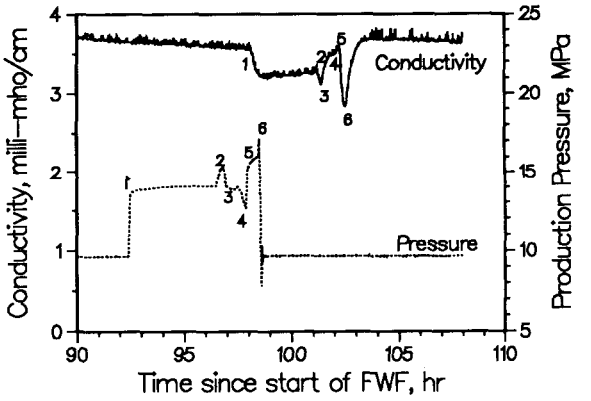

FIGURE 10. Calculated wellbore transit times from various depths to the surface. The points are the measured lag times given in Table 8.

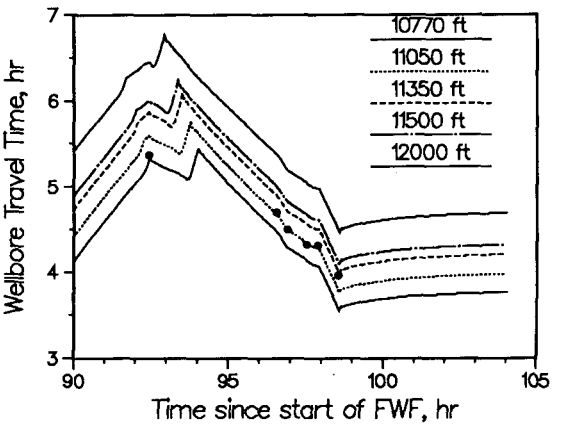

TABLE 8. Times of the Pressure and conductivity transients and lag time for displacing fluid in the wellbore (all times in hours).

Point	Pressure Time	Conductivity Time	Time Difference
1	92.43	97.8	5.37
2	96.55	101.25	4.70
3	96.90	101.40	4.50
4	97.52	101.84	4.32
5	97.89	102.20	4.31
6	98.54	102.50	3.96

Discussion and Conclusions

The three tracer experiments carried out during the LTFT have shown that the reservoir is undergoing dynamic changes during long-term heat extraction. During the 50 day period between the first and second tests, the fluid transit time in the reservoir increased markedly for the shortest residence time flow paths. This result invalidates the theory often raised in criticism of the HDR concept that heat extraction will result in the preferential opening of a short-circuiting path due to thermal contraction of the rock. The trend is in the opposite direction, toward a more uniform sweep of fluid through the rock mass. A similar phenomenon was observed in the Fenton Hill Phase I reservoir (e. g. Robinson and Tester, 1984).

The water consumed during long-term operation can, based on the measured total fracture volume, be apportioned between fluid that expands the volume of active fluid flow paths and fluid that seeps from the boundaries of the reservoir or into the rock blocks within the reservoir. A calculation based on the tracer results shows that 16% of the water loss is actually expansion of the active reservoir volume. The active fracture flow volume is also pressure-dependent: the fracture volume at a lower flow rate and pressure resulted in a lower fracture volume and more direct flow channeling between the wells.

Another use of the fracture volume measurements is to determine the nature of the pressure drop through the reservoir. The storage aperture determined from tracer measurements is at least an order of magnitude larger than the hydraulic aperture measured from pressure drop and flow rate. This result is very common in studies of flow through fractured rock (e. g. Long and Billaux, 1987, Gelhar, 1988, Robinson, 1985), and is likely due to large local pressure drops where fluid is constricted to flow through regions of small aperture. In this fracture network, there may be joints oriented unfavorably with respect to the prevailing earth stresses. These joints could dominate the pressure drop through the reservoir, while other, more open joints account for most of the fluid storage.

The FWF experiment offered a unique opportunity to explore the origins of certain dissolved species in the circulating fluid and to obtain further information about the flow patterns in the reservoir. No specie behaved as would be expected assuming no source or sink for the component. A source of the dissolved specie, postulated to be pore fluid (after Grigsby et al., 1989) is needed to explain the behavior of components such as Cl, B, and Br, which are not present in the rock minerals in sufficient quantities to be produced via dissolution or ion exchange reactions. The calculated fraction of pore fluid in the produced fluid is 4-7%. This result agrees qualitatively with the conceptual model of both direct and long-residence-time flow paths between the wells. The longer, more tortuous flow paths must be sweeping through a very large volume of rock since they are still entraining a significant amount of fluid that was in the rock mass before exploitation. These paths are probably continuously being accessed during heat extraction, and the pore fluid that originally resided in the fractures is continuously swept into the flowing fluid that reaches the production well.

Other dissolved species concentrations are influenced by rock-water interactions over the time scale of the FWF. These include Si (governed by quartz dissolution), Ca (which probably precipitated near the injection well during the FWF), and Na, which appears to have a source term in addition to pore fluid displacement. Feldspar dissolution is a likely additional source mechanism for Na.

Finally, the preferential opening of fractures near the production well was observed in both the hydraulic and geochemical data during the FWF. We were able to pinpoint the uppermost fractures that exhibited this behavior. They were the shallowest fluid entry points in the open hole, suggesting that operating at high production well pressure does not merely open the joints in closest proximity to the injection region, as might be feared. Also, the fact that these uppermost joints had already experienced breakthrough of fresh water after 90 hr shows that the flow through the rock between the wells is fairly evenly distributed.

Acknowledgments

This work was performed under the auspices of the U. S. Department of Energy, Geothermal Technology Division. N. Rodrigues would like to thank the entire staff of the EES-4 division at Los Alamos for their support and for making his stay at Los Alamos so special. Help received from D. Duchane, D. Brown, Z. Dash and R. Duteau was particularly welcome. Mr. Rodrigues' research is sponsored by the British Council (UK), University of Coimbra and INIC (Portugal). For this work he also received partial funding from the Department of Trade and Industry, UK.

References

Abelin, H., L. Birgersson, J. Gidlund, L. Moreno, I. Neretnieks, and S. Tunbrant, "Results from some tracer experiments in crystalline rocks in Sweden", in C.F. Tsang, ed. "Coupled processes associated with nuclear repositories", Academic Press, Orlando, FA, pp 363-379 (1987).

Gelhar, L. W., "Applications of Stochastic Models to Solute Transport in Fractured Rocks," SKB Technical Report 87-05, Swedish Nuclear Fuel and Waste Management Co., Stockholm, Sweden (1988).

Grigsby, C. O., J. W. Tester, P. E. Trujillo, and D. A. Counce, "Rock-Water Interactions in the Fenton Hill, New Mexico, Hot Dry Rock Geothermal Systems I. Fluid Mixing and Chemical Geothermometry", *Geothermics*, 18, 5/6, 629-656 (1989).

Grigsby, C. O., and J. W. Tester, "Rock-Water Interactions in the Fenton Hill, New Mexico, Hot Dry Rock Geothermal Systems II. Modeling Geochemical Behavior", *Geothermics*, 18, 5/6, 657-676 (1989).

Laney, R., A. W. Laughlin, M. J. Aldrich, "Geology and Geochemistry of samples from Los Alamos National Laboratory HDR well EE-2, Fenton Hill, New Mexico", Los Alamos Scientific Laboratory, Report LA-8923-MS (1981).

Long, J. C. S., and D. M. Billaux, "From Field Data to Fracture Network Modeling: An Example Incorporating Spatial Structure," *Water Resour. Res.*, 23, 7, 1201-1216 (1987).

Robinson, B. A., "Non-Reactive and Chemically Reactive Tracers: Theory and Applications", Ph.D. Thesis, Massachusetts Institute of Technology (1985).

Robinson, B. A., and P. Kruger, "Pre-Test Estimates of Temperature decline for the LANL Fenton Hill Long-Term Flow Test", Geothermal Resources Council, 1992 Annual Meeting, San Diego CA (1992).

Robinson, B. A., and J. W. Tester, "Characterization of Flow Maldistribution Using Inlet-Outlet Tracer Techniques: An Application of Internal Residence Time Distributions," *Chem. Engng. Sci.*, 41, 3 (1986).

Robinson, B. A., and J. W. Tester, "Dispersed Fluid Flow in Fractured Reservoirs: An Analysis of Tracer-Determined Residence Time Distributions," *J. Geophys. Res.*, 89, B12, 10374-10384 (1984).

Snow, D. T., "Anisotropic permeability of fractured media" *Water Resour. Res.*, 5, 1273-1289 (1969).

Witherspoon, P. A., J. S. Y. Wang, K. Iwai, and J. E. Gale, "Validity of cubic law for fluid flow in a deformable rock fracture", *Water Resour. Res.*, 16, 1016-1024 (1980).

PROCEEDINGS, Eighteenth Workshop on Geothermal Reservoir Engineering
Stanford University, Stanford, California, January 26-28, 1993
SGP-TR-145

PROGRESS REPORT ON THE LONG-TERM FLOW TESTING OF THE HDR RESERVOIR AT FENTON HILL, NEW MEXICO

Donald W. Brown and Robert DuTeau

Los Alamos National Laboratory
Earth and Environmental Sciences Division
Los Alamos, New Mexico 87545

Abstract

Through mid-December 1992, long-term flow testing of the Phase II Hot Dry Rock (HDR) reservoir at Fenton Hill, NM has been conducted for an aggregate of 24 weeks at near-optimum aseismic injection conditions. This period of flow testing, which began on April 9, 1992, included several reservoir shut-ins due to equipment problems and an intervening lower-injection-rate Interim Flow Test lasting about 6 weeks.

With the exceptions noted above, the majority of the flow testing for that period was conducted at an average injection rate of 7.2 l/s and at pressures up to 27.3 MPa. However, this high level of injection pressure has not produced any discernible reservoir microseismicity, indicating that we have been operating the reservoir at pressures below the threshold for fracture extension. The permeation loss from the boundaries of the reservoir at these elevated pressures has averaged about 0.7 l/s, a very low rate of water loss considering the very large volume of fractured rock (about 16×10^6 m^3) comprising the pressure-stimulated reservoir region.

Temperature logging across the 350-m production interval, centered at a depth of about 3500 m, indicates that there has been no measurable drop in the mixed-mean reservoir production temperature at the top of this interval since the time of our first temperature log in mid July.

Most recently, we have conducted additional intermittent reservoir testing at higher levels of production backpressure during a period of reservoir pressure maintenance using a high-capacity rental triplex mud pump.

Introduction

The present Phase II HDR reservoir at Fenton Hill represents the successful creation and operation of a second, deeper and hotter engineered geothermal system for mining the earth's heat at this site in northern New Mexico. The smaller and shallower Phase I reservoir was flow tested during the period from 1978 to 1980, with the longest flow test lasting over 9 months (Dash et al., 1981).

The primary objective of the present long-term flow testing of the Phase II reservoir is to demonstrate a sustainable level of heat production for a sufficient period of time -- at least for one to two years. The initial phase of this testing began on April 9, 1992 and lasted 16 weeks. Unfortunately, failures of both primary injection pumps caused a premature, but temporary, end to high-injection-pressure flow testing on July 31. This period of testing has previously been referred to as the Long-Term Flow Test (LTFT), and will be so referred to in this paper.

Reservoir flow testing was then continued at a lower rate of 4.3 l/s (68 gpm) for the 6-week period from August 20 to October 2. This period of lower-injection-pressure flow testing, referred to as the Interim Flow Test (IFT), ended when a "terminal" failure occurred to the smaller backup pump. Following the end of the IFT, a used triplex mud pump was leased on a temporary basis to maintain reservoir pressure and to allow a modicum of flow testing until a more suitable replacement pump was located.

There were several ancillary technical objectives for the subsequent flow testing that have been accomplished since the end of the 16-week LTFT on July 31. These objectives focus on the measurement of the reservoir flow performance at other (than LTFT) injection and production pressure levels, and are critical to our overall understanding of how an engineered geothermal system actually performs under a variety of operating conditions. With this knowledge, we will be able to engineer changes in the flow behavior of this specific HDR reservoir in the future to considerably enhance its productivity, as well as to improve the design of future HDR systems.

Reservoir Performance During the LTFT

During 16 weeks of continuous flow testing, the surface injection pressure was maintained at levels up to about 27.3 MPa (3960 psi). This maximum pressure produced no discernible microseismicity indicating stable, nonextensional reservoir operation. That the reservoir was not extending during this period of time is supported by the low and slightly declining rate of reservoir water loss.

Figures 1 and 2 show the surface injection and production pressures and the corresponding injection and production flow rates during the LTFT. As shown in Figure 1, the injection pressure was gradually increased to 27.3 MPa (3960 psi) and then maintained at this level, while the production backpressure was generally maintained at 9.3 MPa (1400 psi). The actual control variables for this phase of flow testing were injection flow rate and production backpressure, the latter being controlled by an automated pressure-regulating system. As shown in Figure 2, both the injection and production flow rates declined by about 10 percent during the LTFT. Tracer evidence indicates that this flow-rate decline resulted from a gradual redistribution of reservoir flow away from the more direct flow paths (Rodrigues et al., 1993).

Figure 1. LTFT Wellhead Pressures

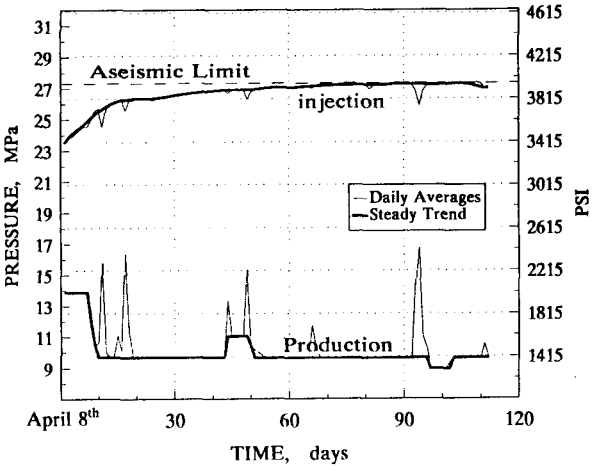

Figure 2. LTFT Flow Rates

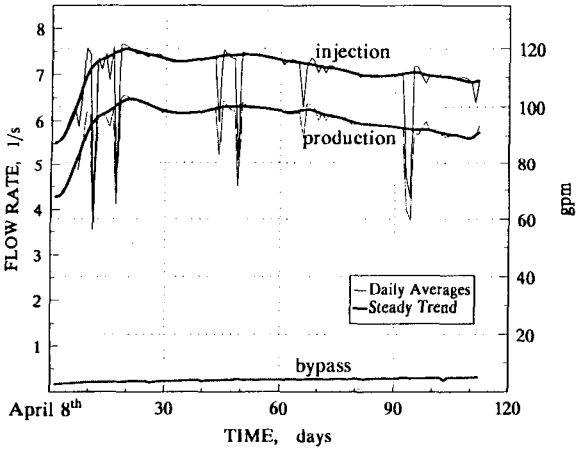

Figure 3 shows the apparent rate of reservoir water loss during the LTFT. This loss is the observed difference between the 24-hour mean injection and production flow rates, corrected for the small (about 0.3 l/s) annular casing bypass flow from the reservoir occurring at the injection well.

Figure 3. LTFT Water Loss

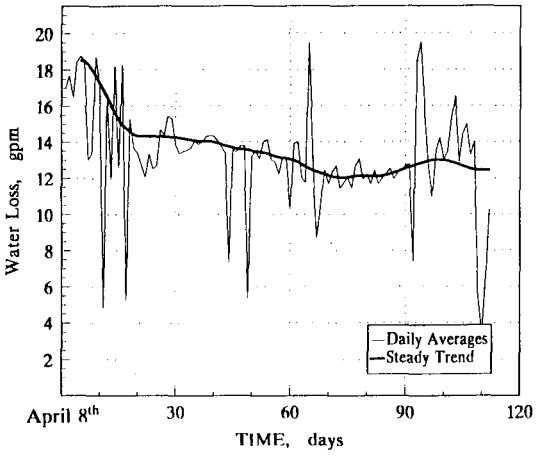

However, this calculated loss rate has not been corrected for the approximately 0.1 l/s of "loss" actually resulting from additional fluid storage within the reservoir due to the continued cooling-induced contraction of the rock blocks near the reservoir entrance region and the accompanying joint dilation (Rodrigues et al., 1993).

As can be seen in Figure 3, the rate of water loss declines quite rapidly during the initial transient period, and then more slowly during the remainder of the test. In contrast, the injection pressure, and therefore the pressure on that part of the reservoir boundary away from the production well where the majority of the diffusional water loss occurs, was rising or constant. (The slight rise in the water loss rate beyond day 90 was caused by the protracted reservoir shutin at about that time, as shown in Figure 2.) The inference is that the reservoir boundary was stable, and that the diffusional portion of the reservoir water loss rate was slowly declining with time as has been observed during previous static reservoir pressure testing (Brown, 1992).

The variation of the surface production temperature and the corresponding thermal power during the LTFT are given in Figures 4a and 4b. As shown, the production temperature first increased as equilibrium was approached, and then very slowly decreased. The slow decline in temperature was undoubtedly due the falloff in production flow rate as shown in Figure 2, and the concomitant increase in the heat loss, per unit flow rate, from the production wellbore to the surrounding rock. As a point of reference, during the 30-day flow test of the Phase II reservoir in mid-1986 (Dash, 1989), the production temperature rose to above 190°C at a flow rate of about 13.9 l/s (220 gpm), giving another example of the dependence of production temperature on flow rate.

Figure 4a. LTFT Wellhead Temperatures

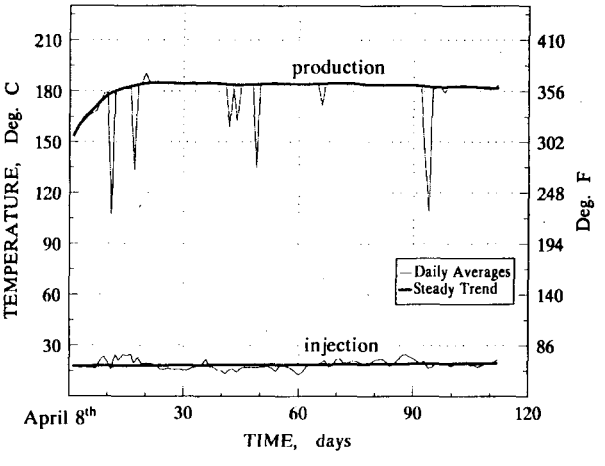

Figure 4b. LTFT Thermal Power

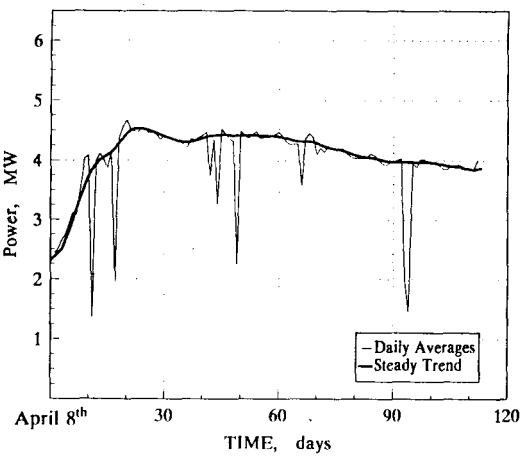

Interim Flow Test

During the 6-week period from August 20 to October 1, referred to as the IFT, reservoir flow testing continued at a lower injection rate of about 4.3 l/s (68 gpm) using a smaller-capacity reserve pump. Also included in this 6-week period was a 1-week reservoir shut-in for necessary pump repairs.

Figure 5 shows the injection and production pressure profiles during the IFT, while the injection and production flow rate profiles are shown in Figure 6. The period of reservoir shut-in is apparent. After establishing steady-state flow conditions near the beginning of the IFT, the injection pressure slowly leveled out at about 22.2 MPa (3220 psi) at an injection rate of 4.3 l/s (68 gpm). Following the shut-in, the injection pressure more rapidly stabilized, but again at a level of 22.2 MPa.

Figure 5. IFT Wellhead Pressures

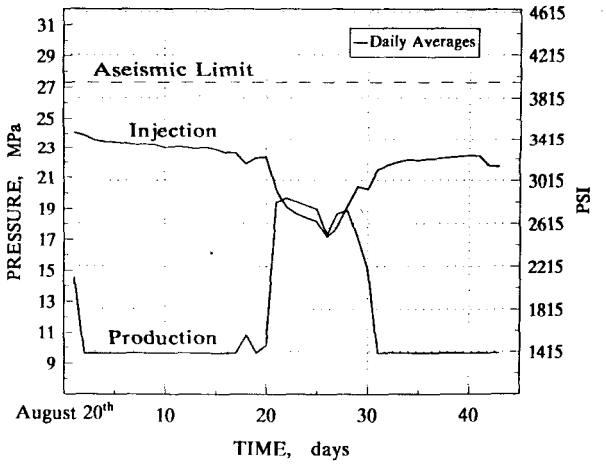

Figure 6. IFT Flow Rates

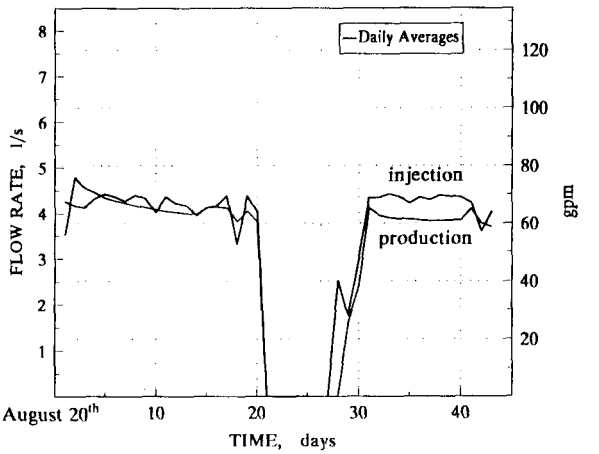

The production temperature variation during the IFT is shown in Figure 7. It is apparent that the 3-week reservoir shut-in following 16 weeks of circulation during the LTFT did not cause a significant perturbation in the temperature field surrounding the production well, since it required only a few days of flow to re-establish a steady-state production temperature at the lower value of about 165°C. This would indicate that the rock surrounding the production wellbore had been considerably heated during the LTFT.

Figure 7. IFT Wellhead Temperatures

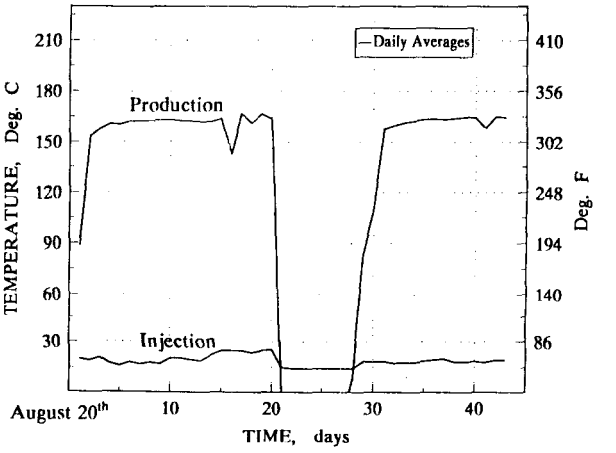

Table I compares the principal reservoir performance data for the LTFT and the IFT. It should be noted that these two flow tests were performed at the same production backpressure level of 9.65 MPa (1400 psi), thus providing a direct measure of the effect of reduced injection pressure on reservoir flow at a constant production backpressure. These data have been essential in validating the GEOCRACK discrete-element reservoir flow/deformation model being developed at Kansas State University (Swenson and Beikmann, 1992).

Table I. Reservoir Performance During the LTFT and the IFT Showing the Variation in Flow Rate as a Function of Injection Pressure

Test	LTFT	IFT
Measured Performance	7/21-29/92	9/29/92
Injection Conditions		
Flow Rate, l/s (gpm)	6.76 (107.1)	4.34 (68.8)
Pressure, MPa (psi)	27.29 (3958)	22.36 (3243)
Production Conditions		
Flow Rate, l/s (gpm)	5.66 (89.7)	3.85 (61.1)
Backpressure, MPa (psi)	9.66 (1401)	9.65 (1399)
Temperature, °C	183	165
Water Loss		
Rate, l/s (gpm)	0.79 (12.5)	0.23 (3.6)
Percent	11.7	5.2

Two observations can be made from the data presented in Table I. First, a 22% increase in the injection pressure between the IFT and the LTFT results in a much larger 56% increase in the injection rate. This shows the strong nonlinear relationship between joint flow and pressure in the body of the reservoir. Second, the rate of peripheral water loss through the microcrack fabric of the rock mass surrounding the HDR reservoir region was markedly decreased by reducing the injection pressure from 27.3 MPa (3960 psi) to 22.4 MPa (3250 psi). The water loss data shows, for matrix flow in this case, the strong nonlinear dependency of permeation outflow on the mean pressure level between the reservoir boundary and the far-field.

Figure 8 shows the wire-line-measured wellbore temperature profiles for corresponding times near the end of the LTFT and the IFT. Even though the surface production temperature for the IFT shows a significant decline from that for the LTFT due to the reduction in flow rate, the corresponding mixed-mean reservoir outlet temperatures at a depth of 3200 m (10,500 ft) indicate no measurable decline. Since the mixed-mean reservoir outlet temperature at 3.85 l/s (61 gpm) should have been about 2°C lower than that at 5.66 l/s (90 gpm) for the same set of distributed wellbore fracture entrances due to additional heat loss as the produced fluid flowed upward through the production interval, one can conclude that the reservoir has experienced no net cooldown between the times of these two temperature surveys.

Figure 8. Production Wellbore Temperature Surveys at 5.82 l/s (7/16) and 3.91 l/s (9/29)

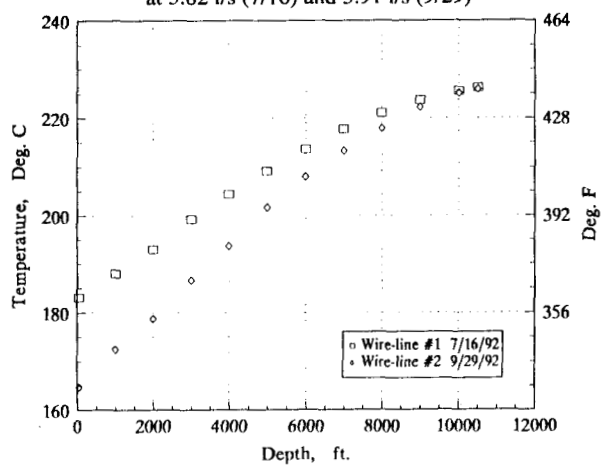

Recent Flow Testing at Higher Backpressures

Following a month of reservoir shut-in, a leased positive-displacement mud pump was brought on line in early November 1992. While re-inflating the reservoir and establishing steady-state flow conditions in November, the pump operated for only a total of 20 days as materials and maintenance issues related to its operation were being addressed. During December, however, with newly designed pump plungers and liners, the pump operated on a near-continuous basis, and we were able to establish two higher-backpressure production flow conditions as shown in Table II.

Table II. Reservoir Flow Performance Under Conditions of Higher Backpressure (15.2 MPa and 12.4 MPa)

Measured Performance	12/10/92	12/27/92
Injection Conditions		
Flow Rate, l/s (gpm)	7.33 (116.2)	7.14 (113.1)
Pressure, MPa (psi)	27.32 (3963)	27.32 (3962)
Production Conditions		
Flow Rate, l/s (gpm)	5.34 (84.6)	5.71 (90.5)
Backpressure, MPa (psi)	15.18 (2201)	12.40 (1798)
Temperature, °C	177.1	182.8

The production data given in Tables I and II indicate that there is a broad maximum in the production flow rate as a function of backpressure, with only a 5% falloff in flow rate as the backpressure is increased from 12.4 MPa (1800 psi) to 15.2 MPa (2200 psi). This would suggest that the decrease in the driving pressure difference across the reservoir, as the backpressure is increased, is about balanced by the decrease in reservoir flow impedance with increasing backpressure. The overall subject of reservoir flow impedance is discussed in a companion paper (DuTeau and Brown, 1993).

Conclusions

To date, long-term flow testing of the Phase II reservoir at Fenton Hill under stable, aseismic conditions has shown no thermal drawdown for an aggregate flow testing period of about 6.3 months. This conclusion is based on both surface production temperature measurements and temperature logs (Refer to Figure 8 and Tables I and II).

During the initial 16-week LTFT, which was conducted at injection pressures up to 27.3 MPa (3960 psi), the production backpressure was generally maintained at 9.65 MPa (1400 psi). The resulting mean production flow rate was 5.8 l/s (92 gpm) at a temperature of 184°C. The mean thermal power production was 4.0 MW, but the actual power level declined by about 10% during the LTFT due to a gradually decreasing production flow rate. This decreasing flow rate in turn reflected a gradual redistribution of flow within the reservoir, away from more direct paths and toward more indirect paths. For the LTFT, the apparent water loss rate averaged about 0.8 l/s (12.5 gpm), of which 0.1 l/s (16%) was actually being stored within the fractured reservoir in thermally dilated joints near the injection interval, and possibly to some extent in new fracture flow paths.

References

Brown, D. W., "Recent Progress in HDR Reservoir Engineering," Proceedings, Geothermal Program Review IX, March 19-21, 1991, San Francisco, CA, US Department of Energy report CONF-913105 (1991).

Brown, D. W., and B. A, Robinson, "The Pressure Dilation of a Deep, Jointed Region of the Earth," in Rock Joints, Proceedings of the International Symposium on Rock Joints, Leon, Norway, June 1990, A. A. Balkema, Rotterdam (1990).

Dash, Z. V. (Ed.), "ICFT: An Initial Closed-Loop Flow Test of the Fenton Hill Phase II HDR Reservoir," Los Alamos National Laboratory Report LA-11498-HDR (1989).

Dash, Z. V., H. D. Murphy and G. M. Cremer (Eds.), "Hot Dry Rock Geothermal Reservoir Testing: 1978 to 1980, "Los Alamos National Laboratory Status Report LA-9080-SR (1981).

DuTeau, R. and D. Brown, "HDR Flow Impedance Variation with Back-pressure," Proceedings, 18th Workshop on Geothermal Reservoir Engineering, Jan. 26-28, 1993, Stanford University, Stanford, CA (1993).

Rodrigues, N. E. V., B. A. Robinson and D. A. Counce, "Tracer Experiment Results During the Long-Term Flow Test of the Fenton Hill Reservoir," Proceedings, 18th Workshop on Geothermal Reservoir Engineering, Jan. 26-28, 1993, Stanford University, Stanford, CA (1993).

Swenson, D., and Mel Beikmann, "An Implicitly Coupled Model of Fluid Flow in Jointed Rock," in Rock Mechanics: Proceedings of the 33rd U.S. Symposium, A. A. Balkema, Rotterdam (1992).

PROCEEDINGS, Eighteenth Workshop on Geothermal Reservoir Engineering
Stanford University, Stanford, California, January 26-28, 1993
SGP-TR-145

CORRELATING QUARTZ DISSOLUTION KINETICS IN PURE WATER FROM 25° TO 625°C

Jefferson W. Tester, W. Gabriel Worley, Bruce A. Robinson,
Charles O. Grigsby, Jeffrey L. Feerer

Massachusetts Institute of Technology
Chemical Engineering Department and Energy Laboratory
Cambridge, MA 02139

BACKGROUND AND MOTIVATION

During the past 50 years, quartz dissolution kinetics and solubility measurements have been the subject of numerous investigations. Researchers have been motivated either because of their interest in understanding important natural geologic processes in the earth or because of a need to quantify dissolution rates for chemical processes above ground or for geothermal heat extraction underground. Our motivation for carrying out experimental studies of quartz dissolution for the last 15 years was driven by engineering issues related to mineral transport in circulating hot dry rock (HDR) geothermal systems (Armstead and Tester, 1987; Grigsby *et al.*, 1989; Charles *et al.*, 1979; Tester *et al.*, 1977). Of critical importance to HDR is the characterization of the rate of dissolution of host reservoir rock as a function of temperature, pressure and liquid phase composition. In general, quartz is a major mineral component in HDR reservoirs in low permeability crystalline rock. Furthermore, quartz is highly reactive relative to other constituent minerals in near neutral (non-acidic/non-basic) aqueous environments at temperatures of interest to HDR geothermal energy extraction (150° to 300°C). Because of these two reasons, we were motivated to understand the quantitative aspects of quartz dissolution in pure water.

More specifically, the analysis and modeling of data from HDR field tests at the Fenton Hill site in New Mexico require that dissolution kinetics be fully characterized in order to predict reservoir performances as well as to size the active reservoir on a volumetric or areal heat sweep efficiency basis (Grigsby and Tester, 1989). Because HDR systems have small circulating fluid volumes and residence times relative to natural hydrothermal systems, dynamic changes in dissolved silica concentration can be created by switching from a normal closed-loop mode of operating to an open-loop mode. In the closed-loop mode with a modest flow of make-up water, silica concentrations approach saturation because of recirculation effects. This permits the use of geothermometry to estimate reservoir temperatures (Fournier and Rowe, 1966). In the open-loop mode, however, fresh water with a low dissolved silica concentration can be flushed through the system. In this case the transport rate of silica into the reservoir fluid can be used as a chemical tracer to aid in estimating the size of the active heat transfer volume and area of the reservoir (Robinson *et al.*, 1988; Grigsby and Tester, 1989).

Given our motivation for examining quartz dissolution kinetics for HDR reservoir modeling needs, we started out in 1977 by carefully reviewing the available literature on this subject. We quickly realized that while a great amount of work had been done with quartz, results from one research group were rarely if ever compared with another group's data. Furthermore, there were only a few investigators who even attempted to correlate their data in a systematic manner. Over the last 15 years the situation has improved with respect to experimental procedures and equipment used along with a much improved appreciation for the importance of surface preparation and characterization. These factors have all contributed to enhancing the quality of the data. However, almost without exception, even recent investigators have not compared or correlated their rate data with others on a fully quantitative basis.

THERMODYNAMICS AND KINETIC CONSIDERATIONS

In order to fully appreciate the manner in which dissolution rate data are correlated, several basic thermodynamic and kinetic issues germane to the quartz-water system are worthy of attention. Quartz dissolves congruently via a global hydrolysis pathway to form silicic acid ($Si(OH)_4$) (Iler, 1955, 1979).

$$SiO_{2(s)} + 2H_2O_{(aq)} \rightleftarrows Si(OH)_{4\,(aq)} \qquad (1)$$

Reaction (1) is reversible in the sense that both dissolution ($\rightarrow$) and precipitation ($\leftarrow$) pathways can occur simultaneously. At saturation, these rates are equivalent and the net rate of reaction is zero with dissolved silica values at levels corresponding to the solubility of quartz in water at a particular temperature, pressure, pH, etc. Studies reported in this paper deal specifically with dissolution measurements conducted in initially distilled and/or deionized water. Under these conditions and assuming that reactor wall materials are chemically inert, one would expect only temperature and, to a lesser extent, pressure to influence rates of dissolution.

Some investigators have employed the concepts of transition state theory to justify the form of a global rate expression for quartz dissolution (Rimstidt and Barnes, 1980; Brady and Walther, 1990; Dove and Crerar, 1990). While these approaches represent noteworthy extensions of transition state theory to heterogeneous (solid-liquid) geochemical kinetic systems, they do not identify rate-controlling elementary reaction steps at a molecular level. A recent treatment by Casey *et al.* (1990) using *ab initio* molecular orbital calculations provides a more realistic representation of possible transition state activated complexes. However, without direct evidence of activated complex structure in this heterogeneous system, a heuristic empirical approach is justified and can be useful in correlating dissolution rate data over a wide temperature range.

Although it is difficult to attribute original authorship to this idea, papers in the mid-1950's began to report a phenomenological rate equation based on de Donder and Nernst-like concepts (see for example, O'Connor and Greenberg, 1958; Iler, 1955). In this treatment, one postulates that reaction (1) is fully reversible; and that at saturation, the rate of dissolution equals the rate of precipitation. At conditions of undersaturation where the bulk concentration of silica in solution is below its solubility, the forward direction dissolution rate is assumed to occur at the same rate that it does at saturation while the precipitation rate decreases in direct proportion to the bulk silica concentration. In simple equation form this is equivalent to saying that the *net* rate of dissolution (R_{diss}) in mol/m^2 s is given at a particular temperature and pressure by the following expression

$$R_{diss} = \frac{-1}{V}\frac{dN_{SiO_2}}{dt} = k_d a^* (C^{sat}_{SiO_2} - C_{SiO_2}) \qquad (2)$$

and by defining $k^*_d \equiv k_d C^{sat}_{SiO_2}$,

$$R_{diss} = k^*_d a^* (1 - C_{SiO_2}/C^{sat}_{SiO_2}) \qquad (3)$$

where

a^* = active quartz surface area per unit of fluid volume (m^2/m^3)

k_d = empirical first-order dissolution rate constant (m/s)

$k^*_d \equiv k_d C^{sat}_{SiO_2}$ = empirical zero-order dissolution rate constant (mol/m^2 s)

C_{SiO_2} = bulk silica concentration (mol/m^3)

$C^{sat}_{SiO_2}$ = saturated silica concentration or solubility (mol/m^3)

V = solution or fluid volume (m^3)

N_{SiO_2} = moles of silica dissolving from quartz (mol)

t = time (s)

The term $(1 - C_{SiO_2}/C^{sat}_{SiO_2})$ can be viewed as the degree of undersaturation. One can see that R_{diss} has a linear or first-order dependence on concentration, and at saturation R_{diss} goes to zero. At the opposite extreme, R_{diss} is maximized when $C_{SiO_2} = 0$. This condition is referred to as "free-dissolution" and is analogous to evaporation of a solid or liquid into a perfect vacuum.

In essence, this phenomenological approach assumes that the forward dissolution process in Reaction (1) occurs at a constant rate, independent of the composition of the surrounding bulk solution. Thus,

$$r_{diss} = r^{max}_{diss} = k_d a^* C^{sat}_{SiO_2} \qquad (4)$$

This forward rate is equal to the maximum, reverse precipitation rate at saturation. Consequently, the net rate $r^{max}_{diss} = k_d a^* C^{sat}_{SiO_2} = 0$ at saturation or

$$r^{max}_{diss} = r^{max}_{pptn} = k_p a^* C^{sat}_{SiO_2} \qquad (5)$$

and $k_d = k_p$. At finite undersaturations, $C_{SiO_2} < C^{sat}_{SiO_2}$ and r_{pptn} is reduced in proportion to the bulk silica concentration:

$$r_{pptn} = k_p a^* C_{SiO_2} = k_d a^* C_{SiO_2} \qquad (6)$$

Therefore, Eqn. (2) can be developed by subtracting Eqn. (6) from Eqn. (5). We want to emphasize that either derivation of Eqn. (2) does not require a molecular-level, elementary reaction description of the quartz dissolution mechanism.

The a* term in Eqns. (2)-(6) underscores the importance of knowing the active dissolving surface area. Many investigators report that the BET-derived surface area from nitrogen or argon gas adsorption is the correct surface area to use -- but they do not provide molecular-based reasoning to justify that claim. At the opposite extreme, a nominal value of the surface area based on the bulk geometric characteristics of the quartz sample can be used depending on whether it is a slab, disc, cylinder or crushed into a quasi-spherical rough particle shape. White and Peterson (1990a, b) give an excellent review of surface area concerns as they apply to geochemical kinetics in natural systems undergoing weathering.

In principle, the forward dissolution rate should depend on the concentration of active ≡ Si-O-Si ≡ sites on the surface. As a first approach, we can assume that the dissolution rate varies linearly with the surface site concentration and that the concentration of active ≡ Si-O-Si ≡ sites scales directly with the *saturation* value of silica dissolved in the bulk aqueous phase. Given these assumptions, classical phase equilibrium considerations enter the picture. The $C^{sat}_{SiO_2}$ term in Eqn. (2) expresses this effect quantitatively, with the forward dissolution rate of Reaction (1) given by Eqn. (4).

Effectively, because we measure the net dissolution rate (R_{diss}) and the bulk silica concentration in solution C_{SiO_2} and estimate a*, in order to extract a first-order rate constant for dissolution (k_d) we need to have an estimate of $C^{sat}_{SiO_2}$ as a function of temperature and pressure in the two-component, binary mixture of quartz (SiO_2) and water (H_2O).

Fournier and Potter (1982) provide an excellent correlation for quartz solubility. Figure 1 compares their solubility correlation at the vapor pressure of the solution and at 1000 bar with experimental data from several investigators (Kennedy, 1950; Crerar and Anderson, 1971; Hemley *et al.*, 1980; Morey and Hesselgesser , 1951; Siever, 1962). Data are given from 25°C to the critical point of pure water at 374°C on the saturation curve, while they extend to 600°C at 1000 bar.

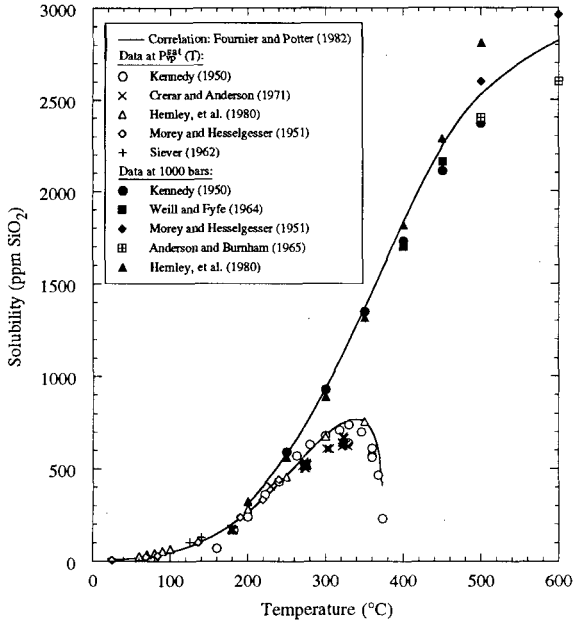

Figure 1. Solubility of quartz in pure water at the saturated solution vapor pressure and at 1000 bar

Figure 2 gives a semi-logarithmic plot of both the vapor pressure (P^{sat}_{vp}) of pure water and the solubility ($C^{sat}_{SiO_2}$) as a function of reciprocal absolute temperature. These so-called Gibbs-Helmholtz coordinates linearize the temperature dependence and provide an estimate of phase transition enthalpies from the slope of the lines -- ΔH (vaporization) from the vapor pressure line and ΔH (solution) from the solubility line. The highly non-linear behavior for solubility near the critical point is indicative of a change in the solvation characteristics of water on a molecular level.

The Fournier and Potter correlation for quartz solubility used in our data analysis is as follows:

$$\log_{10} C_m = A + B\,(\log_{10} v) + C(\log_{10} v)^2 \qquad (7)$$

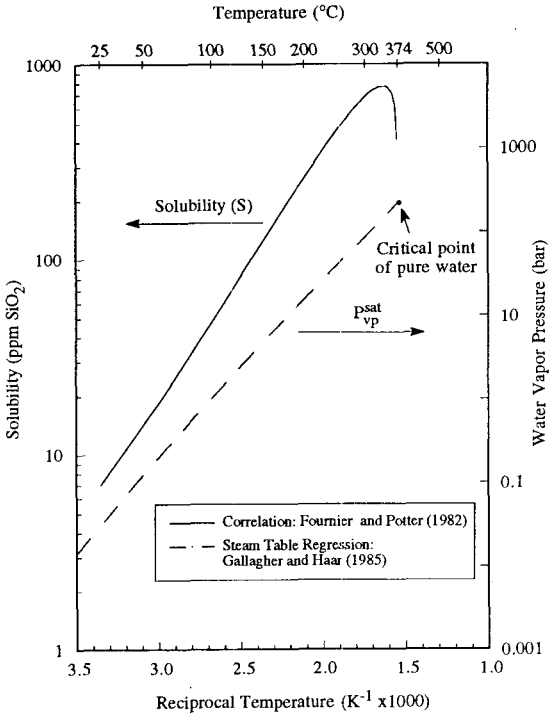

Figure 2. Vapor pressure of pure water and quartz solubility at the saturation vapor pressure from 25°C to the critical point (374°C, 221 bar) using Gibbs-Helmholtz coordinates to linearize temperature dependencies

where A, B, and C are empirical temperature-dependent constants that have been fit to data, C_m is the molal silica concentration (moles SiO_2/1 kg of water), v is the specific volume of water (cc/g) and T is the temperature in Kelvins. The A, B, and C parameters are given by

$$A = 4.66206 + 0.0034063\,T + 2179.7\,T^{-1} - 1.1292 \times 10^6\,T^{-2} + 1.3543 \times 10^8\,T^{-3}$$

$$B = -0.0014180\,T - 806.97\,T^{-1}$$

$$C = 3.9465 \times 10^{-4}\,T$$

We can rewrite Eqn. (2) to express the solubility $C^{sat}_{SiO_2}$ in ppm (parts per million of SiO_2) as:

$$\log_{10} C^{sat}_{SiO_2} = \log_{10}(C_m \times MW) \times 10^3) = 4.7788 + \log_{10} C_m \qquad (8)$$

where MW = molecular weight of SiO_2 = 60.084.

Equations (2) and (3) thus represent an empirical global model for quartz dissolution that can be used to correlate data. If we can show that it is applicable over a wide range of conditions, then one not only gets a useful function for correlating data but its simple mathematical form can be easily incorporated into dynamic reservoir simulation models.

SPECIFIC OBJECTIVES AND APPROACH

Given the motivating factors cited in the previous section, our objectives in preparing this paper were twofold: first to describe our experimental procedures for preparing and characterizing quartz surfaces and carrying out kinetic measurements of dissolution rates from 25° to 255°C and second to compare and correlate our results with kinetic data reported by other investigators in developing a general empirical correlation for intrinsic dissolution kinetics.

Our approach to achieving these objectives consisted of the following key steps:

(1) designing and utilizing five different experimental systems for measuring dissolution rates

(2) developing consistent procedures for sample preparation and composition measurements so that reproducible kinetic data could be obtained

(3) analyzing all existing published kinetic data on quartz dissolution in pure water to determine their suitability for quantitative correlations

(4) conducting dissolution experiments from 25° to 255°C

(5) developing an empirically-based model to correlate our data with those collected in other laboratories

EXPERIMENTAL EQUIPMENT AND PROCEDURES EQUIPMENT

Equipment. Five different apparatus were used in this study to obtain dissolution kinetic data. For purposes of identification we have labeled them:

(1) *Batch Bottle*
(2) *Packed Bed*
(3) *Rocking Autoclave*
(4) *Stirred Autoclave*
(5) *Spinning Basket*

The *Batch Bottle* system is simply a sealed polyethylene bottle (125 ml) that contains the quartz sample in water. This apparatus was used only for measurements in the temperature range of 23° to 50°C. Solution samples were removed periodically for analysis and temperatures were maintained in a constant-temperature water bath to ± 1°C. Typically, experiments at these temperatures were conducted from 4 to 18 months.

The *Packed Bed* system (Grigsby, 1989) used a vertical cylindrical teflon-lined stainless steel reactor (4.13 cm diameter and 15.24 cm long). The reactor contained a 13 cm high packed bed of quartz particles suspended vertically on teflon-coated, stainless steel filter holder. All wetted parts in the system were either polyethylene or Teflon. Water was pumped into the bottom of the bed which contained 288.0 g of quartz sand with a void fraction of 39.2%. Liquid samples were taken from the effluent in the top of the reactor where pH was also measured. All experiments in the *Packed Bed* reactor were conducted at 25°C. Tracer tests indicated that non-ideal flow due to dispersion in the packed bed was insignificant. Ideal plug flow behavior with a uniform fluid velocity in the bed was closely approximated, thus the system could be treated as a plug flow reactor (PFR) for purposes of data analysis.

The *Rocking Autoclave* system (Robinson, 1982) consisted of a small, closed reactor bomb agitated using a reclining arm to raise and lower the vessel which was kept isothermal using band heaters and an Athena differential temperature controller. Alternatively, the bomb was placed in an oven and whole system was rocked to achieve adequate mixing between the solid quartz particles and fluid phase. The bombs used in this study were constructed of titanium with a teflon O-ring used to seal the cover. Their inside dimensions were 2.29 cm diameter with a length of 5.23 cm -- providing a working volume of about 21.5 cm^3. The *Rocking Autoclave* apparatus was used for measurements from 200 to 250°C. Separate runs were carried out over a range of exposure times to obtain rate information as only the final concentration of the solution was determined after the dissolution reaction had been quenched using liquid nitrogen or cold water to cool the bomb.

The *Stirred Autoclave* experimental apparatus (Robinson, 1982) was used to perform batch quartz dissolution experiments in the temperature range from 180° to 255°C. The reactor vessel was a Pressure Products Industries, 316 stainless steel autoclave, with a total usable volume of approximately 1 L. A variable speed D.C. motor drives a rotating magnet to which a six-bladed agitation propeller/shaft assembly is attached. The rotation speed was adjusted from approximately 200-900 rpm to ensure good mixing. Liquid samples were extracted from the autoclave through a sampling valve connected to a small diameter stainless steel tube which was immersed in a cold water bath to cool the liquid sample well below its boiling point. Constant temperature to ± 1°C was maintained using an external electrical resistance heating jacket controlled by an Athena temperature controller, which received its temperature signal from a thermocouple placed in the immersed thermocouple well.

To perform an experiment, a sample of crushed quartz of known weight and size fraction was charged through the top of the reaction vessel. A known amount of distilled, deionized water (usually 500 mL) was then added and the system closed to begin heatup. The water was preheated to cut down on the time required for the system to reach the desired temperature. The reactor and contents were allowed to heat up without turning on the stirrer; this procedure minimized the dissolution rate during the heatup period. Once the desired temperature was reached, samples were taken at regular intervals as follows: the stirrer, which was operating constantly

during the experiment, was shut off for about one minute before a sample was taken to allow the solid particles to settle to the bottom of the autoclave. Then approximately 4 mL of liquid were expelled to displace the stagnant fluid in the sampling tube. Then roughly 3 mL of sample were taken and the stirrer turned back on. At the end of an experiment, the stirrer and controller were turned off and the system allowed to cool just below the boiling point of water. This temperature is high enough that none of the dissolved silica would reprecipitate on the quartz particles upon cooling. The entire contents were then drained and the quartz particles rinsed thoroughly before being used in the next experiment.

The final reactor system used in this study was a *Spinning Basket* flow-through design, developed to improve reaction conditions by reducing the interparticle abrasion that occurs in the other two autoclave systems. Quartz particles were held in an annular fixed bed using a rigid wire screen basket which is rotated within an autoclave vessel to maintain good fluid contact and high mass transfer rates, and to virtually eliminate abrasion effects common to fluidized bed or actively stirred or rocked reactor systems. In the *Spinning Basket* system all wetted parts at dissolution conditions were constructed of CP (commercially pure) titanium.

The Ti *Spinning Basket* reactor system and ancillary equipment are schematically shown in Fig. 3. An Autoclave Engineers magnetic drive unit was modified to provide rotation of the Ti basket containing the quartz sample. A 20 L polypropylene feed tank was used to hold the distilled, deionized water that was fed continuously to the reactor to maintain well-mixed conditions for this open, flow-through design. A charge of approximately 600 g of prepared Ottawa sand was used for all experiments. The reactor has a liquid volume of approximately 1 L; thus a nominal surface area to fluid volume ratio of 19 cm^2/cm^3 could be maintained to permit operation over a wide range of

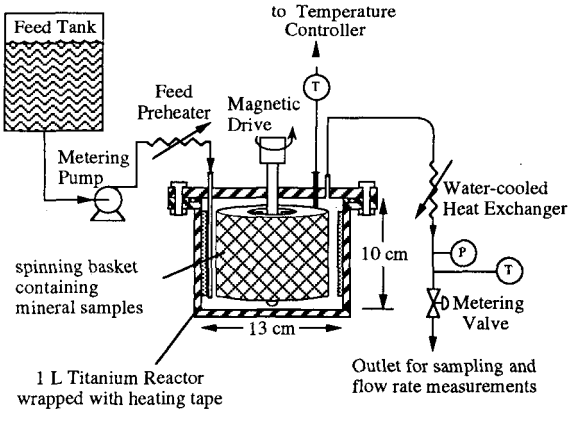

Figure 3. Schematic of the titanium spinning basket continuous flow stirred tank reactor (CSTR) system

temperatures and residence times (τ). At 70°C, the feed water flow rate was 0.3 mL/min (τ = 3300 min) while at the maximum temperature studied of 150°C, the flow rate was 20 mL/min (τ = 50 min). Under these conditions we could maintain ideal back-mixed flow and still observe measurable dissolved SiO_2 concentrations in the product effluent stream from the reactor. The *Spinning Basket* reactor had a maximum operating pressure of 8 bar (116 psia) which limited the temperature to about 150°C for dissolution runs where the vapor pressure of water is 4.75 bar (68.9 psia). The system has now been upgraded to operate at 240°C and 40 bar (600 psia) for experiments currently underway. A Na-fluorescein dye tracer study performed on this reactor indicated that, to within experimental accuracy, ideal continuous stirred tank reactor (CSTR) flow conditions existed with a residence time distribution (RTD) given by:

$$f(t) = 1 - \exp[-t/\tau] \qquad (9)$$

where f(t) maps out the time dependence of the tracer concentration in the product stream in response to a unit concentration step change in the feed and τ is the mean reactor residence time ($V_R/\dot{q}$; V_R = reactor volume and $\dot{q}$ = volumetric flow rate).

Other equipment supporting the *Spinning Basket* reactor included an electrically heated preheater tube for the feed and a water-cooled heat exchanger for the product. Both of these employed CP titanium tubing. The reactor itself was wrapped in heating tape and insulated to maintain isothermal conditions. Following the cool-down section when the product stream reached about 30°C or less, titanium tubing and 316 stainless steel fittings were used.

Sample Preparation. In our experiments two types of quartz were used: crushed, clear, Hot Springs, Arkansas, quartz crystals and Ottawa sand. For both samples cleaning and washing steps were used to ensure well-defined uniform surfaces. Crushing and other types of mechanical deformation can create a disturbed surface layer which, if not taken into account properly, can falsify the data resulting from a quartz dissolution experiment. Other experimenters (Van Lier *et al.*, 1960; Rimstidt and Barnes, 1980) observed initial rapid rates of dissolution as a result of a disturbed layer. Rimstidt and Barnes (1980) hypothesized that these high rates were a result of a thin layer of amorphous silica and used their early time data to obtain an estimate for the dissolution rate of amorphous silica. An equally plausible mechanism would be that the initially high rate is due to a larger a* term in Eqn. (2) that is caused by very small particles (fines) that were created by mechanical deformation during crushing or are present from purely natural causes.

Scanning electron microscope (SEM) photographs were used in the present study to verify the existence of the damaged layer. Figure 4a is a SEM photograph of an unwashed particle of quartz taken using an ISI Model DS-130 scanning electron

(a) Untreated crushed quartz.

(b) Reacted crushed quartz after several dissolution experiments above 150°C.

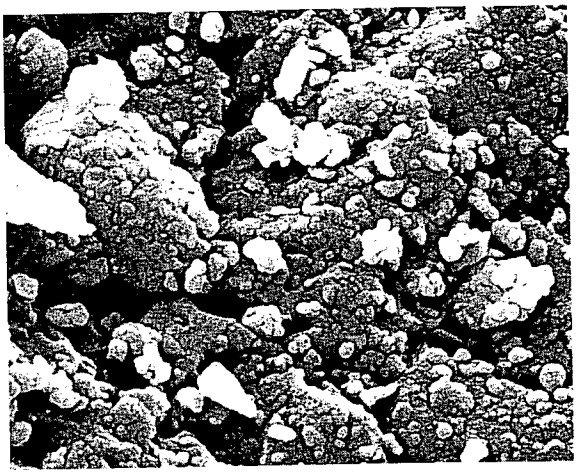

(c) Untreated Ottawa sand.

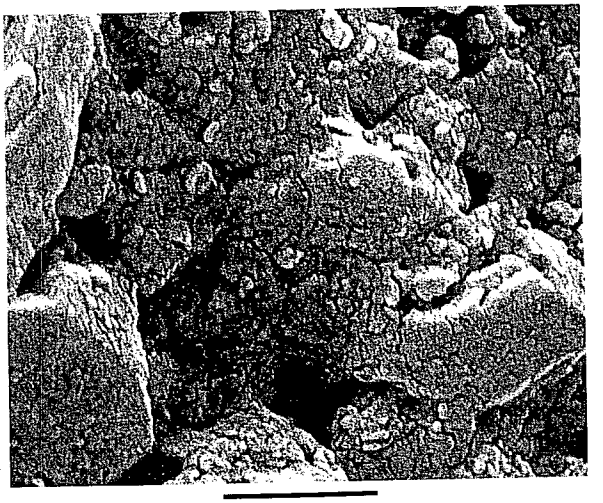

(d) Washed Ottawa sand.

Figure 4. Scanning Electron Microscope (SEM) photograph of typical crushed quartz and Ottawa sand before and after treatment to remove fines.

microscope. Clearly, the damaged layer exists as a discontinuous collection of fines adhering to the surface of the particle. Even if the small fines were pure amorphous silica, obtaining an accurate value for the surface area is not feasible. Thus, extracting meaningful amorphous silica kinetic data from a quartz dissolution experiment using the initial rate data is problematic. Furthermore, some of the fines may have small enough radii of curvature (of the order of 1 μm or less) that surface energy effects could significantly raise their equilibrium solubility in water via a Gibbs-Kelvin-Thompson effect.

The initial rapid dissolution of these small particles suggests an effective method to get around the problem of fines adhering to the quartz surface. If the quartz particles are brought to a high temperature in water (200°C or greater) for several hours, then the fines will dissolve preferentially until they have been totally eliminated. In practice, the method used in this study was simply to reuse the same quartz particles in each experiment. The first experiment using freshly prepared quartz particles always exhibited a rapid initial rate of dissolution. Subsequent experiments did not, suggesting that the small fines had been dissolved completely in the first experiment. Figure 4b is a SEM photograph of a typical crushed quartz particle after several runs at high temperature (> 200°C). The fines have been virtually eliminated, ensuring that the subsequent dissolution experiments are those of the large quartz particles with no interference from the small fines.

Van Lier (1960) showed that treatment with HF will dissolve the fines very rapidly. However, since HF chemically interacts with quartz to accelerate dissolution, an elaborate washing procedure is necessary to ensure that none of the HF is left in the microfractures of the quartz particles. The procedure suggested in the present study is much easier to carry out experimentally, and avoids the problem of HF adsorption into the microfractures.

One piece of empirical evidence obtained from our *Stirred Autoclave* experiments (180° to 255°C) suggests that the small fines are responsible for the rapid initial rate of dissolution. During the 1 to 2 hours required to heat the reactor up to temperature, the amount of dissolution predicted from the rate expression of Eqn. (2) is so small that the initial concentration of dissolved silica (the concentration after the system has reached its ultimate temperature) should still be approximately 0 ppm. Experimentally, this calculation is borne out in the runs performed using annealed quartz, but the first experiment using unwashed quartz shows that the concentration reaches at least 40 ppm during the heatup period. Presumably this initial higher concentration is due to rapid dissolution of the small fines. If Figure 4a is taken as a typical example of the size and quantity of the fines, then it can be calculated that complete dissolution of these small particles during heatup would result in an initial concentration within a factor of 2 of the observed 40 ppm. Given the limited accuracy of such a calculation, the fact that it results in a concentration in the neighborhood of the observed result suggests that rapid dissolution of the small fines is a reasonable explanation of the initial dissolution rate behavior.

Crushed quartz was used for all dissolution experiments conducted in the *Rocking Autoclave* and *Stirred Autoclave*, batch reactor systems. Quartz crystals were crushed, washed and sieved to obtain a desired size range. For the *Rocking Autoclave* experiments, a 53 to 1000 μm size distribution was used; while for the *Stirred Autoclave* runs, a narrower size distribution of 53 to 149 μm was used. These represent overall particle size ranges while actual ranges used in individual experiments were considerably smaller.

Ottawa sand was used for all dissolution experiments carried out in the *Packed Bed* (PFR), *Batch Bottle*, and *Spinning Basket* (CSTR) reactor systems. Samples of Ottawa sand were prepared slightly differently depending on the reactor used. The preparation procedure was as follows:

1. Wash the *as received* 20 to 28 mesh (595 to 841 μm) sand particles for 10 minutes in concentrated nitric acid to remove iron.
2. Tumble for three weeks with continued, periodic fresh water washes (500 mesh silicon carbide grit was used for the sand particles used in the *Packed Bed* reactor runs).
3. Rinse with water.
4. Wash with water for three weeks with fresh water added periodically.
5. Dry at 100°C (an ethanol wash was used before drying for the sand particles used in the Packed Bed reactor runs).

Analytical Methods. Three primary methods -- molybdate yellow and blue spectrophotometric and inductively coupled plasma (ICP) emission spectroscopy -- and one secondary method -- atomic absorption (AA) spectroscopy -- were used to determine dissolved silica concentrations. The molybdate yellow method was used for SiO_2 concentrations in the 1 to 400 ppm range while the molybdate blue and ICP methods were used in the 0.02 to 2.0 ppm range. AA was used periodically to cross-check the molybdate techniques to ensure that silica polymerization was not significantly affecting the determination of dissolved SiO_2.

The color reagent for the molybdate yellow method was prepared by mixing 50 ml of 1.0 N sulfuric acid with 20 ml of a premixed 10 wt% ammonium molybdate solution and diluting to 500 ml with deionized water. The ammonium molybdate solution was prepared by dissolving an appropriate amount of reagent grade ammonium molybdate pellets in deionized water to obtain a 10% by wt. solution. The concentrated sulfuric acid used to prepare the 1.0 N H_2SO_4 solution was also of reagent grade purity.

Fresh quantities of yellow color reagent were prepared every day during an experimental run since it was observed that the transmittance of light in the reagent declines noticeably after a few days. To perform an analysis, 1.0 ml of sample was pipetted and diluted to 50.0 ml in a volumetric flask. Transmittance readings at 6, 9, and 12 minutes after the start of the reaction were taken at a wavelength of 440 nm and 0.098 μm slit width using a Beckman DU-2 spectrophotometer. For almost all samples, two agreeing transmittance readings (to the third decimal place) were obtained in these three readings.

The transmittance readings were converted to concentrations assuming Beer's law was followed. To verify the Beer's law assumption, a 1000 ppm sodium silicate standard was diluted quantitatively to 50, 100, and 200 ppm and the absorbance was found to vary linearly with concentration over this range.

The molybdate blue method utilized absorbance at 815 nm measured on a Schimadzu UV-160U spectophotometer following a ASTM standard technique #D859. Calibration was carried out using quantitative dilutions of a silicon AA standard solution (1010 ppm Si in 2% NaOH) to establish a linear Beer's law region from 0.1 to 2.0 ppm SiO_2. Both molybdate methods are accurate to about ± 3% (with slightly higher errors near the lower detection limit).

ICP measurements were carried out at 251.61 nm for SiO_2 using a Perkin-Elmer model 5500 ICP emission spectrograph for the runs carried out in the *Packed Bed* (PFR) reactor system at 25°C. ICP analyses were performed by D. Counce of Los Alamos National Laboratory. Although a detection level of about 1 ppb is possible for silica, lower limits of 20 ppb (0.02 ppm) were reported for our measurements.

CORRELATION OF EXPERIMENTAL DISSOLUTION KINETICS DATA

Dissolution experiments were performed using the five different reactor systems described in the preceding section. Operating conditions for each system were tabulated in Table 1. Also included are run conditions, reactor designs and mineral descriptions for seven studies of quartz dissolution from other laboratories that were selected for correlation and comparison with our data. As can be seen from Table 1, values for nominal surface area, BET area, and surface area per unit fluid volume are given. The nominal areas are based on average particle sizes using an effective spherical radius (<r>) and the density of quartz (r)

$$\text{Nominal area} = \frac{4\pi(<r>)^2}{(4\pi/3)(<r>)^3\rho} = \frac{3}{<r>\rho} \qquad (10)$$

BET areas reported in our studies used N_2/He adsorption and standard methods. Values for other investigators were cited if available in their published results.

Dissolution rate data as a function of temperature for experiments carried out in this investigation are given in Table 2. Both k_d^* and $C_{SiO_2}^{sat}$ values are provided so that either $k_d = k_d^* / C_{SiO_2}^{sat}$ or k_d^* values can be correlated to temperature. The method used to estimate k_d or k_d^* depends on experimental conditions. Batch experiments in the *Rocking Autoclave*, *Stirred Autoclave*, and *Batch Bottle* systems were analyzed using a time integration of Eqn. (2) that accounted for any volume changes that occured due to periodic sampling (see Robinson, 1982 for details). Continuous flow, open system experiments in the *Packed Bed* (PFR) and *Spinning Basket* (CSTR) system utilized conventional chemical engineering methods for reactor analysis (see Grigsby, 1989 for details).

Table 1. Experimental reaction conditions, reactor designs, and mineral descriptions

Investigator	Reactor Type[1]	Reactor System Wetted Material	Temp Range (°C)	Mineral Type[2]	Particle Size	Specific Surface Area (cm^2/g)		nominal area[3] / fluid volume (cm^2/cm^3)
						nominal	BET	
Present Study:	Rocking Autoclave (B)	Titanium	200-250	Crushed AK	53-1000 μm	12-352	-	1.6
	Stirred Autoclave (B)	316 SS	184-255	Crushed AK	53-149 μm	126-212	-	7-44
	Packed Bed (PFR)	Teflon-lined SS	25	Ottawa Sand	595-841 μm	32	766-903	108
	Batch Bottle (B)	Polyethylene	23-50	Ottawa Sand	595-841 μm	32	766-903	3-48
	Spinning Basket (CSTR)	CP Titanium	70-150	Ottawa Sand	595-841 μm	32	766-903	19
Brady and Walther (1990)	Floating Bottle (B)	"Plastic"	25	Crushed AK	74-149 μm	210	1110	7-32
Dove and Crerar (1990)	Mixed Flow (CSTR)	CP Titanium	200-300	Crushed AK	150-250 μm	116	230	0.76
Kitahara (1960)	Autoclave (B)	Silver-lined steel	400-480	Slab	5x10x15 mm	-	-	0.16
Rimstidt and Barnes (1980)	Rocking Autoclave (B)	---	65-305	Sand (Corning)	100-1000 μm	54	920	67-2600
Siebert, et al. (1963)	Spinning Disc (B)	Stainless Steel	248-332	Disc (0001)	64.8 mm diam	-	-	0.033
van Lier, et al. (1960)	Rotating Tube (B)	Platinum	70-90	Crushed BZ	5-10 mm	3140	3600	290
Weill and Fyfe (1964)	Autoclave (B)	Inconel	400-625	Slab AK (0001)	-	-	-	0.1-0.2

[1] B = batch - closed system
CSTR = *continuous flow stirred tank reactor*
PFR = plug flow reactor

[2] AK = Hot Springs, Arkansas Quartz
BZ = Brazilian Quartz

[3] a*(nominal basis) = nominal area/fluid volume ; 1 cm^2/cm^3 = 100 m^2/m^3

Table 2. Quartz nominal dissolution rate constant data from the present study and earlier investigations plotted in Figure 5

Present Study	Temp (°C)	$\log_{10} k_d^{*}$ [1] (mol/m^2-s)	$C_{SiO_2}^{sat}$ [2] (ppm)	Earlier Studies	Temp (°C)	$\log_{10} k_d^{*}$ [1] (mol/m^2-s)	$C_{SiO_2}^{sat}$ [2] (ppm)
Packed Bed	****25	-11.00	7	Brady and Walther (1990)			
	****25	-11.65	7	*Floating Bottle*	****25	-11.19	7
					****25	-11.73	7
Batch Bottle	****23	-12.58	7	Van Lier, et al. (1960)			
	****23	-12.61	7	*Rotating Tube*	70	-12.16	24
	****23	-12.45	7		80	-11.46	30
	****23	-12.55	7		90	-11.16	38
	23	-13.42	7		***90	-11.64	38
	23	-13.27	7		***90	-11.02	38
	50	-12.19	14		***90	-11.20	38
	50	-12.20	14	Rimstidt and Barnes (1980)			
	50	-12.21	14	*Rocking Autoclave*	*65	-10.60	21
Spinning Basket	70	-11.34	24		**105	-9.14	53
	100	-10.19	48		*105	-9.88	53
	100	-10.22	48		105	-10.27	53
	100	-10.19	48		**105	-10.18	53
	100	-10.44	48		145	-8.36	115
	125	-9.27	79		**145	-9.01	115
	125	-9.19	79		170	-8.43	173
	125	-9.07	79		**187	-8.11	221
	125	-9.16	79		*213	-7.07	311
	125	-9.17	79		265	-6.56	529
	125	-9.53	79		305	-6.14	698
	125	-9.63	79	Dove and Crerar (1990)			
	125	-9.61	79	*Mixed Flow (CSTR)*	200	-7.63	269
	125	-9.81	79		200	-7.35	269
	125	-9.58	79		200	-7.28	269
	150	-8.39	125		200	-7.38	269
	150	-8.46	125		200	-7.26	269
					201	-7.43	272
Stirred Autoclave	184	-7.84	212		250	-6.74	474
	184	-7.98	212		300	-5.97	695
	184.5	-8.20	213		300	-6.01	695
	202	-7.31	270		300	-6.15	695
	202.5	-7.43	272	Siebert et al. (1963)			
	203	-7.24	274	*Spinning Disc*	248	-6.11	476
	215	-7.04	318		250	-5.99	486
	221	-6.75	341		269	-5.85	579
	221	-6.91	341		291	-5.54	688
	221	-7.03	341		315	-5.16	793
	253	-6.36	475		332	-4.96	843
	255	-6.44	485	Kitahara (1960)			
				Autoclave	400	-4.46	†360
Rocking Autoclave	200	-7.04	264		400	-4.37	†800
	200	-7.20	264		440	-4.18	†1840
	200	-7.18	264		440	-4.37	†1100
	250	-6.66	463		440	-4.53	†530
					480	-4.43	†750
					480	-4.21	†1580
				Weill and Fyfe (1964)			
				Autoclave	400	-3.85	2015
					625	-2.54	2896

1 $\log_{10} k_d^{*}$ were calculated using equation (3) and nominal values of a*

2 $C_{SiO_2}^{sat}$ were estimated using correlation by Fournier and Potter (1982) except values preceded by a †.

† Solubility values are based on actual measurements from Kitahara (1960).

Data points with asterisks were omitted from regression for the following reasons:

* ⇒ precipitation experiment
** ⇒ disturbed quartz surface
*** ⇒ experiments not designed to gain kinetic information
**** ⇒ outliers: quartz surfaces probably have not reached a steady state morphology

Figures 5 and 6 correlate the dissolution rate data from 25° to 625°C cited in Table 2 using nominal and BET-derived surface area estimates for the a* term in Eqn. (2). Both figures are in the form of Arrhenius ($\log_{10} k_d^*$ vs 1/T) plots. Data from the five reactor systems of our investigations are combined with the results of the seven previous research groups to arrive at linear-least squares correlations over the entire temperature range.

Empirical equations for k_d^* based on the least-squares lines in Figs. 5 and 6 are given as:

$$k^*_{d,NA} = 475 \pm 356 \exp\left[-\frac{92.2 \pm 2.8}{RT}\right] \quad \text{(nominal area basis)} \qquad (11a)$$

$$k^*_{d,BET} = 597 \pm 1186 \exp\left[-\frac{101.3 \pm 6.6}{RT}\right] \quad \text{(BET area basis)} \qquad (11b)$$

where the error limits represent fits to a 95% confidence level and the units of $k^*_{d,NA}$ and $k^*_{d,BET}$ are mol/m^2 s, T is in Kelvins and R is in units of kJ/mol K. Overall, we estimate $\log_{10} k_d^*$ errors to be ± 0.64 using a nominal area basis and ± 0.98 using a BET area basis.

Although the scatter in the Fig. 5 data where k_d^* is based on nominal area seems somewhat less than in Fig. 6 where k_d^* is based on BET-derived areas, the apparent superior fit may be fortuitous. Nonetheless, both plots confirm the form of Eqn. (3) as a reliable empirical correlation which can be used with confidence to predict the rate of quartz dissolution in pure water over twelve-orders of magnitude of rate change from 25° to 625°C. This rather surprising result suggests that the global averaging effects of Eqns. (2) and (3) provide an accurate representation of dissolution kinetics in a traditional Arrhenius framework. Furthermore, the apparent activation energies of 92.2 ± 2.8 kJ/mol (nominal area basis) and 101.3 ± 6.6 kJ/mol (BET area basis) are reasonable in that they both agree with each other. For comparison, the estimated bond energy for breaking an Si-O bond is about 228 kJ/mole (Robie *et al.*, 1979), which suggests that the activated state to produce a free aqueous species of SiO_2 involves the formation of OH linkages to the dissolving SiO_2 species.

One would expect that the fundamental kinetic processes associated with dissolution would dominate the temperature dependence of Eqns. (2) and (3). These intrinsic kinetic effects are captured in the k_d and k_d^* global rate parameters. The a* term merely scales or normalizes one set of rate data to another and should not be as strongly temperature-dependent as k_d or k_d^*. The observed similar activation energies for nominal- and BET-area normalizations and the similar quality of the correlations themselves shown in Figs. 5 and 6 support these assertions and further substantiate that the form used in Eqns. (2) and (3) is phenomenologically correct.

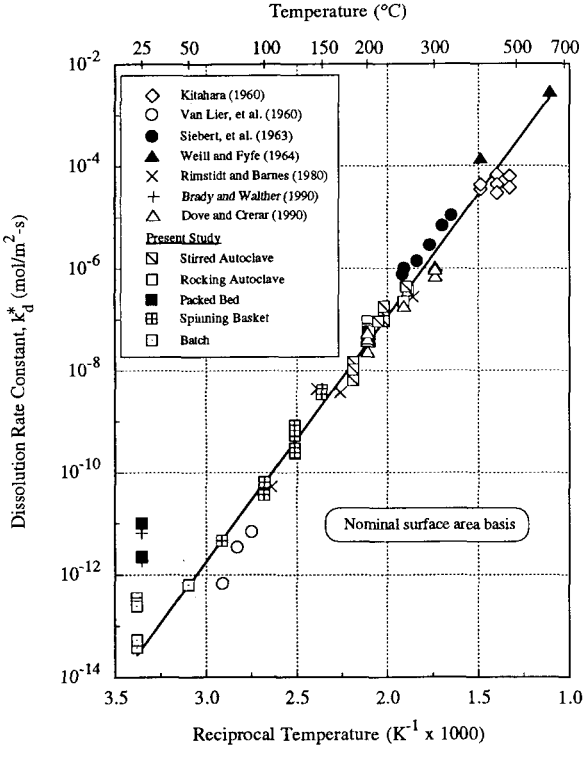

Figure 5. Quartz dissolution kinetics in pure water from 25° to 625°C using a nominal surface area basis and Arrhenius coordinates

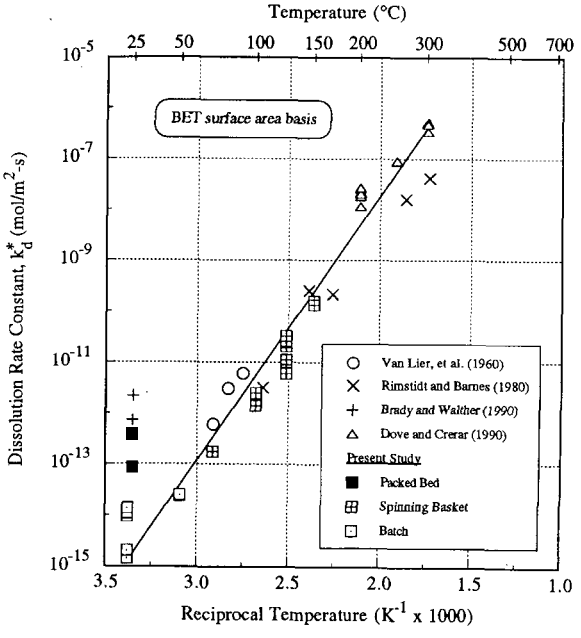

Figure 6. Quartz dissolution kinetics in pure water from 25° to 300°C using a BET-determined surface area basis and Arrhenius coordinates

There are several points that need to be made concerning the data given in Tables 1 and 2. First, not all values of k_d^* available from previous investigators were plotted in Figs. 5 and 6. For example, as indicated in Table 2, several values given by Rimstidt and Barnes (1980) were omitted because a disturbed surface layer existed during their experiments. Also three data points reported by Van Lier *et al.* (1960) at 90°C were deleted because they came from experiments not designed to obtain kinetic information. Although several other investigators report quartz dissolution kinetics at pH's comparable to pure water conditions, they employed buffered solutions (Brady and Walther, 1990; Knauss and Wolery, 1988; Wollast and Chou, 1986). To avoid complications or ambiguities in interpretation, dissolution data obtained in buffered solutions were omitted from our comparisons.

Perhaps the most noteworthy feature in the k_d^* data shown in Figs. 5 and 6 are the *apparent* high dissolution rates at 25°C. We do not believe this behavior is due to fines dissolution, since our sample preparation was very effective in removing fines as verified by SEM observations given in Fig. 4c and d. Apparent high dissolution rates were observed in our experiments with the *Batch Bottle* and *Packed Bed* reactor systems with Ottawa sand as well as by Brady and Walther (1990) who used crushed quartz crystals from Hot Springs, Arkansas. Because dissolution rates are intrinsically very slow at 25°C, surface rearrangements or chemical annealing takes a much longer time than required at higher temperatures. For example, with an activation energy of about 97 kJ/mol, the intrinsic dissolution rate increases 20-fold for a 25°C increase in temperature from 25° to 50°C. Long-term *Batch Bottle* experiments conducted for up to 550 days (18 months) indicate a continual approach to the least-squares regression lines in Figs. 5 and 6. We believe this is due to a gradual annealing process that eventually results in a steady-state surface structure for dissolving quartz.

There are two sets of *Batch Bottle* experiment results plotted in Figures 5 and 6. The first set was performed on Ottawa sand using the standard sample preparation procedures plus an additional soaking in 70°C water for 10 days. Data from this set has the higher dissolution rate constant. The second set of experiments was performed on Ottawa sand taken from the *Spinning Basket* reactor after exposure to temperatures from 70°-150°C for a period of 50 days. This batch of sand should have annealed somewhat with a very low concentration of "high energy" sites remaining. The second data set reached steady state in six months and agrees well with the correlation in Figs. 5 and 6. The first set of experiments have been reacting for 18 months and are still not at steady-state. Nevertheless, we plotted the values in Figs. 5 and 6 for comparison. We anticipate that if we wait long enough, the first set of *Batch Bottle* experiments will agree with the correlations presented in Figures 5 and 6. We could estimate the time required to reach steady-state at 25°C based on our experiments at higher temperatures, but this extrapolation would be inaccurate since the activation energy for removal of the "high energy" sites will be less than for steady-state quartz dissolution.

Clearly more work needs to be done to quantitatively characterize how the surface morphology of quartz on a molecular-level influences these kinetic phenomena. Given the inherently complex nature of quartz hydrolysis and dissolution, the simplicity of the global correlation given by Eqn. (2) is even more striking.

CONCLUSIONS

A general empirical correlation for estimating the intrinsic dissolution rate of quartz in pure water from 25° to 625°C was presented. Data obtained from five different apparatus in this study correlated favorably to rate measurements reported by seven other research groups using both nominal and BET-determined surface area bases. More than eleven orders of magnitude of variation of dissolution rate occur over a 600°C temperature change exhibiting Arrhenius-like behavior with a global activation energy of about 97 kJ/mol SiO_2. Discrepancies in low temperature (25°C) measurements were resolved by waiting sufficiently long to permit annealing processes to produce a "steady-state" dissolving surface.

Acknowledgements. The authors would like to thank our colleagues at Los Alamos National Laboratory who assisted us in carrying out this work. In particular, C. Holley, R.M. Potter, D. Counce, P. Trujillo, the late L. Blatz, R. Charles, M.C. Smith, R.B. Duffield, D. Duchane, J. Albright, J.E. Mock, H. Murphy and A.W. Laughlin provided stimulating discussion, analytical support and critiques of our work over the past 15 years. The U.S. Department of Energy, Geothermal Technology Division, through the hot dry rock geothermal energy project also provided financial support for a portion of the work discussed in this paper. We also gratefully acknowledge the support provided by Alice Colby in preparing the manuscript for publication.

REFERENCES

ANDERSON, G.M. and BURNHAM, C.W. (1965) The solubility of quartz in supercritical water. *Amer. J. Sci.* **263**, 494-511.

ARMSTEAD, H.C.H. and TESTER, J.W. (1987) Heat mining. *E&F N. Spon, London,* Section 10.4.

BRADY, P.V. and WALTHER, J.V. (1990) Kinetics of quartz dissolution at low temperatures. *Chem. Geol.* **82**, 253-264.

CASEY, W.H., LASAGA, A.C., and GIBBS, G.V. (1990) Mechanisms of silica dissolution as inferred from the kinetic isotope effect. *Geochim. Cosmochim. Acta* **54**, 3369-3378.

CHARLES, R.W., HOLLEY, C.E., TESTER, J.W., GRIGSBY, C.O., and BLATZ, L.A. (1979) Experimentally determined rock-fluid interactions applicable to a natural hot dry rock geothermal system. *TMS Paper Selection Report A80-8, The Metallurgical Society of AIME, Warrendale, PA.*

CRERAR, D.A. and ANDERSON, G.M. (1971) Solubility and solvation reactions of quartz in dilute hydrothermal solutions. *Chem. Geol.* **8**, 107-122.

DOVE, P.M. and CRERAR, D.A. (1990) Kinetics of quartz dissolution in electrolyte solutions using a hydrothermal mixed flow reactor. *Geochim. Cosmochim. Acta* **54**, 955-969.

FOURNIER, R.O. and ROWE, J.J. (1966) Estimation of underground temperature from the silica content of water from hot springs and wet-steam wells. *Amer. J. Sci.* **264**, 685-697.

FOURNIER, R.O. and POTTER, R.W. II (1982) An equation correlating the solubility of quartz in water from 25° to 900°C at pressures up to 10,000 bars. *Geochim. Cosmochim. Acta* **46**, 1969-1973.

GALLAGHER, J.S. and HAAR, L. (1985) Steam tables -- NBS standard reference database 10. *U.S. National Institute of Standards and Technology, Thermophysics Division*, Gaithersburg, MD.

GRIGSBY, C.O. (1989) Kinetics of rock-water reactions. *Ph.D. Thesis, Chemical Engineering Department, Massachusetts Institute of Technology*, Cambridge, MA.

GRIGSBY, C.O., TESTER, J.W., TRUJILLO, P.E. and COUNCE, D.A. (1989) Rock-water interactions in the Fenton Hill, New Mexico hot dry rock geothermal system. 1. Fluid mixing and chemical geothermometry. *Geothermics* **18** (5/6), 629-656.

GRIGSBY, C.O., and TESTER, J.W. (1989) Rock-water interactions in the Fenton Hill, New Mexico hot dry rock geothermal system. 2. Modeling geothermal behavior. *Geothermics* **18** (5/6), 657-676.

HEMLEY, J.J., MONTOYA, M., MARINENKO, J.W. and LUCE, R.W. (1980) Equilibria in the system Al_2O_3-SiO_2-H_2O and some general implications for alteration/mineralization processes. *Econ. Geol.* **75**, 210-228.

ILER, R.K. (1955) *The Colloid Chemistry of Silica and the Silicates.* Cornell University Press.

ILER, R.K. (1979) *The Chemistry of Silica..* John Wiley and Sons.

KENNEDY, G.C. (1950) A portion of the system silica-water. *Econ. Geol.* **45**, 629-653.

KITAHARA, S. (1960) The solubility equilibrium and the rate of solution of quartz in water at high temperatures and high pressures. *Rev. Phys. Chem. Japan* **30** (2), 122-130.

MOREY, G.W. and HESSELGESSER, J.M. (1951) The solubility of quartz and some other substances in superheated steam at high pressures. *Amer. Soc. Mech. Eng. Trans.* **73**, 865-872.

O'CONNOR, T.L. and GREENBERG, S.A. (1958) The kinetics for the solution of silica in aqueous solutions. *J. Phys. Chem.* **62** (10), 1195-1198.

RICHARDS, H.G., SAVAGE, D. and ANDREWS, J.N. (1992) Granite-water reactions in an experimental hot dry rock geothermal reservoir, Resernanowes test site, Cornwall, U.K. *Applied Geochem.* **7**, 193-222.

RIMSTIDT, J.D. and BARNES, H.L. (1980) The kinetics of silica-water reactions. *Geochim. Cosmochim. Acta* **44**, 1683-1699.

ROBINSON, B.A. (1982) Quartz dissolution and silica deposition in hot dry rock geothermal systems. *M.S. Thesis, Chemical Engineering Department, Massachusetts Institute of Technology*, Cambridge, MA.

ROBINSON, B.A., TESTER, J.W. and BROWN, L.F. (1988) Reservoir sizing using inert and chemically reacting tracers. *SPE Formation Evaluation* **2**, 227-234.

SIEBERT, H., YOUDELIS, W.V., LEJA, J. and LILGE, E.O. (1963) The kinetics of the dissolution of crystalline quartz in water at high temperatures and high pressures. *Unit Processes in Hydrometallurgy, The Metallurgical Society of AIME Conference* **24**, 284-299.

SIEVER, R. (1962) Silica solubility 0°-200°C and the diagenesis of siliceous sediments. *J. Geol.* **70**, 127-150.

TESTER, J.W., HOLLEY, C.E. and BLATZ, L.A. (1977) Solution chemistry and scaling in hot dry rock geothermal systems. *83rd National Meeting of the American Institute of Chemical Engineers*, Houston.

VAN LIER, J.A., DE BRUYN, P.L. and OVERBEEK, J.Th.G. (1960) The solubility of quartz. *J. Phys. Chem.* **64**, 1675-1682.

WEILL, D.F. and FYFE, W.S. (1964) The solubility of quartz in H_2O in the range 1000-4000 bars and 400-550°C. *Geochim. Cosmochim Acta* **28**, 1243-1255.

WHITE, A.F. and PETERSON, M.L. (1990) The role of reactive-surface-area characterization in geochemical kinetic models. In *Chemical Modeling of Aqueous Systems II (Chapter 35)*, (eds. D.C. Melchior and R.L. Bassett) *ACS Symposium Series 416*, Washington, D.C., 461-475.

WHITE, A.F. and PETERSON, M.L. (1990) The role of reactive surface areas in chemical weathering. *2nd Inter. Symp. Geochemistry of Earth's Surfaces and of Mineral Formation, July 2-8, 1990, Aixen Provences, France*, 334-336.

PROCEEDINGS, Eighteenth Workshop on Geothermal Reservoir Engineering
Stanford University, Stanford, California, January 26-28, 1993
SGP-TR-145

CORRELATION BETWEEN GAS COMPOSITIONS AND PHYSICAL PHENOMENA AFFECTING THE RESERVOIR FLUID IN PALINPINON GEOTHERMAL FIELD (PHILIPPINES).

D'Amore F., Nuti S.*, Ruaya J.R.°, Ramos-Candelaria M.N.°, and Seastres J.S.°*

*CNR, International Institute for Geothermal Researches, Pisa, Italy
°PNOC- Energy Development Corp., Fort Bonifacio, Makati, Philippines

ABSTRACT

Using thermodynamic gas equilibria to calculate temperature and steam fraction in the reservoir, three main physical phenomena due to exploitation of Palinpinon field are identified. 1) Pressure drawdown producing a local increase in the computed steam fraction, with the fluid maintaining high temperature values (close to 300°C). Strong decline in flow rate is observed. 2) Irreversible steam losses from the original high temperature liquid phase during its ascent through fractures in upper zones of the reservoir. Steam is generally lost at temperatures (e.g. 240°C) lower then those of the original aquifer. 3) Dilution and cooling effects due to reinjection fluid returns. These are function of the local geostructural conditions linking through fractures the injectors and production wells. The computed fraction of the recovered reinjected brine can in some case exceed 80% of the total produced fluid. At the same time the computed gas equilibration temperatures can decline from 280-300°C to as low as 215-220°C. Comparing these values with the well bottom measured temperatures, the proposed methodology based on gas chemistry gives more reliable temperature estimate than water chemistry based geothermometers for fluids with high fractions of injected brine.

INTRODUCTION

The Southern Negros geothermal field lies at the southern tip of Negros Island in an andesitic system characterized mostly by a vertically fractured medium (Ruaya et al., 1991). The under study Puhagan zone of the field has been providing steam for the 112.5 MWe Palinpinon I geothermal power plant since June 1983 from its 22 production wells (Fig.1). Ten reinjection wells are located in the identified major outflow region north and northeast of the production area. They accept the separated brine, having a salinity up to about 11,000 mg/kg in chloride content, by gravity flow through two reinjection lines. Injection at high pressure (about 0.8 MPa) started immediately after production. Harper and Jordan (1985) assessed the geochemical changes observed in response to early production and reinjection. The reinjection strategy adopted has been described by Ruaya and Salera (1990).

The hydrothermal system in Palinpinon is a single-phase neutral alkali-Cl hot water with less than 2% by weight in gas content, and an average reservoir Cl concentration, before any injection contribution, of about 4,200 mg/kg at a saturated water temperature of up to 330°C. Typical production temperatures, however, are about 280-300°C at near saturation conditions. For most Puhagan wells, different zones of the reservoir contribute to total production, such as a deep zone at high pressure and temperature close to 300°C, in most cases gas depleted, and a shallow, relatively gas rich, two-phase zone at much lower pressure and a temperature close to 240°C (Ruaya et al., 1991).

From 1983 to October 1989, wastewater injection was confined at the Puhagan sector. During this period rapid fluid communication between the injectors and the production wells was observed, using primarily chloride (Harper and Jordan, 1985). At the end of 1989, the bulk of reinjection was transferred farther away, northeast from the production area, to the Ticala/Malaunay sector to reduce the return of reinjection fluids. With the reduced mass injection at Puhagan the field reinjection fluid returns substantially declined in the production sector down to a maximum of 30-50%.

Table 1 reports gas compositions in total discharges and some physical parameters for selected wells of the field in Puhagan zone. It is evident a quite high variability in fluid production pressures and enthalpies together with an extremely high change in total gas content, H_2/CO_2 and H_2/H_2S ratios.

D'Amore and Truesdell (1985) and D'Amore (1991) proposed a general suitable graphical method in which measurable chemical parameters are represented as coordinates, while physical parameters, such as temperature and steam fraction generate a theoretical "grid" inside the diagram. It involves the use of chemical species ratios derived from chemical reactions. In this paper two chemical reactions are used to represent gaseous species in chemical equilibria. Essentially the method is based on the application of the mass action law on the two following chemical reactions at thermodynamic equilibrium conditions:

$$CO_2 + 4H_2 = 2H_2O + CH_4 \quad (1)$$

$$H_2 + 3/2\ FeS_2 + 2\ H_2O = 3\ H_2S + 1/2\ Fe_3O_4 \quad (2)$$

This paper attempts to model, using gas compositions, the changes due to exploitation covering several years until 1991 affecting production wells at Puhagan sector. The described geochemical models are highly simplified, due to the very little information

available on the kinetics of the single chemical reactions involved. However H_2S species seems to be fastly reequilibrating with respect to H_2 probably because of the high content of sulphydes in the reservoir rock, allowing buffering of H_2S partial pressure. Morerover we try to demonstrate that through the application of gas chemistry it is possible to correlate easily measurable wellhead chemical parameters with physical reservoir parameters, such as temperature and steam fraction useful in evaluating some geothermal well performance. All original chemical data are from D'Amore et al., 1993.

The water stored in this geothermal reservoir is mostly present as a liquid together with a little amount of coexisting vapor phase at equilibrium conditions. In some cases, the vapor formed at equilibrium becomes irreversibly lost during ascent of the fluid to the surface, before the discharge fluid reaches the wellhead. The in-place steam fraction y of the local reservoir, in equilibrium with the liquid (positive y values) or irreversibly lost at a given temperature from the original liquid (negative y values), at phase equilibrium is defined as:

$$y = n_V/(n_V+n_l) \qquad (3)$$

where n represents the number of moles of steam (n_V) or liquid water (n_l), contained in a given volume of rock. Y value can represent an average value of the steam mass fraction, locally present or lost, over the drainage volume of the well.

Through chemical equations (1) and (2) it is possible to develop the FT-HSH grid diagram having as coordinates the following chemical parameters measured at the total discharge point "d":

$$FT_d = 4\ \log(H_2/H_2O) - \log(CH_4/CO_2) \qquad (4)$$

$$HSH_d = 3\ \log(H_2S/H_2O) - \log\ (H_2/H_20) \qquad (5)$$

The following equations are used for positive or negative y values to link the chemical with the physical parameters in the reservoir:

y > 0:

$$FT_d = -15.35\text{-}3952.8/T°+4.635\ \log\ T° + 4\ \log\ (y°+(1\text{-}y°)/B°_H + \log\ (y° + (1\text{-}y°)/B°_{CO2}) - \log\ (y° + (1\text{-}y°)/B°_{CH4}) \qquad (6)$$

$$HSH_d = 6.449\text{-}6149.7/T°\text{-}0.412\ \log\ T° + 3\ \log\ (y°+(1\text{-}y°)/B°_{H2S}) - \log\ (y°+(1\text{-}y°)/B°_{H2}) \qquad (7)$$

y < 0:

$$FT_d = -15.35\text{-}3952.8/T°+4.635\ \log\ T° - 4\ \log\ B°_{H2} - \log\ B°_{CO2} + \log\ B°_{CH4} - 4\ \log\ (1+y\text{-}y\ B_{H2}) - \log\ (1+y\text{-}y\ B_{CO2}) + \log\ (1+y\text{-}y\ B_{CH4}) \qquad (8)$$

$$HSH_d = 6.449\text{-}6149.7/T°\text{-}0.412\ \log\ T° - 3\ \log\ B°_{H2S}\ \log\ B°_{H2} - 3\ \log\ (1+y\ \text{-}y\ B_{H2S}) + \log\ (1+y\text{-}y\ B_{H2}) \qquad (9)$$

In equations (8) and (9), $B_i°$ refers to the original temperature T° of the aquifer, while B_i refers to the temperature of the steam loss.

FT and HSH values from gas data of Table 1 are plotted in Fig.2. Both computed temperatures and steam fractions from these data are quite variable and do not provide much information in characterizing the behavior of each well. This is the main reason why selected wells of the field presenting typical behaviors through several measured data have been chosen to correlate their physical performance with time as function of gas compositions.

In some case, like for well OK-5, gas compositions measured during several years produce a cluster of points in the grid diagram with equilibration temperatures in the range 300-310°C from an almost pure liquid phase (y=0). In these cases the clustering of data indicates that the well draws fluid from deep undisturbed zones of the reservoir, which until the present remains unaffected by exploitation of the field. This is usually observed for wells located in the western zone of Puhagan area, on the border of the still unexploited Sogongon zone of the field, developed to produce about 80 MWe.

In most cases, observed chemical variations from ideal equilibrium behavior in pure liquid, brought about by exploitation of the Puhagan field have been attributed to different physical phenomena. The wells selected in this paper are representative of groups showing similar peculiar time variations both in chemical and physical characteristics.

STEAM ADDITION TO AN ORIGINAL LIQUID DUE TO PRESSURE DRAWDOWN.

During exploitation, several wells show increases in gas content and discharge enthalpies (exceeding 2,000 kj/kg). These wells are found south of Puhagan sector (such as PN20D, 27D, 9D, 13D and 10D). Well PN20D, which is located within the hottest part of the field close to the Lagunao Dome, has been selected as the most representative of this group. The well became a producer in October 1986. The computed FT and HSH values are represented in Fig.3. At starting conditions the gas composition suggests little steam loss in the deep reservoir fluid (y=-0.007) at low flow rate. With time there is a significant increase in steam fraction, up to about 2% in 1991. The computed temperatures in the diagram are quite high, between 287 and 306°C. The lowest temperatures are observed along the y =0 line in the period 1988-89 when the amount of injected brine in Puhagan sector was very high. For this well in that period the fraction of recovered injected water was close to 30% (D'Amore et al., 1993). At the end of 1989 wastewater injection was shifted to Ticala/Malaunay sector and fluid injection was substantially reduced in Puhagan area.

A possible explanation for the observed gas composition can be due to two contemporaneous phenomena.

The first phenomenon affecting fluid composition seems to be due to moderate amount of recovered injected water in this area. Because of the localized high heat flow in this zone, injection produces cooling of only about 15°C

in contrast to the central Puhagan wells showing cooling up to 90°C.

The second one could be the drawdown of the liquid water in the reservoir. During the first months of 1991 compared to early 1990, at the same wellhead pressure of 0.7 MPa, enthalpy increases from about 1800 to about 2,400 kj/kg and the monthly cumulative mass withdrawal declines from about 90,000 tons to less than 20,000 tons. The drawdown hypothesis seem to be supported by the shut-in pressures measured in the monitoring well PN25D. From 1990 to 1991 shut-in pressure declined from about 9 to 6 MPa (Fig. 4). Initially, the well PN20D was producing from two main permeable zones located at vertical depths of 1730-1937 and 1215-1391 m. With time, anhydrite deposits have been detected between these two production zones. Anhydrite deposition is believed to have partly blocked fluid contribution from the deeper permeable zone having y values close to zero. The effect of this phenomenon is a decline in production due to decrease in liquid volume available in the local reservoir because of a decrease of permeability. This local depressuration induced also the inflow of acidic fluids (Gerardo et al., 1993) which probably enhanced the anhydrite deposits. In Palinpinon acidic fluid can be present in upper shallow layers were the lost steam condensates and mixes with local meteoric water. This can form shallow, cold and oxidizing waters with low pH, high content of sulfate as well as low content of H_2 and chloride. These waters were detected during shallow drillings. In 1992, when the contribution of this fluids becomes significant, due to pressure drawdown, the total discharge composition results in lower pH (4-5), lower chloride (< 1.000 mg/kg) and high sulfate (> 200 mg/kg) contents in the liquid fraction. The gas composition is showing lower values in H_2 and higher H_2S content probably because of partial reduction of sulfate.

STEAM LOSSES AT LOWER TEMPERATURES FROM AN ORIGINAL LIQUID

In the Southern sector of Puhagan, several wells (e.g. PN23D, 27D, 30D, 31D) present generally negative values of computed y using FT and HSH chemical parameters under high wellhead pressure condition, and also for a period of time after shut-in (that is when the well is set on-line for production). Well PN30D has been selected as representative of this group.

Its maximum temperature monitored at well bottom is 305°C. Its relatively constant concentration in chloride (in average 4,100 + 400 mg/kg) and enthalpy (1400-1600 kj/kg) exclude any large influence from reinjection fluids. The relative positions of y and temperature on the grid diagram are shown for selected analyses in Fig.5. The scattering in the position of the points show a quite high variability in y values, from about zero to -0.1, with relatively constant values of the computed temperatures between 285 to 300°C. The pre-exploitation fluid temperatures at the main entries were about 250°C at 1340-1440 m and about 300°C at 2770-2865 m (vertical depths). Y values are very negative in the diagram when H_2 concentrations are very low. H_2S content varies correspondingly but to a degree where computed temperature remains almost stable indicating preservation of chemical equilibrium.

A good correlation is observed between H_2 concentration and the cumulative monthly mass withdrawal with time (Fig.6). This indicates that at high wellhead pressure the local deep reservoir liquid looses large amounts of gas boiling during its ascent through fractures. It must be considered that the close by wells are producing generally at low wellhead pressure. Fluid displacement and boiling is then induced by pressure differential at high temperature in the reservoir. Some steam is irreversibly lost at lower temperature from the original fluid moving through fractures towards other wells on line for production, and it can accumulate as a condensate layer in shallow zones with respect to the main reservoir. This process is schematically outlined in Fig.7. Steam separation produces at a given temperature partitioning of gases in the newly formed steam as a function of different gas solubilities. This can explain the observed variability in H_2/H_2S or H_2S/CO_2 ratios. At high production, after some time, gas composition recovers to initial undisturbed conditions attaining the original thermodynamic equilibrium. However, the reequilibration is not completed at a similar rate. H_2S rapidly recovers its original concentration, due probably to the buffering effect of sulphydes minerals, while H_2 takes longer time to recover from water dissociation reaction. In this process ammonia content is almost unaffected by steam losses because of its extremely high solubility relative to other gases: for example at 250°C the ratio of distribution coefficients between H_2 and NH_3 is about 110.

The original undisturbed fluid conditions for well PN30D before any steam loss can be estimated by the use of the data considered during the periods corresponding to the maximum contents of H_2 at high flowrate (September-December 1985, October-December 1986, and June-October 1990). The application of the FT-HSH grid to these data results in a value of y=0 at a computed temperature of 290°C. Fixing then this temperature for the original liquid before steam losses, by the use of equations 8 and 9, it is possible to calculate for any gas composition showing negative y values on the grid, the temperature at which the steam is lost and the corresponding lost steam fraction in non isothermal conditions. Infact the observed extremely high negative y values in the grid are considered to be apparent as computed by the use of the FT and HSH parameters represented in the grid at isothermal conditions. In these cases a more realistic alternative is that steam loss occurs at a much lower temperature than the original reservoir liquid temperature. As an example, the gas composition of April 1987 can be considered. On the grid the corresponding point is consistent with a temperature of 300°C and y=-0.1. Using the non isothermal method, and fixing an original temperature of 290°C in a pure liquid phase, a steam loss temperature of 240°C is computed corresponding with a value of y=-0.025.

WELLS AFFECTED BY REINJECTED BRINE

Most wells (e.g. PN26, PN28, OK7) located in the northeast portion of the field are strongly affected by the separated brine reinjected in Puhagan and then later in the Ticala/Malaunay sector. Gas chemistry may prove useful in monitoring reinjection returns and in providing realistic reservoir temperature estimates .

This section aims to quantify the fraction of produced fluid due to reinjected water (X) and the equilibration temperature in the reservoir (T°) by using gas composition at wellhead.

As a typical example, the method is applied to well PN28. The grid diagram representing the available data is shown in Fig.8. The point representing initial condition (°) is based on the analytical data of the adjacent well PN26 (July 1983) since gas data for PN28 at undisturbed condition are not available. Despite that, an initial temperature close to 280°C for an almost pure liquid phase can be estimated, which is consistent with the temperature evaluated from the SiO_2 content. Based on computed y values, it is evident that this well is little affected by steam losses ($y > -0.01$). The temperatures computed from the grid (Tg) show that the mixing with the injected brine produces a progressive cooling down to 215°C, consistent with well bottom physical measurements (from point 1 to point 14 in Fig.8) in October 1989, when fluid injection was confined at Phuagan sector. This trend (Fig.9) is consistent with the progressive increase in chloride concentration (from less then 5,000 to more then 10,000 mg/kg) and discharge enthalpy decline with time (down to about 1,000 kj/kg). When the bulk of the injected fluid was shifted to the Ticala sector, at northeast, a recovery in grid temperature, Tg, up to about 255°C, and a decline in chloride concentration are observed.

The proposed method consists of a convergence routine to calculate T° when a fraction X of injected brine is contributing to the total produced fluid generating the measured concentrations $C_{H2,d}$ and $C_{H2S,d}$. The equations used (D'Amore et al., 1993) are reported in Table 2. The value of T° is obtained when $X_{FT} = X_{HSH}$. From selected gas analyses of this well computed values of T° and X vs time are reported with computed Tg values and chloride concentrations in Fig.9. The observed trends of all these parameters are consistent among them. The computed T° has a different value than Tg. The T° value represents the theoretical temperature in the fractured medium where the fluid is in contact with the rock; that is the temperature in the producing cell of the reservoir where after mixing the fluid and the rock are in thermodynamical equilibrium. This thermal condition is a function of the balance between the heat lost because of the local inflow of the injected brine and the heat supplied by the local and surroundings rocks in that particular portion of the reservoir where thermodynamical equilibrium is supposed to be attained. The Tg value approaches the actual measurable well bottom temperature after dilution and cooling of the fluid at the moment of sampling. This fluid might not be fully chemically equilibrated because of the high local permeability and the fast recovery of the injected brine. We assume then that the local large fractures allows the transfer of the mixed fluid at well-head in a very short time. For this reason Tg < T°.

CONCLUSIONS

The Puhagan sector at Southern Negros geothermal field shows a large variability of gas composition both in space and time. This may be due to three main physical phenomena affecting the original fluid stored in the deep reservoir. (1) Local pressure drawdown in the original liquid phase present in the reservoir feeding a single well. This phenomenon produces a local increase in the steam fraction in phase equilibrium with the liquid maintaining high measured temperature values. Low local permeability is the main factor producing drawdown. Moreover, drawdown seems to induce inflow of acidic fluids from shallow layers into the main reservoir.(2) Steam loss from an original liquid at high temperature when the wellhead pressure is very high or after shut-in condition. The assumed phenomenon and the applied methodology shows that from a given volume of reservoir with high local permeability feeding a well, the original liquid at high pressure and temperature moves through fractures during low production period towards shallower levels. This movement is induced by pressure differential through fluid communication with adjacent producing wells. The original liquid during rise through local fractures boils at lower temperature irreversibly loosing steam in phase equilibrium. Each gas species partitions between liquid and steam at this new temperature as a function of its solubility. (3) Reinjection of the brine separated at high pressure. This reinjection fluid returns are a function of the local geostructural conditions linking through fractures the injectors and the producers. The production wells affected by this mixing show a well bottom temperature decline from 280-300°C to as low as 215-220°C. These last values are close to the measured temperatures when most of the produced fluid is due to the injected brine. Water-rock equilibration temperature in the reservoir can be computed as well as the contribution of the injected brine to the total produced fluid. The most common water geothermometers seem not applicable to wells highly affected by reinjection returns because of lack of reequilibration.

Using the model based on the grid diagram sketched in Fig.10, gas geochemistry offers interesting and low cost tools to evaluate phenomena occurring in the reservoir particularly usefull in field management.

REFERENCES

D'Amore F. (1991), "Gas geochemistry as a link between geothermal exploration and exploitation". In Application of Geochemistry in Geothermal Reservoir Development (ed. D'Amore F.), Chap. 4, pp.93-144. UNITAR, NewYork.

D'Amore F. and Truesdell A.H. (1985), "Calculation of geothermal reservoir temperatures and steam fractions from gas compositions". Geoth. Resources Council, Trans., V.9, 305-310.

D'Amore F., Nuti S., Ruaya J.R., Ramos-Candelaria M.N. and Seastres J.S. (1993), "Applications of gas chemistry in evaluating physical phenomena in Palinpinon geothermal field (Philippines)". Geothermics, in press.

Gerardo J.Y., Nuti S., D'Amore F., Seastres J.S. and Gonfiantini R. (1993), "Isotopes as a tool in understanding recharge and reservoir processes in the Southern Negros geothermal project (Philippines)". Geothermics, in press.

Harper R.T. and Jordan O.T. (1985), "Geochemical changes in response to production and reinjection for Palinpinon I geothermal field, Negros Oriental, Philippines". Proc. 7th New Zealand Geothermal Workshop, 39-44.

Ruaya J.R. and Salera J.R.M. (1990), "Reinjection strategy for Palinpinon geothermal field, Southern Negros, Philippines". Int. Conf. and Exibition on Energy Supply and Utilization, Jan. 23-26, 1990, Manila, Philippines.

Ruaya J.R., Solis R.P., Solana R.R. and Seastres J.S. (1991), "Simple interpretations of chemical transients in multifeed, two-phase geothermal wells". Geothermics, 20, 135-146.

TABLE 1. Gas composition in total discharge (moles/moles x 10^5), maximum temperature measured at well bottom, and WH pressure and enthalpy for selected wells of Palinpinon geothermal field.

n	Well	Date	(Max) (°C)	P (MPaa)	H (kJ/kg)	CO_2	H_2S	H_2	CH_4	N_2	NH_3
1	OK5	03SEP90	310	3.69	2025	245	14.61	1.42	0.16	1.21	0.65
2	OK10D	04SEP90	270	0.80	1552	153	7.52	0.99	1.99	3.11	1.09
3	PN20D	12MAR91	324	0.71	2393	451	17.31	2.51	0.76	0.84	2.16
4	PN30D	27JAN90	305	2.67	1544	197	7.77	0.31	0.77	0.99	0.83
5	PN31D	05SEP90	322	1.02	1875	263	10.45	0.77	1.31	0.93	1.90
6	PN24D	09MAR91	316	0.83	1585	244	8.73	0.66	1.19	1.35	0.91
7	OK7	19APR90	318	0.68	1350	92	3.73	0.54	0.96	0.43	1.09
8	PN28	02JAN90	303	1.44	1203	60	1.17	0.04	0.58	0.30	1.17
9	PN32D	08AUG91	270	0.88	2524	450	14.83	2.42	2.19	2.20	-

Table 2. Equations used for computation of the recovered fraction of injected water (X) and water-rock equilibration temperature T°.

$$X_{FT} = \left[1 + \frac{exp_{10} - ((FT° + \log (CH_4°/CO°_2))/4)}{1/C_{H2,d} - (exp_{10} ((FT° + \log (CH°_4/CO_2°))/4))} \right]^{-1}$$

$$X_{HSH} = \left[1 + \frac{exp_{10} - ((HSH°/3) + ((FT° + \log(CH_4°/CO°_2))/12))}{(1/C_{H2S,d}) - exp_{10} - ((HSH°/3) + ((FT° + \log(CH°_4/CO_2°))/12))} \right]^{-1}$$

X_{FT} and X_{HSH} are respectively computed starting from chemical reactions (1) and (2). C_{H2} and C_{H2S} are the measured molar concentrations of H_2 and H_2S.

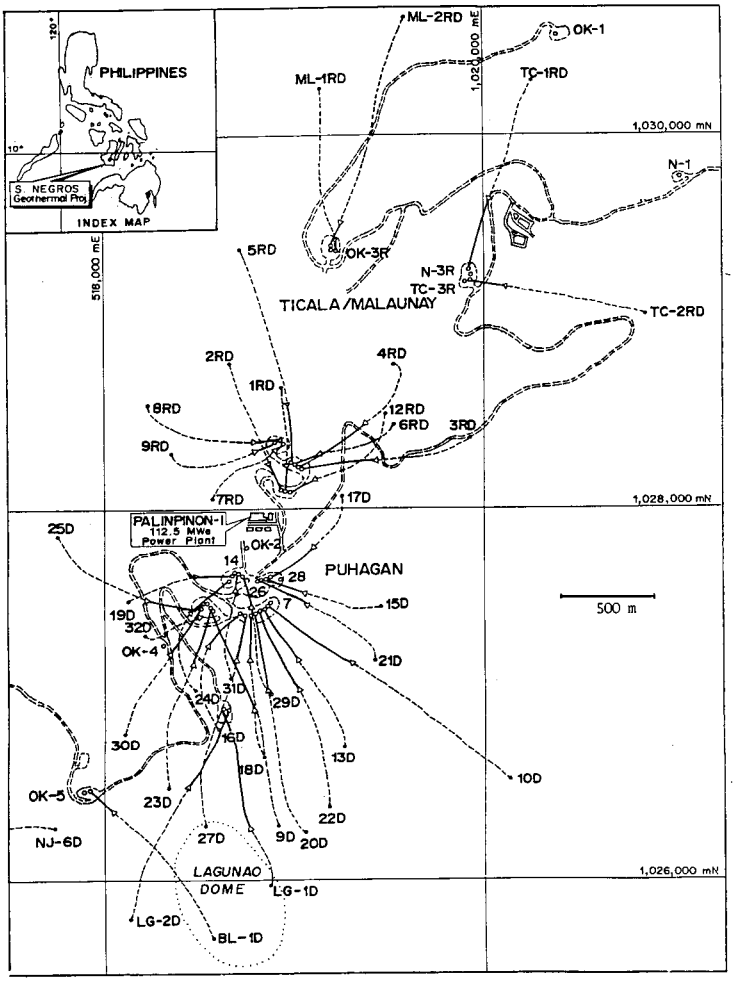

Fig.1. Palinpinon geothermal field in Negros Island (Philippines) and well locations in Puhagan and Ticala areas. Wells drilled directionally are marked with a "D". Reinjection wells are marked with a "R".

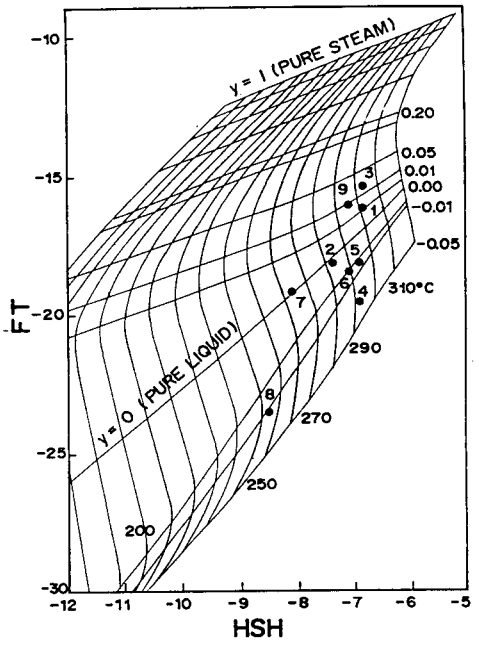

Fig.2. FT-HSH grid diagram from gas composition of wells shown in Tab. 1.

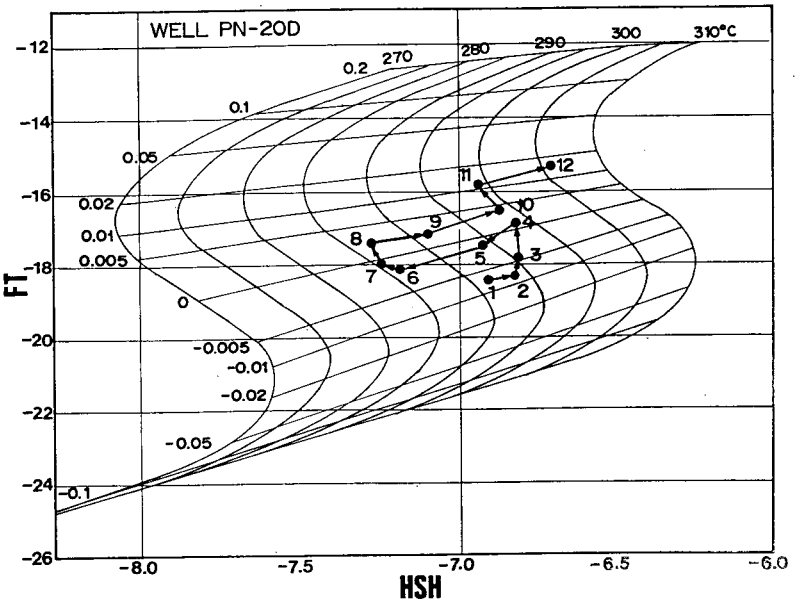

Fig.3. Grid diagram for well PN20D from gas compositions (1986-1992).

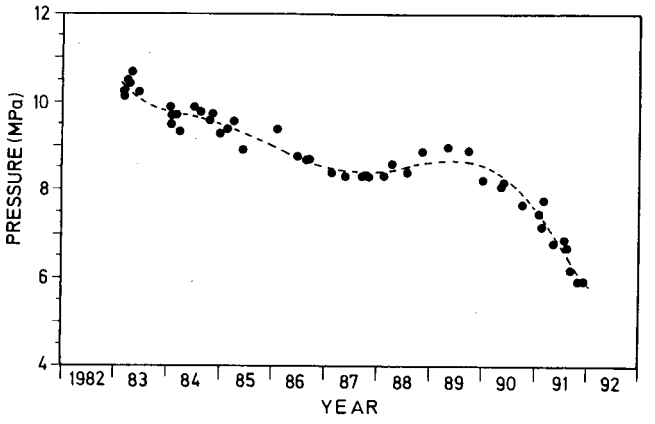

Fig.4. Shut-in pressure values vs time for the monitoring well PN25D.

Fig.5. Grid diagram for well PN30D from gas compositions (1985-1991).

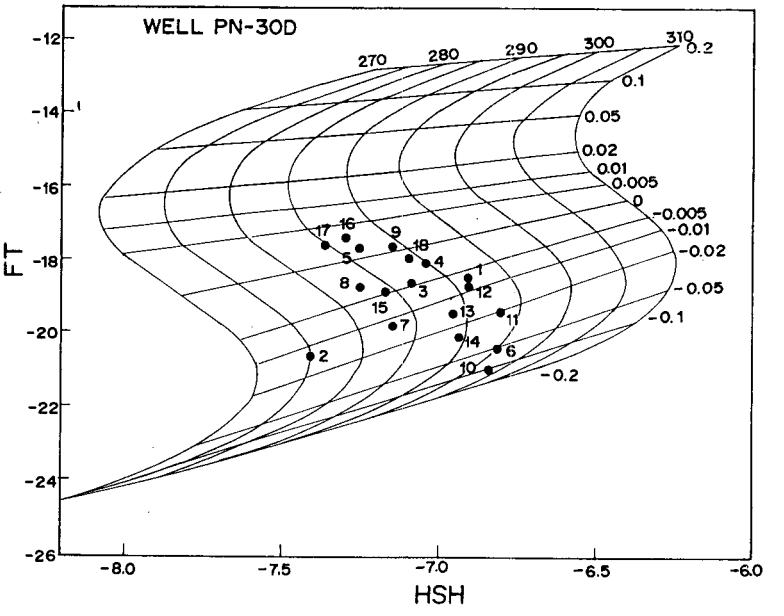

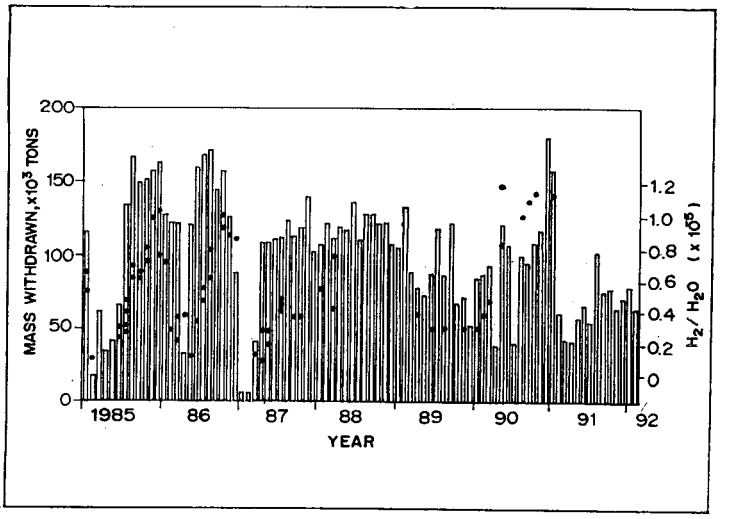

Fig.6. Monthly cumulative mass withdrawal and H_2/H_2O (molar concentration x 10^5) for well PN30D.

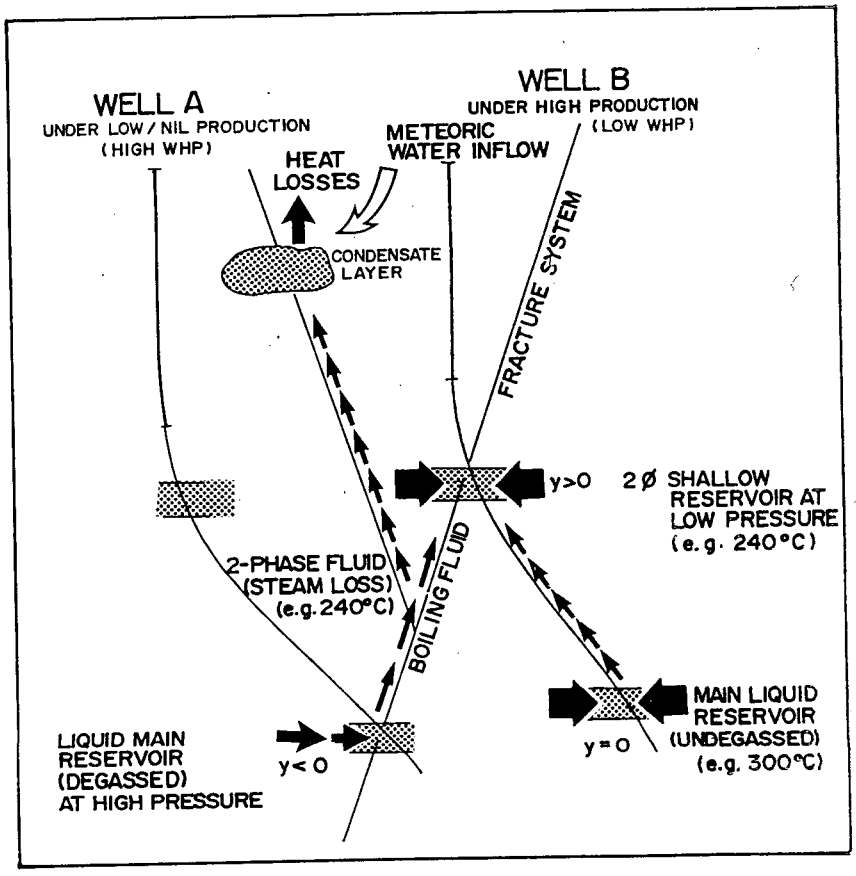

Fig.7. Sketch model for steam losses from well A (at high wellhead pressure) induced by pressure differential in the reservoir with respect to well B producing under low wellhead pressure.

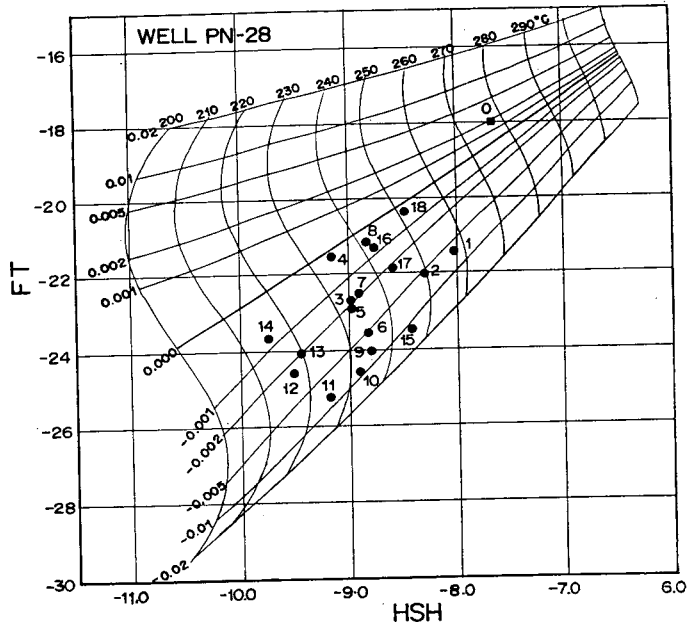

Fig.8. Grid diagram for well PN28 from gas compositions (1983-1991).

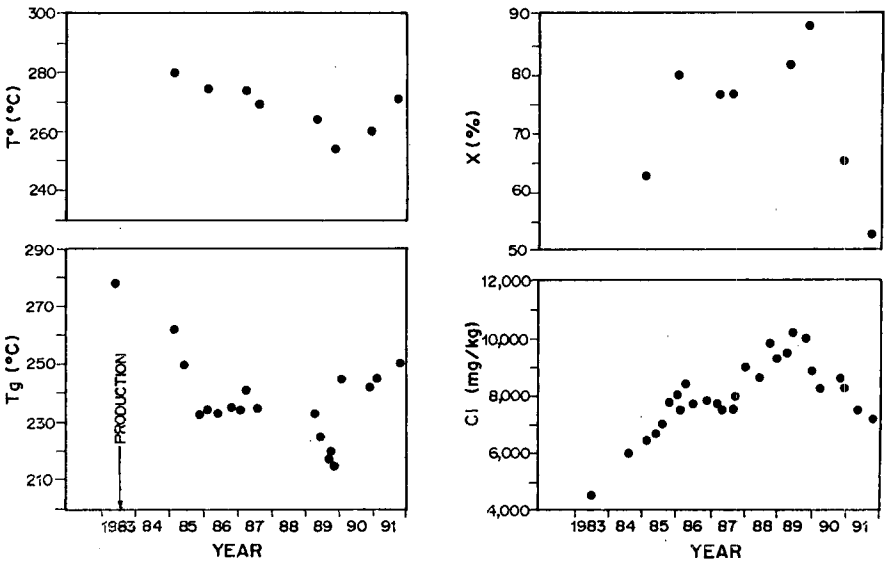

Fig.9. For selected samples following parameters are reported vs time for well PN28: chloride concentration in total discharge, Tg values computed from the grid (Fig.8), computed values of fluid-rock equilibration temperature T° and the corresponding percentage of recovered brine (X%).

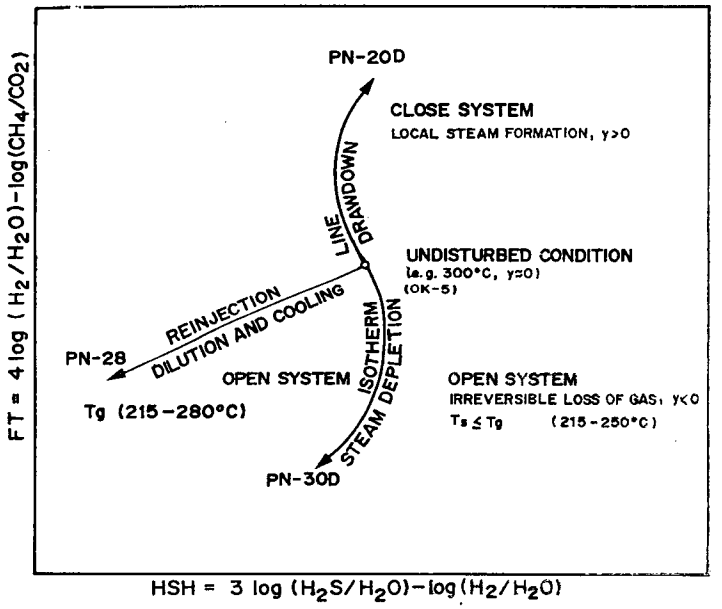

Fig.10. Sketch showing the main phenomena affecting the position of the points in the FT-HSH grid diagram, derived from gas composition. For y < 0,Ts indicates the steam losses temperature from the original liquid.

PROCEEDINGS, Eighteenth Workshop on Geothermal Reservoir Engineering
Stanford University, Stanford, California, January 26-28, 1993
SGP-TR-145

AN EVALUATION OF THE DEEP RESERVOIR CONDITIONS OF THE BACON-MANITO GEOTHERMAL FIELD, PHILIPPINES USING WELL GAS CHEMISTRY

by Franco D'Amore* , Marinela Maniquis-Buenviaje Φ
and Ramonito P. Solis Φ

* CNR-IIRG, 2 Piazza Solferino, 56126 Pisa, Italy
Φ PNOC-EDC, Ft. Bonifacio, Metro Manila, Philippines

ABSTRACT

Gas chemistry from 28 wells complement water chemistry and physical data in developing a reservoir model for the Bacon-Manito geothermal project (BMGP), Philippines. Reservoir temperature, T_{HSH}, and steam fraction, y, are calculated or extrapolated from the grid defined by the Fischer-Tropsch (FT) and H_2-H_2S (HSH) gas equilibria reactions. A correction is made for H_2 that is lost due to preferential partitioning into the vapor phase and the reequilibration of H_2S after steam loss.

INTRODUCTION

The Bacon-Manito geothermal project (BMGP) is located 20 kms southeast of Legazpi City, in the northern Philippine island of Luzon (Fig. 1). Initial geoscientific surveys were conducted in 1977 and exploratory drilling followed in 1978. At present, over 30 wells have been drilled. The 110-MWe BacMan I and 2 x 20 MWe BacMan II geothermal power plants are presently being built and are scheduled for commissioning in 1993.

Fault structures is the major cause of permeability at BMGP (PNOC-EDC, 1988). Based on subsurface geology, permeability is mostly due to the intersection of faults mapped on the surface and faults accompanied by dike intrusions.

The main components of the lithologic unit in BMGP are the Gayong Sedimentary Formation (GSF), Pocdol Volcanics (PV), and Cawayan Intrusive Complex (CIC). The GSF is composed primarily of calcareous sedimentary breccias. The lower PV is composed of hyaloclastites, andesites and basalts; while the upper PV is composed of fresh hornblende-bearing andesite, intensely to completely altered volcanic rock

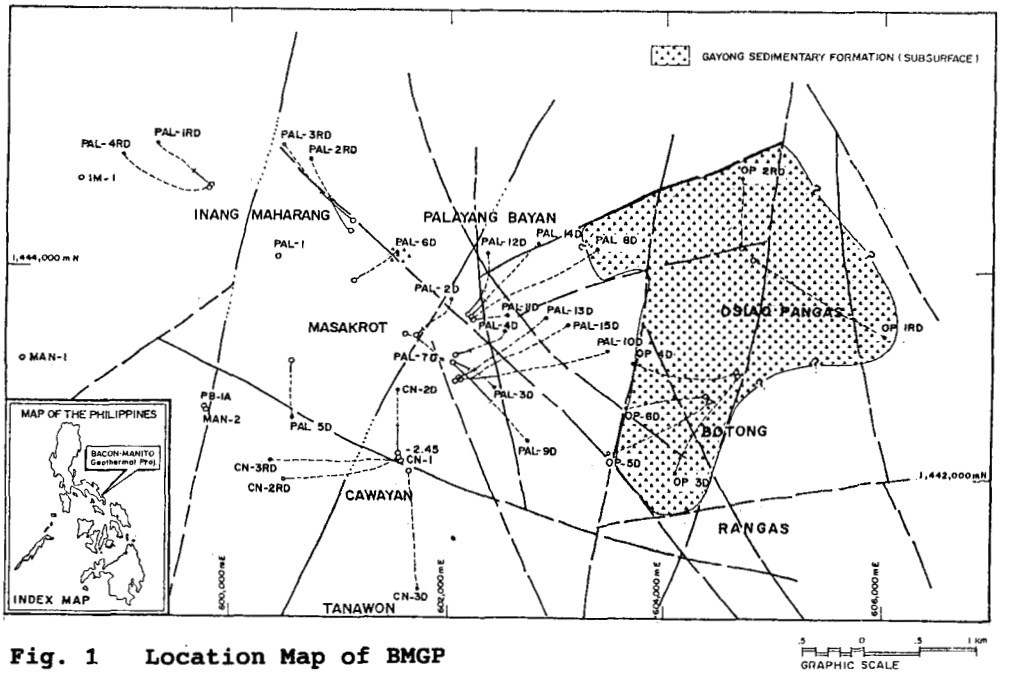

Fig. 1 Location Map of BMGP

intercalated with andesitic breccias, lavas and tuffs. The CIC include all basalt/diabase, microdiorite and plutonic dikes that intrude the GSF and PV.

BACMAN RESERVOIR CHEMISTRY

Except for three wells, Pal-2D, CN-2D and CN-2RD, all of the wells in BMGP discharge near neutral NaCl waters. Several wells, located in Cawayan and Palayang Bayan sectors, encounter cool meteoric or acidic SO_4-rich condensate type fluids at shallower depths.

Geochemical field trends, represented here by reservoir chloride field trend, suggest that the whole BMGP area belong to one geothermal system (Fig. 2). The center of the resource is inferred to be close to wells OP-3D, OP-4D, Pal-8D, Pal-10D and Pal-14D. The deep reservoir chloride of about 6500 mg/kg is almost uniform across the central Palayang Bayan area. The upflowing fluid has a reservoir chloride close to 8000 mg/kg.

The baseline or pre-exploitation steam chemistry of BMGP wells are presented in Table 1. These data are taken when the well is producing from the major feedzone at stabilized conditions during discharge testing. CO_2 comprises 95-98% by volume of the non-condensible gas in the steam phase. The rest is composed of N_2, CH_4, Ar, NH_3 and H_2.

Wells in Palayang Bayan and Cawayan with high gas concentrations produce predominantly from a shallow level, leading early workers to infer the presence of a shallow gassy, two-phase region or a gas cap (PNOC-EDC, 1988; KRTA, 1986).

DATA PROCESSING

Theoretical Background

The following expressions can be used together to calculate the reservoir temperature, T_{HSH} and steam fraction, y:

$$4\log(H_2/H_2O)_d - \log(CH_4/CO_2)_d = FT_d \qquad \text{Eq. (1)}$$

$$3\log(H_2S/H_2O)_d - \log(H_2/H_2O)_d = HSH_d \qquad \text{Eq. (2)}$$

where $(i/H_2O)_d$ is the molar ratio at the disharge point "d".

When $y \geq 0$, the graphical solution is used. The method used by D'Amore and Truesdell (1985) implies isothermal conditions during steam loss. The reservoir temperature for these wells are equal to the temperature at which the fluid boils upon ascent.

In some cases extremely negative values of y are extrapolated and steam loss is not consistent with the local conditions of the reservoir liquid as seen in Southern Negros geothermal project, Philippines (D'Amore et al, in preparation), so that:

$$FT_d = -15.35 - 3952.8/T^\circ + 4.635\log T^\circ - 4\log B^\circ_{H_2} - \log B^\circ_{CO_2} + \log B^\circ_{CH_4} - 4\log(1+y-yB_{H_2}) - \log(1+y-yB_{CO_2}) + \log(1+y-yB_{CH_4}) \qquad \text{Eq. (3)}$$

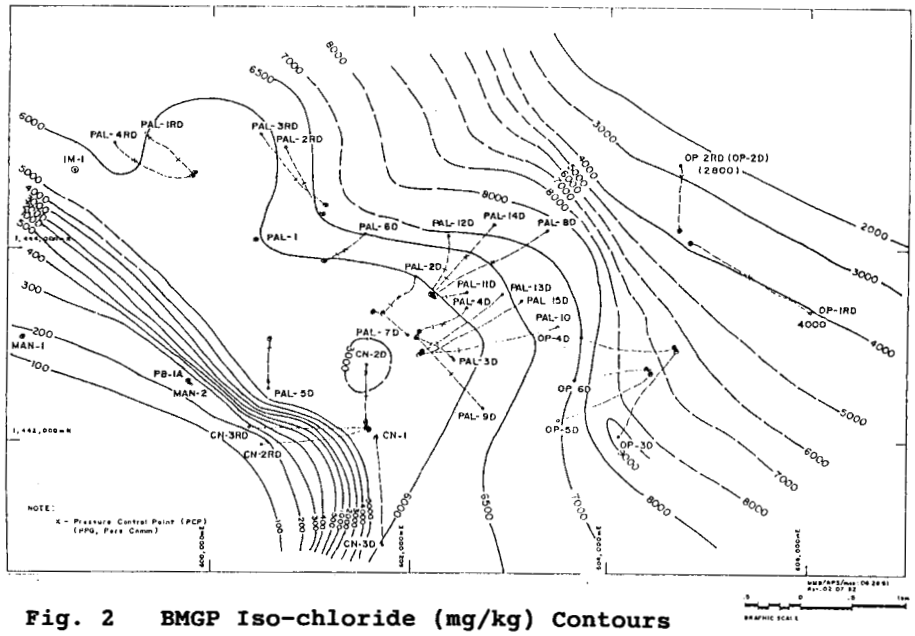

Fig. 2 BMGP Iso-chloride (mg/kg) Contours

TABLE 1: BACON-MANITO BASELINE WELL STEAM CHEMISTRY

WELL	DATE	WHP	H	SP	pH	CO2	H2S	N2	H2	CH4
	mm-dd-yy	MPaa	kJ/kg	MPaa		mmoles/100 moles H2O			at TD	
PAL-1	01-01-83	1.18	1077	0.640	6.87	146	0.90	1.513	0.052	1.660
PAL-2D	03-12-84	2.75	1281	0.611	5.33	1471	13.80	13.27	0.721	10.765
PAL-3D	05-20-83	2.51	1255	0.570	6.38	169	5.55	0.224	0.017	0.163
PAL-4D	12-20-83	3.35	1308	0.349	7.51	321	6.98	0.236	0.108	4.260
PAL-5D	07-12-84	1.82	1230	0.542	7.49	34	0.99	1.070	0.019	0.400
PAL-6D	06-07-84	0.31	1547	0.225	7.01	398	3.29	1.760	0.242	3.047
PAL-7D	08-07-84	1.58	1162	0.832	6.38	218	1.99	1.264	0.086	3.234
PAL-8D	04-12-84	4.44	1479	0.619	7.16	772	9.60	0.374	0.095	1.452
PAL-9D	11-26-86	2.39	1158	0.429	7.68	105	3.98	0.310	0.050	0.800
PAL-10D	12-19-85	1.62	1407	0.904	6.66	620	13.70	0.461	0.863	7.387
PAL-11D	10-31-87	1.09	1526	0.814	6.90	870	11.30	2.090	0.390	11.550
PAL-12D	05-06-88	3.27	1353	0.839	7.03	327	5.76	0.953	0.054	2.914
PAL-13D	03-08-87	3.54	1277	0.910	6.84	264	7.00	0.390	0.203	1.213
PAL-13D	03-17-87	0.88	1345	0.625	6.83	339	7.58	2.530	0.765	5.170
PAL-14D	01-13-89	1.37	1334	0.551	7.15	255	4.39	1.200	0.035	1.703
PAL-15D	12-14-89	2.54	1218	0.504	6.50	196	6.30	0.682	0.044	0.403
PAL-1RD	09-28-84	1.33	1099	0.702	7.41	65	0.85	0.372	0.014	0.409
PAL-3RD	02-04-85	0.32	1280	0.262	7.49	260	1.90	1.490	0.091	6.060
OP-1RD	07-20-88	0.37	1256	0.130	7.95	1409	9.20	0.960	0.220	43.900
OP-2RD	08-18-88	0.48	848	0.391	8.06	613	1.76	0.110	0.025	5.048
OP-3D	01-22-90	1.53	1581	0.413	7.53	1286	31.10	2.060	6.780	35.900
OP-4D	07-16-91	5.65	1478	0.473	6.46	833	18.50	0.570	1.430	3.350
OP-5D	09-21-91	0.27	2457	0.227	6.49	1796	40.10	3.410	7.950	30.200
OP-6D	03-16-91	0.96	2526	0.606	7.74	3592	100.00	4.890	27.03	92.460
CN-1	11-19-82	2.37	1214	0.577	7.71	50	1.85	0.063	0.027	0.917
CN-2D	10-07-82	0.68	1331	0.649	3.79	4381	16.07	5.613	3.557	132.56
CN-3D	10-20-90	2.20	1297	0.825	7.25	70	3.30	0.710	0.090	0.980
CN-2RD	05-10-91	0.51	965	0.433	3.66	68	2.60	4.900	0.560	0.910
CN-3RD	09-13-91	0.35	922	0.333	8.57	80	0.45	7.600	0.218	0.864

$$HSH_d = 6.449 - 6149.7/T^\circ - 0.412\log T^\circ - 3\log B^\circ_{H_2S} + \log B^\circ_{H_2} - 3\log(1+y-yB_{H_2S}) + \log(1+y-yB_{H_2}) \qquad \text{Eq. (4)}$$

where T° = reservoir temperature
B° = gas distribution coefficient at T°
B = gas distibution coefficient at temperature of steam loss
y = reservoir steam fraction

Application

Initially, T_{HSH} and y for these wells were taken from the isotherms in the grid defined by the FT-HSH equilibria at $y \geq 0$. About half of the wells were found to have y values ranging from -0.5% to +5% (Fig. 3). The rest of the wells, however, have highly negative y values.

For the latter wells, HSH_d at $y = 0$ was used to calculate T_{HSH} using Eq. (4). This is taken to be the local tempera-

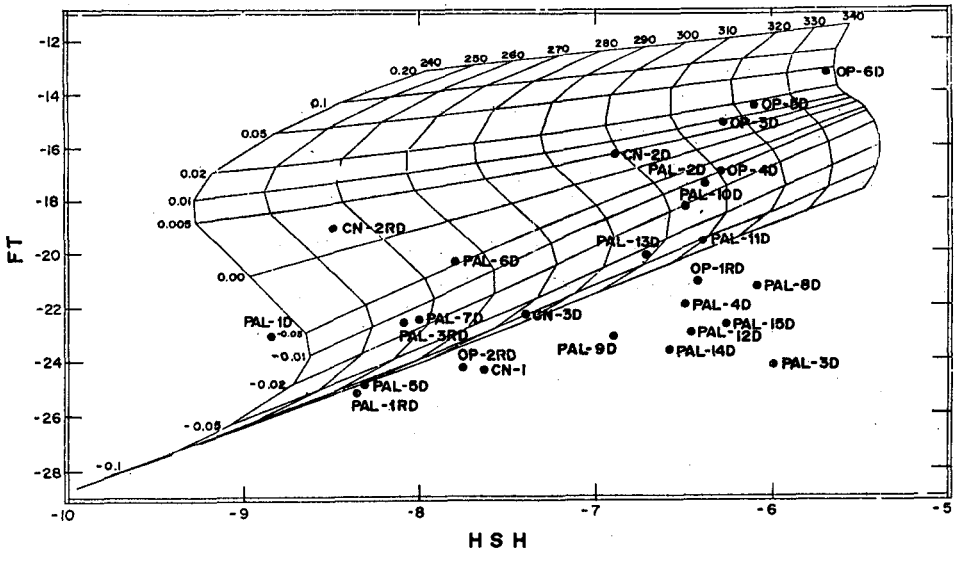

Fig. 3 FT-HSH Plot of BMGP Wells

ture of the aquifer after steam loss, hypothesizing reequilibration of H_2S. Assuming $T° = T_{HSH}$, y is calculated from Eq. (3) using an arbitrary degassing temperature of 240°C.

The use of 240°C as degassing temperature, however, can be justified using the two available analyses for well Pal-13D. At higher wellhead pressure (WHP), a decline in all components, especially in the less soluble H_2, CH_4 and N_2 is seen. In particular, H_2 decreases by about 75% while H_2S decline is small. The FT-HSH grid can be used for the Pal-13D gas data at low WHP. Extrapolation yields a temperature close to 285°C and y value close to zero. This temperature is very close to that measured at depth and also that using quartz geothermometer (Table 2). Assuming 290°C for the undisturbed system and using the first set of gas data at higher WHP in Eqs. (3) and (4), the degassing temperature and y are estimated. Convergency is obtained only at a degassing temperature of 240°C and y = -0.01.

Therefore, a degassing temperature of 240°C is assumed near the vicinity of Pal-13D. Much of the steam loss occurs close to a permeability barrier or shift from limestone sediments to more permeable volcanics, in between wells OP-4D/Pal-10D and Pal-15D, OP-5D and Pal-9D, Pal-8D and Pal-14D. As the hot geothermal fluids flows to the west, this value decreases to about 200°C. If 200°C degassing temperature is assumed, the computed y values will be less negative and probably close to zero.

TABLE 2 : BMGP RESERVOIR TEMPERATURE AND STEAM FRACTION

WELL	DATE mm-dd-yy	STM.FR. y	RESERVOIR TEMPERATURE ESTIMATES TSiO2	Tmax	Tmajor	THSH
PAL-1	01-01-83	-0.004	243	281	240	236
PAL-2D	03-12-84	-0.012	280	293	267	305
PAL-3D	05-20-83	-0.150	270	285	278	308
PAL-4D	12-20-83	-0.027	276	307	286	300
PAL-5D	07-12-84	-0.033	260	270	-	250
PAL-6D	06-07-84	-0.005	273	286	279	266
PAL-7D	08-07-84	-0.015	272	277	277	263
PAL-8D	04-12-84	-0.038	291	313	313	310
PAL-9D	11-26-86	-0.050	275	282	282	288
PAL-10D	12-19-85	-0.004	283	325	283	305
PAL-11D	10-31-87	-0.012	280	270	270	305
PAL-12D	05-06-88	-0.075	282	299	299	300
PAL-13D	03-08-87	-	288	316	283	295
PAL-14D	01-13-89	-0.100	299	301	265	297
PAL-15D	12-14-89	-0.080	285	285	267	306
PAL-1RD	09-28-84	-0.038	245	260	256	250
PAL-3RD	02-04-85	-0.010	235	271	225	260
OP-1RD	07-20-88	-	253	245	230	305
OP-2RD	08-18-88	-0.035	209	216	186	265
OP-3D	01-22-90	0.010	296	300	294	317
OP-4D	07-16-91	-0.001	317	>300	313	313
OP-5D	09-21-91	0.020	279	296	270	323
OP-6D	03-16-91	0.050	290	>300	276	338
CN-1	11-19-82	-0.052	266	271	266	268
CN-2D	10-07-82	0.005	241	246	-	299
CN-3D	10-20-90	-0.018	274	276	272	275
CN-2RD	05-10-91	0.002	247	245	234	256
CN-3RD	09-13-91	0.003	233	239	234	213

TSiO2 = silica temperature (Fournier and Potter, 1982)
Tmax = measured maximum downhole temperature
Tmajor = measured temperature at major production zone
THSH = reservoir temperature based on gas chemistry, assuming FT-HSH equilibria

DISCUSSION

Comparison with Other Reservoir Temperature Values

Fair correlation exists between T_{HSH}, T_{SiO2} (Fournier and Potter, 1982) and measured downhole temperatures (Fig. 4). Temperature differences up to 50°C may be due to the following reasons:

a) discharge enthalpy is greater than 1800 kj/kg and have steam-dominated discharge (OP-5D and OP-6D);

b) excess enthalpy (OP-3D, Pal-2D, Pal-10D, Pal-11D and Pal-15D);

c) the production zone is tapping a cooler reservoir fluid (CN-2RD and Pal-3RD); and

d) high CO_2 content depresses downhole temperatures

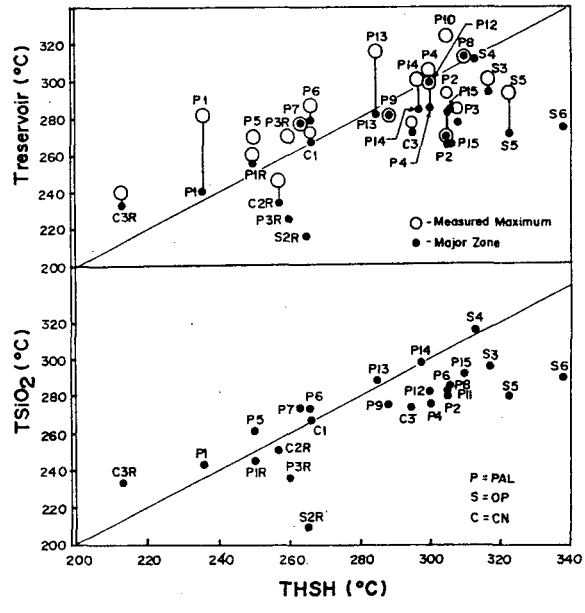

Fig. 4 Comparison of THSH with $TSiO_2$ and Measured Downhole Temperatures

The presence of gas has an effect on the pressure-temperature relationship and depresses the boiling point. The maximum temperature depression is 50°C at OP-2RD (36% by weight of steam). For other gassy wells like Pal-2D, Pal-8D, Pal-10D and Pal-11D, temperature decrease from 10 to 15°C. More specifically, the presence of a gassy, upper feedzone does not significantly affect the pressure profile but affects flow temperature below the gas feedzone (Aunzo, 1990).

e) measured temperatures are that of the steam and not the rock-water system for Botong wells OP-3D, OP-5D and OP-6D

In vapor-dominated systems, lower temperature steam is generated from boiling.

Field Trends

The results of T_{HSH} and y, are plotted across the field and temperature contours are drawn (Fig. 5). The main heat upflow zone as delineated by the tentative 320° contour is near the Botong sector. Reservoir temperature decreases towards the general westward direction. Reservoir steam fraction values, y (enclosed in parenthesis in Fig. 5), show a large variation across the field. Wells located near the heat upflow zone have $y > 0\%$.

Reservoir Model

The above field trends also suggest that the whole BMGP area belongs to one geothermal system. Slightly two-phase (maximum y = 5%) reservoir fluids of temperature ≥ 320°C undergo adiabatic cooling and non-isothermal boiling along a postulated permeability barrier located near wells OP-4D, OP-5D, Pal-8D, Pal-9D, Pal-10D, Pal-13D, Pal-14D and Pal-15D (Fig. 6). The upflow zone is probably located near the vicinity of OP-3D to 6D.

The more mobile vapor phase flows through the shallow layers of the volcanics formation and outflows to the W-NW. This vapor-rich layer is both adiabatically and conductively cooled as it mixes with cool recharge waters from the surface. H_2S is oxidized to SO_4 and the resultant acidic SO_4-rich condensate fluid percolates down vertical structures, appearing as deep acid inflows in wells such as Pal-2D and Pal-9D. In wells CN-2RD and CN-3RD, temperature drops from 250°C to 215°C and y values are already near zero, indicating condensate liquid.

The hot degassing reservoir fluid flows through the lower layers of the volcanics formation and outflows towards the W-NW. This is shown by the negative y values of Pal-1RD, CN-1 and CN-3D. Temperature reversals are observed for the outflow-lying wells, e.g. Pal-1RD and Pal-3RD. These wells encounter cool dilute recharge fluids as well as acidic condensate fluids.

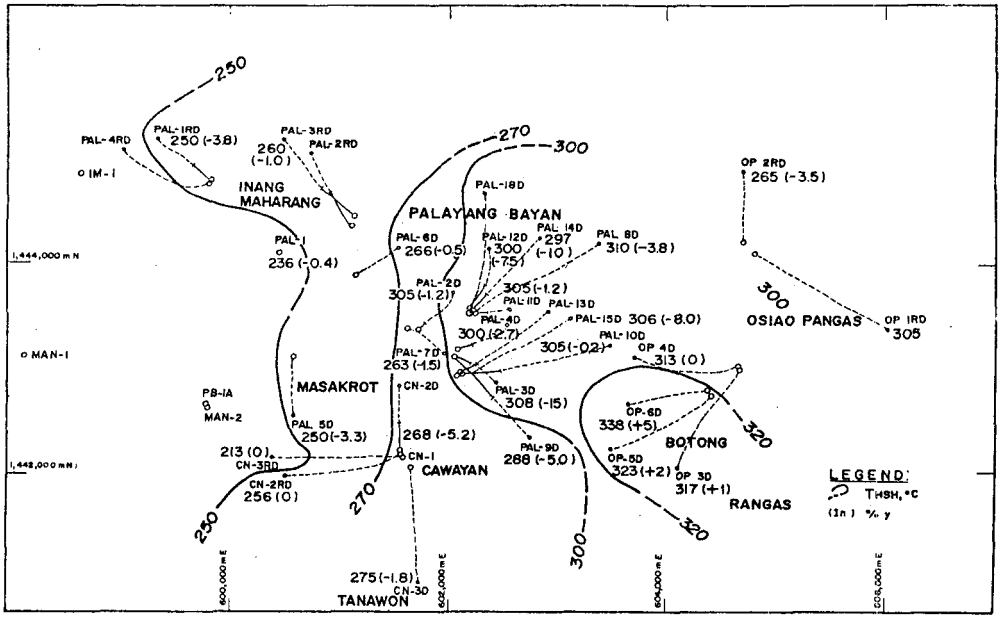

Fig. 5 Field Trends of THSH and Y

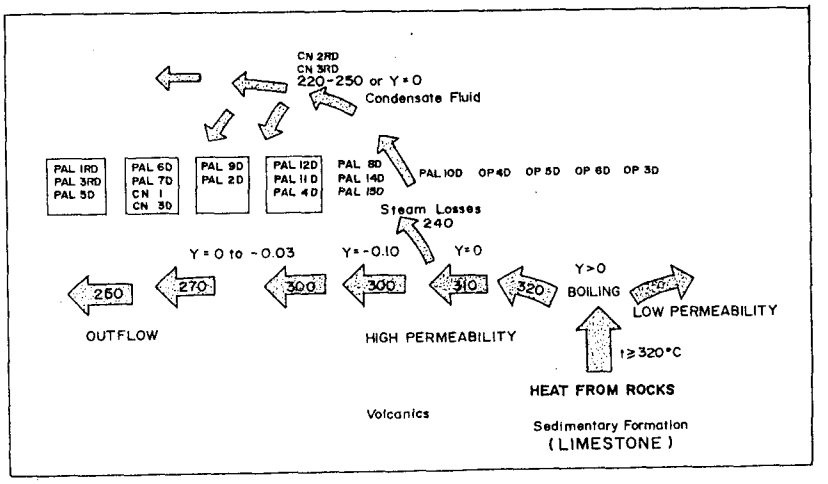

Fig. 6 Proposed BMGP Reservoir Model

CONCLUSIONS

The Fischer-Tropsch (FT) and H_2-H_2S (HSH) gas equilibria reactions are used in evaluating reservoir temperature and steam fraction. For BMGP wells with $y < -0.5\%$, the FT-HSH grid is not used and an approximate correction is made for H_2 that is lost due to preferential partitioning into the vapor phase and for the reequilibration of H_2S after steam loss.

Fair correlation is observed between T_{HSH}, quartz temperature (up to 300-320°C) and measured downhole temperatures in the majority of the wells. T_{HSH} is believed to give a good estimate of the local deep reservoir temperature. T_{HSH} is unaffected by acidic fluids, high discharge enthalpy (>1800 kj/kg), high CO_2 content in the reservoir fluid and despite also the fact that the major feed zone contributes a cooler dilute fluid.

A reservoir model is proposed. The primary reservoir fluid is slightly two-phase (y_{max}= 5%) and the main heat upflow zone is near the area delineated by the Botong wells, OP-3D to 6D. Permeability, as defined by vertical and horizontal structures, exerts control not only on the fluid outflow direction but also the gas composition. Deep reservoir boiling is caused by the shift from a less permeable sedimentary formation to more permeable volcanics. Gas composition is affected by postulated separate flow paths for a) the more mobile vapor phase which eventually forms a shallow condensate layer and, b) the deep hot degassed liquid.

ACKNOWLEDGEMENTS

The authors gratefully acknowledges the facilities, time and data provided by the management and staff of the Philippine National Oil Company- Energy Development Corporation (PNOC-EDC), the International Institute for Geothermal Research (CNR-IIRG) and International Atomic Energy Agency (IAEA).

REFERENCES

Aunzo, Z. P. 1990. GWELL: A Multi-Component Multi-Feedzone Geothermal Wellbore Simulator. M.Sc. Thesis, University of California, Berkeley, USA.

D'Amore, F., Nuti, S., Ruaya, J.R., Ramos-Candelaria, M.N., and Seastres, J.S. Jr., (in preparation) Applications of Gas Chemistry in Evaluating Physical Phenomena in Southern Negros (Palinpinon) Geothermal Field, Philippines.

D'Amore, F. and Truesdell, A.H. 1985. Calculation of geothermal reservoir temperatures and steam fractions from gas compositions. Geothermal Resources Council Transactions, v. 9.

Fournier, R.O. and Potter, R. W. 1982. A revised and expanded silica (quartz) geothermometer. Geotherm. Resource Council Bull., Nov. 1982, 3-12.

KRTA,Ltd., 1986. Bacon-Manito Geothermal Project: A Review of Gas Chemistry of Deep Wells, Internal Report.

PNOC-EDC, 1988. Bacman II Resource Assessment. PNOC Internal Report.

PROCEEDINGS, Eighteenth Workshop on Geothermal Reservoir Engineering
Stanford University, Stanford, California, January 26-28, 1993
SGP-TR-145

The Generation of HCl in the System NaCl–KCl–H_2O–Quartz at 600°C: Implications Regarding HCl in Natural Systems at Lower Temperatures

Robert O. Fournier and J. Michael Thompson

U.S. Geological Survey MS-910, 345 Middlefield Road, Menlo Park, CA 94025

ABSTRACT

In experiments at 600°C in the system NaCl–KCl–H_2O, within the analytical uncertainty, stoichiometric quantities of Cl and total alkali metals (Na+K) appear to dissolve in steam coexisting with chloride-rich brine at high pressures in the absence of solid salt. In contrast, at lower pressures, where steam coexists with precipitated salts, significant excess chloride as associated hydrogen chloride (HCl°) dissolves in steam. The HCl° appears to be generated by the reaction of solid NaCl(*s*) (halite) with steam, producing solid NaOH(*s*) that diffuses into halite, forming a solid solution. Where HCl° is present highly associated NaOH° as well as associated NaCl° appear to dissolve in steam, and the solubility of each is increased as the mole fraction of NaOH(*s*) in halite increases. In our quasi-static experiments, compared to dynamic flow-through experiments of others, higher initial ratios of H_2O/NaCl have resulted in higher mole fractions of NaOH(*s*) in solid solution in halite and, accordingly, higher solubilities of NaCl° and NaOH° dissolved in steam. Addition of quartz to the system NaCl–KCl–H_2O results in the formation of sodium disilicate by reaction of silica with NaOH(*s*) and an order of magnitude increase in the concentration of HCl° dissolved in steam.

In natural hydrothermal systems at lower temperatures where brine or brine plus steam are present in the absence of precipitated salt, the pH of the brine is controlled mainly by base exchange reactions involving a variety of silicates that fix Na^+/H^+ and K^+/H^+ activity ratios. Where feldspars are present pH values generally are near neutral. Where mica, but no feldspar is present pH values may become only moderately acid. High acidity in salt-absent brine systems occurs only where all feldspars and mica have been altered to other minerals (generally pyrophyllite/kaolinite or alunite). The situation changes significantly when salt precipitates. Hydrolysis produces HCl° by the reaction of water with NaCl when halite is present. The NaOH(*s*) that is produced as a byproduct is likely to react with quartz plus various alumino-silicates, producing a variety of alteration products and allowing steam to become greatly enriched in HCl° compared to the composition of steam that is attained in the simple system NaCl–KCl–H_2O with halite present. Also, when a natural high-temperature hydrothermal system changes from one in which the pore fluid is brine to one in which the pore fluid is dry steam there is a drastic change in Na^+/H^+ and K^+/H^+ activity ratios in the pore fluid because the hydrogen ions that were predominantly dissociated species in the brine become predominantly associated species in steam. The net result is the stabilization of alkali feldspars in contact with steam that may contain appreciable HCl° that is produced by the reaction of precipitated salt with the steam.

INTRODUCTION

In 1973 we initiated an experimental study of the partitioning of sodium and potassium between brine and steam and between solid salts and steam in the system NaCl–KCl–H_2O, with the aim of obtaining a better understanding of conditions controlling base exchange reactions involving alkali feldspars and hydrothermal fluids in volcanic and subvolcanic environments. We soon found that our experiments also were providing information about the generation of HCl by hydrolysis of the salt, and the focus of the experiments was shifted somewhat to include a study of this phenomenon. Unfortunately, that work ended prematurely because we were diverted to other activities that had, at the time, higher priority. Although the initial results were very interesting, they were not published then because we considered them very preliminary. It is now evident that we will not resume this experimental study and have decided to publish our results because of increasing concern within the geothermal energy industry about the conditions at which HCl is generated in hydrothermal systems (e.g., Anderson, 1989; Haizlip and Truesdell, 1988; 1989). Although our results are for much higher temperatures than are encountered in the production of geothermal resources they have implications with respect to natural hydrothermal systems at lower temperatures.

The solubility of NaCl in superheated steam at temperatures in excess of 400°C has been investigated by several researchers, including Olander and Liander (1950), Styrikovich *et al.* (1955), Sourirajan and Kennedy (1962), Martynova and Samoilov (1962), Martynova (1964), Galobardes *et al.* (1981), and Armellini and Tester (submitted). The formation of HCl by the hydrolysis of sodium chloride in dry steam was specifically addressed by Galobardes *et al.* (1981) at 350–550°C, by Armellini and Tester (submitted) at 450–550°C, and by Hanf and Sole (1970) at 600–950°C. All of the hydrolyses studies were carried out in a similar manner; dry steam or nitrogen containing steam at a controlled humidity were flowed at constant temperature and pressure through long, pipe-like

reaction vessels packed with sodium chloride. In these dynamic flow-through experiments a given quantity of steam was in contact with salt for a relatively short period of time (a few seconds to a few minutes, depending on flow rate). However, the above investigators concluded that equilibrium solubilities of NaCl in steam are attained very quickly at high temperatures because similar results were obtained at different rates of flow, and in experiments using reaction chambers in which flow paths were of different lengths.

Pitzer and Pabalan (1986) carried out a thermodynamic analysis of the solubility of NaCl in steam and, based on the results of Hanf and Sole (1970) and Galobardes *et al.* (1981), concluded that the effect of hydrolysis on NaCl properties at high temperatures is probably very small. Recently Anderko and Pitzer (in press) formulated an equation of state representation of phase equilibria in the system NaCl–H_2O, and Sterner *et al.* (1992) have reported the results of a thermodynamic analysis of solid-liquid equilibria at high temperatures and pressures in the system NaCl–KCl–H_2O. It is noteworthy that Sourirajan and Kennedy (1962), who investigated the system NaCl–H_2O over widely ranging temperatures and pressures, and with reaction times of a few hours, reported significantly higher solubilities of NaCl in dry steam than those reported by other investigators, except for Alekhin and Vakulenko (1988). Alekhin and Vakulenko (1988) measured solubilities *in-situ* using a radioactive tracer and reported even greater solubilities than those reported by Sourirajan and Kennedy (1962). However, Armellini and Tester (submitted) point out that the Alekhin and Vakulenko (1988) results possibly may be in error due to absorbed NaCl molecules on the inner walls of the reaction vessel.

APPARATUS AND EXPERIMENTAL PROCEDURE

The experiments were carried out using a reaction vessel made of Inconel X with an internal capacity of 68 cm^3. Fluid could be injected into or withdrawn from the vessel through a stainless-steel capillary tube that was inserted into the chamber through the closure plunger, using a high-pressure fitting. The vessel, charged with solid reactants (Table 1), was placed vertically in a doubly wound furnace with one winding heating just the ends of the furnace and a second winding heating the middle portion.

The reaction vessel was heated to about 600°C with the sampling port open to allow escape of air as the internal temperature increased. After attaining a stable temperature of 600°C, measured at the top of the reaction vessel, the sampling port was closed and then known amounts of water were slowly injected into the hot vessel until a desired maximum internal pressure was attained. The water and salt were allowed to equilibrate at about 600°C overnight and then sampling was initiated. At this time the temperature external to the sample chamber at the bottom of the vessel generally was about 10°C hotter than at the top, but the gradient within the sample chamber probably was much less owing to convection of the fluid.

TABLE 1. *Starting materials used in experiment (in grams).*

Experiment No.	NaCl (g)	KCl (g)	Quartz (g)	H_2O (g)	NaCl:KCl (by wt.)	m soln.	NaCl/KCl mole ratio
P42	4.0	---	---	21	---	3.26	---
P23	1.5	0.5	---	14.4	3:1	2.60	3.83
P26	1.5	0.5	---	27	3:1	1.20	3.83
P45	45.0	15.0	---	18	3:1	53.95	3.83
P30	3.0	1.0	1.0	21	3:1	3.08	3.83

Samples were extracted from the top of the vessel; thus the temperature closest to the point of sampling was taken as the experimental temperature, 600 ± 3°C. Generally about every 45 to 60 minutes during the day three separate steam condensate samples were quickly extracted for chemical analyses. However, a few intervals between sampling episodes were more than 16 hours overnight. At the time of sampling, a portion of the capillary tube was placed in an ice bath to quench the sampled fluid to less than about 20°C. It generally took about 5 minutes to extract the three samples. At each sampling episode the first of the three samples generally weighed about 0.6 to 0.8 g and was discarded because it was contaminated with a small amount of condensate that filled the capillary and valve prior to sampling. The next sample also generally weighed about 0.6 to 0.8 g and the last about 0.2 to 0.3 g. The pressure decreased as a consequence of withdrawal of each sample.

The samples were diluted with about 10 g distilled water and analyzed for Na and K by atomic absorption. Cl was determined by potentiometric titration using silver nitrate and a silver reference electrode. Less than 0.5 ppm Ni was found in the samples, indicating that there was no significant attack by the hot brine or steam upon the Inconel X reaction vessel at the conditions of the experiment.

In some experiments the fluid pressure was sufficiently high at the start of an experiment for brine (or brine plus quartz) to fill the reaction chamber. As a result of fluid extraction, pressure declined and a steam cap formed above the brine. Thereafter, only steam was sampled. Continued extraction of steam resulted in the precipitation of salt, and the brine evaporated to dryness so that only steam and solid salt (or salt plus quartz) occupied the reaction chamber during the last few sampling events at low pressures. In the illustrations that follow, the data are plotted at the average pressure during the time that an individual sample was collected.

RESULTS

Figure 1 shows our experimentally determined molal concentrations of Cl (circles) and Na (squares) dissolved in steam in the system NaCl–H_2O (P42, Table 1), compared with experimental results reported by Sourirajan and Kennedy (1962) and by Martynova (1964), and with calculated solubilities of NaCl according to the models of Pitzer and Pabalan (1986) and Anderko and Pitzer (in press). All of the experimental and modeled solubilities are in general agreement at a pressure of about 30 MPa. At

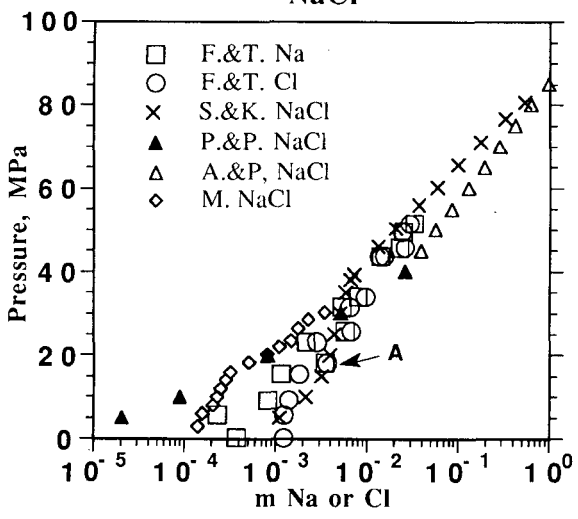

FIG. 1. Experimental results in the system NaCl–H_2O (run P42, Table 1) showing molal Cl or Na dissolved in steam coexisting with brine or halite at 600°C, plotted versus the average vapor pressure during sampling. In the legend F.&T. indicates results of the present investigation; S.&K. indicates results reported by Sourirajan and Kennedy (1962); P.&P. indicate solubilities according to the model of Pitzer and Pabalan (1986); A.&P. indicates solubilities according to the model of Anderko and Pitzer (submitted); and M. indicates results reported by Martynova (1964).

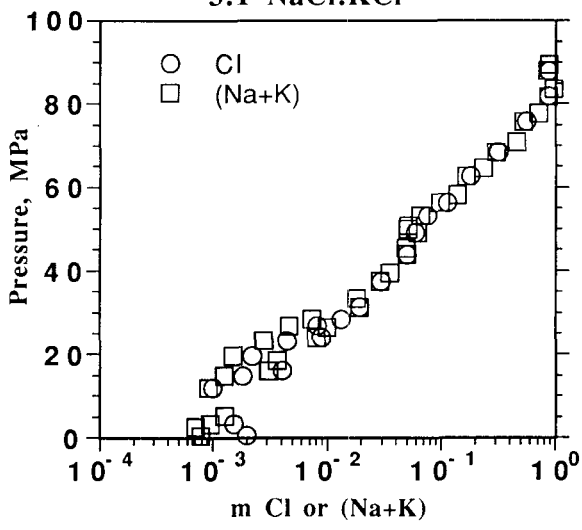

FIG. 2. Experimental results in the system NaCl–KCl–H_2O, starting with a 3:1 mixture of NaCl:KCl by weight (runs P23 and P26, Table 1), showing molal Cl or total alkalies (Na+K) dissolved in steam coexisting with brine and/or halite at 600°C, plotted versus the average vapor pressure during sampling.

other pressures our results generally plot closer to those of Sourirajan and Kennedy (1962) than to those of Martynova (1964), particularly at pressures less than about 25 MPa. Above 30 MPa our measured solubilities are less than the solubilities indicated by the Anderko and Pitzer (in press) model, and below 30 MPa our measured solubilities are considerably greater than the modeled solubilities of Pitzer and Pabalan (1986).

In the system NaCl–H_2O there is an invariant point at a pressure of 39.8 MPa at 600°C where the reactants consist of coexisting gas plus brine plus solid salt (halite). Salt may not exist at higher fluid pressures where only gas plus brine are stable, and brine may not exist at lower pressures where only gas and solid salt are stable. At pressures above 39.8 MPa, where steam coexists with brine, within the analytical uncertainty steam contains molal concentrations of Cl equal to the molal concentration of dissolved Na. At lower pressures where solid salt is a reactant, significantly more Cl generally was found dissolved in steam than Na indicating the presence of HCl°(*g*).

Figure 2 shows our results for Cl and (Na+K) dissolved in steam (at pressures below 80 MPa) in the system NaCl–KCl–H_2O, starting with 3:1 mixtures by weight of NaCl and KCl (P23 and P26, Table 1). At pressures above 80 MPa only one phase (liquid) was present. In the three-component system NaCl–KCl–H_2O at constant temperature, there is still one degree of freedom when brine plus steam plus halite coexist. Therefore, halite (containing KCl in solid solution) may coexist with brine and steam of varying compositions over a range of pressures. The system becomes invariant at a constant temperature and pressure when sylvite precipitates along with halite. However, sylvite did not precipitate in our experiments because there is complete solid solution between halite and sylvite at 600°C. The formation of NaOH and HCl° by hydrolysis reactions is a complicating factor because residual NaOH will impart an extra degree of freedom to the system when HCl° is preferentially removed during sampling of steam. Also, like KCl, NaOH forms a solid solution with halite, and its presence effects the amount of salt that may dissolve in a coexisting gas (discussed later).

Figure 3 shows the results of adding quartz to a 3:1 mixture by weight of NaCl and KCl (P30, Table 1). At pressures below about 30 MPa, addition of quartz to the system NaCl–KCl–H_2O greatly increases the Cl dissolved in steam (Figs. 3 and 4), but has very little, if any, effect on dissolved Na (Fig. 5). Figures 6 and 7 show contrasting concentrations of Cl and Na dissolved in steam starting with 3:1 NaCl:KCl mixtures by weight in which the reaction vessel in one run (P45, Table 1) initially contained 60 g salt (≈54 m Cl) and in two other runs (P23 and P26, Table 1) it initially contained only 2 g salt (<3 m Cl). An important observation is that increased concentrations of both Na and Cl were attained in steam in experiments when initially there was less NaCl present relative to water. In the P23 and P26 experiments (1.5 g NaCl) the initial NaCl/H_2O weight ratios were 0.10 and 0.06 respectively, while in the P45 experiment (45 g NaCl) the initial NaCl/H_2O weight ratio was 2.5.

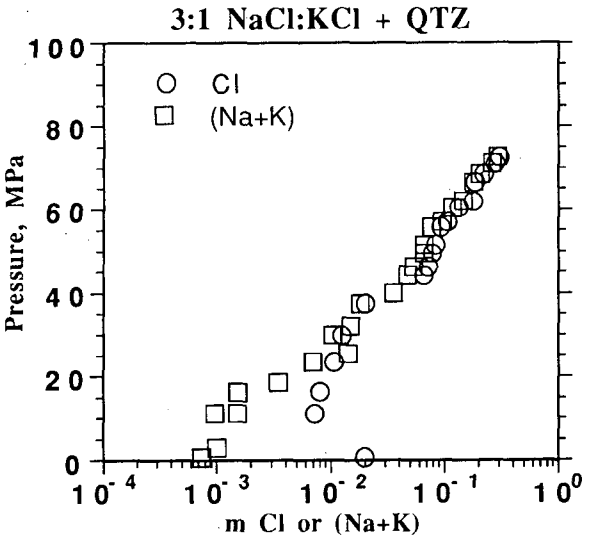

FIG. 3. Experimental results in the system NaCl–KCl–H_2O-quartz, starting with a 3:1 mixture of NaCl:KCl by weight (run P30, Table 1), showing molal Cl or total alkalies (Na+K) dissolved in steam coexisting with brine and/or halite at 600°C, plotted versus the average vapor pressure during sampling.

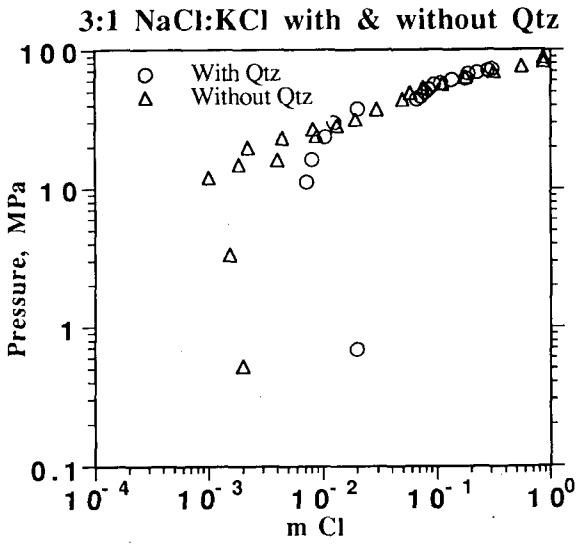

FIG. 4. Comparison of molal concentrations of Cl dissolved in steam starting with 3:1 mixtures by weight of NaCl:KCl with quartz and without quartz.

DISCUSSION

The smaller concentrations of both Na and Cl found dissolved in steam in experiments starting with more salt relative to water indicate that these variations are not likely to be due mainly to kinetic factors. If kinetic factors were dominant, one would expect those systems with the largest surface areas of salt relative to the amount of water present

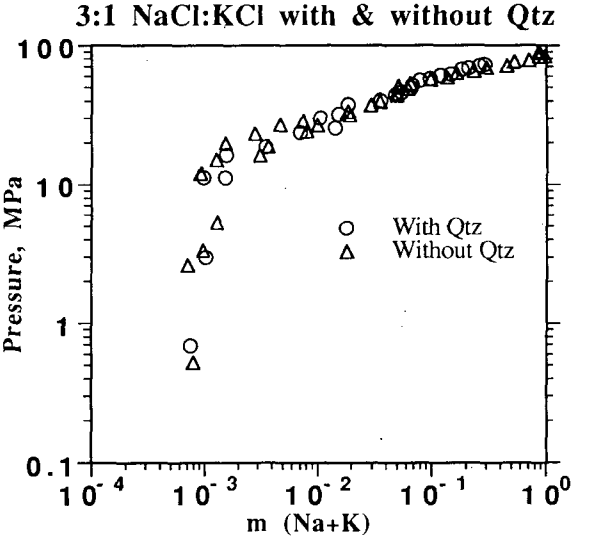

FIG. 5. Comparison of molal concentrations of Na dissolved in steam starting with 3:1 mixtures by weight of NaCl:KCl with quartz and without quartz.

to attain the highest concentrations of dissolved salt most quickly, assuming that higher concentrations of dissolved salt represent a closer approximation to equilibrium conditions. Such was not the case, and below we suggest a model in which equilibrium conditions were approached in most or all of the experiments, with different solubility results mostly caused (1) by variations in the amount of NaOH produced by hydrolysis reactions and (2) by variations in the mole fraction of NaOH(*s*) in solid solution within halite. The following discussion of the solubility results and hydrolysis effects is based mainly on reactions within the system NaCl–H_2O. The addition of KCl to the system is a complicating factor, but this does not appear to change drastically the general conclusions.

In their flow-through experiments in the temperature range 450–550°C both Styrikovich *et al.* (1955) and Martynova and Samoilov (1962) measured Cl^- ion concentrations and calculated NaCl solubilities, assuming that Na^+ and Cl^- ions were present in quenched steam in about equal molal concentrations. Their respective results are in good agreement, but at pressures less than 10 MPa their reported solubilities are significantly higher than those of Galobardes *et al.* (1981). Galobardes *et al.* (1981) calculated NaCl solubilities using measured Na^+ ion concentrations even though they found the ratio of molal chloride to sodium about equal to 1.2 at 450°C and extracted a highly basic solution (pH ~11) when they pumped cold water (as opposed to dry steam) through a salt-packed column that previously had been used for several weeks in their dry steam experiments at 450°C. This clearly shows that solid NaOH(*s*) formed and remained in the column of packed salt during their dry steam flow-through experiments. Also, in flow-through experiments in the same temperature-pressure range as the above experiments, Armellini and Tester (submitted) measured both Na^+ and Cl^- ion concentrations and their

Cl^- results are in agreement with those of Styrikovich *et al.* (1955) and Martynova (1964), and their Na^+ results are in agreement with those of Galobardes *et al.* (1981). The larger molal concentrations of Cl in steam relative to Na in these experiments clearly show the importance of hydrolysis of NaCl at high temperatures and low pressures according to the reaction,

$$NaCl(s) + H_2O(g) = NaOH(s) + HCl°(g). \quad (1)$$

It is not surprising that our results show considerably greater solubilities at comparable temperatures and pressures than the modeled solubilities of Pitzer and Pabalan (1986) because they calibrated their model using experimental results reported by Galobardes *et al.* (1981), who, as noted above, measured dissolved Na and then calculated NaCl solubilities with the assumption that stoichiometric quantities of dissolved Cl were present in solution. Therefore, the Pitzer and Pabalan (1986) model is likely to yield lower than measured solubilities to the extent that NaOH and HCl form by the hydrolysis of NaCl.

In the flow-through experiments of Hanf and Sole (1970), Galobardes *et al.* (1981), and Armellini and Tester (submitted), in which the mass ratio of salt to steam was very large and the transient steam was in contact with solid salt for only a few seconds to a few minutes, equilibrium was attained by dissolving salt, starting with pure steam. Our experimental technique, in which samples of fluids were extracted from a reaction chamber at successively lower pressures, was similar to the technique employed by Sourirajan and Kennedy (1962). In these experiments a maximum amount of salt was dissolved in steam at high pressure at the start of an experiment. During and after each sampling episode a new equilibrium condition was approached from supersaturation toward saturation. Because the concentration of (Na+K) in the third sample collected generally was less than the concentration of (Na+K) dissolved in the second sample that was collected at higher pressures not more than 3 or 4 minutes previously, we conclude that both condensation of brine and precipitation of salt from steam occur rapidly as pressure declines. The 45 to 60 minute (or longer) interval between the start of individual sampling episodes is likely to have been sufficient to achieve equilibrium with respect to the partitioning of Na and K between brine and steam and to attain equilibrium solubilities of salt in dry steam. However, the NaOH(s) that is produced according to equation (1) forms a limited solid solution with the remaining NaCl(s), and the interval between samplings may not have been sufficient for solid state diffusion to result in a uniform mole fraction of NaOH(s) in solid solution within halite. In this regard it is noteworthy that the data point labeled A in Fig. 1, which has about equal amounts of dissolved Na and Cl, and which plots on the Sourirajan and Kennedy (1962) solubility curve, is for a fluid that equilibrated with salt for about 16 hours between sampling episodes. All the other data points shown in Fig. 1 are for fluids that equilibrated with salt for about 30 minutes to 1 hour between sampling episodes and for as little as 2 or 3 minutes between individual sample extractions. It is possible that equilibrium of NaOH in solid solution in halite was attained by diffusion within 16 hours, but not in the runs of shorter duration. This is an important consideration because NaOH° as well as NaCl° dissolve into the steam phase, and the equilibrium concentration of NaOH° dissolved in steam will depend on the mole fraction of NaOH(s) in solid solution in the halite (Hanf and Sole, 1970; Armellini and Tester, submitted). In particular, Armellini and Tester (submitted) noted that limitations imposed by diffusion rates of NaOH(s) into halite "could lead to unsteady behavior and hydrolysis levels which depend on experimental parameters such as salt particle sizes and previous history of the salt bed."

A factor that may be important in explaining the difference in experimental results using flow-through techniques compared to quasi-static experiments is the much larger H_2O/NaCl mass ratio in the latter experiments. When steam is in contact with halite, hydrolysis reactions will proceed until sufficient HCl° is generated to attain equilibrium. The amount of HCl° generated is independent of the amount of halite present, but, as noted above, apparently is highly dependent on the amount of NaOH(s) in solid solution in halite. Figure 8 is a schematic phase diagram for the system NaCl–NaOH–H_2O at a temperature and pressure such that only gas plus solid salt exist. It is drawn to be compatible with the experimental observations and assumes limited solid solution of NaOH(s) within halite. The positions of tie lines show in a general way how solubilities of both Na and Cl in gas may increase as the mole fraction of NaOH(s) in solid solution in halite becomes greater. Furthermore, the mole fraction of NaOH(s) that is attained within halite depends on the mass of NaOH(s) generated by the hydrolysis reaction, the mass of halite remaining after that reaction, and the rate of diffusion of NaOH(s) into the halite. For the same amount of NaOH(s) generated, the resulting mole fraction of NaOH(s) in halite will be smaller when larger amounts of halite are present initially. In our experiments it is likely that diffusion of NaOH(s) into halite generally did not achieve a uniform, equilibrium distribution, but some diffusion appears to have occurred. We suggest that the effective mole fraction of NaOH(s) in halite, as a controlling factor with respect to the gas phase, was much larger in the quasi-static experiments (larger initial H_2O/NaCl mass ratios) than in the flow-through experiments (smaller initial H_2O/NaCl mass ratios).

In our experiments the effects of variations in the initial H_2O/NaCl mass ratio on the amounts of Na and Cl dissolved in steam can be seen in Figs. 6 and 7 that compare the results for experiment P45 (45 g NaCl), in which the initial H_2O/NaCl mass ratio was 0.4, with those for P23 and P26 (both 1.5 g NaCl) in which this ratio was 9.6 and 18, respectively. Clearly, smaller initial H_2O/NaCl mass ratios result in less Na and Cl dissolved in steam. Thus, the equilibrium constant for the hydrolysis reaction shown by equation (1) must take into account the departure of the solid salt from unit activity resulting from the solid solution of NaOH(s) in halite and of the NaCl° and NaOH° that enter the gas phase.

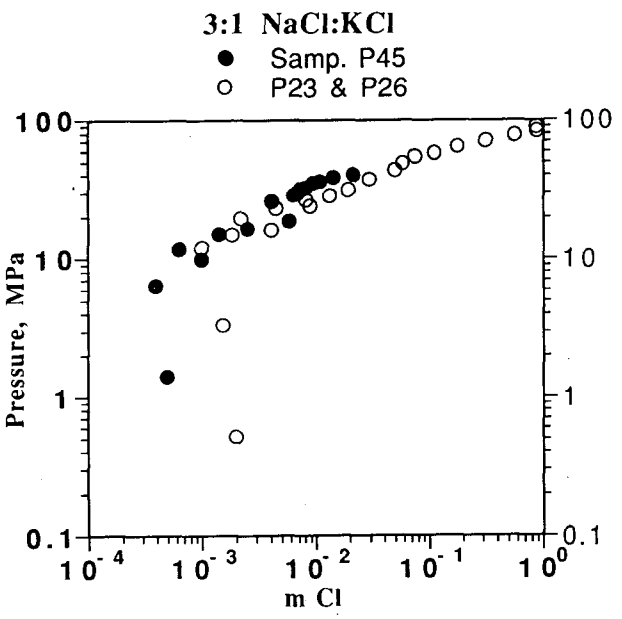

FIG. 6. Molal Cl dissolved in steam as a function of pressure for run P45, starting with 45 g NaCl, compared to runs P23 and P26, each starting with 1.5 g NaCl.

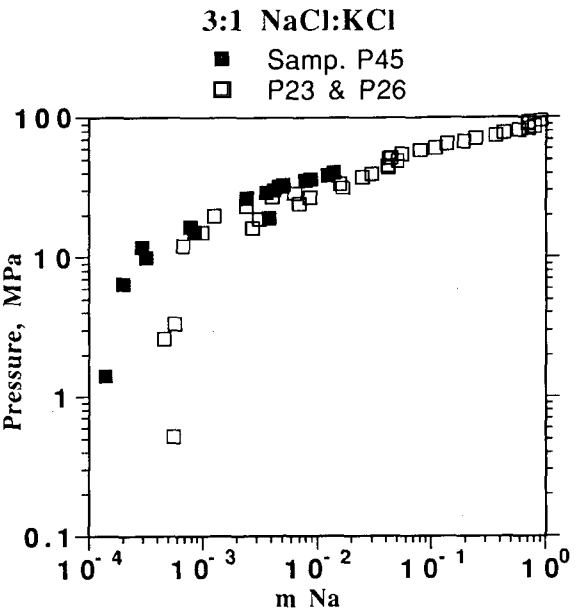

FIG. 7 Molal Na dissolved in steam as a function of pressure for run P45, starting with 45 g NaCl, compared to runs P23 and P26, each starting with 1.5 g NaCl.

To investigate the likely effects of salt hydrolysis reactions in natural systems, we added quartz to a 3:1 mixed salt system, expecting the yield of HCl° to increase because quartz reacts with NaOH to form sparingly soluble sodium disilicate that has a retrograde solubility at high tempera-

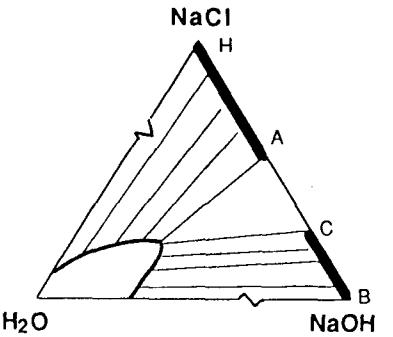

FIG. 8. Triangular diagram showing schematically how gas compositions apparently are affected by solid solution compositions in the system NaCl–NaOH–H_2O at a temperature and pressure such that gas plus solid salt coexist in the absence of brine. Limited solubility of NaOH(s) in halite (H to A) and limited solubility of NaCl(s) in solid NaOH (B to C) is assumed. The heavy curved lines show compositions of the gas phase and the light straight lines show compositions of coexisting gas and solids.

tures (Rowe *et al.*, 1967, and references therein). The reaction is

$$2NaOH(s, l) + 2SiO_2(s) = Na_2Si_2O_5(s) + H_2O(g). \quad (2)$$

Combining equations (1) and (2),

$$2NaCl(s) + 2SiO_2(s) + H_2O(g) = Na_2Si_2O_5(s) + 2HCl(g). \quad (3)$$

Figures 4 and 5 indeed show that at 600°C and pressures below about 40 MPa the addition of quartz to the system NaCl–KCl–H_2O markedly increases dissolved Cl as HCl° in steam with no apparent change in the total dissolved Na.

IMPLICATIONS REGARDING NATURAL SYSTEMS

In natural hydrothermal systems Na^+/K^+ activity ratios in fluids usually are fixed by base exchange reactions involving alkali feldspars (Orville, 1963; Fournier, 1976), while Na^+/H^+ and K^+/H^+ activity ratios are fixed by hydrolysis reactions involving various silicates, including amphiboles, pyroxenes, and especially feldspars and mica (Hemley and Jones, 1964; Hemley and Hunt, 1992). Where micas are present, pH values generally are near neutral or only slightly acidic. Where feldspars have been completely altered to micas, Na^+/H^+ and K^+/H^+ activity ratios are likely to be fixed by hydrolysis reactions involving mica and kaolinite below about 250°C, or mica and pyrophyllite above about 250°C (Hemley and Jones, 1964). In this situation pH values may become moderately acidic. However, extreme acidity can occur only where all feldspars and micas have been altered to pyrophyllite, kaolinite, or alunite.

Pore fluids that evaporate in response to a pressure drop or by boiling in place with escape of steam become ever more saline, and the alkali metal activities in the residual brines increase, thereby increasing Na^+/H^+ and K^+/H^+ activity ratios if compensating reactions do not occur. However, in natural systems compensating reactions are likely to occur. For example, clays and mica are likely to be converted to feldspars by base exchange with release of hydrogen ions, so that an increase in salinity by boiling (implying an increase in Na^+ and K^+ activities) is accompanied by an increase in hydrogen ion activity in order to maintain constant Na^+/H^+ and K^+/H^+ activity ratios. To the extent that the pore fluid initially contained chloride ions, the residual brine becomes slightly richer in hydrochloric acid as boiling progresses, mainly as a result of conversion of mica to feldspar. The evolving steam carries away only a small amount of gaseous HCl° because most hydrochloric acid remains dissolved in the brine. However, exceedingly acid brines generally are not generated by this process because acidity is buffered by rock-water interactions (Hemley and Hunt, 1992), and the rock/water ratio is large where there is sufficient thermal energy to allow large increases in salinity of brine by boiling in place in the formation.

The situation changes drastically when a brine boils dry; the precipitated salts react with steam and silicates with release of gaseous HCl° that is an associated, relatively unreactive, neutral species. The NaCl° and KCl° dissolved in dry steam, however, are appreciably reactive and dissociate to a somewhat greater extent, as shown by fast rates of reaction observed in base exchange experiments involving alkali feldspars at 400–700°C and low pressure (Fournier, 1976). Because hydrogen chloride is present in dry steam mainly as HCl° at high temperatures, its formation by hydrolysis reactions is not likely to significantly decrease Na^+/H^+ and K^+/H^+ activity ratios in the steam. Therefore, alkali feldspars in contact with evaporating brines and dry steam remain stable. In experiments in which only Na- and K-feldspars were in contact with steam plus brine plus alkali metal salt, Na-feldspar was converted to K-feldspar as a consequence of brine and steam becoming relatively enriched in potassium owing to precipitation of NaCl(*s*) (Fournier, 1976).

In a natural system instead of forming sodium disilicate as a reaction product, as in equations (2) and (3), it is likely that salt and quartz would react with various aluminum-rich silicates, forming alkali feldspars and other common hydrothermal alteration products, with release of HCl°. For example, a net reaction might involve NaCl, quartz and calcium feldspar, forming albite and epidote, or NaCl, quartz and muscovite, forming K-feldspar and albite. These net reactions are:

$$4CaAl_2Si_2O_8 + 4SiO_2 + 2NaCl + 2H_2O = 2NaAlSi_3O_8 + 2Ca_2Al_3Si_3O_{12}(OH) + 2HCl°, \quad (4)$$

and

$$2KAl_2(AlSiO_{10})(0H)2 + 12SiO_2 + 4NaCl = 2KAlSi_3O_8 + 4NaAlSi_3O_8 + 2HCl°. \quad (5)$$

When chloride-rich brine boils to dryness, the HCl° that forms by reactions involving salt and silicates, such as (4) and (5), is carried along with steam that escapes from the system. At higher and cooler levels in the system where steam condenses, HCl° is highly fractionated into the liquid condensate where the HCl° dissociates, becoming very reactive and corrosive at these conditions.

An unexpected result shown by the experimental work is that the amount of NaCl° and NaOH° dissolved in steam is inversely proportional to the initial salinity of a Cl-rich brine. This is because of the greater mole fraction of NaOH(*s*) that is attained in solid solution within halite when the initial salt/water ratio is lower. Thus, in a natural system where Cl-rich saline water initially fills all pore spaces, subsequent depressurization that allows steam to form and eventually salt to precipitate may result in higher concentrations of NaCl° and NaOH° dissolved in steam where there are lower initial salinities of pore fluid, provided that all NaOH(*s*) that is generated by hydrolysis reactions is not removed from the system by reaction with silicates.

CONCLUSIONS

At 600°C in the simple system NaCl–H_2O, steam in equilibrium with chloride-rich brine in the absence of halite at high pressures dissolves alkali metals and chloride in approximately stoichiometric quantities. In contrast, at lower pressures excess chloride as HCl° is found dissolved in dry steam in contact with halite. The hydrolysis reaction that produces the HCl° also produces NaOH(*s*) that diffuses into halite, forming a solid solution. Both NaCl° and NaOH° are found dissolved in steam, and the solubility of each is increased as the mole fraction of NaOH(*s*) in halite increases. In the quasi-static experiments, compared to dynamic flow-through experiments, higher initial ratios of H_2O/NaCl have resulted in higher mole fractions of NaOH(*s*) in solid solution in halite and, accordingly, higher reported solubilities of NaCl dissolved in steam. Addition of KCl to the system is a complicating factor, but it does not appear to change these conclusions significantly. In contrast, addition of quartz to the system NaCl–KCl–H_2O greatly increases the amount of HCl° produced by the hydrolysis of NaCl.

In natural systems at lower temperatures, brines generally are not likely to become very acid because their pH values are buffered by mineral reactions involving feldspars and micas. Hydrolysis reactions, that produce HCl° dissolved in steam, are likely to occur only where halite has precipitated as a result of boiling accompanying depressurization. However, the system need not have boiled dry to produce HCl in significant concentrations in steam because halite may coexist with brine of varying composition over a finite pressure range at a constant temperature. Most NaOH, that forms as a byproduct of the hydrolysis of NaCl, is likely to react quickly with quartz and other minerals, forming sparingly soluble alteration products (particularly alkali feldspars), and resulting in increased amounts of HCl° dissolved in steam. Thus, in natural systems NaOH° generally is not likely to

be available for transport along with HCl° in steam, and steam condensates may be very acidic.

The experimental results reported here are in agreement with empirical observations that HCl corrosion problems seem to become greater for steam produced from the hottest parts of The Geysers geothermal field where pressures are well below the boiling-point curve for pure water. Although there is general agreement that HCl is an important gas evolved from cooling magmas, a magmatic source is not required for the attainment of significant quantities of HCl° in steam. All that is required is that steam come in contact with precipitated chloride-rich salt within hot rock that contains reactive silicates.

Acknowledgments—J. L Bischoff and J. J. Hemley provided very helpful reviews of the first draft of the manuscript. Bischoff called our attention to the important related work of Armellini and Tester (submitted) and secured permission from them to show us an early version of their manuscript on the solubility of sodium chloride in sub- and supercritical water vapor. K. S. Pitzer kindly supplied us with a preprint of Anderko and Pitzer (in press).

REFERENCES

Alekhin, Yu.V. and Vakulenko, A.G. (1988) Thermodynamic parameters and solubility of NaCl in water vapor at 300–500°C up to 300 bar. *Geochem. Intl.* **25**, 97–110.

Anderko, A. and Pitzer, K. S. (in press) Equation of state representation of phase equilibria and volumetric properties of the system NaCl-H_2O above 573 K. *Geochim. Cosmochim. Acta.*

Anderson, G. (1989) A thermodynamic model for predicting HCl partial pressure above a high-temperature hypersaline geothermal fluid. *Geotherm. Resourc. Counc. Trans.* **13**, 221–225.

Armellini, F.J. and Tester, J.W. (submitted) Solubility of sodium chloride in sub- and supercritical water vapor. *Fluid Phase Equilibria* .

Fournier, R.O. (1976) Exchange of Na^+ and K^+ between water vapor and feldspar phases at high temperature and low vapor pressure. *Geochim. Cosmochim. Acta* **40**, 1553–1561.

Galobardes, J.F., Van Hare, D.R., and Lockhart, B.R. (1981) Solubility of sodium chloride in dry steam. *J. Chem. Eng. Data* **26**, 363–366.

Haizlip, J.R. and Truesdell, A.H. (1988) Hydrogen chloride in superheated steam and chloride in deep brine at The Geysers geothermal field, California. *Proc. 13th Workshop Geotherm. Reservoir Eng.*, Stanford Univ. **SGP-TR-113**, 93–99.

Haizlip, J.R. and Truesdell, A.H. (1989) The correlation of noncondensable gas and chloride in steam at The Geysers. *Geotherm. Resourc. Counc. Trans.* **13**, 455–460.

Hanf, N.W. and Sole, M.J. (1970) High-temperature hydrolysis of sodium chloride. *Trans. Faraday Soc.* **66**, 3065–3074.

Hemley, J.J. and Hunt, J.P. (1992) Hydrothermal ore-forming processes in the light of studies in rock-buffered systems: II. Some general geologic applications. *Econ. Geol.* **87**, 23–43.

Hemley, J.J. and Jones, W.R. (1964) Chemical aspects of hydrothermal alteration with emphasis on hydrogen metasomatism. *Econ. Geol.* **59**, 538–569.

Martynova, O.I. (1964) Some problems of the solubility of inorganic compounds in water vapor at high temperatures and pressures. *Russ. J. Phys. Chem.* **38**, 587–592.

Martynova, O.I., and Samoilov, Yu.F. (1962) The formation of solutions of inorganic substances in water vapor. *Russ. J. Inorg. Chem.* **7**, 372–375.

Olander, A. and Liander, H. (1950) The phase diagram of sodium chloride and steam above the critical point. *Acta Chim. Scand.* **4**, 1437–1445.

Orville, P.M. (1963) Alkali ion exchange between vapor and feldspar phases. *Amer. J. Sci.* **261**, 201–237.

Pitzer, K.S. and Pabalan, R.T. (1986) Thermodynamics of NaCl in steam. *Geochim. Cosmochim. Acta* **50**, 1445–1454.

Rowe, J.J., Fournier, R.O., and Morey, G.W. (1967) The system water-sodium oxide-silicon dioxide at 200, 250, and 300. *Inorg. Chem.* **6**, 1183–1199.

Sourirajan, S. and Kennedy, G.C. (1962) The system H_2O–NaCl at elevated temperatures and pressures. *Amer. J. Sci.* **260**, 115–141.

Sterner, M.S., Chou, I-M., Downs, R.T., and Pitzer, K.S. (1992) Phase relations in the system NaCl-KCl-H_2O. V. Thermodynamic-PTX analyses of solid-liquid equilibria at high temperatures and pressures. *Geochim. Cosmochim. Acta* **56**, 2295–2309.

Styrikovich, M.A., Khaibullin, I.Kh., and Tschvirachvili, D.G. (1955) Solubility of salts in high pressure steam. *Akad. Nauk. SSSR Doklady* **100**, 1123–1126 (in Russian).

PROCEEDINGS, Eighteenth Workshop on Geothermal Reservoir Engineering
Stanford University, Stanford, California, January 26-28, 1993
SGP-TR-145

A FLUID PROPERTY MODULE FOR THE TOUGH2 SIMULATOR FOR SALINE BRINES WITH NON-CONDENSIBLE GAS

A. Battistelli (§), C. Calore (*), and K. Pruess (%)

(§) Aquater S.p.A. - ENI Group, 61047 S. Lorenzo in Campo (PS), Italy.
(*) Istituto Internazionale per le Ricerche Geotermiche - CNR, Piazza Solferino 2,56126, Pisa, Italy.
(%) Earth Sciences Division, Lawrence Berkeley Laboratory, Berkeley, CA, 94720.

ABSTRACT

A new equation-of-state module has been developed for the TOUGH2 simulator, belonging to the MULKOM family of computer codes developed at LBL. This EOS module is able to handle three-component mixtures of water, sodium chloride, and a non-condensible gas. It can describe liquid and gas phases, and includes precipitation and dissolution of solid salt.

The dependence of density, viscosity, enthalpy, and vapor pressure of brine on salt concentration is taken into account, as well as the effects of salinity on gas solubility in the liquid phase and related heat of solution. The main assumptions made in developing this EOS module are discussed, together with the correlations employed to calculate the thermophysical properties of multiphase multicomponent mixtures.

At present the non-condensible gas can be chosen to be air, CO_2, CH_4, H_2, or N_2. This paper focuses on H_2O-NaCl-CO_2 mixtures and describes new correlations obtained from fitting of published experimental data.

Illustrative results for geothermal reservoir depletion in the presence of salinity and non-condensible gas are presented. We demonstrate and analyze effects of vapor pressure lowering and gas solubility decrease from salinity, and loss of reservoir porosity and permeability from salt precipitation during boiling of brines.

INTRODUCTION

The thermodynamic and transport properties of geothermal fluids are very important for determining the natural state of a geothermal system and its behaviour under exploitation. Such fluids consist usually of complex mixtures of water, non-condensible gases (NCG) and salts dissolved in the liquid phase. As water always represents the main mixture component, its thermophysical properties are customarily used to model geothermal reservoirs. In some cases the content of other components is such that they can alter the reservoir performance significantly. The effects of CO_2 have been analyzed with numerical studies by several authors. The importance of salt content has not received as much attention in reservoir modeling, mainly because only a few high salinity reservoirs have been exploited up to now.

Even though the main effects of dissolved solids and NCG on fluid mixture properties are well-known, the quantitative evaluation of the effect of variable proportion of both salinity and NCG on reservoir conditions and performance requires additional studies.
For the compositional simulation approach required to study high-salinity natural systems containing also NCG, an EOS module for the LBL's multipurpose TOUGH2 numerical simulator has been developed.

MODELING APPROACH

The TOUGH2 code implements the general MULKOM architecture for coupled multiphase, multicomponent fluid and heat flows (Pruess, 1983, 1991a). This new EOS module has been developed to simulate flow problems in which the transport of a variable salinity brine and a NCG occurs.
In this formulation the multiphase system is assumed to be composed of three mass components: water, sodium chloride and CO_2, or some other NCG. Whereas water and the NCG components may be present only in the liquid and gas phases, the salt component may be present dissolved in the liquid phase or precipitated to form a solid salt phase. The solubility of NaCl in the gas phase is neglected.

The three mass components formulation employed has been developed by enhancing an already existing EOS module for simulating the non- isothermal flow of saline water and air (Pruess, 1991b). The treatment of precipitation/dissolution of sodium chloride has been introduced using the method employed to treat similar phenomena occurring for water-silica mixtures (Verma and Pruess, 1988). The reduction of rock porosity because of salt precipitation is taken into account, as well as the related decrease of formation permeability.
The formulation of H_2O-CO_2 fluid mixture basically follows that described by O'Sullivan et al. (1985). The

dependence of brine thermophysical properties on salt concentration has been included following an updated version of the thermophysical package developed by Aquater for a wellbore numerical simulator (Battistelli, 1991).
All relevant thermophysical properties are evaluated using a subroutine by subroutine structure, so that the correlations employed at present can be easily modified.

The dependence of brine enthalpy, density, viscosity and vapor pressure on salt concentration has been accounted for, as well as the effect on NCG solubility and heat of solution in the brine. Transport of the mass components occurs by advection in liquid and gas phases; binary diffusion in the gas phase for steam and the NCG is accounted for. Diffusive and dispersive processes in the liquid phase are not included in the present TOUGH2 code formulation. It is assumed that the three phases (gas, liquid, and solid) are in local chemical and thermal equilibrium and that no chemical reactions take place other than interphase mass transfer.

In the integral finite differences formulation used by TOUGH2, the mass balance equations are written in the following general form (Pruess, 1991a):

$$\frac{d}{dt}\int_{Vn} M^{(k)}\, dV = \int_{\Gamma n} F^{(k)} \bullet \mathbf{n}\, d\Gamma + \int_{Vn} Q^{(k)} dV \qquad (1)$$

where k=1,2,3, indicates water, NaCl and NCG components, respectively. A complete description of the nomenclature used is given at the end of the paper. The accumulation and mass flux terms for the NaCl component (k=2) are written as follows:

$$M^{(2)} = \phi\, S_s\, \rho_s + \phi\, S_l\, \rho_l\, X_l^{(2)} \qquad (2)$$

$$F^{(2)} = -\,k\,\frac{k_{rl}}{\mu_l}\,\rho_l\, X_l^{(2)}\,(\,\mathbf{grad}P_l - \rho_l\,\mathbf{g}\,) \qquad (3)$$

where S_s is the "solid saturation", defined as the fraction of pore volume occupied by solid salt.

THERMODYNAMIC PACKAGE DESCRIPTION

The primary variables used for single phase conditions are total pressure of reference phase, P, salt mass fraction, $X^{(2)}$, NCG mass fraction, $X^{(3)}$, and temperature, T. If the solid salt is present, the second primary variable is switched to solid saturation S_s. In two-phase conditions the third primary variable is switched from NCG mass fraction to gas phase saturation S_g .

Mass balances of water, salt and NCG components, together with the heat balance, are set up and solved by TOUGH2 using the Newtown-Raphson iteration method. During the iteration process, the EOS module must be capable of recognizing the appearance and disappearance of phases, and of providing all thermophysical properties of phases present, pertaining to the last updated primary variables. A description of the main tests performed to recognize the phase transitions and of the equations used to calculate phases properties is given below.

Liquid conditions

First the test for phase change to two-phase conditions is made checking if total pressure exceeds the boiling pressure of fluid mixture:

$$P \overset{?}{\geq} P_{boil}(T, X_l^{(2)}, X_l^{(3)}) \qquad (4)$$

The liquid phase boiling pressure is calculated according to:

$$P_{boil} = P_{b\ sat}(T, X_l^{(2)}) + P^{(3)}(T, X_l^{(2)}, X_l^{(3)}) \qquad (5)$$

If the test fails, a change to the two-phase state is made initializing the gas phase saturation to a small non zero quantity. The bubbling pressure of NCG, $P^{(3)}$, is calculated according to Henry's law and accounting for the salting-out effect.

The solid salt phase appears if the salt mass fraction in the liquid phase exceeds the halite solubility. If:

$$X_l^{(2)} > X^{(2)}{}_{sol}(T) \qquad (6)$$

precipitation starts and the second primary variable is switched from salt mass fraction $X^{(2)}$ to "solid saturation" S_s. (Actually, $10+S_s$ is then used as second primary variable, so that by the fact that this is large than 1 it can be distinguished from mass fractions, which are always between 0 and 1) When Eq. (6) indicates that precipitation is starting S_s is initialized to a small non zero value. Conversely, when solid phase is present, its disappearance is recognized simply by $S_s<0$. In this case the second primary variable is switched back to $X^{(2)}$, and is initialized with a value slightly smaller than the equilibrium solubility $X_{sol}^{(2)}(T)$.

The thermophysical properties of the liquid phase are calculated as follows. The density and viscosity are assumed to be the same as those for brine, with the assumption that the effect of dissolved gas can be neglected because of low gas solubility. Liquid phase density, viscosity and enthalpy are given by:

$$\rho_l = \rho_b(P, T, X_l^{(2)}) \qquad (7)$$

$$\mu_l = \mu_b(P, T, X_l^{(2)}) \qquad (8)$$

$$H_l = (1-X_l^{(3)})\, H_b(P, T, X_l^{(2)}) + X_l^{(3)}\, H_l^{(3)}(P^{(3)}, T) \quad (9)$$

Gas conditions

In single-phase gas conditions the salt component can be present only as solid precipitate, having neglected its (very small) solubility in the gas phase. The appearance of the liquid phase is tested checking the partial pressure of steam, $P^{(1)}$, against the vapor brine pressure:

$$P^{(1)} \overset{?}{<} P_{b\ sat}(T, X^{(2)}_{eq}) \quad (10)$$

The brine vapor pressure is calculated using $X^{(2)}_{eq} = 0$ if no solid phase is present in the element, otherwise it is assumed to be the solubility of NaCl at element temperature. Partial pressure of water component is calculated using an iterative procedure from total pressure, temperature and NCG mass fraction. If the above test fails, a transition to two-phase conditions is diagnosed, initializing the third variable as a gas phase saturation slightly lower than one.

Density, enthalpy and viscosity of single-phase gas fluid mixtures are calculated as follows:

$$\rho_g = \rho_g^{(1)}(P^{(1)}, T) + \rho_g^{(3)}(P^{(3)}, T) \quad (11)$$

$$H_g = (1-X_g^{(3)})\, H_g^{(1)}(P^{(1)}, T) + X_g^{(3)}\, H_g^{(3)}(P^{(3)}, T) \quad (12)$$

$$\mu_g = (1-X_g^{(3)})\, \mu_g^{(1)}(P^{(1)}, T) + X_g^{(3)}\, \mu_g^{(3)}(P^{(3)}, T) \quad (13)$$

Liquid-gas mixtures

For elements with two-phase fluid the phase transition test is made checking the gas phase saturation that is used as third primary variable. If $S_g \geq 1 - S_s$, then the liquid phase disappears and a transition to single-phase gas conditions is made. If $S_g \leq 0$, then the gas phase disappears and a transition to single-phase liquid conditions is made. Appearance or disappearance of a precipitated solid phase is handled as in liquid conditions.

With the assumption of additivity of partial pressures, the partial pressure of NCG is given by:

$$P^{(3)} = P - P_{b\ sat}(T, X_l^{(2)}) \quad (14)$$

The mole fraction of NCG in the liquid phase is calculated according to Henry's law:

$$Y_l^{(3)} = P^{(3)} / K_{hb}(T, m) \quad (15)$$

where m is the salt molality. Then the mass fraction of NCG in the liquid phase is calculated in an obvious way. The mass fraction of NCG in the gas phase is calculated from the density of fluid mixture, computed considering an ideal mixture of steam and gas:

$$\rho_g = \rho_g^{(1)}(P_{b\ sat}, T) + \rho_g^{(3)}(P^{(3)}, T) \quad (16)$$

then:

$$X_g^{(3)} = \rho_g^{(3)} / \rho_g \quad (17)$$

The specific enthalpy and viscosity of vapor phase are calculated using Eq. 12 and 13 respectively, with $P^{(1)} = P_{b\ sat}$.
The density, viscosity and enthalpy of liquid phase are calculated with Eq. 7, 8 and 9 respectively, using the component mass fractions in the liquid phase.

THERMODYNAMIC PROPERTIES OF MIXTURE COMPONENTS

The correlations used to evaluate the thermophysical properties of mixture components are described below. References are given for all those correlations available in the technical literature, whereas new correlations obtained through the regression of published experimental data are presented in detail.

Water and salt component properties

The pure water properties are always computed using the International Formulation Committee (1967) correlations implemented in the TOUGH2 code.

- **Brine vapor pressure.** The vapor pressure of sodium chloride solutions is calculated according to the equation presented by Haas (1976). It can be used in the temperature range from -11 to 300 °C; as stated by Haas, extrapolation to 325°C still seems acceptable. The salt content can range from 0 to halite saturation. The equations implemented differ from the original ones used by Haas as the IFC correlation has been used to compute pure water saturation pressure. Figure 1 shows the vapor saturated brine pressure vs temperature at different NaCl mass fractions.
It is seen that dissolved solids generally reduce the vapor pressure. The salinity-induced vapor pressure lowering (VPL) effects can be large, reducing vapor pressure to as little as 2/3 of the vapor pressure of pure water. To put this number in perspective, it is of interest to make a comparison with VPL effects from capillarity and adsorption-induced suction pressure. From the data given by Pruess and O'Sullivan (1992) it can be seen that a reduction of vapor pressure to 2/3 of the value for "bulk" pure water would require extremely strong suction pressures approaching -100 MPa! Thus it appears that salinity-induced VPL effects are likely to be more important in the depletion of

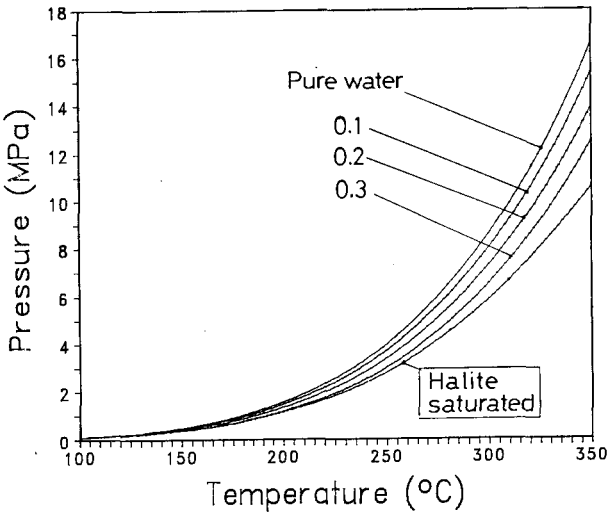

Figure 1. Vapor pressure of NaCl solutions from 0 mass fraction to halite saturation at 100° to 350°C.

vapor-dominated reservoirs than the capillarity/ adsorption induced effects.

- **Brine density.** The density of vapor-saturated brine is calculated using the equations presented by Haas (1976). They can be applied in the temperature range from 75 to 325 °C whereas the salt content can vary from 0 to 7.3 molal, or up to halite saturation if the corresponding molal concentration is lower. The density of vapor-saturated pure water is computed using the IFC formulation.
The effect of pressure on brine density is estimated with the assumption that brine compressibility is the same as that of pure water from the vapor-saturated pressure to current pressure.

- **Brine enthalpy.** The enthalpy of vapor-saturated sodium chloride solutions is calculated using the correlation of Michaelides (1981) based on the thermodynamic data presented by Silvester and Pitzer (1976). The corrections of typing errors in the Michaelides paper, presented by Gudmundsson and Thrainsson (1989), have been considered. The correlation should be applied in the temperature range from 100 to 300 °C. The compressed brine enthalpy is estimated assuming a similar pressure dependence for brine and pure water.

- **Brine viscosity.** The dynamic viscosity of vapor-saturated brine for salt mass fraction up to 0.30, is estimated using an equation quoted by Chierici et al. (1981), which applies a correction as a function of salt mass fraction to the dynamic viscosity of vapor saturated pure water. The latter is computed according to the IFC formulation.
The dynamic viscosity of compressed brine is calculated assuming a similar pressure dependence for brine and pure water.

- **Halite solubility.** The concentration of solutions that are both vapor- and halite-saturated is evaluated using an equation due to Potter and quoted by Chou (1987), who recommends the use of this equation from 0 to 382 °C.

- **Density and enthalpy of halite.** The density of halite is considered independent on pressure and temperature: a constant value of 2160 kg/m^3 is used (Deer et al., 1966).
The enthalpy of halite is calculated integrating the equation of heat capacity at constant pressure reported by Silvester and Pitzer (1976). The equation is valid from 25 to 800 °C (Palaban and Pitzer, 1987).

Carbon dioxide component

The equations used to calculate the carbon dioxide thermodynamical and transport properties are given below. A similar approach can be followed for other gases: this has already been done for air, methane, hydrogen and nitrogen.

- **Density and enthalpy of gaseous carbon dioxide.** The density and enthalpy of CO_2 as a function of temperature and its partial pressure are calculated from equations reported by Sutton and McNabb (1977). These equations are already used by the H_2O-CO_2 EOS module described by O'Sullivan et al. (1985).

- **Viscosity of gaseous carbon dioxide.** The CO_2 dynamic viscosity is calculated using the correlation quoted by Pritchett et al. (1981) and already implemented in the TOUGH2 H_2O-CO_2 EOS module.

- **Henry's law constant.** Dissolution of carbon dioxide in pure water and sodium chloride brines is described using Henry's law and the concept of salting-out; the Henry's constant is then calculated as:

$$K_{hb}(T, X_l^{(2)}) = K_h(T)\ 10^{(\ m\ k_b(T)\ )} \qquad (18)$$

where k_b is the salting-out coefficient. Several approximations are implicit in this formulation: the most important is the application of the formula at other than very small solute gas concentrations. Henry's law constant for the dissolution of carbon dioxide in pure water and the salting-out coefficient are calculated using polynomial regressions of data from 0 to 300 °C published by Cramer (1982). To extend the temperature range of Henry's constant correlation, the values reccomended by D'Amore and Truesdell (1988) from 300 °C to the critical point of water were also considered. The polynomial fit of Henry's constant is shown in Figure 2. The standard deviation is 4.74 MPa. The equation is as follows:

$$K_h(T) = \sum_{i=0}^{5} [\ A(i)\ T^i\ ] \qquad (19)$$

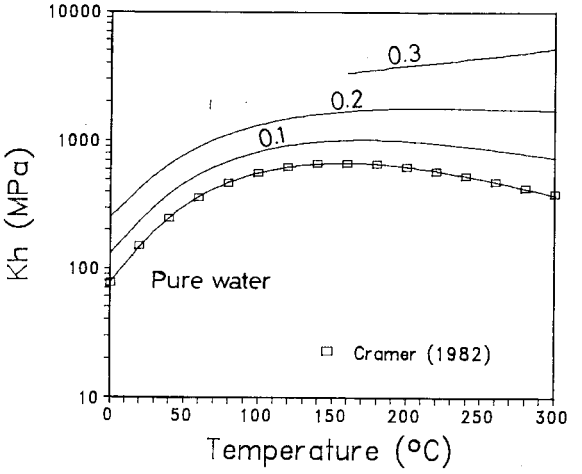

Figure 2. Henry's law constant for CO_2 in NaCl solutions from 0 to 0.3 mass fraction at 0° to 300°C.

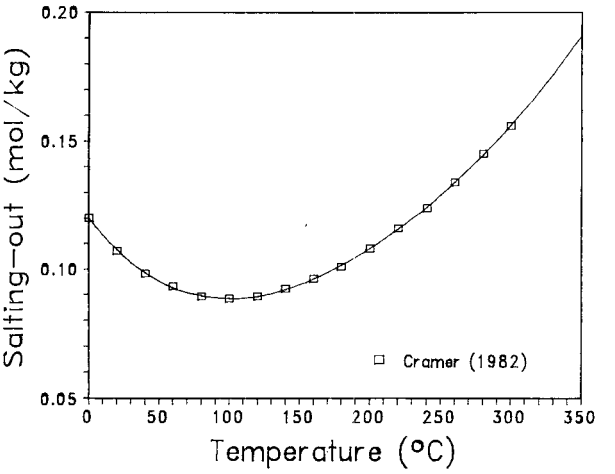

Figure 3. Salting-out coefficient for CO_2 dissolved in NaCl solutions from 0° to 350°C.

where the coefficients A(i) have the following values:

A(0) = 7.83666 E+8
A(1) = 1.96025 E+6
A(2) = 8.20574 E+4
A(3) = -7.40674 E+2
A(4) = 2.18380 E+0
A(5) = -2.20999 E-3

The equation for the salting-out coefficient is:

$$k_b(T) = \sum_{i=0}^{4} [\, B(i)\, T^i \,] \qquad (20)$$

The polynomial fit is shown in Figure 3. Standard deviation is 3.09 E-4 kg/mol. The coefficients B(i) have the following values:

B(0) = 1.19784 E-1
B(1) = -7.17823 E-4
B(2) = 4.93854 E-6
B(3) = -1.03826 E-8
B(4) = 1.08233 E-11

- Enthalpy of dissolved carbon dioxide. The enthalpy of carbon dioxide dissolved in pure water is calculated adding the heat of solution to the enthalpy of carbon dioxide in the gaseous state, according to the expression:

$$H_l^{(3)}(P^{(3)}, T) = H_g^{(3)}(P^{(3)}, T) + \Delta H_{sol}^{(3)}(T) \qquad (21)$$

The heat of solution can be calculated using the expression of temperature dependence of the equilibrium constant for the chemical reaction of solution:

$$CO_{2\,(g)} \text{---} > CO_{2\,(l)}$$

The equation that relates the heat of solution of a gas to its Henry's constant has been presented, among others, by Himmelblau (1959):

$$\left(\frac{\delta \ln K_h(T)}{\delta T}\right)_p = -\frac{\Delta H_{sol}^{(3)}(T)}{R\ TK^2} W^{(3)} \qquad (22)$$

In the above equation the molecular weight $W^{(3)}$ of CO_2 has been added to convert the heat of solution from J/mol to J/kg units. Eq. (22) is used to derive the heat of solution for carbon dioxide in sodium chloride brines using the Henry's constant K_{hb} given by Eq. (18). Figure 4 shows the heat of solution of CO_2 as a function of temperature at different salt mass fractions.

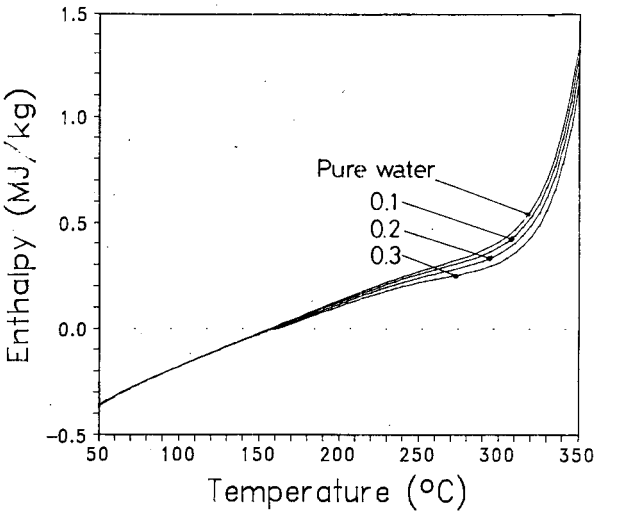

Figure 4. Heat of solutions for CO_2 dissolved in NaCl solutions from 0 to 0.3 mass fraction at 50° to 350°C.

NUMERICAL SIMULATIONS

It is well known that the main effects of solids dissolved in the liquid phase are the decrease of vapor pressure and enthalpy, and the increase of density and viscosity in the liquid phase. Furthermore, the NCG solubility in the liquid brine decreases (salting-out effect). We have performed numerical simulations to show some of the capabilities of the new EOS module to model the effects of dissolved solids and NCG on the behavior of geothermal reservoirs. For this purpose the examples presented are not designed to represent site-specific cases.

Depletion of zero-dimensional reservoir

The first simulations consider constant rate production from a zero-dimensional 'lumped-parameter' reservoir model in order to show the effects of salinity and CO_2 due to differences in the thermodynamic properties and mobilities of liquid and gas phases.

A block of 1 km^3 volume is considered initially in single-phase liquid conditions with a temperature of 260 °C and a pressure of 8 MPa. The formation parameters are the following: rock grain density 2600 kg/m^3, rock specific heat 920 J/(kg °C), formation thermal conductivity 2.51 W/(m °C), rock porosity 5%, Corey's relative permeability curves with residual liquid saturation of 0.3 and residual gas phase saturation of 0.05. Capillary pressure effects and VPL due to suction pressure are not included. Production occurs at a constant rate of 41.5 kg/s to attain the complete depletion in about 30 years when the block is filled with pure water.

A first series of simulations considers the two-component H_2O-NaCl system with salt mass fraction of 0 (pure water case), 0.01, 0.05, 0.10, 0.20 and 0.30 respectively. Figure 5 shows the pressure during block depletion as a function of time for the six cases. The time necessary for complete fluid depletion increases with increasing NaCl content as the fluid reserves stored initially increase from 39.41 E+9 kg for the pure water case up to 53.05 E+9 kg for the 0.30 salt mass fraction case. Two-phase conditions develop in the block for all cases within a few months; the boiling of fluid occurs at different pressure because of VPL due to salinity. Then the pressure remains almost constant for about 10 to 13 years until the gas phase mobility increases as shown by the enthalpy of produced fluid (Fig. 6). In this period the salinity of the reservoir liquid phase is almost constant (Fig. 7) as the salt mass

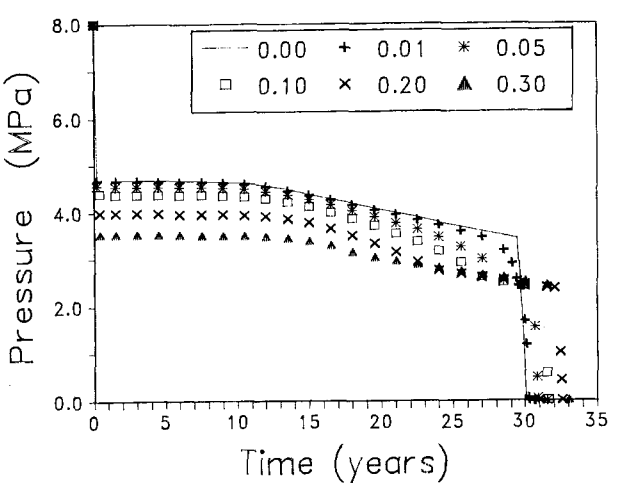

Figure 5. Depletion of zero-dimensional reservoir at different NaCl mass fractions for the H_2O-NaCl mixture.

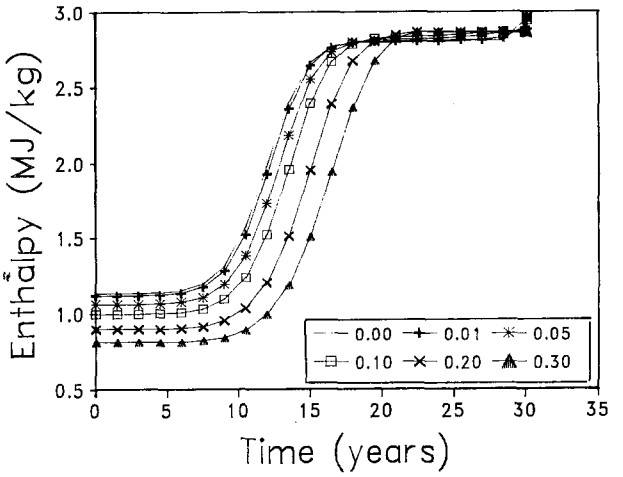

Figure 6. Production enthalpy as a function of time during reservoir depletion.

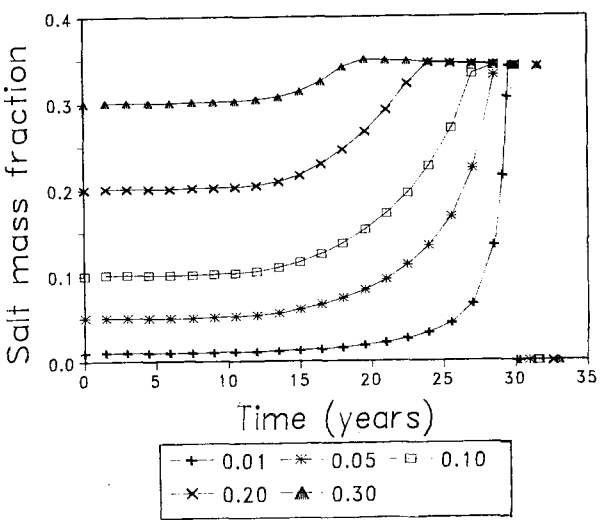

Figure 7. NaCl mass fraction in the liquid phase as a function of time during reservoir depletion.

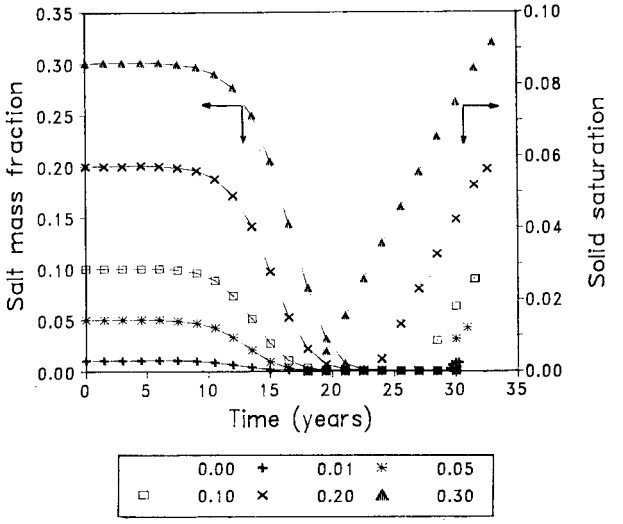

Figure 8. NaCl mass fraction in produced fluid and solid saturation as a function of time during reservoir depletion.

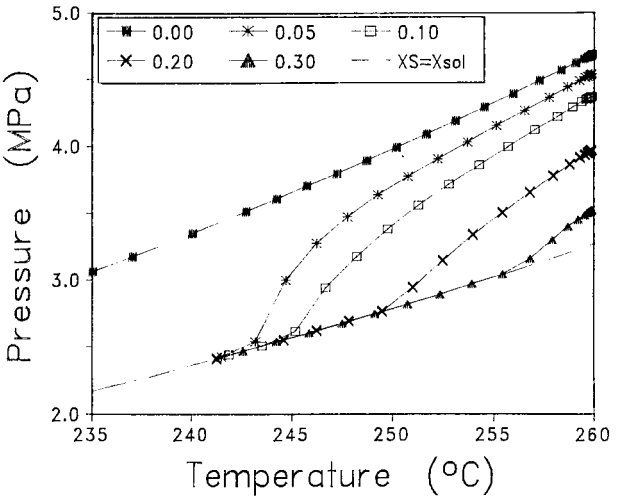

Figure 9. Brine vapor pressure as a function of reservoir temperature during reservoir depletion.

fraction in the produced fluid (Fig. 8).

The increase of gas phase mobility determines the rise of produced fluid enthalpy; then the reservoir temperature starts to decline significantly, also reducing reservoir pressure. The salt mass fraction in produced fluid declines as it can be extracted only dissolved in the less mobile liquid phase. This and the continous vaporization of water in the liquid phase determines the increase of salt concentration until it equals the halite solubility. Obviously the precipitation of solid salt occurs earlier depending on the initial salt content (see Figure 8). Figure 7 shows that for a complete drying process a solid salt phase can develop even for a very low initial salt concentration; in this case the increase of liquid phase salinity occurs close to the complete vaporization of liquid phase.

Figure 5 shows the pressure decline due to both temperature decline and salinity increase; when solid salt is present, the pressure becomes almost the same for the different cases because the salt mass fraction in the liquid phase is controlled by the solubility of halite and reservoir temperature differs only slightly. Figure 9 shows the brine vapor pressure as a function of reservoir temperature for the two-phase mixture. It shows the maximum VPL due to salt content, which is limited by the presence of solid salt phase.

Because of different initial fluid reserves, the liquid phase disappears over longer periods as the initial salt content increases. The increase in reservoir life is not proportional to the initial fluid reserves, as more and more salt is precipitated to form the solid phase that cannot be produced.

The second series of simulation considers the previous cases with the addition of 0.002 (2000 ppm) CO_2 mass fraction to the fluid mixture. The effect of NCG on reservoir pressure decline is shown in Figure 10. The salting-out effect increases the CO_2 bubbling pressure: up to a salt content of about 0.10 this increase balances the VPL. Then the increase of CO_2 bubbling pressure is higher and the fluid boiling pressure increases. Initial pressure depletion is governed by the exsolution of CO_2 from the liquid phase. The partial pressure of NCG declines as soon as the gas phase forms, as the NCG is partititioned preferentially in the gas phase. After 1.5 years, the NCG mass fraction into the gas phase is about 0.13 for the zero salinity case, but rises to 0.60 for the highest salinity. Figure 11 shows the decrease of NCG mass fraction in the liquid phase due to increasing salt contents. Considering the production characteristics, this effect determines a lower NCG content in produced fluid, as the low gas content liquid phase is initially produced (see Figure 12).

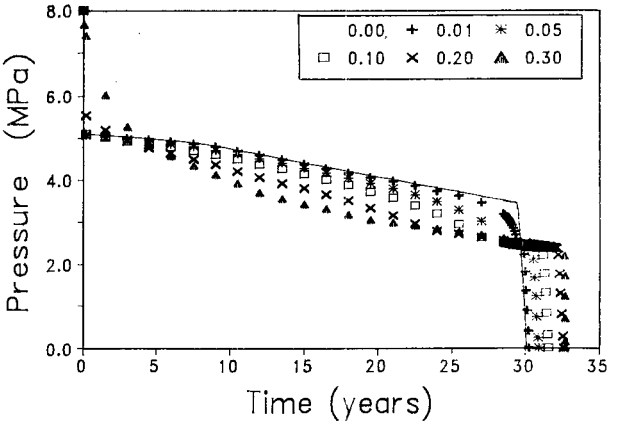

Figure 10. Depletion of zero-dimensional reservoir at different NaCl mass fractions in the presence of 2,000 ppm of CO_2.

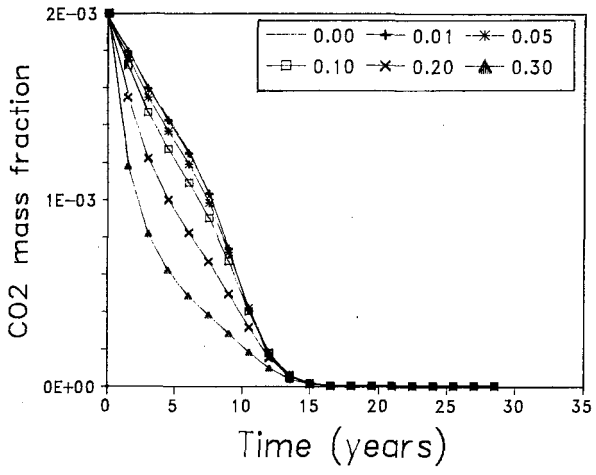

Figure 11. CO_2 mass fraction in the liquid phase as a function of time during reservoir depletion.

When its mobility increases, the rich NCG vapor phase is produced determining the sharp increase of NCG in produced fluid with higher concentrations for higher salt content; the position of maximum CO_2 mass fraction is also dependent on the salt content. Then the NCG declines with time and after about 15 years the carbon dioxide content in the liquid phase becomes negligible.
As expected, with respect to the previous series of simulations, the addition of NCG affects the initial reservoir pressure depletion until the partial pressure of NCG declines. These effects are concentrated in the first 10 years; after 15 years the pressure decline for all the cases is coincident to that of corresponding free-gas case.

For the parameters used in these simulations, excluding the last depletion period when the liquid phase is almost

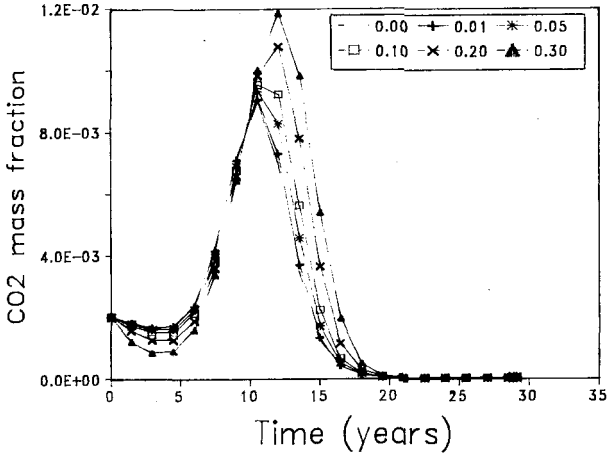

Figure 12. CO_2 mass fraction in produced fluid as a function of time during reservoir depletion.

completely vaporized, the effect of salt becomes important when its initial concentration exceeds about 50,000 ppm. The main effects on production characteristics are lower enthalpy and lower reservoir pressure for the cases with higher salinity; both can be considered as negative features of reservoirs containing brine.

Depletion of tight matrix blocks

We have simulated fluid production from tight matrix blocks under conditions considered representative of vapor dominated systems to show some effects of VPL and permeability reduction due to salinity.
Changes in formation permeability due to precipitation or dissolution of sodium chloride are modeled in the present EOS module formulation using the porosity-permeability correlations given in the paper by Verma and Pruess (1988). We used the 'series model' for tubular flow for the simulations presented here, with fractional lenght=0.8 and critical porosity fraction=0.8.

We have used the same model system as previously studied by Pruess and O'Sullivan (1992). The model consists of a single cubic block of rock matrix with side lenght D=50 m, surrounded by fractures wich have a fractional volume of 1E-4. The matrix block is discretized according to the MINC method (Pruess and Narasimhan, 1985) with 9 nested cubes of 2%, 4%, 6%, 8%, 10%, 13%, 16%, 20%, and 21% volume fractions. Matrix permeability and porosity are 5 E-18 m^2 and 5%, respectively. Liquid relative permeability and capillary pressure are taken as the van Genuchten form. Gas relative permeability is given by $k_{rg}=1-k_{rl}$. VPL due to suction pressure effects is not included. The system is initially in two-phase conditions at temperature of 240 °C, with liquid saturation of 80% in the matrix block, and 1% in the fractures.
Block depletion occurs by a 'well' on deliverability placed in the fractures (bottomhole pressure of 1 MPa, productivity index of 1.788E-13 m^3). Additional parameter specifications are given in the paper by Pruess and O'Sullivan (1992).

Three different cases were simulated: (Case 1) reservoir fluid is pure water; (Case 2) liquid phase is a brine with 0.20 salt mass fraction; (Case 3) same as Case 2 but permeability reduction due to salt precipitation is considered. Initial fluid pressure is 3.348 MPa for Case 1 and 2.838 MPa for Cases 2 and 3 because of VPL effects due to brine salinity. Initial fluid reserves are 4.089E+6 kg for Case 1, and 4.948E+6 kg (of which 3.962E+6 kg is water) for Cases 2 and 3.

Figure 13 shows the well production as a function of time for the 3 cases. The higher production rate for Case 1 occurs because of the higher initial pressure in the system; this causes a faster recovery of fluid

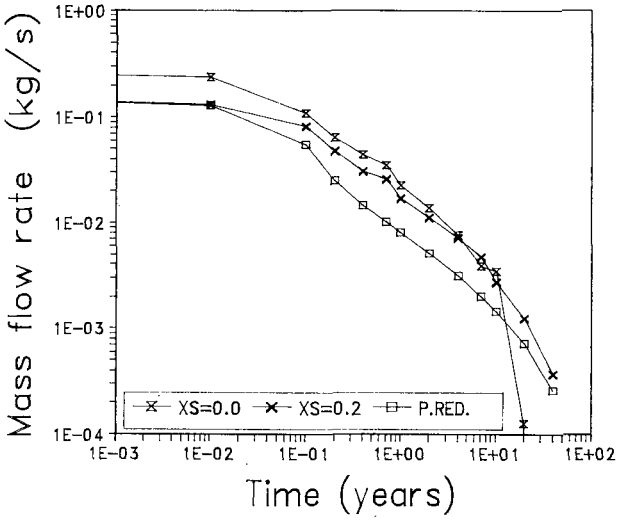

Figure 13. Production flow rate as a function of time during depletion of a tight matrix block.

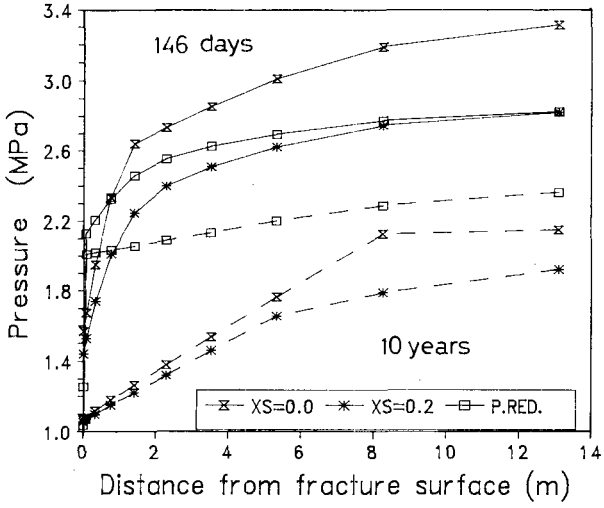

Figure 15. Pressure distribution as a function of distance from fracture at 146 days and 10 years in matrix block depletion problem.

reserves and the system is depleted after about 20 years, when all the matrix elements are in single-phase gas conditions. The same occurs for Case 2 after about 40 years. At this time the cumulative mass production for Case 1 and 2 are almost the same (Figure 14), as the initial reserves of pure water are almost the same. In fact the salt dissolved into the liquid phase is not recovered as the well produces steam from the beginning of exploitation. This is because the initial relative permeability to the liquid phase is low and the liquid phase is held by capillary forces in the matrix block. The introduction of permeability reduction in

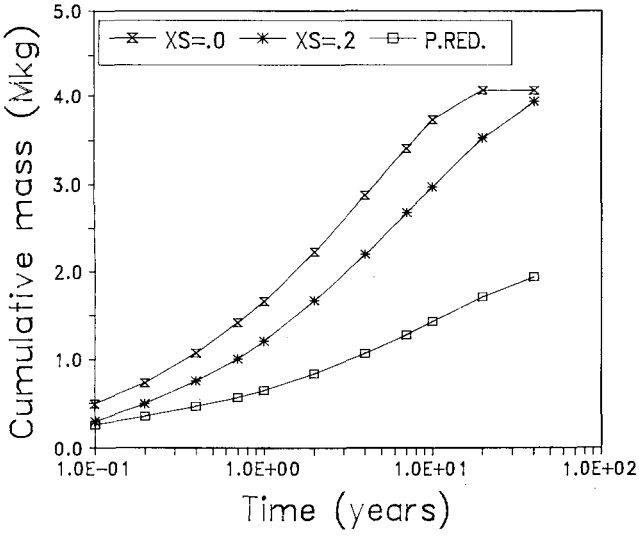

Figure 14. Cumulative fluid recovery as a function of time in matrix block depletion problem.

Case 3 is responsible for a faster decline in well production. After 40 years cumulative production for Case 3 is about 50% of that of Case 2.

For Case 3, after about 13 days the salt precipitation starts in the first matrix element. After 36.5 days, the solid saturation in this element is 0.11, causing a reduction of formation permeability to about 25% of its initial value. In both Case 2 and 3 the precipitation of solid salt close to the fracture surface continues as additional liquid phase flows towards the outermost element. There the vaporization produces the accumulation of sodium chloride and its precipitation. If the related permeability reduction is considered, the solid 'skin' at the fracture surface gives rise to a lower decrease of pressure in the interior of matrix block than in Case 2. Figure 15 shows the pressure distribution as a function of distance from the fracture surface after 146 days and 10 years, respectively. It is seen that when permeability reduction from solid precipitate is taken into account, most of the pressure drop occurs near the block surface.

After 40 years the well production for Case 3 is decreased by a factor of 1E+3. Even though about 50% of the original water reserves are still stored in the matrix block, they are produced only very slowly as the permeability of the outermost region of the matrix block is reduced to 0.6% of its initial value.

CONCLUSIONS

A thermophysical properties package for saline brines with non-condensible gas, that had been developed for a wellbore flow code "PROFILI", has been incorporated into the general-purpose multiphase fluid and heat flow

code TOUGH2. Our formulation includes a comprehensive suite of multiphase mixture effects, including density, viscosity, and enthalpy effects from salt dissolution, reduction in non-condensible gas solubility due to salinity, vapor pressure lowering due to salinity, and porosity and permeability reduction from the precipitation of salt.

Numerical simulations of reservoir depletion have demonstrated important effects from reduction in the solubility of non-condensible gas due to salinity. Vapor pressure lowering effects from salinity are very strong, and are likely to have a large impact on the depletion of vapor-dominated systems. In the depletion of fractured reservoirs, persistent boiling near the surfaces of matrix blocks will lead to concentration and ultimately precipitation of solids. This may cause a severe loss in permeability, and may considerably slow the rates at which fluid reserves can be recovered.

The simulation capabilities presented here will be of interest not only for geothermal reservoir studies, but also for analysis of fluid and heat flow conditions near high-level nuclear waste repositories.

ACKNOWLEDGEMENTS

This work was supported by Aquater S.p.A. of the Italian National Hydrocarbons Agency (ENI), by the International Institute for Geothermal Research of the Italian National Research Council (CNR), and by the Assistant Secretary for Conservation and Renewable Energy, Geothermal Division, of the U.S. Department of Energy under Contract No. DE-AC03-76SF00098. The authors would like to aknowledge the hospitality of the Institute for Fluid Mechanics, University of Hanover, Germany, where part of this work was performed.

NOMENCLATURE

$\mathbf{F}^{(i)}$ mass flux of component i, kg/(s m^2).
$\mathbf{g}$ acceleration of gravity, m^2/s.
k intrinsic permeability, m^2.
k_{rg} relative permeability to gas phase.
k_{rl} relative permeability to liquid phase.
k_b salting-out coefficient, kg/mol.
K_h Henry constant, Pa.
H specific enthalpy, J/kg.
m salt molality, mol/kg.
$M^{(i)}$ accumulation term of component i, kg/m^3.
$\mathbf{n}$ unit normal vector.
P pressure, Pa.
$Q^{(i)}$ source term for component i, kg/(s m^3).
R universal gas constant, J/(mol K).
S saturation.
T temperature, °C.
TK temperature, K.
V_n volume of grid element n, m^3.
$X^{(i)}$ mass fraction of component i.
$Y^{(3)}$ mole fraction of NCG.
$W^{(3)}$ molecular weight of NCG, kg/mol.
Γ_n surface area of grid element n, m^2.
ϕ porosity.
μ dynamic viscosity, Pa s.
ρ density, kg/m^3.

Subscripts and Superscripts

b brine.
boil boiling.
eq equivalent salt mass fraction.
g gas phase.
l liquid phase.
s solid salt phase.
sat vapor-saturated.
sol halite solubility.
1 water component, H_2O.
2 salt component, NaCl.
3 gas component, NCG.

REFERENCES

Battistelli, A., "PROFILI code: the thermodynamical package for H_2O-NaCl-CO_2 fluid mixtures". Unpublished Aquater report H 6046, Nov., 1991.

Chierici, G. L., Giannone, G., and Sclocchi G., "A Wellbore Model for Two-Phase Flow in Geothermal Reservoirs". SPE 10315, 1981.

Chou, I.- M., "Phase relations in the system NaCl-KCl-H_2O. III : Solubilities of halite in vapor-saturated liquids above 445 °C and redetermination of Phase equilibrium properties in the system NaCl-H_2O". Geoch. et Cosm. Acta, Vol. 51, pp. 1965-1975, 1987.

Cramer, S. D., "The solubility of methane, carbon dioxide and oxigen in brines from 0° to 300 °C". US Bureau of Mines, report No. 8706, 1982.

D'Amore, F., and Truesdell, A. H., "A rewiew of solubilities and equilibrium constants for gaseous species of geothermal interest". Sci. Geol. Bull., 41, 3-4, pp. 309-332, Strasbourg, 1988.

Deer, W. A., Howie, R. A., and Zussman, J., "An Introdution to the Rock-Forming Minerals". Longman Group Limited, London, 1966.

Gudmundsson, J.- S., and Thrainsson H., "Power potential of two-phase geothermal wells". Geothermics, Vol. 18, No. 3, pp 357-366, 1989.

Haas, J. L. Jr., "Physical Properties of the Coexisting Phases and Thermodynamical Properties of the H_2O Component in Boiling NaCl Solutions". USGS Bulletin

1421-A, 1976.

Himmelblau, D. M., "Partial molal heats and entropies of solution for gases dissolved in water from the freezing to the near critical point". J. Phys. Chem., Vol. 63, pp. 1803-1808, 1959.

International Formulation Committe, "A Formulation of the Thermodynamic Properties of Ordinary Water Substance". IFC Secretariat, Düsseldorf, Germany, 1967.

Michaelides, E. E., "Thermodynamic properties of geothermal fluids". GRC Transactions, Vol. 5, Oct. 1981.

O'Sullivan, M. J., Bodvarsson, G. S., Pruess, K., and Blakeley, M. R., "Fluid and Heat Flow in Gas-Rich Geothermal Reservoirs". SPE J., pp. 215-226, Apr. 1985.

Palaban, R. T., and Pitzer, K. S., "Thermodynamics of concentrated electrolyte mixtures and the prediction of mineral solubilities to high temperatures for mixtures in the system Na-K-Mg-Cl-SO_4-OH-H_2O". Geoch. et Cosm. Acta, Vol. 51, pp.2429-2443, 1987.

Pritchett, J. W., Rice, M. H., and Riney T. D., "Equation-of-state for water-carbon$_3$ dioxide mixtures: implications for Baca reservoir". S^3 report SSS-R-81-4870, report DOE/ET/27163-8, UC-66a, Feb. 1981.

Pruess, K., "Development of the General Purpose Simulator MULKOM". Annual report 1982, Earth Sci. Div., Lawrence Berkeley Lab. report, LBL-15500, Berkeley, CA, 1983.

Pruess, K. and Narashiman, T. N., "A Practical Method for Modeling Fluid and Heat Flow in Fractured Porous Media". Soc. Pet. Eng. J., Vol. 25, N. 1, pp. 14-26, 1985.

Pruess, K., "TOUGH2 - A General-Purpose Numerical Simulator for Multiphase Fluid and Heat Flow", Earth Sci. Div., Lawrence Berkeley Lab. report LBL-29400, Berkeley, CA, 1991a.

Pruess, K., "EOS7 - An Equation-of-State Module for the TOUGH2 Simulator for Two-Phase Flow of Saline Water and Air", Earth Sci. Div., Lawrence Berkeley Lab. report LBL-31114, Berkeley, CA, 1991b.

Pruess, K., and O'Sullivan, M., "Effects of Capillarity and Vapor Adsorption in the Depletion of Vapor-Dominated Geothermal Reservoirs". 17th Workshop on Geoth. Res. Eng., Stanford University, Stanford, CA, Jan., 29-31, 1992.

Silvester, L. F., and Pitzer, K. S., "Thermodynamics of geothermal brines - I. Thermodynamic properties of vapor-saturated NaCl (aq) solutions from 0-300 °C". Lawrence Berkeley Lab. report LBL-4456, UC-66, TID-4500-R64, 1976.

Sutton, F. M., and McNabb, A., "Boiling Curves at Broadlands Field". New Zealand J. of Sci., Vol. 20, pp. 333-337, 1977.

Verma, A., and Pruess, K., "Thermohydrological Conditions and Silica Redistribution Near High-Level Nuclear Wastes Emplaced in Saturated Geological Formations". J. of Geophys. Res., Vol.93, No. B2, pp. 1159-1173, Feb. 10, 1988.

PROCEEDINGS, Eighteenth Workshop on Geothermal Reservoir Engineering
Stanford University, Stanford, California, January 26-28, 1993
SGP-TR-145

WELLBORE SIMULATION - CASE STUDIES

Derek Freeston and Calum Gunn[1]
Geothermal Institute, University of Auckland, Auckland, New Zealand
[1] Geothermal Energy New Zealand Limited, Auckland, New Zealand

ABSTRACT

The use of a wellbore simulator, WELLSIM, to characterise the effects of multi-feed inflow on wellbore pressure-temperature characteristics, and diameter changes to a well on the deliverability curve, is discussed. Matching analyses are performed with the simulator on a well which has a number of two-phase and liquid infeeds, and it is demonstrated that good matches to both pressure and temperature profiles can be achieved. The significance of the reservoir/feed response curve for a steam well is illustrated, and the optimisation of wellbore diameter is shown to be related to whether the discharge is wellbore or reservoir controlled.

INTRODUCTION

Studies of flow in a wellbore have become important in recent years as reservoir engineers and operators have sought to improve reservoir simulation techniques and the corresponding results, and to optimise well output. This study is based on a wellbore simulator, of which a number are described in the literature (e.g. Barelli et al., 1982; Bjornsson, 1987; and Hadgu, 1989).

The basis of most of these simulators is the one-dimensional steady flow momentum equations, with closing equations provided from the two-phase flow literature for wells supplying fluid from a liquid or two-phase reservoir. In general, for such a simulator, five flow regimes are recognised: bubble, slug, churn, annular and mist, with transition and pressure drop relationships dependent on the user's choice. A full discussion of some of the available regime transition equations, and pressure drop predictions is in Hadgu (1989).

Fluid composition, that is, the water and gas chemistry, has a significant influence on the well performance. Well geometry and the location and number of feed zones are other major factors influencing well performance. Modern wellbore simulators will therefore have a pressure/temperature/volume (PVT) package capable of accurately specifying fluid properties over a range of pressure and chemistry. The wellbore simulator used in this study is a commercially-available software package, WELLSIM, developed by Geothermal Energy New Zealand Limited (GENZL) and Auckland UniServices Limited, based on the work of Hadgu (1989). The structure of the program is described in Gunn and Freeston (1991a). The latest version of the WELLSIM simulator gives the user: a choice of five different two-phase flow correlations for evaluating pressure drop; the PVT package for H_2O-CO_2-NaCl systems described in Andersen et al. (1992); a pre-processing module to check the accuracy of input data; a matching analysis module; and, a method for assessing the consistency of downhole pressure and temperature measurements, termed lower bound analysis.

A comparison of the five two-phase flow correlations as implemented in WELLSIM has been performed by Probst et al. (1992), and a description of the preprocessor, matching and lower bound modules is in Gunn et al. (1992). WELLSIM is also capable of analysing multi-feed zone wells, although in order to accurately and uniquely characterise flow in such a well, feed zone input data has to be known precisely; such data is not often available.

WELLSIM is a steady-state wellbore simulator, and so assumes that the simulated conditions do not vary significantly with respect to time, and thus the discharge is considered to be "stable". The changes with time that occur in wellhead conditions due to changes in the reservoir are outside the scope of this study.

The wellhead or deepest feed input parameters to the simulator, include: pressure; temperature; enthalpy; mass flowrate; fluid type (i.e. liquid, superheated steam, or two-phase); fluid impurity content (i.e. the amount of dissolved solids and non-condensable gases); and, dryness fraction.

OUTPUT CURVES

The output curve for a well is the plotted relationship of discharging mass flowrate against wellhead pressure. This is sometimes referred to as either a "deliverability curve" or "productivity curve". The form of this relationship can determine the suitability of a well for energy production. The wellhead pressure can be controlled through choke valves which in turn alters the discharging mass flowrate of the well, and thus the output curve can be found directly from well testing.

Wellbore simulators can be used to estimate the full output curve based on one or two measured points, saving additional well tests. Furthermore, a simulator can be applied to predicting the effects of changes in well design on well productivity. Hadgu and Freeston (1986) and Freeston and Hadgu (1986) describe the application of wellbore simulators to management problems in a geothermal field, and in particular examine the effects of changes in well design. Barnett (1989) describes a theoretical study of the effect of wellbore diameter on well output for a well in the Eburru geothermal field in Kenya.

Barnett (1989) discusses that where a reservoir is sufficiently permeable it can supply fluid at a greater rate than that which the well is able to deliver to the surface. Such behaviour is termed *wellbore controlled flow*, as it occurs when the pressure drop up the well is substantially greater than the *pressure drawdown*. Pressure drawdown in this study does not refer to pressure changes in the reservoir over time, but to the pressure difference between the static reservoir pressure at the primary feed zone when the well is shut-in, and the pressure at that feed whilst the well is discharging. It can be inferred that when wellbore controlled flow occurs, larger well diameters should provide more favourable well output characteristics than smaller wells. However, the important consideration is as to whether the increased cost of the larger wellbore is sufficiently offset by the value of the greater rate of steam flow that might be delivered.

RESERVOIR/FEED RESPONSE CURVES

The reservoir/feed response curve is similar to an output curve for the well, but at depth, rather than at the wellhead. It is also a function of mass flowrate against pressure, although in this case it is the pressure at the feed that is of interest.

The most desirable method of determining the reservoir/feed response curve is to measure it directly. By taking downhole pressure and temperature measurements during discharge of the well at a number of different mass flowrates, pairs of mass flowrate and feed pressure can be observed. In general, if these measurements have been taken with suitable accuracy, the data can be fitted to one of a number of typical equations describing the reservoir/feed response curve. The equations used to fit such curves are termed "drawdown relationships".

Drawdown relationships express the pressure drawdown as a function of the mass flowrate of the fluid entering the wellbore from the reservoir. This pressure drop or drawdown from undisturbed (i.e. static) conditions in the reservoir, to full flow in the wellbore, is caused by a combination of laminar, turbulent, and wellbore entrance effects, amongst others.

For two-phase feeds, or feeds with high mass flowrates, one general form of this relationship is shown in equation (1) (e.g. Gunn and Freeston, 1991b).

$$p_r - p_f = aW + bW^2 \qquad (1)$$

where: p_r = undisturbed (static) reservoir pressure; p_f = feed zone pressure; W = feed zone mass flowrate; a = first order drawdown parameter (a constant); and, b = second order drawdown parameter (a constant).

Drawdown relationships for dry or superheated steam feeds have another form that is also second order, but in addition includes a "drawdown exponent" as seen below in equation (2), (e.g. Bodvarsson and Witherspoon, 1985).

$$W = C(p_r^2 - p_f^2)^n \qquad (2)$$

where: C = steam drawdown parameter/coefficient; and n = steam drawdown exponent.

Where feed zone mass flowrate and pressure measurements are available, the unknown drawdown parameters in the appropriate expression from above can be found directly. It is unlikely that the relationships will fit the measured data exactly, but the unknown parameters can be varied until the best fit is found.

It is generally assumed that the reservoir/feed response can be considered independent of well design and diameter. This assumption means that once appropriate drawdown parameters are established for a particular well, based on observed conditions, then the effect that any desired change in well design has on the output curve for that well can be predicted. This can be done by performing a series of wellbore simulations over a range of mass flowrates using deepest feed zone conditions as the input parameters, and by specifying the change in well design. The results of the simulations provide the estimated new wellhead pressure for each discharging mass flowrate and thus the output curve for the new design. The change in productivity can be found by comparing the new and existing output curves at the operating wellhead pressure.

PRESSURE/TEMPERATURE PROFILES

Measurements of downhole pressure and temperature are difficult to obtain in a flowing well; they are mass flow limited where wireline-type logging is used, due to drag of the toolhead. Simulation at higher mass flowrates is therefore useful in characterising feed zone characteristics.

The mass and energy equations governing the conditions at a secondary feed are presented in Bjornsson (1987), who postulates six possible flow directions and conditions in the wellbore close to the feed zone, depending on the

characteristics of the feed zones (inflow or outflow) and the type of well behaviour, production or injection. As noted above, the values of secondary feed enthalpy and mass flowrate are not usually available as simulator input conditions, but Bjornsson (1987) suggested that varying their magnitude until good matching is achieved can at least provide feasible estimates. However, the solution can be non-unique because more than one set of feed zone parameters might satisfy the data. The decision as to which set of parameters is the most accurate may require other independent data, such as the use of geochemical information at a feed zone to define an enthalpy.

The feed zone is generally assumed in a wellbore simulator to act at a point around which pressures are invariant. In reality, mixing of fluids and the subsequent changes in properties of the mixed fluid will occur over a zone or region rather than at a point.

Where two feeds contribute fluids of different temperature, it is possible that the downhole temperature profile will exhibit a discontinuity about the feed point. Such discontinuities will be pronounced where the fluid causes a phase transition at the feed. This will occur when a high enthalpy two-phase fluid enters the well above a liquid feed, or alternatively a lower enthalpy liquid feed overlies a two-phase zone. The well examined in Case Study 2 of this paper exhibits such a temperature discontinuity.

CASE STUDY 1 - WELL OUTPUT

For the first case study, WELLSIM has been used to assess the possible benefits of drilling larger wells in a vapor-dominated field. The field already has a number of producing wells, each with a $9\frac{5}{8}$" production casing and 7" liner. The proposed larger well design involves a $13\frac{3}{8}$" casing and $10\frac{3}{4}$" liner. Measured output curves are available for most wells, but measurements of feed mass flowrate and pressure are not.

WELLSIM has initially been used to determine the reservoir/feed response curves for each well, based on the observed wellhead conditions. The results of these simulations thus produce a typical range of responses throughout the reservoir. A "representative well" can then be modelled. This well has been simulated over the range of typical feed responses and depths for both the current well design and the proposed larger well design, in order to predict the relative increase in production that might be recognised by drilling larger wells in future.

Points on the reservoir/feed response curves for each well are estimated from the results of a series of wellhead/down simulations, using points on each measured output curve as simulator input parameters. The casing and liner sizes and the feed depth are also specified, assuming a single feed, as are the other input parameters such as enthalpy and gas content. WELLSIM contains a preprocessing module which ensures that wellhead or feed input parameters are complete and/or consistent. For each pair of output mass flow and pressure measurements, the simulation produces pairs of feed mass flow rate and pressure at the feed depth. With an assumed undisturbed reservoir pressure, values of C and n can be estimated from equation (2). A least squares best fit value for these drawdown parameters can then be determined.

The representative well has been modelled with a typical feed enthalpy of 2800 kJ/kg, a gas content of 0.15% by weight, and no salts. An undisturbed reservoir pressure of 36 bara has been assumed.

Once the values of the feed productivity (C) were determined for the actual wells, three different values of C were selected for the representative well as being typical of actual well behaviour. A value of $n = 0.75$ was used in all cases, as it was found that this value was applicable to all the actual wells. As noted also by Rumi (1972), using a field-wide value for n, reduces the complexity of the problem, and allows all the values to be compared on the same basis, as they all have the same units.

The first value is $C = 0.75$ t/(hr.bara$^{1.5}$). It is suggested that this value can be considered to relate to a steam well that is a good producer (around 8 MW), either with a fairly good permeability, or with a fairly large negative skin factor.

The second value used is $C = 0.375$ t/(hr.bara$^{1.5}$) which is half the previous value. This value is probably more typical of the mean value of C for wells drilled in the production phase. The final value used is $C = 1.5$ t/(hr.bara$^{1.5}$) and it is suggested that this value is typical of the most productive wells in the field.

The current and larger well designs have both been modelled as having a casing shoe at 900m. For each value of C, three cases have been simulated with the primary feed at 1000 m, 1300 m, and also at 1600 m.

RELATIONSHIP BETWEEN PERMEABILITY AND WELL PRODUCTIVITY

The effect of a variation in feed productivity on the predicted increase in production from the current to the larger well design is shown in Figure 1. For each case the increase in production is considered at the three different primary feed depths and at operating pressures of 10 bara and 15 bara.

It can be clearly seen that the more productive the feed, then the greater is the increase in production between two

well designs. From this conclusion it can be inferred that a well that intersects highly permeable regions stands to benefit significantly from a larger casing and liner.

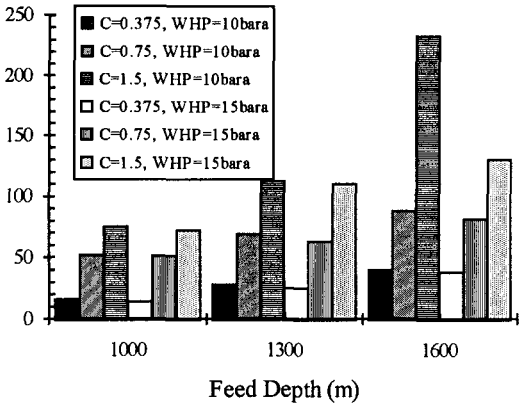

Figure 1: Effects of variations in feed productivity (C) and feed depth, on the production increase between the current and larger well designs for the representative well.

This result demonstrates the effect of wellbore controlled flow, because the wellbore has more control over the flow for high values of C. In other words, the wellbore diameter affects the flow more where the feed zones are highly productive. The converse is also true. Where C is low, then the flow is controlled more by the reservoir/feed response relationship. This is clearly illustrated in Figure 2, which presents a selection of the cases run. Of the cases where C = 0.375 t/(hr.bara$^{1.5}$) the reservoir/feed response curve lies only just above the output curve that provides the greatest well productivity. At a particular operating pressure any well must have an output that is less than the feed mass flowrate found at that pressure on the response curve.

For example, with C = 0.375, the feed mass flowrate at a feed pressure of 15 bara is 70 t/hr. This means that the production can never be more than 70 t/hr if the wellhead operating pressure is 15 bara. From Figure 2, the most productive output curve where C = 0.375 is for the larger well design with a 1000 m feed. The difference between the production at 15 bara, and the feed mass flowrate at 15 bara is only 4 t/hr. This means that increasing the diameter of the well any further serves little purpose.

In general the output curves for the larger well design where C = 0.375 come very close to the reservoir/feed response curve. The feed zone depth has less effect on the production with the larger well design. This indicates that using a $13\frac{3}{8}$" casing and $10\frac{3}{4}$" liner can be considered relatively optimal for these type of vapor-dominated reservoir conditions, as a bigger well cannot improve production significantly. Such fairly "flat" reservoir/feed response curves can be considered more indicative of reservoir controlled flow.

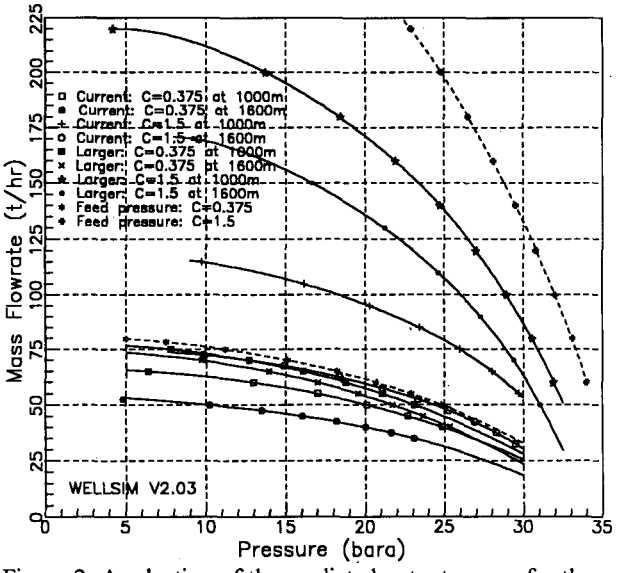

Figure 2: A selection of the predicted output curves for the representative well.

CASE STUDY 2 - MULTIPLE FEED WELL

In the second case study WELLSIM has been used to attempt to characterise a multiple feed well. The well selected is from a liquid-dominated reservoir with very low concentrations of dissolved salts and non-condensable gases. The production casing is $9\frac{5}{8}$", and the liner is $7\frac{5}{8}$" running from 1218 m to 2879 m. The well deviates by 23° from the vertical below 500 m. The main permeable zone lies between 1898 - 2084 m. Minor permeable zones are found between 1384 - 1430 m, 1522 - 1720 m, 2226 - 2321 m, and 2506 - 2592 m. The discharge data available for the well is for a mass flowrate of 58 kg/s and enthalpy of 1313 kJ/kg, at a wellhead pressure of 2.5 MPag.

WELLSIM has five different two-phase flow correlations that can be used. Using the input data above, a comparison of each correlation was made with the measured downhole pressure and temperature profiles, and it was decided to use the Duns and Ros correlation, as this gave the better match for pressure and temperature above the shallowest feed zone. Probst et al. (1992) also recommend using Duns and Ros for wells exhibiting similar characteristics.

The approach used was to characterise each feed in turn, beginning with the shallowest feed and working down to the wellbottom. The possible conditions at the feed for enthalpy can be indicated by carefully studying the measured temperature profile for changes in gradient. The measured profile is Curve 4 shown in Figure 3. Based on the measured wellhead conditions, the simulated temperature profile found by assuming only a single feed at

2600 m, is Curve 1 in Figure 3. It can be seen that this starts to deviate from the measured profile below 1700 m, which is near the location of the two shallowest feed zones.

The first noticeable change in the measured temperature gradient occurs just below 1200 m, and this is most likely due to the transition from liner to casing. This conclusion is confirmed by studying the change in measured pressure gradient at this depth (see Curve 4 in Figure 4).

The measured temperature gradient continues to change below 1200 m, and this will be due to the two shallowest feeds. The enthalpy at the major feed between 1898 and 2084 m is clearly indicated by the minimal change in temperature between 1900 and 2100 m, which only varies from 288 to 289°C. Such a small change in temperature represents liquid flow, and the enthalpy of the major feed is thus the liquid phase enthalpy of pure water at 289°C, about 1280 kJ/kg. Just above 1900 m the fluid flashes.

It was decided to model the two shallowest feeds at a single point, 1400 m, as it is not really possible to distinguish between them, given the only small change in temperature gradient that is observed. The conditions of the fluid entering at this point must be such that they mix with the fluid from below, which has an enthalpy around 1280 kJ/kg, and results in a fluid which has an enthalpy of 1313 kJ/kg at the wellhead. The other constraint is that these feeds are minor feeds, so it can probably be assumed that they contribute less than half the total flow.

Performing a mass and energy balance about the 1400 m feed point, given the above constraints, provides a functional relationship between the enthalpy and mass flowrate of the feed. Various values of feed flowrate at 1400 m were tested with the simulator, and the resultant pressure and temperature profiles were compared with the measured profiles from the wellhead down to the next feed at 2100 m. The most reasonable match was found for a mass flowrate of 15 kg/s and enthalpy of 1459 kJ/kg. This result is shown in Curve 2 for both Figures 3 and 4.

To characterise the major feed at 2100 m, requires matching the pressure and temperature profiles from 2100 m to the next significant feed. If the fluid below 2100 m is in fact flowing, then from the measured temperature profile, it appears to be two-phase until a depth of around 2500 m. The temperature below this depth remains fairly constant at 318 °C, indicating an enthalpy of around 1450 kJ/kg. If the fluid were in fact static then it is less likely that the temperature gradient would remain constant.

Like the two shallow permeable feed zones, it is difficult to distinguish the two lower permeable zones. These have been modelled together at 2600 m. The conditions of the fluid entering at the major feed at 2100 m must be such that they mix with the fluid from the lowest feed at 2600 m, with an enthalpy of 1450 kJ/kg, and results in a fluid which has an enthalpy of 1280 kJ/kg above the major feed. As this feed is considered to be the major feed, it probably contributes more than half the total flow.

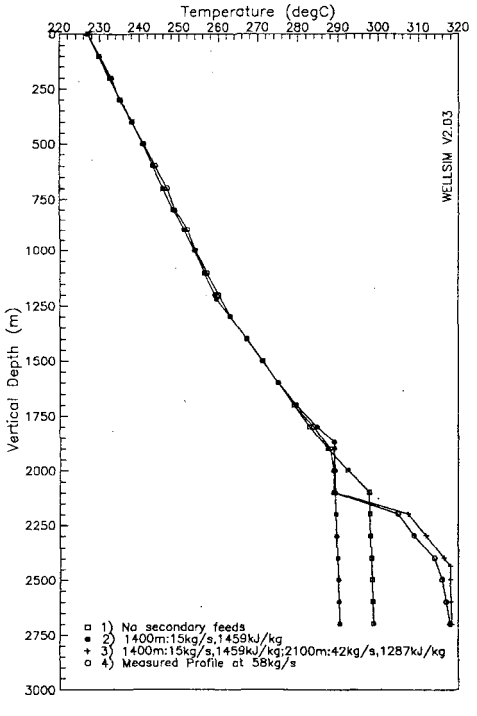

Figure 3: Simulated vs measured temperature profiles.

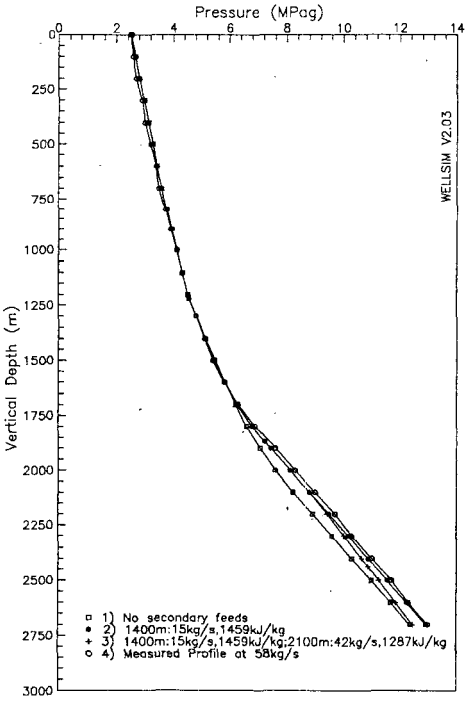

Figure 4: Simulated vs measured pressure profiles.

A functional relationship between the enthalpy and mass flowrate at the 2100 m feed point again can be derived by performing a mass and energy balance. Various values of feed flowrate at 2100 m were tested with the simulator, and the most reasonable matches were found at high mass flowrates. Conditions of 42 kg/s and 1287 kJ/kg were found to give the excellent match shown by each of Curves 3 in Figures 3 and 4. The simulated pressures are within 4.5% of the measured values from wellhead to 2600 m, and the temperatures are within 0.5%.

CONCLUSIONS

The first case study has demonstrated the use of WELLSIM to characterising reservoir/feed response relationships, and then using these relationships to compare the potential production differences between two sizes of wells. From the results, it can be inferred that wells which intersect highly permeable and productive feed zones and exhibit *wellbore controlled flow*, will benefit significantly from a large wellbore design. Where wells consistently intersect producing zones of low to intermediate permeability the additional increase is unlikely to be justified, as productivity gains are limited by the reservoir/feed response relationship.

From the second case study, it has been demonstrated that feed zone conditions can be characterised by a combination of, examining changes in the measured temperature gradient, and performing matching analyses with a wellbore simulator. Where liquid flow exists in a part of the well it becomes fairly simple to derive a relationship between the mass flowrate and enthalpy at each feed, and then use the simulator to determine the most suitable pair of flowrate and enthalpy values. It is clear that for this procedure to be successful, accurate downhole data must be available.

ACKNOWLEDGEMENTS

The authors gratefully acknowledge the management of GENZL for permission to publish this paper. Also, thanks are expressed to R.E. Tilos (PNOC-EDC, Philippines) for performing many of the simulations used for Case Study 2.

REFERENCES

Andersen, G., Probst, A., Murray, L. and Butler, S. (1992) "An Accurate Model for Geothermal Fluids as Represented by H_2O-CO_2-NaCl Mixtures". Proc. 17th Workshop on Geothermal Reservoir Engineering, Stanford University.

Barnett, B. (1989) "A Theoretical Study of the Effect of Bore Diameter on Well Outputs". Proc. 11th N.Z Geothermal Workshop, Auckland University, pp. 181-187.

Bodvarsson, G.S. and Witherspoon, P.A. (1985) "Flowrate Decline of Steam Wells in Fractured Geothermal Reservoirs". Proc. 10th Workshop on Geothermal Reservoir Engineering, Stanford University, pp. 105-112.

Barelli, A., Corsi, R., Del Pizzo, G. and Scali, C. (1982) "A Two-Phase Flow Model for Geothermal Wells in the Presence of a Non-Condensable Gas". Geothermics 11, 175-191.

Bjornsson, G. (1987) "A Multi-Feed Zone Wellbore Simulator". Masters Thesis, University of California, Berkeley.

Freeston, D. and Hadgu, T. (1986) "Calculation of Output Characteristics of Shallow Wells". Proc. 8th N.Z. Geothermal Workshop, Auckland University, pp. 69-73.

Gunn, C. and Freeston, D. (1991a) "An Integrated Steady-State Wellbore Simulation and Analysis Package". Proc. 13th N.Z. Geothermal Workshop, Auckland University, pp. 161-166.

Gunn, C. and Freeston, D. (1991b) "Applicability of Geothermal Inflow Performance and Quadratic Drawdown Relationships to Wellbore Output Curve Prediction". Geothermal Resources Council Trans., Vol. 15, pp. 471-475.

Gunn, C., Freeston, D. and Hadgu, T. (1992) "Principles for Wellbore Simulator Validation and Calibration Using Matching Analysis - I: Analytical Techniques". Geothermics 21, 363-376.

Hadgu, T. (1989) "Vertical Two-Phase Flow Studies and Modelling of Flow in Geothermal Wells". Ph.D. Thesis, Auckland University.

Hadgu, T. and Freeston, D. (1986) "Application of Wellbore Simulators to Management Problems for a Geothermal Field - Case Studies". Proc. 9th Australasian Fluid Mechanics Conference, Auckland University, pp. 204-207.

Probst, A., Gunn, C. and Andersen, G. (1992) "A Preliminary Comparison of Pressure Drop Models Used in Simulating Geothermal Production Wells". Proc. 14th N.Z. Geothermal Workshop, Auckland University, pp. 139-144.

Rumi, O. (1972) "Some Considerations on the Flowrate/Pressure Curve of the Steam Wells at Larderello". Geothermics 1, 13-23.

PROCEEDINGS, Eighteenth Workshop on Geothermal Reservoir Engineering
Stanford University, Stanford, California, January 26-28, 1993
SGP-TR-145

INTERFERENCE TEST ANALYSIS AT THE TAKIGAMI GEOTHERMAL FIELD, JAPAN

Ryuichi ITOI(1), Michihiro FUKUDA(1), Kenji JINNO(2) and Hiroki Gotoh(3)

(1)Geothermal Research Center, Kyushu University, Kasuga, JAPAN 816
(2)Faculty of Engineering, Kyushu University, Fukuoka, JAPAN 812
(3)Idemitsu Geothermal Co. Ltd, Chiyodaku, Tokyo, JAPAN 100

ABSTRACT

A long term interference test was conducted under conditions of multiwell variable flow rate at Takigami for about ten months in 1987. The test data have been analyzed with an on-line analysis method on the basis of the line-source solution. This method employs Kalman filtering to process the data and then provides the best estimates of reservoir transmissivity and storativity when a new pressure data at an observation well becomes available. The pressure changes measured at seven observation wells have been analyzed with the present method using an infinite reservoir model. The data from one observation well have been further analyzed assuming a presence of a linear boundary. Performances of the parameters estimated for different reservoir models are compared. Fairly good estimates of reservoir parameters are obtained on the basis of an infinite reservoir model for two wells using the entire pressure data whereas for other five wells using a part of the pressure data.

INTRODUCTION

Pressure interference tests have advantages in providing information on average values of reservoir parameters such as transmissivity(T) and storativity(S) in the area where observation and active wells are located(Leaver et al., 1988; Gotoh, 1990). Computer assisted methods to analyze the test data are powerful tools for reservoir engineers. This is because that conventional methods of type curve matching have some difficulties in processing actual situations such as multiple active wells varying their flow rate with time. Two computer codes have been developed on the basis of the line-source solution derived under assumptions of homogeneous, isotropic, and porous type of reservoir (McEdwards and Benson, 1981;Arellano et al., 1990). This solution is superposed both in time and space to meet the situation above and the presence of hydrologic boundary by introducing image well(s). These codes have employed the nonlinear least squares method for parameter determination, because the solution is nonlinear with respect to the reservoir parameters. These programs, however, store all the pressure data at an observation well during computation, requiring a large memory on a computer. Furthermore, poor initial guesses of the parameters may lead to the failure in determining good estimates.

In order to cope these problems, particularly for the analysis using personal computers, we have developed methods to analyze interference test data using Kalman filtering(Itoi et al., 1990; Itoi et al., 1992). On the assumption of a series of pressure data measured at an observation well, these methods yield best estimates of unknown parameters at every moment when a new pressure value becomes available. In this paper, we have analyzed the interference test data at the Takigami geothermal field with the method which is an expansion of the Sen's work (Sen,1984;Itoi et al., 1992). The results indicate that the estimated transmissivity from seven observation wells varies in the range from 1.04×10^{-7} to 8.91×10^{-7} $m^3/Pa \cdot s$.

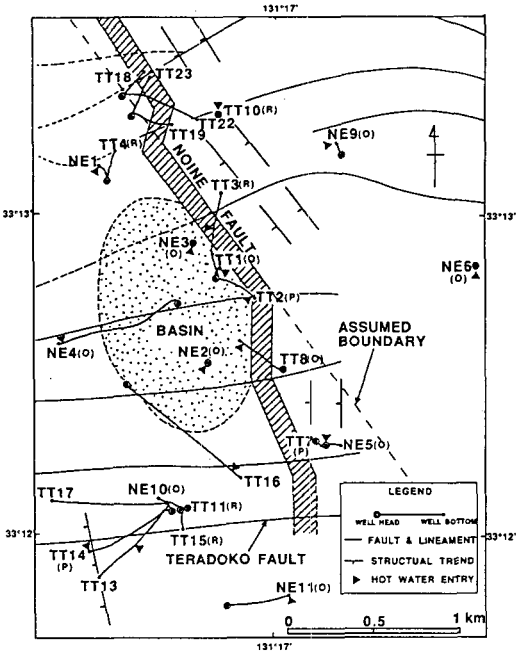

Fig.1 Location map of wells at the Takigami geothermal field. Signs of (P) denote the production well, (R) the reinjection well, and (O) the observation well during the interference test(modified after Hayashi et al., 1988)

INTERFERENCE TEST AT TAKIGAMI

The Takigami geothermal field is located in the Beppu-Shimabara graben in Kyushu Island, Japan. This field has been under exploration for power generation since 1979, and a power plant of installed capacity 25 MW is expected starting its operation in 1996. The interference test in 1987 was conducted with three production wells which discharged enough fluids to generate 26 MW of electricity. The fluid production had been continued for about six months, and the separated water was reinjected through five

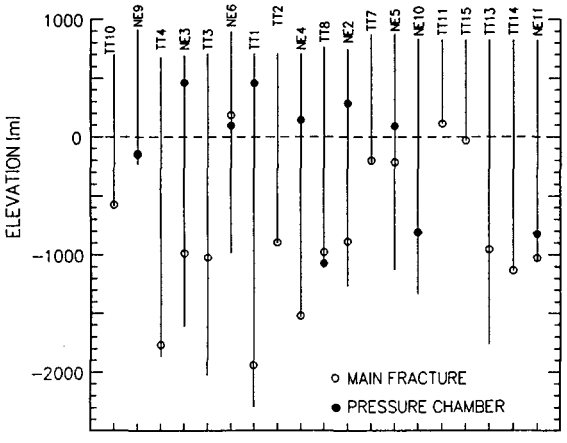

Fig.2 Depths of well, main fracture(open circle), and pressure chamber(solid circle).

reinjection wells(Hayashi et al., 1988). The pressure changes caused by operating these wells had been monitored at seventeen wells including these active wells with pressure measurement apparatus of capillary tube type. Seven out of ten observation wells presented apparent pressure response during the test.

Fig. 1 shows the location map of wells and geological features at Takigami. The reservoir is of water dominated type, and is divided into two areas by the Noine fault running NNW to SSE as shown in Fig.1. High temperature zone at about 250 °C has been found in the south-western part of the field and lower temperature zone in the north-eastern part(Hayashi et al.,1988). Therefore, a reservoir management will be designed to separate production and reinjection zones horizontally by 1 to 2 km to avoid the inflow of reinjected water into the production zone. Fig.2 shows the depths of main fracture or main water loss zone, indicated by the open circle, of the wells which were used during the test in 1987. The solid circle represents the installed depths of pressure chamber for downhole pressure measurement at the observation wells.

Figs.3(a) and (b) show the flow rate history of production and reinjection wells, respectively. Flow rate of production wells was kept almost constant during the test except TT14 ranging its flow rate 200 -270 m^3/h. On the other hand, all reinjection wells show highly variable flow rates with time. Both production and reinjection wells were stopped their operation by about 2.8×10^5 min since the start of the test. Very good communication between the two reinjection wells, TT11 and TT15, was confirmed, thus their flow rates are added and presented as a single flow rate shown in Fig.3(b).

ANALYSIS METHOD OF INTERFERENCE TEST

Pressure response at an observation well caused by producing or reinjecting fluids at a constant flow rate at an active well can be expressed by the line-source solution on the basis of isotropic, homogeneous, and infinite porous type of reservoir. The effects of multiple active wells and their flow rate change with time on the pressure response can be expressed by superposing the line-source solution

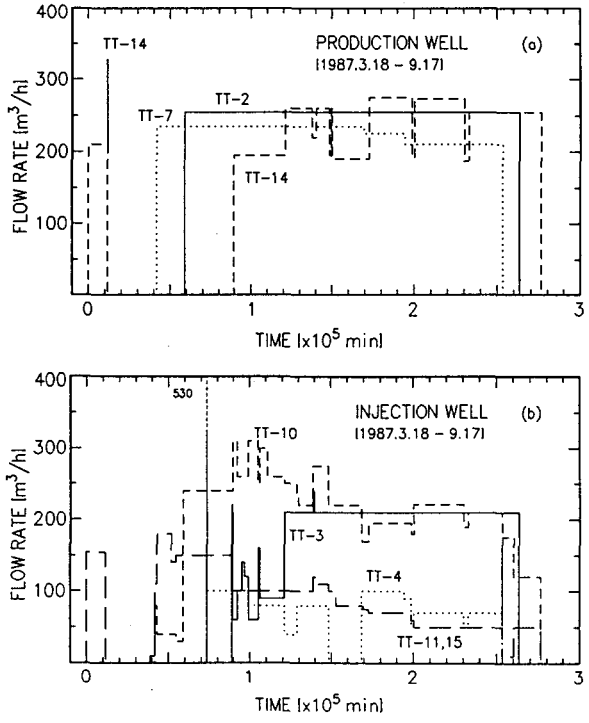

Fig.3 Flow rate history of (a)production wells and (b) reinjection wells.

both in time and space. Moreover, the variable flow rates can be processed by dividing these into a series of linear segments of flow(McEdwards and Benson, 1981). Thus, pressure change at an observation well at time t_k (k=1,2, •, •) can be expressed as

$$\Delta p(t_k) = \frac{1}{4\pi T}\sum_{n=1}^{N}\left(\sum_{j=1}^{J} C_{n,j}\right) \qquad (1)$$

where $\Delta p(t_k)$ is the pressure change at the observation well at time t_k, T is the transmissivity(=kh/μ, k:permeability, h:reservoir thickness, μ:viscosity of fluid). N is the total number of active wells, j is the number of flow segments, and J is the total number of flow segments prior to the time t_k. $C_{n,j}$ is expressed as follows

for $1 \le j \le J-1$

$$C_{n,j} = \left[A_{n,j} + B_{n,j}(t_k - \tau_{n,j})(1 + u_{n,j})\right]\left[Ei(-u_{n,j+1}) - Ei(-u_{n,j})\right]$$
$$- B_{n,j}\left[(t_k - \tau_{n,j})exp(-u_{n,j}) - (t_k - \tau_{n,j+1})exp(-u_{n,j+1})\right] \qquad (2)$$

for $j = J$

$$C_{n,j} = \left[A_{n,j} + B_{n,j}(t_k - \tau_{n,j})(1 + u_{n,j})\right]\left[-Ei(-u_{n,j})\right]$$
$$- B_{n,j}\left[(t_k - \tau_{n,j})exp(-u_{n,j})\right] \qquad (3)$$

and $u_{n,j}$ and u_{nj+1} are

$$u_{n,j}=\frac{Sr_n^2}{4T(t_k-\tau_{n,j})} \quad (4) \qquad u_{n,j+1}=\frac{Sr_n^2}{4T(t_k-\tau_{n,j+1})} \quad (5)$$

where $A_{n,j}$ is the flow rate of j-th segment of n-th active well at time t_k, $B_{n,j}$ is the inclination of this flow segment, $\tau_{n,j}$, $\tau_{n,j+1}$ are the time when j-th flow segment of n-th active well begins and ends, respectively. $Ei(-u)$ is the exponential function of u, S is the storativity(=ϕch, ϕ: porosity, c:compressibility), and r_n is the radial distance between n-th active well and the observation well.

A presence of a hydrologic boundary in the test area can be modelled by assuming it as a linear vertical boundary. The effects of the presence of the linear boundary on pressure behavior at the observation well can be generated by locating image well(s) at a symmetric position across the boundary(Matthews and Russell, 1967; Sageev, et al., 1985). To simplify the subsequent notation , we denote the time t_k by expressing variables with subscript k. Therefore, the pressure response in the presence of the linear boundary is given

$$\Delta p_k = \Delta p_{aw} \pm \Delta p_{im} \quad (6)$$

where Δp_{aw} represents the pressure change caused by operating active wells and Δp_{im} by image wells. Positive sign is for the impermeable boundary and negative one for the constant pressure boundary. Further formulation is developed on the basis of Eq.(1) for the simplicity.

Eq.(1) represents a relation between the measured pressure change at an observation well and the reservoir parameters, T and S, to be estimated, thus this equation corresponds to the measurement equation to form Kalman filtering. This relation, however, is apparently nonlinear with respect to the reservoir parameters. Thus, this equation should be linealized to form Kalman filtering. For this purpose, we have adopted and modified Sen's technique(Sen, 1984) in which he analyzed a pumping well test to estimate aquifer parameters using Kalman filtering under conditions of constant flow rate from a single pumping well. In order to form the observation equation, an additional formula defining u_k is introduced

$$u_k = \sum_{n=1}^{N} u_{n,J} = \frac{S}{T}\sum_{n=1}^{N}\frac{r_n^2}{4(t_k-\tau_J)} \quad (7)$$

Taking logarithms of both side of Eqs.(1) and (7), and by rearranging, we obtain

$$\log \Delta p_k - \log\left[\frac{1}{4\pi}\sum_{n=1}^{N}\left(\sum_{j=1}^{J} C_{n,j}\right)\right] = -\log T \quad (8)$$

$$\log u_k - \log\left[\sum_{n=1}^{N}\frac{r_n^2}{4(t_k-\tau_J)}\right] = -\log T + \log S \quad (9)$$

Writing the left side of the equations as y_1 and y_2 leads to the observation equation in a vector form:

$$\mathbf{y}_k = H_k\mathbf{x}_k + \mathbf{v}_k \quad (10)$$

where $\mathbf{y}_k = [y_1, y_2]^T$ $\mathbf{x}_k = [\log T, \log S]^T$

H_k is the observation matrix and is time invariant as

$$H_k = \begin{bmatrix} -1 & 0 \\ -1 & 1 \end{bmatrix} \quad (11)$$

$[\,]^T$ indicates transposition. Eq.(10) is apparently a linear function of $\mathbf{x}$ whose components are logarithms of T and S. The reservoir parameters, T and S, can be assumed to be constant during the test, and hence the state equation can be written

$$\mathbf{x}_{k+1} = \mathbf{x}_k + \mathbf{w}_k \quad (12)$$

where $\mathbf{v}_k$ and $\mathbf{w}_k$ are the measurement and state noises assumed to be zero-mean, mutually uncorrelated, white noise of covariance matrices V_k and W_k, respectively.
On the basis of the reservoir system described by Eqs.(10) and (12), the algorithm of Kalman filtering provides the best estimate of state vector at time t_k when a new measurement becomes available. By denoting the best estimate at t_k as $\hat{\mathbf{x}}_{k/k}$ where the "hat" indicates estimate, this will be given by updating the previous estimate, $\hat{\mathbf{x}}_{k/k-1}$, as follows

$$\hat{\mathbf{x}}_{k/k} = \hat{\mathbf{x}}_{k/k-1} + K_k(\mathbf{y}_k - H_k\hat{\mathbf{x}}_{k/k-1}) \quad (13)$$

where K_k is the Kalman gain matrix and is given as

$$K_k = P_{k/k-1}H_k^T\left[H_kP_{k/k-1}H_k^T + V_k\right]^{-1} \quad (14)$$

Superscript -1 denotes inversion. The error covariance matrix associated with the present estimate is expressed as

$$P_{k/k} = P_{k/k-1} - K_kH_kP_{k/k-1} \quad (15)$$

For estimating process at the next time step, the state vector is predicted by

$$\hat{\mathbf{x}}_{k+1/k} = \hat{\mathbf{x}}_{k/k} \quad (16)$$

and the error covariance matrix is given as

$$P_{k+1/k} = P_{k/k} + W_k \quad (17)$$

Calculations of parameter estimating can be started by giving initial values for P and $\mathbf{x}$. The components of the observation vector expressed by the left-hand sides of Eqs.(8) and (9) can not be calculated even when a new pressure value at time t_k becomes available, because these components include the parameters to be estimated. Hence these values are substituted by the prior estimates: $\mathbf{x}_{k/k-1}$ (Sen, 1984). This substitution may introduce false information into the components of the observed vector when the poor initial guesses of parameters are given. As a result, the method fails to determine the good estimates at each time step. To overcome this deficiency, we repeat a whole calculation process in which parameters are estimated using pressure data from beginning to end of the measurement. Here, we define the last estimates of parameters determined at a time when the last pressure

value is measured. Then, these final estimates obtained during the present iteration are given as the initial guesses for the next iteration process. Calculations are iterated until the differences between the newly obtained final estimates and the previous ones to satisfy a given convergence criterion. Fig.4 shows a flow chart for the calculation of parameter estimation above.

ANALYSIS OF INTERFERENCE DATA

The pressure data from seven observation wells(NE2, NE3, NE4, NE5, NE10, NE11, TT1) have been analyzed with the method in the preceding section on the basis of an infinite reservoir model. The data from NE11 have been further analyzed by assuming a presence of a linear boundary indicated by the dotted line in Fig.1.

The pressure data were recorded at an interval of six hours, and the total number of data collected for one observation well reached up to 1200 at maximum during the test. The data were, then, processed to extract one from every 10 pressure values and to remove faulty values apparently caused by malfunctioning of the measurement apparatus. The present method has been demonstrated that a convergence of estimation may be guaranteed as far as the ratio of initial guesses of T and S (S/T) being given to be one or less(Itoi et al., 1992). Thus, all calculations are started by giving initial values of $T=1\times10^{-5}$ m^3/Ps•s and $S=1\times10^{-5}$ m/Pa. In addition, initial values of diagonal and nondiagonal components of matrix P are given as 100 and 0, respectively. Covariance matrices of the measurement and the state noises are set to be constant as 0.01 and 0 for diagonal and nondiagonal parts.

In the following, the analyses of the data from NE11 are described in detail on the basis of an infinite reservoir model and of a model in the presence of a linear boundary. NE11 is a deviated well and located southern most part of Takigami as shown in Fig.1. Main water loss zone of this well seems to be on southward extension of the Noine fault. A careful examination of the measured pressure data of NE11 and the flow rate history of active wells seems to support the effects of interference by active wells TT14, and TT7 which is located eastern side of the Noine fault. Therefore, we have analyzed the pressure data by assigning the flow rates of these two active wells. The number of the pressure data used is 75. The data are first analyzed on the basis of an infinite reservoir model. Convergence of calculations is attained after four iterations of estimating process, and the final estimates obtained are $T=2.41\times10^{-7}$ m^3/Pa•s and $S=1.78\times10^{-7}$ m/Pa.

The present method provides estimates at each time step when a new pressure value becomes available, thus the estimated values of T and S are used to predict the pressure value at the next time step, $p_{k+1/k}$, which is compared with the measured value, p_{k+1}. Fig. 5(a) shows a comparison between the two kinds of pressure values during the fourth iteration process. The circle represents the measured pressure and the solid line the predicted one. The predicted pressure values show a fairly good match with the measured ones throughout the test period except in the later times when the pressure recovery starts. During this period, small discrepancies between the two kinds of pressures are recognized. The result implies that the estimated values at the present time are good enough to achieve nearly perfect prediction of the pressure value at the next time. Fig.5(b) shows the performances of estimated values of parameters

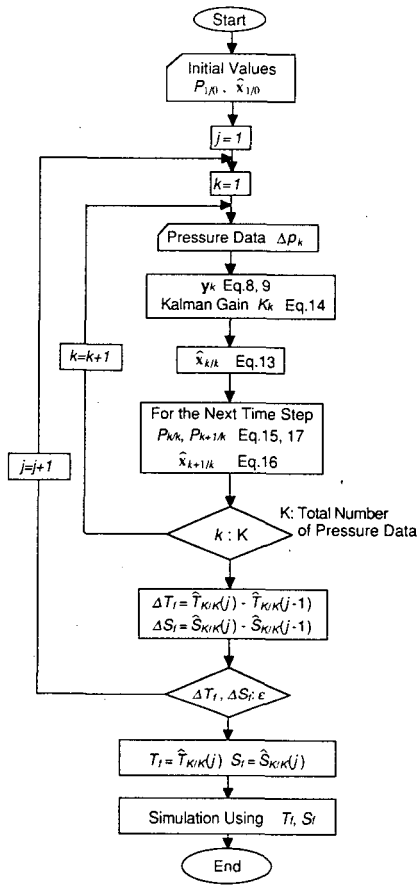

Fig.4 Flow chart for parameter estimation using Kalman filtering.

at each time step during the fourth iteration process. The circle represents the estimated transmissivity(T) and the triangle the estimated storativity(S). Small variations in both estimates can be seen in the early times of the data. This variation may be attributed to the flow rate history of TT14 which stopped and resumed discharging and that of TT7 which started discharging during this period as shown in Fig.3(a). Then, the estimates show gradual increases followed by stabilized values up to about 2.5×10^5 min. In turn, they exhibit continuous decreases as approaching the end of the measurement. The final estimates obtained are $T=2.41\times10^{-7}$ m^3/Pa•s and $S=1.78\times10^{-7}$ m/Pa. The pressure response was simulated using these final estimates, and the result is compared with the measured pressure values in Fig.5(c). Good matches are observed only for short periods in the very early and later times. The simulated pressure departs markedly with time from the measured ones up to 2.5×10^5 min. Then, the discrepancies between the two kinds of pressures become small as it approaches the end of the measurement. This poor match is attributed to the final estimates of T and S used for simulating the entire pressure data are lower than the estimates at the middle times. However, major features of the measured values such as sharp drop at about 0.4×10^5 min and start of pressure recovery when fluids production stopped are successfully reproduced.

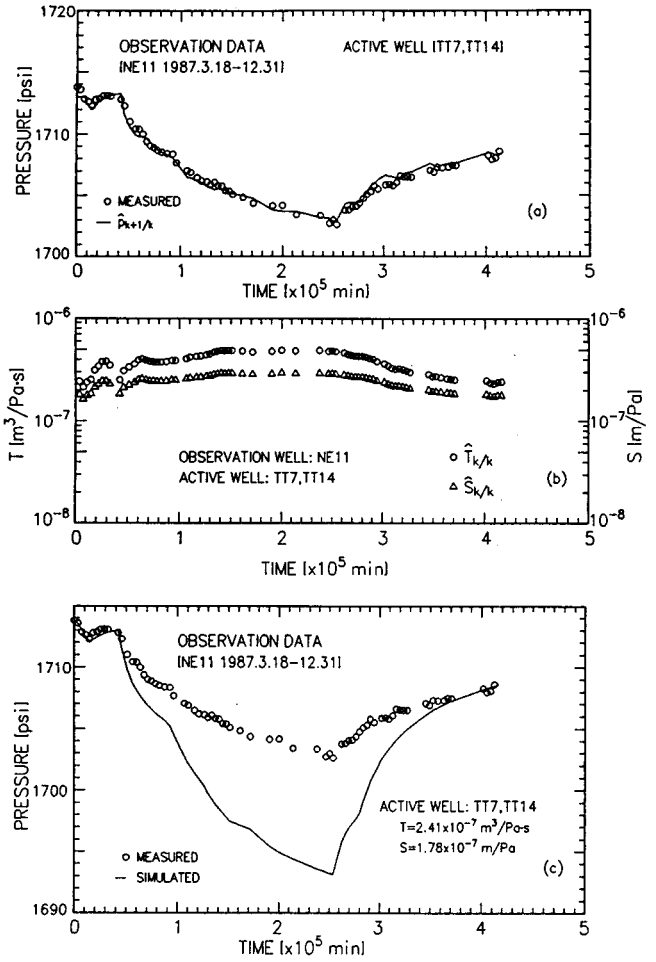

Fig.5 Results of analysis of the pressure data from NE11, (a)predicted pressure(solid line) compared with measured one during the fourth iteration process of parameter estimating, (b) performance of estimated transmissivity(T) and storativity(S) with time, (c) comparison of simulated pressure values using the final estimates of T and S with measured ones.

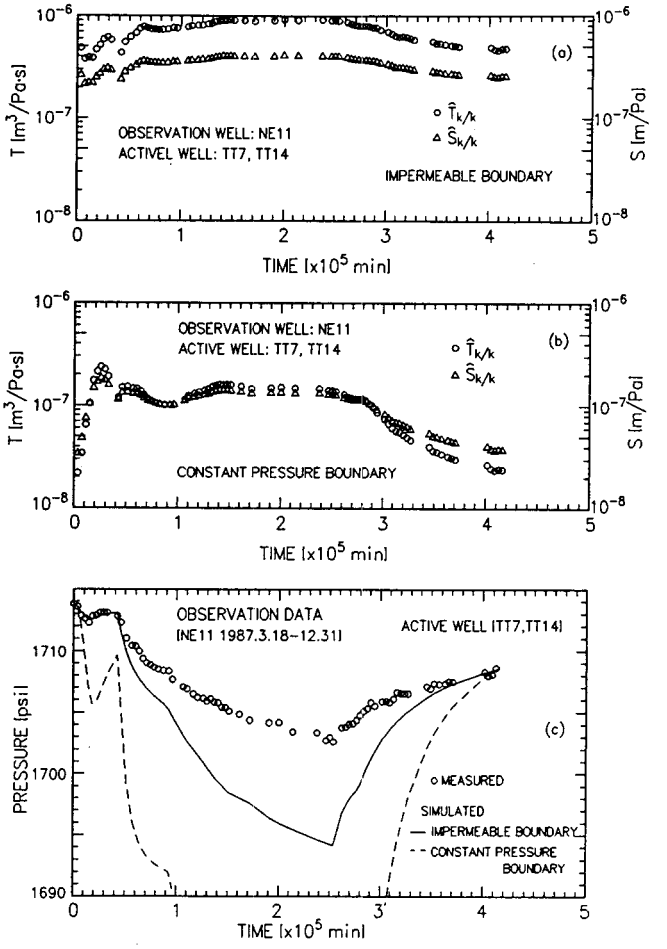

Fig.6 Results of analysis in a presence of a linear boundary for NE11, (a)performance of estimated transmissivity(T) and storativity(S) with time for the case of impermeable boundary, (b) for the case of constant pressure boundary, (c) comparison of simulated pressure values using the final estimates of T and S determined for the cases above.

Next, we have analyzed the data of NE11 with an infinite reservoir model in the presence of the linear boundary located as shown in Fig.1. NE11 is apparently received interference from both production wells of TT14 and TT7, and thus it may be reasonable to assume the presence of the boundary on the eastern side of TT7 if existed. Two kinds of linear boundaries, impermeable and constant pressure, are considered during the analysis. Figs.6(a) and (b) show performances of estimated parameter values of T and S for the cases of impermeable boundary(IB) and of constant pressure boundary(CPB), respectively. The result for the case of IB shows similar performance to that of the infinite reservoir case in Fig.5(b), but both estimates show larger values in comparison with those in Fig.5(b) throughout the test period. On the other hand, the case of CPB shows rapid rise in both estimates at the beginning followed by fairly stabilized values during the middle times. Decrease rates of estimates in the later times are, however, much larger compared with the case of IB. The final estimates attained are 1) T=4.75x10^{-7} m^3/Pa·s and S=2.55x10^{-7} m/Pa for the IB case, 2)2.40x10^{-8} m^3/Pa·s and 3.74x10^{-8} m/Pa for the CPB case. Both values of estimated transmissivity and storativity of the IB case are larger than those of the CPB case by an order of magnitude. These parameter values are used for simulating the pressure

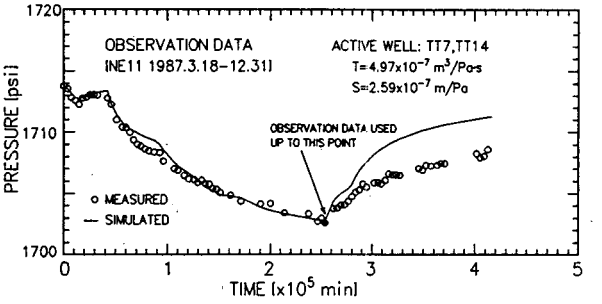

Fig.7 Comparison of simulated pressure values using the final estimates of T and S with measured ones for NE11.

response for each reservoir model, and the results are compared with measured data in Fig. 6(c). Discrepancies between the measured and the simulated values for the case of IB are similar to the result of an infinite reservoir model as shown in Fig.5(c). On the other hand, discrepancies between the two kinds of pressures for the CPB case are much larger than those for the IB case, implying that a constant pressure boundary is not likely to present at this part of the area. Therefore, these results suggest that no models could fully express the entire pressure data of NE11.

A careful examination of the estimation behaviors of T and S in Fig. 5(b) suggests that monotonous decreases in the estimates in the later times may be affected by faulty data since the preceding estimates remain relatively stable. The faulty data may be attributed to the measurement error caused by mulfunctioning of the apparatus. Another possible reason is the fact that the real system do not satisfy the reservoir models used during the analysis. Therefore, calculations for parameter estimation are repeated using the pressure data from the beginning up to 2.54×10^5 min, indicated by the solid circle in Fig.7. Final estimates obtained after five iterations of calculations are $T=4.97 \times 10^{-7}$ $m^3/Pa \cdot s$ and $S=2.59 \times 10^{-7}$ m/Pa. Simulated pressure values using these estimates are compared with measured ones in Fig. 7. The solid line representing the simulated pressure shows a satisfactory match to the measured pressure until the time indicated by the solid circle. The simulated values, however, gradually depart from the measured ones with time. This result indicates that the early half of the data can be fully expressed using an infinite reservoir model.

Analyses of the pressure data from other observation wells also provide fairly good estimates if only a part of the pressure data is used except NE4 and NE10 for which entire pressure data are used. The results of the estimated values are summarized in Table.1. The estimated transmissivity varies in the range 1.04×10^{-7} - 8.91×10^{-7} $m^3/Pa \cdot s$ and the storativity in the range 2.62×10^{-8} - 1.34×10^{-6} m/Pa. Estimated storativity of NE5 shows large value of 3.79×10^{-3} m/Pa which may be physically unrealistic. These transmissivities give kh values in the range from 11.7 to 100.6 darcy•m when the viscosity of water at 240 °C is employed.

Table 1 Estimated transmissivity(T) and storativity(S) on the basis of an infinite reservoir model.

Observation Well	Active Well	Estimates	
		T ($m^3/Pa \cdot s$)	S (m/Pa)
NE2	TT2, TT7, TT14	4.60×10^{-7}	1.34×10^{-6}
NE3	TT3, TT14	2.24×10^{-7}	2.62×10^{-8}
NE4	TT14	1.04×10^{-7}	1.07×10^{-7}
NE5	TT7	2.68×10^{-7}	3.79×10^{-3}
NE10	TT14	1.23×10^{-7}	8.74×10^{-8}
NE11	TT7, TT14	4.97×10^{-7}	2.59×10^{-7}
TT1	TT2, TT14	8.91×10^{-7}	2.08×10^{-7}

CONCLUSIONS

1) Interference test analysis using Kalman filtering provides good estimates of transmissivity(T) and storativity(S) at each moment when a new pressure value at an observation well is measured.

2)Simulated pressure changes using the final estimates of T and S do not always show a satisfactory match to the entire pressure data even the estimates at every moment are good.

3)A careful examination of performances of estimated T and S with time may provide information on the effects of using inadequate reservoir model during the analysis or the faulty data caused by mulfunctioning of measurement apparatus.

4) Estimated permeability-thickness product(kh) from the analyses of seven observation wells varies in the range 11.7 to 100.6 darcy•m.

REFERENCES

Arellano, V.M., Iglesias, E.R., Arellano, J. and Perez, M.R.(1990) ANAPPRES V3.0: Automatic Interference-Test Analysis in Personal Computers, *GRC Trans.*, Vol.14, PartII, 1271-1278.

Gotoh, H.(1990) Reinjection Plan for the Takigami Geothermal Field Oita Prefecture, Japan, *GRC Trans.*, Vol.14, Part II, 897–899.

Hayashi, J., Motomatsu, T. and Kondo, M.(1988) Geothermal Resources in the Takigami Geothermal Area, Kyushu, Japan., *Chinetsu*, Vol.25, No.2, 1–27(in Japanese with English abstract).

Itoi, R., Arakawa, H., Fukuda, M. and Jinno, K.(1990) The Application of Kalman Filter to Pressure Interference Test Analysis, *GRC Trans.*, Vol.14, Part II, 1207– 1210.

Itoi, R., Fukuda, M., Jinno, K. and Gotoh, H.(1992) Interference Test Analysis Method Using the Kalman Filtering and Its Application to the Takigami Geothermal Field, JAPAN, *GRC Trans.*, Vol.16, 657– 662.

Leaver, J.D., Grader, A. and Ramey Jr., H.J.(1998) Multiple-Well Interference Testing in the Ohaaki Geothermal Field, *SPE FE*, Vol.3, No.2, 429-437.

Matthews, C.S. and Russell, D.G.(1967) Pressure Buildup and Flow Tests in Wells, *Monograph Series*, SPE of AIME

McEdwards, D.G. and Benson, S.M.(1981) User's Manual for ANALYZE – – A Variable- Rate, Multiple-Well, Least Squares Matching Routine for Well-Test Analysis, *LBL*-10907.

Sageev, A., Horne, R.N. and Ramey Jr., H.J.(1985) Detection of Linear Boundaries by Drawdown Tests:A Semilog Type Curve Matching Approach, *Water Resources Research*, Vol.21, No.3, 305-310.

Sen, Z.(1984) Adaptive Pumping Test Analysis, *J. of Hydrology*, Vol.74, 259-270.

PROCEEDINGS, Eighteenth Workshop on Geothermal Reservoir Engineering
Stanford University, Stanford, California, January 26-28, 1993
SGP-TR-145

ACCURACY OF RESERVOIR PREDICTIONS FOR THE NESJAVELLIR GEOTHERMAL FIELD, ICELAND

G. S. Bodvarsson,[1] G. Gislason,[2] E. Gunnlaugsson,[2]
O. Sigurdsson,[3] V. Stefansson[3] and B. Steingrimsson,[3]

[1]Earth Sciences Division, Lawrence Berkeley Laboratory,
Berkeley, CA 94720
[2]District Heating Service, Reykjavik, Iceland
[3]National Energy Authority, Reykjavik, Iceland

ABSTRACT

The performance of the 1986 three-dimensional numerical model of the Nesjavellir geothermal field for predicting the deliverabilities and pressure decline of the wells during the period 1987 through 1991 is investigated. The model predicted adequately the flow rate and enthalpy transients of most wells, but overpredicted the pressure decline by 3 to 4 bars.

INTRODUCTION AND FIELD DEVELOPMENT

The Nesjavellir geothermal field is situated north of the Hengill volcano in southwestern Iceland. It is a part of the Hengill geothermal area. Hitaveita Reykjaviku (HR; Reykjavik District Heating) purchased the Nesjavellir farm in 1964, and started to explore the field and develop it to provide hot water for space heating in Reykjavik and vicinity.

Nesjavellir is a high-temperature field, so that it was understood from the start that the geothermal fluid would not be used directly for space heating due to problems of silica scaling and high gas content. Utilization of the field would therefore be based on using the geothermal fluid to heat up fresh water in heat exchangers. In 1974-1990 a pilot heating plant was operated at Nesjavellir, where experiments were carried out with several types of heat exchangers and deaerators (Gunnarsson et al., 1992).

Drilling began at Nesjavellir in 1965 and five exploration wells had been drilled by 1972. Drilling was resumed ten years later and by the end of 1986 a total of eighteen wells had been completed; the deepest well being 2.2 km deep. The Nesjavellir wells are highly productive, and out of the eighteen wells, thirteen are commercial producers with an average thermal output of 60 MW_t per well, or 9 MW_e per well.

Concurrent with the drilling of the field and the utilization experiments in the pilot plant, a thorough geothermal exploration program was carried out (Arnason et al., 1986; Arnason, 1990; Gunnarsson et al., 1992). The exploration and well results have been summarized in a conceptual model of the field (Figure 1). It features a two-phase upflow zone under the Hengill volcano, and lateral fluid flow along the SW-NE fissure system that intersects the volcano.

The conceptual model formed the basis for the development of a three dimensional simulation model of the field (Bodvarsson et al., 1990 and 1991). The main objective of the modeling studies was to predict the response of the field to fluid extraction and to estimate the generating capacity of the field, before any decisions were made on the future power plant size at Nesjavellir. By 1986 it became clear from the modeling studies that the field could supply a 300 MW_t power plant for at least 30 years. Any plans for a larger plant would, according to the simulation model, require reinjection into the reservoir.

The City Council of Reykjavik decided on 20 November 1986 to begin the construction of a power plant at Nesjavellir. The plant was to be built in stages, the first phase being a thermal power plant of 100 MW_t, which amounts to production of 560 l/s of 85°C hot water. The construction work started in early 1987. The first phase was completed and the plant went into operation in September 1990. Additional 100 MW_t are being developed under phase two of which 50 MW_t went on-line in November 1991 and the remainder is scheduled to be in operation by 1994. The planned capacity of the power plant when fully developed is for 400 MW_t thermal power for district heating and 80-90 MW_e for electric generation (expected completion date 2010). A plant of this size would call for a reinjection scheme, according to the numerical modeling results from 1986.

The three-dimensional model was calibrated against all available data up to the end of 1986, and matched well flow rate and enthalpy data from all wells, the initial (natural state) temperature and pressure distributions and pressure interference data between wells. Since 1986 considerable new information has been collected at Nesjavellir, as some of the wells have been continuously flowing and two new wells have been drilled

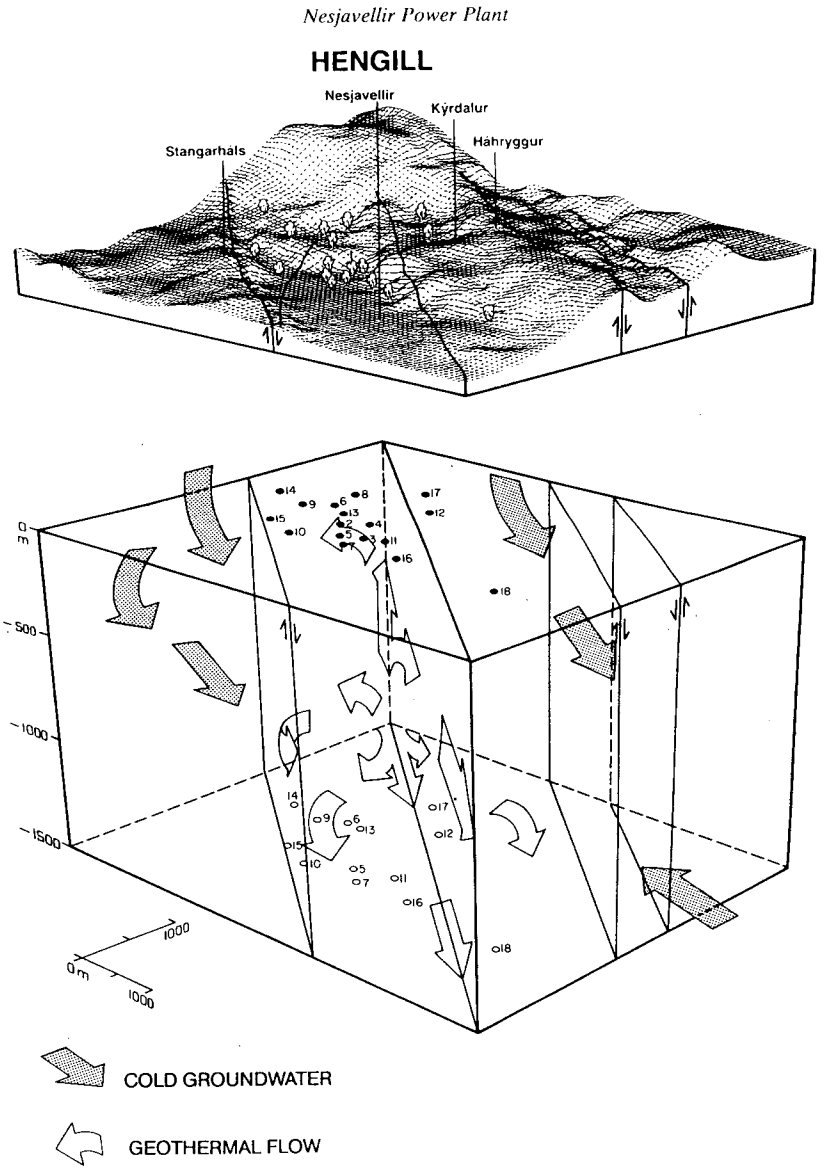

Fig. 1. A three-dimensional conceptual model of the Nesjavellir geothermal field.

(wells 17 and 18). All of these new data require that the three-dimensional model be updated, so that the model is consistent with all available data, and thus provides the best possible reservoir management tool.

In this paper the reservoir predictions for the Nesjavellir field are evaluated. The performance of the 1986 model is evaluated in terms of the its predictions compared to the actual observed flow rates, enthalpies and pressure decline data for the last six years. The recalibration of the model and new performance predictions for the Nesjavellir field are given by Bodvarsson et al. (1993).

THE THREE-DIMENSIONAL MODEL

Figure 2 shows an areal view of the basic grid used. The grid was designed to allow the modeling of each well individually, and to have reasonably small elements in the anticipated wellfield region. Note that the element numbers, for elements 2 through 16 correspond to the number of the well located within the element. It should be noted that Figure 2 only shows the central part of the grid used; the total grid extended 100 km in all directions in order to avoid boundary effects.

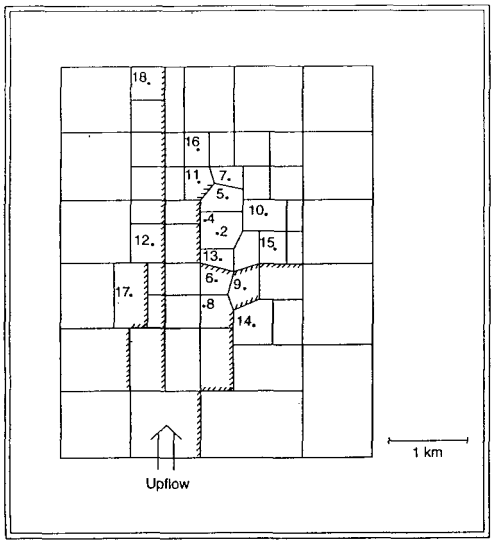

Fig. 2. Areal view of the central part of the numerical grid used in the simulations.

The three-dimensional model consisted of four layers, three of which were 400 m in thickness, while the bottom layer was 800 m thick. The choice of the number of layers and their respective thicknesses was made based on the observed thermodynamic conditions in the field and the locations of major feed zones in the wells.

The two bottom layers represent the main reservoir located below a depth of 800 m. It should be emphasized that it was assumed that no fluid recharge from depth (except for the upflow zone) would occur anywhere in the system. This is certainly a conservative assumption, but other assumptions regarding the deep end of the system are speculative and would lead to "unwanted" optimistic results. The upflow zone was assumed to be located south of the wellfield, which geographically represents a part of the Hengill volcano, east of Skeggi (Figures 1 and 2). For further details of the numerical grid and the three-dimensional model the reader is referred to Bodvarsson et al. (1990).

Various reservoir parameters were adjusted during the natural state and history match simulations, including permeabilities and porosities, the production indices for the wells and the mass recharge rate and the enthalpy of the upflow zone. The relative permeability curves used are the same as those used in the earlier simulations of Nesjavellir (Bodvarsson et al., 1990). The basic characteristics of the curves are that the sum of the relative permeabilities for the two-phases is unity for all values of saturation.

The reservoir fluid was assumed to be pure water. Thus, the effects of noncondensible gases and dissolved solids are neglected. These effects are not believed to be important at Nesjavellir because of low concentrations of these "impurities" in discharge fluids. The computer code MULKOM (Pruess, 1982) was used in this work.

"NEW" NESJAVELLIR FIELD DATA

The most important data for a numerical reservoir model of a geothermal system are the production data from wells (flow rates and enthalpies), and the pressure decline data collected at idle (observation) wells. Wells 5, 6, 11, 13 and 16 have been continuously produced since 1986; the last four wells have provided hot fluids for the 100 MW_t power plant since it commenced in September 1990. Production from well 9 was stopped in 1988, and production testing of recent wells 17 and 18 was carried out in 1987 and 1988. Periodic flow rate and enthalpy measurements are made for all of the flowing wells.

The pressure decline in the reservoir in response to production is monitored through periodic pressure surveys of the idle wells (wells 7, 10, 12, 14, 15, 17 and 18). The observed pressure decline varies greatly between the wells, being largest in well 7 (about 8 bars), considerable in well 10 (3 to 4 bars), observable in wells 14 and 15 (about 2 bars), and marginally detected in wells 12, 17 and 18 (see Table 1). These total pressure decline values were estimated from pressure surveys taken in October 1991.

The production records for the wells are annually compiled and show that the wells decline in flow rate very

Table 1: Observed and predicted total pressure decline in idle Nesjavellir wells from 1984 to late 1991.

Well	Observed Pressure Decline (bars)	Calculated Pressure Decline (bars)
7	8.5	7.5
10	3.0	6.5
12	1.0	1.0
14	1.5	6.0
15	2.0	6.5

gradually, but that the enthalpy of the wells is slowly declining. The data from recent wells 17 and 18 indicate that these wells are relatively colder than the other wells, with maximum temperatures of 240°C and 220°C, respectively. Most of the other Nesjavellir wells have maximum temperatures exceeding 300°C. These results are to be expected for well 18, which is located more than 1 km north of well 16. Well 17, however, is colder than expected given the observed temperature of well 12, and the fact that well 17 is located closer to the inferred upflow zone under the Hengill volcano than well 12. It is likely that the bottomhole location of well 17 lies west of one of the many N-S faults in the area, and that this fault zone partly or fully seals the flow of geothermal fluids to the west.

Natural state heat losses from the geothermal system control the mass and heat flow through the system in its undisturbed state. Modeling the natural thermodynamic conditions of a geothermal system requires reasonably accurate data regarding mass and heat flows from surface springs and fumaroles. For the 1986 model, estimates of surface discharge of springs and fumaroles were obtained from Arnason et al. (1986), and more recent studies have verified these estimates (Gudmundsdottir, 1988).

Franzson (1988) published a summary report on the interpretation of geological data from the Nesjavellir wells in terms of geological structures and fluid flow patterns. The results of his studies provide evidence for possible barriers to fluid flow that may be needed in the numerical model in order to match the available data, especially the observed thermal plume.

Hersir et al. (1990) give a comprehensive and detailed summary of the various geophysical measurements that have been done around the Hengill volcano, including results of resistivity, magnetic, gravity and microearthquake studies. Finally, Gudmundsson and Sigurdsson (1987) present the results of the drilling of two shallow "injection" wells, NN-1 and NN-2, located near wells 5 and 7, respectively. Although the wells are only 300 to 400 m deep, fluid samples taken from the wells show significant component of hot geothermal fluids, estimated to be about 10%. The wells must therefore have some hydrological connectivity to the main geothermal reservoir.

PERFORMANCE OF THE 1986 MODEL

It is of interest to investigate how well (or poorly) the predictions made using the 1986 model have agreed with the observed behavior of the Nesjavellir wells during the last 6 years (1987 to 1992). An evaluation of the predictive capabilities of the 1986 model is obtained by prescribing the actual flow periods for all of the wells and then compare the calculated flow rates and enthalpies of the flowing wells with those observed during the last six years. In addition, one can compare the computed pressure decline at all of the observation wells with observed values. As an example Figures 3 and 4 show the comparison between observed and calculated flow rates and enthalpies for wells 5 and 6. In general, the model results are in acceptable agreement with the observed data, especially since the prediction period (about 6 years) is considerably longer than the calibration period for most of the wells (one to two years). The "rule of thumb" is that a model cannot be expected to predict accurately for a period longer than the calibration period. The model over estimates the flow rate decline of well 6 considerably, and this was found to be the case for many of the other wells. The model also overestimated the enthalpy of the produced fluids for some of the wells.

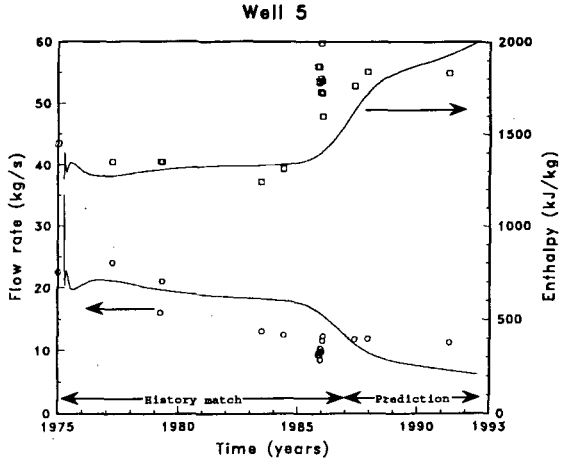

Fig. 3. Comparison between predicted and observed flow rate and enthalpy transients for well 5.

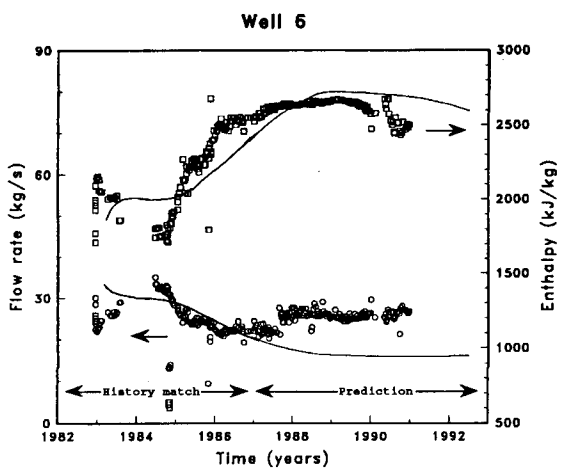

Fig. 4. Comparison between predicted and observed flow rate and enthalpy transients for well 6.

Table 1 shows the estimated observed pressure decline of wells 7, 10, 12, 14 and 15 as of October 1991 as well as the results of the 1986 model. The data given in Table 1 show that the 1986 model overpredicted significantly the pressure decline for most of the wells. The model predicted the pressure decline for well 7 reasonably well, but overestimated the pressure decline for wells 10, 14, and 15 by a factor of 2 to 4. The model predicted the pressure decline for well 12 acceptably well, or practically no pressure decline, as this well is separated from the producing wells by faults acting as permeability barriers. These results strongly suggest that the 1986 model is based on permeabilities that are too low, and consequently the performance predictions based on the 1986 model are conservative for the Nesjavellir reservoir system.

CONCLUSIONS

(1) The 1986 model model predicted remarkably well the flow rate and enthalpy behavior of most of the Nesjavellir wells for the period 1987 to 1992, although the data available for calibration for most of the wells was very limited.

(2) The 1986 model overestimated the pressure decline in the Nesjavellir reservoir during the period 1987 to 1992. This was to be expected since the available pressure decline data in 1986 were very limited, and actually the trend was mislead by the data from well 7 which showed relatively large pressure decline. The observed pressure decline of well 7 is now believed to be controlled by one of the actively producing wells, assumed to be well 16 in the 1992 numerical model.

ACKNOWLEDGEMENTS

The authors thank E. Antunez and C. H. Lai for their critical review of this work. This work was supported by Reykjavik District Heating and in part by the Assistant Secretary of Conservation and Renewable Energy, Office of Renewable Energy Technologies, Geothermal Technology Division of the U. S. Department of Energy under Contract No. DE-AC03-76SF00098.

REFERENCES

Arnason, K., 1990, "Central-loop Transient Electromagnetic Soundings in Geothermal and Ground Water Exploration, a Step Forward," *Geothermal Resources Council, Trans., 14,* (II) 845-851.

Arnason, K., Haraldsson, G. I., Johnsen, G. V., Thorbergsson, G., Hersir, G. P., Saemundsson, K., Georgsson, L. S. and Snorrason, S. P., 1986, Nesjavellir - Geological and geophysical study in 1985, (Icelandic National Energy Authority report OS-86014/JHD-02 (in Icelandic), 125 pp.

Bodvarsson, G. S., Bjornsson, S., Gunnarsson, A., Gunnlaugsson, E., Sigurdsson, O., Stefansson, V. and Steingrimsson, B., 1990, "The Nesjavellir Geothermal Field, Iceland; 1. Field Characteristics and Development of a Three-dimensional Numerical Model," *J. Geothermal Science and Technology, 2,* (3) 189-228.

Bodvarsson, G. S., Bjornsson, S., Gunnarsson, A., Gunnlaugsson, E., Sigurdsson, O., Stefansson, V. and Steingrimsson, B., 1991, "The Nesjavellir Geothermal Field, Iceland; 2. Evaluation of the Generating Capacity of the System," *J. Geothermal Science and Technology, 2,* (4) 229-261.

Bodvarsson, G. S., Gislason, G., Gunnlaugsson, E Sigurdsson, O., Stefansson, V. and Steingrimsson, B., 1993, Predictions and Recalibration of the Three-Dimensional Numerical Model of the Nesjavellir Geothermal Field, Iceland," paper submitted to *Geothermics.*

Franzson, H., 1988, Nesjavellir - Borholujardfraedi - vatnsgengd i jardhitageymi, report issued by the National Energy Authority, OS-88046/JHD-09, (in Icelandic) 58 pp.

Gudmundsdottir, A. L., 1988, Natturulegt varmastreymi til yfirbords a jardhitasvaedum i landi Nesjavalla, Reykjavik Municipal District Heating Service report, (in Icelandic), 38 pp.

Gudmundsson, A. and Sigurdsson, O., 1987, Nesjavellir nidurrennslisholur - borun, jardlog og vatnsstada, National Energy Authority report OS-87043/JHD-25, (in Icelandic), 50 pp.

Gunnarsson, A., Steingrimsson, B., Maack, R., Gunnlaugsson, E., and Magnusson, J., 1992, "Nesjavellir Geothermal Co-generation Power Plant," *Geothermics, 21,* 559-583.

Hersir, G. P., Bjornsson, G. and Bjornsson, A., 1990, Eldstodvar og jardhiti a Hengilsvaedi - jardedlisfraedileg konnun, National Energy Authority report, OS-90031/JHD-06, (in Icelandic), 93 pp.

Pruess, K., 1983, Development of the General Purpose Simulator MULKOM, 1982 Annual report, Earth Sciences Division, Lawrence Berkeley Laboratory, Berkeley, California, LBL-15500, pp. 133-134.

PROCEEDINGS, Eighteenth Workshop on Geothermal Reservoir Engineering
Stanford University, Stanford, California, January 26-28, 1993
SGP-TR-145

DEVELOPMENT OF A DUAL-POROSITY MODEL FOR VAPOR-DOMINATED FRACTURED GEOTHERMAL RESERVOIRS USING A SEMI-ANALYTICAL FRACTURE/MATRIX INTERACTION TERM

Robert W. Zimmerman, Teklu Hadgu, and Gudmundur S. Bodvarsson

Earth Sciences Division, Lawrence Berkeley Laboratory
University of California, Berkeley, CA 94720

ABSTRACT

A new type of dual-porosity model is being developed to simulate two-phase flow processes in fractured geothermal reservoirs. At this time it is assumed that the liquid phase in the matrix blocks remains immobile. By utilizing the effective compressibility of a two-phase water/steam mixture in a porous rock, flow within the matrix blocks can be modeled by a single diffusion equation. This equation in turn is replaced by a nonlinear ordinary differential equation that utilizes the mean pressure and mean saturation in the matrix blocks to calculate the rate of fluid flow between the matrix blocks and fractures. This equation has been incorporated into the numerical simulator TOUGH to serve as a source/sink term for computational gridblocks that represent the fracture system. The new method has been compared with solutions obtained using fully-discretized matrix blocks, on a problem involving a three-dimensional vapor-dominated reservoir containing an injection and a production well, and has been found to be quite accurate.

INTRODUCTION

Although most geothermal reservoirs reside in fractured rocks, most models that have been developed to analyze their behavior have been based on porous medium approximations. In these models, the hydraulic behavior of the fractures and the matrix blocks are modeled together as a locally-homogeneous porous medium. It is well-known, however, that porous medium models are poorly suited for predicting certain aspects of the behavior of geothermal wells, especially enthalpy transients, thermal front migration due to injection, and chemical tracer movement. Nevertheless, in many cases the porous medium approximation must be invoked, due to constraints of computer time or cost. There is, consequently, a great need for improved numerical capabilities for the modeling of fractured geothermal reservoirs, using accurate and appropriate models.

In this paper we discuss our on-going research aimed at improved methods of simulating processes in fractured geothermal reservoirs. The main concept behind our approach is to analyze the heat and mass flow processes occurring within the matrix blocks by simplified equations that enable us to avoid detailed discretization of the individual matrix blocks. These processes are generally governed by diffusion-type partial differential equations. We model these diffusive processes with nonlinear ordinary differential equations that relate the average thermodynamic properties in the block to those at the outer boundary (in the fractures). The first stage of our work, dealing with isothermal flow of a single-phase fluid, was described at the 17th Stanford Workshop (Zimmerman et al., 1992). We have since extended the general approach to treat thermal conduction within the matrix blocks. This extension is straightforward, as shown by Pruess and Wu (1989), since the governing equation for conduction is exactly analogous to that for single-phase flow. In this paper we describe a further extension of this approach to processes involving two-phase conditions in which the liquid phase is immobile.

DUAL–POROSITY MODELS

We now briefly describe the main ideas behind dual-porosity models for fractured reservoirs; for further details, see Barenblatt et al. (1960), Warren and Root (1963), and Duguid and Lee (1977). In order to avoid a cumbersome notation, we will discuss these models with specific reference to single-phase, isothermal flow of a slightly-compressible fluid. Consider first a fracture network, and assume temporarily that the matrix blocks are impermeable. A basic assumption underlying the use of dual-porosity models is that there exists a scale at which it is possible to assign macroscopic properties to the fracture network, such as a permeability k_f, etc. Although it does not seem to be true that such a length-scale always exists (cf., Long and Witherspoon, 1985), standard dual-porosity models assume that such a scale does exist. This scale then serves as a representative elementary volume (REV; see Bear, 1972) upon which a continuum formulation can be based. "Points" in the fracture network are then denoted by the vector x_f, where it is understood that properties defined at point x_f are averaged over an REV centered at that point.

When a single-phase, slightly compressible fluid flows through such a fractured medium, the fluid pressure in the fractures is governed by the following equation (Matthews and Russell, 1967):

$$\phi_f \beta_f \frac{\partial P_f(x_f,t)}{\partial t} = \frac{k_f}{\mu} \nabla_f^2 P_f(x_f,t) + Q(x_f,t), \qquad (1)$$

where ϕ_f is the total fracture porosity, and β_f is the total compressibility of the fractures and the fluid within them. The product $\phi_f \beta_f$ serves as the capacitance term in the diffusion-type equation (1). The pressure P_f is the mean value of the fluid pressure in the fractures, averaged over some REV. The operator ∇_f^2 is the Laplacian with respect to the coordinates x_f. The term Q is a source/sink term representing the net volumetric addition of fluid to the fracture system, per unit of total volume. Although we assume here that the fracture continuum is isotropic, this assumption is not necessary.

Now assume that at each point x_f in the fracture continuum, there is located a permeable matrix block of some specified shape. These matrix blocks can exchange fluid with the fracture continuum; hence we can identify the source/sink term Q in equation (1) with the fluid exchange between the fractures and matrix blocks. Inside each matrix block the fluid pressure P_m will, in general, vary from point to point. Points inside the matrix block are identified by two position variables: x_m locates the point within the block relative to its centroid, and x_f is used to locate that particular block within the fracture continuum. Fluid flow *within* each matrix block is governed by an equation analogous to (1):

$$\phi_m \beta_m \frac{\partial P_m(x_m,t;x_f)}{\partial t} = \frac{k_m}{\mu} \nabla_m^2 P_m(x_m,t;x_f). \qquad (2)$$

The spatial derivatives are in this case taken with respect to the local variable x_m. The fracture/matrix interflow term Q does not appear in equation (2) since, whereas the interflow is assumed to be *distributed* throughout the fracture continuum as a source/sink term, the interflow enters the matrix blocks only at their *boundaries*. If the existence of a fracture skin is ignored (cf., Moench, 1984; deSwaan, 1990), then the pressure at the outer boundary of a given matrix block is equal to the local fracture pressure: i.e., if x_m is on the boundary of the matrix block, then $P_m(x_m,t;x_f)=P_f(x_f,t)$.

The system of equations (1) and (2) are coupled through the term Q, which can be found in principle by integrating the flux out of the boundary of each matrix block, ∂V_m, using Darcy's law (Duguid and Lee, 1977):

$$Q(x_f,t) = \frac{-1}{V_m} \int_{\partial V_m} \frac{k_m}{\mu} \frac{\partial P_m}{\partial n} dA, \qquad (3)$$

where n is measured along the outward unit normal to the boundary of the block. If the system of equations (1-3) were solved with a numerical simulator such as the integral-finite-difference simulator TOUGH (Pruess, 1987), the reservoir would be discretized into a number of gridblocks, each representing a macroscopic region that contained a portion of the fracture continuum. Each of these regions would also therefore contain a certain number of matrix blocks, within which the flow will be governed by equation (2). For some problems the matrix blocks can be replaced, for computational purposes, by a single equivalent matrix block having the same volume and same fracture/matrix interface area as does the collection of actual matrix blocks. In order to accurately resolve the pressure gradients within the matrix blocks, this equivalent matrix block must be discretized into a number of concentric gridblocks. One efficient way of creating this type of dual-porosity grid is the MINC (Multiple INteracting Continua) method, which is described by Pruess and Narasimhan (1985). We have found that accurate MINC simulations over large time scales require roughly ten gridblocks in each equivalent matrix block. The total number of gridblocks used in a simulation will therefore be $11N$, where N is the number of fracture gridblocks. For three-dimensional problems, this number will usually be impractically large, which suggests the desirability of replacing the fine-gridding in the matrix blocks with a readily-computed source/sink term.

LUMPED–PARAMETER MODELS

The earliest double-porosity models, developed by Barenblatt et al. (1960) and Warren and Root (1963), treated the matrix blocks in a lumped-parameter fashion. The equations of such an approach can be derived as follows. We first integrate equation (2) over an entire matrix block, and use the divergence theorem to convert the volume integral on the right into a surface integral, to find

$$\phi_m \beta_m \frac{\partial \bar{P}_m(x_f,t)}{\partial t} = \frac{1}{V_m} \int_{\partial V_m} \frac{k_m}{\mu} \frac{\partial P_m}{\partial n} dA, \qquad (4)$$

where the average pressure P_m is defined by

$$\bar{P}_m(x_f,t) = \frac{1}{V_m} \int_{V_m} P_m(x_m,t;x_f)\, dV. \qquad (5)$$

Comparison of equations (3) and (4) shows that P_m is governed by the following equation:

$$\phi_m \beta_m \frac{d\bar{P}_m(x_f,t)}{dt} = -Q(x_f,t). \qquad (6)$$

Equations (1) and (6) provide two equations for the three variables P_f, $\bar{P}_m$, and Q. To complete the system of equations, Q must be expressed as a function of P_f and $\bar{P}_m$.

Barenblatt et al. (1960) and Warren and Root (1963) assumed that Q is proportional to the difference between P_f and $\bar{P}_m$, so that

$$Q(x_f,t) = \frac{-\alpha k_m}{\mu}(P_f - \bar{P}_m)\,, \tag{7}$$

where α is a parameter that depends on block shape, and has dimensions of area^{-1}. The governing equation (6) for $\bar{P}_m$ then takes the form

$$\phi_m \beta_m \frac{d\bar{P}_m(x_f,t)}{dt} = \frac{\alpha k_m}{\mu}(P_f - \bar{P}_m)\,. \tag{8}$$

For a given shape of the matrix block, α can be chosen such that equation (8) is asymptotically accurate at late times (see Zimmerman et al., 1992). For spherical matrix blocks of radius a_m, which will be used in this paper for illustrative purposes, $\alpha = \pi^2/a_m^2$.

The Warren-Root equation is known to be inaccurate in the early stages of diffusion into a matrix block (Streltsova, 1983; Dykhuizen, 1990). A more accurate interaction equation is that proposed by Vermeulen (1953):

$$\phi_m \beta_m \frac{d\bar{P}_m}{dt} = \frac{\pi^2 k_m [(P_f - P_i)^2 - (\bar{P}_m - P_i)^2]}{2\mu a_m^2 (\bar{P}_m - P_i)}\,, \tag{9}$$

where P_i is the initial pressure in the matrix block. This interaction equation was shown to be fairly accurate for a wide range of boundary conditions (see Zimmerman et al., 1992). Recognizing that the combination $\pi^2 k_m/\phi_m \beta_m \mu a_m^2$ is the product of the shape-factor α and the hydraulic diffusivity $D = k_m/\phi_m \mu \beta_m$, we see that equation (9) can be used for other diffusive processes, such as heat conduction.

TWO–PHASES, IMMOBILE LIQUID

Porous media generally have a minimum value of the liquid saturation S_l, below which the relative permeability of the liquid phase is zero. If the water saturation in the matrix blocks is at this irreducible level, then only the vapor phase (steam) will be mobile. However, although the water cannot flow out of the matrix blocks in the liquid state, water can be produced from the blocks by first vaporizing into the (mobile) steam phase. This is believed to be the case within vapor-dominated geothermal systems, where only steam is produced at the wells (Pruess and Narasimhan, 1982). In such cases, the flow can still be modeled by a single diffusion equation. This requires modifying the compressibility term in the diffusion equation to account for the phase change.

Grant and Sorey (1979) derived an expression for the effective compressibility of the water/steam mixture, based on the following analysis. Imagine that the pressure increases, in which case the temperature will also increase, since the water and steam remain in thermodynamic equilibrium. Heat will then flow from the fluid into the rock matrix, causing some of the vapor to condense. Since liquid water is denser than steam, the overall volume of fluid will decrease, giving rise to an apparent compressibility effect. The resulting expression for the effective compressibility is

$$(\phi\beta)_{eff} = \frac{<\rho C> T v_{lv}^2}{h_{lv}^2}\,, \tag{10}$$

where $v_{lv} = v_v - v_l$ is the difference between the specific volume of the vapor and the liquid, $h_{lv} = h_v - h_l$ is the latent heat of vaporization, and $<\rho C>$ is the overall heat capacity of the system, which is given by

$$<\rho C> = (1-\phi)\rho_r C_r + \phi S_v \rho_v C_v + \phi(1-S_v)\rho_l C_l\,, \tag{11}$$

where C is the specific heat, ρ is the density, and the subscripts r,l,v denote rock, liquid and vapor. This apparent compressibility is usually at least an order of magnitude greater than that of single-phase water or steam. Since the diffusivity is inversely proportional to $(\phi\beta)$, diffusive processes involving two-phase mixtures will proceed relatively slowly.

When the liquid phase is immobile, the flow of the vapor is therefore governed by an equation analogous to equation (2), with the following modifications. The compressibility $(\phi\beta)$ must be replaced by the expression in equation (10), k_m must be multiplied by the relative permeability of the rock to the vapor phase, k_{rv}, and the viscosity must be taken as that of the vapor, μ_v. The relative permeability k_{rv} will vary with vapor saturation, the viscosity μ_v will vary with pressure, and $(\phi\beta)_{eff}$ will vary with both saturation and pressure. In the context of the lumped-parameter approximation, we evaluate these parameters at pressure $\bar{P}_m$ and $\bar{S}_v$, where $\bar{S}_v$ is the mean vapor saturation in the matrix block. During a numerical simulation, these parameters can be re-evaluated at each time step, as $\bar{P}_m$ and $\bar{S}_v$ change with time.

DUAL–POROSITY SIMULATOR

Numerical reservoir simulators used for porous-medium reservoirs typically solve equation (1), and analogous equations for energy balance, etc., by first discretizing the reservoir into a number of computational gridblocks. A numerical scheme such as finite-differences (Huyakorn and Pinder, 1983), finite elements (Pinder and Gray, 1977), or integral finite-differences (Edwards,

1972), is then used to reduce the partial differential equations to a set of algebraic equations. These algebraic equations are solved at each time-step t_n, in order to yield the pressures, temperatures, saturations, etc., in each gridblock at time-step $t_{n+1} = t_n + \Delta t$.

We have implemented our semi-analytical dual-porosity model as a modification to the TOUGH simulator (Pruess, 1987), an integral-finite-difference code that has been widely used to simulate the behavior of geothermal reservoirs. The fracture/matrix interaction equations have been incorporated as an option in the source/sink subroutine that is normally used to represent injection or withdrawal of fluid from a well, etc. In our dual-porosity simulations, each computational gridblock represents a region that has properties corresponding to the fractured continuum, such as k_f, ϕ_f, etc., averaged over a suitably-large REV. Each gridblock will also have associated with it three new variables, $\bar{P}$, $\bar{T}$ and $\bar{S}_v$, that represent the (average) thermodynamic state of the fluid in those matrix blocks that are located within that gridblock. Here we drop the subscript m used to denote "matrix", since the overbar serves the purpose of distinguishing the matrix variables from fracture variables. We calculate the pressure change in the matrix blocks, at each time step and for each gridblock, from equation (9), modified as described above:

$$(\phi\beta)_{eff}\frac{d\bar{P}}{dt} = \frac{\alpha k_m k_{rv}[(P_f - P_i)^2 - (\bar{P} - P_i)^2]}{2\mu_v(\bar{P} - P_i)}, \qquad (12)$$

where $(\phi\beta)_{eff}$ is found from equation (10), and $\alpha = \pi^2/a_m^2$ (if the matrix blocks are assumed to be spheres of radius a_m). The term on the right-hand side of equation (12) then represents the volumetric fluid flux Q, as shown by equation (6). The integration of equation (12) must be done implicitly, in order to avoid numerical instabilities. This means that in passing from t_n to t_{n+1}, the terms on the right-hand side of equation (12) are evaluated under the conditions that exist at time t_{n+1}. An iterative process is therefore required for convergence to the correct new values (see Pruess, 1987). The new saturation at time t_{n+1} is found by applying a mass balance to the matrix block. The mass flux of vapor out of the matrix block into the fracture network also carries with it a sensible heat flux of the amount $\rho_v h_v Q$, where Q is the volumetric flux. This term must be included in the energy balance equation.

EXAMPLE OF RESERVOIR SIMULATIONS

To test the accuracy and computational efficiency of the above-described modifications to the TOUGH code, we have simulated some problems using, with some modifications, the computational grid and reservoir properties that were proposed by Spivak (1991) to test geothermal simulators. This is a three-dimensional model of a vapor-dominated geothermal reservoir, with

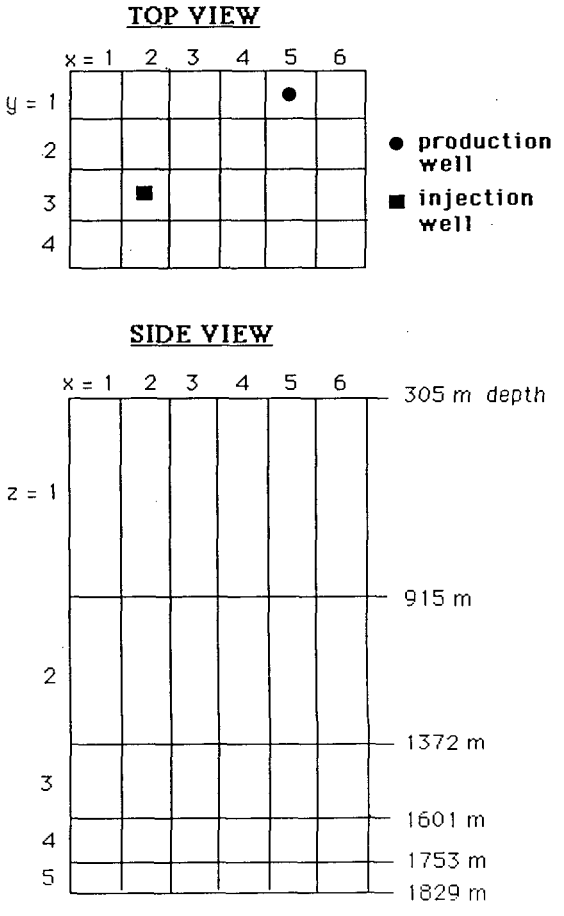

Fig. 1. Schematic diagram of the grid used in simulations of a hypothetical geothermal reservoir. Dimensions of the gridblocks, and the physical properties of the fractures and the matrix blocks, are listed in the text.

properties corresponding to those believed to be applicable to The Geysers geothermal field in California. This hypothetical reservoir (see Fig. 1) is 1524 m thick, and extends from a depth of 305 m to 1829 m below the surface. The cross-sectional shape in any horizontal plane is a rectangle with sides of 914.4 m and 609.6 m. Each layer is broken up into 24 gridblocks, each of length 152.4 m in the two horizontal directions. The thicknesses of the five layers are as shown in Fig. 1. A production well (Well #1) and an injection well (Well #2) are located in gridblocks $xyz = 511$ and $xyz = 231$ (see Fig. 1), and are completed only in the topmost layer of the reservoir.

The matrix blocks are cubes of 67 m on each side, with matrix permeability $k_m = 1 \times 10^{-19}\,\mathrm{m}^2$, matrix porosity $\phi_m = 0.04$. (A somewhat low matrix permeability is used so as to avoid having the liquid saturation rise above its irreducible value near the injection well). The

rock has density $\rho_r = 2648\,\text{kg/m}^3$, and heat capacity $C_r = 1000\,\text{J/kg K}$. The fracture network has an overall porosity $\phi_f = 0.01$, and permeability $k_f = 2.0\times10^{-14}\,\text{m}^2$. The relative permeabilities of both the fracture network and matrix blocks are taken to be linear functions of saturation, with the irreducible saturations for the liquid phase, and for the vapor phase in the matrix blocks, set to zero. The irreducible saturation for the liquid in the matrix blocks is 0.25. In this example, capillary pressure effects and thermal conductivity effects are neglected in both the fractures and matrix blocks.

The initial conditions are that the liquid saturation in the matrix blocks is at its irreducible value of 0.25, and the pressure in the uppermost layer is 3.45 MPa. The initial temperature in the uppermost layer is therefore equal to the saturation temperature at this pressure, which is 242 C. All outer boundaries of the reservoir are impermeable to fluid flow, and the lateral boundaries are also impermeable to heat conduction. A heat flux of $0.5\,\text{W/m}^2$ is conducted vertically upwards through the reservoir. The remaining initial conditions, such as the pressures in the lower layers and the saturations in the fractures, are found by running a simulation to steady state, with no injection or production from the wells.

In the sample problem whose results are shown in Figs. 2-4, Well #1 produces 5 kg/s of fluid, and Well #2 injects 5 kg/s of liquid water at 95 C. The vapor saturation and pressure for the fractures in gridblock 231 are shown in Figs. 2 and 3, respectively, for elapsed times from $10^1 - 10^8$ s (about 38 months). The solid lines denote the values computed using TOUGH with the modifications described above, whereas the open circles denote values computed with TOUGH using the MINC method to discretize each equivalent matrix block into ten concentric gridblocks. The fracture pressure in gridblock 511 is shown in Fig. 4. The vapor saturation in the fractures in gridblock 511 remains very close to 100% through both simulations, and is not shown. The predictions of the new method are in all cases very close to those of the MINC simulations. Due to the relatively complex geometry of this problem, and the physical nonlinearities arising from phase-changes, etc., no analytical solution is available for comparison.

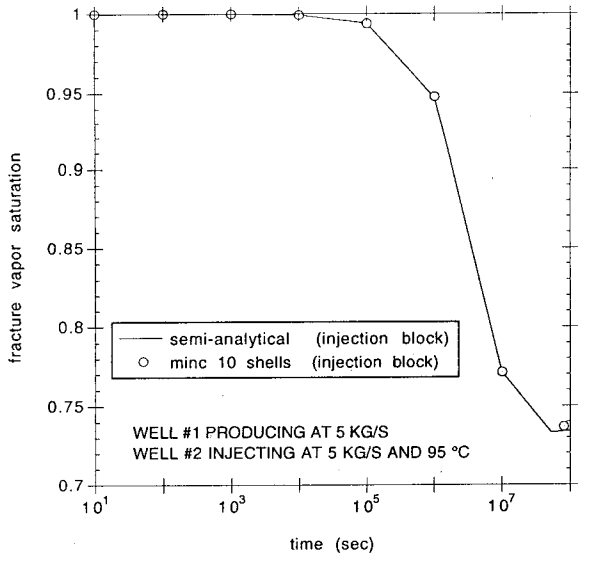

Fig. 2. Vapor saturation in the fractures of gridblock 231, for the problem described in the text.

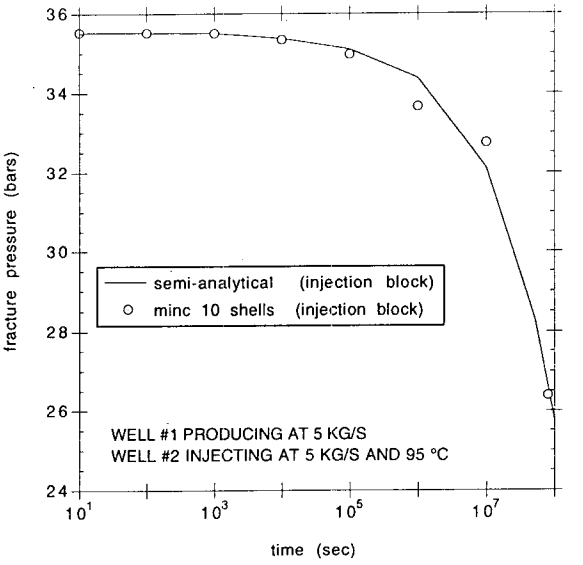

Fig. 3. Pressure in the fractures of gridblock 231, for the problem described in the text.

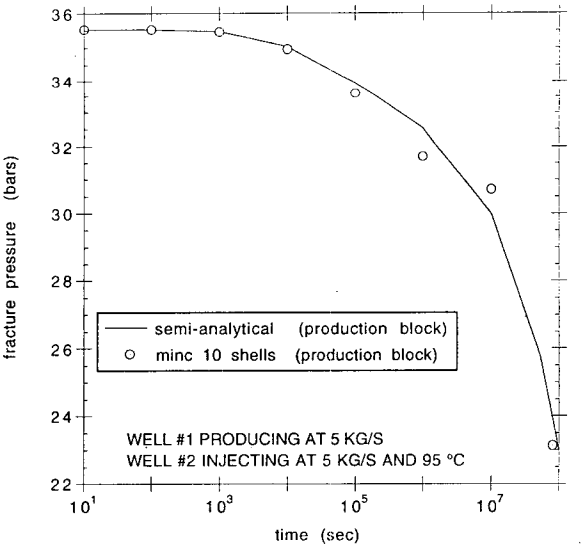

Fig. 4. Pressure in the fractures of gridblock 511, for the problem described in the text.

CONCLUSIONS

A new type of dual-porosity model is being developed for two-phase flow processes in fractured geothermal reservoirs. At this time, the model is limited by the assumption that the liquid phase in the matrix blocks remains immobile. By utilizing the effective compressibility concept developed for water/steam mixtures in porous rocks (Grant and Sorey, 1979), flow within the matrix blocks can be modeled by a single diffusion equation. This equation is in turn replaced by a non-linear ordinary differential equation that utilizes the mean pressure and mean saturation in the matrix blocks to find the rate of fluid flow between the matrix blocks and fractures. This equation has been incorporated into the numerical simulator TOUGH (Pruess, 1987), as a source/sink term for computational gridblocks that represent the fracture system. The accuracy of this new method has been tested by simulating a three-dimensional reservoir containing partially-penetrating injection and production wells, and comparing the results to simulations in which the matrix blocks are each discretized into ten concentric shells.

ACKNOWLEDGMENTS

This work was supported by the Assistant Secretary for Conservation and Renewable Energy, Geothermal Division, U.S. Department of Energy, under Contract No. DE-AC03-76SF00098, with the Lawrence Berkeley Laboratory. The authors thank C. H. Lai and Emilio Antunez of LBL for reviewing this paper.

REFERENCES

Barenblatt, G. E., Zheltov, Y. P., and Kochina, I. N. (1960), "Basic concepts in the theory of seepage of homogeneous liquids in fissured rocks," *J. Appl. Math. Mech., 24,* 1286-1303.

Bear, J. (1972), *Dynamics of Fluids in Porous Media,* Elsevier, New York.

deSwaan, A. (1990), "Influence of shape and skin of matrix-rock blocks on pressure transients in fractured reservoirs," *SPE Form. Eval., 5,* 344-352.

Duguid, J. O., and Lee, P. C. Y. (1977), "Flow in fractured porous media," *Water Resour. Res., 13,* 558-566.

Dykhuizen, R. C, (1990), "A new coupling term for dual-porosity models," *Water Resour. Res., 26,* 351-356.

Edwards, A. L. (1972), "TRUMP: A computer program for transient and steady state temperature distribution in multidimensional systems," *Rep. UCRL-14754,* Lawrence Livermore Laboratory, Livermore, Calif.

Grant, M. A., and Sorey, M. L. (1979), "The compressibility and hydraulic diffusivity of a water-steam flow," *Water Resour. Res., 15,* 684-686.

Huyakorn, P. S., and Pinder, G. F. (1983), *Computational Methods in Subsurface Flow,* Academic Press, San Diego, Calif.

Long, J. C. S., and Witherspoon, P. A. (1985), "The relationship of the degree of interconnection to permeability in fracture networks," *J. Geophys. Res., 90,* 3087-3098.

Matthews, C. S., and Russell, D. G. (1967), *Pressure Buildup and Flow Tests in Wells,* Society of Petroleum Engineers, Dallas.

Moench, A. F. (1984), "Double-porosity models for a fissured groundwater reservoir with fracture skin," *Water Resour. Res., 20,* 831-846.

Pinder, G. F., and Gray, W. G. (1977), *Finite Element Simulation in Surface and Subsurface Hydrology,* Academic Press, San Diego, Calif.

Pruess, K. (1987), "TOUGH User's Guide," *Rep. LBL-20700,* Lawrence Berkeley Laboratory, Berkeley, Calif.

Pruess, K., and Narasimhan, T. N. (1982), "On fluid reserves and the production of superheated steam from fractured, vapor-dominated geothermal reservoirs," *J. Geophys. Res., 25,* 9329-9339.

Pruess, K., and Narasimhan, T. N. (1985), "A practical method for modeling heat and fluid flow in fractured porous media," *SPE J., 25,* 14-26.

Pruess, K. P., and Wu, Y.-S. (1989), "A new semi-analytical method for numerical simulation of fluid and heat flow in fractured reservoirs," *Paper SPE-18426,* Society of Petroleum Engineers, Dallas.

Spivak, A. (1991), "Evaluation of Unocal and LBL models for predicting performance of the Geysers geothermal reservoir," Intera West, Los Angeles, Calif.

Streltsova, T. D. (1983), "Well pressure behavior of a naturally fractured reservoir," *SPE J., 23,* 769-780.

Vermeulen, T. (1953), "Theory of irreversible and constant-pattern solid diffusion," *Ind. Eng. Chem., 45,* 1664-1670.

Warren, J. E., and Root, P. J. (1963), "The behavior of naturally fractured reservoirs," *SPE J., 3,* 245-255.

Zimmerman, R. W., Chen, G., and Bodvarsson, G. S. (1992), "A dual-porosity reservoir model with an improved coupling term," 17th Workshop on Geothermal Reservoir Engineering, Stanford, Calif.

PROCEEDINGS, Eighteenth Workshop on Geothermal Reservoir Engineering
Stanford University, Stanford, California, January 26-28, 1993
SGP-TR-145

AN APPROACH FOR GEOCHEMICAL ASSESSMENT OF CHIPILAPA GEOTHERMAL FIELD

D Nieva, M P Verma, E Portugal and V Torres

Departamento de Geotermia, Instituto de Investigaciones Eléctricas,
Apartado Postal 475, Cuernavaca, Mor. 62000, Mexico.

ABSTRACT

It presents a systematic methodology to evaluate the reservoir characteristics of Chipilapa-Ahuachapan geothermal field through the highly diluted natural manifestations (springs and domestic wells) in its surroundings. The manifestations are classified in three main groups according to their mechanism of formation: *high salinity water (HSW), medium salinity water (MSW)*, and *Sulfated Water (SW)*. The reservoir temperature at Chipilapa geothermal field is around 220°C which is estimated with application of various chemical geothermometers. The isotopic studies indicate that the heating of local meteoric water with the separated steam of deep reservoir fluids is a dominating process in the formation of springs and domestic wells fluids. The process of formation of primary and secondary vapor explains the isotopic composition of fumaroles.

INTRODUCTION

To evaluate prospects of a geothermal field, the geochemical studies of natural manifestations, springs and fumaroles are of great help as they provide preliminary estimates of reservoir characteristics and hydrothermal model of the system. As geochemistry of fumaroles is yet not very clear, the geochemical exploration is basically based on spring water samples. If the springs are highly diluted (i.e. containing a very small component of deep reservoir fluid), it is quite difficult to obtain concrete results. Thus it requires a special attention in interpretation of the data of such highly diluted natural manifestations.

The Chipilapa geothermal field is located in the western part of El Salvador, in north-west of the coastal cordillera, the east of Ahuachapan City, and south-west of Turin and Atiquizaya localities (Nieva et al, 1990). Ahuachapan geothermal system is located west of Chipilapa geothermal field and its has an installed capacity of 90 MWe. Chemical analyses of production fluids from Ahuachapan geothermal system indicate a gradient in temperature and calculated reservoir chloride concentration from 265°C and 9000 ppm Cl in the western part to 235°C and 6000 ppm Cl in the eastern part (Truesdell, 1989). This is considered as a mixing of cooler and less saline water.

Stewart (1990) reassessed the isotopic work of Nuti et al (1986) with the aim to obtain reservoir conditions. The isotopic composition of the fumaroles indicates their formation from high temperature (200°C) steam within the geothermal aquifer.

In the present article we report the results of geochemical studies obtained under the project "Geoscientific and Reservoir Engineering Studies of the Chipilapa Geothermal Field". This project contemplates Geochemical, Geophysical, Geological and Reservoir Engineering studies to estimate geothermal potential of the Chipilapa system to produce electricity.

GEOCHEMICAL EVALUATION OF NATURAL MANIFESTATIONS

The hydrothermal activities at Chipilapa geothermal field are evident in the form of a number of fumaroles, cold and hot springs, and hot water domestic wells. A program of continuous monitoring the chemical behavior of natural manifestations has been carried out by 'Comisión Ejecutiva Hidroeléctrica del Río Lempa' (CEL) during 1980 and 1983. These data have been compiled by Nieva et al (1990) to define the program of sampling of the manifestations for chemical and isotopic studies in order to assess geothermal potential of the field.

The chemical and isotopic ($\delta^{18}O$ and δD) analyses of the samples collected during 1990 are given in the Table 1. The chemical analyses were performed at 'Centro de Investigaciones

Geotérmicos de CEL, El Salvador', whereas the isotopic analyses are carried out at 'Instituto de Investigaciones Eléctricas, México'. There is a good agreement in the chemical analyses of these samples and that of the sampling points analyzed during 1980 and 1983.

Classification of the Manifestations

In an internal report of CEL, it has been observed the existence of various types of waters from Ca-Mg-HCO_3 type to Na-Cl type, and sulfated waters (CEL, 1986). This classification is based on the utilization of comparative diagrams such as Pipper diagram. Nieva et al (1990) have shown that the springs waters have a very small percentage of deep geothermal fluid, one has to take care in case of classification of such manifestations.

Giggenbach (1988) proposed a triangular diagram of Na, K, and Mg, using the thermodynamic properties of stable minerals to distinguish waters in equilibrium with high temperature minerals, waters formed of partial equilibrium, dilution or mixing, and shallow waters. The fluids from Chipilapa-Ahuachapan geothermal system are plotted in this triangular diagram (Figure 1). The fluids obtained from the drilled wells of Ahuachapan geothermal system are situated at the rock-water equilibrium curve. It also indicates the equilibrium temperature of 260°C. Whereas the fluids from the springs fall in the region of shallow waters. This may be due to high dilution with superficial water or re-equilibrium with rocks at low temperature. However, there exists a good correlation in concentration of Na and K, which supports the highly dilution of geothermal fluid with local meteoric water.

With bi-variable diagrams of concentration of dissolved species in the fluids of the manifestations, Nieva et al (1990, 1990a) have shown the existence of various types of geothermal waters, although the fluids are highly diluted with local meteoric water. The manifestations may be grouped in the following dominant types: *High Salinity Water* (**HSW**) *which are derived with mixing of high saline water (separated fluid of deep reservoir fluid) and meteoric water , Medium Salinity Water* (**MSW**), *formed with dilution of medium saline geothermal component with meteoric water* and *Sulfated Water* (**SW**), and mixture of these waters. Under this classification the meteoric waters belongs to both groups, HSW and MSW as they are end member of tendencies of the groups in bi-variable diagrams. The SW manifestations have very low salinity, but high concentration of

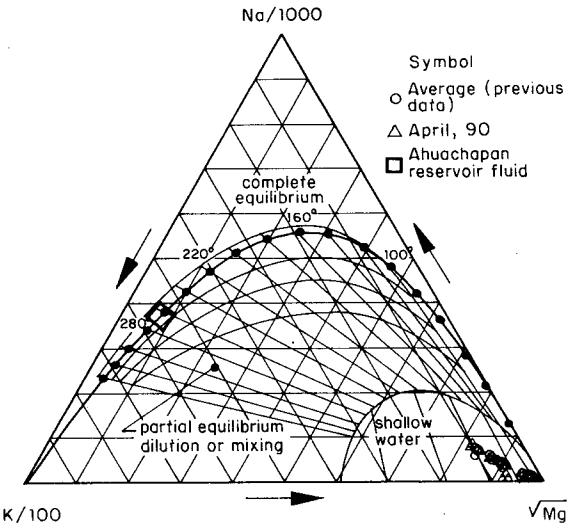

Fig. 1: Triangular diagram in relative contents of Na, K, and Mg to evaluate rock-water interaction equilibrium temperature of a geothermal system (Giggenbach and Stewart, 1982).

bicarbonates and sulfates. These are in general located in the high mountain range in the south of the Chipilapa-Ahuachapan geothermal field, whereas the manifestations related to HSW and MSW are located in the low elevation part in the north the geothermal system.

Chemical Geothermometers

The reservoir temperature of Chipilapa geothermal system is estimated by applying Na-K-Ca (Fournier and Truesdell, 1973), Na-K-Ca with Mg correction (Fournier and Potter, 1979), Cation Concentration (Na-K-Ca-Mg, Nieva and Nieva, 1987) and Na-K (Fournier, 1979) geothermometers. These geothermometers show a wide variation in underground temperature. The Na-K-Ca geothermometer indicates temperatures up to 215°C, whereas the temperatures measured by the Na-K geothermometer are mostly around 260°C. However, the geothermometers which consider the correction of Mg, such as Na-K-Ca with Mg correction and Cation Concentration (CCG) geothermometers, show quite low temperature. The high concentration of Mg in these samples, relatively, indicates that the thermal component of water might have suffered a re-equilibrium at low temperature during ascending to surface or its composition has been altered sufficiently with mixing of high proportion of superficial cold waters.

It has been observed that the temperature measured for the high concentration samples of MSW

Table 1: Chemical and isotopic analysis of natual manifestations in surroundings of Chipilapa-Ahuachapan geothermal system.

Sample	Date	Na	K	Ca	Mg	Cl	SO4	CO3	HCO3	SiO2	B	Fe	Li	Sr	pH	Elec. Cond.	T (°C)	Charge bal.( )	$\delta^{18}O$	δD
Meteoric water with very low proportion of geothermal component																				
F724	11/04/90	22.6	5.6	25.0	11.7	6.5	12.5	2.5	156	90	0.07	ND	ND	0.12	8.54	318	30.3	3.9	-7.89	-57.3
F737	11/04/90	25.3	5.7	37.5	18.2	22.9	18.7	3.6	182	89	0.07	ND	ND		8.58	460	28.2	5.4	-7.32	-53.4
P438	11/04/90	37.0	6.9	22.0	11.0	23.2	14.0	5.4	150	94	0.38	ND	0.06	0.13	8.54	380	31.5	2.9	-7.43	-56.5
P448	10/04/90	37.2	9.6	28.8	13.1	26.9	12.0	7.2	183	85	0.36	0.9	0.08	0.17	8.57	420	30.4	1.6	-7.48	-52.7
P457	27/06/90	38.2	7.4	29.0	13.6	27.7	12.0		200	89	0.5	0.76	0.08		8.16	400	30.0	1.7	-7.62	-57.3
P481	27/06/90	37.2	7.5	30.0	11.2	43.5	11.3		209	89	0.3	0.21	0.07		7.26	390	29.4	-3.1	-7.54	-54.0
M2	11/04/90	35.4	6.2	24.6	10.0	23.9	13.3	3.6	156	96	0.31	ND	0.06	0.13	8.50	370	30	1.8	-7.50	-55.7
Thermal water belongs to MSW group																				
F717	11/04/90	201.0	23.0	13.9	3.6	75.0	29.9		461	143	2.70	0.3	0.67	0.12	8.26	968	62.3	0.7	-7.21	-50.6
F730	11/04/90	187.0	23.6	15.1	3.5	81.8	27.9	22.8	394	156	2.70	ND	0.66	0.13	8.74	940	57.6	-1.1	-7.39	-51.7
F733	11/04/90	128.0	20.8	34.0	7.0	80.7	30.4	10.8	337	137	1.50	ND	0.46	0.27	8.64	810	50.6	-2.0	-7.24	-50.6
F733E	11/04/90	132.0	21.0	34.0	7.2	78.2	29.7	4.8	358	152	1.52	ND	0.48	0.23	8.54	824	50.6	-1.2	-7.26	-52.4
F734	11/04/90	164.0	23.0	23.4	4.7	80.2	29.3	10.8	387	150	2.20	0.2	0.59	0.18	8.69	919	57.6	-1.1	-7.29	-50.1
F735	11/04/90	175.0	22.8	20.4	4.2	86.9	28.7	15.6	376	143	2.40	ND	0.60	0.13	8.69	940	59.3	-0.4	-7.28	-52.2
F757	11/04/90	109.0	17.5	22.4	4.6	46.7	26.0	13.8	265	128	0.92	0.3	0.32	0.18	8.64	640	40.3	0.5	-7.22	-52.5
F760	11/04/90	100.0	15.2	18.7	4.6	37.2	22.2	6.0	256	128	0.68	1.3	0.32	0.18	8.37	588	38.4	1.6	-6.91	-51.7
P468	27/06/90	174	20	23.8	6.0	61.8	25.4		447	132	2.1	ND	0.53		7.88	880	44.2	2.2	-7.07	-51.3
Thermal water belongs HSW group																				
F719	27/06/90	154	25.2	29.8	12.1	185	17.8	2.4	254	128	4.3	0.06	0.4		8.34	940	42.4	0.3	-7.41	-52.8
F740	20/06/90	229.0	39.0	28.0	10.3	342.0	19.9		244	133	6.5		0.12		8.00	1400	37		-7.04	-51.4
F741	27/06/90	70	15.7	26.8	12.8	104	10.7		162	96	1.6	0.1	0.11		7.83	597	29.3	1.0	-7.47	-53.3
P412	11/04/90	139.0	25.2	36.8	12.6	183.0	16.4	12.0	220	133	4.20	1.6	0.40	0.25	8.64	960	34.3	0.6	-7.26	-53.0
P413	11/04/90	154.0	24.4	30.4	10.0	170.0	9.5	12.0	232	118	3.90	0.5	0.41	0.20	8.62	962	36.3	2.8	-6.39	-51.3
M1	11/04/90	148	23.6	28.4	10.6	187	17.1	4.8	265	136	3.9	ND	0.47		8.43	1000	44.4	-3.7	-7.21	-54.5
Sulphate water (SUL)																				
F716	11/04/90	16.2	7.5	43.0	12.8	4.0	49.8	1.2	136	102	0.07	ND	ND		8.46	387	40.0	9.0	-7.42	-51.4
F720	11/04/90	24.0	5.6	20.9	9.2	9.6	20.6		122	92	0.22	ND	0.05	0.12	7.95	295	28.3	5.9	-7.07	-51.3
F726	10/04/90	29.9	9.5	53.0	11.2	0.4	95.4	6.1	158	81	0.03	ND	0.06	0.07	8.56	460		3.3	-7.91	-55.6
F727	10/04/90	29.3	9.6	49.0	10.8	0.3	98.3	3.6	153	76	0.02	ND	0.04	0.12	8.49	454	33.3	1.8	-7.94	-55.3
F728	10/04/90	12.0	2.7	36.4	8.3	3.5	33.4		133	64	0.02	ND	ND	0.20	6.98	300	24.4	9.4	-7.14	-50.6
F729	10/04/90	11.5	2.2	39.5	8.4	4.0	40.6	1.8	132	64	0.01	ND	ND	0.17	8.42	310	28	0.6	-7.27	-52.5
F747	5/04/90	23.4	6.2	64.0	14.2	2.3	138	1.2	168	121	0.06	3.5	0.04		8.49	522	38.6	-1.7	-7.71	-49.4
P469	11/04/90	15.1	4.5	28.2	8.2	2.0	48.4		101	87	0.04	ND	ND	0.25	8.09	309	27.5	2.8	-5.97	-47.3
P526	10/04/90	12.5	4.1	22.6	10.8	2.7	2.6	3.0	135	102	0.04	ND	ND	0.12	8.48	250	24.9	4.3	-7.06	-48.9
M28	05/04/90	49.8	17.8	24.6	5.9	2.6	126.0		85	219	0.48	ND	0.04	0.20	7.48	455	81	4.1	-6.43	-49.0
Water formed with mixing of HSW-MSW																				
F722	11/04/90	165.0	23.4	21.4	6.5	136.0	21.4		301	146	3.60	ND	0.56	0.13	8.14	940	45.6	1.6	-7.10	-50.1
F725	10/04/90	8.7	4.1	21.0	6.5	3.1	22.1		52	64	0.03	ND	ND		8.03	250		19.7	-7.69	-52.7
F752	11/04/90	167.0	20.8	20.0	6.3	105.0	21.7		371	133	2.80	0.3	0.59		8.28	940	51.3	-0.4	-7.30	-51.5
F754	11/04/90	167.0	22.2	15.0	7.0	118.0	22.0	15.0	331	146	3.60	0.2	0.59	0.13	8.70	959	59.6	-2.5	-6.99	-53.2
P410	11/04/90	71.5	16.6	36.4	16.0	140.0	12.7	4.2	139	101	2.30	0.3	0.08	0.32	8.48	700	28.8	0.4	-7.08	-54.2
P414	11/04/90	166.0	23.6	22.4	7.0	149.0	20.9	24.0	248	144	3.70	0.4	0.56	0.15	8.66	462	41.3	0.5	-6.99	-55.8
P414	27/06/90	164	24.2	22.8	7.8	152	20.5		297	139	3.7	0.14	0.49		7.62	860	41.7	1.4	-6.99	-52.5
F744	10/04/90	10.2	3.3	21.2	3.9	1.9	27.5		76	54	ND	ND	ND		8.22	235	21.7	1.1	-7.74	-54.6

group with various geothermometers are quite consistence. The geothermometers CCG and Na-K-Ca with Mg correction show very low temperature except samples 717 and 730. It may be concluded that the samples 717 and 730 have little effect in alteration of chemical composition due to mixing of cold waters. Thus the samples (717 and 730) provide information about deep temperature as in the range 220-230°C.

ISOTOPE HYDROLOGY OF CHIPILAPA-AHUACHAPAN GEOTHERMAL SYSTEM

The isotope compositions ($\delta^{18}O$ and δD) of the springs and the domestic wells, together with the condensed waters from fumaroles (Stewart, 1989) and the total discharge composition of five productive wells (AH-6, AH-19, AH-22, AH-24, and AH-31) of Ahuachapan geothermal system (Nieva et al, 1990) are shown in Figure 2.

Stewart (1990) has reported the isotopic compositions of rainfall at different altitude in the region, which were collected and analyzed by Nuti et al (1986). These samples fall close to the global meteoric water line ($\delta = 8\ \delta^{18}O + 10$) with a mean deuterium excess of 10.3‰. He argued that these samples should not be used to determine the mean isotopic composition of local meteoric water as the average isotopic composition of these rainfalls because they only cover three months of one year. The weighted mean isotopic composition ($\delta D = -47.0$, $\delta^{18}O = -7.0$) of six years rainfall at San Salvador, which is about 120 km from the studied area and has a very similar geographic setting, is a good alternative to consider the average meteoric water composition and the local meteoric line as passing through this point with a gradient of 8. The meteoric line and this point are also shown in the Figure 2.

MIXING MODELS

The geothermal fluids are, in general, formed by an interaction of hot rocks and local meteoric water which infiltrates through faults and fractures in the field. During their ascent to superficies, these fluids cool to a temperature equal or less than the local boiling point by the three important processes: *(i) Adiabatic cooling:* steam separation due to adiabatic expansion of the fluid with decreasing pressure, *(ii) Mixing:* dilution and mixing with waters derived from shallow sources, and *(iii) Conductive cooling:* heat loss in heating country rocks. Normally, the three processes take place in formation of manifestations. However, it is possible to understand mechanism occurred during ascent of the

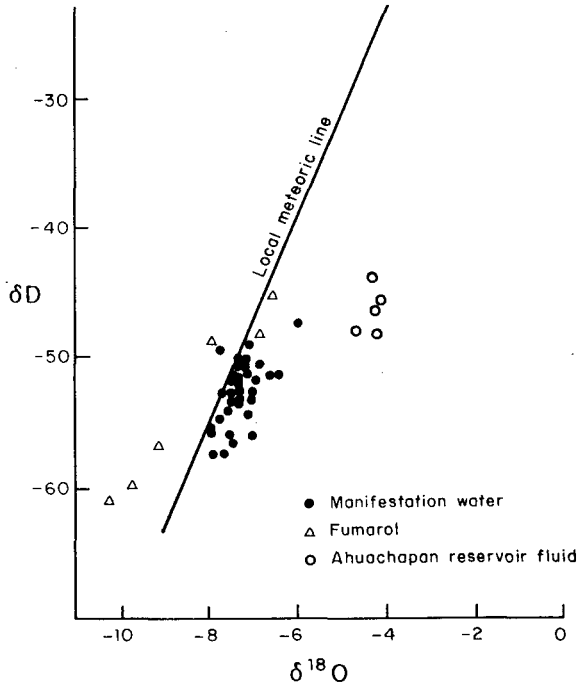

Fig. 2: The isotopic relation ($\delta^{18}O$ vrs. δD) of Chipilapa geothermal field.

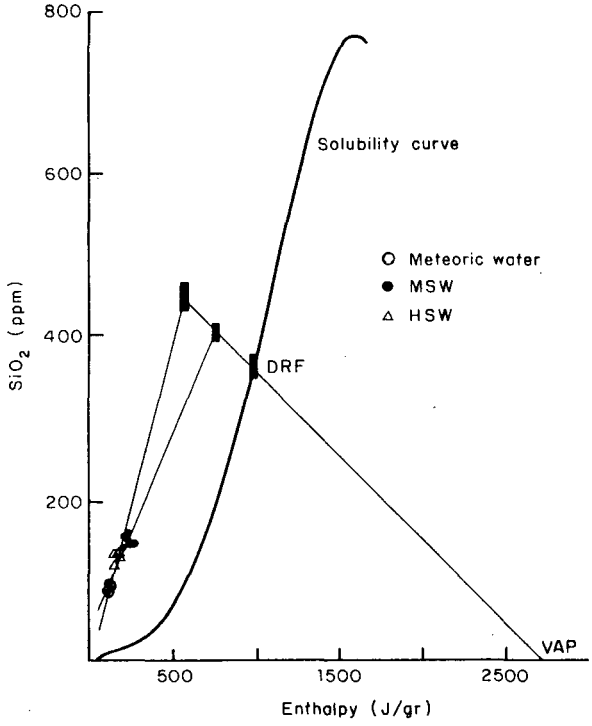

Fig. 3: A mixing model diagram of Enthalpy vrs. SiO_2. It demonstrates the formation of the HSW and MSW groups with mixing of meteoric water and separated deep reservoir fluid at 130-140°C, and 170-180°, respectively.

deep fluids through mass and energy balance equations, if the first two processes have major contribution.

The formation of the two groups manifestations, HSW, and MGW is demonstrated through an quartz solubility vrs. enthalpy diagram (Figure 3). The solubility curve of quartz is a locus of all the points of quartz concentration which are in equilibrium at corresponding enthalpy or temperature (Fournier and Potter, 1982). The reservoir temperature between 220–230°C suggests the equilibrium concentration of SiO_2 in reservoir fluid in between 340–360 ppm. The extrapolated least square fitted lines in the points corresponding the two groups are also shown in the Figure 3. According to this mixing model the reservoir fluid flushes in two phases (vapor and liquid) and then the flushed liquid mixes with the local water in formation of natural manifestations. The model indicates that the group HSW formed by flushing at 130–140°C, whereas MSW formed by flushing at 170–180°C.

The evidences obtained during drilling of wells CH-7 and CH-8 at Chipilapa geothermal field also support the reservoir temperature around 220°C. The chloride concentration of reservoir fluid, calculated according to this model from HSW, should be in between 2200–2450 ppm, whereas MSW indicates only 380–400 ppm (Nieva et al, 1990a). This anomaly arises on account of differences in formation mechanism of these two groups of water and it is used in nomenclature of these groups.

The isotopic mixing model provides an important clue to understand the mechanism of natural manifestation formation. The isotopic composition of condensed waters from fumaroles in the Ahuachapan-Chipilapa field has been explained with a hypothesis of mechanism of formation of primary and secondary vapor in the hydrothermal system (Stewart, 1990). The primary steam originates from the separation of geothermal fluids. This steam may be absorbed in superficial aquifer and may cause its boiling. The steam produced through the boiling this superficial aquifer is named as secondary steam (Giggenbach and Stewart, 1982). Stewart (1990) postulated existence of underground water of 80°C with isotopic composition ($\delta D = -48$, $\delta^{18}O = -7.25$) to explain the phenomenon in formation of manifestations in Ahuachapan-Chipilapa geothermal field.

Nieva et al (1992) explain the evolution of isotopic composition of fumaroles and the waters of groups, HSW and MSW through the mixing mechanism of local meteoric water and components of geothermal fluid according to model proposed by Giggenbach and Stewart (1982). The isotopic composition of deep geothermal water ($\delta^{18}O = -4$ and $\delta D = -45$) is chosen same as reported by Stewart (1990) and the local meteoric water is considered as a cold, low saline spring with isotopic composition ($\delta^{18}O = -7.5$ and $\delta D = -54$). The data points corresponding to the fumaroles, lie in between the curves related to isotopic composition of primary steams from undiluted deep water and secondary steam from primary undiluted steam.

HYDROGEOTHERMAL MODEL OF CHIPILAPA FIELD

Figure 4 shows a schematic diagram of the Chipilapa's hydrogeothermal model which is an outcome of the above evidences. The local meteoric water infiltrates deeply in formation of deep reservoir fluid (DRF) which is reservoir at Ahuachapan geothermal system at 260°C. This DRF separates at 220–230°C in formation fumaroles in the high mountain range and reservoir fluid at Chipilapa geothermal system. A mixture of DRF and primary and secondary condensed vapor (PCV and SCV) are diluted with meteoric water (MW) in formation of the two HSW and MSW. The manifestations of the group are located at low elevation part in the north of the field . The springs associated with sulfated water are found generally near to these mountains. The sulfated water formed by heating of meteoric water with the separated steam. This explains existence a heat source under the mountainous part of the field which is located in the south of the Chipilapa-Ahuachapan geothermal reservoir. The fluid is flowing laterally from the high elevation to low elevation in the north of the system.

CONCLUSIONS

The geothermal model of Chipilapa is a lateral flow model. The local meteoric water infiltrates deeply through faults and fracture in the upper part of mountain range and gets heated up to 260°C. The reservoir fluid at Ahuachapan geothermal system are in rock-water interaction equilibrium at 260°C. As chemical geothermometers indicates 250–270°C reservoir temperature and all the data points corresponding to geothermal wells fall near to the equilibrium curve at the point of 270°C. The chemical geothermometers indicate the reservoir temperature of 220–230°C at Chipilapa geothermal field. The most of the manifestations (springs and domestic wells) in the lower portion of the

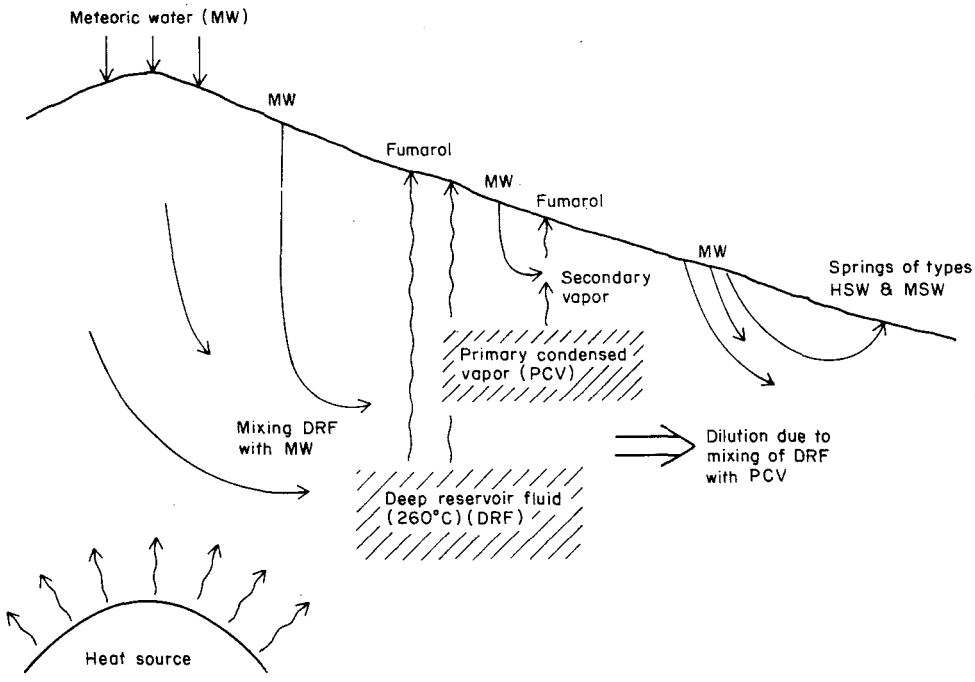

Fig. 4: Sketch diagram of hydrothermal model of Ahuachapan-Chipilapa geothermal system.

field are grouped in two classes, high salinity water (HSW) and medium salinity water (MSW), according to their formation mechanism. The chemical and isotopic studies of the fluid obtained through the drilled wells at Chipilapa geothermal field will contribute significantly in improvement of the presently preliminary model of the system.

REFERENCES

Fournier, R.O. (1979) 'Magnesium correction to the Na-K-Ca chemical geothermometer', Geochim. Cosmochim. Acta, Vol. 43, pp. 1543-1550.

Fournier, R.O. and Potter II, R.W. (1979) 'An equation correlating the solubility of quartz in water from 25° to 900°C at pressure up to 10,000 bars', Geochim. Cosmochim. Acta, vol. 46, pp. 1969–1974.

Fournier, R.O. and Truesdell, A.H. (1973) 'An empirical Na-K-Ca geothermometer for natural waters', Geochim. Cosmochim. Acta, vol. 37, pp. 515–525.

Giggenbach, W.F. (1988) 'Geothermal solute equilibria. Derivation of Na-K-Mg-Ca geoindicators', Geochim. Cosmochim. Acta, Vol. 52, pp. 2749–2765.

Giggenbach, W.F. and Stewart, M.K. (1982) 'Processes controlling the isotope composition of steam and water discharges form steam vents and steam-heated pools in geothermal areas', Geothermics, Vol. 11, pp. 71–80.

Nieva, D. and Nieva, R. (1987) 'Developments in geothermal energy in Mexico. XII. A cationic composition geothermometer for prospection of geothermal resources', Heat Recovery Systems & CPH, Vol. 7, pp. 243-258.

Nieva, D., Verma, M.P. and Portugal, E. (1990) 'Informe de revisión de evidencia previa para el estudio geoquímico', Informe GQM-IF-001 del proyecto de estudio geocientíficos y de ingeniería de reservorios del campo geotérmico de Chipilapa.

Nieva, D., Verma, M.P., Portugal, E. and Santoyo, E. (1990a) 'Estudio Geoquímico: informe final', Informe GQM-IF-002 del proyecto de estudio geocientíficos y de ingeniería de reservorios del campo geotérmico de Chipilapa.

Nuti, S., Martinez, J.A., Campos., A., and Luna, L.A. (1986) Isótopos en estudios geotérmicos. Actividad: estudios de los isótopos ambientales en el área geotérmico de Ahuachapan, IAEA Scientific Report ELS/8/002-01

Truesdell,A.H., Aunzo, A., Bodvarsson, G., Alonso, J. and Campos, A. (1989) 'The use of Ahuachapan fluid chemistry to indicate natural state conditions and reservoir processes during exploitation', XIV Workshop on Geothermal Reservoir Engineering, Stanford University, Stanford, Cal.

Stewart, M.K. (1990) 'Environmental isotope study of Ahuachapán geothermal area: a reassessment' Manuscript provided by CEL.

PROCEEDINGS, Eighteenth Workshop on Geothermal Reservoir Engineering
Stanford University, Stanford, California, January 26-28, 1993
SGP-TR-145

NEW PROJECT FOR HOT WET ROCK GEOTHERMAL RESERVOIR DESIGN CONCEPT

Hideaki Takahashi and Toshiyuki Hashida

Research Institute for Fracture Technology
Tohoku University
Sendai/980, Japan

ABSTRACT

This paper presents the outlines of a new Hot Wet Rock (HWR) geothermal project. The goal of the project is to develop a design methodology for combined artificial and natural crack geothermal reservoir systems with the objective of enhancing the thermal output of existing geothermal power plants. The proposed concept of HWR and the research tasks of the project are described.

INTRODUCTION

It is well known that the productivity of geothermal wells is strongly dependent on the existence of cracks in rock masses. The concept of Hot Dry Rock (HDR) has been proposed in an attempt to create an artificial heat exchanging circulation system by means of well stimulation techniques such as hydraulic fracturing. This idea has attracted considerable interests and resulted in large-scale research projects in the U.S., Europe and Japan. The majority of currently operating geothermal power plants in Japan heavily rely on natural geothermal fluid stored in the existing subsurface crack network. However, the potential thermal energy from the surrounding areas is typically not fully utilized and remains unexploited. The thermal power output is therefore limited, unfortunately. Thus, there is a strong need for enhancing the thermal power of the existing geothermal reservoirs and for extending their operation life.

In response to the need, a new academic research project has been launched at Tohoku University, Japan. This research project is directed towards establishing an engineering design methodology for the further development of existing natural geothermal reservoirs. We have adopted the basic idea of HDR, and combined the existing available geothermal reservoir in the developments. As a result, the new concept of Hot Wet Rock (HWR) is created. The schematic of the concept is illustrated in Fig. 1. The HWR system refers to the combined natural and artificial crack network.

In this paper, the outlines of the new research project for HWR are presented, and the research tasks of working groups formed in the project are briefly described.

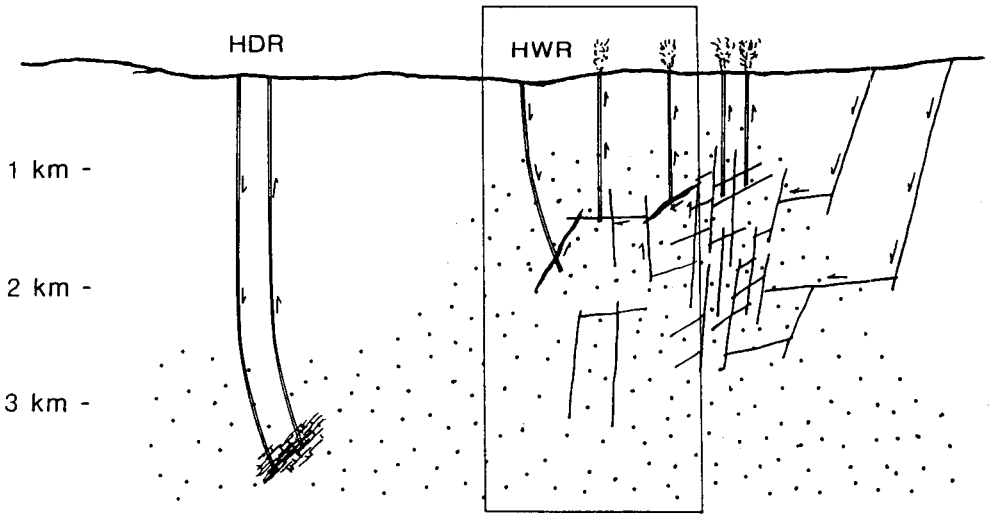

Fig. 1. The concept of Hot Wet Rock (HWR) geothermal reservoir

OUTLINES OF HWR PROJECT

The HWR project is being carried out in close cooperation with the MITI-NEDO geothermal energy development program (1989-1993). Fig. 2 shows the project organization structure. A research group of geothermal energy extraction engineering (GEEE) has been formed at Tohoku University. This research group is composed of several interdisciplinary teams, and plays a technical leading role in the project. As indicated in Fig. 2, a number of private companies and national research laboratories are also participating in the project.

The HWR concept specifically aims to connect a designed artificial crack with a preexisting geothermal reservoir in order to take full advantage of the surrounding area which is full of potential thermal energy. The establishment of the combined methodology for HWR systems calls for several element technologies. The following investigations form the major research tasks of the project:

(1) Monitoring and modelling of natural crack networks
(2) Design methodology of artificial heat exchange surfaces: optimization of the location and size of artificial cracks
(3) Heat extraction simulation from the combined geothermal reservoir
(4) Methods for predicting long-term reservoir performance

The methods listed above are being developed through working group activities in GEEE as shown in Table 1. The table also shows key personnels and their contributions. The GEEE team has carried out a research project on the design methodology of artificial crack-like reservoir for HDR geothermal energy extraction, which was a grant-in-aid for special distinguished research supported by the Government of Japan, Ministry of Education, Science and Culture (Abé , H. and Takahashi, H., 1983, Takahashi, H. and Abé , H., 1987, Niitsuma, H., 1989). The former project is called Γ-project. A crustal rock fracture mechanics approach has been proposed for HDR systems, and verified through field experiments. In the research task (2) of the HWR project, the fracture mechanics methodology is employed and further extended to the combined geothermal reservoir system.

The methodology is scheduled to be applied in the Yunomori geothermal field of the MITI-NEDO program. The temperature in the field is estimated to be about 200 ℃ at a depth of 1500 m. The time schedule of well drilling and experimentation is shown in Table 2. The HWR project provides academic supports for designing a geothermal reservoir in the model field along the time schedule.

RESEARCH ACTIVITIES IN GEEE

In this section a brief description of the individual research task is presented together with some results obtained to date. Given the importance of the natural crack characterization on the proposed combined geothermal reservoir performance, various crack monitoring techniques and modeling methods are being developed within the WG research activities. Fig. 3 illustrates a process for the development of design methodology for HWR systems. The WG researches

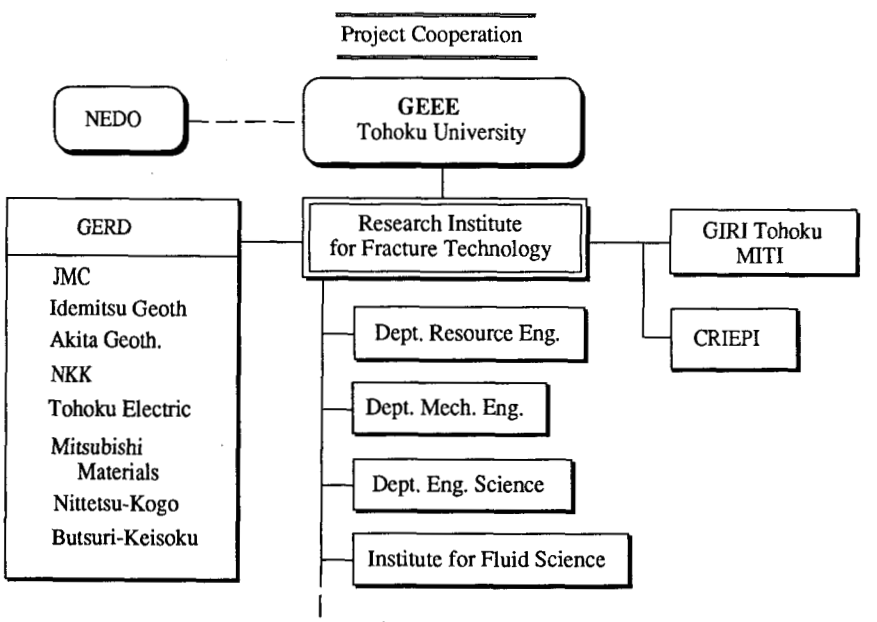

Fig. 2. Research organization structure of HWR project and project cooperation

Table 1. Research group of geothermal energy extraction engineering (GEEE), Tohoku University

Project Chairman	Prof. H. Takahashi (Research Inst. for Fracture Technology)
Project Vice-Chairman	Prof. K. Nakatsuka (Dept. of Resource Eng.)

Working Group	Personnels and Organization	
	WG Leader	WG Subleader
Subsurface Structure Evaluation WG	Prof. H. Niitsuma (Dept. of Resource Eng.)	Ass. Prof. M. Sato (Dept. of Resource Eng.)
Subsurface Crack Design WG	Prof. K. Hayashi (Inst. for Fluid Science)	Ass. Prof. T. Hashida (RIFT*)
Rock Mass Property Evaluation WG	Ass. Prof. K. Matsuki (Dept. of Resource Eng.)	Ass. Prof. T. Hashida (RIFT)
Thermal Design and Evaluation WG	Prof. T. Shoji (RIFT*)	Prof. K. Hayashi (Inst. for Fluid Science)

* RIFT: Research Institute for Fracture Technology

Table 2. Time schedule of MITI-NEDO project: Yunomori field experiments

Year	Schedule
1989	Selection of model field: Yunomori field
1990	Test drilling
1991	Drilling of production well
1992	Hydraulic fracturing (#1)
	Drilling of reinjection well
1993	Hydraulic fracturing (#2)
1994	Circulation test

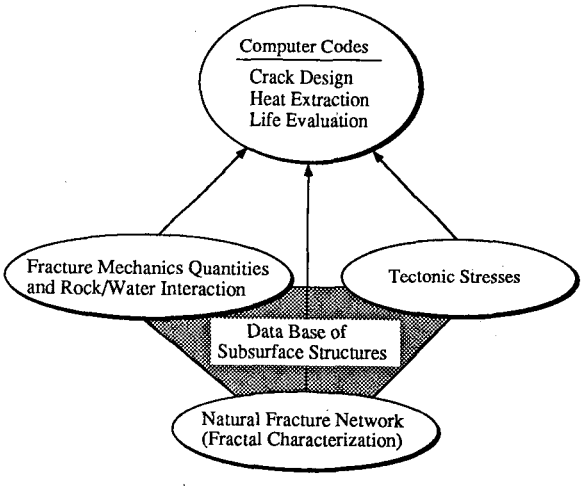

Fig. 3. Flow of research and data base

are also designed to establish a data base of subsurface structures.

(1) Subsurface Structure Evaluation WG

Development of methods for monitoring subsurface cracks is a key issue for the design and performance evaluation of HWR systems. In this project extensive experimental and theoretical investigations are programmed in order to develop reliable methods for evaluating preexisting fracture networks and for detecting artificial cracks induced by hydraulic fracturing technique. The methods being developed are listed in the following:

(a) Monitoring of Preexisting Fractures
- ○ Triaxial shear shadow
- ○ Shear wave splitting
- ○ Acoustic emission monitoring of drilling
- ○ Borehole radar
- ○ Magnetic tracer test.

(b) Monitoring of Artificial Fractures
- ○ Downhole acoustic imaging (triaxial hodogram AE source location); Theoretical study on AE source mechanism is also supporting the development of the method.

For each method, suitable signal detectors and signal processing techniques are being developed. For example, a wideband and high sensitive triaxial seismic detector has been developed for downhole AE source location. In conjunction with the sensor development a new calibration technique for detectors has been devised, which utilizes the spectral matrix analysis to improve the accuracy of the detection of P-wave direction in the triaxial hodogram analysis. The usefulness of the new detector and analyzing technique has been verified through experiments in the GEEE Higashihachimantai model field (Moriya et al., 1990, Niitsuma et al., 1991). In the tests seismic sources were simulated using an air gun in a borehole, and signals from the artificial source were monitored by the triaxial AE sensor set in an another borehole. Fig. 4 compares the results of source location evaluated by the spectral matrix analysis with those obtained by the conventional method in time

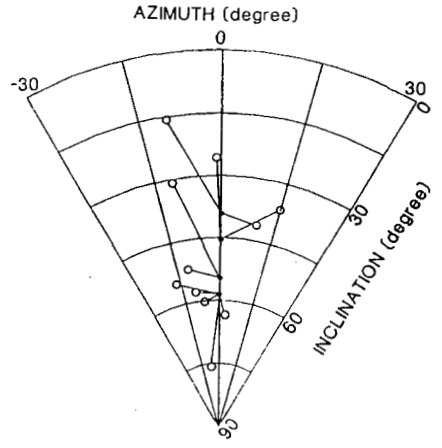

(a) conventional method,

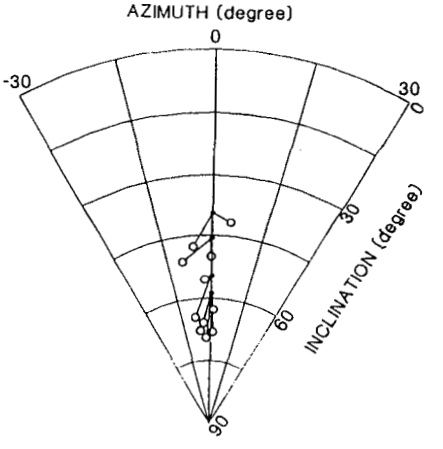

(b) spectral matrix method

Fig. 4. Results of AE source location in calibration tests

domain. The points along the vertical axis indicates the actual location of the artificial seismic sources. It is seen that the new signal processing technique reduces significantly the error in the source location. Furthermore, a triaxial shear shadow technique has been applied to delineate the single crack created by hydraulic fracturing in the Higashihachimantai model field in the course of Γ-project (Niitsuma, H. and Saito, H., 1991). It has been demonstrated that the crack orientation determined by this technique was consistent with that predicted by tectonic stress measurements and core sample observation. The technique is currently being extended to cover more complex fracture networks.

(2) Subsurface Crack Design WG

The research items are outlined below.

(a) Tectonic stress determination; There has been no analyzing method applicable to determine in-situ stresses under the influence of thermal stresses in hydraulic fracturing method. Such a method is now under investigation.

(b) Subsurface crack evaluation based on pressure-flow rate-time records; Computer codes are under development to simulate the crack growth induced by hydraulic fracturing in HWR systems on the basis of the fracture mechanics approach. In order to support the development experimentally, a downhole devise for measuring the crack opening displacement has been fabricated.

(c) Percolation modeling for predicting reservoir performances; Percolation theory is employed to characterize fracture type reservoir and to predict reservoir performance (Usui, T. et al., 1991). Fig. 5 shows a model to examine the effect of an artificial crack on the reservoir permeability. The rectangular inspection area around the injection well is divided into 60×60 grids and the artificial crack is envisioned to extend horizontally towards existing reservoir from the injection well. Natural cracks within the inspection area were generated by using the percolation theory. Namely, the existence or absence of natural crack at the grid point was determined on the basis of the probability density, p. The value of p corresponds to the natural crack density. One segment of grid line whose both ends are

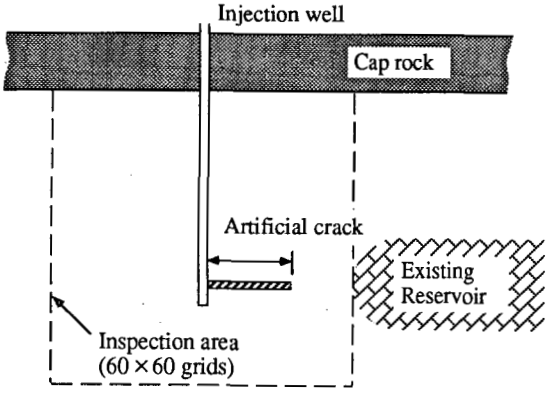

Fig. 5. Reservoir model for examining the effect of an artificial crack on the flow impedance

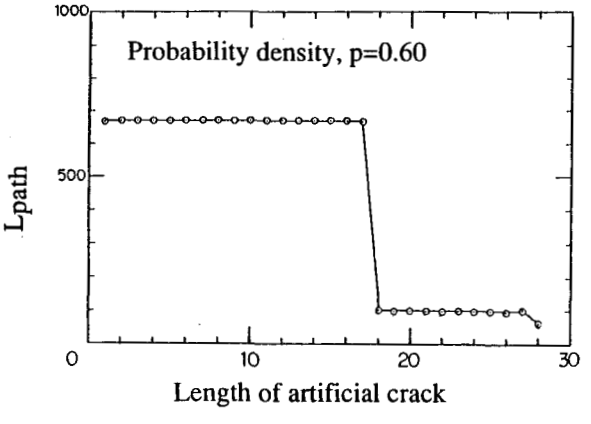

Fig. 6. Example of numerical results based on percolation theory

assigned under a given value of p is taken as an unit of natural crack. Fig. 6 gives an example of result predicted by the model, where L_{path} represents the minimum length of connected paths between injection well and existing reservoir in terms of grid numbers. Higher value of L_{path} can be taken as reflecting higher flow impedance. It is seen that the L_{path} drops rapidly as the artificial crack length reaches 18 grid length. As exemplified in the above example, the percolation model enables an quantitative prediction of an improvement of reservoir permeability by artificial cracks.

(3) Rock Mass Property WG

In order to provide rock mass property and rock/interaction data necessary for the subsurface crack design and thermal extraction analysis, the following investigations are being carried out:

(a) Development of fracture toughness testing method; Core-based test methods are being developed to determine the fracture toughness K_{Ic} under confining pressures. In addition to ISRM suggested core specimens, i.e. short rod and chevron bend, round compact tension specimens are used to evaluate the K_{Ic} in the mutually orthogonal orientations from one piece of core sample.

(b) Determination of tectonic stresses by use of rock core; Various methods including ASR, AE, DSA and DRA will be utilized to finally develop an integrated technique for determining accurate tectonic stresses in addition to the hydraulic fracturing method mentioned above.

(c) Water-rock interaction; Autoclave experiments are performed to determine the kinetics of dissolution and scaling. Investigation of the effect of dissolution on the permeability and the slip resistance along preexisting fractures is also included.

(d) Fractal geometry characterization of geothermal reservoir fracture network: Recent geophysical investigations have revealed that subsurface fracture network could be described by a fractal geometry. In the following a fractal geometry based approach is briefly presented (Watanabe, K. and Takahashi, H., 1991). The fractal relation between fracture length r and the number of fractures N whose length is equal to or larger than r may be expressed by

$$N = Cr^{-D} \qquad (1)$$

where D is fractal dimension and C is a constant which depends on the fracture density of rock mass. Fig. 7 shows an example of fracture network generated by the developed method on the basis of the fractal relation. Based on the recent observation (Meredith, P.G., 1990), the D is assumed to be 1.0 in the computation. The parameter C may be related to the number of fractures measured along a scan-line (as illustrated in Fig. 7) by the following equation

$$C = m / \left\{ \overline{\cos\theta_i} (1 - \ln r_{min}) \right\} \qquad (2)$$

where m is the number of fracture per unit length of the scan-line and $\overline{\cos\theta_i}$ represents an average of $\cos\theta_i$ with θ_i being fracture angle. r_{min} is the smallest observable

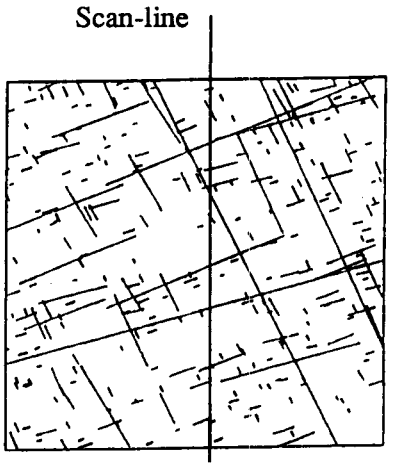

Fig. 7. Fracture network simulated by means of fractal relation

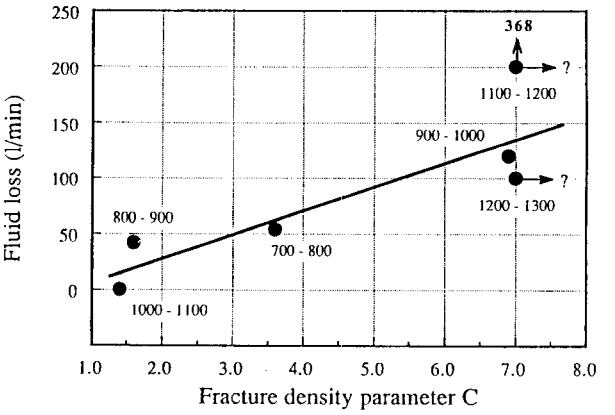

Fig. 8. Comparison between computed fracture density and fluid loss observed during well drilling

length of fracture and depends on the resolution of measurement. The equation allows the parameter C to be determined from the observation of core samples. The above method for characterizing the fracture network has been applied to Kakkonda geothermal field in Japan. The result is shown in Fig. 8 in terms of a comparison between the computed fracture density parameter and the fluid loss observed during well drilling in the field. The general correspondence suggests that the modeling procedure provides a reasonable means for characterizing geothermal subsurface fracture networks.

(4) Thermal Design and Evaluation WG

It is well accepted that the primary fluid flows occur not through homogeneous rock formation, but through fracture networks in fracture type geothermal reservoirs. Considering the complex geometry of fracture networks, it is essential to develop an efficient numerical method for analyzing the heat and fluid flows in HWR reservoirs. LINK (Line-Source and/or Sink Implanted Networks for Fractured Continua) method based on a

double porosity and double permeability model has been developed (Kimura, S. et al, 1991, Masuda, Y.et al, 1991). The concept of the numerical method is shown in Fig. 9. In the method the heat and fluid flows in the fracture, and those in the less permeable rock are calculated separately. As schematically illustrated in Fig. 9, the transport between the rock and fracture network is modelled through one dimensional links. Specifically, the interaction between the fractures and the rock formation is taken into account through sink and source terms in a set of governing equations, describing the transport in the respective system. The present method has been proven to be ten times more efficient than a conventional algorithm by carrying out FEM

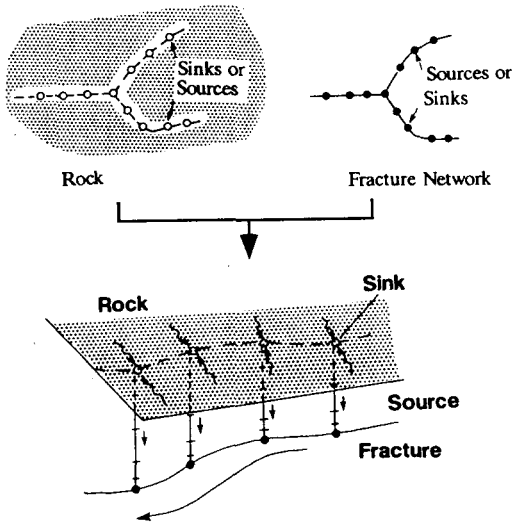

Fig. 9. Concept of proposed LINK method

computations on a simple two-dimensional model. The method is currently being extended to three-dimensional and complex fracture networks. Furthermore, experimental results of dissolution and scaling kinetics are incorporated into the simulator to develop a method for predicting the long-term reservoir behavior based on the rock-water interactions.

Preceding the massive hydraulic fracturing in the Yunomori field, some element technologies above mentioned are being tested in the GEEE Higashihachimantai geothermal model field and Kamaishi test field. Ultimately, the outputs of each individual groups will be integrated to form the foundation of the design methodology for HWR systems.

CONCLUDING REMARKS

The HWR research project outlined in this paper focuses on the development of an engineering methodology for combined fracture type geothermal reservoirs. The technology is expected to enable the further development and enhancement of the thermal power of existing geothermal reservoirs, and then to extend their operation life time. The interdisciplinary approach of the project would facilitate to establish a useful data base of geothermal subsurface structure, which is needed to determine the optimal artificial crack and to design the well stimulation procedure. A comprehensive HWR design methodology, coupled with a subsurface structure data base should be evolved and verified through the field experiment in the course of this project.

REFERENCES

Abé, H. and Takahashi, H. (1983), "Crustal Rock Fracture Mechanics for Design and Control of Artificial Subsurface Cracks if Geothermal Energy Extraction Engineering (G-Project)," Proc. 9th Workshop on Geothermal Reservoir Engineering, Stanford University, pp. 403-408.

Kimura, S., Masuda, Y. and Hayashi, K. (1991), "An Efficient Numerical Method Based on Double Porosity Model to Analyze Heat and Fluid Flows in Fractured Rock Formation," Transactions of the Japan Society of Mechanical Engineers (B), 57-538, pp. 2083-2087 (in Japanese).

Masuda, Y., Kimura, S. and Hayashi, K. (1991), "Heat Extraction Simulation from Fractured Rock by a Double Porosity and Double Permeability Model," Journal of the Geothermal Research Society of Japan, 13-3, pp. 179-190 (in Japanese).

Meredith, P.G., "Cracking, Damage and Fracture in Stressed Rock: A Holistic Approach," Proc. of Nato Advanced Research Workshop on Toughening Mechanisms in Quasi-Brittle Materials, Northwestern University, July 16-20, 1990, pp. 73-104.

Moriya, H., Nagano, K. and Niitsuma, H. (1990),"Precise Estimation of AE Source Direction by Spectral Matrix Analysis," Progress in Acoustic Emission V, Proc. the 10th Int. Acoustic Emission Symposium, Sendai, Japan, Oct. 22-25, 1990, The Japanese Society for Non-Destructive Inspection, pp. 244-251.

Niitsuma, H. (1989),"Fracture Mechanics Design and Development of HDR Reservoirs -Concept and Results of the G-Project, Tohoku University, Japan," Int. J. Rock Mech. Min. Sci. & Geomech. Abstr., 26-3/4, pp. 169-175.

Niitsuma, H., Moriya, H. and Nagano, K. (1991), "Calibration Method Using the Spectral Matrix for Downhole Triaxial Seismic Detectors," in Preprint of 5th Conf. on AE/MA in Geological Structures and Materials, June, 1991.

Niitsuma, H. and Saito, H. (1991),"Evaluation of the Three dimensional Configuration of a Subsurface Artificial Fracture by the Triaxial Shear Shadow Method," Geophysics, in press.

Takahashi, H. and Abé, H. (1987), "Fracture Mechanic Applied to Hot Dry Rock Geothermal Energy," in Fracture Mechanics of Rock, pp. 241-276, B.K. Atkinson ed, Academic Press London, 1987.

Usui, T., Shoji, T. and Hayashi, K. (1991), "Percolation Modeling of a Fracture Type Reservoir -Prediction of an Improvement of Reservoir Productivity by an Artificial Crack," in Preparation.

Watanabe, K. and Takahashi, H. (1991),"Fractal Geometry Characterization of Geothermal Reservoir Fracture Network," Submitted to Journal of Geophysical Research.

EIGHTEENTH ANNUAL WORKSHOP ON GEOTHERMAL RESERVOIR ENGINEERING STANFORD UNIVERSITY

Participants List

Michael C. Adams
University of Utah Research Institute
391 Chipeta Way, Suite A
Salt Lake City, UT 84108
801/584-4435 FAX 801/584-4453

Greg Andersen
UNOCAL
376 S. Valencia
Brea, CA 92621
714/577-2279

Michio Aoki
New Energy & Industrial Technology
29th Floor, Sunshine 60, 1-1, 3-chome
Higashi-Ikebukuro, Toshima-ku
Tokyo 170, Japan
03-3987-9451 FAX 03-3986-8197

Norio Arihara
Waseda University
Dept. Mineral Resources Engineering
3-4-1 Ohkubo, Shinjuku-ku
Tokyo 169, Japan
81-3-3203-4141 FAX 81-3-3200-2567

Paul Atkinson
UNOCAL
3576 Unocal Place
Santa Rosa, CA 95403-1774
707/545-7600 FAX 707/545-8746

Gudni Axelsson
Orkustofnun
Grensásvegur 9
108 Reykjavik, Iceland
354-1-696060 FAX 354-1-688896

Daniel B. Ballantine
Pacific Gas and Electric
Box 456
Healdsburg, CA 95448
707/431-6044 FAX 707/431-6066

Ben Barker
UNOCAL
3576 Unocal Place
Santa Rosa, CA 95403-1774
707/545-7600 FAX 707/545-8746

Alfredo Battistelli
Aquater S.p.A., ENI Group
61047 San Lorenzo in C. (PS)
Italy
39-721-731-326 FAX 39-721-731-308

Joe Beall
Calpine Corporation
P.O. Box 11279
Santa Rosa, CA 95401
707/527-6700 FAX 707/544-2422

Kit Bloomfield
Pacific Gas and Electric
Box 456
Healdsburg, CA 95448
707/431-6000 FAX 707/431-4066

Gudmundur Bodvarsson
Lawrence Berkeley Laboratory
1 Cyclotron Road, MS-50E
Berkeley, CA 94720
510/486-4789 FAX 510/486-5686

Kenneth Bonin
Naval Air Weapons Station
Geothermal Program Office, Code C8306
China Lake, CA 93555-6001
619/939-4049 FAX 619/939-2449

Tom Box
Calpine Corporation
P.O. Box 11279
Santa Rosa, CA 95406-1279
707/527-6700 FAX 707/544-2422

Donald Brown
Los Alamos National Laboratory
Group EES-4, MS-D443
Los Alamos, NM 87545
505/667-1926 FAX 505/667-8487

Patrick Browne
University of Auckland, Geoth. Inst.
Private Bag 92019
Auckland, New Zealand
64-9-373-799

Marinela M. Buenviajie
Philippine National Oil Co.
Energy Development Corporation
Merritt Road, Ft. Bonifacio, Makati
Metro Manila, Philippines
632-815-8961 FAX 632-815-2747

Steve Butler
UNOCAL
3576 Unocal Place
Santa Rosa, CA 95403-1774
707/545-7600 FAX 707/545-8746

Gian Mavro Cameli
E.N.E.L. / S.P.A. - V.D.A.G.
Via A. Pisano 120
56127 Pisa, Italy
050-535-780 FAX 050-533-290

Bill Christensen
UNOCAL
c/o PGI, Room M-20A, P.O. Box 7600
Los Angeles, CA 90051
632/817-8876 FAX 632/817-8622

Jim Combs
Geo Hills Associates
27790 Edgerton Road
Los Altos Hills, CA 94022-3212
415/941-5480 FAX 415/941-5480

Jean Cook
Stanford Geothermal Program
Dept. of Pet. Eng., Stanford University
Stanford, CA 94305
415/723-4745 FAX 415/725-2099

John F. Copp
California Energy Company
900 N. Heritage, Building D
Ridgecrest, CA 93555
619/499-2336 FAX 619/499-2308

John R. Counsil
Consultant
1148 Shadyoak Place
Santa Rosa, CA 95404
707/538-2288

Franco D'Amore
Int. Inst. Geothermal Res.-CNR
Piza Solferino 2
56126 Pisa, Italy
39-50-46069 FAX 39-50-47055

William L. D'Olier
Geothermal Energy Consultant
310 Hume Lane
Bakersfield, CA 93309-2427
805/832-5786 FAX 805/837-1478

Charles Darby
Conservation Development Services Ltd.
79 Olsen Ave.
Auckland 4, New Zealand
64-9-6243140 FAX 64-9-6243140

Nobuhiro Demboya
New Energy & Industrial Tech. Dev. Org.
29th Floor, Sunshine 60, 1-1, 3-chome
Higashi-Ikebukuro, Toshima-ku
Tokyo 170, Japan
03-3987-9451 FAX 03-3986-8197

David V. Duchane
Los Alamos National Laboratory
MS-D443
Los Alamos, NM 87545
505/667-9893FAX 505/667-8487

Robert DuTeau
Los Alamos National Laboratory
Group EES-4, MS-D443
Los Alamos, NM 87545
505/667-1914FAX 505/667-8487

Herman Dykstra
Consultant
4180 Treat Boulevard, Suite 1
Concord, CA 94518
510/676-7464

Kathleen L. Enedy
PG& E
111 Stony Circle
Santa Rosa, CA 95401
707/577-7066FAX 707/577-7067

Steve Enedy
N.C.P.A.
P.O. Box 663
Middletown, CA 95461
707/987-3101FAX 707/987-2088

Iraj Ershaghi
U.S.C., Pet. Eng. Prog.
University Park, HED 316
Los Angeles, CA 90089-1211
213/740-0322FAX 218/740-0324

David Faulder
INEL
P.O. Box 1625
Idaho Falls, ID 83415-2107
208/526-0674FAX 208/526-9822

Shaun Fitzgerald
University of Cambridge
Department of Earth Sciences
Downing Street
Cambridge CB2 3EQ, England
02-23-33-3419FAX 02-23-33-3450

Robert O. Fournier
U.S. Geological Survey
345 Middlefield Road, MS-910
Menlo Park, CA 94025
415/329-5205FAX 415/329-5203

D.H. Freeston
Univ. of Auckland, Geothermal Institute
Private Bag
Auckland, New Zealand
64-9-373-7599FAX 64-9-373-7436

Ingvar B. Fridleifsson
United Nations Univeristy
Orkustofnun, Grensásvegur 9
108 Reykjavik, Iceland
354-1-69-6000FAX 354-1-68-8896

Dr. Sabodh K. Garg
S-Cubed
P.O. Box 1620
La Jolla, CA 92038-1620
619/587-8438FAX 619/755-0474

Colin Goranson
Consultant
1498 Aqua Vista Rd.
Richmond, CA 94805
510/234-0522FAX 510/234-5881

Keshav Goyal
Calpine Corporation
P.O. Box 11279
Santa Rosa, CA 95406-1279
707/527-6700FAX 707/544-2422

Mohinder S. Gulati
UNOCAL
P.O. Box 7600
Los Angeles, CA 90051
213/977-7496FAX 213/977-6333

Héctor Gutiérrez Puente
Comisión Federal de Electricidad
Alejandro Volta 655, Col. Elec.
Morelia, Mich. C.P. 58290
Mexico
91-43-15-6782FAX 91-43-14-4735

Teklu Hadgu
L.B.L., Earth Sciences Division
1 Cyclotron Rd. Bldg. 50E
Berkeley, CA 94720
510/486-6474FAX 510/486-5686

Mineyuki Hanano
JMC Geothermal Res. & Div. Co., Ltd.
72-2-Sasamori, Ukai
Takizawa-mura
Iwate 020-01, Japan
81-196-84-4114FAX 81-196-84-6231

Paul Hirtz
Thermochem
5347 Skylane Boulevard
Santa Rosa, CA
707/575-1310

John W. Hornbrook
Stanford Geothermal Program
Dept. of Pet. Eng., Stanford University
Stanford, CA 94305
415/723-4745FAX 415/725-2099

Roland N. Horne
Stanford Geothermal Program
Dept. of Pet. Eng., Stanford University
Stanford, CA 94305
415/723-4745FAX 415/725-2099

Christy Hunter
California Div. of Oil and Gas
485-B Broadway
El Centro, CA 92243
619/353-9900FAX 619/353-9594

Eduardo R. Iglesias
Inst. de Investigaciones Elec.
Apdo Postal 475
62000 Cuernavaca
Morelia, Mexico
52-73-18-3811 x7305FAX 52-73-18-2526

Steve Ingebritsen
U.S. Geological Survey
345 Middlefield Road, MS-439
Menlo Park, CA 94025
415/329-4422FAX 415/329-4463

Tsuneo Ishido
Geological Survey of Japan
1-1-3 Higashi, Tsukuba
Ibaraki 305
Japan
298-54-3736FAX 298--54-3533

Ryuichi Itoi
Kyushu University
Geothermal Research Center
6-1, Kasuga Koen
Kasuga City, Japan 816
81-92-573-9611x207FAX 81-92-501-3026

Elizabeth Johnson
California Div. of Oil and Gas
20th Floor, MS-21, 801 K Street
Sacramento, CA 95814
916/323-1786FAX 916/323-0424

Steve Jones
N.C.P.A.
P.O. Box 663
Middletown, CA 95426
707/987-3101FAX 707/987-2088

Dennis Kaspereit
California Energy Company, Inc.
900 N. Heritage Dr., Building D
Ridgecrest, CA 93555
619/499-2300FAX 619/499-2308

M. Ali Khan
State of California, Dept. of Conservation
50 "D" Street, No. 300
Santa Rosa, CA 95404
707/576-2385FAX 707/576-2611

Michael Kramer
California Energy Commission
P.O. Box 446
Clarksburg, CA 95612
916/744-1131

Paul Kruger
Civil Engineering Dept.
Stanford University
Stanford, CA 94305
415/725-2382FAX 415/725-8662

Joe La Fleur
Consultant
36700 Oak Point Road
Springfield, OR 97478
503-741-7198

Pete Ledingham
Geoscience, Ltd.
Falmouth Business Park
Bickland Water Road, Falmouth
Cornwall TR11 452 U.K.
44-326-21-1070FAX 44-326-21-1073

Marcelo J. Lippmann
L.B.L., Earth Sciences Division
1 Cyclotron Rd., Bldg. 50-E
Berkeley, CA 94720
510/486-5035FAX 510/486-5686

James Lovekin
California Energy Company
900 N. Heritage, Building D
Ridgecrest, CA 93555
619/499-2322FAX 619/499-2308

H.K. "Pete" McCluer
Consultant
P.O. Box 650
Mt. Aukum, CA 95656
209/245-4171FAX 209/245-4623

Greg McFadden
Philippine Geothermal, Inc.
c/o UNOCAL, P.O. Box 7600
Los Angeles, CA 90051
63-2-817-8876FAX 63-2-817-8622

Lynn McLarty
Meridian Corporation
4300 King Street, Suite 400
Alexandria, VA 22302
703/998-3691FAX 703/998-0887

David Meade
Naval Air Weapons Sta., Geoth. Program Office
Code 8306
China Lake, CA 93555-6001
619/939-4057FAX 619/939-2449

Ricardo Marquez Medina
C.F.E.
P.O. Box 248
Calexico, CA 92231
619/536-870FAX 619/536-269

Tony Menzies
GeothermEx, Inc.
5221 Central Avenue, Suite 201
Richmond, CA 94804
510/527-9876FAX 510/527-8164

Luis Merida
Cordon Y. Merida
6 Calle 6-38, zona 9
Edificio Plaza Tivoli, Oficina 503-4
Guatemala, Guatemala, Central America
502-2-31-7972FAX 502-2-34-0627

Donald Michels
Don Michels Associates
P.O. Box 8652
Missoula, MT 59807
406/728-2576FAX 406/721-7671

John E. Mock
U.S. Department of Energy, Geoth. Div.
1000 Independence Ave.
Washington, DC 20585
202/586-5340FAX 202/586-5124

Phil Mogen
UNOCAL
3576 Unocal Place
Santa Rosa, CA 95403-1774
707/545-7600FAX 707/545-8746

Joseph N. Moore
University of Utah Research Institute
391 Chipeta Way, Suite A
Salt Lake City, UT 84108
801/584-4428FAX 801/584-4453

Paul B. Mount II
State Lands Commission
245 W. Broadway, Suite 425
Long Beach, CA 90802
310/590-5201FAX 310/590-5295

Cuong Nghiem
105 Marina Lakes Drive
Richmond, CA 94804
510/215-7972

Dennis L. Nielson
University of Utah Research Institute
391 Chipeta Way, Suite C
Salt Lake City, UT 84108
801/584-4438 FAX 801/584-4453

Gerald Niimi
Thermasource, Inc.
P.O. Box 1236
Santa Rosa, CA 95402
707/523-2960 FAX 707/523-1029

Harry Olson
University of Hawaii, H.N.E.I.
Look Laboratory, 811 Olomehani Street
Honolulu, HI 96813
808/522-5620 FAX 808/522-5618

Will Osborn
California Energy Company
900 N. Heritage, Building D
Ridgecrest, CA 93555
619/765-2551

Carel Otte
4261 Commonwealth Avenue
La Cañada, CA 91011
818/952-0176

Lawrence A. Owusu
S-Cubed
P.O. Box 1620
La Jolla, CA 92038-1620
619/587-7207 FAX 619/755-0474

Jens K. Pedersen
UNOCAL
3576 Unocal Place
Santa Rosa, CA 95403-1774
707/545-7600 FAX 707/544-6855

Minh Pham
GeothermEx, Inc.
5221 Central Avenue, Suite 201
Richmond, CA 94804
510/527-9876 FAX 510/527-8164

John W. Pritchett
S-Cubed
P.O. Box 1620
La Jolla, CA 92038-1620
619/587-8440 FAX 619/755-9474

Karsten Pruess
L.B.L., Earth Sciences Division
1 Cyclotron Rd., Bldg. 50E
Berkeley, CA 94720
510/486-6732 FAX 510/486-5686

Marshall Reed
U.S. Department of Energy, Geoth. Div.
CE-122
Washington, DC 20585
202/586-8076 FAX 202/586-5124

Joel Renner
INEL
P.O. Box 1625
Idaho Falls, ID 83415-3526
208/526-9824 FAX 208/526-0969

Miguel D. Ribó
C.F.E.
P.O. Box 248
Calexico, CA 92231
53-68-70 FAX 53-62-69

Ken Riedel
UNOCAL Production Technology
P.O. Box 76
Brea, CA 92621
714/528-7201

Ann Robertson-Tait
GeothermEx, Inc.
5221 Central Avenue, Suite 201
Richmond, CA 94804
510/527-9876 FAX 510/527-8164

Bruce Robinson
Los Alamos National Laboratory
MS-D443
Los Alamos, NM 87545
505/667-1910 FAX 505/667-8487

Tim Rossknecht
UNOCAL, Geothermal of Indonesia, Ltd.
c/o UGI Room M-20
P.O. Box 7600
Los Angeles, CA 90051
62-21-750-1957 FAX 62-21-720-4498

Subir K. Sanyal
GeothermEx, Inc.
5221 Central Avenue, Suite 201
Richmond, CA 94530
510/527-9876 FAX 510/527-8164

Alexander Schriener, Jr.
UNOCAL
81711 Highway 111
Indio, CA 92201
619/342-4723 FAX 619/347-4224

Hiroshi Shigeno
Geological Survey of Japan
Hokkaido Branch
Nishi-2, Kita-8, Kita-ku
Sapporo 060, Japan
81-11-709-1814 FAX 81-11-709-1817

Mike Shook
INEL
P.O. Box 1625, MS 2107
Idaho Falls, ID 83404
208/526-6945 FAX 208/526-9822

J.L. Bill Smith
N.C.P.A.
P.O. Box 663
Middletown, CA 95461
707/987-3101 FAX 707/987-2088

Jeffry L. Stevens
S-Cubed
P.O. Box 1620
La Jolla, CA 92038-1620
619/587-8442 FAX 619/755-0474

Ed Stockman
CCPA No. 1/SMUD
9500 Coldwater Creek Road
Kelseyville, CA 95451
707/928-5291 FAX 707/928-5144

Calvin J. Strobel
UNOCAL Geothermal
3576 Unocal Place
Santa Rosa, CA 95403-1774

Mario César Suárez Arriaga
Comisión Fed. de Elec.
AP 31-C
Morelia, Mich.
58290 Mexico
43-156782 FAX 43-154735

Alfred H. Truesdell
Entropy, Inc.
700 Hermosa Way
Menlo Park, CA 94023
415/322-6135 FAX 415/324-4009

Marina M. Voskanian
State Lands Commission
245 W. Broadway, Suite 425
Long Beach, CA 90802
310/590-5201 FAX 310-590-5295

Mark Walters
Russian River Energy Company
1573 Manzanita Avenue
Santa Rosa, CA 95404
707/527-4134 FAX 707/545-8470

Kimio Watanabe
Tohoku University
Aramaki Aoba, Aoba-ku
Sendai 980
Japan
022-222-1800 x4184 FAX

Gary Whitnack
Naval Air Weapons Station
Geoth. Program Office, Code C8306
China Lake, CA 93555-6001
619/939-4060 FAX 619/939-2449

Colin Williams
U.S. Geological Survey
345 Middlefield Road, MS-923
Menlo Park, CA 94025
415/329-4881 FAX 415/329-4876

Ken Williamson
UNOCAL
3576 Unocal Place
Santa Rosa, CA 95405
707/545-7600 FAX 707/545-8746

W. Gabriel Worley
M.I.T., Dept. of Chemical Engineering
77 Massachusetts Avenue, 66-553
Cambridge, MA 02139-4307
617-253-6445 FAX 617-253-8013

Phillip M. Wright
Univ. of Utah Research Institute
391 Chipeta Way, Suite C
Salt Lake City, UT 84108
801/584-4439 FAX 801/584-4453

Yusaku Yano
Geological Survey of Japan, LBL
50E Earth Sciences Division
Berkeley, CA 94720
510/486-6950 FAX 510/486-5686

Kasumi Yasukawa
Lawrence Berkeley Laboratory
1 Cyclotron Road, MS-50E
Berkeley, CA 94720
510/486-4160 FAX 510/486-5686

Elliot Yearsley
California Energy Company, Inc.
900 N. Heritage Dr., Building D
Ridgecrest, CA 93555
619/499-2327 FAX 619/499-2308

Yanis C. Yortsos
University of Southern California
HED 216 USC
Los Angeles, CA 90089-1211
213/740-0317 FAX 218/740-8053

R.W. Zimmerman
Lawrence Berkeley Laboratory
1 Cyclotron Road, MS-50E
Berkeley, CA 94720
510/486-7106 FAX 510/486-5686

SUBJECT INDEX

AUTHOR INDEX